Nonlocal Transport in Magnetised and Multi-Species Plasmas

Nicholas Terence Mitchell

2026

IMPERIAL

Department of Natural Sciences

Imperial College London

Thesis submitted in part fulfilment of the requirements for the degree of

Doctor of Philosophy

and the **Diploma of Imperial College London**

© Nicholas Mitchell, 2026

Abstract

A reduced kinetic method (RKM) for describing nonlocal transport in magnetised plasmas is derived from first principles and considered in a 1D3V geometry. The key feature of this RKM in contrast to other nonlocal closures is using the linearised Fokker-Planck collision operator, which can be shown to match the full, first-principles collision operator for the tail of the particle distributions even with order unity deviation from thermodynamic equilibrium. In a nonlocal transport scenario within a broad hydrodynamic framework, it is the tails of the velocity distributions that are responsible for the relevant transport fluxes, making this description first-principle yet relatively computationally inexpensive. An inhibited peak heat flux and preheat of the conductive heat flux are observed, which are expected from physical arguments and previous kinetic studies. Nonlocal behavior of other transport fluxes, namely the Righi-Leduc, Peltier, Ettingshausen, Nernst, thermal force, friction, cross friction, viscous stress, and gyroviscous stress terms are also demonstrated. A novel nonlocal effect on current-driven transport, in particular the Ettingshausen heat flow, is found and investigated. Nonlocal transport in ionic mixtures is also described by the RKM, including ordinary, thermo-, and baro-diffusion, and ion conductive, Dufour, and pressure-driven heat flow. Novel nonlocal features associated with multiple species, as opposed to single species, are demonstrated, as well the impact of ion-electron collisions on nonlocal ion transport.

Role of the Author

This work is centred around an approach called the RKM. The derivation of the RKM, numerical implementation, and code outputs are solely the work of the author. Much of the content of this thesis is included in the papers:

- [1] N. T. Mitchell, D. A. Chapman, C. J. McDevitt, M. P. Read, and G. Kagan. *A reduced kinetic method for investigating non-local ion heat transport in ideal multi-species plasmas*, Plasma Physics and Controlled Fusion (2024), IOP Publishing.
- [2] N. T. Mitchell, D. A. Chapman, and G. Kagan. *Nonlocal current-driven heat flow in ideal plasmas.* Physical Review E (2025), American Physical Society.
- [3] N. T. Mitchell, D. A. Chapman, and G. Kagan. *A First-Principles Closure for Nonlocal Magnetized Transport*, Plasma Physics and Controlled Fusion (2026), IOP Publishing.
- [4] N. T. Mitchell, D. A. Chapman, and G. Kagan. *Impact of ion-electron collisions on nonlocal ion heat conduction, viscous stress, and diffusion.* To be submitted.

These works have been written with the supervision, input, and comments from coauthors, but written by the first author.

Copyright Statement

The copyright of this thesis rests with the author. Unless otherwise indicated, its contents are licensed under a Creative Commons Attribution-Non Commercial 4.0 International Licence (CC BY-NC). Under this licence, you may copy and redistribute the material in any medium or format. You may also create and distribute modified versions of the work. This is on the condition that: you credit the author and do not use it, or any derivative works, for a commercial purpose. When reusing or sharing this work, ensure you make the licence terms clear to others by naming the licence and linking to the licence text. Where a work has been adapted, you should indicate that the work has been changed and describe those changes. Please seek permission from the copyright holder for uses of this work that are not included in this licence or permitted under UK Copyright Law.

Declaration

I hereby declare that, unless otherwise acknowledged, all material used and information reported in this thesis is entirely original.

Nicholas Mitchell

June 26, 2026

Acknowledgments

The work behind this thesis has been a long road and I am immensely grateful to all those who have supported me along the way. Firstly, I would like to thank Dr. Grigory Kagan and Dr. David Chapman for being excellent supervisors. On top of insightful physics discussions, they have provided the healthiest balance of mentorship and research independence which has made the last four years thoroughly enjoyable and rewarding. I am also grateful to First Light Fusion (FLF) for providing my studentship, without which this work would not have been possible.

I am fortunate to have conducted my PhD in a research group full of such great people, and I would like to thank the whole of the Plasma group at Imperial for making me part of a welcoming community. To name a few, thank you to Adam, Ben, Brian, Kas, Katie, Phil, and Niki for all the laughs. You make the office something I look forward to each morning.

During my PhD, I have taken on the role of Subwarden at Xenia Hall and Wilson House which has provided me with great experience and provided a residence. Thank you to the Subwardening teams and especially Andrea and Luke for being great and supportive Wardens. I have also greatly enjoyed the teaching opportunities I have undertaken during my time at Imperial.

Outside of Imperial, thank you to Meg and Jonny for your friendship. Finally, thank you to my family: Clare, Dom, Jemma, Sam, Harry, Elly, Rosie, and Hobbes. You have all been endlessly supportive and caring and I can't express how grateful I am.

Contents

1 Introduction **11**

2 Background **16**

2.1 Inertial Confinement Fusion 16

2.1.1 ICF schemes 19

2.1.2 Transport in ICF 22

2.1.3 Modelling fusion plasmas 23

2.2 Basic Plasma Theory 25

2.2.1 Debye shielding 26

2.2.2 Plasma oscillations 27

2.2.3 Collisions 29

2.2.4 Magnetic fields 31

2.2.5 Other regimes 32

2.3 Kinetic Theory 34

2.3.1 Origin of the Vlasov-Fokker-Planck equation 34

2.3.2 Fokker-Planck collision operator 39

2.4 Chapman-Enskog Expansion 42

2.4.1 Outline of procedure 42

2.4.2 Multi-fluid equations 44

2.4.3 Fluid equations for ionic mixtures 44

2.4.4 Fluid equations for electrons 46

2.5 Electron Transport 46

2.5.1 Physical description 46

2.5.2 Local problem 49

2.5.3 Transport calculation for a Lorentz plasma 50

2.5.4 Local closures 52

2.5.5 Single species ion transport 53

2.5.6 Heat exchange . . . 55
2.6 Ionic Mixture Transport . . . 55
2.7 Magnetohydrodynamics (MHD) . . . 58
2.7.1 Ideal MHD . . . 60
2.7.2 Resistive diffusion . . . 61
2.7.3 Biermann battery . . . 62
2.7.4 Nernst effect . . . 62
2.7.5 Hall effect . . . 63
2.7.6 MHD effects in ICF . . . 63
2.8 Nonlocal Transport . . . 63
2.8.1 Previous studies and closures . . . 66

3 Reduced Kinetic Method Framework 70
3.1 Reducing Kinetic Equations . . . 70
3.1.1 Electron RKM . . . 70
3.1.2 Multi-species RKM . . . 74
3.2 Local Limit . . . 76
3.3 Expansion in Spherical Harmonics . . . 77
3.3.1 Projection of terms . . . 78
3.3.2 Recovering hydrodynamic and transport quantities . . . 80
3.4 Numerical Implementation . . . 83
3.4.1 Nondimensionalisation . . . 83
3.4.2 Discretising and finite-differencing . . . 83
3.4.3 Field-particle term . . . 86
3.4.4 Boundary conditions . . . 86
3.4.5 Enforcing solvability conditions . . . 87
3.5 Spherical and Cylindrical Geometries . . . 89
3.5.1 Spherical spatial coordinates . . . 90
3.5.2 Cylindrical spatial coordinates . . . 91

4 Unmagnetised Single Species Results 93
4.1 Nonlocal Transport Fluxes . . . 93
4.2 Nonlocal Distribution Function . . . 95
4.2.1 Angle-averaged distribution function . . . 95
4.2.2 First angular moment of distribution function . . . 96
4.2.3 First angular moment across space . . . 97
4.2.4 Heat flux integrand . . . 98

4.2.5 Validity of linearising collision operator . . . 99
4.3 Convergence Studies . . . 101
4.4 Isobaric versus Isochoric . . . 103
4.5 Operator Comparison . . . 104
4.6 SNB Comparison . . . 106
4.7 Solving for Nonlocal Deviation . . . 107
4.8 Cylindrical and Spherical Geometries . . . 108

5 Nonlocal Electron Transport Results **110**
5.1 Thermally-Driven Terms . . . 110
5.2 Current-Driven Terms . . . 113
5.3 Impact of Fast Flows on Current-Driven Transport . . . 113
5.4 Strongly Magnetised Nonlocal Transport . . . 118
5.5 Nonlocal Distribution Function . . . 120
5.6 Heat Flux Integrands . . . 121
5.7 Collision Operator Verification . . . 123

6 Nonlocal Ion Transport Results **124**
6.1 RKM for Single Species Ions . . . 124
6.2 Magnetised Viscous Stress . . . 125
6.3 Impact of Ion-Electron Collisions on Ion Transport . . . 126
6.4 Impact of Sonic Flows on Nonlocal Ion Heat Flow . . . 132
6.5 Multi-Species Heat Flow . . . 135
6.6 Nonlocal Diffusion . . . 136
6.7 Multi-Species Transport with Ion-Electron Collisions . . . 141

7 Discussion **144**
7.1 Summary of Results . . . 144
7.1.1 Reduced kinetic method . . . 144
7.1.2 Nonlocal electron transport . . . 144
7.1.3 Nonlocal ion transport . . . 146
7.2 Future Implications . . . 147
7.3 Final Remarks . . . 149

A Fluid Equations for Ionic Mixtures **150**
A.1 Definitions of Hydrodynamic Quantities . . . 150
A.2 Mass Continuity Equations . . . 151
A.3 Momentum Equation . . . 151

A.4 Pressure Equation . . . 152

B Fokker-Planck Collision Operator **155**

B.1 Derivation of Fokker-Planck Collision Operator . . . 155

B.1.1 Collision dynamics . . . 156

B.1.2 Collision statistics . . . 157

B.1.3 Landau form . . . 158

B.1.4 Rosenbluth form . . . 159

B.2 Properties of the Fokker-Planck Collision Operator . . . 160

B.2.1 Particle number conservation . . . 160

B.2.2 Momentum conservation . . . 160

B.2.3 Energy conservation . . . 161

B.2.4 Maxwellians are equilibrium distributions . . . 162

B.2.5 H-theorem . . . 162

B.3 Linearised Landau Collision Operator . . . 164

B.3.1 Test-particle collision operator . . . 164

B.3.2 Field-particle collision operator . . . 168

B.3.3 Electron-ion collision operator . . . 168

B.3.4 Ion-electron collision operator . . . 170

B.3.5 Electron-ion Maxwellian exchange terms . . . 171

B.3.6 Expansion in spherical harmonics . . . 171

C Local Transport Derivation **175**

C.1 Local Electron Transport . . . 175

C.2 Local Ionic Transport in Mixture Formalism . . . 184

Table of Mathematical Symbols **189**

List of Acronyms **193**

List of Figures **194**

List of Tables **202**

Bibliography **203**

“Everything should be made as simple as possible, but not simpler!”

- Attributed to (but likely paraphrased from) Albert Einstein

CHAPTER 1

Introduction

Nuclear fusion is often regarded as the ultimate source of practically unlimited sustainable energy. Achieving fusion requires confining a gas of light isotopes, typically deuterium and tritium, at extremely high temperatures where the gas is ionised, i.e. a plasma. Plasma theory and modelling are therefore of the utmost importance to achieving fusion energy. Collisional transport processes play a key role in the dynamics of plasmas and therefore help determine the viability and performance of various approaches to fusion energy. Such transport phenomena include heat conduction, which is a key mechanism by which fusion plasmas transport thermal energy and cool. Although there are other transport mechanisms such as radiation and turbulence in plasmas, 'transport' in this work broadly refers to non-turbulent collisional transport processes.

Plasmas are often modelled with a fluid description which solves for hydrodynamic state variables, namely density, flow velocity, and temperature. The governing fluid equations contain transport terms such as the heat flux $\boldsymbol{q}$ that require a closure in terms of hydrodynamic quantities. If the plasma is sufficiently collisional, the Chapman-Enskog expansion of the Vlasov-Fokker-Planck (VFP) equation (or, more generally for dilute gases, the Boltzmann equation) is valid, providing analytic transport closures such as Fourier's law $\boldsymbol{q} = -\kappa \boldsymbol{\nabla} T$ which describes heat conduction in a simple gas with thermal conductivity κ. These transport closures are called 'local' since the transport fluxes at a spatial position $\boldsymbol{x}$ (e.g. $\boldsymbol{q}(\boldsymbol{x})$) can be expressed in terms of the hydrodynamic quantities and their gradients at that spatial position ($n(\boldsymbol{x})$, $T(\boldsymbol{x})$, $\boldsymbol{\nabla} T(\boldsymbol{x})$, etc.). Here, 'sufficiently' collisional requires that the mean free paths (MFPs) λ of particles relevant to heat and momentum transport are shorter than typical length scales L over which fluid quantities such as density and temperature vary, i.e. $\lambda / L \ll 1$. In addition, the collision time is required to be shorter than characteristic hydrodynamic timescales.

If the plasma is not sufficiently collisional, analytic local transport results become invalid. Since the MFP of a single particle in an ideal plasma scales strongly with particle speed as $\lambda \propto v^4$, suprathermal particles in the tail of the velocity distribution that contribute significantly to heat and momentum transport are far less

collisional than the bulk. These tail particles may therefore stream across temperature gradients before they collide, depositing their energy and momentum far away from their origin. The resulting transport fluxes at a spatial position then depend on the profiles of hydrodynamic quantities away from that position, and are therefore 'nonlocal'.

Transport fluxes are often sourced from higher velocity particles than those responsible for determining the hydrodynamic state variables. Because of this, there is a semi-collisional regime where the thermal MFP λ_{th} relevant to state variables is still shorter than gradient length scales $\lambda_{\text{th}}/L \sim 1/100 - 1/10$ while the suprathermal MFPs relevant to transport $\lambda_{\text{transport}} \sim 10 - 100\,\lambda_{\text{th}}$ are longer than those length scales $\lambda_{\text{transport}}/L \gtrsim 1$. In this semi-collisional regime, the bulk of the distribution is kept near-Maxwellian by collisions and the fluid description is still valid, yet transport fluxes can be nonlocal since they are carried largely by less-collisional suprathermal particles.

Nonlocal transport can significantly influence the conductive heat flux, suppressing the peak heat flow and preheating colder regions, both of which directly impact hydrodynamic evolution and therefore fusion yield. Nonlocal effects are particularly prevalent in regions with low density, high temperature, and sharp gradients, all of which are often encountered in confined fusion plasmas. Understanding and appropriately modelling nonlocal heat transport is therefore an important consideration for hydrodynamic simulations to accurately model, design, and optimise confined fusion schemes.

Kinetic effects such as nonlocal heat flow are not accounted for in a standard fluid framework. Full kinetic approaches such as VFP and particle-in-cell (PIC) simulations naturally include these kinetic effects. However, full kinetic codes are often computationally intractable for large-scale integrated simulations of fusion-relevant scenarios such as inertial confinement fusion (ICF) implosions, leaving fluid simulations as the preferred approach. An intermediate approach is a fluid simulation with a nonlocal transport closure which provides transport fluxes to the fluid model for a given set of hydrodynamic profiles. Since transport quantities such as the heat flux are typically more sensitive to streaming suprathermal particles than hydrodynamic quantities such as temperature, the fluid description of hydrodynamic quantities can remain valid while transport fluxes become nonlocal. This hybrid approach then includes nonlocal transport effects while maintaining computational tractability. Developing an accurate nonlocal closure requires a thorough investigation of transport in nonlocal scenarios.

Previous literature is rich in nonlocal transport studies and closures that focus almost entirely on the electron conductive heat flux [5–13], neglecting the suite of other transport fluxes which may be influenced by nonlocal behaviour. These closures almost always rely on simplified model collision operators and diffusive approximations and therefore do not naturally reproduce local transport results in the short MFP limit and likely miss some aspects of nonlocal physics and behaviour. These approaches also overlook current-driven transport, which appears naturally in local analytic closures. Currents generate magnetic fields and therefore a closure including current-driven transport must include magnetic field effects. To the author's knowledge, there is little previous literature that addresses nonlocal ion transport, with only one closure for nonlocal ion

viscous stress [14] and no known previous discussion or closure for nonlocal multi-species transport.

This work develops a first-principles reduced kinetic method (RKM) that acts as a nonlocal transport closure, and then applies it to investigate novel nonlocal transport phenomena. Chapter 2 covers relevant background on inertial confinement fusion and plasma theory with a focus on the VFP equation and transport closures. The remaining chapters present and discuss novel results, many of which have already been presented in first-author papers published in or submitted to peer-reviewed journals [1–4]. Chapter 3 derives the RKM framework from the VFP equation for electrons and ionic mixtures, and describes its numerical implementation. Chapter 4 presents the RKM in the simplest case of unmagnetised electrons subject to a temperature gradient. Chapters 5 and 6 then apply the RKM to investigate novel features of nonlocal electron transport and ion transport, respectively. These chapters are summarised as follows:

Chapter 2: Background

The background relevant to the thesis is presented, starting with a basic introduction to ICF. Basic plasma theory concepts such as Debye shielding, plasma oscillations, and collisions are discussed, with relevant results derived. An overview of the VFP framework governing weakly coupled plasmas is given, leading to fluid equations describing plasmas with multiple ion species. Both the multi-fluid and mixture formalisms are initially presented, but the mixture formalism is adopted for the remainder of this work. A qualitative introduction to local transport mechanisms in magnetised and multi-species plasmas is presented, along with a summary of the local analytic results for these transport quantities in the collisional limit. Nonlocal transport is described physically, and a brief overview of previous literature is given. Relevant but involved mathematical derivations for the chapter are presented in the appendices, namely deriving fluid equations from the VFP equation, deriving and linearising the Landau collision operator, and deriving local electron transport fluxes and transport coefficients.

Chapter 3: Reduced Kinetic Method Framework

Starting from the electron VFP equation, the governing equations of the RKM are derived. The derivation is mathematically involved, but follows a few conceptually straightforward steps: the VFP equation is written in the centre-of-momentum (CoM) frame, then the distribution function (DF) is decomposed into a Maxwellian part plus a deviation, and finally the deviation is expanded over spherical harmonics in velocity-angle space. The key assumption of the RKM in this derivation is neglecting the nonlinear component of the collision operator, which is justified *a posteriori* in Chapter 4. The derivation is repeated for ionic mixtures, which requires the same procedure applied to a set of coupled VFP equations for each ion species. The numerical implementation of the RKM is described. Explicit expressions appearing in the spherical harmonic projection of the transport fluxes and Vlasov operator are presented. The form of the Vlasov operator in 1D spherical and cylindrical coordinates is derived and presented.

Chapter 4: Unmagnetised Single Species Results

The RKM is initially demonstrated for unmagnetised electrons subject to a temperature gradient. This allows both the underlying physics behind nonlocal transport and the RKM itself to be demonstrated in a simple case. Both nonlocal transport fluxes and distribution functions are shown to demonstrate the underlying kinetic physics. The assumption of neglecting the nonlinear component of the collision operator is justified *a posteriori* in nonlocal cases by showing that the Rosenbluth potentials do not deviate far from their Maxwellian results. Convergence studies for the RKM are presented over the number of spherical harmonics in the DF expansion, the number of iterations for self-consistent momentum exchange, the upper bound of the velocity domain, and the velocity grid resolution. A more computationally efficient formulation of the RKM is derived and demonstrated, solving only for the nonlocal deviation of the DF instead of the whole deviation from Maxwellian. Nonlocal heat flow in spherical and cylindrical geometries is also shown.

Chapter 5: Nonlocal Electron Transport Results

A uniform magnetic field is applied to the temperature-gradient case of Chapter 4, and the resulting physics of nonlocal magnetised transport is discussed. Nonlocal current-driven transport is also investigated. An especially novel aspect of nonlocal current-driven transport is presented, where a new dimensionless number describing the strength of the relative flow N_u is shown to give rise to new nonlocal behaviour in addition to the conventional Knudsen number N_K.

Chapter 6: Nonlocal Ion Transport Results

Results from the multi-species extension of the RKM with two ion species are presented. Nonlocality is demonstrated not only due to temperature gradients but also due to pressure and concentration gradients. Both near-symmetric (DT) and asymmetric (CH) mixtures are considered. Novel single-ion-species effects are also shown, namely nonlocal heat flow accounting for ion-electron collisions and nonlocal viscous stress. The impact of sonic flows on nonlocal ion heat flow is also shown.

Chapter 7: Discussion

The results of the thesis and their relevance to confined fusion plasmas are discussed.

Appendix A: Fluid Equations for Ionic Mixtures

By taking velocity moments of the VFP equation, fluid equations for an ionic mixture are obtained. Here, the mixture formalism is presented, where the fluid variables include the common ion temperature and CoM velocity rather than individual temperatures and flow velocities.

Appendix B: Fokker-Planck Collision Operator

The Fokker-Planck collision operator for a weakly coupled plasma is derived. Key properties (conservation of

particle number, momentum, and energy, and the H-theorem) are proved, and the explicit form of the linearised Fokker-Planck operator is derived for a multi-species plasma. The projection of the linearised Fokker-Planck operator onto the spherical harmonic basis used in this work is presented.

Appendix C: Local Transport Derivation

Local analytic closures are explicitly derived for magnetised electron transport and multi-species ion transport. For electron transport, the derivation follows the style of Braginskii [15] with calculations presented explicitly, including a short Python routine that computes the required matrix elements for the collision operator and transport coefficients. For multi-species ion transport, the derivation follows the style of Ferziger and Kaper [16], with the form of the local closures presented but expressions for the transport coefficients not explicitly derived. Their explicit solution is provided in other literature [17–22].

CHAPTER 2

Background

2.1 Inertial Confinement Fusion

Nuclear fusion is a process where two light nuclei are fused together to form a heavier, more stable nucleus, excess particles such as neutrons and protons, and energy. For example, a Deuterium nucleus and Tritium nucleus may fuse (D+T $\rightarrow$ n + ^{4}He), releasing a total of 17.6 MeV [23]. Fusing a single gram of DT fuel would therefore release only neutrons, helium, and more than 300 GJ of energy, roughly the same energy released from 50 barrels of crude oil. Since fusion releases such large amounts of energy without the use or production of heavy radioactive isotopes, it is a prime candidate for clean energy production.

The difficulty with fusion is that there is a very high energy barrier to fuse two nuclei together due to their Coulomb repulsion. The two nuclei must be brought together to within a distance $d \sim 1$ fm for the strong nuclear force to overcome the Coulomb barrier. If the electrostatic potential energy $U \sim Z_1 Z_2 e^2 / 4\pi\varepsilon_0 d$ is considered classically, the nuclei must collide with $E_{\text{barrier}} \sim$ MeV energies. Fortunately, quantum tunneling allows for incident energies under this threshold to still overcome the Coulomb barrier and fuse with some probability. For a gas of light nuclei with temperatures lower than this classical requirement $k_{\text{B}}T \ll E_{\text{barrier}}$, which is still much less than the classical barrier, suprathermal particles have a slight chance of fusing which results in a non-negligible fusion rate. For temperatures $k_{\text{B}}T \sim 1$ keV, this fusion rate can be significant enough to overcome various cooling mechanisms and heat the gas further. These required temperatures are much greater than the ionisation energy of these light atoms $\sim 13.6\ Z^2$ eV, therefore a gas heated to thermonuclear fusion conditions will almost always be ionised, or a *plasma*.

For a high fusion yield of a confined plasma, the plasma should be dense, hot, and confined for a long period of time. The product of the number density, temperature, and confinement time $n_i T_i \tau_{\text{conf.}}$ then serves as a rough quantity that should be maximised for a fusion plasma [24]. There are two main approaches to confined fusion which aim to maximise this product. The first is ICF, which compresses a plasma, typically

using high intensity lasers, to high density and temperature, which will then burn for a short period of time before rapidly expanding and cooling. The second is magnetic confinement fusion (MCF), which confines a relatively low density plasma at high temperature for a long period of time. The motivation of this work is primarily ICF, although methods and results may be readily applicable to an MCF context.

Thermonuclear burn occurs naturally in stars, where large densities and temperatures are confined by the extreme weight of the star itself, and in thermonuclear weapons, where an exploding fission bomb generates a burst of high intensity radiation that implodes a nearby mass of fusion fuel. To achieve confined fusion on Earth for energy production, neither of these approaches is feasible since the former relies on extreme gravitational fields and the latter is extremely destructive and restricted by international treaties. With the advent of laser technology in the 1960s [25], it was realised [26, 27] that high intensity lasers could be used as alternative drivers for compressing fuel to achieve fusion-relevant conditions for energy production with implosions on much smaller scales.

Basic principles

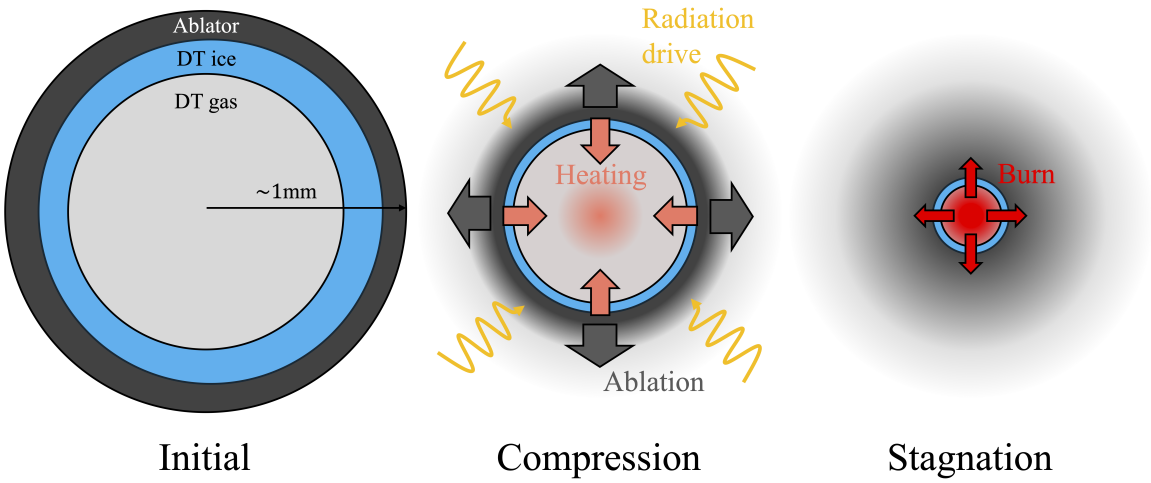


Figure 2.1: Depiction of a basic ICF capsule implosion (not to scale).

Figure 2.1 depicts the basic steps behind an ICF implosion of a spherical capsule [28–30]. The capsule typically consists of a large spherical volume of DT gas contained within a thin DT ice layer and high-density ablator. The ablator is usually made of high-density carbon (HDC, i.e. diamond), plastic (CH), or beryllium.

The outer layer is then ablated by an external radiation drive. The ablating material generates a rocket effect that compresses the DT fuel inside to higher densities. Compressive heating and heat conduction from the hotter outer layers heat the core during the implosion. As the density and temperature of the DT core increases, the resulting thermal pressure pushes back on the imploding fuel and ablator, decelerating the implosion until stagnation. Near stagnation, the fuel at the centre reaches extremely high densities ($n \sim 10^{30}\,\mathrm{m}^{-3}$) and temperatures ($T \gtrsim 1\,\mathrm{keV}$) at which a significant fusion rate can be achieved. Fusion reactions release various energetic products such as gamma radiation, neutrons, and light nuclei such as ^{4}He, i.e. alpha particles. These

light nuclei quickly collide with the dense fuel and heat it further. If this heating from fusion reactions exceeds energy losses of the hotspot such as radiative and conductive losses, the reaction is self-sustaining and achieves thermonuclear burn. In this common approach known as hotspot ignition, this burning can then spread out to the outer gas and ice layers, fusing most of the fuel and releasing a large amount of energy from fusion reactions. Alternatively, the whole fuel may be uniformly compressed and heated to fusion conditions, known as volume ignition. The fusion energy released from these implosions could then be captured by a surrounding blanket of material and harnessed for energy production.

Physics challenges

There are a number of physics challenges that stand in the way of reliable ICF for energy production. One of the major challenges of ICF is hydrodynamic instabilities [31]. Hydrodynamic instabilities refer to a set of mechanisms which cause perturbations in fluids to grow. These drive the implosion away from the ideal uniform picture outlined above, resulting in asymmetries and mix which are detrimental to fusion yield.

The Rayleigh-Taylor instability (RTI) arises at the boundary between two fluids where the heavier fluid pushes against the lighter fluid. If the boundary has perturbations, they grow due to the RTI, with shorter wavelength or higher-mode perturbations growing faster. In ICF, the ablator layer pushes against the less dense fuel inside, leading to RTI growth of the ablation front during the compression phase. Low-mode perturbations of these boundaries then lead to a non-spherical implosion which reduces the final compression ratio of the capsule. High-mode growth tears the outer shell which then acts as a less effective piston or ruins confinement entirely, as well as mixing high-Z impurities into the hotspot which increase radiative losses. The RTI is typically the most problematic hydrodynamic instability to ICF schemes.

Laser-plasma instabilities (LPIs) are another key physics challenge for ICF [32, 33]. LPIs are a set of unstable wave-plasma interactions that are often detrimental to the idealised ICF implosion above. There are a few LPIs of particular relevance to ICF. Stimulated Raman Scattering (SRS) and Stimulated Brillouin Scattering (SBS) describe scattering of electromagnetic waves off electron plasma waves and ion acoustic waves, respectively. Two-Plasmon Decay (TPD) describes a single photon exciting two electron plasma waves. SRS and TPD may then cause incident lasers to generate high-energy near-collisionless electrons that preheat fuel in an ICF capsule in the early stages of compression, as well as reflecting incident laser energy away from the target. Cross-Beam Energy Transfer (CBET) describes how energy is transferred from shorter to longer electromagnetic waves via an ion acoustic wave, which causes driving laser beams to transfer energy between each other, often away from the target.

ICF implosions are usually considered and modelled hydrodynamically. However, kinetic effects are known to significantly influence the macroscopic behaviour of the implosion and often have a deleterious impact on yield [34–36]. Relevant kinetic effects include reactivity reduction due to Knudsen layer effects [37–40], species separation and interpenetration [41–43], kinetic shock structure [44–50], and the focus of this thesis, nonlocal heat transport [51–53].

2.1.1 ICF schemes

Direct drive

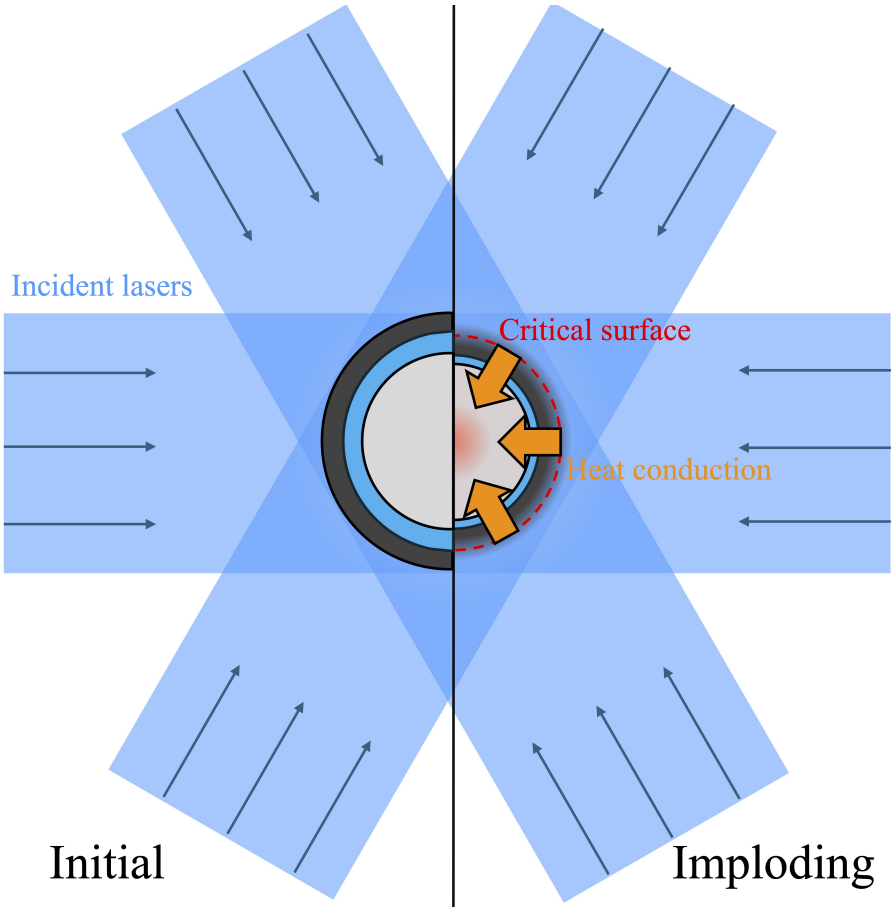


Figure 2.2: Depiction of a direct drive implosion.

Perhaps the most obvious ICF scheme is direct drive [54], where lasers are directly incident on a spherical capsule to drive an implosion as depicted in Figure 2.2. A large number of laser beams, typically $\sim 10 - 200$, are arranged to provide roughly uniform illumination of the capsule. As described above, the capsule implodes subject to these lasers ablating the outer layer, which drives the outer shell inwards and compresses the fuel. Direct drive has the advantage that the laser energy is coupled efficiently to the implosion since the lasers are directly incident. The design of an Inertial Fusion for Energy production (IFE) power plant using direct drive targets is straightforward to imagine; capsules could be shot rapidly into a target chamber, imploded by a spherical array of lasers, and the resulting energetic neutrons could be captured by a blanket of material such as liquid lithium to extract heat.

Direct drive has limiting physics challenges. Since lasers of a given wavelength λ may not propagate in plasmas denser than a critical density $n_e \geq n_{\text{crit.}}(\lambda) \propto \lambda^{-2}$, most of the laser energy is deposited on the critical surface where the plasma is at this critical density. Heating the fuel inside the critical surface then relies on other mechanisms to transport heat radially inwards, predominantly heat conduction. Non-uniformity of the laser drive often seeds the RTI which is highly detrimental to compression and the resulting fusion yield.

Lasers do not provide a perfectly smooth spatial intensity profile, but contain small scale variations known as laser speckles. These speckles seed high mode perturbations which grow quickly under compression due to the RTI. In addition, as the capsule compresses and becomes smaller, the overlapping behaviour of the incident lasers changes. Even if an initial laser configuration is chosen that gives near-perfect uniform illumination of the surface, the intensity distribution on the surface changes as the capsule shrinks if the laser configuration remains fixed. Laser zooming, where the laser focus is varied during the implosion, may be employed to combat this but adds additional complications to the laser drive. LPIs such as TPD and SRS generate fast near-collisionless electrons near the quarter-critical surface which may travel radially inwards and preheat the fuel before the main compression wave reaches it. This increases the temperature and therefore pressure inside the capsule, which pushes outwards and inhibits compression. CBET causes outgoing reflected beams to absorb energy from ingoing incident beams, reducing deposited laser energy and heating of the capsule. To avoid these challenges, different ICF schemes are also studied, the arguably most prevalent being indirect drive.

Indirect drive

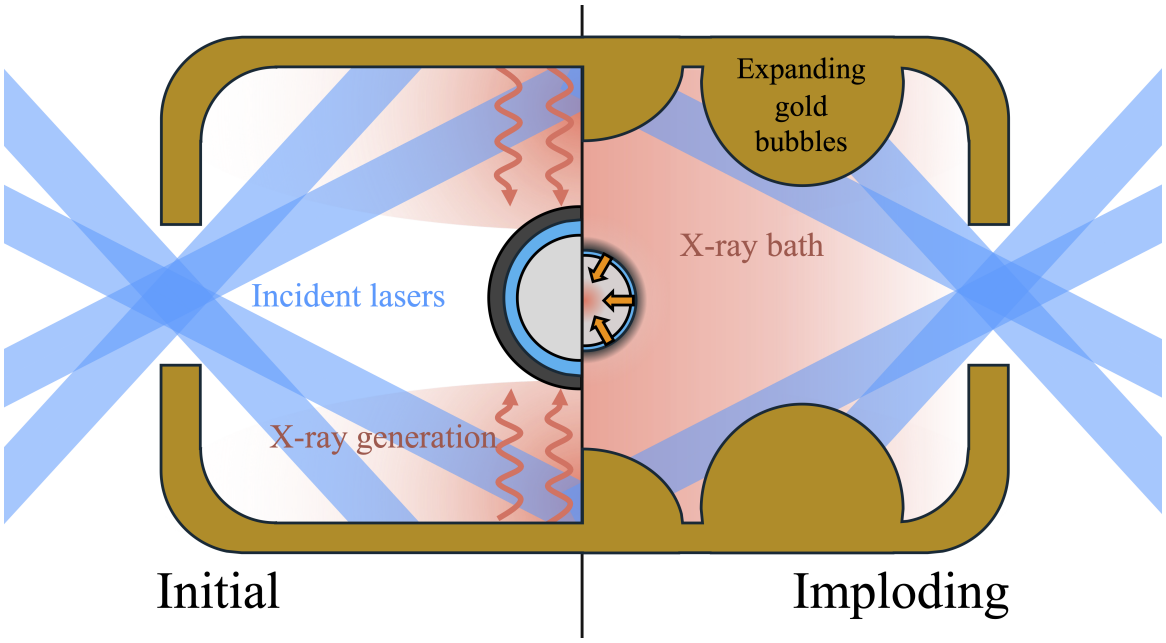


Figure 2.3: Depiction of an indirect drive implosion using a hohlraum through the xz plane, where the hohlraum is cylindrically symmetric around the horizontal z axis.

Figure 2.3 depicts a typical indirect drive scheme. The capsule is surrounded by a large cylinder of high-Z material, often gold, known as a 'hohlraum', a German loanword meaning a cavity or empty region. Rather than lasers being directly incident on the capsule, the lasers arrive through open windows at the ends of the hohlraum and heat the inner walls. The hot high-Z material generates a bath of X-rays that drives the implosion of the capsule. The benefit of the X-ray bath is that it is far more uniform than the lasers themselves, therefore does not seed strong high-mode perturbations when driving the implosion of the capsule. The

shorter wavelength of the radiation drive also means a higher critical density, so X-rays may penetrate deeper into the capsule, improving the efficiency of the ablation process relative to direct drive. These improvements come with two main drawbacks: firstly, the additional step of converting laser energy to X-rays by heating the gold walls is particularly inefficient, only transferring on the order of $\sim 10\%$ of the laser energy to the capsule. Secondly, the additional target complexity of the hohlraum makes the practicality and economics of indirect drive far less attractive for IFE than direct drive. CBET still transfers energy between incident and outgoing beams, but with careful design can be utilised to transfer energy past the expanding gold bubbles to illuminate the capsule waist, improving ablation uniformity. The complexity of indirect drive also faces new issues working against the drive such as the expanding gold blocking off lasers at late times. Regardless of these challenges, indirect drive is the only confined fusion scheme to date to achieve the Lawson criterion and then net target gain with the groundbreaking N210808 and N221205 shots on the National Ignition Facility (NIF), respectively [55–58].

Magneto-inertial schemes

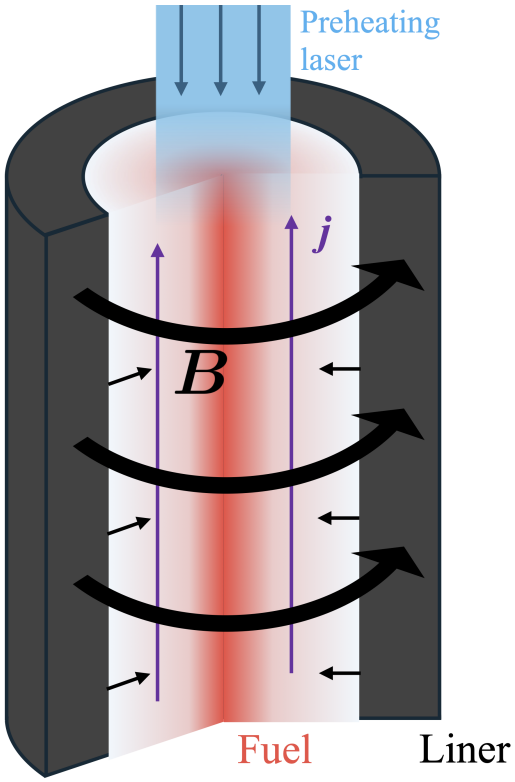


Figure 2.4: Depiction of a Magnetized liner inertial fusion (MagLIF)-like implosion.

As illustrated in Figure 2.4, an axial current may be applied through a conducting tube, generating an azimuthal magnetic field. The resulting Lorentz force, or equivalently magnetic pressure, acts radially inwards and compresses the tube. This setup is known as a Z-pinch. Early research in the 1950s attempting to achieve thermonuclear burn with Z-pinches quickly found that hydrodynamic instabilities shred the material apart before fusion-relevant densities and temperatures could be reached, and the scheme was abandoned in favour

of laser-driven ICF. However, cylindrical current-driven ICF has received new interest over the last couple of decades with the MagLIF concept [59–61] in which the fuel is preheated with lasers and an external axial magnetic field is applied to suppress conductive heat losses. MagLIF has since inspired private fusion startups to develop similar cylindrical magneto-inertial fusion schemes [62–65].

We can argue geometrically that the ratio of final to initial density is related to the ratio of final to initial radius as

$$\frac{\rho_{\text{final}}}{\rho_{\text{initial}}} = \left(\frac{R_{\text{initial}}}{R_{\text{final}}}\right)^{(D+1)}, \tag{2.1}$$

where $(D+1) = 2$ for a cylindrical geometry and $(D+1) = 3$ for a spherical geometry, assuming that the cylinder maintains its length during compression. We may expect some axial extension during radial compression of a cylindrical target, which only decreases the effective value of D. For a given density compression ratio $\rho_{\text{final}}/\rho_{\text{initial}}$, a cylindrical implosion therefore requires a significantly greater compression in radius $R_{\text{initial}}/R_{\text{final}}$. Cylindrical implosions are therefore far more susceptible to hydrodynamic instabilities such as RTI that mix layers and shred the target apart during implosion. This is arguably the key disadvantage of cylindrical rather than spherical ICF schemes. However, magnetic fields are naturally suited to a cylindrical rather than spherical geometry. Since magnetic fields provide the advantages of compression with magnetic pressure and inhibited conductive heat losses, cylindrical schemes are a competitive approach to ICF.

2.1.2 Transport in ICF

Collisional transport of heat and momentum is an essential piece of physics for understanding and modelling of the collective behaviour of plasmas, and therefore of great practical significance for confined fusion schemes. As well as being generally important to the overall hydrodynamic evolution of the plasma, there are specific effects in ICF where transport plays a significant role [28].

As previously discussed, the incident lasers or radiation cannot transport energy beyond the critical surface of the capsule. Thermal conduction is therefore left as the dominant mechanism that transports heat further inwards beyond the critical surface to the ablation front. Once the capsule temperature increases as a result of compressional heating and heating from fusion reactions, heat conduction then cools the capsule. Heat transport is therefore a key mechanism in both initiating burn and loss of confinement, both of which directly impact the fusion yield.

Collisional transport is also responsible for viscous effects in a plasma. Viscous effects exert stresses, i.e. transport momentum, due to gradients in flow. Physical viscosity is often not included in fluid simulations and models of ICF implosions, although viscosity can indeed play a notable role in implosion dynamics [66]. Viscous effects also heat the fluid due to gradients in flow. Fluid simulations often require artificially imposed viscosity to smear out sharp discontinuities that would otherwise lead to undesired and unphysical numerical artefacts and instabilities.

Collisional shocks are present in most ICF implosions since the rapid compression of the outer layers

of the target often generates shocks. Shocks are often thought of as perfect discontinuities in fluid profiles. Such discontinuities are permitted as solutions to the ideal fluid (or Euler) equations, however transport fluxes introduce diffusive terms that smear out the shock to have continuous fluid profiles. The transport fluxes dictate the structure of the shock front, which in turn have an impact on fluid and implosion dynamics [47, 67].

Magnetic fields are often applied externally to ICF implosions to suppress thermal transport or compress a liner with magnetic pressure. Even initially unmagnetised implosions can self-generate magnetic fields due to the Biermann battery effect [68]. Near peak compression in spherical or cylindrical implosions, the magnetic pressure is usually dominated by thermal pressure, i.e. the plasma beta is large $\beta_{\text{th}} \equiv \frac{p}{B^2/\mu_0} \gg 1$, so the magnetic field does not typically directly affect hydrodynamic behaviour. Although not strong enough to contribute significantly to plasma pressure, the magnetic field can still be strong enough to magnetise transport, with Hall parameters of $\chi_e \sim 1 - 100$ being achieved in magnetised fusion schemes such as MagLIF. The magnetic field suppresses transport perpendicular to the field, which can dramatically reduce conductive heat losses during the implosion. Other transport quantities such as electron-ion dynamic friction and thermal forces directly impact magnetic field transport. For example, the cross thermal force term gives rise to the Nernst effect which advects the magnetic field down temperature gradients, reducing magnetisation of the hotspot at peak compression and increasing conductive heat losses. These transport terms that influence magnetic field transport are therefore also of key significance in ICF implosions.

2.1.3 Modelling fusion plasmas

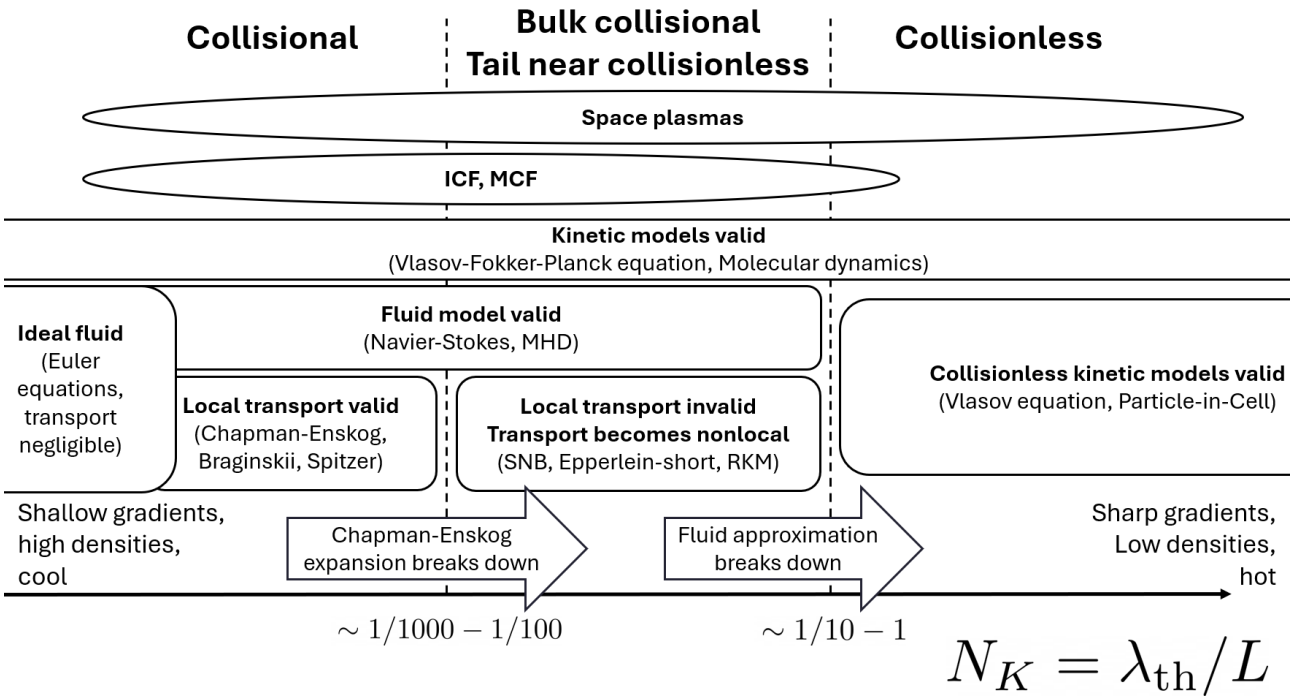


Figure 2.5: Validity of models across different regimes of collisionality parametrised by the Knudsen number N_K.

To design and optimise a confined fusion scheme, physics models and simulations that accurately describe

the physical behaviour of a plasma must be developed. Various descriptions are valid over different regimes of collisionality, as illustrated by Figure 2.5. The Knudsen number $N_K = \lambda_{\text{th}}/L$, the ratio of a characteristic thermal MFP λ_{th} to a characteristic gradient lengthscale $L \sim |\boldsymbol{\nabla} \ln T|^{-1}$, is the relevant parameter for describing collisionality, with large and small N_K corresponding to collisionless and collisional plasmas, respectively.

The conceptually simplest approach to modelling a plasma would be to simulate the motion of each ion and electron under Newton's laws of motion. This approach is typically known as molecular dynamics (MD). For a classical plasma, this approach is first-principles and captures the essential physics; however, the sheer number of particles required for a complex system such as an ICF implosion typically leaves this approach computationally intractable. MD is almost always limited to microscopic studies of thermodynamic properties rather than macroscopic behaviour.

A more computationally tractable approach, similar to MD, is a PIC approach. This method evolves 'macroparticles', each of which model the behaviour of many particles. Electromagnetic fields are determined on a grid from the charge and current distributions of these macroparticles, from which the macroparticles then evolve in time, although gridless macroparticle approaches also exist [69]. PIC codes are especially applicable to collisionless plasmas, with extensions to account for collisions requiring additional corrections [70, 71]. With collisional corrections included, PIC approaches can be applied to study collisional plasmas relevant to ICF. By their nature, PIC simulations are subject to statistical noise due to the limited number of macroparticles which diminishes their utility for studying collisional phenomena.

Instead of describing the motion of each particle in a particular realisation of the system, the plasma may be described by a macroscopic continuous distribution of particles. This distribution function describes the distribution of particles in phase space (i.e. position and velocities), and its evolution may be described by a six-dimensional (three position coordinates and three velocity coordinates) partial differential equation (PDE) known as Boltzmann's equation, or for weakly coupled plasmas, the VFP equation. This kinetic description provides a mathematically rigorous macroscopic description of plasmas and many-particle systems in general across all regimes of collisionality.

Although a kinetic description is first-principles, its high dimensionality and complicated mathematical formulation leaves it often intractable for analytic work and large scale simulations. A fluid description is far more tractable and can be derived phenomenologically or directly from kinetic theory in the highly collisional limit. Fluid equations are a set of PDEs in position space describing the evolution of the fluid density, momentum density (or flow velocity), and energy density (or internal energy density or temperature). Mathematically, these three quantities may be viewed as the first three velocity moments of the DF which parameterise the leading order Maxwellian behaviour. Evolving the fluid equations for these three moments then describes the DF to leading order.

The finite collisionality of the plasma leaves microscopic particle behaviour able to transport heat and momentum across space and between species. A classic example of such transport is heat conduction, where

heat diffuses down temperature gradients. The mathematical description of heat conduction takes the form of Fourier's law, where the heat flux entering the temperature equation as $dT/dt \propto -\boldsymbol{\nabla} \cdot \boldsymbol{q}$ has the closure $\boldsymbol{q} = -\kappa \boldsymbol{\nabla} T$. The Chapman-Enskog expansion [16, 72] is a formal mathematical procedure that derives local closures for transport fluxes and provides explicit expressions for their transport coefficients such as the heat conductivity κ. Like the fluid description itself, these transport closures become invalid when the plasma is not sufficiently collisional. However, since transport quantities such as the heat flux usually depend on higher velocity moments than the bulk fluid quantities such as temperature, these local transport closures break down at higher collisionalities ($N_K \sim 1/100$) than the fluid description ($N_K \sim 1$). There is therefore an intermediate regime between highly collisional and collisionless plasmas where the plasma can be described as a fluid with a 'nonlocal' transport closure. To understand how a plasma is modelled, an understanding of basic plasma theory is necessary.

2.2 Basic Plasma Theory

A plasma is a collection of a large number of charged particles, or ionised gas, that exhibits collective behaviour. Plasmas typically consist of a mixture of negatively charged electrons and one or more ion species. Plasmas may still contain neutral particles, but these are ignored for the purposes of this work where we assume the plasma is sufficiently hot and collisional that all neutral atoms are quickly ionised. Since many of these particles will be identical to each other, they are often grouped together according to their species (electrons, deuterons, tritons, etc.). A species with label α is characterised by a particle charge q_α and mass m_α.

One of the main features of a plasma in contrast with a neutral gas is long-range interactions between particles via electric and magnetic fields. For plasmas described in this work, we assume that the thermal energy dominates the pairwise Coulomb potential energy between particles, i.e. the coupling parameter $\Gamma \equiv U/k_\mathrm{B}T \sim e^2 n^{1/3}/k_\mathrm{B}T \ll 1$, where T is the temperature. Such a plasma is known as weakly coupled, and is the type of plasma usually encountered in a confined fusion context[1].

Since plasmas typically originate from heating a neutral gas to sufficiently high temperatures to ionise all neutral atoms $k_\mathrm{B}T \gtrsim 13.6$ eV, they are usually neutral on macroscopic scales, or 'quasineutral'. Although quasineutral, the net charge of different species allows both microscopic and macroscopic electric and magnetic fields to impact the collective dynamics. This is the key feature that makes plasmas exhibit a rich variety of phenomena compared to neutral gases. Defining a macroscopic number density $n_\alpha = \frac{1}{|V|}\int_V d^3\boldsymbol{r}\; n_\alpha^{\text{micro.}}$ by coarse graining the microscopic number density over some sufficiently large volume V, the quasineutrality condition is

$$\sum_\alpha q_\alpha n_\alpha = 0. \tag{2.2}$$

[1]Moderately and strongly coupled plasmas where $\Gamma \gtrsim 1$ are still frequently encountered in ICF in cold dense regions, but nonlocal transport effects are usually only present in weakly coupled plasmas and therefore this treatment suffices for the scope of this thesis

Here, 'sufficiently large' will turn out to be on spatial scales greater than some minimum length scale known as the Debye length.

2.2.1 Debye shielding

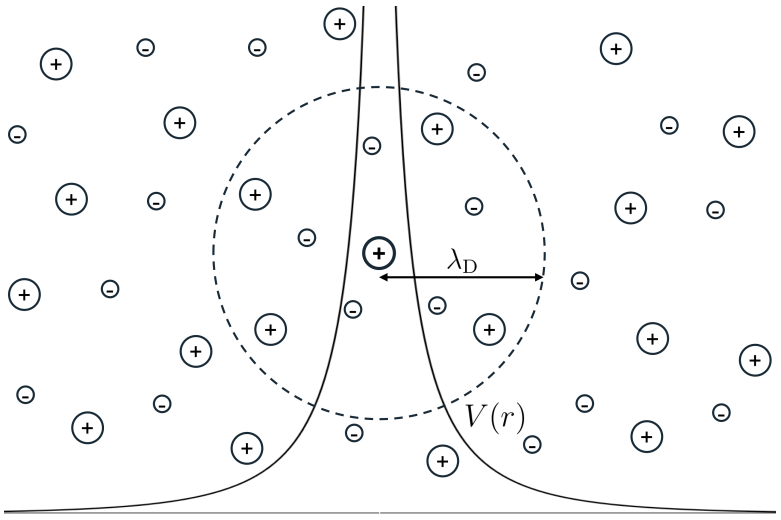


Figure 2.6: Debye shielding in a simple plasma due to a positive charge at the centre. Negative charges shift towards this central positive charge, forming a shielded potential $V(\boldsymbol{r}) \propto e^{-r/\lambda_{\mathrm{D}}}/r$. Inside the Debye sphere, charged particles experience the individual Coulomb force of the central charge. Outside the Debye sphere $r \gtrsim \lambda_{\mathrm{D}}$, the potential is exponentially small, and charged particles are shielded from the individual effect of the central charge.

Consider a plasma in thermodynamic equilibrium. As illustrated in Figure 2.6, we focus on a particular particle at the origin with charge q_α that generates an electric potential $V(\boldsymbol{r})$ to which other particles in the vicinity respond by redistributing themselves. From statistical mechanics, the equilibrium arrangement of these other particles obeys a Boltzmann distribution $n_\alpha^{\text{micro.}} \propto \exp(-q_\alpha V(\boldsymbol{r})/k_{\mathrm{B}}T_\alpha)$, with the potential determined self-consistently from Gauss' law. The potential and number density are then governed by

$$\nabla^2 V = -\frac{1}{\varepsilon_0}\left(q_\alpha \delta(\boldsymbol{r}) + \sum_\beta q_\beta n_\beta^{\text{micro.}}\right), \quad n_\beta^{\text{micro.}} = n_\beta \exp(-q_\beta V(\boldsymbol{r})/k_{\mathrm{B}}T_\beta), \tag{2.3}$$

where $\delta(\boldsymbol{r})$ is the Dirac delta distribution. Assuming weak coupling ($\Gamma \ll 1$), the exponential may be Taylor expanded as $\exp(-\frac{q_\beta V(\boldsymbol{r})}{k_{\mathrm{B}}T_\beta}) = 1 - \frac{q_\beta V(\boldsymbol{r})}{k_{\mathrm{B}}T_\beta} + \mathcal{O}(\Gamma^2)$, which may be substituted into Gauss' law to find

$$\nabla^2 V \approx -\frac{q_\alpha}{\varepsilon_0}\delta(\boldsymbol{r}) - \frac{1}{\varepsilon_0}\underbrace{\sum_\beta q_\beta n_\beta}_{\text{quasineutral, }=0} + \underbrace{\left(\sum_\beta \frac{n_\beta q_\beta^2}{\varepsilon_0 k_{\mathrm{B}} T_\beta}\right)}_{=1/\lambda_{\mathrm{D}}^2} V. \tag{2.4}$$

The last term introduces a characteristic length scale

$$\lambda_{\mathrm{D}} \equiv \left(\sum_\beta \frac{n_\beta q_\beta^2}{\varepsilon_0 k_{\mathrm{B}} T_\beta}\right)^{-1/2}, \tag{2.5}$$

known as the Debye length. The solution should then be spherically symmetric $V = V(r)$, therefore satisfying

$$\frac{1}{r^2}\frac{\partial}{\partial r}\left(r^2 \frac{\partial V}{\partial r}\right) - \frac{1}{\lambda_{\mathrm{D}}^2} V = -\frac{q_\alpha}{\varepsilon_0}\delta(\boldsymbol{r}), \quad V(r \ll \lambda_D) \approx \frac{q_\alpha}{4\pi\varepsilon_0 r}, \quad V(r \to \infty) = 0. \tag{2.6}$$

The solution for the potential is

$$V(\boldsymbol{r}) = \frac{q_\alpha}{4\pi\varepsilon_0}\frac{e^{-r/\lambda_\mathrm{D}}}{r}, \tag{2.7}$$

which highlights that the potential is screened by other charges on length scales larger than the Debye length $\sim \lambda_\mathrm{D}$, or outside the Debye sphere (defined as a sphere of radius λ_D). For this argument to be valid, there must be many particles within the Debye sphere $N_\mathrm{D} = n\lambda_\mathrm{D}^3 \gg 1$, which turns out to be equivalent to weak coupling $\Gamma \sim N_\mathrm{D}^{-2/3} \ll 1$.

Since the plasma is weakly coupled, the thermal energy is primarily tied to the kinetic energy associated with random motion within the plasma $k_\mathrm{B}T_\alpha \sim \frac{1}{2}m_\alpha v^2$. This then defines a characteristic speed for a species

$$v_{\mathrm{th},\alpha} \equiv \sqrt{\frac{2k_\mathrm{B}T_\alpha}{m_\alpha}}, \tag{2.8}$$

known as the thermal velocity. This is the characteristic speed which most particles of species α travel with if the plasma is near local thermal equilibrium (LTE), although some particles in the distribution will have speeds significantly faster than this.

2.2.2 Plasma oscillations

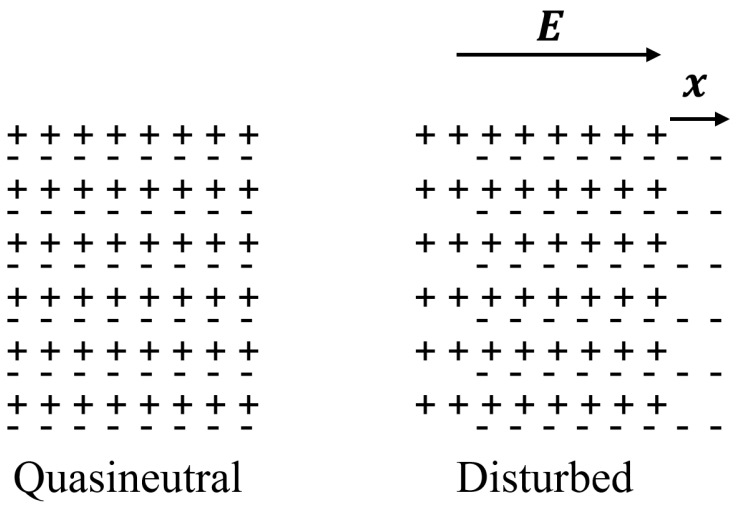


Figure 2.7: Slab of plasma disturbed from quasineutrality

Consider a slab of plasma that is initially quasineutral, but is then disturbed by shifting the electrons by a small displacement $\boldsymbol{x}$. From Gauss' law, a restoring electric field $\boldsymbol{E} = \frac{en_e}{\varepsilon_0}\boldsymbol{x}$ is generated by the charge separation. Ignoring other forces, each electron has an equation of motion $\ddot{\boldsymbol{x}} = -\frac{e}{m_e}\boldsymbol{E} = -\frac{e^2 n_e}{\varepsilon_0 m_e}\boldsymbol{x}$, and therefore oscillates with a frequency

$$\omega_{\mathrm{p},e} = \sqrt{\frac{e^2 n_e}{\varepsilon_0 m_e}}, \tag{2.9}$$

known as the plasma frequency. This is then the inverse timescale on which departures from quasineutrality are restored.

This derivation may appear inadequate since electrons do not remain in a fixed rigid structure which generates a macroscopic electric field. For an alternative derivation, consider similarly an initially quasineutral plasma with a fixed background of ions and 'cold' electrons such that their thermal motion can be neglected compared to the phase velocity of any modes. An electromagnetic wave $\boldsymbol{E}(t,\boldsymbol{x}) = \boldsymbol{E}_0 \exp(i(\boldsymbol{k}\cdot\boldsymbol{x} - \omega t))$ is applied. Each electron then has an equation of motion as before $\ddot{\boldsymbol{x}} = -\frac{e}{m_e}\boldsymbol{E}$, where $\boldsymbol{x}$ is the displacement from equilibrium. Considering modes $\boldsymbol{x} = \boldsymbol{x}_0 \exp(i(\boldsymbol{k}\cdot\boldsymbol{x} - \omega t))$, we have

$$\boldsymbol{x} = \frac{e}{m_e\omega^2}\boldsymbol{E}. \tag{2.10}$$

Each electron generates a dipole moment $\boldsymbol{p} = -e\boldsymbol{x}$, and therefore the plasma gains a polarisation density $\boldsymbol{P} = n_e\boldsymbol{p} = -\frac{n_e e^2}{m_e\omega^2}\boldsymbol{E}$ and therefore an electric displacement field

$$\boldsymbol{D} = \varepsilon_0\boldsymbol{E} + \boldsymbol{P} = \varepsilon_0\left(1 - \frac{n_e e^2}{\varepsilon_0 m_e\omega^2}\right)\boldsymbol{E} = \varepsilon(\omega)\varepsilon_0\boldsymbol{E}, \quad \text{where} \quad \varepsilon(\omega) \equiv 1 - \frac{\omega_{\mathrm{p},e}^2}{\omega^2}, \tag{2.11}$$

which defines the dielectric function $\varepsilon(\omega)$. Faraday's and Maxwell-Ampère's law in media are

$$\boldsymbol{\nabla}\times\boldsymbol{E} = -\partial_t\boldsymbol{B}, \quad \boldsymbol{\nabla}\times\boldsymbol{H} = \boldsymbol{j}_{\text{free}} + \partial_t\boldsymbol{D}. \tag{2.12}$$

Ignoring free charge and currents, taking ∂_t of Maxwell-Ampère's law, and substituting in Faraday's law yields

$$-\boldsymbol{\nabla}\times(\boldsymbol{\nabla}\times\boldsymbol{E}) = \nabla^2\boldsymbol{E} - \boldsymbol{\nabla}(\boldsymbol{\nabla}\cdot\boldsymbol{E}) = \mu_0\partial_t^2\boldsymbol{D} \quad \Rightarrow \quad (k^2\mathrm{I} - \boldsymbol{k}\boldsymbol{k})\cdot\boldsymbol{E} = -\frac{\omega^2}{c^2}\varepsilon(\omega)\boldsymbol{E}. \tag{2.13}$$

For longitudinal modes with $\boldsymbol{k} \parallel \boldsymbol{E}$, the dispersion relation for a nontrivial electric field simply becomes

$$\varepsilon(\omega) = 0 \quad \Rightarrow \quad \omega = \omega_{\mathrm{p},e}, \tag{2.14}$$

i.e. longitudinal modes, or 'Langmuir oscillations', vibrate at the plasma frequency. For transverse modes with $\boldsymbol{k} \perp \boldsymbol{E} = 0$, the dispersion relation becomes

$$(\omega^2\varepsilon(\omega) - k^2c^2)\boldsymbol{E} = 0. \tag{2.15}$$

Substituting in the form of the dielectric function above and demanding a nontrivial electric field yields the dispersion relation

$$\omega^2 = \omega_{\mathrm{p},e}^2 + k^2c^2. \tag{2.16}$$

The plasma frequency is therefore the cutoff frequency for electromagnetic waves propagating in a plasma. This is particularly relevant in ICF, since laser light of a given frequency cannot pass deeper into a capsule and deposit energy beyond the critical surface.

Since the electron population has a characteristic random speed $v_{\mathrm{th},e}$, departures from quasineutrality occur on length scales

$$v_{\mathrm{th},e}\omega_{\mathrm{p},e}^{-1} \sim \sqrt{\frac{k_\mathrm{B}T_e}{m_e}\frac{\varepsilon_0 m_e}{e^2 n_e}} \sim \sqrt{\frac{\varepsilon_0 k_\mathrm{B}T_e}{e^2 n_e}} \sim \lambda_\mathrm{D}. \tag{2.17}$$

The Debye length, as before, is then the distance over which microscopic electric fields are shielded and therefore the minimum length scale on which the plasma can be considered quasineutral.

2.2.3 Collisions

In a neutral gas, particles collide with each other on short distances comparable to their size. In a plasma, particles are charged, and therefore experience the effect of each other at much larger distances due to electromagnetic interactions. Electromagnetic interactions include those on short length scales due to the interaction of individual particles and those on large length scales due to macroscopic electric and magnetic fields. The length scale that separates these two interactions is the Debye length; individual particle effects are apparent on length scales shorter than the Debye length, but screened on larger length scales. Electromagnetic interactions between particles on sub-Debye length scales are interpreted as collisions, dependent on the plasma being made of many particles, and interactions on larger scales are deemed macroscopic interactions.

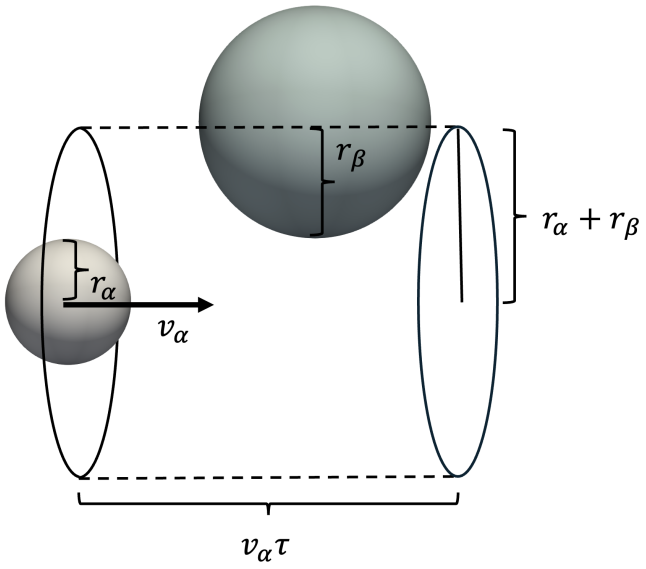


Figure 2.8: The cylinder traced out describing the collision of two hard spheres of species α (white ball) against species β (blue ball).

To understand collisions, first consider a multi-species gas made of hard spheres of radius r_α which then collide like billiard balls if their surfaces touch. We ask if a single particle of species α will collide against another particle of species β. As depicted in Figure 2.8, if the first particle moving in a straight line traces a cylinder with cross-sectional area $\sigma_{\alpha\beta} = \pi\big(r_\alpha + r_\beta\big)^2$, a collision will occur if the second particle lies in this imaginary cylinder. For the first particle streaming with a speed v_α for a duration τ, a volume $V = \sigma_{\alpha\beta} v_\alpha \tau$ is traced out. The number of particles of species β in this cylinder is then $n_\beta \sigma_{\alpha\beta} v_\alpha \tau$. The collision time is the characteristic time for a single collision, so where there is a single particle in this cylinder, i.e. where $1 \sim n_\beta \sigma_{\alpha\beta} v_\alpha \tau$. The collision frequency for collisions between α and β is then $\nu_{\alpha\beta} \sim \tau^{-1} \sim n_\beta \sigma_{\alpha\beta} v_\alpha$.

Considering a Coulomb collision between a particle of species α and another of species β, where we imagine that the species β particle is fixed in place, the distance of closest approach d may be found from energy considerations

$$\frac{1}{2} m_\alpha v_\alpha^2 \sim \frac{1}{4\pi\varepsilon_0} \frac{q_\alpha q_\beta}{d} \quad \Rightarrow \quad d \sim \frac{2 q_\alpha q_\beta}{4\pi\varepsilon_0 m_\alpha v_\alpha^2}. \tag{2.18}$$

This distance of closest approach is then the analogue of the sum of the hard sphere radii $d = r_\alpha + r_\beta$. Using the characteristic distance of closest approach, the collision frequency then becomes

$$\nu_{\alpha\beta} \sim \frac{n_\beta q_\alpha^2 q_\beta^2}{4\pi\varepsilon_0^2 m_\alpha^2 v_\alpha^3}, \tag{2.19}$$

which is a characteristic collision frequency describing collisions between species α and β at a particle speed v_α.

A more detailed analysis, presented in Appendix B, yields the same collision frequency but with an additional factor $\ln\Lambda_{\alpha\beta}$ known as the Coulomb logarithm. This factor comes from integrating over different impact parameters for small-angle Coulomb collisions rather than using only the distance of closest approach. The integral that appears is

$$\int_{b_{\min}}^{b_{\max}} \frac{db}{b} = \ln(b_{\max}/b_{\min}). \tag{2.20}$$

For the integral over the impact parameter to converge, both a minimum and maximum cutoff have been introduced for b, resulting in the Coulomb logarithm $\ln(b_{\max}/b_{\min}) = \ln\Lambda_{\alpha\beta}$. Specific forms of the Coulomb logarithm follow from physical arguments about the cutoffs. For a Debye-shielded Coulomb potential, the maximum cutoff becomes the Debye length, since particles beyond this impact parameter do not experience the collision. The lower cutoff may be chosen to be the classical distance of closest approach $d_\alpha \sim q_\alpha q_\beta/4\pi\varepsilon_0 k_\mathrm{B} T_\alpha$, since collisions with smaller impact parameters experience large-angle deflections. However, when the de Broglie wavelength exceeds the classical distance of closest approach, quantum effects become significant and instead one should take $b_{\min} = \lambda_{Q,\alpha}$, where $\lambda_{Q,\alpha} = \hbar\sqrt{2\pi/\mu_{\alpha\beta}k_\mathrm{B}T_\alpha}$ is the de Broglie wavelength of a thermal particle and $\mu_{\alpha\beta}$ is the reduced mass of the colliding particles [73]. The standard prescription for the minimum cutoff is $b_{\min} = \max(d_\alpha, \lambda_{Q,\alpha})$, although in the following only the classical cutoff is used for simplicity.

For a single species, using $b_{\max} = \lambda_\mathrm{D}$ and $b_{\min} = d$, we have

$$\Lambda = \frac{b_{\max}}{b_{\min}} \sim \frac{1}{\sqrt{n}}\left(\frac{\varepsilon_0 k_\mathrm{B} T}{q^2}\right)^{3/2} \sim N_\mathrm{D}, \tag{2.21}$$

therefore the Coulomb logarithm $\ln\Lambda$ is a measure of the magnitude of the number of particles in the Debye sphere, and therefore a measure of coupling, with larger $\ln\Lambda$ being more weakly coupled.

Using this scaling for the Coulomb logarithm, we may estimate [74]

$$\ln\Lambda \approx 26.7 - \frac{1}{2}\ln\left(\frac{n}{[1\mathrm{m}^{-3}]}\right) + \frac{3}{2}\ln\left(\frac{T}{[1\mathrm{eV}]}\right). \tag{2.22}$$

This estimate does not include quantum effects that change the scaling of the Coulomb logarithm at different densities and temperatures, but provides a decent estimate for our arguments. High-energy-density plasmas encountered in ICF have typical densities and temperatures of $n \sim 10^{29} - 10^{31}\,\mathrm{m}^{-3}$ and $T \sim 1 - 10\,\mathrm{keV}$, and therefore a Coulomb logarithm of $\ln\Lambda \gtrsim 2$ which is mostly within the weakly coupled regime, with moderate-coupling effects in cold and dense regions of the plasma. The subject matter of this thesis, nonlocal

transport, is most relevant in high temperatures and low density regions where a weak coupling treatment is valid. For the results of this work, a common uniform Coulomb logarithm is always assumed $\ln \Lambda_{\alpha\beta}(\boldsymbol{r}) = \ln \Lambda$ for simplicity, although the RKM can straightforwardly include a specified form of $\ln \Lambda_{\alpha\beta}(\boldsymbol{r})$.

The lower limit for the impact parameter $b \geq b_{\min}$ removes the larger angle deflections from consideration. To justify this, we consider the differential cross section for a Coulomb collision, or the Rutherford cross section, which has the standard result

$$\left(\frac{d\sigma}{d\Omega}\right)_{\text{Coulomb}} = \frac{1}{4}\left(\frac{q_\alpha q_\beta}{4\pi\varepsilon_0 \mu_{\alpha\beta} u^2}\right)^2 \frac{1}{\sin^4(\delta/2)}, \tag{2.23}$$

as shown in Appendix B, where δ is the scattering angle, and $\mu_{\alpha\beta}$ is the reduced mass of the two colliding particles. Due to the strong divergence $\sim \delta^{-4}$ for small scattering angles, these types of collisions dominate over large angle deflections.

The basic collision frequency of species α against species β is then

$$\hat{\nu}_{\alpha\beta} = \frac{n_\beta q_\alpha^2 q_\beta^2 \ln \Lambda_{\alpha\beta}}{4\pi\varepsilon_0^2 m_\alpha^2 v_{\text{th},\alpha}^3}, \tag{2.24}$$

which includes the Coulomb logarithm and the thermal velocity of species α. Considering only collisions of a particle of species α against species β, the average distance it travels before colliding, the MFP, is

$$\lambda_{\text{th},\alpha\beta} = \frac{v_{\text{th},\alpha}}{\hat{\nu}_{\alpha\beta}} = \frac{4\pi\varepsilon_0^2 m_\alpha^2 v_{\text{th},\alpha}^4}{n_\beta q_\alpha^2 q_\beta^2 \ln \Lambda_{\alpha\beta}} = \frac{16\pi\varepsilon_0^2 (k_\text{B} T_\alpha)^2}{n_\beta q_\alpha^2 q_\beta^2 \ln \Lambda_{\alpha\beta}}. \tag{2.25}$$

For a non-thermal particle with speed v, we recall $\nu \propto v^{-3}$ so its MFP scales as

$$\lambda_{\alpha\beta}(v) \sim \left(\frac{v}{v_{\text{th},\alpha}}\right)^4 \lambda_{\text{th},\alpha\beta}. \tag{2.26}$$

The MFP is independent of particle mass, so electrons and singly charged ions are equally sensitive to nonlocal kinetic effects.

2.2.4 Magnetic fields

In the presence of a magnetic field $\boldsymbol{B}$, a particle gyrates around field lines with a gyrofrequency

$$\omega_{\text{c},\alpha} \equiv \frac{q_\alpha B}{m_\alpha}. \tag{2.27}$$

The characteristic number of gyro-orbits between collisions of a thermal particle is then

$$\chi_\alpha \equiv \omega_{\text{c},\alpha} \tau_{\alpha\alpha}, \tag{2.28}$$

which defines the Hall parameter χ_α. This parameter then quantifies how strongly magnetic fields influence particle motion between collisions. For $\chi_\alpha \ll 1$, the plasma is weakly magnetised. For $\chi_\alpha \sim 1$ or $\chi_\alpha \gg 1$, the plasma is moderately or strongly magnetised, respectively. Although the Hall parameter may be defined for each species, we typically focus on the electron Hall parameter $\chi = \chi_e$.

Collisions were considered to be purely electrostatic in the treatment above. If the magnetic field is sufficiently strong, it can affect particles during the collision and must therefore be accounted for in a proper treatment. Magnetic fields impact collisions where the gyroradius $\rho_{\mathrm{L},\alpha}$ of a particle is smaller than or comparable to the Debye sphere $\rho_{\mathrm{L},\alpha} \lesssim \lambda_D$. In terms of timescales, magnetic fields impact collisions where the gyrofrequency is faster than the plasma frequency $\omega_{c,\alpha} \gtrsim \omega_{\mathrm{p},\alpha}$ so particles experience gyroorbits during a single plasma oscillation, i.e. during the average crossing time of the Debye sphere. By comparing length scales $\rho_{\mathrm{L},\alpha} = v_{\mathrm{th},\alpha}/\omega_{\mathrm{c},\alpha}$, we may also find how large the magnetic field must be for collisions to be electromagnetic:

$$\sqrt{\frac{k_{\mathrm{B}}T}{m}}\frac{m}{qB} \lesssim \sqrt{\frac{\varepsilon_0 k_{\mathrm{B}}T}{nq^2}} \quad \Rightarrow \quad \frac{B^2}{\mu_0} \gtrsim \rho c^2, \tag{2.29}$$

i.e. where the magnetic energy density is comparable to or dominates the mass energy density. Such strong magnetic fields can be encountered in astrophysical environments but not in ICF plasmas, therefore the standard electrostatic treatment of collisions is sufficient for the scope of this work. Note that this is a distinct and much stricter criterion than the magnetisation of the plasma over a collision time. Moderate magnetic fields frequently encountered in ICF plasmas still have an impact on collision-dependent phenomena such as transport.

2.2.5 Other regimes

Quantum and relativistic physics results in new regimes of plasma. For example, if the plasma is sufficiently hot $k_{\mathrm{B}}T_e \gtrsim m_e c^2 \approx 0.511\,\mathrm{MeV}$, electrons become relativistic. Relativistic plasmas are more complicated since single particles are required to be described relativistically, but also since particle-antiparticle pairs may be produced spontaneously. Quantum mechanical effects also give rise to new behaviour. The de Broglie wavelength of a thermal electron, or the 'quantum wavelength', is

$$\lambda_{\mathrm{Q},e} = \hbar\sqrt{\frac{2\pi}{m_e k_{\mathrm{B}}T_e}}. \tag{2.30}$$

If the quantum wavelength is much larger than the average interatomic spacing $\lambda_{\mathrm{Q},e} \gtrsim n_e^{-1/3}$, electron wavefunctions overlap and interfere, giving rise to quantum collective behaviour. This is quantified by the electron degeneracy parameter $\Theta = n_e\lambda_{\mathrm{Q},e}^3 \propto n_e T_e^{-3/2}$, which considers the average number of electrons occupying a single-particle quantum state. If $\Theta \ll 1$, the system is classical, and if $\Theta \gtrsim 1$, quantum effects are significant. Metals are a familiar example of degenerate electrons where $\Theta \gtrsim 1$. Although metals are not plasmas, plasmas can exist at high temperatures and densities where $\Theta \gtrsim 1$, known as quantum plasmas. The state in which matter is moderately coupled $\Gamma \sim 1$ and moderately degenerate $\Theta \sim 1$ is known as warm dense matter (WDM). This regime of matter linking neutral gases, solids, and weakly coupled plasmas is encountered in ICF and planetary cores, and is therefore a particularly active research topic.

Figure 2.9 shows a parameter space over temperature and number density with relevant regimes of matter indicated. Physical regimes include regions with unionised matter, relativistic thermal electrons, strong

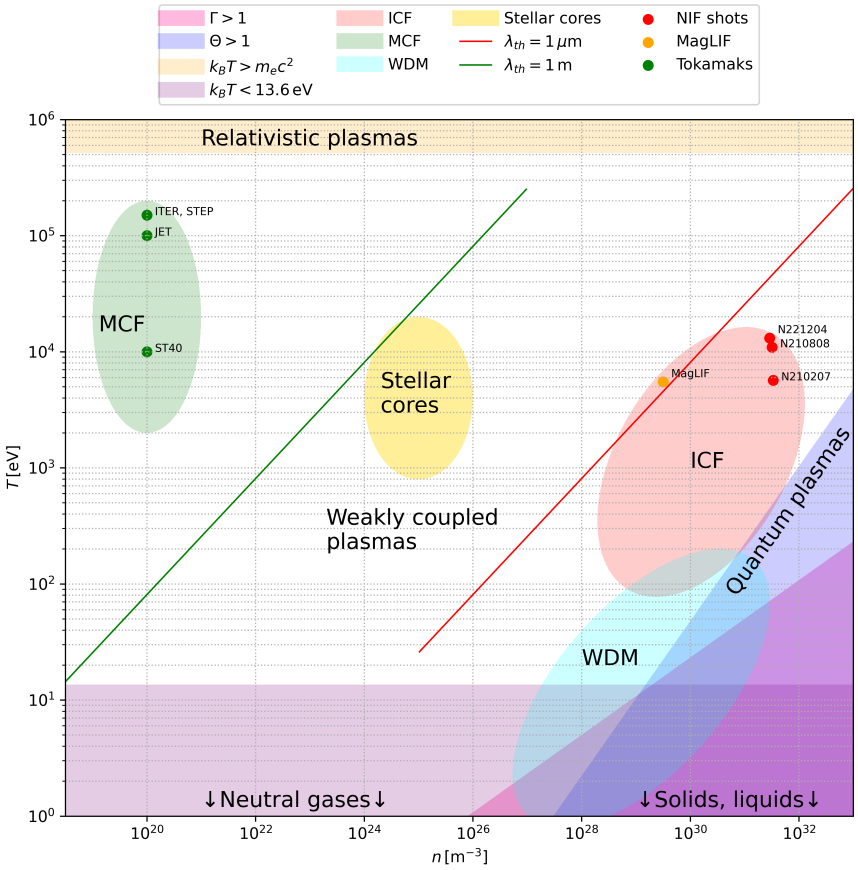


Figure 2.9: Parameter space of plasma temperature versus number density with different regimes, confined fusion schemes, and relevant scales roughly indicated. The indicated regions for ICF, MCF, stellar cores, and WDM are a rough quantitative guide rather than strict definitions of these types of plasma. The indicated ICF refers to the plasma during the implosion; before the implosion, the material is not ionised, but quickly transitions to the plasma regime during laser heating.

coupling, quantum degeneracy, and WDM. Typical regions in parameter space for confined fusion schemes and stellar cores are shown, with a few examples of notable ICF experiments and tokamaks.

The solid red and green lines indicate where the thermal MFP is $\lambda_{\mathrm{th}} = 1\,\mu\mathrm{m}$ and $\lambda_{\mathrm{th}} = 1\,\mathrm{m}$, respectively. Below the red $\lambda_{\mathrm{th}} = 1\,\mu\mathrm{m}$ line, plasma behaviour on length scales much longer than this is collisional and fluid-like. Below but near this boundary, suprathermal particles with longer MFPs give rise to nonlocal transport on these length scales, and above the boundary the plasma is collisionless and kinetic on those length scales. ICF targets tend to have shortest length scales $L \gtrsim 1\,\mu\mathrm{m}$ during implosions, therefore most of the ICF parameter space is collisional. There is still a significant region, at lower densities and higher temperatures just below the boundary, where nonlocal effects are expected to be significant. In contrast, MagLIF appears to be significantly collisionless and MCF appears entirely kinetic. However, strong external magnetic fields in these confined fusion schemes cause particles to gyrate much faster than the collision frequency, introducing the gyroradius as a shorter length scale that restores collisionality.

This work focuses on this regime especially relevant to ICF where the plasma is often weakly coupled,

classical, and mostly collisional, but is sometimes subject to short length scales where transport becomes nonlocal. Such plasmas are described by kinetic theory.

2.3 Kinetic Theory

2.3.1 Origin of the Vlasov-Fokker-Planck equation

The fundamental object of kinetics is the DF $f_\alpha(\boldsymbol{x}, \boldsymbol{v}, t)$, a probability density distribution over physical space and velocity space defined such that $f_\alpha(\boldsymbol{x}, \boldsymbol{v}, t) d^3\boldsymbol{x} d^3\boldsymbol{v}$ is the expected number of particles of species α in the infinitesimal phase space volume $d^3\boldsymbol{x} d^3\boldsymbol{v}$ at $(\boldsymbol{x}, \boldsymbol{v}, t)$. The evolution of the DF with binary collisions is governed by the Boltzmann equation. Ideal, weakly coupled plasmas may be described by the VFP equation, which is the Boltzmann equation for a plasma with a Fokker-Planck collision operator as a consequence of long-range Coulomb collisions with multiple species. The VFP equation for a species α in laboratory-frame phase-space coordinates $(t, \boldsymbol{x}, \boldsymbol{v})$ for particle position $\boldsymbol{x}$ and particle velocity $\boldsymbol{v}$ is

$$\partial_t f_\alpha + \boldsymbol{v} \cdot \boldsymbol{\nabla} f_\alpha + \frac{q_\alpha}{m_\alpha} (\boldsymbol{E} + \boldsymbol{v} \times \boldsymbol{B}) \cdot \boldsymbol{\nabla}_{\boldsymbol{v}} f_\alpha = \sum_\beta C_{\alpha\beta}\{f_\alpha, f_\beta\}\,, \tag{2.31}$$

where f_α is the DF of species α. The FP collision operator $C_{\alpha\beta}\{f_\alpha, f_\beta\}$ represents collisions of species β acting on species α, with the sum over all species β including α.

Conservation in phase space

An intuitive derivation of the kinetic equation comes from particle number conservation in phase space. Consider a single spatial coordinate x and velocity coordinate v, and a rectangle in this reduced phase space $\{x, v \mid x_0 \leq x < x_0 + \Delta x,\ v_0 \leq v < v_0 + \Delta v\}$. The rate of change of the number of particles in the volume

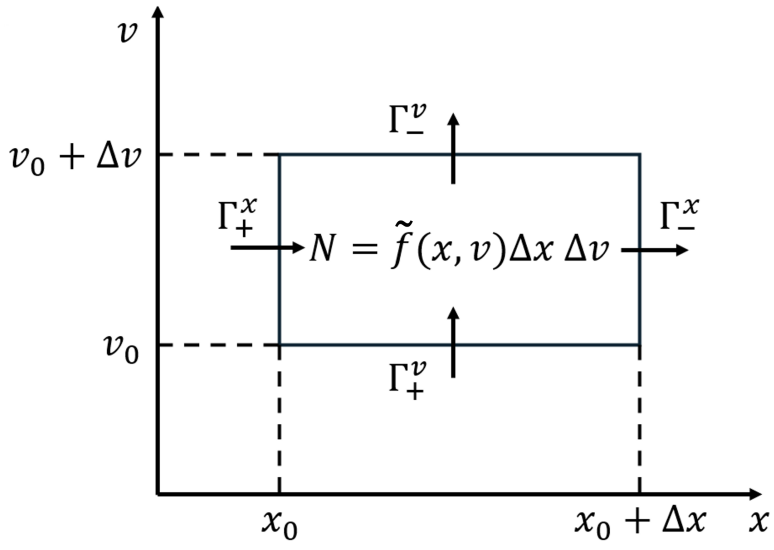


Figure 2.10: Rectangular region in phase space with particle fluxes in and out.

is given as

$$\partial_t N_\alpha = \Gamma^x_{\alpha,+} - \Gamma^x_{\alpha,-} + \Gamma^v_{\alpha,+} - \Gamma^v_{\alpha,-}. \tag{2.32}$$

The flux of particles on each of the four edges may be written as

$$\begin{aligned} \Gamma^x_{\alpha,+} &= \dot{x}_\alpha(x_0, v_0)\tilde{f}_\alpha(x_0, v_0)\Delta v, \quad \Gamma^x_{\alpha,-} = \dot{x}_\alpha(x_0 + \Delta x, v_0)\tilde{f}_\alpha(x_0 + \Delta x, v_0)\Delta v, \\ \Gamma^v_{\alpha,+} &= \dot{v}_\alpha(x_0, v_0)\tilde{f}_\alpha(x_0, v_0)\Delta x, \quad \Gamma^v_{\alpha,-} = \dot{v}_\alpha(x_0, v_0 + \Delta v)\tilde{f}_\alpha(x_0, v_0 + \Delta v)\Delta x, \end{aligned} \tag{2.33}$$

i.e. the product of the flow of particles ($\dot{x}_\alpha$ or $\dot{v}_\alpha$), phase-space number density $\tilde{f}_\alpha$ at the face, and size of the face (Δv or Δx). Substituting into Equation 2.32 and dividing by the phase space volume $\Delta x \Delta v$ to obtain the phase-space number density $\tilde{f}_\alpha = N_\alpha / \Delta x \Delta v$ yields

$$\begin{aligned} \partial_t \tilde{f}_\alpha = &\frac{\dot{x}_\alpha(x_0, v_0)\tilde{f}_\alpha(x_0, v_0) - \dot{x}_\alpha(x_0 + \Delta x, v_0)\tilde{f}_\alpha(x_0 + \Delta x, v_0)}{\Delta x} \\ &+ \frac{\dot{v}_\alpha(x_0, v_0)\tilde{f}_\alpha(x_0, v_0) - \dot{v}_\alpha(x_0, v_0 + \Delta v)\tilde{f}_\alpha(x_0, v_0 + \Delta v)}{\Delta v}. \end{aligned} \tag{2.34}$$

Taking the limit as Δx and Δv tend to zero results in the continuity equation

$$\partial_t \tilde{f}_\alpha + \partial_x(\dot{x}_\alpha \tilde{f}_\alpha) + \partial_v(\dot{v}_\alpha \tilde{f}_\alpha) = 0. \tag{2.35}$$

For more spatial and velocity dimensions, the additional terms due to fluxes in these dimensions are added. The sum of these terms is naturally written as divergences in physical space $\sum_{i=1,2,3} \partial_{x_i}(\dot{x}_{\alpha,i} f) = \boldsymbol{\nabla} \cdot (\dot{\boldsymbol{x}}_\alpha f)$ and velocity space $\sum_{i=1,2,3} \partial_{v_i}(\dot{v}_{\alpha,i} f) = \boldsymbol{\nabla}_{\boldsymbol{v}} \cdot (\dot{\boldsymbol{v}}_\alpha f)$. Also using the equations of motion $\dot{\boldsymbol{x}}_\alpha = \boldsymbol{v}$ and $\dot{\boldsymbol{v}}_\alpha = \boldsymbol{F}_\alpha / m$, where $\boldsymbol{F}_\alpha$ is the force on a particle of species α, we obtain a continuity equation

$$\partial_t \tilde{f}_\alpha + \boldsymbol{\nabla} \cdot (\boldsymbol{v} \tilde{f}_\alpha) + \boldsymbol{\nabla}_{\boldsymbol{v}} \cdot \left(\frac{1}{m_\alpha} \boldsymbol{F}_\alpha \tilde{f}_\alpha \right) = 0. \tag{2.36}$$

Finally, noting that the Lorentz force $\boldsymbol{F}_\alpha = q_\alpha(\tilde{\boldsymbol{E}} + \boldsymbol{v} \times \tilde{\boldsymbol{B}})$ is divergence-free in velocity space since $\boldsymbol{\nabla}_{\boldsymbol{v}} \cdot (\tilde{\boldsymbol{E}} + \boldsymbol{v} \times \tilde{\boldsymbol{B}}) = \varepsilon_{ijk} \partial_{v_i} v_j \tilde{B}_k = \varepsilon_{ijk} \delta_{ij} \tilde{B}_k = \varepsilon_{iik} \tilde{B}_k = 0$, we are left with the kinetic equation

$$\partial_t \tilde{f}_\alpha + \boldsymbol{v} \cdot \boldsymbol{\nabla} \tilde{f}_\alpha + \frac{q_\alpha}{m_\alpha} (\tilde{\boldsymbol{E}} + \boldsymbol{v} \times \tilde{\boldsymbol{B}}) \cdot \boldsymbol{\nabla}_{\boldsymbol{v}} \tilde{f}_\alpha = 0, \tag{2.37}$$

where $\boldsymbol{v}$ can be taken outside of the spatial gradient since it is an independent variable from $\boldsymbol{x}$. The tildes on the phase-space number density $\tilde{f}_\alpha$ and electromagnetic fields $\tilde{\boldsymbol{E}}$ and $\tilde{\boldsymbol{B}}$ indicate that they are exact, in particular that they include microscopic fluctuations on top of macroscopic behaviour. The kinetic equation in tandem with Maxwell's equations

$$\boldsymbol{\nabla} \cdot \tilde{\boldsymbol{E}} = \frac{1}{\varepsilon_0} \sum_\alpha q_\alpha \int d^3\boldsymbol{v}\, \tilde{f}_\alpha, \tag{2.38}$$

$$\boldsymbol{\nabla} \cdot \tilde{\boldsymbol{B}} = 0, \tag{2.39}$$

$$\boldsymbol{\nabla} \times \tilde{\boldsymbol{E}} = -\partial_t \tilde{\boldsymbol{B}}, \tag{2.40}$$

$$\boldsymbol{\nabla} \times \tilde{\boldsymbol{B}} = \mu_0 \varepsilon_0 \partial_t \tilde{\boldsymbol{E}} + \mu_0 \sum_\alpha q_\alpha \int d^3\boldsymbol{v}\, \boldsymbol{v} \tilde{f}_\alpha, \tag{2.41}$$

provide an exact description of the plasma. This derivation gives an intuitive understanding that the kinetic equation is a continuity equation of particles in phase space. This may be made even more explicit by writing the kinetic equation in terms of phase space coordinates $\boldsymbol{Z} = (\boldsymbol{x}, \boldsymbol{v})$ as

$$\partial_t \tilde{f}_\alpha + \boldsymbol{\nabla}_{\boldsymbol{Z}} \cdot (\dot{\boldsymbol{Z}} \tilde{f}_\alpha) = 0, \tag{2.42}$$

i.e. is a distribution obeying Liouville's theorem.

Klimontovich's distribution

Klimontovich [75] presented a more rigorous derivation to the exact kinetic equation 2.37. Suppose we have N particles of species α indexed by k. The exact behaviour of particle k is described by its position $\boldsymbol{x}_\alpha^k$ and velocity $\boldsymbol{v}_\alpha^k$ which evolve according to

$$\dot{\boldsymbol{x}}_\alpha^k = \boldsymbol{v}_\alpha^k, \quad \dot{\boldsymbol{v}}_\alpha^k = \frac{q_\alpha}{m_\alpha}\Big(\tilde{\boldsymbol{E}}(t, \boldsymbol{x}_\alpha^k) + \boldsymbol{v}_\alpha^k \times \tilde{\boldsymbol{B}}(t, \boldsymbol{x}_\alpha^k)\Big). \tag{2.43}$$

We may construct a single distribution which contains the exact positions of all of the particles as

$$\tilde{f}_\alpha(t, \boldsymbol{x}, \boldsymbol{v}) = \sum_k \delta^3(\boldsymbol{x} - \boldsymbol{x}_\alpha^k(t))\delta^3(\boldsymbol{v} - \boldsymbol{v}_\alpha^k(t)), \tag{2.44}$$

which is known as Klimontovich's distribution. Taking the time derivative, we find

$$\partial_t \tilde{f}_\alpha = -\sum_k \left[\dot{\boldsymbol{x}}_\alpha^k \cdot \boldsymbol{\nabla}_{\boldsymbol{x}}\Big(\delta^3(\boldsymbol{x} - \boldsymbol{x}_\alpha^k)\delta^3(\boldsymbol{v} - \boldsymbol{v}_\alpha^k)\Big) + \dot{\boldsymbol{v}}_\alpha^k \cdot \boldsymbol{\nabla}_{\boldsymbol{v}}\Big(\delta^3(\boldsymbol{x} - \boldsymbol{x}_\alpha^k)\delta^3(\boldsymbol{v} - \boldsymbol{v}_\alpha^k)\Big)\right]. \tag{2.45}$$

The equations of motion for each individual particle (Equation 2.43) are substituted in to replace $\dot{\boldsymbol{x}}_\alpha^k$ and $\dot{\boldsymbol{v}}_\alpha^k$. Since these expressions are not explicitly dependent on the phase space coordinates $\boldsymbol{x}$ and $\boldsymbol{v}$, the gradients may be moved outside of the summation. This yields

$$\partial_t \tilde{f}_\alpha + \boldsymbol{\nabla}_{\boldsymbol{x}} \cdot \sum_k \left[\boldsymbol{v}_\alpha^k\Big(\delta^3(\boldsymbol{x} - \boldsymbol{x}_\alpha^k)\delta^3(\boldsymbol{v} - \boldsymbol{v}_\alpha^k)\Big)\right] \tag{2.46}$$

$$+ \boldsymbol{\nabla}_{\boldsymbol{v}} \cdot \sum_k \left[\frac{q_\alpha}{m_\alpha}\Big(\tilde{\boldsymbol{E}}(t, \boldsymbol{x}_\alpha^k) + \boldsymbol{v}_\alpha^k \times \tilde{\boldsymbol{B}}(t, \boldsymbol{x}_\alpha^k)\Big)\Big(\delta^3(\boldsymbol{x} - \boldsymbol{x}_\alpha^k)\delta^3(\boldsymbol{v} - \boldsymbol{v}_\alpha^k)\Big)\right] = 0. \tag{2.47}$$

Now, the Dirac deltas are employed to replace $\boldsymbol{x}_\alpha^k \to \boldsymbol{x}$ and $\boldsymbol{v}_\alpha^k \to \boldsymbol{v}$, yielding

$$\partial_t \tilde{f}_\alpha + \boldsymbol{\nabla}_{\boldsymbol{x}} \cdot \left(\boldsymbol{v} \sum_k \delta^3(\boldsymbol{x} - \boldsymbol{x}_\alpha^k)\delta^3(\boldsymbol{v} - \boldsymbol{v}_\alpha^k)\right) \tag{2.48}$$

$$+ \boldsymbol{\nabla}_{\boldsymbol{v}} \cdot \left(\frac{q_\alpha}{m_\alpha}\Big(\tilde{\boldsymbol{E}} + \boldsymbol{v} \times \tilde{\boldsymbol{B}}\Big) \sum_k \delta^3(\boldsymbol{x} - \boldsymbol{x}_\alpha^k)\delta^3(\boldsymbol{v} - \boldsymbol{v}_\alpha^k)\right) = 0, \tag{2.49}$$

which, upon recognising the reappearance of the Klimontovich distribution in the second and third terms, reproduces the exact kinetic equation

$$\partial_t \tilde{f}_\alpha + \boldsymbol{v} \cdot \boldsymbol{\nabla} \tilde{f}_\alpha + \frac{q_\alpha}{m_\alpha}(\tilde{\boldsymbol{E}} + \boldsymbol{v} \times \tilde{\boldsymbol{B}}) \cdot \boldsymbol{\nabla}_{\boldsymbol{v}} \tilde{f}_\alpha = 0. \tag{2.50}$$

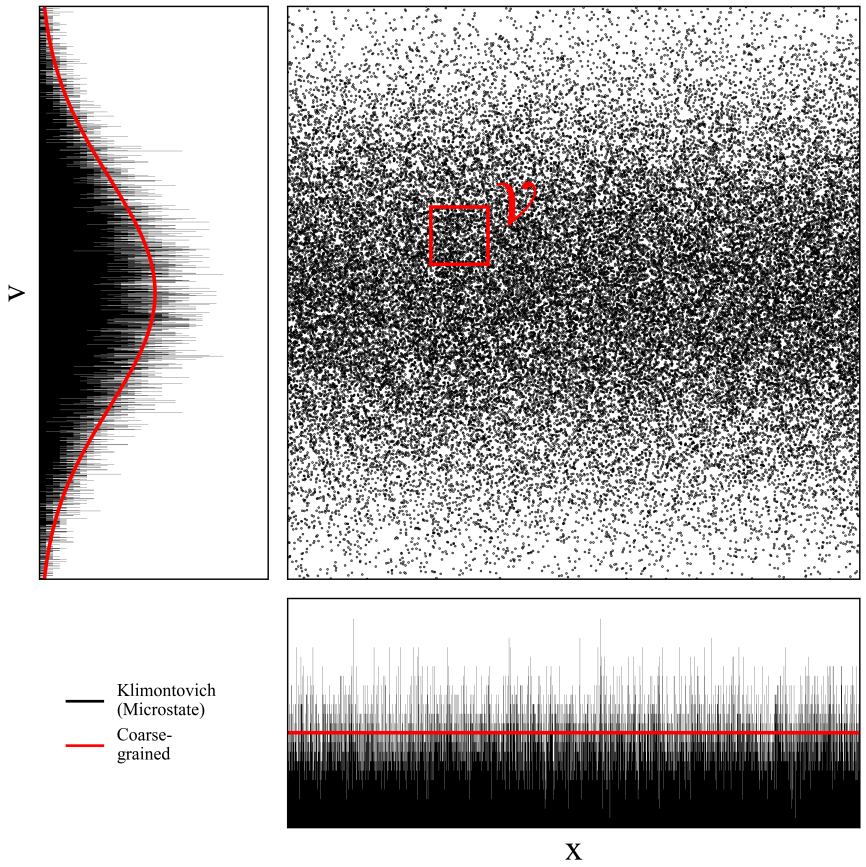


Figure 2.11: Depiction of the Klimontovich distribution (black) for a particular microstate over phase space. In the top right plot, each dot represents a Dirac delta at that location in phase space, with histograms in space and velocity shown below and to the left, respectively. The red box shows the coarse-graining volume $\mathcal{V}$ from which the smooth distribution function is obtained.

Coarse graining

The descriptions above have not resulted in an explicit description of collisions. 'Collisions' in the plasma context refer to particles being deflected by microscopic fluctuating electromagnetic fields on scales smaller than the Debye length. The last term in the exact kinetic equation 2.50 therefore includes these microscopic collisions on top of the macroscopic fields. However, we are interested in the behaviour of the distribution on scales much larger than the Debye length, and it is therefore convenient to average over these scale lengths. We define a phase space volume average $\langle \dots \rangle = \frac{1}{|\mathcal{V}|} \int_{\mathcal{V}} \dots d^3\boldsymbol{r} d^3\boldsymbol{v}$ over a small phase space volume $\mathcal{V}$ centred at $\boldsymbol{x}, \boldsymbol{v}$ of size $\sim l_x, l_v$ in physical space and velocity space, respectively. The spatial scale l_x should be much larger than the interparticle spacing to average over many particles but much smaller than the Debye length $n^{-1/3} \ll l_x \ll \lambda_\mathrm{D}$. The velocity scale l_v should be smaller than the velocity scale of the distribution, i.e. the thermal velocity, but larger than velocity changes over a microscopic fluctuation of the distribution. This coarse graining, depicted in Figure 2.11, may instead be viewed as taking an ensemble average over microstates, but here we more simply treat it as smoothing out over phase space for a given microstate.

We decompose the DF into a smooth coarse-grained part and the remaining sub-Debye microscopic

fluctuations as

$$\tilde{f}_\alpha = \langle \tilde{f}_\alpha \rangle + \delta \tilde{f}_\alpha. \tag{2.51}$$

By definition, the average of the fluctuating part vanishes since $\langle \delta \tilde{f}_\alpha \rangle = \langle \tilde{f}_\alpha - \langle \tilde{f}_\alpha \rangle \rangle \equiv 0$. Similarly, the fields are also decomposed as

$$\tilde{\boldsymbol{E}} = \langle \tilde{\boldsymbol{E}} \rangle + \delta \tilde{\boldsymbol{E}}, \quad \tilde{\boldsymbol{B}} = \langle \tilde{\boldsymbol{B}} \rangle + \delta \tilde{\boldsymbol{B}}, \tag{2.52}$$

where $\langle \delta \tilde{\boldsymbol{E}} \rangle = 0$ and $\langle \delta \tilde{\boldsymbol{B}} \rangle = 0$ by definition. Since Maxwell's equations are linear, they may be rewritten as two decoupled sets, one in terms of 'coarse-grained' quantities $(\langle \tilde{f}_\alpha \rangle, \langle \tilde{\boldsymbol{E}} \rangle, \langle \tilde{\boldsymbol{B}} \rangle)$ and one in terms of sub-Debye fluctuating quantities $(\delta \tilde{f}_\alpha, \delta \tilde{\boldsymbol{E}}, \delta \tilde{\boldsymbol{B}})$. Fluctuations in the electromagnetic fields are then determined directly from the fluctuations in the DF, and the coarse-grained fields are determined directly from the coarse-grained DF via

$$\boldsymbol{\nabla} \cdot \langle \tilde{\boldsymbol{E}} \rangle = \frac{1}{\varepsilon_0} \sum_\alpha q_\alpha \int d^3\boldsymbol{v}\, \langle \tilde{f}_\alpha \rangle, \qquad \boldsymbol{\nabla} \cdot \delta \tilde{\boldsymbol{E}} = \frac{1}{\varepsilon_0} \sum_\alpha q_\alpha \int d^3\boldsymbol{v}\, \delta \tilde{f}_\alpha, \tag{2.53}$$

$$\boldsymbol{\nabla} \cdot \langle \tilde{\boldsymbol{B}} \rangle = 0, \qquad \boldsymbol{\nabla} \cdot \delta \tilde{\boldsymbol{B}} = 0, \tag{2.54}$$

$$\boldsymbol{\nabla} \times \langle \tilde{\boldsymbol{E}} \rangle = -\partial_t \langle \tilde{\boldsymbol{B}} \rangle, \qquad \boldsymbol{\nabla} \times \delta \tilde{\boldsymbol{E}} = -\partial_t \delta \tilde{\boldsymbol{B}}, \tag{2.55}$$

$$\boldsymbol{\nabla} \times \langle \tilde{\boldsymbol{B}} \rangle = \mu_0 \varepsilon_0 \partial_t \langle \tilde{\boldsymbol{E}} \rangle + \mu_0 \sum_\alpha q_\alpha \int d^3\boldsymbol{v}\, \boldsymbol{v} \langle \tilde{f}_\alpha \rangle, \qquad \boldsymbol{\nabla} \times \delta \tilde{\boldsymbol{B}} = \mu_0 \varepsilon_0 \partial_t \delta \tilde{\boldsymbol{E}} + \mu_0 \sum_\alpha q_\alpha \int d^3\boldsymbol{v}\, \boldsymbol{v}\, \delta \tilde{f}_\alpha. \tag{2.56}$$

Taking this average of the exact kinetic equation, we have

$$\partial_t \langle \tilde{f}_\alpha \rangle + \boldsymbol{v} \cdot \boldsymbol{\nabla} \langle \tilde{f}_\alpha \rangle + \frac{q_\alpha}{m_\alpha} (\langle \tilde{\boldsymbol{E}} \rangle + \boldsymbol{v} \times \langle \tilde{\boldsymbol{B}} \rangle) \cdot \boldsymbol{\nabla}_{\boldsymbol{v}} \langle \tilde{f}_\alpha \rangle + \left\langle \frac{q_\alpha}{m_\alpha} (\delta \tilde{\boldsymbol{E}} + \boldsymbol{v} \times \delta \tilde{\boldsymbol{B}}) \cdot \boldsymbol{\nabla}_{\boldsymbol{v}} \delta \tilde{f}_\alpha \right\rangle = 0, \tag{2.57}$$

where the terms linear in fluctuating quantities have vanished under the average. This equation describes how the coarse-grained DF evolves in phase space subject to macroscopic fields but also due to microscopic fluctuations from the last term that is quadratic in sub-Debye quantities and therefore quadratic in $\delta \tilde{f}_\alpha$. This last term is the one that describes collisions. We therefore put it on the right hand side of the equation and call it the 'collision operator', since it is determined from the coarse-grained DF. Finally, we drop the averaging notation by writing the coarse-grained DF as $f_\alpha = \langle \tilde{f}_\alpha \rangle$ and coarse-grained electromagnetic fields as $\boldsymbol{E} = \langle \tilde{\boldsymbol{E}} \rangle$ and $\boldsymbol{B} = \langle \tilde{\boldsymbol{B}} \rangle$. This yields the VFP equation

$$\partial_t f_\alpha + \boldsymbol{v} \cdot \boldsymbol{\nabla} f_\alpha + \frac{q_\alpha}{m_\alpha} (\boldsymbol{E} + \boldsymbol{v} \times \boldsymbol{B}) \cdot \boldsymbol{\nabla}_{\boldsymbol{v}} f_\alpha = C_\alpha, \tag{2.58}$$

where the collision term

$$C_\alpha = -\left\langle \frac{q_\alpha}{m_\alpha} (\delta \tilde{\boldsymbol{E}} + \boldsymbol{v} \times \delta \tilde{\boldsymbol{B}}) \cdot \boldsymbol{\nabla}_{\boldsymbol{v}} \delta \tilde{f}_\alpha \right\rangle. \tag{2.59}$$

The collision term makes it clear that microscopic fluctuations still impact the coarse-grained distribution due to correlations in $\delta \tilde{f}_\alpha$ and the resulting fluctuations in the fields. Finding an explicit expression for the

collision term requires evaluating correlations of the fluctuations $\langle \delta\tilde{f}_\alpha \delta\tilde{f}_\beta \rangle$ from f_α and f_β. If collisions are assumed to be binary and the colliding particles are initially uncorrelated before the collision, the collision term has the form of the Boltzmann collision operator. For a weakly coupled plasma with a Debye-shielded Coulomb potential, the Boltzmann operator reduces to the Fokker-Planck collision operator $C_\alpha = \sum_\beta C_{\alpha\beta}\{f_\alpha, f_\beta\}$ [75–77] which is used for the remainder of this work. A derivation of the Fokker-Planck collision operator following Helander and Sigmar [78] is presented in Appendix B.

A more rigorous derivation of the Boltzmann equation is provided by the Bogoliubov–Born–Green–Kirkwood–Yvon (BBGKY) hierarchy [16]. This treatment starts from Liouville's theorem for an $\mathcal{N}$-particle system in $6\mathcal{N}$-dimensional phase space

$$\partial_t f^{(\mathcal{N})} + \{f^{(\mathcal{N})}, H^{(\mathcal{N})}\} = 0, \tag{2.60}$$

where $f^{(\mathcal{N})}$ and $H^{(\mathcal{N})}$ are the $\mathcal{N}$-particle DF and Hamiltonian, respectively, and $\{\dots,\dots\}$ is the Poisson bracket over the appropriate coordinates. By integrating over successive particle coordinates, a hierarchy of coupled equations is obtained, in which the evolution of the s-particle distribution $f^{(s)}$ depends on $f^{(s+1)}$. The BBGKY hierarchy can be truncated by introducing a suitable closure for a chosen DF $f^{(k)}$, which leaves the $s = 1, \dots, k-1$ coupled equations to be solved.

A naïve closure would be that the particles remain uncorrelated, i.e.

$$f^{(2)}(t, \boldsymbol{x}_1, \boldsymbol{v}_1, \boldsymbol{x}_2, \boldsymbol{v}_2) = f^{(1)}(t, \boldsymbol{x}_1, \boldsymbol{v}_1) f^{(1)}(t, \boldsymbol{x}_2, \boldsymbol{v}_2). \tag{2.61}$$

However, this closure contains no information about microscopic collisions and therefore yields the Vlasov equation for a collisionless plasma. To include collisions, a more informed closure is to assume uncorrelated particles only immediately before each collision, i.e. the closure for $f^{(2)}$ before a collision is given by Equation 2.61. After a binary collision, the two particles are then correlated, with the closure for $f^{(2)}$ after the collision determined by the collision dynamics. This assumption of no correlations before collisions, commonly known as 'molecular chaos' or the *Stosszahlansatz*, yields a closed kinetic equation for the single-particle distribution function $f = f^{(1)}$ including binary collisions, i.e. Boltzmann's equation.

2.3.2 Fokker-Planck collision operator

The Fokker-Planck collision operator, originally derived in 1936 [79], describes binary long-range small-angle Debye-shielded Coulomb collisions. It has the form

$$C_{\alpha\beta}\{f_\alpha, f_\beta\} = -\frac{q_\alpha^2 q_\beta^2 \ln\Lambda_{\alpha\beta}}{8\pi\varepsilon_0^2 m_\alpha} \frac{\partial}{\partial v_i} \int d^3\boldsymbol{v}' \, \frac{u^2\delta_{ij} - u_i u_j}{u^3} \left(\frac{f_\alpha(\boldsymbol{v})}{m_\beta} \frac{\partial f_\beta(\boldsymbol{v}')}{\partial v_j'} - \frac{f_\beta(\boldsymbol{v}')}{m_\alpha} \frac{\partial f_\alpha(\boldsymbol{v})}{\partial v_j} \right), \tag{2.62}$$

where $u = |\boldsymbol{v} - \boldsymbol{v}'|$, with a derivation provided in Appendix B. The Fokker-Planck collision operator is a special case of the more general Boltzmann collision operator describing binary collisions, however this work focuses entirely on weakly coupled plasmas, therefore only uses the Fokker-Planck operator. The collision operator may also be written in the Rosenbluth form [80]

$$C_{\alpha\beta}\{f_\alpha, f_\beta\} = \frac{1}{4\pi} \left(\frac{q_\alpha q_\beta}{\varepsilon_0 m_\alpha} \right)^2 \ln\Lambda_{\alpha\beta} \frac{\partial}{\partial v_i} \left[-\frac{m_\alpha}{m_\beta} \frac{\partial \mathcal{H}\{f_\beta\}}{\partial v_i} f_\alpha + \frac{1}{2} \frac{\partial^2 \mathcal{G}\{f_\beta\}}{\partial v_i \partial v_j} \frac{\partial f_\alpha}{\partial v_j} \right], \tag{2.63}$$

where the Rosenbluth potentials

$$\mathcal{H}\{f_\beta\} \equiv \int d^3\boldsymbol{v}'\, \frac{1}{u} f_\beta(\boldsymbol{v}'), \quad \mathcal{G}\{f_\beta\} \equiv \int d^3\boldsymbol{v}'\, u f_\beta(\boldsymbol{v}'). \tag{2.64}$$

These objects are called 'potentials' since they satisfy the relations

$$\nabla_v^2 \mathcal{H}\{f_\beta\} = -4\pi f_\beta, \quad \nabla_v^2 \mathcal{G}\{f_\beta\} = 2\mathcal{H}\{f_\beta\}, \tag{2.65}$$

which are Poisson equations in velocity space, similarly to Gauss' law for the electric potential in physical space $\nabla^2 V = -\sigma/\varepsilon_0$. Analogously to V being the electric potential sourced from the charge distribution σ, the first Rosenbluth potential $\mathcal{H}$ is the potential sourced from the DF f, and the second Rosenbluth potential $\mathcal{G}$ is the potential sourced from the first Rosenbluth potential $\mathcal{H}$, up to constant factors.

Properties of Fokker-Planck collision operator

The Fokker-Planck collision operator has some important conservation properties. As shown in Appendix B, it satisfies

$$\begin{aligned}
&\int d^3\boldsymbol{v}\, C_{\alpha\beta}\{f_\alpha, f_\beta\} = 0, \\
&\int d^3\boldsymbol{v}\, m_\alpha \boldsymbol{v} C_{\alpha\beta}\{f_\alpha, f_\beta\} + \int d^3\boldsymbol{v}\, m_\beta \boldsymbol{v} C_{\beta\alpha}\{f_\beta, f_\alpha\} = 0, \\
&\int d^3\boldsymbol{v}\, \frac{1}{2} m_\alpha v^2 C_{\alpha\beta}\{f_\alpha, f_\beta\} + \int d^3\boldsymbol{v}\, \frac{1}{2} m_\beta v^2 C_{\beta\alpha}\{f_\beta, f_\alpha\} = 0,
\end{aligned} \tag{2.66}$$

which correspond to conservation of particle number, momentum, and energy, respectively.

Collisions naturally drive the local velocity distribution towards a Maxwellian distribution

$$f_\alpha^M(t, \boldsymbol{x}, \boldsymbol{v}) = n_\alpha(t, \boldsymbol{x}) \left(\frac{m_\alpha}{2\pi T_\alpha(t, \boldsymbol{x})} \right)^{3/2} \exp\left(- \frac{m_\alpha |\boldsymbol{v} - \boldsymbol{u}_\alpha(t, \boldsymbol{x})|^2}{2T_\alpha(t, \boldsymbol{x})} \right), \tag{2.67}$$

where n_α, $\boldsymbol{u}_\alpha$, and T_α are parameters of the distribution that physically represent the number density, flow velocity, and temperature (in energy units, i.e. $k_\mathrm{B} = 1$) of species α. This is manifested mathematically through the H-theorem of the collision operator, which states that the rate of entropy production due to the collision operator,

$$\left. \frac{dS}{dt} \right|_{\text{collisions}} = -\sum_\alpha \sum_\beta \int d^3\boldsymbol{v}\, C_{\alpha\beta}\{f_\alpha, f_\beta\} \ln f_\alpha \geq 0, \tag{2.68}$$

with the equality being satisfied if and only if the DFs are all local Maxwellians with common flow velocities and temperatures as shown in Appendix B.

This work focuses on collisional plasmas where collisions are the dominant influence on the DF. This then suggests that the DF in a sufficiently collisional plasma is near Maxwellian $f_\alpha \approx f_\alpha^M$, and therefore may be described effectively through the parameters n_α, $\boldsymbol{u}_\alpha$, and T_α. By taking appropriate velocity moments of Boltzmann's equation, evolution equations for these parameters may be obtained, thereby leaving a much more tractable fluid description.

Here we introduce the peculiar velocity $\boldsymbol{w} = \boldsymbol{v} - \boldsymbol{u}$, i.e. the velocity in the frame comoving with some local flow velocity $\boldsymbol{u}$. Different species may have different flow velocities, but within this work $\boldsymbol{u}$ is always

either the electron flow velocity $\boldsymbol{u} = \boldsymbol{u}_e$ or the ion CoM flow velocity $\boldsymbol{u} = \boldsymbol{u}_i = \sum_\alpha \rho_\alpha \boldsymbol{u}_\alpha$. The velocity space is then written in spherical polar coordinates of the peculiar velocity (w, ϑ, φ) such that

$$\boldsymbol{w} = w\sin\vartheta\cos\varphi\,\hat{\boldsymbol{w}}_x + w\sin\vartheta\sin\varphi\,\hat{\boldsymbol{w}}_y + w\cos\vartheta\,\hat{\boldsymbol{w}}_z. \tag{2.69}$$

The velocity basis vectors $\hat{\boldsymbol{w}}_{x,y,z}$ are simply aligned with the spatial basis vectors $\{\hat{\boldsymbol{x}}, \hat{\boldsymbol{y}}, \hat{\boldsymbol{z}}\}$ in planar cases, with spherical and cylindrical cases discussed later. Often, the velocity coordinate $\mu \equiv \cos\vartheta \equiv \boldsymbol{w}\cdot\hat{\boldsymbol{z}}/w$ is used for convenience.

Linearised Fokker-Planck Collision Operator

If the DFs are expanded as its deviation away from Maxwellian $f_\alpha = f_\alpha^M + \delta f_\alpha$, the Fokker-Planck collision operator splits into four parts

$$C_{\alpha\beta}\{f_\alpha, f_\beta\} = \underbrace{C_{\alpha\beta}\{f_\alpha^M, f_\beta^M\}}_{\substack{\text{Maxwellian-Maxwellian}\\ \text{collisions } C_{\alpha\beta}^M}} + \underbrace{C_{\alpha\beta}\{\delta f_\alpha, f_\beta^M\}}_{\substack{\text{Test-particle}\\ \text{operator } \hat{C}_{\alpha\beta}^T\delta f_\alpha}} + \underbrace{C_{\alpha\beta}\{f_\alpha^M, \delta f_\beta\}}_{\substack{\text{Field-particle}\\ \text{operator } \hat{C}_{\alpha\beta}^F\delta f_\beta}} + \underbrace{C_{\alpha\beta}\{\delta f_\alpha, \delta f_\beta\}}_{\substack{\text{Nonlinear}\\ \text{operator}}}, \tag{2.70}$$

where we have used the bilinearity of the collision operator. The test-particle collision operator represents the effect on species α of a distribution of test-particles of species α colliding against a Maxwellian background of species β. It has the form [74, 78]

$$\hat{C}_{\alpha\beta}^T\delta f_\alpha = \frac{1}{2}\nu_D^{\alpha\beta}\hat{\mathcal{L}}\delta f_\alpha + \frac{1}{w^2}\partial_w\left(\tilde{\nu}_s^{\alpha\beta}w^3\delta f_\alpha + \frac{1}{2}\nu_\parallel^{\alpha\beta}w^4\partial_w\delta f_\alpha\right), \tag{2.71}$$

where the three collision frequencies are defined via

$$\begin{aligned}
\nu_D^{\alpha\beta} &= \hat{\nu}_{\alpha\beta}\frac{\mathrm{erf}(\xi_\beta) - G(\xi_\beta)}{\xi_\alpha^3},\\
\tilde{\nu}_s^{\alpha\beta} &= \frac{m_\alpha}{m_\alpha + m_\beta}\nu_s^{\alpha\beta} = 2\hat{\nu}_{\alpha\beta}\frac{G(\xi_\beta)}{\xi_\alpha},\\
\nu_\parallel^{\alpha\beta} &= 2\hat{\nu}_{\alpha\beta}\frac{G(\xi_\beta)}{\xi_\alpha^3},
\end{aligned} \tag{2.72}$$

where $\xi_\alpha = w/v_{\mathrm{th},\alpha}$, $G(\xi)$ is the Chandrasekhar function [74, 78, 81], and the pitch-angle scattering operator

$$\hat{\mathcal{L}}f = (\boldsymbol{w}\times\boldsymbol{\nabla}_{\boldsymbol{w}})^2 f = \partial_\mu\big((1-\mu^2)\partial_\mu f\big) + \frac{1}{1-\mu^2}\partial_\varphi^2 f. \tag{2.73}$$

The name 'pitch-angle scattering' refers to the impact of the operator in the kinetic equation. We may recognise the second expression as the two angular components of the Laplacian in spherical polar coordinates. This suggests that the pitch-angle scattering operator diffuses the DF in velocity-angle space towards an isotropic distribution, but does not scatter the energy of particles, as depicted in Figure 2.12. Energy drag and diffusion are manifested through the slowing and parallel collision terms, respectively.

The field-particle collision operator represents the effect on species α of a Maxwellian of species α colliding against a non-Maxwellian distribution of species β. It has the form [82, 83]

$$\hat{C}_{\alpha\beta}^F\delta f_\beta = \left(\frac{q_\alpha q_\beta}{\varepsilon_0 m_\alpha}\right)^2 \ln\Lambda_{\alpha\beta}\frac{m_\alpha f_\alpha^M}{T_\alpha}\left[\frac{T_\alpha}{m_\beta}\delta f_\beta - \delta\mathcal{H}_\beta + \left(\frac{m_\alpha}{m_\beta} - 1\right)w\partial_w\delta\mathcal{H}_\beta + \frac{m_\alpha w^2}{2T_\alpha}\partial_w^2\delta\mathcal{G}_\beta\right], \tag{2.74}$$

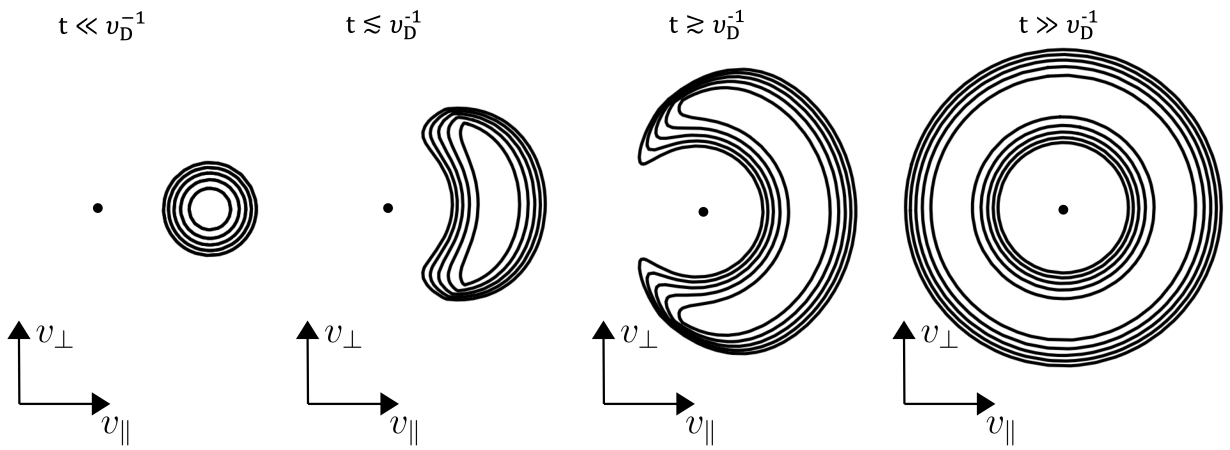


Figure 2.12: Depiction of contours of a beam-like DF subject to pitch-angle scattering due to collisions against a fixed Dirac-delta-like distribution.

where $\delta\mathcal{H}_\beta$ and $\delta\mathcal{G}_\beta$ are the Rosenbluth potentials sourced from δf_β.

The nonlinear component requires evaluating the full Fokker-Planck operator. For both local analytic transport calculations and the RKM of this work, the nonlinear component is neglected, but both the test-particle and field-particle terms are kept since they are both required to correctly reproduce local transport results.

2.4 Chapman-Enskog Expansion

The Chapman-Enskog expansion [15, 16, 72] is a formal mathematical procedure for finding transport coefficients of near-LTE kinetic systems, including neutral gases and plasmas. The Chapman-Enskog approach is valid where the system is highly collisional. Physically, this requires that relevant collision times and MFPs are much shorter than relevant hydrodynamic timescales and length scales, respectively.

2.4.1 Outline of procedure

To outline the general mathematical procedure, we write the Boltzmann equation for a single species in the form

$$\partial_t f + \hat{V} f = \frac{1}{\varepsilon} C\{f, f\}, \tag{2.75}$$

where $\hat{V} = \boldsymbol{v} \cdot \boldsymbol{\nabla} + (\boldsymbol{F}/m) \cdot \boldsymbol{\nabla}_{\boldsymbol{v}}$ is the Vlasov operator with a body force $\boldsymbol{F}$, and the parameter ε has been introduced to indicate the presence of a small parameter since collisions dominate. For $\varepsilon \ll 1$, a solution may be sought as a perturbation expansion in this small parameter

$$f = \sum_{n=0}^{\infty} \varepsilon^n f_n = f_0 + \varepsilon f_1 + \varepsilon^2 f_2 + \ldots, \tag{2.76}$$

alongside a multiple scales expansion of the time variable

$$t_n = \varepsilon^n t, \quad \text{i.e.} \quad t_0 = t,\ t_1 = \varepsilon t,\ t_2 = \varepsilon^2 t,\ \ldots \tag{2.77}$$

where t_n are treated as independent variables. The secular conditions

$$n = \int d^3\boldsymbol{v} f_0, \quad n\boldsymbol{u} = \int d^3\boldsymbol{v}\ \boldsymbol{v} f_0, \quad \frac{3}{2}nT = \int d^3\boldsymbol{v}\ \frac{1}{2}m(\boldsymbol{v}-\boldsymbol{u})^2 f_0, \tag{2.78}$$

are also required such that the fluid quantities are determined from the leading order term. Substituting into the Boltzmann equation yields

$$(\partial_{t_0} + \varepsilon\partial_{t_1} + \dots)(f_0 + \varepsilon f_1 + \dots) + \hat{V}(f_0 + \varepsilon f_1 + \dots) = \frac{1}{\varepsilon}C\{f_0 + \varepsilon f_1 + \dots,\ f_0 + \varepsilon f_1 + \dots\}. \tag{2.79}$$

To leading order $\mathcal{O}(\varepsilon^{-1})$, we obtain

$$0 = C\{f_0, f_0\}, \tag{2.80}$$

the solution of which is a Maxwellian $f_0 = f^M$ from the H-theorem. A Maxwellian distribution as described by Equation 2.67 has three free parameters, namely n, $\boldsymbol{u}$, and T. To describe the DF to leading order in ε, we do not need to solve Boltzmann's equation in its six-dimensional entirety, but instead only three evolution equations for these lowest moments called hydrodynamic or fluid equations. Taking the 1, $m\boldsymbol{v}$, and $\frac{1}{2}mv^2$ velocity moments of Equation 2.75 yields evolution equations for n, $\boldsymbol{u}$, and T. These fluid equations are

$$\begin{aligned}
\int d^3\boldsymbol{v}\ m(2.75): &\qquad \partial_t\rho + \boldsymbol{\nabla}\cdot(\rho\boldsymbol{u}) = 0,\\
\int d^3\boldsymbol{v}\ m\boldsymbol{v}\ (2.75): &\qquad \rho(\partial_t\boldsymbol{u} + \boldsymbol{u}\cdot\boldsymbol{\nabla}\boldsymbol{u}) = -\boldsymbol{\nabla}p - \boldsymbol{\nabla}\cdot\Pi + qn(\boldsymbol{E} + \boldsymbol{u}\times\boldsymbol{B}),\\
\int d^3\boldsymbol{v}\ \frac{1}{2}mv^2(2.75): &\quad \partial_t\left(\frac{3}{2}nT\right) + \boldsymbol{\nabla}\cdot\left(\frac{3}{2}nT\boldsymbol{u}\right) = -\boldsymbol{\nabla}\cdot\boldsymbol{q} - p\boldsymbol{\nabla}\cdot\boldsymbol{u} - \Pi\colon\boldsymbol{\nabla}\boldsymbol{u},
\end{aligned} \tag{2.81}$$

where $\rho = nm$ is the mass density, $p = nT$ is the thermal pressure, $\boldsymbol{q} = \int d^3\boldsymbol{v}\ \frac{1}{2}mw^2\boldsymbol{w}f$ is the heat flux, and $\Pi = \int d^3\boldsymbol{v}\ (\boldsymbol{w}\boldsymbol{w} - \frac{1}{3}w^2\mathrm{I})f$ is the viscous stress. These last two quantities $\boldsymbol{q}$ and $\hat{\Pi}$ are known as transport quantities, since they are responsible for transporting heat and momentum within the fluid. If these transport quantities are neglected, which is valid in the limit of infinite collisionality, the remaining set of equations are known as the Euler equations.

Due to the streaming operator $\boldsymbol{v}\cdot\boldsymbol{\nabla}f$ and interspecies collision operators, higher-order velocity moments than n, $\boldsymbol{u}$, and T are present in their evolution equations, leaving an underdetermined system of equations. The Chapman-Enskog method solves for f_1 as a perturbation away from Maxwellian, from which these higher-order velocity moments, or transport terms, may be evaluated. The next order $\mathcal{O}(1)$ term of Boltzmann's equation is

$$(\partial_{t_0} + \hat{V})f^M = C\{f_1, f^M\} + C\{f^M, f_1\} \equiv \hat{C}f_1 \tag{2.82}$$

This is a linear problem that may then be solved for f_1, and therefore transport quantities. Although required for the mathematical formalism, the expansion of timescales and terms $\mathcal{O}(\varepsilon^2)$ do not impact the evaluation of transport quantities in practice. Therefore, we instead write $f_1 = \delta f^{\text{local}}$ and write $t_0 = t$ to yield the local problem

$$(\partial_t + \hat{V})f^M = \hat{C}\delta f^{\text{local}}. \tag{2.83}$$

To apply the Chapman-Enskog approach to a plasma of electrons and ions, the same essential procedure as above is applied, but now to the VFP equation 2.31 of each species. Solving multiple coupled VFP equations brings additional complications, in particular new transport terms that exchange heat and momentum between species. For plasmas, the magnetic field term also introduces complications to both the fluid equations and the transport closures.

2.4.2 Multi-fluid equations

For N_s species with labels α, the set of fluid equations is [84, 85]

$$\begin{aligned}
\int d^3\boldsymbol{v}\; m_\alpha (2.31): &\qquad \partial_t \rho_\alpha + \boldsymbol{\nabla}\cdot(\rho_\alpha \boldsymbol{u}_\alpha) = 0, \\
\int d^3\boldsymbol{v}\; m_\alpha \boldsymbol{v}\; (2.31): &\qquad \rho_\alpha(\partial_t \boldsymbol{u}_\alpha + \boldsymbol{u}_\alpha\cdot\boldsymbol{\nabla}\boldsymbol{u}_\alpha) = -\boldsymbol{\nabla}p_\alpha - \boldsymbol{\nabla}\cdot\Pi_\alpha + q_\alpha n_\alpha(\boldsymbol{E} + \boldsymbol{u}_\alpha\times\boldsymbol{B}) + \sum_\beta \boldsymbol{R}_{\alpha\beta}, \\
\int d^3\boldsymbol{v}\; \frac{1}{2}m_\alpha v^2\; (2.31): &\qquad \frac{3}{2}n_\alpha(\partial_t T_\alpha + \boldsymbol{u}_\alpha\cdot\boldsymbol{\nabla}T_\alpha) = -\boldsymbol{\nabla}\cdot\boldsymbol{q}_\alpha - p_\alpha\boldsymbol{\nabla}\cdot\boldsymbol{u}_\alpha - \Pi_\alpha : \boldsymbol{\nabla}\boldsymbol{u}_\alpha + \sum_\beta \tilde{W}_{\alpha\beta}
\end{aligned} \tag{2.84}$$

For each species α, the set of 5 equations are identical to the single fluid case (Equation 2.81) but with additional source terms that exchange momentum ($\boldsymbol{R}_{\alpha\beta}$) and heat ($\tilde{W}_{\alpha\beta}$) between species. The set of N_s fluid equations for a general gas mixture may be evolved in time with these interspecies coupling terms.

2.4.3 Fluid equations for ionic mixtures

In a collisional plasma with species with similar masses, such as ions in a plasma, the momentum exchange $\boldsymbol{R}_{\alpha\beta}$ and heat exchange $\tilde{W}_{\alpha\beta}$ are dominant unless there is a large separation in flows $|\boldsymbol{u}_\alpha - \boldsymbol{u}_\beta| \ll v_{\text{th},\alpha}$ or temperatures $|T_\alpha - T_\beta| \ll T_\alpha$. Between two Maxwellians, the exchange terms have the form

$$\boldsymbol{R}^M_{\alpha\beta} = -\bar{\nu}^{\alpha\beta}_s \rho_\alpha(\boldsymbol{u}_\alpha - \boldsymbol{u}_\beta), \quad \tilde{W}^M_{\alpha\beta} = -\bar{\nu}^{\alpha\beta}_\epsilon n_\alpha(T_\alpha - T_\beta), \tag{2.85}$$

where the momentum and heat exchange frequencies are comparable to the basic collision frequency $\bar{\nu}^{\alpha\beta}_s \sim \bar{\nu}^{\alpha\beta}_\epsilon \sim \hat{\nu}_{\alpha\beta}$ [76]. If the flows or temperatures are disparate between species, these terms then quickly relax the two distributions to near-LTE where the flows and temperatures are similar. For a near-LTE collisional plasma with multiple ion species, the deviation of their flows away from their CoM velocity should then be much smaller than their thermal velocities, and their temperatures should be roughly equal. This suggests that instead of solving this set of equations $(1+3+1)N_s = 5N_s$ for the density, flow, and temperature of each individual ion species, a reduced set of $N_s + 3 + 1 = N_s + 4$ equations may be solved for each species' density and a CoM velocity and common ion temperature. This approach, known as the mixture formalism, has the clear advantage of solving for fewer fluid variables, and therefore evolving fewer PDEs than the multi-fluid formalism.

There are additional advantages of the mixture formalism over the multi-fluid formalism. Since the characteristic timescale on which these momentum exchange and heat exchange terms act is the collision time

$\tau_{\alpha\beta} \sim \hat{\nu}_{\alpha\beta}^{-1}$, this timescale should be resolved in a fluid simulation to capture multi-species effects such as diffusion. When simulating a collisional plasma, this timestep may be very restrictive. The mixture formalism can be viewed as the quasistatic approximation of these momentum and heat exchange processes which naturally orders out these short collisional timescales. The mixture formalism also has multi-species effects such as diffusion that appear explicitly through transport quantities, whereas in the multi-fluid formalism these effects are not explicit but result from an interplay of flows and momentum exchanges. It is therefore easier to study these multi-species effects through the mixture framework.

This set of fluid equations for the electrons and ionic mixture then require a closure for the electric and magnetic fields $\boldsymbol{E}$ and $\boldsymbol{B}$ and the transport quantities $\boldsymbol{V}_\alpha$, $\boldsymbol{R}_e$, $\Pi_{e,i}$, $\boldsymbol{q}_{e,i}$, and $\tilde{W}_{ie}$. The closure for the electromagnetic fields may be provided by Maxwell's equations. Most of these transport quantities vanish identically for a Maxwellian distribution due to its isotropy, therefore to leading order are determined from the next term in the perturbation expansion δf_α. The order $\mathcal{O}(\varepsilon)$ equation of the Chapman-Enskog expansion then provides a set of equations which, when solved, provide δf_α, and therefore a closure to these transport quantities.

The exceptions to the above statement are the momentum exchange $\boldsymbol{R}_e$ and heat exchange $\tilde{W}_{ie}$ terms between electrons and ions. The ion-electron heat exchange can be evaluated between an electron and ion Maxwellian with different temperatures to leading order, with corrections from δf_e and δf_i being negligible. In contrast, the momentum exchange $\boldsymbol{R}_e$ can be evaluated between an electron and ion Maxwellian with different flows, but the correction from δf_e is of the same order so must still be accounted for.

The ionic mixture equations are derived in Appendix A by directly taking the relevant mixture moments of the VFP equation, as opposed to first taking individual species moments to obtain the multi-fluid equations, then combining to form the mixture equations. The resulting mixture equations are

$$\begin{aligned}
\int d^3\boldsymbol{v}\; m_\alpha (2.31): \qquad & \partial_t \rho_\alpha + \boldsymbol{\nabla}\cdot(\rho_\alpha(\boldsymbol{u}_i + \boldsymbol{V}_\alpha)) = 0, \\
\sum_\alpha \int d^3\boldsymbol{v}\; m_\alpha \boldsymbol{v}\; (2.31): \qquad & \rho_i(\partial_t \boldsymbol{u}_i + \boldsymbol{u}_i\cdot\boldsymbol{\nabla}\boldsymbol{u}_i) = -\boldsymbol{\nabla} p_i - \boldsymbol{\nabla}\cdot\Pi_i \\
& \qquad + \sigma_i(\boldsymbol{E} + \boldsymbol{u}_i\times\boldsymbol{B}) + \boldsymbol{j}_D\times\boldsymbol{B} - \boldsymbol{R}_e, \\
\sum_\alpha \int d^3\boldsymbol{v}\; \frac{1}{2} m_\alpha v^2\; (2.31): \quad & \partial_t\left(\frac{3}{2} n_i T_i\right) + \boldsymbol{\nabla}\cdot\left(\frac{3}{2} n_i T_i \boldsymbol{u}_i\right) = -\boldsymbol{\nabla}\cdot\boldsymbol{q}_i - p_i \boldsymbol{\nabla}\cdot\boldsymbol{u}_i - \Pi_i : \boldsymbol{\nabla}\boldsymbol{u}_i \\
& \qquad + \boldsymbol{j}_D\cdot(\boldsymbol{E} + \boldsymbol{u}_i\times\boldsymbol{B}) + \tilde{W}_{ie},
\end{aligned} \tag{2.86}$$

where $\rho_i = \sum_\alpha \rho_\alpha$ is the total ion density, $\boldsymbol{u}_i = \sum_\alpha \frac{\rho_\alpha}{\rho_i}\boldsymbol{u}_\alpha$ is the ion CoM velocity, $\sigma_i = \sum_\alpha q_\alpha n_\alpha$ is the ion charge density, and $\boldsymbol{j}_D = \sum_\alpha q_\alpha n_\alpha \boldsymbol{V}_\alpha$ is the current associated with ionic diffusion. The rest of this work proceeds with the mixture formalism rather than the multi-fluid formalism, although the RKM could likely be formulated within the multi-fluid formalism without major additional complications.

2.4.4 Fluid equations for electrons

The electron fluid equations are

$$\begin{aligned}\partial_t \rho_e + \boldsymbol{\nabla}\cdot(\rho_e \boldsymbol{u}_e) &= 0\\ \rho_e(\partial_t \boldsymbol{u}_e + \boldsymbol{u}_e\cdot\boldsymbol{\nabla}\boldsymbol{u}_e) &= -\boldsymbol{\nabla}p_e - \boldsymbol{\nabla}\cdot\Pi_e - en_e(\boldsymbol{E}+\boldsymbol{u}_e\times\boldsymbol{B}) + \boldsymbol{R}_e\\ \partial_t\left(\frac{3}{2}n_eT_e\right) + \boldsymbol{\nabla}\cdot\left(\frac{3}{2}n_eT_e\boldsymbol{u}_e\right) &= -\boldsymbol{\nabla}\cdot\boldsymbol{q}_e - p_e\boldsymbol{\nabla}\cdot\boldsymbol{u}_e - \Pi_e\colon\boldsymbol{\nabla}\boldsymbol{u}_e - \tilde{W}_{ie} - \boldsymbol{R}_e\cdot(\boldsymbol{u}_e-\boldsymbol{u}_i).\end{aligned} \tag{2.87}$$

The set of electron and ionic mixture fluid equations may then be solved in tandem with Maxwell's equations for the mixture

$$\boldsymbol{\nabla}\cdot\boldsymbol{E} = (\sigma_i - en_e)/\varepsilon_0, \tag{2.88}$$

$$\boldsymbol{\nabla}\cdot\boldsymbol{B} = 0, \tag{2.89}$$

$$\boldsymbol{\nabla}\times\boldsymbol{E} = -\partial_t\boldsymbol{B}, \tag{2.90}$$

$$\boldsymbol{\nabla}\times\boldsymbol{B} = \mu_0\boldsymbol{j} + \mu_0\varepsilon_0\partial_t\boldsymbol{E}. \tag{2.91}$$

Fluid simulations rarely solve the fluid equations for the ionic mixture 2.86 and electrons 2.87 and Maxwell's equations for the electromagnetic fields 2.88 all together. Since electrons are much lighter than ions, they evolve on faster timescales and shorter lengthscales than ions and are thus often assumed to enforce quasineutrality ($n_e = \sum_\alpha Z_\alpha n_\alpha$) and be quasistatic, i.e. the left hand side of the momentum equation is zero. Similarly, the displacement current $\varepsilon_0\partial_t\boldsymbol{E}$ is also often neglected, leading to a magnetohydrodynamics (MHD) description.

2.5 Electron Transport

2.5.1 Physical description

Here, we consider an unmagnetised simple plasma to gain a physical understanding of local electron transport [15].

Heat conduction

Figure 2.13 illustrates the physical origin of the conductive heat flux. Particles travel a distance comparable to a MFP before colliding and depositing heat. Particles from the right and left will carry energies $E_\pm \sim T(z_0 \pm \lambda/2)$, respectively. For particles moving with a characteristic speed v, the flux of particles is $\sim nv$, the net flux of heat through the surface at $z = z_0$ is then

$$\boldsymbol{q}^T \sim (nvE_- - nvE_+)\hat{\boldsymbol{z}} \sim -nv\lambda\frac{T(z_0+\lambda/2) - T(z_0-\lambda/2)}{\lambda}\hat{\boldsymbol{z}} \sim -nv\lambda\frac{\partial T}{\partial z}\hat{\boldsymbol{z}} \sim -\kappa\boldsymbol{\nabla}T, \tag{2.92}$$

where we assume the spatial scales of interest are larger than the MFP λ so the derivative appears, and we have introduced the heat conductivity $\kappa \sim nv\lambda$. Taking the characteristic particle speed $v \sim v_{\text{th}} = \sqrt{2T/m}$ and MFP $\lambda \sim \lambda_{\text{th}} \propto T^2/n$ as their thermal values, we find that the heat conductivity in a plasma scales as

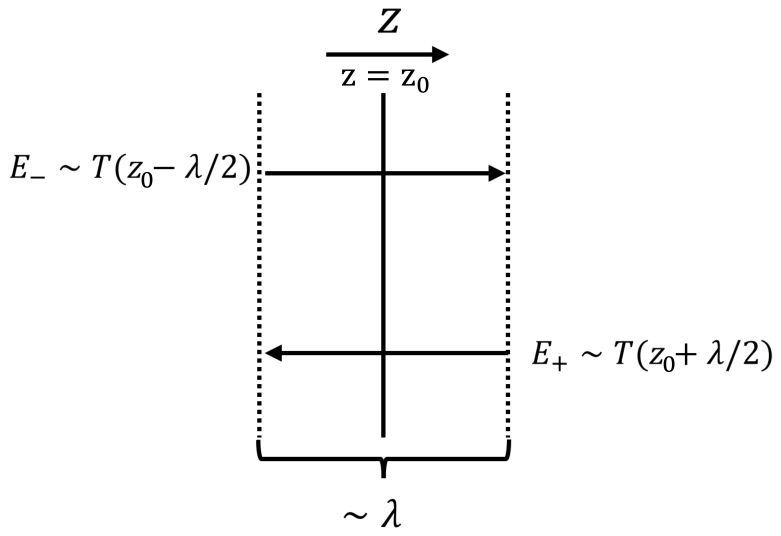


Figure 2.13: Two particles transporting energy through a surface at $z = z_0$.

$\kappa \sim nT\tau/m \propto T^{5/2}/\sqrt{m}$, and is independent of density. Since this argument is true for either electrons and ions, and electrons and ions typically have similar temperatures $T_i \sim T_e$, the electron heat flux is often dominant over the ion heat flux ($\kappa_e \gg \kappa_i$ and $|\boldsymbol{q}_e^T| \gg |\boldsymbol{q}_i^T|$) for weak and moderate magnetic fields $\chi_e \lesssim 1$.

This derivation is only intended to illustrate the physics and scaling behind heat conduction, and does not provide the numerical prefactor $\hat{\kappa}$ in front of $\boldsymbol{q}^T = -\hat{\kappa}\frac{nT\tau}{m}\boldsymbol{\nabla}T$. Even if a more detailed but similar calculation is carried out, accounting for velocity-dependence of the MFP, the Maxwellian distribution of particles, and angular distribution, the final answer would still be incorrect. To obtain the correct numerical prefactor for the heat conductivity, the VFP equation must be solved for δf, from which the heat flux and conductivity may be determined.

Dynamic friction

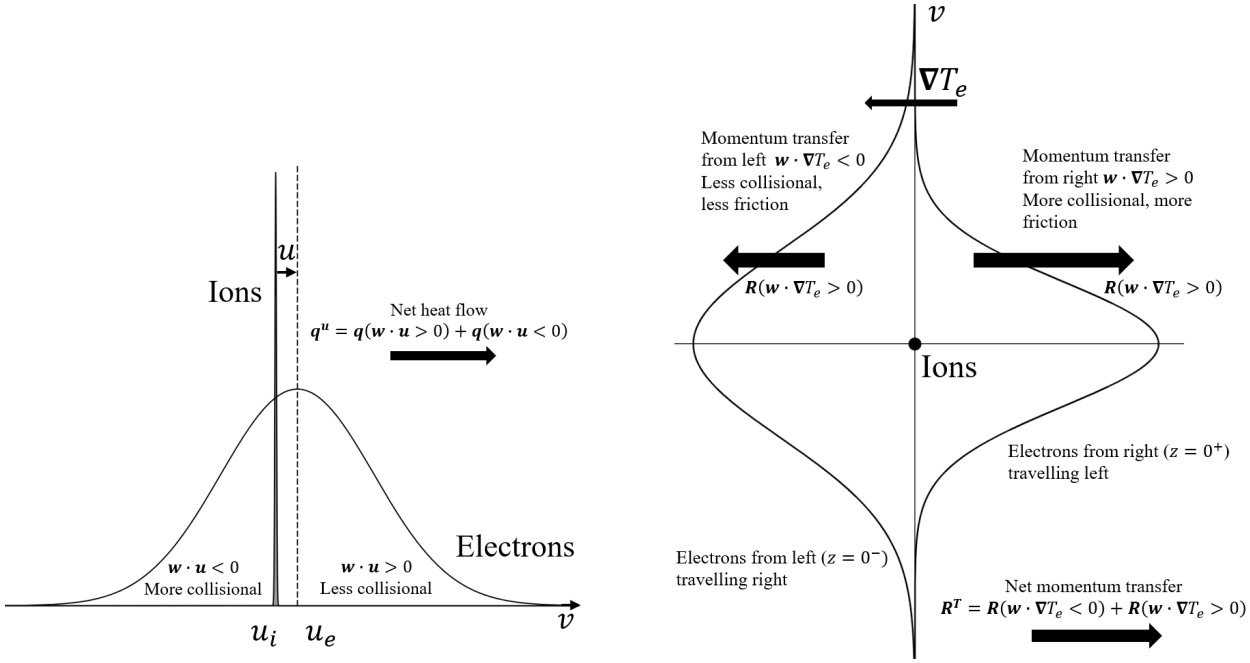
Let us now consider an electron population with a net relative flow $\Delta\boldsymbol{u} = \boldsymbol{u}_e - \boldsymbol{u}_i$ against the ion population. Since the ions are much heavier than electrons and Coulomb collisions are elastic, collisions of electrons against ions only change the direction and not the speed of electrons. The electrons therefore gradually lose their relative flow $\Delta\boldsymbol{u}$ on the timescale of the electron-ion collision time τ_{ei}. Each electron loses a momentum $m_e\Delta\boldsymbol{u}$ during this time, so there is a force per unit volume

$$\boldsymbol{R}_e^u \sim -\frac{n_e m_e}{\tau_{ei}}\Delta\boldsymbol{u}, \tag{2.93}$$

which is the origin of the friction force $\boldsymbol{R}_e^u$. Braginskii defines the electron-ion collision time τ_{ei} such that the numerical prefactor here is unity when evaluated between an electron and ion Maxwellian. Even though the friction force between Maxwellians with different mean velocities is nonzero, the next order correction to the electron DF δf_e has an additional contribution to the same order, leaving again a nontrivial numerical prefactor.

Peltier heat flux

If the collision frequency was independent of particle velocity, these above terms (heat flux driven by temperature gradients $\boldsymbol{q}^T \propto -\boldsymbol{\nabla} T$ and friction driven by flows $\boldsymbol{R}_e^u \propto -\Delta \boldsymbol{u}$) would be the only electron transport fluxes. However, since the electron-ion collision frequency is velocity-dependent $\nu_{ei} \propto 1/|\boldsymbol{v} - \boldsymbol{u}_i|^3$, there are additional 'off-diagonal' transport terms where flows drive heat flux $\boldsymbol{q}_e^u \propto \Delta \boldsymbol{u}$ and temperature gradients drive an electron-ion momentum exchange $\boldsymbol{R}_e^T$.



(a) Current-driven heat flow

(b) Thermal force

Figure 2.14: Physical origin of 'off-diagonal' transport terms $\boldsymbol{q}_e^u$ and $\boldsymbol{R}_e^T$.

Figure 2.14(a) illustrates an electron and ion Maxwellian with relative drift $\Delta \boldsymbol{u}$. In the electron's frame $\boldsymbol{w} = \boldsymbol{v} - \boldsymbol{u}_e$, we compare the two halves of the electron population moving with $\boldsymbol{w} \cdot \Delta \boldsymbol{u} > 0$ and against $\boldsymbol{w} \cdot \Delta \boldsymbol{u} < 0$ the relative flow (on the right and left of the dashed line, respectively). The population moving with the flow $\boldsymbol{w} \cdot \Delta \boldsymbol{u} > 0$ is, on average, less collisional against the ions than the half moving against the flow $\boldsymbol{w} \cdot \Delta \boldsymbol{u} < 0$, and therefore the heat flux carried by these two halves do not perfectly cancel. There will therefore be a current-driven heat flux

$$\boldsymbol{q}_e^u \sim n_e T_e \Delta \boldsymbol{u} \tag{2.94}$$

in the direction of the relative flow, since the $\boldsymbol{w} \cdot \Delta \boldsymbol{u} > 0$ side of the population is less collisional.

Thermal force

Figure 2.14(b) illustrates an electron Maxwellian from a slightly hotter (left) and slightly cooler (right) part of the plasma. Similarly to the origin of the current-driven heat flux, these two halves of the electron population

are considered. The population from $z = 0^{\pm}$ experience friction forces $R_{\pm} \sim -\frac{n_e m_e v_{\mathrm{th},e}}{\tau_{ei}}\big|_{\pm}$ against the background ions. The difference in these forces then leaves the momentum exchange

$$\boldsymbol{R}_e^T = \boldsymbol{R}_+ - \boldsymbol{R}_- \sim -\frac{n_e m_e v_{\mathrm{th},e}}{\tau_{ei}} \frac{\lambda_{\mathrm{th},e}}{T_e} \boldsymbol{\nabla} T_e \sim -n_e \boldsymbol{\nabla} T_e, \tag{2.95}$$

known as the thermal force. Although $\boldsymbol{q}_e^u$ and $\boldsymbol{R}_e^T$ do not have the collision time appearing explicitly in their expressions, they are still collisional phenomena. The thermal force is of comparable order as pressure gradients $|\boldsymbol{R}_e^T| \sim n_e T_e / L \sim |\boldsymbol{\nabla} p_e|$, therefore is significant in a wide variety of collisional plasmas.

Magnetised transport

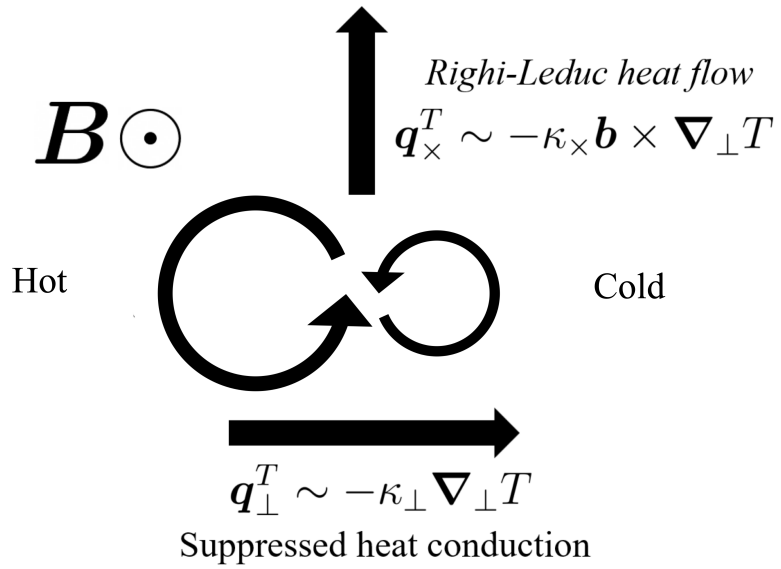


Figure 2.15: Magnetised electron heat conduction. For ions, the direction of the gyro-orbits is reversed so the ion Righi-Leduc heat flow is in the $+\boldsymbol{b} \times \boldsymbol{\nabla} T_i$ direction.

Magnetic fields cause electrons to undergo gyro-orbits around the magnetic field lines, suppressing heat transport in the direction perpendicular to the field. The component of the transport flux parallel to the magnetic field is unaffected. The gyro-orbits also generate particle motion in the direction perpendicular to both the magnetic field and temperature gradient or relative flow, therefore an additional 'cross' component to each of the above transport fluxes is gained in this direction. For the conductive heat flux, this is illustrated in Figure 2.15; magnetic fields suppress heat transfer down the temperature gradient, but the imbalance of gyromotion (shown here for electrons) between the hot and cold sides yields an additional component of heat flow in the $\boldsymbol{b} \times (-\boldsymbol{\nabla} T_e)$ direction.

2.5.2 Local problem

The first order Chapman-Enskog equation, analogous to Equation 2.83, for electrons [15] is

$$\begin{aligned} &f_e^M \left(\left[\boldsymbol{R}_e / p_e + \left(\frac{w^2}{v_{\mathrm{th},e}^2} - \frac{5}{2} \right) \boldsymbol{\nabla} \ln T_e \right] \cdot \boldsymbol{w} + \frac{2}{v_{\mathrm{th},e}^2} \boldsymbol{\nabla} \boldsymbol{u}_e : \left(\boldsymbol{w}\boldsymbol{w} - \frac{1}{3} w^2 \mathrm{I} \right) \right) - C_{ei}^M \\ &= \hat{C}_{ee} \delta f_e^{\mathrm{local}} + \hat{C}_{ei} \delta f_e^{\mathrm{local}} + \frac{e}{m_e} (\boldsymbol{w} \times \boldsymbol{B}) \cdot \boldsymbol{\nabla}_{\boldsymbol{w}} \delta f_e^{\mathrm{local}}, \end{aligned} \tag{2.96}$$

where $C_{ei}^M = C_{ei}\{f_e^M, f_i^M\}$. This linear problem can then be solved directly for $\delta f_e^{\text{local}}$ from which local transport fluxes are evaluated. This derivation, provided in Appendix C for the vectorial fluxes, is reasonably mathematically involved. To get a taste of a local transport calculation without the mathematical complexity of the full derivation, let us consider the example of an unmagnetised plasma in the Lorentz limit ($Z \gg 1$) with viscosity ignored.

2.5.3 Transport calculation for a Lorentz plasma

In the Lorentz limit, electron-ion collisions dominate over electron-electron collisions. This leaves only the electron-ion collision operator which has the analytically simple form

$$\hat{C}_{ei} f_e = \frac{\hat{\nu}_{ei}}{2\xi^3}\hat{\mathcal{L}} f_e = \frac{3\sqrt{\pi}}{8\tau_{ei}}\frac{1}{\xi^3}\hat{\mathcal{L}} f_e. \tag{2.97}$$

Ignoring the term responsible for viscosity $\boldsymbol{\nabla}\boldsymbol{u}_e$, Equation 2.96 becomes

$$\left[\boldsymbol{R}_e/p_e + \frac{3\sqrt{\pi}}{4}\frac{v_{\text{th},e}}{\tau_{ei}w^3}\Delta\boldsymbol{u} + \left(\frac{w^2}{v_{\text{th},e}^2} - \frac{5}{2}\right)\boldsymbol{\nabla}\ln T_e\right]\cdot\boldsymbol{w} f_e^M = \frac{3\sqrt{\pi}}{8\tau_{ei}}\frac{1}{\xi^3}\hat{\mathcal{L}}\delta f_e, \tag{2.98}$$

where $\boldsymbol{\xi} = \boldsymbol{w}/v_{\text{th},e}$ and we have used the form of C_{ei}^M derived in Appendix B. We recognise that there are only two independent thermodynamic drives on the left hand side: $\Delta\boldsymbol{u}$ and $\boldsymbol{\nabla}\ln T_e$. The momentum exchange $\boldsymbol{R}_e$ is not an independent thermodynamic force since it is determined from δf_e as

$$\boldsymbol{R}_e = \int d^3\boldsymbol{v}\, m_e\boldsymbol{v} C_{ei}\{f_e, f_i\}, \tag{2.99}$$

and therefore from $\Delta\boldsymbol{u}$ and $\boldsymbol{\nabla}T_e$. Although we may write out this explicitly and solve the remaining integral problem, an alternative approach is to write the momentum exchange as

$$\boldsymbol{R}_e = -\hat{\alpha}_L\frac{n_e m_e}{\tau_{ei}}\Delta\boldsymbol{u} - \hat{\beta}_L n_e\boldsymbol{\nabla}T_e, \tag{2.100}$$

with the dimensional prefactors based on the physical arguments above, with the Lorentz transport coefficients $\hat{\alpha}_L$ and $\hat{\beta}_L$ being determined self-consistently later. If the form of these dimensional prefactors was not known beforehand, we could still write an uninformed linear combination of the thermodynamic drives $\boldsymbol{R}_e = -A\Delta\boldsymbol{u} - B\boldsymbol{\nabla}T_e$ and determine the coefficients A and B in an identical manner.

Since $\boldsymbol{\xi}$ is an eigenfunction of the pitch-angle scattering operator via $\hat{\mathcal{L}}(f(\xi)\hat{\boldsymbol{\xi}}) = -2f(\xi)\hat{\boldsymbol{\xi}}$, we are motivated to provide an ansatz

$$\delta f_e = -\left[\phi^u(\xi)\frac{\Delta\boldsymbol{u}}{v_{\text{th},e}} + \phi^T(\xi)v_{\text{th},e}\tau_{ei}\boldsymbol{\nabla}\ln T_e\right]\cdot\hat{\boldsymbol{\xi}} f_e^M, \tag{2.101}$$

constructed such that $\phi^u(\xi)$ and $\phi^T(\xi)$ are dimensionless scalar functions of ξ corresponding to the two independent thermodynamic drives. Substituting in, we obtain the solutions for each function by straightforward algebra as

$$\phi^u(\xi) = 2\left(\xi - \frac{4}{3\sqrt{\pi}}\hat{\alpha}_L\xi^4\right), \quad \phi^T(\xi) = \frac{4}{3\sqrt{\pi}}\xi^4\left(\xi^2 - \frac{5}{2} - \hat{\beta}_L\right). \tag{2.102}$$

In order to find the self-consistent $\hat{\alpha}_L$ and $\hat{\beta}_L$, we enforce the zero-flow condition in the CoM frame

$$\int d^3\boldsymbol{w}\, \boldsymbol{w}\delta f_e = 0 \quad \Rightarrow \quad \int_0^\infty d\xi\, e^{-\xi^2}\xi^3\phi^{u,T}(\xi). \tag{2.103}$$

Enforcing this condition yields

$$\hat{\alpha}_L = \frac{3\sqrt{\pi}}{4}\frac{\int_0^\infty e^{-\xi^2}\xi^4 d\xi}{\int_0^\infty e^{-\xi^2}\xi^7 d\xi} = \frac{3\pi}{32}, \quad \hat{\beta}_L = \frac{\int_0^\infty e^{-\xi^2}\xi^7(\xi^2-5/2) d\xi}{\int_0^\infty e^{-\xi^2}\xi^7 d\xi} = \frac{3}{2}. \tag{2.104}$$

The solutions to the perturbed distribution are therefore

$$\phi^u(\xi) = 2\bigg(\xi - \frac{\sqrt{\pi}}{8}\xi^4\bigg), \quad \phi^T(\xi) = \frac{4}{3\sqrt{\pi}}\xi^4\bigg(\xi^2 - 4\bigg). \tag{2.105}$$

From these solutions, we then compute the transport fluxes, namely the momentum exchange and heat flux. The momentum exchange is

$$\begin{aligned}
\boldsymbol{R}_e &= -\frac{n_e m_e}{\tau_{ei}}\Delta\boldsymbol{u} + \int d^3\boldsymbol{w}\, m_e \boldsymbol{w}\hat{C}_{ei}\delta f_e && (2.106)\\
&= n_e m_e v_{\mathrm{th},e}\pi^{-3/2}\underbrace{\int d\Omega\, \hat{\boldsymbol{\xi}}\hat{\boldsymbol{\xi}}}_{=\frac{4\pi}{3}\mathrm{I}}\cdot\int_0^\infty d\xi\, \frac{3\sqrt{\pi}}{4\tau_{ei}}\bigg[\phi^u(\xi)\frac{\Delta\boldsymbol{u}}{v_{\mathrm{th},e}} + \phi^T(\xi)v_{\mathrm{th},e}\tau_{ei}\boldsymbol{\nabla}\ln T_e\bigg]e^{-\xi^2} && (2.107)\\
&= -\underbrace{\bigg(1 - \int_0^\infty d\xi\, 2\bigg(\xi - \frac{\sqrt{\pi}}{8}\xi^4\bigg)e^{-\xi^2}\bigg)}_{=3\pi/32=\hat{\alpha}_L}\frac{n_e m_e}{\tau_{ei}}\Delta\boldsymbol{u} + \underbrace{\frac{8}{3\sqrt{\pi}}\int_0^\infty d\xi\, \xi^4\bigg(\xi^2-4\bigg)e^{-\xi^2}}_{=-3/2=-\hat{\beta}_L} n_e\boldsymbol{\nabla}T_e && (2.108)\\
&= -\hat{\alpha}_L\frac{n_e m_e}{\tau_{ei}}\Delta\boldsymbol{u} - \hat{\beta}_L n_e\boldsymbol{\nabla}T_e, && (2.109)
\end{aligned}$$

which is self-consistent with the coefficients $\hat{\alpha}_L$ and $\hat{\beta}_L$ found earlier. The heat flux is

$$\begin{aligned}
\boldsymbol{q}_e &= \int d^3\boldsymbol{w}\, \frac{1}{2}m_e w^2\boldsymbol{w}\delta f_e && (2.110)\\
&= -n_e T_e v_{\mathrm{th},e}\frac{4}{3\sqrt{\pi}}\int_0^\infty d\xi\, \bigg[\phi^u(\xi)\frac{\Delta\boldsymbol{u}}{v_{\mathrm{th},e}} + \phi^T(\xi)v_{\mathrm{th},e}\tau_{ei}\boldsymbol{\nabla}\ln T_e\bigg]\xi^5 e^{-\xi^2} && (2.111)\\
&= \underbrace{-\frac{4}{3\sqrt{\pi}}\int_0^\infty d\xi\, 2\bigg(\xi - \frac{\sqrt{\pi}}{8}\xi^4\bigg)\xi^5 e^{-\xi^2}}_{=3/2=\hat{\beta}_L} n_e T_e\Delta\boldsymbol{u} - \underbrace{\frac{8}{3\sqrt{\pi}}\int_0^\infty d\xi\, \phi^T(\xi)\xi^5 e^{-\xi^2}}_{=128/3\pi\equiv\hat{\kappa}_L}\frac{n_e T_e\tau_{ei}}{m_e}\boldsymbol{\nabla}T_e && (2.112)\\
&= \hat{\beta}_L n_e T_e\Delta\boldsymbol{u} - \hat{\kappa}_L\frac{n_e T_e\tau_{ei}}{m_e}\boldsymbol{\nabla}T_e, && (2.113)
\end{aligned}$$

where the heat conductivity coefficient is $\hat{\kappa}_L = 128/3\pi$. From this simple calculation, we see that the expected effects of dynamic friction, thermal force, Peltier heat flow, and heat conduction emerge with the same scalings as argued earlier on physical grounds. The reappearance of $\hat{\beta}_L = 3/2$ is not a coincidence but a manifestation of Onsager symmetry. The coefficients of the thermal force and Peltier heat flow terms are then directly related.

Taking the unmagnetised Lorentz limit allowed for this simpler calculation where the perturbations $\phi^{u,T}$ can be solved for exactly by solving an algebraic equation. Magnetic fields can be included in the Lorentz limit and still leave an algebraic problem, but one that requires additional care with forming and solving equations with complex numbers. For finite Z, the resulting equations are now differential rather than algebraic. These

equations may be solved by direct numerical solutions to the equations [86] or, more commonly and elegantly, expanding the functions $\phi^{u,T}(\xi)$ over a set of orthogonal functions (the generalised Laguerre or Sonine polynomials), truncating the expansion, and solving the finite set of coefficients as a matrix problem [15]. This derivation is provided in Appendix C, and the resulting local closures for transport fluxes are summarised here.

2.5.4 Local closures

Electron vectorial fluxes

The local electron heat flux and momentum exchange may be written as the linear combination of thermodynamic drives $\boldsymbol{q}_e^{\text{local}} = \boldsymbol{q}_e^T + \boldsymbol{q}_e^u$ and $\boldsymbol{R}_e^{\text{local}} = \boldsymbol{R}_e^T + \boldsymbol{R}_e^u$. The closure for these four components are

$$\begin{aligned}
\boldsymbol{q}_e^T &= -\kappa_0^e\big(\underbrace{(\hat{\kappa}_\parallel \boldsymbol{bb} + \hat{\kappa}_\perp(\mathrm{I}-\boldsymbol{bb}))\cdot\boldsymbol{\nabla}T_e}_{\text{Heat conduction}} + \underbrace{\hat{\kappa}_\times \boldsymbol{b}\times\boldsymbol{\nabla}T_e}_{\text{Righi-Leduc}}\big) = -\kappa_0^e \underline{\underline{\hat{\kappa}}}\cdot\boldsymbol{\nabla}T_e,\\
\boldsymbol{q}_e^u &= n_e T_e\big(\underbrace{(\hat{\beta}_\parallel \boldsymbol{bb} + \hat{\beta}_\perp(\mathrm{I}-\boldsymbol{bb}))\cdot\Delta\boldsymbol{u}}_{\text{Peltier}} + \underbrace{\hat{\beta}_\times \boldsymbol{b}\times\Delta\boldsymbol{u}}_{\text{Ettingshausen}}\big) = n_e T_e \underline{\underline{\hat{\beta}}}\cdot\Delta\boldsymbol{u},\\
\boldsymbol{R}_e^T &= -n_e\big(\underbrace{(\hat{\beta}_\parallel \boldsymbol{bb} + \hat{\beta}_\perp(\mathrm{I}-\boldsymbol{bb}))\cdot\boldsymbol{\nabla}T_e}_{\text{Thermal force}} + \underbrace{\hat{\beta}_\times \boldsymbol{b}\times\boldsymbol{\nabla}T_e}_{\text{Nernst}}\big) = -n_e \underline{\underline{\hat{\beta}}}\cdot\boldsymbol{\nabla}T_e,\\
\boldsymbol{R}_e^u &= -\frac{n_e m_e}{\tau_{ei}}\big(\underbrace{(\hat{\alpha}_\parallel \boldsymbol{bb} + \hat{\alpha}_\perp(\mathrm{I}-\boldsymbol{bb}))\cdot\Delta\boldsymbol{u}}_{\text{Friction}} - \underbrace{\hat{\alpha}_\times \boldsymbol{b}\times\Delta\boldsymbol{u}}_{\text{Cross-friction}}\big) = -\frac{n_e m_e}{\tau_{ei}}\underline{\underline{\hat{\alpha}}}\cdot\Delta\boldsymbol{u},
\end{aligned} \tag{2.114}$$

where the dimensionless rank-2 tensors,

$$[\underline{\underline{\hat{\alpha}}}]_{ij} = \hat{\alpha}_\parallel b_i b_j + \hat{\alpha}_\perp(\delta_{ij} - b_i b_j) - \hat{\alpha}_\times \varepsilon_{ikj} b_k, \tag{2.115}$$

$$[\underline{\underline{\hat{\beta}}}]_{ij} = \hat{\beta}_\parallel b_i b_j + \hat{\beta}_\perp(\delta_{ij} - b_i b_j) + \hat{\beta}_\times \varepsilon_{ikj} b_k, \tag{2.116}$$

$$[\underline{\underline{\hat{\kappa}}}]_{ij} = \hat{\kappa}_\parallel b_i b_j + \hat{\kappa}_\perp(\delta_{ij} - b_i b_j) + \hat{\kappa}_\times \varepsilon_{ikj} b_k, \tag{2.117}$$

where ε_{abc} is the Levi-Civita symbol. In a local right-handed coordinate system with $\boldsymbol{b}$ aligned with the $\hat{\boldsymbol{z}}$ direction, these tensors may be written in matrix notation as

$$\underline{\underline{\hat{\alpha}}} = \begin{pmatrix} \hat{\alpha}_\perp & -\hat{\alpha}_\times & 0 \\ \hat{\alpha}_\times & \hat{\alpha}_\perp & 0 \\ 0 & 0 & -\hat{\alpha}_\parallel \end{pmatrix}, \quad \underline{\underline{\hat{\beta}}} = \begin{pmatrix} \hat{\beta}_\perp & -\hat{\beta}_\times & 0 \\ \hat{\beta}_\times & \hat{\beta}_\perp & 0 \\ 0 & 0 & \hat{\beta}_\parallel \end{pmatrix}, \quad \text{and} \quad \underline{\underline{\hat{\kappa}}} = \begin{pmatrix} \hat{\kappa}_\perp & -\hat{\kappa}_\times & 0 \\ \hat{\kappa}_\times & \hat{\kappa}_\perp & 0 \\ 0 & 0 & \hat{\kappa}_\parallel \end{pmatrix}. \tag{2.118}$$

The dimensionless coefficients $\hat{\alpha}_{(\parallel,\perp,\times)}$, $\hat{\beta}_{(\parallel,\perp,\times)}$, and $\hat{\kappa}_{(\parallel,\perp,\times)}$ depend only on the effective ionisation $Z^* = \sum_\alpha \frac{n_\alpha Z_\alpha^2 \ln\Lambda_{e\alpha}}{n_e \ln\Lambda_{ee}}$[2] and, for perpendicular $\perp$ and cross $\times$ terms, the Hall parameter $\chi = \omega_{\mathrm{c},e}\tau_{ee}$. Braginskii gives fits for these coefficients as functions of (Z,χ). This work compares with the coefficients given by Ji and Held [87, 88] which are provided as Padé approximants that are extremely well converged ($\lesssim 0.1\%$) over the number of Sonine polynomials kept in the expansion of δf_e or δf_i. The electron transport fluxes are summarised in Table 2.1 and a derivation for these local transport terms and coefficients can be found in Appendix C.

[2] In an ionic mixture, the electrons 'see' only the effective ionisation Z^* equivalent to a simple plasma with ionisation $Z = Z^*$, so these symbols are often used interchangably for results on electron transport.

		Electron transport flux	
		Heat flux $\boldsymbol{q}_e$	Momentum exchange $\boldsymbol{R}_e$
Thermodynamic drive	Temperature gradient $-\boldsymbol{\nabla} T_e$	Heat conduction $\hat{\kappa}_{(\parallel,\perp)}$, *Righi-Leduc* $\hat{\kappa}_\times$	Thermal force $\hat{\beta}_{(\parallel,\perp)}$, *Nernst force* $\hat{\beta}_\times$
	Relative flow (current) $\Delta \boldsymbol{u}$	Peltier $\hat{\beta}_{(\parallel,\perp)}$, *Ettingshausen* $\hat{\beta}_\times$	Dynamic friction $\hat{\alpha}_{(\parallel,\perp)}$, *cross-friction* $\hat{\alpha}_\times$

Table 2.1: Summary of local vectorial electron transport. The 'cross' $\times$ terms gained in the $\boldsymbol{b} \times (-\boldsymbol{\nabla} T_e, \Delta \boldsymbol{u})$ direction are shown in italics. The relevant transport coefficients for each term are also indicated, highlighting the Onsager symmetry between the off-diagonal terms.

2.5.5 Single species ion transport

Heat conduction

The local ion heat flux in a simple plasma has the form

$$\boldsymbol{q}_i^T = -\kappa_c^i \big(\underbrace{(\hat{\kappa}_\parallel^i \boldsymbol{bb} + \hat{\kappa}_\perp^i (\mathrm{I} - \boldsymbol{bb})) \cdot \boldsymbol{\nabla} T_i}_{\text{Heat conduction}} - \underbrace{\hat{\kappa}_\times^i \boldsymbol{b} \times \boldsymbol{\nabla} T_i}_{\text{Righi-Leduc}} \big), \tag{2.119}$$

where $\hat{\kappa}^i_{(\parallel,\perp,\times)}$ are a similar set of dimensionless coefficients [88]. In Braginskii's work, where ion-electron collisions are neglected, the dimensionless coefficient $\hat{\kappa}^i_\parallel / \sqrt{2} = 3.906$ is a constant, i.e. even independent of ionisation. However, as shown by Ji and Held, ion-electron collisions have a non-negligible impact on ion transport which leads to a dependence of $\hat{\kappa}^i_{(\parallel,\perp,\times)}$ on the combination $\frac{1}{Z}\sqrt{\frac{m_e}{m_i}}$ and temperature ratio $\frac{T_i}{T_e}$. Ion-electron collisions noticeably suppress these ion transport coefficients by $\sim 10\%$ even for equal electron and ion temperatures $T_i = T_e$. For hotter ions $T_i > T_e$, this suppression becomes even more pronounced. These effects are readily included in the RKM.

Viscous stress

Viscous stress, the anisotropic component of the pressure tensor, is another transport quantity that requires a closure within a hydrodynamic framework. In an ideal plasma, ion viscous stress almost always dominates over electron viscous stress; therefore, it is only considered here in the context of ions.

Consider a species with a shearing flow profile $\boldsymbol{u} = u_x(y)\hat{\boldsymbol{x}}$ as depicted in Figure 2.16. A particle from the faster region of flow $y = y_0 + \lambda/2$ may stream kinetically, as opposed to hydrodynamically, to a slower

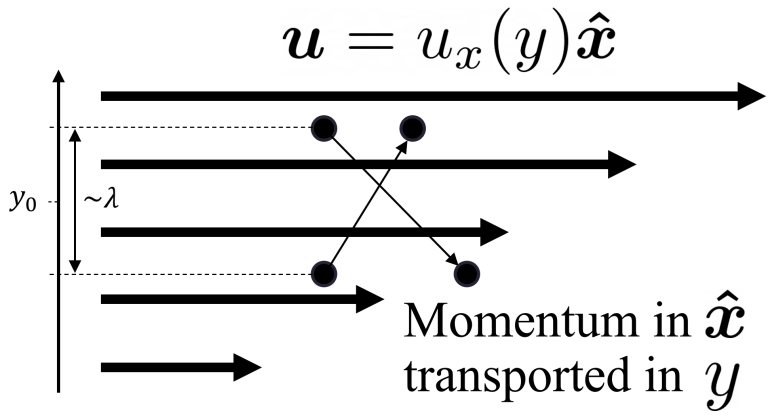


Figure 2.16: Physical origin of viscous stress.

region of flow $y = y_0 - \delta y$. This particle carries a momentum $\hat{\boldsymbol{x}}$-direction momentum $\sim mu_x(y_0 + \lambda/2)\hat{\boldsymbol{x}}$. It streams roughly a MFP $\sim \lambda$ before colliding. Again considering a total particle flux $\sim nv$, with particles travelling in the other direction carrying a momentum $mu_x(y_0 - \lambda/2)\hat{\boldsymbol{x}}$, the overall $\hat{\boldsymbol{x}}$-direction momentum transported through the surface $y = y_0$ is

$$\Pi_{yx} \sim nvm(u_x(y_0 - \lambda/2) - u_x(y_0 + \lambda/2)) = -nvm\lambda\frac{u_x(y_0 + \lambda/2) - u_x(y_0 - \lambda/2)}{\lambda} \sim -nvm\lambda\frac{\partial u_x}{\partial y}. \tag{2.120}$$

As before, the characteristic speed is the thermal velocity $v \sim v_{\text{th}} \sim \sqrt{T/m}$ and distance transported before colliding is a MFP $\lambda \sim v_{\text{th}}\tau$, leaving

$$\Pi_{yx} \sim -\eta\frac{\partial u_x}{\partial y}, \quad \eta \sim nT\tau, \tag{2.121}$$

which introduces the viscosity $\eta \sim nT\tau$. More generally, the viscous stress is a rank-two tensor $\Pi \sim -\eta\boldsymbol{\nabla}\boldsymbol{u}$. Ion viscous stress typically dominates electron viscous stress since $|\Pi^i/\Pi^e| \sim \eta_i/\eta_e \sim \tau_i/\tau_e \sim \sqrt{m_i/m_e} \gtrsim 40$.

Braginskii's closure for the ion viscous stress tensor, valid for order-unity Mach number, can be expressed in the form

$$\Pi_i^{\text{local}} = -\eta_c^i\Big(\underbrace{\hat{\eta}_0^i\mathrm{W}_0^i + \hat{\eta}_1^i\mathrm{W}_1^i + \hat{\eta}_2^i\mathrm{W}_2^i}_{\text{Ordinary viscous stress}}\underbrace{-\hat{\eta}_3^i\mathrm{W}_3^i - \hat{\eta}_4^i\mathrm{W}_4^i}_{\text{Gyroviscous stress}}\Big) \tag{2.122}$$

where $\eta_c^i = n_iT_i\tau_{ii}$ is the basic viscosity and $\hat{\eta}_{(0,\ldots,4)}^i$ are a set of dimensionless viscosity coefficients. $\mathrm{W}_{(0,\ldots,4)}^i$ are various contractions of $\boldsymbol{b}$ with the ion rate-of-strain tensor $\mathrm{W}^i = \boldsymbol{\nabla}\boldsymbol{u}_i + (\boldsymbol{\nabla}\boldsymbol{u}_i)^{\mathrm{T}} - \frac{2}{3}(\boldsymbol{\nabla}\cdot\boldsymbol{u}_i)\mathrm{I}$, defined by Braginskii as

$$\mathrm{W}_{0,ab}^i = \frac{3}{2}\left(b_ab_b - \frac{1}{3}\delta_{ab}\right)\left(b_cb_d - \frac{1}{3}\delta_{cd}\right)\mathrm{W}_{cd}^i,$$
$$\mathrm{W}_{1,ab}^i = \left(\delta_{ac}^\perp\delta_{bd}^\perp + \frac{1}{2}\delta_{ab}^\perp b_cb_d\right)\mathrm{W}_{cd}^i,$$

$$\begin{aligned}
\mathrm{W}^i_{2,ab} &= \left(\delta^\perp_{ac} b_b b_d + \delta^\perp_{bd} b_a b_c\right) \mathrm{W}^i_{cd}, \\
\mathrm{W}^i_{3,ab} &= \frac{1}{2}\left(\delta^\perp_{ac} \varepsilon_{bed} + \delta^\perp_{bd} \varepsilon_{aec}\right) h_e \mathrm{W}^i_{cd}, \\
\mathrm{W}^i_{4,ab} &= \left(b_a b_c \varepsilon_{bed} + b_b b_d \varepsilon_{aec}\right) h_e \mathrm{W}^i_{cd}.
\end{aligned} \tag{2.123}$$

where index summation convention is employed, $\delta^\perp_{ab} \equiv \delta_{ab} - b_a b_b$ is the rejection dyad, and ε_{abc} is the Levi-Civita symbol. Similarly to the vectorial transport fluxes, this local closure contains parallel, perpendicular, and cross terms [89]. The coefficient $\hat{\eta}^i_0$ is independent of the Hall parameter since it represents the parallel components unaffected by the magnetic field. The $\hat{\eta}^i_{(1,2)}$ terms represent the perpendicular components of the viscous stress tensor suppressed by the magnetic field. The $\hat{\eta}^i_{(3,4)}$ terms are the additional cross components gained due to gyromotion, analogously to the cross components of vectorial transport fluxes such as the Righi-Leduc term.

2.5.6 Heat exchange

Finally, the ion-electron heat exchange [15, 85] has the closure

$$\tilde{W}_{ie} = \frac{4}{\sqrt{\pi}} n_e \hat{\nu}_{ei} \frac{m_e}{m_i} (T_e - T_i), \tag{2.124}$$

which is directly evaluated from Maxwellian distributions since the leading order Chapman-Enskog solution contains no $l = 0$ term and therefore does not provide a leading order correction to $\tilde{W}_{ie}$. Since the heat exchange is not dependent on $\delta f_{(e,i)}$ to leading order in m_e/m_i or N_K, it is not studied in a nonlocal context.

2.6 Ionic Mixture Transport

Considering the heat flux in a multi-species plasma has further complications in comparison to the single species case. A single species may only experience self-collisions whereas multi-species transport requires also considering collisions with other species. For electron transport described above, electron-ion collisions are significant and included. However, the significant mass disparity between electrons and ions means that the electron-ion collision operator does not depend on the non-Maxwellian part of the ion distribution to leading order, therefore is effectively a single species problem requiring solving a single VFP equation. The same is not true when solving for multi-species ion transport where there is a set of coupled kinetic equations which must be solved simultaneously. Furthermore, different species in mixtures diffuse in the CoM frame which gives rise to an additional source of heat transport of generally comparable magnitude. Experimental evidence for various types of ICF implosions indicates that multi-species effects can directly affect the yield [90–93], further motivating the present study.

Ion transport becomes magnetised when the ion Hall parameter $\chi_i = \omega_{\mathrm{c},i}\tau_{ii} \gtrsim 1$. Due to the large mass ratio between electrons and ions, much stronger magnetic fields are required to magnetise ions. Ion transport results in this work mostly focus on unmagnetised cases, but magnetised ion transport is still described by

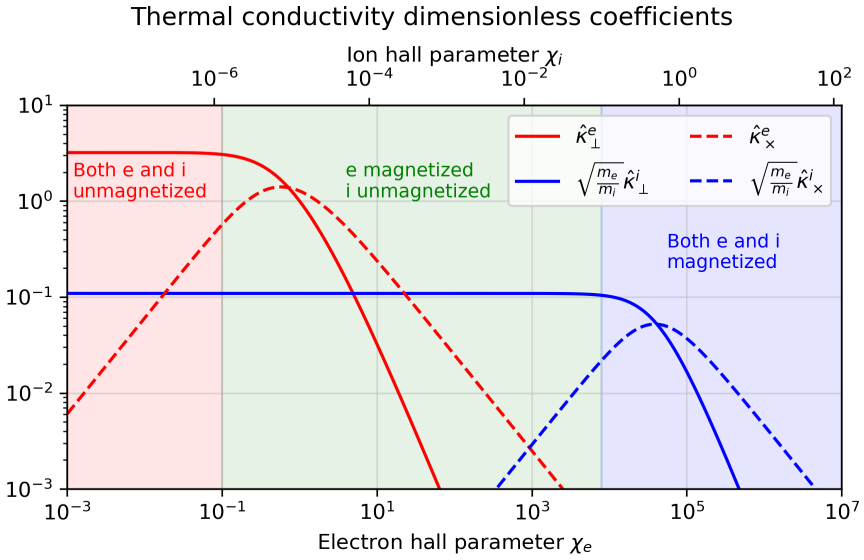


Figure 2.17: Dimensionless conductivities for electrons and ions for a simple hydrogen plasma ($Z = 1$, $m_i/m_e \approx 1840$, $T_i/T_e = 1$) as a function of Hall parameters. Electron heat transport dominates for $\chi_e \lesssim 10$, but ion heat transport dominates at larger magnetizations. For $10^{-4} \lesssim \chi_i \lesssim 10^{-1}$, ion transport dominates but is still unmagnetised, then becomes magnetised beyond $\chi_i \gtrsim 10^{-1}$. In these regimes, nonlocal unmagnetised and magnetised ion transport are both relevant.

the RKM locally and nonlocally. Figure 2.17 shows the electron and (single-species) ion heat conductivity coefficients for hydrogen ($Z = 1$) over a wide range of Hall parameters. There exists a wide parameter space for which electron transport is significantly magnetised ($\chi_e \gtrsim 1$) and ions are unmagnetised ($\chi_i \ll 1$), and therefore ion transport should have a significant impact on the evolution of the plasma. When magnetic fields are present in ICF plasmas from external application or spontaneous production due to the Biermann effect, the plasma is usually sufficiently collisional such that the blue region is never reached.

In the mixture formalism, only the total ion heat flux $\boldsymbol{q}_i$ enters the total temperature equation. The total ion heat flux is defined in the CoM frame as $\boldsymbol{q}_i = \sum_\alpha \int d^3\boldsymbol{w}\, \frac{1}{2} m_\alpha w^2 \boldsymbol{w} f_\alpha$. In a simple plasma featuring electrons and a single ion species, there is no heat flux associated with the flow since the only ion species velocity is identical to the hydrodynamic velocity. On the other hand, in a multi-species plasma, each species α has an individual diffusive flow defined as $\boldsymbol{V}_\alpha = \boldsymbol{u}_\alpha - \boldsymbol{u}_i$ relative to the hydrodynamic velocity. This introduces a component to the heat flux in multi-species cases due to the diffusion of different species in the CoM frame transporting energy, which does not occur in the single-species case. This additional contribution to the heat flux associated with diffusion is called the enthalpy flux.

The total ion heat flux $\boldsymbol{q}_i$ may be decomposed into two parts via $\boldsymbol{q}_i = \boldsymbol{q}'_i + \boldsymbol{h}_i$, the reduced heat flux and enthalpy flux respectively, defined as

$$\begin{aligned} \boldsymbol{q}'_i &= \sum_\alpha \int d^3\boldsymbol{w} \left(\frac{1}{2} m_\alpha w^2 - \frac{5}{2} T_i \right) \boldsymbol{w} f_\alpha \,, \\ \boldsymbol{h}_i &= \sum_\alpha \frac{5}{2} T_i \int d^3\boldsymbol{w}\, \boldsymbol{w} f_\alpha = \sum_\alpha \frac{5}{2} n_\alpha T_i \boldsymbol{V}_\alpha \,, \end{aligned} \tag{2.125}$$

both of which are summed over all ion species. The enthalpy flux has been written in terms of the diffusive velocities $\boldsymbol{V}_\alpha$ to emphasise its physical significance as heat flow carried via diffusion. The significance of the $5/2$ factor arises physically from the enthalpy contribution, as well as mathematically from the form of the Sonine expansion in the local analytic calculation. Although it is not necessary to decompose $\boldsymbol{q}_i = \boldsymbol{q}'_i + \boldsymbol{h}_i$, it improves physical interpretation and provides an additional flux to benchmark the RKM with against the local analytic result.

The Chapman-Enskog expansion [16, 72] of multi-species Boltzmann equations yields local results for transport quantities, in particular the local reduced heat flux

$$\boldsymbol{q'}_i^{\text{local}} = -\lambda'_i \boldsymbol{\nabla} T_i - n_i T_i \sum_\alpha D_\alpha^T \boldsymbol{d}_\alpha \,, \tag{2.126}$$

and local diffusive velocities

$$\boldsymbol{V}_\alpha^{\text{local}} = -D_\alpha^T \boldsymbol{\nabla} \ln T_i - \sum_\beta D_{\alpha\beta} \boldsymbol{d}_\beta \,, \tag{2.127}$$

where λ'_i, D_α^T, and $D_{\alpha\beta}$ are the partial coefficient of thermal conductivity, multi-species thermo-diffusion coefficients, and multi-species ordinary diffusion coefficients respectively, with the sign convention following Ferziger and Kaper [16]. These transport coefficients are determined from the collision operator $C_{\alpha\beta}$. For the full Fokker-Planck collision operator with Debye shielding, these may be provided analytically. The diffusive driving forces

$$\boldsymbol{d}_\alpha \equiv \frac{\boldsymbol{\nabla} p_\alpha - c_\alpha \boldsymbol{\nabla} p_i}{p_i} - c_\alpha \frac{\rho_i}{p_i} (\boldsymbol{X}_\alpha - \sum_\beta c_\beta \boldsymbol{X}_\beta), \tag{2.128}$$

where $c_\alpha = \rho_\alpha / \rho_i$ is the mass concentration of species α and $\boldsymbol{X}_\alpha$ is the external body force acting on species α. If electromagnetic fields and electrons are included[3], these external body forces are

$$\boldsymbol{X}_\alpha = \frac{1}{\rho_\alpha} \boldsymbol{R}_{\alpha e} + \frac{e Z_\alpha}{m_\alpha} \boldsymbol{E}' = -\frac{Z_\alpha^*}{Z^*} \frac{1}{\rho_\alpha} \boldsymbol{R}_e + \frac{e Z_\alpha}{m_\alpha} \boldsymbol{E}', \tag{2.129}$$

where $\boldsymbol{E}' = \boldsymbol{E} + \boldsymbol{u}_i \times \boldsymbol{B}$ is the effective electric field, and $\boldsymbol{R}_{\alpha e}$ is the collisional force exerted on species α by electrons. This collisional force can be shown to be

$$\boldsymbol{R}_{\alpha e} = -\boldsymbol{R}_{e\alpha} = -\frac{Z_\alpha^*}{Z^*} \boldsymbol{R}_e, \quad \text{where} \quad Z_\alpha^* = \frac{\hat{\nu}_{e\alpha}}{\hat{\nu}_{ee}} = \frac{n_\alpha Z_\alpha^2 \ln \Lambda_{e\alpha}}{n_e \ln \Lambda_{ee}}, \quad Z^* = \sum_\alpha Z_\alpha^* \tag{2.130}$$

In the local limit, ion transport coefficients for a simple plasma of electrons and a single ion species are provided by Braginskii [15]. Practically exact fits are provided by Ji and Held [88], which accounts for ion-electron collisions. Comprehensive formalisms and practical prescriptions for calculations of local ionic transport processes in an unmagnetised plasma with multiple ion species are given by Chapman and Cowling [72], Ferziger and Kaper [16], Zhdanov [84], with compact formulae provided by Kagan and Baalrud [94], and Kagan and Tang [95].

In the local single ion species case, the only two gradients available to induce heat flux are the temperature and pressure gradients. By assuming force balance, the single-species ion heat flux may be expressed purely in

[3] Still with ion Hall parameter $\chi_i \ll 1$.

terms of the temperature gradient. In contrast, the multi-species case involves more gradients on which the heat flux may be dependent, such as concentration gradients. In addition, for single species cases the external force $\boldsymbol{X}$ does not appear explicitly in the kinetic equation for δf due to force balance. For multi-species cases, the force $\boldsymbol{X}_\alpha$ may vary for different species, such as different specific charges q_α/m_α, giving different electrostatic forces on each species. These forces then appear explicitly in the kinetic equation for δf_α and therefore affect the heat flux. The result is that not only can temperature gradients drive ion heat flow, but also the diffusive driving force $\boldsymbol{d}_\alpha$ which allows pressure gradients, concentration gradients, electric fields, and ion-electron momentum exchange to drive heat flow.

Similarly to heat flow, temperature gradients and the diffusive driving force also drive the diffusive velocity. To make the physical mechanisms clearer, we consider a two-component mixture with a light (l) and heavy (h) species. The diffusive mass flux of the lighter species $\boldsymbol{i} = \rho_l \boldsymbol{V}_l = -\rho_h \boldsymbol{V}_h$ may be written in the Landau form [96]

$$\boldsymbol{i}^{\text{local}} = -\rho_i D \Bigg(\underbrace{\boldsymbol{\nabla} c}_{\substack{\text{Ordinary} \\ \text{diffusion}}} + \underbrace{k_T \boldsymbol{\nabla} \ln T_i}_{\substack{\text{Thermo-} \\ \text{diffusion}}} + \underbrace{k_p \boldsymbol{\nabla} \ln p_i}_{\substack{\text{Baro-} \\ \text{diffusion}}} \underbrace{- k_E \frac{e}{T_i} \boldsymbol{E}'}_{\substack{\text{Electro-} \\ \text{diffusion}}} \Bigg), \tag{2.131}$$

where $c = c_l$. The ordinary diffusion coefficient D is defined such that the concentration gradient inside the bracket has a prefactor of unity. The other drives then have nontrivial dimensionless coefficients, namely the baro-diffusion ratio k_p, thermo-diffusion ratio k_T, and electro-diffusion ratio k_E. A different basis of drives may be chosen in other works, so the exact appearance of these terms may vary. This form emphasises that there are different thermodynamic forces that can drive interspecies diffusion. For example, even in a uniform 50:50 DT mixture, a temperature gradient will drive thermo-diffusion which can separate the species, which would directly reduce fusion reactivity and yield.

If ions are magnetised $\chi_i \gtrsim 1$, then additional cross $\times$ components are gained for each flux such as a Righi-Leduc heat flux, but also physically new terms such as cross-diffusion terms for each thermodynamic drive and a cross-diffusive heat flux. The RKM has been implemented with magnetised multi-species capability, however these cases are not considered here since ions are practically almost never magnetised in ICF experiments. A summary of unmagnetised multi-species transport is provided by Table 2.2.

2.7 Magnetohydrodynamics (MHD)

Electrons may be treated as a fluid evolving according to the fluid equations 2.87. Due to the small inertia of electrons compared to ions m_e/m_i, the electron density and flow evolve on much faster timescales than the ion fluid, relaxing quickly to a state that satisfies quasineutrality and electron pressure balance. MHD then treats the electron density and flow as quasistatic, determined by the quasineutrality and electron pressure balance conditions.

		Ion transport flux	
		Reduced heat flux $\boldsymbol{q}_i'$	Diffusive velocity $\boldsymbol{V}_\alpha$
Thermodynamic drive	Temperature gradient $-\boldsymbol{\nabla} T_i$	Heat conduction λ_i'	Thermo-diffusion D_α^T (Soret effect)
	Diffusive driving force $\boldsymbol{d}_\beta$	Diffusive heat flux D_β^T (Dufour effect, baro-heat flow)	Ordinary, baro-, and electro-diffusion $D_{\alpha\beta}$

Table 2.2: Summary of local vectorial ionic mixture transport. Note that the diffusive driving forces $\boldsymbol{d}_\alpha$ are linear combinations of concentration gradients $\boldsymbol{\nabla} c_\alpha$, pressure gradients $\boldsymbol{\nabla} p_\alpha$, the electric field $\boldsymbol{E}$, and electron-ion momentum exchange $\boldsymbol{R}_e$. The relevant transport coefficients for each term are also indicated, highlighting the Onsager symmetry between the off-diagonal terms.

The quasineutrality condition determining the electron density is simple:

$$n_e \approx \sum_\alpha Z_\alpha n_\alpha. \tag{2.132}$$

The electron pressure balance condition in general requires careful treatment. For our purposes, we simply start from the electron flow equation

$$\rho_e(\partial_t \boldsymbol{u}_e + \boldsymbol{u}_e \cdot \boldsymbol{\nabla} \boldsymbol{u}_e) = -\boldsymbol{\nabla} p_e - \boldsymbol{\nabla} \cdot \Pi_e - e n_e(\boldsymbol{E} + \boldsymbol{u}_e \times \boldsymbol{B}) + \boldsymbol{R}_e, \tag{2.133}$$

and neglect the electron inertia terms on the left hand side and electron viscosity, leaving

$$0 \approx -\boldsymbol{\nabla} p_e - e n_e(\boldsymbol{E} + \boldsymbol{u}_e \times \boldsymbol{B}) + \boldsymbol{R}_e, \tag{2.134}$$

which we may then rearrange to find a closure for the electric field $\boldsymbol{E}$. We rewrite the electron flow in terms of the electric current in the centre-of-momentum frame

$$\boldsymbol{j} = -e n_e(\boldsymbol{u}_e - \boldsymbol{u}_i) \quad \Rightarrow \quad \boldsymbol{u}_e \approx \boldsymbol{u} - \frac{1}{e n_e}\boldsymbol{j}, \tag{2.135}$$

where we have taken the ion CoM velocity to be the total plasma CoM velocity $\boldsymbol{u}_i \approx \boldsymbol{u}$, with next order corrections being small due to the mass ratio $\sim \mathcal{O}(m_e/m_i)$. This yields a form of the generalised Ohm's law

$$\boldsymbol{E} \approx \underbrace{-\boldsymbol{u} \times \boldsymbol{B}}_{\text{'frozen-in flow'}} \underbrace{-\frac{1}{e n_e}\boldsymbol{\nabla} p_e}_{\text{'Biermann battery'}} \underbrace{+\frac{1}{e n_e}\boldsymbol{R}_e^u}_{\text{'Resistive diffusion'}} \underbrace{+\frac{1}{e n_e}\boldsymbol{R}_e^T}_{\text{'Nernst' and 'cross Nernst'}} \underbrace{+\frac{1}{e n_e}\boldsymbol{j} \times \boldsymbol{B}}_{\text{'Hall effect'}}, \tag{2.136}$$

where terms have been labelled according to the physical effects they give rise to[4]. To identify what these physical effects are, we substitute in this closure of the electric field $\boldsymbol{E}$ into Faraday's law

$$\partial_t \boldsymbol{B} = -\boldsymbol{\nabla} \times \boldsymbol{E}, \tag{2.137}$$

yielding the induction equation

$$\partial_t \boldsymbol{B} \approx \underbrace{\boldsymbol{\nabla} \times (\boldsymbol{u} \times \boldsymbol{B})}_{\text{'frozen-in flow'}} \underbrace{+\boldsymbol{\nabla} \times \left(\frac{1}{en_e}\boldsymbol{\nabla} p_e\right)}_{\text{'Biermann battery'}} \underbrace{-\boldsymbol{\nabla} \times \left(\frac{1}{en_e}\boldsymbol{R}_e^u\right)}_{\text{'Resistive' diffusion'}} \underbrace{-\boldsymbol{\nabla} \times \left(\frac{1}{en_e}\boldsymbol{R}_e^T\right)}_{\text{'Nernst' and 'cross Nernst'}} \underbrace{-\boldsymbol{\nabla} \times \left(\frac{1}{en_e}\boldsymbol{j} \times \boldsymbol{B}\right)}_{\text{'Hall effect'}}. \tag{2.138}$$

Ampère's law with the displacement current neglected (where flow velocities are non-relativistic) to relate the current and magnetic field directly via

$$\boldsymbol{j} \approx \frac{1}{\mu_0}\boldsymbol{\nabla} \times \boldsymbol{B}. \tag{2.139}$$

This approach, known as MHD, then does not require evolving the ion fluid, electron fluid, and Maxwell's equations all in tandem, but only the ion fluid, electron temperature, and magnetic field. This can be beneficial from a computational viewpoint since fewer PDEs are required to be solved and short electron timescales and length scales are averaged out. It is also helpful from a theoretical perspective since different phenomena are clearly captured by different terms in the induction equation or the generalised Ohm's law. Now, we look at the effect of each term individually.

2.7.1 Ideal MHD

If all other terms are neglected, the frozen-in-flow term leaves ideal MHD described by the ideal induction equation

$$\partial_t \boldsymbol{B} = \boldsymbol{\nabla} \times (\boldsymbol{u} \times \boldsymbol{B}). \tag{2.140}$$

Expanding the curl and noting $\boldsymbol{\nabla} \cdot \boldsymbol{B} = 0$, we may write the ideal induction equation as

$$\partial_t \boldsymbol{B} + \underbrace{\boldsymbol{u} \cdot \boldsymbol{\nabla} \boldsymbol{B}}_{\text{advection}} = \underbrace{(\boldsymbol{B} \cdot \boldsymbol{\nabla})\boldsymbol{u}}_{\text{field stretching}} \underbrace{-\boldsymbol{B}(\boldsymbol{\nabla} \cdot \boldsymbol{u})}_{\text{compression}}, \tag{2.141}$$

which describes how magnetic fields are advected by flows, but also stretched by straining flows and enhanced by compressive flows. In magnetised ICF implosions, these terms tell us that the initial magnetic field is dramatically enhanced with the implosion, allowing for large magnetic fields that suppress heat transport to be achieved with a realistic seed field.

[4]There are additional terms in the generalised Ohm's law that have not appeared above to our simpler treatment, however the above treatment suffices for our purposes. A proper derivation forms an evolution equation for the current $\boldsymbol{j}$ using the electron and ion momentum equations which itself is rearranged for the electric field $\boldsymbol{E}$. This approach is not much more complicated than the above for a simple plasma, but does become notably more complicated for ionic mixtures.

Some straightforward algebra [77] and using the mass continuity equation yields

$$\frac{d}{dt}\left(\frac{\boldsymbol{B}}{\rho}\right) = \frac{\boldsymbol{B}}{\rho}\cdot\boldsymbol{\nabla}\boldsymbol{u}. \tag{2.142}$$

where $d/dt = \partial_t + \boldsymbol{u}\cdot\boldsymbol{\nabla}$ is the Lagrangian derivative.

Suppose that two nearby fluid elements have positions $\boldsymbol{r}_1(t)$ and $\boldsymbol{r}_2(t)$ which evolve according to the flow $\boldsymbol{u}(t,\boldsymbol{r})$. The displacement between these two elements $\delta\boldsymbol{r}(t) = \boldsymbol{r}_2(t) - \boldsymbol{r}_1(t)$ evolves as

$$\frac{d}{dt}\delta\boldsymbol{r} = \boldsymbol{u}(t,\boldsymbol{r}+\delta\boldsymbol{r}) - \boldsymbol{u}(t,\boldsymbol{r}) \approx \delta\boldsymbol{r}\cdot\boldsymbol{\nabla}\boldsymbol{u}, \tag{2.143}$$

which has the same form as the ideal induction equation in the form written above. This tells us that if these two fluid elements are initially on the same field line, they remain on the same field line since $\delta\boldsymbol{r} \propto \boldsymbol{B}/\rho$, i.e. their separation remains in the direction of the magnetic field. Alfvén's theorem is a similar statement, which proves that the magnetic flux through any closed loop moving with the fluid flow is conserved in ideal MHD, i.e. the magnetic flux is frozen into the flow. MHD becomes non-ideal when other terms in the induction equation are included. In ideal MHD, flows may then continuously enhance magnetic fields. This process cannot go on forever, with eventually non-ideal effects such as resistive diffusion coming into effect and slowing magnetic field growth.

2.7.2 Resistive diffusion

The friction term $\boldsymbol{R}_e^u$ results in the decay of relative flows between electrons and ions, and therefore resists currents. This is a dissipative process which can limit the otherwise unbounded enhancement of magnetic fields by field stretching and compression in ideal MHD.

In the generalised Ohm's law, the resistive diffusion term has the form

$$\boldsymbol{E} = \frac{1}{en_e}\boldsymbol{R}_e^u + \text{other terms} = -\frac{m_e}{e\tau_{ee}}\underline{\underline{\hat{\alpha}}}\cdot\Delta\boldsymbol{u} + \text{other terms} = \underline{\underline{\eta}}\cdot\boldsymbol{j} + \text{other terms}, \tag{2.144}$$

where $\underline{\underline{\eta}} = \frac{m_e}{e^2 n_e \tau_{ee}}\underline{\underline{\hat{\alpha}}}$ is the resistivity tensor. This emphasises that the friction term directly gives rise to electrical resistivity (or conductivity) in a plasma. Using the local closure for the friction force, the resistive diffusion term appearing in the induction equation has the form

$$-\boldsymbol{\nabla}\times\left(\frac{1}{en_e}\boldsymbol{R}_e^u\right) = -\frac{1}{\mu_0}\boldsymbol{\nabla}\times\left(\underline{\underline{\eta}}\cdot\boldsymbol{\nabla}\times\boldsymbol{B}\right). \tag{2.145}$$

The curl may be expanded with $\underline{\underline{\eta}}$ following the same form as $\underline{\underline{\hat{\alpha}}}$ before. For our purposes, let us briefly assume that the resistivity is isotropic $\underline{\underline{\eta}} = \eta\mathrm{I}$, yielding

$$-\frac{1}{\mu_0}\boldsymbol{\nabla}\times\Big(\eta\boldsymbol{\nabla}\times\boldsymbol{B}\Big) = -\frac{1}{\mu_0}\eta\boldsymbol{\nabla}\times\Big(\boldsymbol{\nabla}\times\boldsymbol{B}\Big) + \frac{1}{\mu_0}\Big(\boldsymbol{\nabla}\times\boldsymbol{B}\Big)\times\boldsymbol{\nabla}\eta = \frac{\eta}{\mu_0}\nabla^2\boldsymbol{B} + \frac{1}{\mu_0}\Big(\boldsymbol{\nabla}\times\boldsymbol{B}\Big)\times\boldsymbol{\nabla}\eta. \tag{2.146}$$

Here, the $\frac{\eta}{\mu_0}\nabla^2\boldsymbol{B}$ gives rise to diffusion of the magnetic field.

2.7.3 Biermann battery

The Biermann battery term may be rewritten using vector identities as

$$\boldsymbol{\nabla} \times \left(\frac{1}{en_e}\boldsymbol{\nabla} p_e\right) = \frac{1}{e}\boldsymbol{\nabla} \times (\boldsymbol{\nabla} T_e + T_e \boldsymbol{\nabla} \ln n_e) = \frac{1}{e}\boldsymbol{\nabla} T_e \times \boldsymbol{\nabla} \ln n_e. \tag{2.147}$$

The term therefore is nonzero when electron temperature and density gradients are unaligned.

Suppose we have a highly collisional (i.e. transport is local) plasma with initially zero magnetic field, and therefore zero current from Ampère's law. The induction equation becomes

$$(\partial_t \boldsymbol{B})|_{B=0} = \frac{1}{e}\boldsymbol{\nabla} T_e \times \boldsymbol{\nabla} \ln n_e + \boldsymbol{\nabla} \times \left(\frac{1}{en_e}\boldsymbol{R}_e^T|_{B=0}\right). \tag{2.148}$$

These terms can then spontaneously generate magnetic fields even if a plasma is initially unmagnetised. The Biermann battery term shows that misaligned electron temperature and density gradients spontaneously generate magnetic fields. In ICF implosions, even initially unmagnetised targets can become magnetised during stagnation due to the Biermann battery effect, where the magnetic field can then influence heat transport and introduce asymmetries in the implosion [68].

Using the local result for the unmagnetised thermal force $\boldsymbol{R}_e^T$, the second term becomes

$$\boldsymbol{\nabla} \times \left(\frac{1}{en_e}\boldsymbol{R}_{e,\parallel}^T\right) = -\frac{1}{e}\boldsymbol{\nabla} \times \left(\hat{\beta}_\parallel(Z)\boldsymbol{\nabla} T_e\right) = \frac{1}{e}\hat{\beta}_\parallel'(Z)\boldsymbol{\nabla} T_e \times \boldsymbol{\nabla} Z, \tag{2.149}$$

where $\boldsymbol{\nabla} \times \boldsymbol{\nabla} T_e \equiv 0$ by vector identity. For uniform effective ionisation Z^*, this term vanishes and the Biermann battery is the main term in highly collisional plasmas that can spontaneously produce magnetic fields. Effective ionisation can vary at material boundaries which are common in ICF targets or variation in Coulomb logarithms, and therefore can give rise to non-Biermann spontaneous field production [97, 98]. One could imagine an interesting interplay between multi-species ion dynamics which generates variations in Z, which then spontaneously generates magnetic fields through this term, although this is beyond the scope of this thesis.

2.7.4 Nernst effect

In the induction equation, the local Nernst term has the form

$$-\boldsymbol{\nabla} \times \left(\frac{1}{en_e}\boldsymbol{R}_e^T\right) = \frac{1}{e}\boldsymbol{\nabla} \times \left(\underline{\underline{\hat{\beta}}} \cdot \boldsymbol{\nabla} T_e\right) \tag{2.150}$$

$$= \frac{1}{e}\boldsymbol{\nabla} \times \left([\hat{\beta}_\parallel \boldsymbol{bb} + \hat{\beta}_\perp(\mathrm{I} - \boldsymbol{bb})] \cdot \boldsymbol{\nabla} T_e + \hat{\beta}_\times \boldsymbol{b} \times \boldsymbol{\nabla} T_e\right) \tag{2.151}$$

$$= \boldsymbol{\nabla} \times (\boldsymbol{v}_N \times \boldsymbol{B}), \tag{2.152}$$

where we define the Nernst velocity

$$\boldsymbol{v}_N = \underbrace{-\frac{\hat{\beta}_\times}{eB}\boldsymbol{\nabla} T_e}_{\text{Nernst}} \underbrace{-\frac{\hat{\beta}_\parallel - \hat{\beta}_\perp}{eB}(\boldsymbol{b} \times \boldsymbol{\nabla} T_e)}_{\text{Cross Nernst}}. \tag{2.153}$$

Since this form is the same as the frozen-in flow term with the hydrodynamic flow $\boldsymbol{u}$ replaced with the Nernst velocity $\boldsymbol{v}_N$, the physical interpretation of this term is that magnetic fields are advected down electron temperature gradients due to the Nernst term, and in the $-\boldsymbol{b} \times \boldsymbol{\nabla} T_e$ direction by the cross Nernst term.

2.7.5 Hall effect

Similarly to the Nernst term, the Hall term may be written in terms of an advection velocity

$$-\boldsymbol{\nabla} \times \left(\frac{1}{e n_e} \boldsymbol{j} \times \boldsymbol{B} \right) = \boldsymbol{\nabla} \times (\boldsymbol{v}_H \times \boldsymbol{B}), \quad \boldsymbol{v}_H = -\frac{1}{e n_e} \boldsymbol{j} = \Delta \boldsymbol{u}, \tag{2.154}$$

which shows that magnetic fields are advected along with the electron fluid rather than the ions.

2.7.6 MHD effects in ICF

Electron heat conduction is a primary energy loss mechanism in ICF implosions, rapidly transporting heat away from the hotspot during compression and stagnation [28]. This typically reduces the peak hotspot temperature and therefore the fusion yield of the implosion. To mitigate conductive losses, external magnetic fields may be applied to the target pre-implosion, inhibiting the conductive heat flux ($\hat{\kappa}_\perp \leq \hat{\kappa}_\parallel$). Although the initial seed fields are relatively weak, they are dramatically enhanced by field compression as they move with the radially inwards flow. Even in implosions without externally applied magnetic fields, they may be spontaneously generated during the implosion by the Biermann battery effect [99]. All of the above MHD induction effects influence the magnetic field behaviour during the implosion [68]. The resistive diffusion and Nernst terms originate from the electron-ion momentum exchange, which is a transport quantity. Nonlocal behaviour of these terms then gives rise to nonlocal behaviour in the induction equation, disturbing the magnetic field which in turn impacts heat transport.

2.8 Nonlocal Transport

Consider the unmagnetised conductive heat flux with the local closure $\boldsymbol{q}^T = -\kappa \boldsymbol{\nabla} T$. At a point in space, for a given density and temperature, there is a maximum possible heat flux $q^{\text{free}} \sim n T v_{\text{th}}$ corresponding to all particles streaming freely at the thermal speed. For a sufficiently sharp gradient, the local result will exceed the free-streaming limit where $\kappa |\boldsymbol{\nabla} T| > n T v_{\text{th}}$, thereby becoming unphysical. Nonlocal effects then have a tendency to inhibit the maximum heat flux to remain physical, which is supported by simulations and Fokker-Planck codes [5]. This observation motivates a flux-limiter approach [100, 101], where local transport coefficients are limited in nonlocal cases by a fitted function compared to full FP methods. Although computationally cheap, flux limiters are physically inaccurate and fail to capture other features of nonlocal transport such as preheating in cold regions. More advanced models, such as the Schurtz-Nicolaï-Busquet (SNB) approach [6, 7], provide a more physically accurate description of nonlocal transport for electrons but not ions. For ion transport, this leaves flux limiters as the usual practical option implemented in hydrodynamics codes.

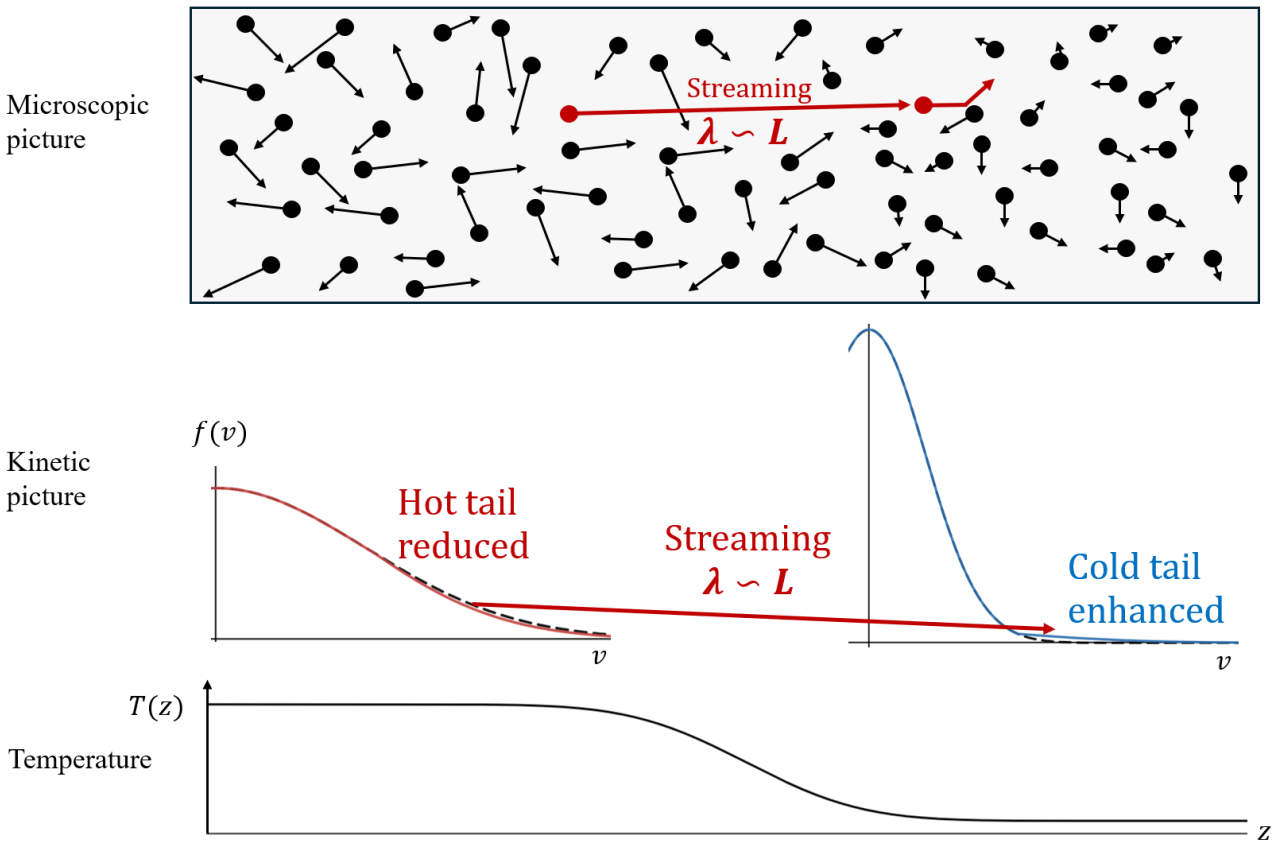


Figure 2.18: Depiction of streaming suprathermal particles in the tail of the distribution giving rise to nonlocal effects.

Hydrodynamic quantities such as density and temperature are populated predominantly by thermal particles in the bulk of the velocity distribution, whereas the heat flux is sourced primarily by suprathermal particles in the tail of the distribution. In a plasma, the MFP of a particle against a Maxwellian background scales as $\lambda \sim \lambda_{\text{th}}(v/v_{\text{th}})^4$, where λ_{th} is the MFP of a thermal particle with speed $v = v_{\text{th}}$. Nonlocal effects are therefore most apparent in the tail of the DF where particle MFPs may be comparable to length scales on which hydrodynamic quantities vary, allowing these suprathermal particles to stream across these profiles before colliding. This leads to a regime where the bulk is strongly collisional and therefore near-Maxwellian, but where the tail of the DF may experience nonlocal kinetic effects which modifies the heat flux. This regime is illustrated in Figure 2.18. A set of fluid equations describing evolution of hydrodynamic quantities may then remain a valid description of the plasma, but with a nonlocal prescription for the heat flux.

In the more mathematical context of the Chapman-Enskog expansion, nonlocal transport simply means that the parameter ε (which was effectively Knudsen number) in the expansion of the DF and timescales is no longer sufficiently small for the perturbative solution to be valid. In particular, the leading-order term in the perturbation expansion $f \approx f^M(x|n, \boldsymbol{u}, T)$ is no longer successfully described by evolving its first three moments via the fluid equations with local closures. Consider the $\mathcal{O}(1)$ equation obtained from the Chapman-Enskog expansion 2.82 while keeping next order $\mathcal{O}(\varepsilon)$ Vlasov term

$$(\partial_{t_0} + \hat{V})f^M + \varepsilon\hat{V}\delta f = C\{\delta f, f^M\} + C\{f^M, \delta f\}. \tag{2.155}$$

The term $\varepsilon\hat{V}\delta f$ was previously neglected on the basis that ε is small, so this term was subleading compared to the linear collision operator $\varepsilon|\hat{V}\delta f|/|\hat{C}\delta f| \ll 1$. However, the linear Fokker-Planck collision operator decays as $\sim v^{-3}$ similarly to the collision frequency we found for Coulomb collisions. The Vlasov operator contains the spatial advection term $\hat{V} = \boldsymbol{v}\cdot\boldsymbol{\nabla} + \ldots$, which grows with v. There will then always exist some sufficiently large v beyond which this ordering is violated and the Chapman-Enskog expansion breaks down. Local closures are still valid under the assumption that the Chapman-Enskog expansion breaks down at high enough v as to not significantly alter the relevant moments appearing in the fluid equations, the highest moment being the heat flux.

Nonlocal effects are expected to impact regions of phase space where the advection term $\boldsymbol{w}\cdot\boldsymbol{\nabla}\delta f$ becomes comparable to the collision term $\hat{C}\delta f$, and therefore phase space where

$$\frac{|\boldsymbol{w}\cdot\boldsymbol{\nabla}\delta f|}{|\hat{C}\delta f|} \sim \left(\frac{w}{v_{\text{th},e}}\right)^4 N_K \tag{2.156}$$

is comparable to or greater than unity. Since transport fluxes often depend on suprathermal particles $w > v_{\text{th}}$, nonlocal effects can occur for N_K significantly less than unity. Heat flux is the transport flux evaluated from the largest velocity moment of the distribution, having the form

$$\boldsymbol{q} = \int d^3\boldsymbol{w}\,\frac{1}{2}mw^2\boldsymbol{w}\delta f \propto \int d\Omega\int dw\,w^4\boldsymbol{w}\delta f \propto \int d\xi\,\xi^5 e^{-\xi^2}\phi(\xi), \tag{2.157}$$

where $\xi = w/v_{\text{th}}$ is the normalised velocity coordinate and $\delta f = \phi(\xi)f^M$. By determining the window of the integrand that provides most of the contribution to the heat flux integral, the relevant velocities that contribute to the heat flux are determined. Nonlocality of heat flow is then expected for $N_K \gtrsim \xi_+^{-4}$, where ξ_+ is the upper limit of this window. Here, we define this upper limit such that the contribution to the integral above $\xi > \xi_+$ is 10% of the total integral.

To estimate the heat flux window, we consider the solution $\phi(\xi)$ obtained from the unmagnetised Lorentz problem 2.5.3 which had the solution $\phi^T(\xi) \propto \xi^4(\xi^2 - 4)$ for temperature-gradient-driven transport. The conductive heat flux integrand therefore scales as $dq^T/d\xi \propto \xi^9(\xi^2-4)e^{-\xi^2}$, which provides the window of the heat flux integrand in the Lorentz limit.

Figure 2.19 shows the integrand windows for the unmagnetised Lorentz limit result and the actual integrands obtained from the local analytic calculation for the electron conductive heat flux in a simple hydrogen plasma. The Lorentz limit and hydrogen plasma results are similar, both having their majority contribution to the heat flux from particles with $1 \lessapprox \xi \lessapprox 3.3$. We therefore expect nonlocal effects on the unmagnetised electron heat flux to emerge for Knudsen numbers $N_K \gtrsim 3.3^{-4} \approx 1/100$. For moderate magnetisation $\chi = 1$, the perpendicular heat flux integrand is shifted to much lower velocities, therefore becoming far more insensitive to nonlocal effects. The Righi-Leduc heat flux for $\chi = 1$ has a higher velocity window, therefore is expected to be more sensitive to nonlocal effects than the perpendicular heat flow at similar magnetisation.

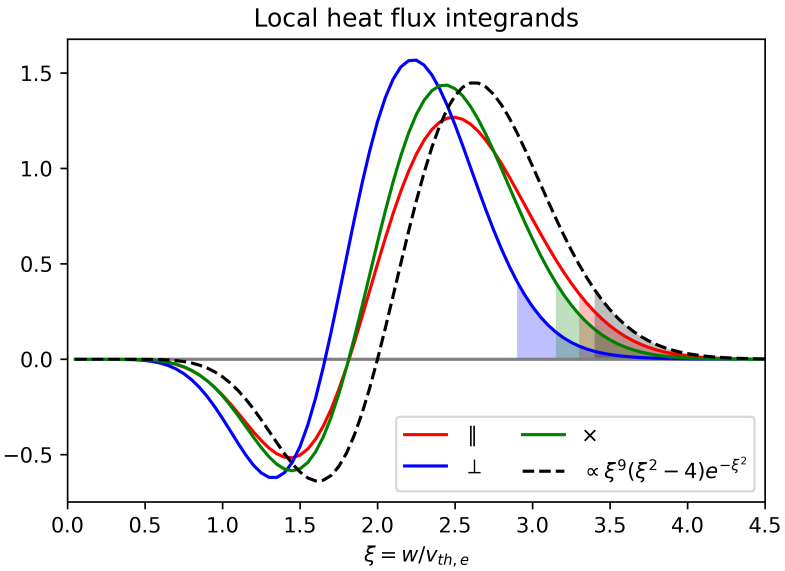


Figure 2.19: Integrands of the local electron conductive heat flux for $Z = 1$, $\chi = 1$, normalised to have equal area when integrated over ξ. The parallel component is unaffected by magnetisation, therefore corresponds to the unmagnetised result. The shaded areas represent the highest velocity section of the tail that provides 10% contribution to the whole heat flux integral.

2.8.1 Previous studies and closures

Plenty of previous literature investigates nonlocal transport via full kinetic simulations. Early work includes that of Bell et al. [102], which demonstrated nonlocal heat transport in ICF-relevant plasmas due to sharp temperature gradients through VFP simulations. Similar work by Matte et al. [103] uses VFP simulations to justify an $l = 1$ expansion even in nonlocal cases and a particular flux-limited closure for the heat flux.

One of the first nonlocal transport closures was developed by Luciani et al. [104]. This closure, known as LMV, assumes that the nonlocal heat flux can be provided by the spatial convolution of the local heat flux with a suitable kernel

$$\boldsymbol{q}(\boldsymbol{x}) = \int d^3\boldsymbol{x}'\, G(\boldsymbol{x}, \boldsymbol{x}')\boldsymbol{q}^{\text{local}}(\boldsymbol{x}'), \tag{2.158}$$

where the form of the LMV kernel in 1D is argued heuristically as

$$G^{\text{LMV}}(x, x') = \frac{1}{2a\lambda_e(x')} e^{-\theta(x,x')}, \quad \text{where} \quad \theta(x, x') = \left| \frac{1}{a\lambda_e(x')n_e(x')} \int_{x'}^{x} dx''\, n_e(x'') \right|, \tag{2.159}$$

and a is a free parameter, chosen as $a = 32$ by comparison with VFP simulations. Albritton et al. provide the AWBS closure, which starts from a simplified form of the VFP equation to derive a similar convolution closure. Epperlein and Short provide yet another convolution closure, determining their kernel

$$G^{\text{ES}}(x, x') = -\frac{\sin(\theta)\text{si}(\theta) + \cos(\theta)\text{Ci}(\theta)}{\pi a\lambda(x')}, \quad \text{where} \quad \text{Ci}(\theta) \equiv -\int_\theta^\infty \frac{\cos t}{t} dt, \quad \text{si}(\theta) \equiv -\int_\theta^\infty \frac{\sin t}{t} dt, \tag{2.160}$$

from fits to a set of VFP simulations of a relaxing temperature perturbation, which are found to be inconsistent with both the LMV and AWBS closures. As Epperlein and Short themselves state: "since the *correct* kernel is problem dependent, caution is necessary when applying nonlocal transport models to situations previously untested by the more accurate FP simulations". Although these kernels may provide the correct results in the idealised cases in which they are simplified and provide the correct qualitative behaviour, there is no guarantee or reassurance that they provide the correct nonlocal behaviour in other cases.

A more modern and perhaps the most widely used nonlocal transport closure is the Schurtz-Nicolaï-Busquet (SNB) closure [6]. The original SNB paper provides a heuristic derivation, starting by presenting a multidimensional extension to the LMV convolution kernel. This convolution is then shown to be the solution of a linear diffusion equation. The convolution is then applied to individual velocity (or energy) groups with a velocity-dependent MFP, which leaves a linear diffusion equation for each velocity group, capturing the correct physical picture of suprathermal particles giving rise to nonlocal effects. A secondary derivation from kinetics is also provided, also with a magnetised extension [7], which fundamentally relies on a heavily simplified collision operator for appropriate algebraic manipulations. Other models follow a similar framework to SNB, but with different model collision operators or a minimum entropy closure for the $l = 2$ mode.

Since these approaches rely on a simplified form of the collision operator, local analytic transport results are not naturally recovered. Some of these approaches still produce local transport results, but only by construction since they are based on a convolution of the local analytic result or find the correction to the heat flux $\Delta \boldsymbol{q}$ which automatically recovers the local limit when finding the total heat flux $\boldsymbol{q} = \boldsymbol{q}^{\text{local}} + \Delta \boldsymbol{q}$. SNB and similar approaches expand the DF in spherical harmonics to the first harmonic $l = 1$ as $f_e = f^0 + \hat{\boldsymbol{v}} \cdot \boldsymbol{f}^1$ and use a rescaled Lorentz-like collision term

$$\hat{C}_e^{\text{SNB}} \boldsymbol{f}^1 = -\nu_{ei}^* \boldsymbol{f}^1, \quad \text{where} \quad \nu_{ei}^* = \zeta(Z) \left(\frac{v_{\text{th},e}}{w} \right)^3 \hat{\nu}_{ei}, \tag{2.161}$$

where $\zeta(Z)$ is an ionisation-dependent numerical prefactor. In the Lorentz limit $Z \to \infty$, this is the leading order result for the $l = 1$ component of the linearised Fokker-Planck collision operator, therefore reproduces the correct heat conductivity in this large Z limit. In SNB and similar approaches, the ionisation-dependent prefactor is chosen such that the local analytic result for the heat conductivity $\hat{\kappa}_{\parallel}^e$ is appropriately recovered by setting

$$\zeta(Z) = \frac{(Z \hat{\kappa}_e^{\parallel})|_{Z \to \infty}}{Z \hat{\kappa}_e^{\parallel}} \approx \frac{Z + 4.2}{Z + 0.24}. \tag{2.162}$$

This forces the correct Z scaling for the parallel heat conductivity. However, the underlying behaviour of the collision operator in velocity space is not captured by this Lorentz-like operator. The full linearised Fokker-Planck operator contains the test-particle term, which includes velocity-space friction and diffusion terms, and the field-particle term, which includes integral operators in velocity space. There is therefore no guarantee that this collision operator should then capture nonlocal behaviour accurately. In addition, the collision frequency has been scaled to recover the correct parallel heat conductivity, but all other transport

coefficients such as $\hat{\kappa}_{(\perp,\times)}$, $\hat{\alpha}_{(\parallel,\perp,\times)}$, and $\hat{\beta}_{(\parallel,\perp,\times)}$ have different nontrivial Z scalings that are not matched by this ad-hoc scaling. Finally, it is unlikely that these types of closures would be able to fully capture $l = 2$ behaviour which is necessary for describing viscous stress.

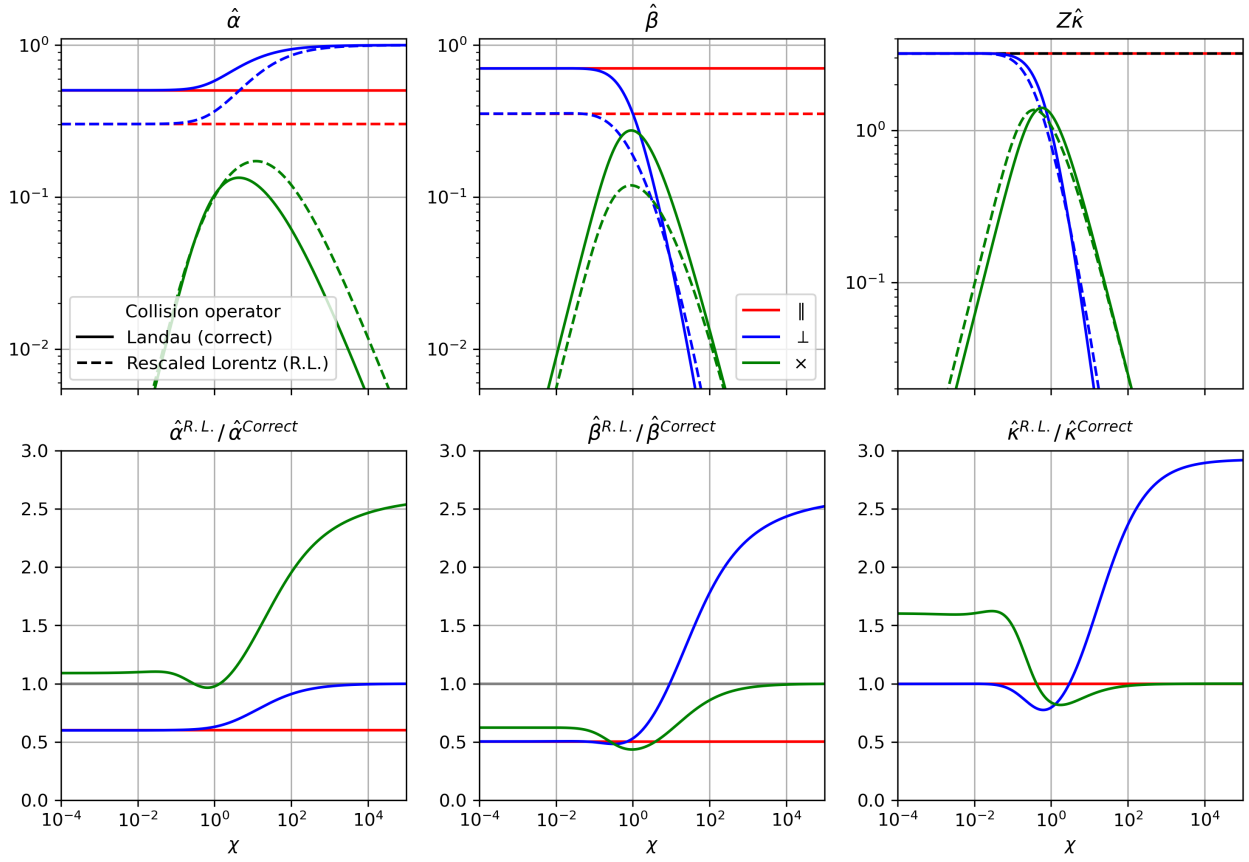


Figure 2.20: Comparison of correct transport coefficients for $Z = 1$ (solid lines) to transport coefficients obtained with the rescaled Lorentz collision operator (dashed lines).

Figure 2.20 demonstrates this issue by comparing the correct electron transport coefficients for a simple hydrogen plasma $Z = 1$ to the coefficients obtained from the rescaled Lorentz-like collision operator. The three different components $\parallel$, $\perp$, and $\times$, for each coefficient are shown in red, blue, and green, respectively. The Lorentz-like results are rescaled such that the parallel heat conductivity coefficient $\hat{\kappa}_{\parallel}$ matches the result obtained from the Fokker-Planck collision operator corresponding to Braginskii's 3.16 by choosing $\zeta(Z) = (Z + 4.2)/(Z + 0.24)$ as discussed above. All other Lorentz-like coefficients then follow this same scaling.

The perpendicular heat conductivity coefficient $\hat{\kappa}_{\perp}$ matches the parallel coefficient $\hat{\kappa}_{\parallel}$ for low magnetisations $\chi \lesssim 0.1$, therefore the rescaled Lorentz result matches the correct result obtained from the Fokker-Planck collision operator. However, the magnetised behaviour of the perpendicular coefficient is noticeably different. The rescaled Lorentz coefficient reduces with Hall parameter slightly faster than the correct result as it becomes magnetised. At very large magnetisations $\chi \gg 1$, both collision models obtain the correct $\hat{\kappa}_{\perp} \propto \chi^{-2}$ scaling, but the Lorentz model is ≈ 2.9 times larger than the correct result. At low magnetisations, the cross heat

conductivity coefficient $\hat{\kappa}_\times$ that describes the Righi-Leduc heat flow is $\sim 60\%$ larger than the correct result. At order-unity Hall parameter $\chi \sim 1$, this ratio drops to $\sim 20\%$ less than the correct result. These differences highlight that although the $\zeta(Z)$ rescaling forces a correct result for $\hat{\kappa}_\parallel$, this agreement does not hold for the other magnetised components of the heat conductivity.

At very high magnetisations $\chi \gg 1$, the rescaled Lorentz result tends to the correct result $Z\hat{\kappa}_\times \sim \frac{5}{2}\frac{1}{\chi}$. For the correct result of $Z\hat{\kappa}(Z)$, this asymptotic behaviour holds for all Z regardless, so it is not surprising that it is recovered here. The correct asymptotic behaviour of $\hat{\beta}_\times \sim \frac{3}{2}\frac{1}{\chi}$ for $\chi \gg 1$ is also recovered by the reduced Lorentz model for the same reason. The $\hat{\alpha}_\perp$ coefficient is also recovered in this limit, but this is due to the non-Maxwellian correction to $\hat{\alpha}_\perp$ becoming subleading for large χ. Aside from these matching asymptotic behaviours, discrepancies in $\hat{\alpha}$ and $\hat{\beta}$ are clear for low, moderate, and high magnetisations.

These plots emphasise that nonlocal closures based on a rescaled Lorentz collision operator do not reproduce local transport coefficients. If such a closure is used in a hydrodynamic code, local transport will not be correctly described, and the nonlocal behaviour is not accurately described either due to the limited collision model.

There are numerous works that compare a set of nonlocal transport closures against each other and to full VFP simulations for ICF-relevant test problems. Work by Marocchino et al. [12] compares SNB, another model known as CMG, and flux-limited Spitzer-Härm heat flow against the full kinetic code OSHUN. Both of the nonlocal closures capture the correct qualitative behaviour, but there are quantitative discrepancies. Work by Sherlock et al. in 2017 [105] compares SNB to the VFP code K2. Here, mostly good qualitative agreement is found between the models, but there are still significant quantitative differences between the heat flow predicted by SNB compared to K2. It is worth emphasising that the K2 simulations of this work do not use proper electron-electron collisions, but rely on the same rescaled Lorentz collision operator discussed above. Another comparison by Brodrick et al. [10] compares SNB and a couple of other closures against kinetic simulations from the IMPACT, SPRING, and KIPP codes. Again, decent agreement of SNB with VFP simulations is shown but with notable discrepancies. These works also emphasise a free parameter 'r' appearing in the collision operators of SNB-like closures. Finally, recent work by Arran et al. in 2025 [11] compares two SNB-like closures, M1 and hybrid-AWBS-BGK, against the VFP codes IMPACT and K2 for magnetised heat conduction. Comparisons are carried out at extremely high ionisations so the VFP simulations essentially use Lorentz collision operators. Similar to other comparisons, agreement is decent but there are noticeable differences in both unmagnetised and magnetised nonlocal cases. Full VFP OSHUN simulations by Zhao et al. [106] demonstrate nonlocal transport in magnetised plasmas. Although these works are effectively first-principles studies, they employ VFP simulations as numerical experiments rather than closures for nonlocal heat transport. For simulating large-scale plasma systems such as an ICF implosion, hydrodynamics codes are required, leaving a requirement for nonlocal closures.

CHAPTER 3

Reduced Kinetic Method Framework

3.1 Reducing Kinetic Equations

The RKM reduces the VFP equation to a tractable linear problem for the deviation of distribution function from Maxwellian (DDF) δf_α from which transport fluxes may be evaluated. Deriving the RKM equation follows three key steps: firstly, the distribution function is decomposed as $f_\alpha = f_\alpha^M + \delta f_\alpha$. Secondly, the nonlinear component of the collision operator $\sim C_{\alpha\beta}\{\delta f_\alpha, \delta f_\beta\}$ is neglected, which is justified for $N_K \lesssim 1/10$. Finally, the DDF is expanded over spherical harmonics in velocity space, where truncating to the first N_l terms leaves a set of PDEs for the projections of the DDF $\delta f_\alpha^{(l,m)}(\boldsymbol{x}, w)$ that may be solved over the spatial domain and single speed coordinate. For this work, a one-dimensional spatial geometry is always considered for simplicity, although the RKM may be straightforwardly extended to two or three spatial dimensions.

3.1.1 Electron RKM

Starting with the electron VFP equation

$$\partial_t f_e + \boldsymbol{v}\cdot\boldsymbol{\nabla} f_e - \frac{e}{m_e}\big(\boldsymbol{E}+\boldsymbol{v}\times\boldsymbol{B}\big)\cdot\boldsymbol{\nabla}_{\boldsymbol{v}} f_e = C_{ee}\{f_e, f_e\} + C_{ei}\{f_e, f_i\}, \tag{3.1}$$

we change coordinates $(t, \boldsymbol{x}, \boldsymbol{v})$ to $(t' = t, \boldsymbol{x}' = \boldsymbol{x}, \boldsymbol{w} = \boldsymbol{v} - \boldsymbol{u}_e(t, \boldsymbol{x}))$. Derivatives transform as

$$\partial_t = (\partial_t t')\partial_{t'} + (\partial_t \boldsymbol{x}')\cdot\boldsymbol{\nabla}_{\boldsymbol{x}'} + (\partial_t \boldsymbol{w})\cdot\boldsymbol{\nabla}_{\boldsymbol{w}} = \partial_{t'} - (\partial_t \boldsymbol{u}_e)\cdot\boldsymbol{\nabla}_{\boldsymbol{w}}, \tag{3.2}$$

$$\boldsymbol{\nabla}_{\boldsymbol{x}} = (\boldsymbol{\nabla}_{\boldsymbol{x}} t')\partial_{t'} + (\boldsymbol{\nabla}_{\boldsymbol{x}} \boldsymbol{x}')\cdot\boldsymbol{\nabla}_{\boldsymbol{x}'} + (\boldsymbol{\nabla}_{\boldsymbol{x}} \boldsymbol{w})\cdot\boldsymbol{\nabla}_{\boldsymbol{w}} = \boldsymbol{\nabla}_{\boldsymbol{x}'} - (\boldsymbol{\nabla}_{\boldsymbol{x}} \boldsymbol{u}_e)\cdot\boldsymbol{\nabla}_{\boldsymbol{w}}, \tag{3.3}$$

$$\boldsymbol{\nabla}_{\boldsymbol{v}} = (\boldsymbol{\nabla}_{\boldsymbol{v}} t')\partial_{t'} + (\boldsymbol{\nabla}_{\boldsymbol{v}} \boldsymbol{x}')\cdot\boldsymbol{\nabla}_{\boldsymbol{x}'} + (\boldsymbol{\nabla}_{\boldsymbol{v}} \boldsymbol{w})\cdot\boldsymbol{\nabla}_{\boldsymbol{w}} = \boldsymbol{\nabla}_{\boldsymbol{w}}. \tag{3.4}$$

Dropping primes, this yields the electron VFP equation in the electron CoM frame as

$$\partial_t f_e - (\partial_t \boldsymbol{u}_e)\cdot\boldsymbol{\nabla}_{\boldsymbol{w}} f_e + (\boldsymbol{w}+\boldsymbol{u}_e)\cdot(\boldsymbol{\nabla} - (\boldsymbol{\nabla}\boldsymbol{u}_e)\cdot\boldsymbol{\nabla}_{\boldsymbol{w}}) f_e - \frac{e}{m_e}\big(\boldsymbol{E}+(\boldsymbol{w}+\boldsymbol{u}_e)\times\boldsymbol{B}\big)\cdot\boldsymbol{\nabla}_{\boldsymbol{w}} f_e = C_{ee}\{f_e, f_e\} + C_{ei}\{f_e, f_i\}. \tag{3.5}$$

The electron momentum equation, obtained as the $m_e\boldsymbol{v}$ moment of the electron kinetic equation 3.1 or $m_e\boldsymbol{w}$ moment of 3.5, is

$$\partial_t \boldsymbol{u}_e + \boldsymbol{u}_e \cdot \boldsymbol{\nabla}\boldsymbol{u}_e = \frac{1}{\rho_e}\bigg(- \boldsymbol{\nabla} p_e - \boldsymbol{\nabla}\cdot\Pi_e - e n_e\big(\boldsymbol{E} + \boldsymbol{u}_e \times \boldsymbol{B}\big) + \boldsymbol{R}_e\bigg), \tag{3.6}$$

where $p_e = n_e T_e$ is the electron pressure, Π_e is the electron viscous stress tensor, and $\boldsymbol{R}_e$ is the electron-ion momentum exchange defined as $\boldsymbol{R}_e = \int d^3\boldsymbol{v}\; m_e \boldsymbol{v} C_{ei}$. Substituting in $\partial_t \boldsymbol{u}_e$ from the electron momentum equation 3.6 into Equation 3.5 cancels various terms, yielding

$$\partial_t f_e + \hat{V}_e f_e + \hat{B}_e f_e = C_{ee}\{f_e, f_e\} + C_{ei}\{f_e, f_i\}, \tag{3.7}$$

where the unmagnetised electron Vlasov operator in the CoM frame is

$$\hat{V}_e = (\boldsymbol{w} + \boldsymbol{u}_e)\cdot\boldsymbol{\nabla} - \bigg[\boldsymbol{w}\cdot(\boldsymbol{\nabla}\boldsymbol{u}_e) + \frac{1}{\rho_e}\bigg(- \boldsymbol{\nabla} p_e - \boldsymbol{\nabla}\cdot\Pi_e + \boldsymbol{R}_e\bigg)\bigg]\cdot\boldsymbol{\nabla}_{\boldsymbol{w}}, \tag{3.8}$$

and the magnetic field term

$$\hat{B}_e = -\frac{e}{m_e}(\boldsymbol{w}\times\boldsymbol{B})\cdot\boldsymbol{\nabla}_{\boldsymbol{w}}. \tag{3.9}$$

The electron DF is then decomposed as $f_e = f_e^M + \delta f_e$, where the electron Maxwellian distribution is $f_e^M = n_e(\sqrt{\pi}v_{\mathrm{th},e})^{-3}\exp(-(w/v_{\mathrm{th},e})^2)$ with thermal velocity $v_{\mathrm{th},e} = \sqrt{2T_e/m_e}$. Unlike the Chapman-Enskog expansion, this decomposition does not assume a small deviation from Maxwellian $|\delta f_e/f_e^M| \ll 1$. This expands the collision terms as

$$\begin{aligned} C_{ee}\{f_e, f_e\} &\approx \underbrace{C_{ee}\{\delta f_e, f_e^M\}}_{=C_{ee}^T\{\delta f_e\}} + \underbrace{C_{ee}\{f_e^M, \delta f_e\}}_{=C_{ee}^F\{\delta f_e\}} = \hat{C}_{ee}\delta f_e, \\ C_{ei}\{f_e, f_i\} &\approx \underbrace{C_{ei}\{f_e^M, f_i^M\}}_{=C_{ei}^M} + \underbrace{C_{ei}\{\delta f_e, f_i^M\}}_{=C_{ei}\{\delta f_e\}} = C_{ei}^M + \hat{C}_{ei}\delta f_e, \end{aligned} \tag{3.10}$$

where $C_{ee}\{f_e^M, f_e^M\} = 0$ identically, and the collision term between an electron Maxwellian and ion Maxwellian with relative flow $\Delta\boldsymbol{u}$ is

$$C_{ei}^M = -2\hat{\nu}_{ei}\frac{\boldsymbol{w}\cdot\Delta\boldsymbol{u}}{\xi_e^3} f_e^M. \tag{3.11}$$

Even for large non-Maxwellian deviations in the tail of the distribution, the nonlinear electron-electron term $C_{ee}\{\delta f_e, \delta f_e\}$ may be neglected. This is justified *a posteriori* in Sections 4.2.5 and 5.7 for the unmagnetised and magnetised cases, respectively. On scales relevant to electron transport $w \sim v_{\mathrm{th},e} \gg v_{\mathrm{th},i}$, the electron-ion collision operator to leading order in mass ratio $m_e/m_i \ll 1$ reduces to the same form as colliding against a Maxwellian ion distribution, i.e. $C_{ei}\{f_e, f_i\} \approx C_{ei}\{f_e, f_i^M\}$. Even if multiple ion species are present or the plasma is not quasineutral, the electron-ion collision operator against individual ion species is in a form that allows the total electron-ion collision operator to be written in the same form as a single-species electron-ion collision operator with effective ionisation $Z^* = \sum_\alpha \hat{\nu}_{e\alpha}/\hat{\nu}_{ee} = \sum_\alpha Z_\alpha^2 \frac{n_\alpha}{n_e}\frac{\ln\Lambda_{e\alpha}}{\ln\Lambda_{ee}}$ for ions with labels α. Equation 3.7 becomes

$$\partial_t f_e^M + \hat{V}_e f_e^M - C_{ei}^M = \big(\hat{C}_{ee} + \hat{C}_{ei} - \partial_t - \hat{V}_e - \hat{B}_e\big)\delta f_e \tag{3.12}$$

The time derivative of the DDF may be taken to be zero $\partial_t \delta f_e = 0$ as the transport closure may be assumed to be local in time [107]. In a fluid simulation, the effect of the history of the DDF may still be taken into account by writing

$$\partial_t \delta f_e \approx \frac{\delta f_e(t) - \delta f_e(t - \Delta t)}{\Delta t}, \tag{3.13}$$

where Δt is the current hydrodynamic timestep, and $\delta f_e(t - \Delta t)$ has already been determined by the RKM on the previous timestep. The $\delta f_e(t - \Delta t)/\Delta t$ term is then moved to the left hand side into the driving terms, and $\delta f_e(t)/\Delta t$ is kept on the right hand side as an operator. For the purposes of this work, these terms are ignored, but could be straightforwardly included when integrating the RKM into a fluid simulation.

The Maxwellian terms on the left hand side may be evaluated using

$$\begin{aligned}
\partial_t f_e^M &= \left(\partial_t \ln n_e + \left(\frac{w^2}{v_{\text{th},e}^2} - \frac{3}{2}\right)\partial_t \ln T_e\right) f_e^M \\
&= \left(- \boldsymbol{\nabla}\cdot\boldsymbol{u}_e - \boldsymbol{u}_e\cdot\boldsymbol{\nabla}\ln n_e + \left(\frac{w^2}{v_{\text{th},e}^2} - \frac{3}{2}\right)\left(- \boldsymbol{u}_e\cdot\boldsymbol{\nabla}\ln T_e - \frac{2}{3}\boldsymbol{\nabla}\cdot\boldsymbol{u}_e + K_e\right)\right) f_e^M, \\
\boldsymbol{\nabla} f_e^M &= \left(\boldsymbol{\nabla}\ln n_e + \left(\frac{w^2}{v_{\text{th},e}^2} - \frac{3}{2}\right)\boldsymbol{\nabla}\ln T_e\right) f_e^M, \\
\boldsymbol{\nabla}_{\boldsymbol{w}} f_e^M &= -\frac{2}{v_{\text{th},e}^2} f_e^M \boldsymbol{w},
\end{aligned} \tag{3.14}$$

where the time derivatives of the density and temperature have been rewritten using the electron density and temperature fluid equations which may be written in the form

$$\begin{aligned}
\partial_t \ln n_e &= -\boldsymbol{\nabla}\cdot\boldsymbol{u}_e - \boldsymbol{u}_e\cdot\boldsymbol{\nabla}\ln n_e, \\
\partial_t \ln T_e &= -\boldsymbol{u}_e\cdot\boldsymbol{\nabla}\ln T_e - \frac{2}{3}\boldsymbol{\nabla}\cdot\boldsymbol{u}_e + K_e,
\end{aligned} \tag{3.15}$$

where the $\mathcal{O}(N_K^2)$ transport terms are written together as

$$K_e = \frac{2}{3p_e}\left[- \boldsymbol{\nabla}\cdot\boldsymbol{q}_e - \Pi_e : \boldsymbol{\nabla}\boldsymbol{u}_e - \boldsymbol{R}_e\cdot(\boldsymbol{u}_e - \boldsymbol{u}_i) - \tilde{W}_{ie}\right], \quad \tilde{W}_{ie} = \frac{4}{\sqrt{\pi}} n_e \hat{\nu}_{ei}\frac{m_e}{m_i}(T_e - T_i). \tag{3.16}$$

Combining these together, the terms on the left hand side become

$$\begin{aligned}
D_e &\coloneqq \partial_t f_e^M + \hat{V}_e f_e^M - C_{ei}\{f_e^M, f_i^M\} - \frac{1}{\Delta t}\delta f_e(t - \Delta t) \\
&= \left[\left(\frac{w^2}{v_{\text{th},e}^2} - \frac{3}{2}\right)K_e + \frac{2}{v_{\text{th},e}^2}\boldsymbol{\nabla}\boldsymbol{u}_e : \left(\boldsymbol{w}\boldsymbol{w} - \frac{1}{3}w^2\mathbb{I}\right)\right. \\
&\left. + \left(\left(\frac{w^2}{v_{\text{th},e}^2} - \frac{5}{2}\right)\boldsymbol{\nabla}\ln T_e + \frac{1}{p_e}\left(- \boldsymbol{\nabla}\cdot\Pi_e + \boldsymbol{R}_e\right) + 2\hat{\nu}_{ei}\frac{v_{\text{th},e}}{w^3}\Delta\boldsymbol{u}\right)\cdot\boldsymbol{w}\right] f_e^M - \frac{1}{\Delta t}\delta f_e(t - \Delta t),
\end{aligned} \tag{3.17}$$

leaving the kinetic equation

$$D_e = \left(\hat{C}_e - \hat{V}_e - \hat{B}_e - (\Delta t)^{-1}\right)\delta f_e. \tag{3.18}$$

The driving term D_e and CoM Vlasov operator $\hat{V}_e$ are dependent on transport quantities which themselves are determined from moments of δf_e. For Knudsen numbers $N_K \lesssim 1/10$, almost all of these terms are subleading and may be neglected as they are in the Chapman-Enskog expansion. The exception to this is the momentum exchange $\boldsymbol{R}_e$ appearing in the electron driving term D_e, which depends on δf_e to leading order.

Braginskii [15] solves this by taking the integral part of $\boldsymbol{R}_e$ acting on δf_e to the right hand side, then solving the resulting linear problem. Although a similar approach may be employed here, we keep these transport terms within D_e on the left hand side. In cases with high Knudsen numbers, the appearance of additional transport terms under spatial derivatives appearing in D_e such as $\boldsymbol{\nabla} \cdot \Pi_e$ would introduce much more complicated and dense matrix operators if included in the right hand side, and the appearance of transport quantities in $\hat{V}_e$ yields a nonlinear problem. These complications are only small corrections to the kinetic equations, therefore they may be handled by solving the equations iteratively. The electron DDF equation 3.18 is first solved with the local results for transport quantities to obtain the DDF δf_e. From the DDF, transport quantities may be recomputed. In the local limit, these are expected to be self-consistent. In nonlocal cases, the transport quantities may have modifications, so the solution is inconsistent. These computed transport quantities may be then fed back into the same DDF equation to be solved again. This procedure is iterated until all transport quantities are self-consistent over the spatial domain within some tolerance. In most cases, neglecting $\mathcal{O}(N_K^2)$ terms is sufficient, leaving $D_e \approx D_e^{(0)}$ where

$$\begin{aligned} D_e^{(0)} = \Bigg[& \frac{2}{v_{\mathrm{th},e}^2} \boldsymbol{\nabla} \boldsymbol{u}_e : \left(\boldsymbol{w}\boldsymbol{w} - \frac{1}{3} w^2 \mathbb{I} \right) \\ & + \left(\left(\frac{w^2}{v_{\mathrm{th},e}^2} - \frac{5}{2} \right) \boldsymbol{\nabla} \ln T_e + \frac{\boldsymbol{R}_e}{p_e} + 2\hat{\nu}_{ei} \frac{v_{\mathrm{th},e}}{w^3} \Delta \boldsymbol{u} \right) \cdot \boldsymbol{w} \Bigg] f_e^M. \end{aligned} \tag{3.19}$$

In the local limit, i.e. for $N_K \lll 1$, the Vlasov term $\hat{V}_e \delta f_e \sim \mathcal{O}(N_K^2)$ is subleading, and therefore the electron DDF equation becomes

$$D_e^{(0)} = (\hat{C}_e - \hat{B}_e) \delta f_e, \tag{3.20}$$

which is exactly the first-order Chapman-Enskog equation for the local electron problem.

Repeating the procedure for a single ion species yields the ion kinetic equation for $\delta f_i = f_i - f_i^M$ as

$$D_i = \left(\hat{C}_{ii} + \hat{C}_{ie} - \hat{V}_i - \hat{B}_i - (\Delta t)^{-1} \right) \delta f_i, \tag{3.21}$$

where

$$\begin{aligned} \boldsymbol{w} &= \boldsymbol{v} - \boldsymbol{u}_i, \\ D_i &= \left[\left(\frac{w^2}{v_{\mathrm{th},i}^2} - \frac{3}{2} \right) K_i + \frac{2}{v_{\mathrm{th},i}^2} \boldsymbol{\nabla} \boldsymbol{u}_i : \left(\boldsymbol{w}\boldsymbol{w} - \frac{1}{3} w^2 \mathbb{I} \right) + \left(\left(\frac{w^2}{v_{\mathrm{th},i}^2} - \frac{5}{2} \right) \boldsymbol{\nabla} \ln T_i - \frac{1}{p_i} \boldsymbol{\nabla} \cdot \Pi_i \right) \cdot \boldsymbol{w} \right] f_i^M \\ &\quad - \frac{1}{\Delta t} \delta f_i(t - \Delta t), \\ K_i &= \frac{2}{3 p_i} \left[- \boldsymbol{\nabla} \cdot \boldsymbol{q}_i - \Pi_i : \boldsymbol{\nabla} \boldsymbol{u}_i \right], \\ \hat{V}_i &= (\boldsymbol{w} + \boldsymbol{u}_i) \cdot \boldsymbol{\nabla} - \left[\boldsymbol{w} \cdot (\boldsymbol{\nabla} \boldsymbol{u}_i) + \frac{1}{\rho_i} \left(- \boldsymbol{\nabla} p_i - \boldsymbol{\nabla} \cdot \Pi_i \right) \right] \cdot \boldsymbol{\nabla}_{\boldsymbol{w}}, \\ \hat{B}_i &= \frac{Ze}{m_i} (\boldsymbol{w} \times \boldsymbol{B}) \cdot \boldsymbol{\nabla}_{\boldsymbol{w}}, \end{aligned} \tag{3.22}$$

where the ion-electron Maxwellian collision terms $C_{ei}\{f_i^M, f_e^M\}$ have cancelled exactly with the $\boldsymbol{R}_e$ and $\tilde{W}_{ie}$ terms in D_i, and similarly the $\boldsymbol{R}_e$ term in $C_{ie}\{\delta f_i, f_e^M\}$ and $\hat{V}_i$ have cancelled. These cancellations mean that

all electron transport terms have vanished from the ion DDF equation so the ion solution does not require solving for electron transport first. The only appearance of electrons in the ion DDF equation is through the ion-electron collision term $\hat{C}_{ie}\delta f_i = C_{ie}\{f_i, f_e^M\}$. The ion-electron collision terms are neglected by Braginskii [15] since they are small by a factor of mass-ratio, however Ji and Held have shown that ion-electron collisions have a significant impact ($\sim 10\%$) on ion transport coefficients [87, 88], especially for larger ion temperatures $T_i > T_e$.

3.1.2 Multi-species RKM

Starting from the ion VFP equations in a multi-species plasma for each ion species α

$$\partial_t f_\alpha + \boldsymbol{v}\cdot\boldsymbol{\nabla} f_\alpha + \frac{q_\alpha}{m_\alpha}\bigg(\boldsymbol{E} + \boldsymbol{v}\times\boldsymbol{B}\bigg)\cdot\boldsymbol{\nabla}_{\boldsymbol{v}} f_\alpha = \sum_\beta C_{\alpha\beta}\{f_\alpha, f_\beta\} + C_{\alpha e}\{f_\alpha, f_e\}, \tag{3.23}$$

where the sum over β includes all ion species but not electrons. The ion-electron collision operator has been written separately. Changing coordinates to the frame comoving with the ion CoM velocity via $(t, \boldsymbol{x}, \boldsymbol{v}) \to (t' = t, \boldsymbol{x}' = \boldsymbol{x}, \boldsymbol{w} = \boldsymbol{v} - \boldsymbol{u}_i(t, \boldsymbol{x}))$, the derivatives transform the same as before. Transforming the ion VFP equations to these new coordinates and dropping primes yields

$$\begin{aligned}&\partial_t f_\alpha + (\boldsymbol{w}+\boldsymbol{u}_i)\cdot\boldsymbol{\nabla} f_\alpha + \bigg[-(\partial_t \boldsymbol{u}_i) - (\boldsymbol{w}+\boldsymbol{u}_i)\cdot(\boldsymbol{\nabla}\boldsymbol{u}_i) + \frac{q_\alpha}{m_\alpha}\bigg(\boldsymbol{E} + (\boldsymbol{w}+\boldsymbol{u}_i)\times\boldsymbol{B}\bigg)\bigg]\cdot\boldsymbol{\nabla}_{\boldsymbol{w}} f_\alpha \\ &= \sum_\beta C_{\alpha\beta}\{f_\alpha, f_\beta\} + C_{\alpha e}\{f_\alpha, f_e\}\end{aligned} \tag{3.24}$$

Using the mixture momentum equation to replace the flow time derivative

$$\partial_t \boldsymbol{u}_i + \boldsymbol{u}_i\cdot\boldsymbol{\nabla}\boldsymbol{u}_i = \frac{1}{\rho_i}\bigg(-\boldsymbol{\nabla} p_i - \boldsymbol{\nabla}\cdot\Pi_i + \sigma_i(\boldsymbol{E} + \boldsymbol{u}_i\times\boldsymbol{B}) + \boldsymbol{j}_D\times\boldsymbol{B} - \boldsymbol{R}_e\bigg), \tag{3.25}$$

where $\sigma_i = \sum_\beta q_\beta n_\beta$ and $\boldsymbol{j}_D = \sum_\beta q_\beta n_\beta \boldsymbol{V}_\beta$, we obtain

$$\begin{aligned}&\partial_t f_\alpha + (\boldsymbol{w}+\boldsymbol{u}_i)\cdot\boldsymbol{\nabla} f_\alpha + \bigg[-\boldsymbol{w}\cdot(\boldsymbol{\nabla}\boldsymbol{u}_i) + \frac{1}{\rho_i}\bigg(\boldsymbol{\nabla} p_i + \boldsymbol{\nabla}\cdot\Pi_i\bigg) - \frac{\sigma_i}{\rho_i}(\boldsymbol{E} + \boldsymbol{u}_i\times\boldsymbol{B}) - \frac{1}{\rho_i}\boldsymbol{j}_D\times\boldsymbol{B} \\ &+ \frac{1}{\rho_i}\boldsymbol{R}_e + \frac{q_\alpha}{m_\alpha}\bigg(\boldsymbol{E} + (\boldsymbol{w}+\boldsymbol{u}_i)\times\boldsymbol{B}\bigg)\bigg]\cdot\boldsymbol{\nabla}_{\boldsymbol{w}} f_\alpha = \sum_\beta C_{\alpha\beta}\{f_\alpha, f_\beta\} + C_{\alpha e}\{f_\alpha, f_e\}.\end{aligned} \tag{3.26}$$

Collating terms, this becomes

$$\begin{aligned}&\partial_t f_\alpha + (\boldsymbol{w}+\boldsymbol{u}_i)\cdot\boldsymbol{\nabla} f_\alpha + \bigg[-\boldsymbol{w}\cdot(\boldsymbol{\nabla}\boldsymbol{u}_i) + \frac{1}{\rho_i}\bigg(\boldsymbol{\nabla} p_i + \boldsymbol{\nabla}\cdot\Pi_i + \boldsymbol{R}_e\bigg) + \tilde{\boldsymbol{Y}}_\alpha + \frac{q_\alpha}{m_\alpha}(\boldsymbol{w}\times\boldsymbol{B})\bigg]\cdot\boldsymbol{\nabla}_{\boldsymbol{w}} f_\alpha \\ &= \sum_\beta C_{\alpha\beta}\{f_\alpha, f_\beta\} + C_{\alpha e}\{f_\alpha, f_e\},\end{aligned} \tag{3.27}$$

where

$$\tilde{\boldsymbol{Y}}_\alpha = \bigg(\frac{q_\alpha}{m_\alpha} - \sum_\beta c_\beta \frac{q_\beta}{m_\beta}\bigg)(\boldsymbol{E} + \boldsymbol{u}_i\times\boldsymbol{B}) - \bigg(\sum_\beta c_\beta \frac{q_\beta}{m_\beta}\boldsymbol{V}_\beta\bigg)\times\boldsymbol{B} \tag{3.28}$$

Each ion DF is then decomposed into a Maxwellian (with the mixture temperature and flow) and a deviation $f_\alpha = f_\alpha^M + \delta f_\alpha$, where each ion Maxwellian

$$f_\alpha^M = n_\alpha\bigg(\frac{m_\alpha}{2\pi T_i}\bigg)^{3/2}\exp\bigg(-\frac{m_\alpha w^2}{2T_i}\bigg). \tag{3.29}$$

Substituting into the ion kinetic equations in the CoM frame,

$$
\begin{aligned}
&(\partial_t + \boldsymbol{u}_i\cdot\boldsymbol{\nabla})f_\alpha^M + \boldsymbol{w}\cdot\boldsymbol{\nabla}f_\alpha^M + \left[-\boldsymbol{w}\cdot(\boldsymbol{\nabla}\boldsymbol{u}_i) + \frac{1}{\rho_i}\left(\boldsymbol{\nabla}p_i + \boldsymbol{\nabla}\cdot\Pi_i + \boldsymbol{R}_e\right) + \tilde{\boldsymbol{Y}}_\alpha + \frac{q_\alpha}{m_\alpha}(\boldsymbol{w}\times\boldsymbol{B})\right]\cdot\boldsymbol{\nabla}_{\boldsymbol{w}}f_\alpha^M \\
&+ \partial_t\delta f_\alpha + (\boldsymbol{w}+\boldsymbol{u}_i)\cdot\boldsymbol{\nabla}\delta f_\alpha + \left[-\boldsymbol{w}\cdot(\boldsymbol{\nabla}\boldsymbol{u}_i) + \frac{1}{\rho_i}\left(\boldsymbol{\nabla}p_i + \boldsymbol{\nabla}\cdot\Pi_i + \boldsymbol{R}_e\right) + \tilde{\boldsymbol{Y}}_\alpha + \frac{q_\alpha}{m_\alpha}(\boldsymbol{w}\times\boldsymbol{B})\right]\cdot\boldsymbol{\nabla}_{\boldsymbol{w}}\delta f_\alpha \\
&= \sum_\beta\left(C_{\alpha\beta}\{f_\alpha^M, f_\beta^M\} + C_{\alpha\beta}\{\delta f_\alpha, f_\beta^M\} + C_{\alpha\beta}\{f_\alpha^M, \delta f_\beta\}\right) + C_{\alpha e}\{f_\alpha^M, f_e\} + C_{\alpha e}\{\delta f_\alpha, f_e\}.
\end{aligned}
\tag{3.30}
$$

The first line involves derivatives acting on the Maxwellian which may be evaluated using the particle continuity equation

$$
\partial_t n_\alpha = -\boldsymbol{\nabla}\cdot(n_\alpha(\boldsymbol{u}_i + \boldsymbol{V}_\alpha)) \quad\Rightarrow\quad (\partial_t + \boldsymbol{u}_i\cdot\boldsymbol{\nabla})\ln n_\alpha = -\boldsymbol{\nabla}\cdot(\boldsymbol{u}_i + \boldsymbol{V}_\alpha) - \boldsymbol{V}_\alpha\cdot\boldsymbol{\nabla}\ln n_\alpha \tag{3.31}
$$

and temperature equation

$$
\begin{aligned}
&\partial_t\left(\frac{3}{2}n_iT_i\right) + \boldsymbol{\nabla}\cdot\left[\frac{3}{2}n_iT_i\boldsymbol{u}_i + \boldsymbol{q}_i\right] = -p_i\boldsymbol{\nabla}\cdot\boldsymbol{u}_i - \Pi_i\colon\boldsymbol{\nabla}\boldsymbol{u}_i + \boldsymbol{j}_D\cdot(\boldsymbol{E}+\boldsymbol{u}_i\times\boldsymbol{B}) + \tilde{W}_{ie} \\
\Rightarrow\quad &(\partial_t + \boldsymbol{u}_i\cdot\boldsymbol{\nabla})\ln T_i = \\
&\frac{2}{3}\left[-\boldsymbol{\nabla}\cdot\boldsymbol{u}_i - \frac{1}{p_i}\boldsymbol{\nabla}\cdot\boldsymbol{q}_i - \frac{1}{p_i}\Pi_i\colon\boldsymbol{\nabla}\boldsymbol{u}_i + \frac{1}{p_i}\boldsymbol{j}_D\cdot(\boldsymbol{E}+\boldsymbol{u}_i\times\boldsymbol{B}) + \frac{1}{p_i}\tilde{W}_{ie}\right] + \boldsymbol{\nabla}\cdot\left(\sum_\beta\frac{n_\beta}{n_i}\boldsymbol{V}_\beta\right)
\end{aligned}
\tag{3.32}
$$

where the total number density derivative is evaluated using

$$
\partial_t n_i + \boldsymbol{\nabla}\cdot(n_i\boldsymbol{u}_i) = -\boldsymbol{\nabla}\cdot\left(\sum_\beta n_\beta\boldsymbol{V}_\beta\right). \tag{3.33}
$$

The relevant Maxwellian derivatives are then evaluated as

$$
\boldsymbol{\nabla}f_\alpha^M = \left[\boldsymbol{\nabla}\ln n_\alpha + \left(\frac{w^2}{v_{\mathrm{th},\alpha}^2} - \frac{3}{2}\right)\boldsymbol{\nabla}\ln T_i\right]f_\alpha^M, \quad \boldsymbol{\nabla}_{\boldsymbol{w}}f_\alpha^M = -\frac{2}{v_{\mathrm{th},\alpha}^2}f_\alpha^M\boldsymbol{w}, \tag{3.34}
$$

and

$$
\begin{aligned}
(\partial_t + \boldsymbol{u}_i\cdot\boldsymbol{\nabla})f_\alpha^M &= \left[(\partial_t + \boldsymbol{u}_i\cdot\boldsymbol{\nabla})\ln n_\alpha + \left(\frac{w^2}{v_{\mathrm{th},\alpha}^2} - \frac{3}{2}\right)(\partial_t + \boldsymbol{u}_i\cdot\boldsymbol{\nabla})\ln T_i\right]f_\alpha^M \\
&= \left[-\frac{2}{3}\frac{w^2}{v_{\mathrm{th},\alpha}^2}\boldsymbol{\nabla}\cdot\boldsymbol{u}_i - \boldsymbol{\nabla}\cdot\boldsymbol{V}_\alpha - \boldsymbol{V}_\alpha\cdot\boldsymbol{\nabla}\ln n_\alpha + \left(\frac{w^2}{v_{\mathrm{th},\alpha}^2} - \frac{3}{2}\right)\left(\frac{2}{3}\left[-\frac{1}{p_i}\boldsymbol{\nabla}\cdot\boldsymbol{q}_i\right.\right.\right. \\
&\left.\left.\left. - \frac{1}{p_i}\Pi_i\colon\boldsymbol{\nabla}\boldsymbol{u}_i + \frac{1}{p_i}\boldsymbol{j}_D\cdot(\boldsymbol{E}+\boldsymbol{u}_i\times\boldsymbol{B}) + \frac{1}{p_i}\tilde{W}_{ie}\right] + \boldsymbol{\nabla}\cdot\left(\sum_\beta\frac{n_\beta}{n_i}\boldsymbol{V}_\beta\right)\right)\right]f_\alpha^M.
\end{aligned}
\tag{3.35}
$$

The ion-electron collision terms are

$$
\begin{aligned}
C_{\alpha e}\{\delta f_\alpha, f_e\} &= \frac{1}{\rho_\alpha}\boldsymbol{R}_{e\alpha}\cdot\boldsymbol{\nabla}_{\boldsymbol{w}}\delta f_\alpha + \hat{C}_{\alpha e}^T\delta f_\alpha, \\
C_{\alpha e}\{f_\alpha^M, f_e\} &= \left[-\frac{1}{p_\alpha}\boldsymbol{R}_e\cdot\boldsymbol{w} - \frac{8}{3\sqrt{\pi}}\hat{\nu}_{e\alpha}\frac{\rho_e}{\rho_\alpha}\left(1 - \frac{T_e}{T_i}\right)\left(\frac{w^2}{v_{\mathrm{th},\alpha}^2} - \frac{3}{2}\right)\right]f_\alpha^M \\
&= \left[-\frac{1}{p_\alpha}\boldsymbol{R}_{e\alpha}\cdot\boldsymbol{w} + \frac{2}{3p_\alpha}\tilde{W}_{\alpha e}\left(\frac{w^2}{v_{\mathrm{th},\alpha}^2} - \frac{3}{2}\right)\right]f_\alpha^M,
\end{aligned}
\tag{3.36}
$$

where

$$
\tilde{W}_{\alpha e} = \frac{4}{\sqrt{\pi}}\frac{m_e}{m_\alpha}n_e\hat{\nu}_{e\alpha}(T_e - T_i) = \frac{4}{\sqrt{\pi}}\frac{\rho_e}{\rho_\alpha}p_\alpha\hat{\nu}_{e\alpha}\left(\frac{T_e}{T_i} - 1\right), \quad \tilde{W}_{ie} = \sum_\beta\tilde{W}_{\beta e}. \tag{3.37}
$$

The inhomogeneous terms on the LHS become

$$\begin{aligned} D_\alpha \equiv (\partial_t + \boldsymbol{u}_i \cdot \boldsymbol{\nabla}) f_\alpha^M + \boldsymbol{w} \cdot \boldsymbol{\nabla} f_\alpha^M + \Bigg[- \boldsymbol{w} \cdot (\boldsymbol{\nabla} \boldsymbol{u}_i) + \frac{1}{\rho_i} \Big(\boldsymbol{\nabla} p_i + \boldsymbol{\nabla} \cdot \Pi_i + \boldsymbol{R}_e \Big) \\ + \tilde{\boldsymbol{Y}}_\alpha + \frac{q_\alpha}{m_\alpha} (\boldsymbol{w} \times \boldsymbol{B}) \Bigg] \cdot \boldsymbol{\nabla}_{\boldsymbol{w}} f_\alpha^M - C_{\alpha e} \{ f_i^M, f_e^M \} \\ \approx \left(\boldsymbol{w} \cdot \frac{n_i}{n_\alpha} \boldsymbol{d}_\alpha + \left(\frac{w^2}{v_{\mathrm{th},\alpha}^2} - \frac{5}{2} \right) \boldsymbol{w} \cdot \boldsymbol{\nabla} \ln T_i + \frac{2}{v_{\mathrm{th},\alpha}^2} \left(\boldsymbol{w}\boldsymbol{w} - \frac{1}{3} \mathbb{I} \right) : \boldsymbol{\nabla} \boldsymbol{u}_i + \frac{c_\alpha}{p_\alpha} \boldsymbol{w} \cdot (\boldsymbol{j}_D \times \boldsymbol{B}) \right) f_\alpha^M \end{aligned} \tag{3.38}$$

where

$$\boldsymbol{d}_\alpha = \frac{\boldsymbol{\nabla} p_\alpha - c_\alpha \boldsymbol{\nabla} p_i}{p_i} - \frac{\rho_\alpha}{p_i} \left(\boldsymbol{X}_\alpha - \sum_\beta c_\beta \boldsymbol{X}_\beta \right), \quad \boldsymbol{X}_\alpha = \frac{q_\alpha}{m_\alpha} (\boldsymbol{E} + \boldsymbol{u}_i \times \boldsymbol{B}) - \frac{1}{\rho_\alpha} \boldsymbol{R}_{e\alpha}. \tag{3.39}$$

The final line contains only the leading order $\mathcal{O}(N_K)$ terms, with the other $\mathcal{O}(N_K^2)$ terms kept in the previous line to identify the neglected terms, which may be readily included in the RKM. The Vlasov operator terms are all put on the right hand side and combined into a single operator

$$\begin{aligned} \hat{V}_\alpha = (\boldsymbol{w} + \boldsymbol{u}_i) \cdot \boldsymbol{\nabla} + \Bigg[- \boldsymbol{w} \cdot (\boldsymbol{\nabla} \boldsymbol{u}_i) + \frac{1}{\rho_i} (\boldsymbol{\nabla} p_i + \boldsymbol{\nabla} \cdot \Pi_i) + \boldsymbol{Y}_\alpha + \frac{q_\alpha}{m_\alpha} (\boldsymbol{w} \times \boldsymbol{B}) \Bigg] \cdot \boldsymbol{\nabla}_{\boldsymbol{w}}, \\ \text{where} \quad \boldsymbol{Y}_\alpha = \left(\frac{q_\alpha}{m_\alpha} - \sum_\beta c_\beta \frac{q_\beta}{m_\beta} \right) (\boldsymbol{E} + \boldsymbol{u}_i \times \boldsymbol{B}) + \frac{1}{\rho_i} \boldsymbol{R}_e - \frac{1}{\rho_\alpha} \boldsymbol{R}_{e\alpha}. \end{aligned} \tag{3.40}$$

We also note that the test-particle collision operators may be combined into a single test-particle-like operator

$$\hat{C}_\alpha^T \equiv \sum_\beta \hat{C}_{\alpha\beta}^T + \hat{C}_{\alpha e}^T \tag{3.41}$$

The DDF equation for species α is therefore

$$\partial_t \delta f_\alpha + D_\alpha = \hat{C}_\alpha^T \delta f_\alpha + \sum_\beta \hat{C}_{\alpha\beta}^F \delta f_\beta - \hat{V}_\alpha \delta f_\alpha. \tag{3.42}$$

As before, the closure is assumed to be stationary $\partial_t \delta f_\alpha = 0$. However, to include non-stationary effects, this time derivative may be taken as

$$\partial_t \delta f_\alpha = \frac{\delta f_\alpha(t) - \delta f_\alpha(t - \Delta t)}{\Delta t}, \tag{3.43}$$

where Δt is the timestep from the previous RKM evaluation where $\delta f_\alpha(t - \Delta t)$ is known. These two terms may be split up, leaving the DDF equation as

$$D_\alpha - (\Delta t)^{-1} \delta f_\alpha(t - \Delta t) = \hat{C}_\alpha^T \delta f_\alpha + \sum_\beta \hat{C}_{\alpha\beta}^F \delta f_\beta - (\hat{V}_\alpha + (\Delta t)^{-1}) \delta f_\alpha, \tag{3.44}$$

which may still be solved as a linear problem.

3.2 Local Limit

Here we emphasise that the local limit ($N_K \lll 1$) naturally recovers the first-order Chapman-Enskog equation. Consider the electron DDF equation

$$D_e = \big(\hat{C}_{ee} + \hat{C}_{ei} - \hat{V}_e - \hat{B}_e \big) \delta f_e. \tag{3.45}$$

with

$$\begin{aligned} D_e = \Bigg[&\left(\frac{w^2}{v_{\mathrm{th},e}^2} - \frac{3}{2}\right) K_e + \frac{2}{v_{\mathrm{th},e}^2} \boldsymbol{\nabla} \boldsymbol{u}_e : \left(\boldsymbol{w}\boldsymbol{w} - \frac{1}{3} w^2 \mathbb{I} \right) \\ &+ \left(\left(\frac{w^2}{v_{\mathrm{th},e}^2} - \frac{5}{2}\right) \boldsymbol{\nabla} \ln T_e + \frac{1}{p_e} \left(- \boldsymbol{\nabla} \cdot \Pi_e + \boldsymbol{R}_e \right) + Z \hat{\nu}_{ee} v_{\mathrm{th},e} \frac{1}{w^3} \Delta \boldsymbol{u} \right) \cdot \boldsymbol{w} \Bigg] f_e^M, \end{aligned} \tag{3.46}$$

and

$$\hat{V}_e = (\boldsymbol{w} + \boldsymbol{u}_e) \cdot \boldsymbol{\nabla} - \left[\boldsymbol{w} \cdot (\boldsymbol{\nabla} \boldsymbol{u}_e) + \frac{1}{\rho_e} \left(- \boldsymbol{\nabla} p_e - \boldsymbol{\nabla} \cdot \Pi_e + \boldsymbol{R}_e \right) \right] \cdot \boldsymbol{\nabla}_{\boldsymbol{w}}, \tag{3.47}$$

and the magnetic field term

$$\hat{B}_e = -\frac{e}{m_e} (\boldsymbol{w} \times \boldsymbol{B}) \cdot \boldsymbol{\nabla}_{\boldsymbol{w}}. \tag{3.48}$$

For $N_K \lll 1$, the K_e and $\boldsymbol{\nabla} \cdot \Pi_e$ terms appearing in D_e become subleading, as does the whole Vlasov term $\hat{V}_e \delta f_e$. The remaining equation is

$$\begin{aligned} &f_e^M \left(\left[\boldsymbol{R}_e / p_e + \left(\frac{w^2}{v_{\mathrm{th},e}^2} - \frac{5}{2} \right) \boldsymbol{\nabla} \ln T_e \right] \cdot \boldsymbol{w} + \frac{2}{v_{\mathrm{th},e}^2} \boldsymbol{\nabla} \boldsymbol{u}_e : \left(\boldsymbol{w}\boldsymbol{w} - \frac{1}{3} w^2 \mathbb{I} \right) \right) - C_{ei}\{f_e^M\} \\ &= C_{ee}\{\delta f_e\} + C_{ei}\{\delta f_e\} + \frac{e}{m_e} (\boldsymbol{w} \times \boldsymbol{B}) \cdot \boldsymbol{\nabla}_{\boldsymbol{w}} \delta f_e \end{aligned} \tag{3.49}$$

which is exactly the local problem 2.96 obtained from the Chapman-Enskog procedure [15], and similarly for the multi-species RKM. This emphasises a key feature of the RKM: in the local limit, the approach naturally becomes the local problem, rather than requiring construction of the solution in a way such that the local limit is recovered for small Knudsen number. This recovery of the local limit is demonstrated in later chapters.

3.3 Expansion in Spherical Harmonics

The DDF is then expanded in spherical harmonics in velocity space as

$$\delta f_\alpha = \sum_{k=0}^{\infty} \sum_{n=-k}^{k} \frac{2k+1}{4\pi} \frac{(k-n)!}{(k+n)!} P_k^n(\cos\vartheta) e^{in\varphi} \delta f_\alpha^{(k,n)}, \tag{3.50}$$

where P_k^n are the associated Legendre functions [108] and ϑ, φ are the polar and azimuthal velocity coordinates, respectively. The orientation of the spherical velocity coordinates is chosen such that the pole ($\vartheta = 0$) is aligned with the z axis via $\mu = \cos\vartheta = \boldsymbol{w} \cdot \hat{\boldsymbol{z}}/w$, and $\varphi = 0$ is contained within the xz plane via $\cos\varphi = (\boldsymbol{w} \cdot \hat{\boldsymbol{x}})/(w \sin\vartheta)$. The components of the spherical harmonic expansion may be recovered by an appropriate moment of the DDF over velocity angle space

$$\delta f_\alpha^{(l,m)} = \int d^2\Omega \, e^{-im\varphi} P_l^m(\mu) \delta f_\alpha = \langle l, m | \delta f_\alpha \rangle, \tag{3.51}$$

for $l, m \in \mathbb{Z}$ with $l \geq 0$ and $|m| \leq l$, where $d^2\Omega = \sin\vartheta d\vartheta d\varphi = -d\mu d\varphi$ is the velocity angle element and Dirac notation is introduced for brevity. The DDF equation may be projected onto the spherical harmonic basis by taking the same moment $\int d^2\Omega \, e^{-in\varphi} P_k^n(\mu)(\dots)$, yielding a set of PDEs for the modes of the electron DDF of the form

$$\mathcal{D}_e^{(l,m)} = \mathcal{C}_e^{(l,m)} - \mathcal{V}_e^{(l,m)} - \mathcal{B}_e^{(l,m)}, \tag{3.52}$$

where calligraphic characters represent the projections of the corresponding terms onto the spherical harmonic basis. The form of most of these projections are provided by Swanekamp et al. [109], with other terms not provided in the literature derived in Section 3.5. The spherical harmonic expansion is then truncated to the first N_l modes for the l index, leaving N_l^2 PDEs in (z, w) that may be solved numerically for δf_e, and therefore transport quantities. For this work, $N_l = 4$ is typically used which has been shown in previous work [1, 110] to demonstrate good convergence of transport quantities for Knudsen numbers $N_K \lesssim 1/10$. The solvability conditions 3.87 become

$$\begin{aligned} &\int_0^\infty dw\, w^2 \delta f_e^{(0,0)} = 0, \quad \int_0^\infty dw\, w^4 \delta f_e^{(0,0)} = 0, \\ &\int_0^\infty dw\, w^3 \delta f_e^{(1,m)} = 0, \quad m = -1, 0, 1, \end{aligned} \tag{3.53}$$

and the transport fluxes become 1D w moments of particular components of $\delta f_e^{(l,m)}$ as given in Section 3.3.2. In principle, the DDF equation expanded in spherical harmonics 3.52 may be solved in full 3D3V space. Three velocity dimensions are required to fully realise magnetic field effects, however a single spatial dimension is suitable for investigating nonlocal transport. The spatial geometry is therefore reduced to a single spatial dimension z, with translational symmetry assumed in the x and y directions, leaving a 1D3V space.

3.3.1 Projection of terms

Here, we summarise the explicit form of the terms appearing in the DDF equation projected onto the spherical harmonic basis.

Driving terms

The driving term may be written as

$$D_\alpha = \left[d_\alpha^0 + \boldsymbol{d}_\alpha^1 \cdot \hat{\boldsymbol{w}} + \boldsymbol{d}_{\alpha,z}^2 \cdot \left(\hat{\boldsymbol{w}}\hat{\boldsymbol{w}} - \frac{1}{3}\mathbb{I} \right) \cdot \hat{\boldsymbol{z}} \right] f_\alpha^M, \tag{3.54}$$

where the components of the driving force are

$$\begin{aligned} d_\alpha^0 &= \left(\frac{w^2}{v_{\mathrm{th},\alpha}^2} - \frac{3}{2} \right) K_\alpha, \quad \boldsymbol{d}_e^1 = w \left(\left(\frac{w^2}{v_{\mathrm{th},e}^2} - \frac{5}{2} \right) \boldsymbol{\nabla} \ln T_e + \frac{1}{p_e} \left(-\boldsymbol{\nabla} \cdot \Pi_e + \boldsymbol{R}_e \right) + 2\hat{\nu}_{ei} \frac{v_{\mathrm{th},e}}{w^3} \Delta \boldsymbol{u} \right), \\ \boldsymbol{d}_{\alpha,z}^2 &= 2 \frac{w^2}{v_{\mathrm{th},\alpha}^2} \boldsymbol{u}_\alpha', \quad \boldsymbol{d}_i^1 = w \left(\left(\frac{w^2}{v_{\mathrm{th},i}^2} - \frac{5}{2} \right) \boldsymbol{\nabla} \ln T_i - \frac{1}{p_i} \boldsymbol{\nabla} \cdot \Pi_i \right), \end{aligned} \tag{3.55}$$

with $\boldsymbol{u}_\alpha' = \partial_z \boldsymbol{u}_\alpha$.

The projection of the driving term is therefore

$$\mathcal{D}_\alpha^{(l,m)} = \int d^2\Omega\, e^{-im\varphi} P_l^m(\mu) D_\alpha = \left[d_\alpha^0 \delta_{l,0} \delta^{m,0} + \boldsymbol{d}_\alpha^1 \cdot \langle l, m | \hat{\boldsymbol{w}} \rangle + \boldsymbol{d}_{\alpha,z}^2 \cdot \langle l, m | \left(\hat{\boldsymbol{w}}\hat{\boldsymbol{w}} - \frac{1}{3}\mathbb{I} \right) \cdot \hat{\boldsymbol{z}} \rangle \right] f_\alpha^M, \tag{3.56}$$

where we find

$$\begin{aligned} \langle l, m | \hat{\boldsymbol{w}} \rangle &= \frac{2\pi}{3} \left[-2\delta^{m,1} (\hat{\boldsymbol{x}} - i\hat{\boldsymbol{y}}) + \delta^{m,-1} (\hat{\boldsymbol{x}} + i\hat{\boldsymbol{y}}) + 2\delta^{m,0} \hat{\boldsymbol{z}} \right] \delta_{l,1}, \\ \langle l, m | \left(\hat{\boldsymbol{w}}\hat{\boldsymbol{w}} - \frac{1}{3}\mathbb{I} \right) \cdot \hat{\boldsymbol{z}} \rangle &= \frac{4\pi}{15} \left[-6\delta^{m,1} (\hat{\boldsymbol{x}} - i\hat{\boldsymbol{y}}) + \delta^{m,-1} (\hat{\boldsymbol{x}} + i\hat{\boldsymbol{y}}) + 4\delta^{m,0} \hat{\boldsymbol{z}} \right] \delta_{l,2} \end{aligned} \tag{3.57}$$

by writing

$$\hat{\boldsymbol{w}} = \sqrt{1-\mu^2}\cos\varphi\,\hat{\boldsymbol{x}} + \sqrt{1-\mu^2}\sin\varphi\,\hat{\boldsymbol{y}} + \mu\hat{\boldsymbol{z}} \tag{3.58}$$

and evaluating the relevant integrals.

Vlasov terms

The projections of the unmagnetised Vlasov and magnetic field terms are

$$\begin{aligned}
\mathcal{V}_\alpha^{(l,m)} &= u_{\alpha,z}\partial_z\delta f_\alpha^{(l,m)} + w\partial_z\langle l,m|\mu\delta f_\alpha\rangle - w\boldsymbol{u}'_\alpha\cdot\langle l,m|\mu\boldsymbol{\nabla}_{\boldsymbol{w}}\delta f_\alpha\rangle - \boldsymbol{F}_\alpha\cdot\langle l,m|\boldsymbol{\nabla}_{\boldsymbol{w}}\delta f_\alpha\rangle,\\
\mathcal{B}_\alpha^{(l,m)} &= -\boldsymbol{\omega}_\alpha\cdot\langle l,m|\boldsymbol{w}\times\boldsymbol{\nabla}_{\boldsymbol{w}}\delta f_\alpha\rangle,
\end{aligned} \tag{3.59}$$

where vectors have been condensed to

$$\boldsymbol{F}_e = \frac{1}{\rho_e}\Big(-\boldsymbol{\nabla}p_e - \boldsymbol{\nabla}\cdot\Pi_e + \boldsymbol{R}_e\Big),\quad \boldsymbol{F}_i = \frac{1}{\rho_i}\Big(-\boldsymbol{\nabla}p_i - \boldsymbol{\nabla}\cdot\Pi_i\Big),\quad \boldsymbol{\omega}_e = -\frac{e}{m_e}\boldsymbol{B},\quad \boldsymbol{\omega}_i = \frac{Ze}{m_i}\boldsymbol{B}. \tag{3.60}$$

and components

$$\begin{aligned}
\langle l,m|\mu\delta f_e\rangle &= \frac{l+1-m}{2l+1}\delta f_e^{(l+1,m)} + \frac{l+m}{2l+1}\delta f_e^{(l-1,m)},\\
\langle l,m|\boldsymbol{\nabla}_{\boldsymbol{w}}\delta f_e\rangle &= \frac{1}{2}(\hat{\boldsymbol{x}}+i\hat{\boldsymbol{y}})\sum_{k=0}^{\infty}\left[a_{l,k}^{+}(m)\partial_w\delta f_e^{(k,m+1)} + (-c_{l,k}^{+}(m)+(m+1)d_{l,k}^{+}(m))\frac{1}{w}\delta f_e^{(k,m+1)}\right]\\
&\quad+\frac{1}{2}(\hat{\boldsymbol{x}}-i\hat{\boldsymbol{y}})\sum_{k=0}^{\infty}\left[a_{l,k}^{-}(m)\partial_w\delta f_e^{(k,m-1)} + (-c_{l,k}^{-}(m)-(m-1)d_{l,k}^{-}(m))\frac{1}{w}\delta f_e^{(k,m-1)}\right]\\
&\quad+\hat{\boldsymbol{z}}\left[\frac{l+1-m}{2l+1}\frac{1}{w^{l+2}}\partial_w\Big(w^{l+2}\delta f_e^{(l+1,m)}\Big) + \frac{l+m}{2l+1}w^{l-1}\partial_w\Big(\frac{1}{w^{l-1}}\delta f_e^{(l-1,m)}\Big)\right],\\
\langle l,m|\mu\boldsymbol{\nabla}_{\boldsymbol{w}}\delta f_e\rangle &= \frac{1}{2}(\hat{\boldsymbol{x}}+i\hat{\boldsymbol{y}})\sum_{k=0}^{\infty}\left[\tilde{a}_{l,k}^{+}(m)\partial_w\delta f_e^{(k,m+1)} + (-\tilde{c}_{l,k}^{+}(m)+(m+1)\tilde{d}_{l,k}^{+}(m))\frac{1}{w}\delta f_e^{(k,m+1)}\right]\\
&\quad+\frac{1}{2}(\hat{\boldsymbol{x}}-i\hat{\boldsymbol{y}})\sum_{k=0}^{\infty}\left[\tilde{a}_{l,k}^{-}(m)\partial_w\delta f_e^{(k,m-1)} + (-\tilde{c}_{l,k}^{-}(m)-(m-1)\tilde{d}_{l,k}^{-}(m))\frac{1}{w}\delta f_e^{(k,m-1)}\right]\\
&\quad+\hat{\boldsymbol{z}}\sum_{k=0}^{\infty}\left[\tilde{b}_{l,k}(m)\partial_w\delta f_e^{(k,m)} + \tilde{g}_{l,k}(m)\frac{1}{w}\delta f_e^{(k,m)}\right],\\
\langle l,m|\boldsymbol{w}\times\boldsymbol{\nabla}_{\boldsymbol{w}}\delta f_e\rangle &= \frac{1}{2i}(\hat{\boldsymbol{x}}+i\hat{\boldsymbol{y}})\sum_{k=0}^{\infty}\left[(C_{l,k}^{+}(m)-(m+1)D_{l,k}^{+}(m))\delta f_e^{(k,m+1)}\right]\\
&\quad+\frac{1}{2i}(\hat{\boldsymbol{x}}-i\hat{\boldsymbol{y}})\sum_{k=0}^{\infty}\left[(-C_{l,k}^{-}(m)-(m-1)D_{l,k}^{-}(m))\delta f_e^{(k,m-1)}\right]\\
&\quad-im\delta f_e^{(l,m)}\hat{\boldsymbol{z}},
\end{aligned} \tag{3.61}$$

where the matrix elements follow the same definition as Swanekamp et al. [109] with the tilde coefficients indicating an additional factor of μ in the integrand of their definitions, e.g.

$$\begin{aligned}
a_{l,k}^{\pm}(m) &\coloneqq \frac{2k+1}{2}\frac{(k-(m\pm1))!}{(k+(m\pm1))!}\int_{-1}^{1}d\mu\,P_l^m(\mu)\sqrt{1-\mu^2}P_k^{m\pm1}(\mu),\\
\tilde{a}_{l,k}^{\pm}(m) &\coloneqq \frac{2k+1}{2}\frac{(k-(m\pm1))!}{(k+(m\pm1))!}\int_{-1}^{1}d\mu\,P_l^m(\mu)\mu\sqrt{1-\mu^2}P_k^{m\pm1}(\mu).
\end{aligned} \tag{3.62}$$

Collision terms

The projection of the test-particle collision operator is

$$\mathcal{C}^{T,(l,m)}_{\alpha\beta} = -\frac{1}{2}l(l+1)\nu_D^{\alpha\beta}\delta f_\alpha^{(l,m)} + \frac{1}{w^2}\partial_w\left(\tilde{\nu}_s^{\alpha\beta}w^3\delta f_\alpha^{(l,m)} + \frac{1}{2}\nu_\parallel^{\alpha\beta}w^4\partial_w\delta f_\alpha^{(l,m)}\right), \tag{3.63}$$

where we have used that spherical harmonics are eigenfunctions of the pitch-angle scattering operator via $\hat{\mathcal{L}}(P_l^m e^{im\varphi}) = -l(l+1)P_l^m e^{im\varphi}$.

The spherical harmonic projection of the field-particle collision operator is

$$\begin{aligned}\mathcal{C}^{F,(l,m)}_{\alpha\beta} = \hat{\nu}_{\alpha\beta}\frac{4}{\sqrt{\pi}}\frac{n_\alpha}{n_\beta}e^{-(w/v_{\text{th},\alpha})^2}\Bigg[&\frac{m_\alpha}{m_\beta}\delta f_\beta^{(l,m)} + \left(-1+\left(\frac{m_\alpha}{m_\beta}-1\right)l + \frac{(l+1)(l+2)}{2l+3}\frac{w^2}{v_{\text{th},\alpha}^2}\right)\frac{1}{v_{\text{th},\alpha}^2}\Psi_{\beta,1}^{(l,m)}(w)\\ &+\left(-1-\left(\frac{m_\alpha}{m_\beta}-1\right)(l+1) - \frac{l(l-1)}{2l-1}\frac{w^2}{v_{\text{th},\alpha}^2}\right)\frac{1}{v_{\text{th},\alpha}^2}\Psi_{\beta,2}^{(l,m)}(w)\\ &-\frac{l(l-1)}{2l-1}\frac{1}{v_{\text{th},\alpha}^4}\Psi_{\beta,3}^{(l,m)}(w) + \frac{(l+1)(l+2)}{2l+3}\frac{1}{v_{\text{th},\alpha}^4}\Psi_{\beta,4}^{(l,m)}(w)\Bigg].\end{aligned} \tag{3.64}$$

where we have defined the integrals

$$\begin{aligned}\Psi_{\beta,1}^{(l,m)}(w) &= \frac{2}{2l+1}w^l\int_w^\infty du\, u^{1-l}\delta f_\beta^{(l,m)}(u), \quad \Psi_{\beta,2}^{(l,m)}(w) = \frac{2}{2l+1}\frac{1}{w^{l+1}}\int_0^w du\, u^{2+l}\delta f_\beta^{(l,m)}(u),\\ \Psi_{\beta,3}^{(l,m)}(w) &= \frac{2}{2l+1}w^l\int_w^\infty du\, u^{3-l}\delta f_\beta^{(l,m)}(u), \quad \Psi_{\beta,4}^{(l,m)}(w) = \frac{2}{2l+1}\frac{1}{w^{l+1}}\int_0^w du\, u^{4+l}\delta f_\beta^{(l,m)}(u).\end{aligned} \tag{3.65}$$

3.3.2 Recovering hydrodynamic and transport quantities

Once the DDF equation has been solved for $\delta f_\alpha^{(l,m)}$, transport terms may be recovered as appropriate velocity moments of δf_α

$$\begin{aligned}\boldsymbol{q}_\alpha &= \int d^3\boldsymbol{w}\,\frac{1}{2}m_\alpha w^2\boldsymbol{w}\delta f_\alpha,\\ \Pi_\alpha &= \int d^3\boldsymbol{w}\, m_\alpha\left(\boldsymbol{w}\boldsymbol{w} - \frac{1}{3}w^2\mathbb{I}\right)\delta f_\alpha,\\ \boldsymbol{R}_e &= \boldsymbol{R}_e^0 + \int d^3\boldsymbol{w}\, m_e\boldsymbol{w}\hat{C}_{ei}\delta f_e.\end{aligned} \tag{3.66}$$

Using orthogonality relations for spherical harmonics, these may be expressed directly as integrals over $\delta f_\alpha^{(l,m)}$. Writing the velocity integrals in spherical velocity coordinates with $d^3\boldsymbol{w} = w^2 dw\, d^2\Omega$, the fluxes become

$$\begin{aligned}\boldsymbol{q}_\alpha &= \frac{1}{2}m_\alpha\int_0^\infty dw\, w^5\boldsymbol{S}_{1,\alpha},\\ \boldsymbol{R}_e &= \boldsymbol{R}_e^0 - \hat{\nu}_{ei}v_{\text{th},e}^3\int_0^\infty dw\,\boldsymbol{S}_{1,e},\\ \Pi_\alpha &= m_\alpha\int_0^\infty dw\, w^4\mathrm{S}_{2,\alpha},\end{aligned} \tag{3.67}$$

where the rank-1 and rank-2 fluxes

$$\begin{aligned}
\boldsymbol{S}_{1,\alpha} &= \int d^2\Omega\, \hat{\boldsymbol{w}}\delta f_\alpha = -\mathrm{Re}\{\delta f_\alpha^{(1,1)}\}\hat{\boldsymbol{x}} + \mathrm{Im}\{\delta f_\alpha^{(1,1)}\}\hat{\boldsymbol{y}} + \delta f_\alpha^{(1,0)}\hat{\boldsymbol{z}}, \\
\mathrm{S}_{2,\alpha} &= \int d^2\Omega \left(\hat{\boldsymbol{w}}\hat{\boldsymbol{w}} - \frac{1}{3}\mathbb{I}\right)\delta f_\alpha \\
&= \left(\frac{1}{12}\mathrm{Re}\{\delta f_\alpha^{(2,2)}\} - \frac{1}{3}\delta f_\alpha^{(2,0)}\right)\hat{\boldsymbol{x}}\hat{\boldsymbol{x}} + \left(-\frac{1}{12}\mathrm{Re}\{\delta f_\alpha^{(2,2)}\} - \frac{1}{3}\delta f_\alpha^{(2,0)}\right)\hat{\boldsymbol{y}}\hat{\boldsymbol{y}} + \frac{2}{3}\delta f_\alpha^{(2,0)}\hat{\boldsymbol{z}}\hat{\boldsymbol{z}} \\
&\quad - \frac{1}{12}\mathrm{Im}\{\delta f_\alpha^{(2,2)}\}(\hat{\boldsymbol{x}}\hat{\boldsymbol{y}} + \hat{\boldsymbol{y}}\hat{\boldsymbol{x}}) - \frac{1}{6}\mathrm{Re}\{\delta f_\alpha^{(2,1)}\}(\hat{\boldsymbol{x}}\hat{\boldsymbol{z}} + \hat{\boldsymbol{z}}\hat{\boldsymbol{x}}) + \frac{1}{6}\mathrm{Im}\{\delta f_\alpha^{(2,1)}\}(\hat{\boldsymbol{y}}\hat{\boldsymbol{z}} + \hat{\boldsymbol{z}}\hat{\boldsymbol{y}}).
\end{aligned} \tag{3.68}$$

as shown on the next page, and

$$\boldsymbol{R}_e^0 = -\frac{4}{3\sqrt{\pi}}\hat{\nu}_{ei}\rho_e\Delta\boldsymbol{u}, \tag{3.69}$$

is the friction force between an electron Maxwellian and ion Maxwellian with relative flow $\Delta\boldsymbol{u}$.

In the mixture framework, we also define the diffusive velocities $\boldsymbol{V}_\alpha$, reduced heat flux $\boldsymbol{q}_i'$, and enthalpy flux $\boldsymbol{h}_i$ as

$$\boldsymbol{V}_\alpha = \frac{1}{n_\alpha}\int d^3\boldsymbol{w}\, \boldsymbol{w}\delta f_\alpha, \tag{3.70}$$

$$\boldsymbol{q}_i' = \sum_\alpha \int d^3\boldsymbol{w} \left(\frac{1}{2}m_\alpha w^2 - \frac{5}{2}T_i\right)\boldsymbol{w}\delta f_\alpha, \tag{3.71}$$

$$\boldsymbol{h}_i = \sum_\alpha \frac{5}{2}n_\alpha T_i \boldsymbol{V}_\alpha \tag{3.72}$$

such that the total ion heat flux $\boldsymbol{q}_i = \boldsymbol{q}_i' + \boldsymbol{h}_i$. After expanding in spherical harmonics, these integrals become

$$\boldsymbol{V}_\alpha = \frac{1}{n_\alpha}\int_0^\infty dw\, w^3 \boldsymbol{S}_{1,\alpha}, \quad \boldsymbol{q}_i' = \sum_\alpha \int_0^\infty dw\, w^3 \left(\frac{w^2}{v_{\mathrm{th},\alpha}^2} - \frac{5}{2}\right)T_i\boldsymbol{S}_{1,\alpha}. \tag{3.73}$$

We wish to express the fluxes

$$\boldsymbol{S}_{1,\alpha}(w) = \int d^2\Omega\, \hat{\boldsymbol{w}}\delta f_\alpha, \quad \mathrm{S}_{2,\alpha}(w) = \int d^2\Omega \left(\hat{\boldsymbol{w}}\hat{\boldsymbol{w}} - \frac{1}{3}\mathbb{I}\right)\delta f_\alpha. \tag{3.74}$$

in terms of the spherical harmonic projection of the DF $\delta f_\alpha^{(l,m)}$. These two terms may be simplified using orthogonality relations. Since δf_α is real, we must have

$$\delta f_\alpha^{(l,-m)} = (-1)^m \frac{(l-m)!}{(l+m)!}(\delta f_\alpha^{(l,m)})^*, \tag{3.75}$$

where * denotes the complex conjugate. We also note some relevant associated Legendre functions in Table 3.1.

$\ell\backslash m$	$m=-2$	$m=-1$	$m=0$	$m=1$	$m=2$
$l=0$			1		
$l=1$		$\sqrt{1-\mu^2}$	μ	$-\sqrt{1-\mu^2}$	
$l=2$	$\frac{3}{24}(1-\mu^2)$	$\frac{1}{2}\mu\sqrt{1-\mu^2}$	$\frac{1}{2}(3\mu^2-1)$	$-3\mu\sqrt{1-\mu^2}$	$3(1-\mu^2)$

Table 3.1: Associated Legendre functions $P_\ell^m(\mu)$ for $\ell = 0, 1, 2$.

Rank-1 flux

Writing in matrix notation in the $\{\hat{\boldsymbol{x}}, \hat{\boldsymbol{y}}, \hat{\boldsymbol{z}}\}$ basis,

$$\boldsymbol{S}_{1,\alpha} = \int d^2\Omega \begin{pmatrix} \sin\vartheta\cos\varphi \\ \sin\vartheta\sin\varphi \\ \cos\vartheta \end{pmatrix} \delta f_\alpha = \int d^2\Omega \begin{pmatrix} \sqrt{1-\mu^2}\frac{1}{2}(e^{i\varphi}+e^{-i\varphi}) \\ \sqrt{1-\mu^2}\frac{1}{2i}(e^{i\varphi}-e^{-i\varphi}) \\ \mu \end{pmatrix} \delta f_\alpha$$

$$= \begin{pmatrix} \frac{1}{2}(\langle 1,-1| - \langle 1,1|) \\ \frac{1}{2i}(\langle 1,-1| + \langle 1,1|) \\ \langle 1,0| \end{pmatrix} \delta f_\alpha = \begin{pmatrix} -\mathrm{Re}\{\delta f_\alpha^{(1,1)}\} \\ \mathrm{Im}\{\delta f_\alpha^{(1,1)}\} \\ \delta f_\alpha^{(1,0)} \end{pmatrix} = -\mathrm{Re}\{\delta f_\alpha^{(1,1)}\}\hat{\boldsymbol{x}} + \mathrm{Im}\{\delta f_\alpha^{(1,1)}\}\hat{\boldsymbol{y}} + \delta f_\alpha^{(1,0)}\hat{\boldsymbol{z}} \quad (3.76)$$

Rank-2 flux

Writing in matrix notation in the $\{\hat{\boldsymbol{x}}, \hat{\boldsymbol{y}}, \hat{\boldsymbol{z}}\}$ basis,

$$\mathrm{S}_{2,\alpha} = \int d^2\Omega \left(\hat{\boldsymbol{w}}\hat{\boldsymbol{w}} - \frac{1}{3}\mathbb{I}\right)\delta f_\alpha$$

$$= \int d^2\Omega \begin{pmatrix} (1-\mu^2)\cos^2\varphi - \frac{1}{3} & (1-\mu^2)\cos\varphi\sin\varphi & \mu\sqrt{1-\mu^2}\cos\varphi \\ (1-\mu^2)\cos\varphi\sin\varphi & (1-\mu^2)\sin^2\varphi - \frac{1}{3} & \mu\sqrt{1-\mu^2}\sin\varphi \\ \mu\sqrt{1-\mu^2}\cos\varphi & \mu\sqrt{1-\mu^2}\sin\varphi & \mu^2 - \frac{1}{3} \end{pmatrix} \delta f_\alpha$$

$$= \int d^2\Omega \begin{pmatrix} 2P_2^{-2}e^{2i\varphi} + \frac{1}{12}P_2^2e^{-2i\varphi} - \frac{1}{3}P_2^0 & \frac{1}{i}(2P_2^{-2}e^{2i\varphi} - \frac{1}{12}P_2^2e^{-2i\varphi}) & P_2^{-1}e^{i\varphi} - \frac{1}{6}P_2^1e^{-i\varphi} \\ \frac{1}{i}(2P_2^{-2}e^{2i\varphi} - \frac{1}{12}P_2^2e^{-2i\varphi}) & -2P_2^{-2}e^{2i\varphi} - \frac{1}{12}P_2^2e^{-2i\varphi} - \frac{1}{3}P_2^0 & \frac{1}{i}(P_2^{-1}e^{i\varphi} + \frac{1}{6}P_2^1e^{-i\varphi}) \\ P_2^{-1}e^{i\varphi} - \frac{1}{6}P_2^1e^{-i\varphi} & \frac{1}{i}(P_2^{-1}e^{i\varphi} + \frac{1}{6}P_2^1e^{-i\varphi}) & \frac{2}{3}P_2^0 \end{pmatrix} \delta f_\alpha$$

$$= \begin{pmatrix} 2\langle 2,-2| + \frac{1}{12}\langle 2,2| - \frac{1}{3}\langle 2,0| & \frac{1}{i}(2\langle 2,-2| - \frac{1}{12}\langle 2,2|) & \langle 2,-1| - \frac{1}{6}\langle 2,1| \\ \frac{1}{i}(2\langle 2,-2| - \frac{1}{12}\langle 2,2|) & -2\langle 2,-2| - \frac{1}{12}\langle 2,2| - \frac{1}{3}\langle 2,0| & \frac{1}{i}(\langle 2,-1| + \frac{1}{6}\langle 2,1|) \\ \langle 2,-1| - \frac{1}{6}\langle 2,1| & \frac{1}{i}(\langle 2,-1| + \frac{1}{6}\langle 2,1|) & \langle 2,0| \end{pmatrix} \delta f_\alpha$$

$$= \begin{pmatrix} \frac{1}{12}\mathrm{Re}\{\delta f_\alpha^{(2,2)}\} - \frac{1}{3}\delta f_\alpha^{(2,0)} & -\frac{1}{12}\mathrm{Im}\{\delta f_\alpha^{(2,2)}\} & -\frac{1}{6}\mathrm{Re}\{\delta f_\alpha^{(2,1)}\} \\ -\frac{1}{12}\mathrm{Im}\{\delta f_\alpha^{(2,2)}\} & -\frac{1}{12}\mathrm{Re}\{\delta f_\alpha^{(2,2)}\} - \frac{1}{3}\delta f_\alpha^{(2,0)} & \frac{1}{6}\mathrm{Im}\{\delta f_\alpha^{(2,1)}\} \\ -\frac{1}{6}\mathrm{Re}\{\delta f_\alpha^{(2,1)}\} & \frac{1}{6}\mathrm{Im}\{\delta f_\alpha^{(2,1)}\} & \delta f_\alpha^{(2,0)} \end{pmatrix}$$

$$= \left(\frac{1}{12}\mathrm{Re}\{\delta f_\alpha^{(2,2)}\} - \frac{1}{3}\delta f_\alpha^{(2,0)}\right)\hat{\boldsymbol{x}}\hat{\boldsymbol{x}} + \left(-\frac{1}{12}\mathrm{Re}\{\delta f_\alpha^{(2,2)}\} - \frac{1}{3}\delta f_\alpha^{(2,0)}\right)\hat{\boldsymbol{y}}\hat{\boldsymbol{y}}$$
$$+ \frac{2}{3}\delta f_\alpha^{(2,0)}\hat{\boldsymbol{z}}\hat{\boldsymbol{z}} - \frac{1}{12}\mathrm{Im}\{\delta f_\alpha^{(2,2)}\}(\hat{\boldsymbol{x}}\hat{\boldsymbol{y}} + \hat{\boldsymbol{y}}\hat{\boldsymbol{x}}) - \frac{1}{6}\mathrm{Re}\{\delta f_\alpha^{(2,1)}\}(\hat{\boldsymbol{x}}\hat{\boldsymbol{z}} + \hat{\boldsymbol{z}}\hat{\boldsymbol{x}}) + \frac{1}{6}\mathrm{Im}\{\delta f_\alpha^{(2,1)}\}(\hat{\boldsymbol{y}}\hat{\boldsymbol{z}} + \hat{\boldsymbol{z}}\hat{\boldsymbol{y}}). \quad (3.77)$$

3.4 Numerical Implementation

3.4.1 Nondimensionalisation

Before finite differencing and implementing numerically, we note that the DDF equation has a certain scale invariance that allows for nondimensionalisation. In particular, for each dimensionful quantity Q (which may be space and/or velocity dependent), we define a characteristic quantity Q_0 to define a nondimensionalised quantity $\bar{Q} = Q/Q_0$.

For the characteristic length, one might be tempted to define the characteristic scale length from the number density as $l_0 = n_0^{-1/3}$, but lengths and number densities always appear independently in the VFP equation so it is still appropriate and more convenient to define them separately.

3.4.2 Discretising and finite-differencing

To discretise the spatial and velocity coordinates, we define a uniform grid via $z = z_{\min} + i\Delta z$, $w = (j+1)\Delta w$, where i and j are the spatial and velocity indices, respectively. Derivatives of a quantity Q are estimated via the finite difference scheme

$$\partial_z Q_{i,j} = \frac{Q_{i+1,j} - Q_{i-1,j}}{2\Delta z}, \quad \partial_w Q_{i,j} = \frac{Q_{i,j+1/2} - Q_{i,j-1/2}}{\Delta w}, \quad (3.78)$$

where the velocity cell-face values are linearly interpolated from cell-centre values as

$$Q_{i,j+1/2} = (1 - \delta^w_{i,j+1/2})Q_{i,j+1} + \delta^w_{i,j+1/2}Q_{i,j}\,. \quad (3.79)$$

The coefficient $\delta^w_{i,j}$, which is a function of grid position, specifies the linear interpolation scheme. A Chang-Cooper-inspired [111] scheme $\delta^w_{p,q} = 1/u - 1/(e^u - 1)$, where $u = 2(\Delta w)^2 j/[v_{\mathrm{th},\alpha}]_i^2$ is chosen for velocity derivatives. This choice improves stability and convergence with respect to a simpler finite difference scheme with fixed $\delta^w_{i,j}$. Reshaping $F_{i,j,l,m,s}$ into a vector $\boldsymbol{F}$, the set of PDEs is discretised to $\boldsymbol{D} = \hat{M}\boldsymbol{F}$, where $\hat{M}$ is the linear operator representing the discretised right side of the DDF equation acting on $\delta f_\alpha^{(l,m)}$, or Jacobian, and $\boldsymbol{D}$ is the inhomogeneous driving term $\mathcal{D}_\alpha^{(l,m)}$ reshaped as a vector. The solution may be found via standard linear solvers. Here, SciPy's sparse matrix suite is used.

To reshape $\delta f_\alpha^{(l,m)}$ into a vector $\boldsymbol{F}$, the relevant indices i (spatial index), j (velocity index), l, m (spherical harmonic indices), and s (species index) must be flattened to a single index k. We focus on two separate cases, namely the magnetised single-species case which requires the i, j, l, m indices, and the unmagnetised multi-species case, which requires the i, j, l, s indices. A magnetised multi-species solver has still been implemented, but it is unnecessary to consider both magnetised and multi-species effects here.

Nondimensionalising quantities		
Type of quantity	Quantities (Q)	Characteristic scale (Q_0)
Mass	Species masses m_α	m_0, typically lightest particle mass $m_0 = \min_\alpha(m_\alpha)$ (i.e. electron mass for electron RKM, lightest ion mass for ion RKM)
Charge	Species charges q_α	Magnitude of charge of electron e
Temperature and energy	Temperature T_α	T_0, typically $T_0 = T_{e,i}(z = -\infty)$
Velocity	Particle velocities $\boldsymbol{w}$, $\boldsymbol{v}$ Flow velocities $\boldsymbol{u}_\alpha$ Diffusive velocities $\boldsymbol{V}_\alpha$	$v_0 = \sqrt{2T_0/m_0}$
Number density	Species number densities n_α	n_0, typically $n_0 = n_{e,i}(z = -\infty)$
Frequency	Time derivatives ∂_t Collision frequencies $\hat{\nu}_{\alpha\beta}$ Collision operators $C_{\alpha\beta}$	$\nu_0 = C_0 = \frac{n_0 e^4 \ln\Lambda_0}{4\pi\varepsilon_0^2 m_0^2 v_0^3}$
Length	MFPs $\lambda_{\text{th},\alpha}$ Spatial coordinate z Gradient scale length L	$\lambda_0 = v_0/\nu_0$
Distribution function	f_α, f_α^M, δf_α	$f_0 = n_0 v_0^{-3}$
Heat flux	Heat fluxes $\boldsymbol{q}_\alpha$, $\boldsymbol{h}_\alpha$	$q_0 = n_0 T_0 v_0$
Force density	Momentum exchange $\boldsymbol{R}_e$ Lorentz force $q_\alpha n_\alpha(\boldsymbol{E} + \boldsymbol{v} \times \boldsymbol{B})$	$R_0 = n_0 m_0 \nu_0 v_0$
Electric field strength	$\boldsymbol{E}$	$E_0 = \frac{m_0 v_0 \nu_0}{e}$
Magnetic field strength	$\boldsymbol{B}$	Enters via Hall parameter $\chi_\alpha = \frac{q_\alpha B}{m_\alpha}\tau_{\alpha\alpha}$

Table 3.2: Conventions for nondimensionalising quantities in the RKM for numerical implementation.

Flattening the indices $(i, j, l, m, s) \to k$ with some linear mapping, the matrix equation can be written as

$$D_{k_1} = \sum_{k_2} \hat{M}_{k_1,k_2} F_{k_2}. \tag{3.80}$$

The vector F_k will be of size $N_k = N_i N_j N_l N_l N_s$, therefore the matrix $\hat{M}$ will therefore be of size $N_k^2 = (N_i N_j N_l N_l N_s)^2$ which is extremely large. For a moderate choice of $N_i = N_j = 100$ spatial and velocity

b index \ a index	0	1	2	3
(l,m)				
0	(0,0)	(1,1)	(2,2)	(3,3)
1	(1,-1)	(1,0)	(2,1)	(3,2)
2	(2,-2)	(2,-1)	(2,0)	(3,1)
3	(3,-3)	(3,-2)	(3,-1)	(3,0)

Table 3.3: Relationship between (l,m) and (a,b) indices.

gridpoints, $N_l = 4$ orders in spherical harmonics, and a single species $N_s = 1$, already the vectors D_{k_1} and F_{k_2} have $N_k = 160,000$ elements and the matrix $\hat{M}$ has $N_k^2 = 2.56 \times 10^{10}$ elements. However, since various indices are only coupled to their neighbours (e.g. i is only coupled to nearest neighbours $i_2 = i_1 \pm 1$ through the spatial derivative), the matrix will be sparse. The remaining linear problem is therefore tractable to solve using sparse matrix solvers.

For the unmagnetised (1D2V) multi-species RKM, the indices are flattened as

$$k(i,l,s,j) = j + N_j(s + N_s(l + N_l(i))), \tag{3.81}$$

analogous to the numerical value for a number with digits i,l,s,j with appropriate weighting. The velocity index j is chosen as the first (least weighted) digit since the collision operators, particularly the field-particle operator, couple all $\boldsymbol{F}$ for fixed i,l,s. If j were chosen as a later (higher weighted) digit, then the matrix M_{k_1,k_2} would have components very far away from the main diagonal, which should slow down the SciPy solver. The spatial index i is chosen as the last digit (highest weighted) since it only couples to nearest neighbours as mentioned above. In addition, for $N_K \lll 1$, spatial derivatives of δf_α vanish. As i is chosen as the last digit, the matrix $\hat{M}_{k_1,k_2}$ naturally becomes block diagonal, where each block solves the local problem for that i.

For the magnetised (1D3V) single species RKM, the number of m indices required are dependent on l via $N_m = 2l+1$. To handle this efficiently, l,m are remapped to a convenient pair of indices a,b via

$$a,b = \begin{cases} l, & l-m, & m \geq 0 \\ l+m, & l, & m < 0 \end{cases}, \quad \text{with inverse} \quad l,m = \begin{cases} a, & a-b, & a \geq b \\ b, & a-b, & a < b \end{cases}, \tag{3.82}$$

such that the indices (a,b) are square with $N_a = N_b = N_l$. This conversion is provided clearly in table 3.4.2 for the first few lowest orders. The indices are then flattened as

$$k(i,a,b,j) = j + N_j(b + N_l(a + N_l(i))). \tag{3.83}$$

The distribution function is real, which yields a direct relationship between positive and negative m, which may be used to again reduce the requirement on the number of equations. This is not considered here since it

adds additional complexity. For the magnetised (1D3V) multi-species case, the indices are flattened as

$$k(i,a,b,s,j) = j + N_j(s + N_l(b + N_l(a + N_l(i)))). \tag{3.84}$$

3.4.3 Field-particle term

Implementing the operator then requires discretising the integrals $\Psi^{(l,m)}_{\beta,(1,2,3,4)}$ from Equation 3.65 as

$$\Psi_{1,k_1} = \frac{2}{2l_1+1} w_{j_1}^{l_1} \sum_{j_2>j_1} \Delta w\, w_{j_2}^{1-l_1} F_{k_2}, \quad \Psi_{2,k_1} = \frac{2}{2l_1+1} w_{j_1}^{-(l_1+1)} \sum_{j_2\leq j_1} \Delta w\, w_{j_2}^{2+l_1} F_{k_2} \tag{3.85}$$

$$\Psi_{3,k_1} = \frac{2}{2l_1+1} w_{j_1}^{l_1} \sum_{j_2>j_1} \Delta w\, w_{j_2}^{3-l_1} F_{k_2}, \quad \Psi_{4,k_1} = \frac{2}{2l_1+1} w_{j_1}^{-(l_1+1)} \sum_{j_2\leq j_1} \Delta w\, w_{j_2}^{4+l_1} F_{k_2}, \tag{3.86}$$

which densely populates the (j_1, j_2) sub-block of the Jacobian. Since j is chosen as the least weighted index when flattening, these dense elements are kept as close to the leading diagonal $k_1 = k_2$ as possible, which is preferred for linear solvers.

3.4.4 Boundary conditions

The RKM solves for the DDF from the set of PDEs 3.52 over the spatial domain $z_{\text{min}} < z < z_{\text{max}}$ and velocity domain $0 < w < w_{\text{max}}$. The spatial bounds are chosen to be sufficiently far away from the gradient region around $z = 0$ such that the local result for the distribution function is restored due to collisions. The high velocity cutoff w_{max} is chosen to capture the part of the tail of the DF that contributes to the heat flux, beyond which the DF may be taken to be zero. The boundary condition for the DF at and above the high velocity cutoff is therefore fixed at zero $\delta f_\alpha(z, w \geq w_{\text{max}}, \mu) = 0$ with a default value $w_{\text{max}} = 5\,\max_z(v_{\text{th}})$, which is verified *a posteriori* to capture the full integrand of the heat flux.

The stencil for an arbitrary set of indices (i, j, l) is shown in Figure 3.1, where multi-species (linking different s) and magnetised (linking different m) effects are not shown. Nearest neighbours in space $(i \pm 1, j, l)$ are required for terms such as $\boldsymbol{u} \cdot \boldsymbol{\nabla} \delta f_\alpha^{(l,m)}$. Nearest neighbours in velocity space $(i, j \pm 1, l)$ are required for velocity gradients in the test-particle collision operator, as well as all (i, j_2, l) entering the field-particle collision operator (in multi-species cases, this also links different s). Spatial and velocity nearest neighbours in space and velocity space are also required from nearest neighbours in the Legendre index, i.e. $(i \pm 1, j, l \pm 1)$ and $(i, j \pm 1, l \pm 1)$ from spatial and velocity derivatives in the Vlasov operator. In the local limit, only the stencil along j remains.

Figure 3.2 shows the Jacobian $\hat{M}_{k_1,k_2}$ for the RKM with an artificially small grid size with $N_k = 72$. Nonzero elements belonging to the advection operator and both components of the linearised collision operator are indicated. The larger square blocks contain cells of $i_1 = i_2$, and the smaller blocks contain cells of $i_1 = i_2$ and $l_1 = l_2$. We observe that the Jacobian is indeed sparse and the approach for larger grid sizes may still be tractable. The ordering of digits of $k(i, l, j)$ is demonstrated to be a good choice, since the nonzero elements remain close to the main diagonal. If another ordering were chosen, say $k(j, l, i)$ (where j is the highest-weighted index), nonzero elements far off the main diagonal would be populated by the linear collision operator.

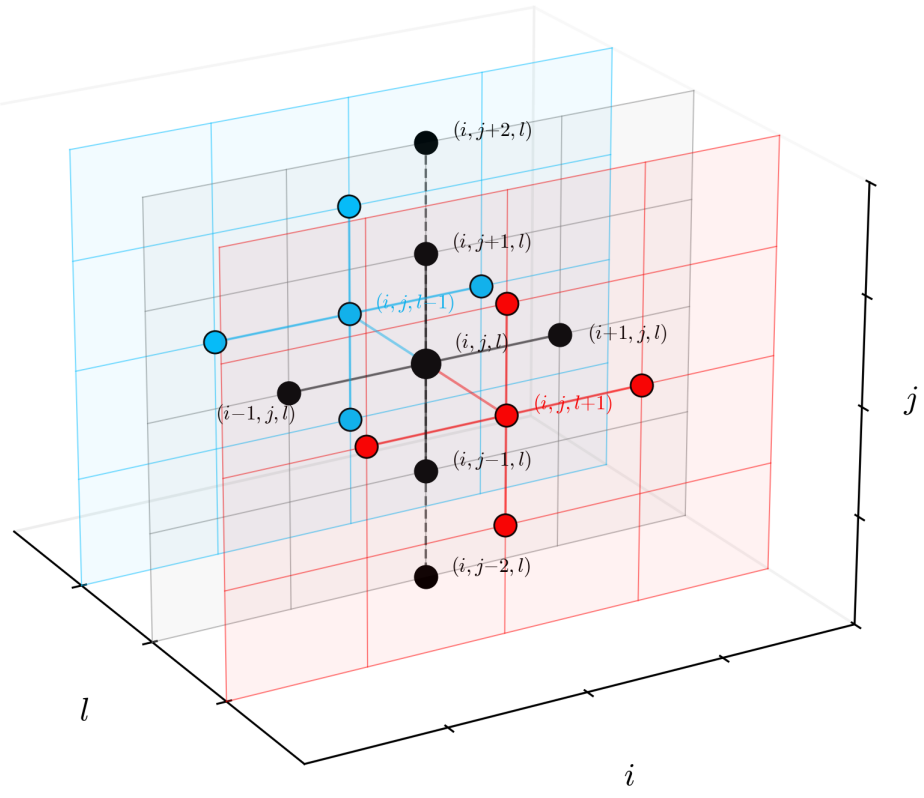


Figure 3.1: Stencil for cell (i, j, l).

In the local limit, the advection operator $\boldsymbol{w} \cdot \boldsymbol{\nabla} \delta f_\alpha$ becomes negligible, and the green elements vanish. This then leaves the Jacobian as block diagonal with only the smaller blocks. In this limit, each of these blocks is solved independently for the local solution. Since only the $l = 1, 2$ modes are driven ($l = 1$ from $\boldsymbol{\nabla} T_{e,i}$, $\boldsymbol{u}$, and $\boldsymbol{d}_\alpha$, and $l = 2$ from $\boldsymbol{\nabla} \boldsymbol{u}_{e,i}$) by the left hand side D_{k_1}, the local limit only requires solving the $l = 1$ block for a non-trivial solution (and $l = 2$ if gradients in flow generating viscous stress are included).

3.4.5 Enforcing solvability conditions

The DDF equation should be solved with the same solvability conditions as the Chapman-Enskog solution, namely constraining that the solution δf_α does not modify the number density, hydrodynamic flow, or temperature. For the single species case, these solvability conditions are

$$\int d^3\boldsymbol{w}\ \delta f_\alpha = 0, \quad \int d^3\boldsymbol{w}\ \boldsymbol{w} \delta f_\alpha = 0, \quad \int d^3\boldsymbol{w}\ w^2 \delta f_\alpha = 0, \tag{3.87}$$

respectively. On the spherical harmonic expansion, these conditions become

$$\int_0^\infty dw\ w^2 \delta f_\alpha^{(0,0)} = 0, \quad \int_0^\infty dw\ w^3 \delta f_\alpha^{(1,m)} = 0, \quad \int_0^\infty dw\ w^4 \delta f_\alpha^{(0,0)} = 0, \tag{3.88}$$

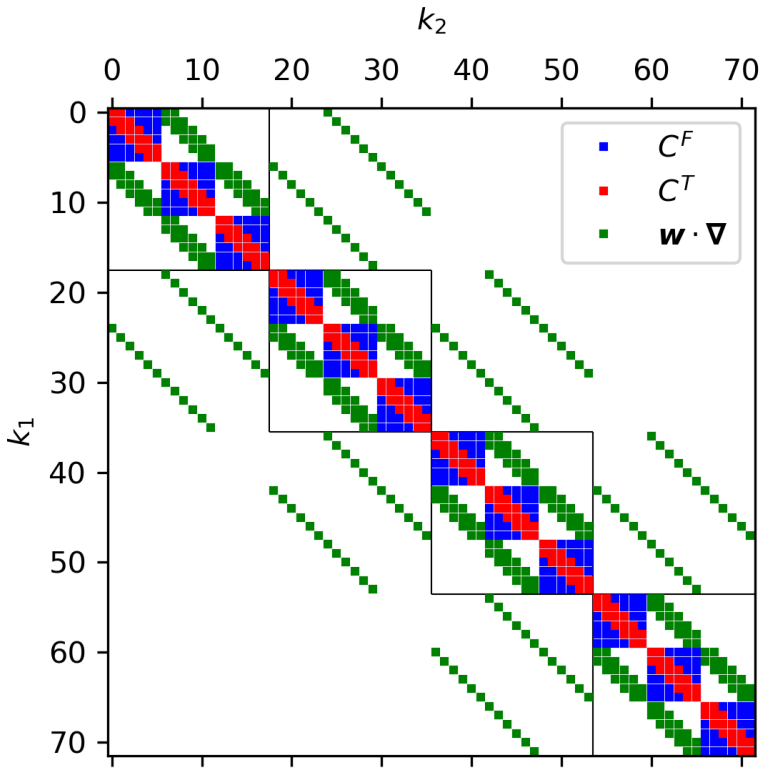


Figure 3.2: Nonzero elements in the Jacobian $\hat{M}_{k_1,k_2}$ for the RKM with $N_l = 3$, $N_i = 4$, $N_j = 6$ for the unmagnetised single species solver. Elements are arranged according to $k(i,l,j) = j + N_j(l + N_l(i))$.

where the flow constraint holds for $m = 0, \pm 1$. For the discretised DDF, these conditions become

$$\sum_{j_2} c_{j_2} w_{j_2}^2 F_{k_2(l_2=0)} = 0, \quad \sum_{j_2} c_{j_2} w_{j_2}^3 F_{k_2(l_2=1)} = 0, \quad \sum_{j_2} c_{j_2} w_{j_2}^4 F_{k_2(l_2=0)} = 0. \tag{3.89}$$

The matrix $\hat{M}_{k_1,k_2}$ is then modified to enforce these conditions. In particular, at each spatial index i, a row of the matrix is replaced to enforce each of these conditions as

$$\hat{M}_{k_1,k_2} = c_{j_2} w_{j_2}^2, \quad D_{k_1} = 0, \quad \text{where} \quad l_1 = l_2 = 0, \quad m_1 = m_2 = 0, \quad j_1 = j_n, \tag{3.90}$$

$$\hat{M}_{k_1,k_2} = c_{j_2} w_{j_2}^3, \quad D_{k_1} = 0, \quad \text{where} \quad l_1 = l_2 = 0, \quad m_1 = m_2 = 0, \pm 1, \quad j_1 = j_u, \tag{3.91}$$

$$\hat{M}_{k_1,k_2} = c_{j_2} w_{j_2}^4, \quad D_{k_1} = 0, \quad \text{where} \quad l_1 = l_2 = 0, \quad m_1 = m_2 = 0, \quad j_1 = j_T, \tag{3.92}$$

where $j_{(n,u,T)}$ are some chosen velocity coordinates at which to enforce the constraint, chosen as the coordinate with the thermal velocity $w_{j_1} = [v_{\text{th},\alpha}]_{i_1}$.

For the multi-species solver in the mixture formalism, the density and temperature conditions are enforced on each species. For the flow constraint, the condition is instead

$$\sum_\alpha \int d^3\boldsymbol{w}\, m_\alpha \boldsymbol{w} \delta f_\alpha = 0 \quad \Rightarrow \quad \sum_\alpha \int_0^\infty dw\, m_\alpha w^3 \delta f_\alpha^{(1,m)} = 0, \tag{3.93}$$

since only the hydrodynamic velocity $\boldsymbol{u}_i$ is constrained, but each species may have a diffusive velocity relative

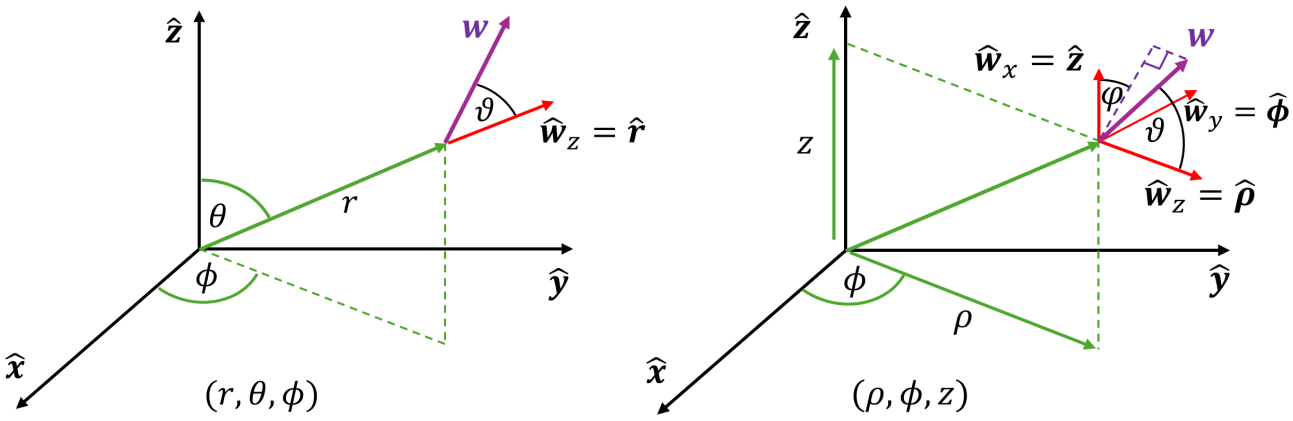
to this. This constraint is enforced in the matrix $\hat{M}_{k_1,k_2}$ as

$$\hat{M}_{k_1,k_2} = c_{j_2} m_{s_2} w_{j_2}^3, \quad D_{k_1} = 0, \quad \text{where} \quad l_1 = l_2 = 0, \quad m_1 = m_2 = 0, \pm 1, \quad s_1 = 0, \quad j_1 = j_u, \tag{3.94}$$

which sums over s_2 and enforces the constraint on the first species $s_1 = 0$.

3.5 Spherical and Cylindrical Geometries

Other spatial geometries can be described using 1D3V coordinates, provided there are spatial symmetries that allow position space to be described using one spatial coordinate. Two standard curvilinear geometries are spherical and cylindrical.



(a) Spherical spatial and spherical velocity coordinates

(b) Cylindrical spatial and spherical velocity coordinates

Figure 3.3: Diagrams visualizing spherical and cylindrical spatial coordinates with spherical velocity coordinates.

A spherical geometry is particularly relevant to ICF, where targets and implosions are usually ideally spherical. Spherical coordinates are denoted (r, θ, ϕ) as standard and depicted in Figure 3.3a, with spherical symmetry over θ, ϕ, leaving the radial coordinate r as the single spatial coordinate. The pole of the spherical velocity coordinates is then aligned with the local radial direction $\hat{\boldsymbol{w}}_z = \hat{\boldsymbol{r}}$. The presence of a magnetic field or non-radial components of flows would violate spherical symmetry in space, therefore may not be included in the 1D spherical coordinates. There is then an azimuthal symmetry over the azimuthal angle in the velocity space φ. The phase space in a spherical geometry is then described by 1D2V coordinates (r, w, ϑ).

A cylindrical geometry is particularly relevant to Z-pinches and magneto-inertial schemes such as MagLIF [59]. Cylindrical coordinates are denoted (ρ, ϕ, z) as standard and depicted in Figure 3.3b, with cylindrical symmetry over the spatial azimuthal angle ϕ and axial symmetry over the axial coordinate z. The pole of the spherical velocity coordinates is then aligned with the local radial direction $\hat{\boldsymbol{w}}_z = \hat{\boldsymbol{\rho}}$. Unlike planar or spherical spatial coordinates, a cylindrical spatial geometry requires 1D3V coordinates even without flows or magnetic fields, since the z axis provides a second preferential direction that breaks the azimuthal symmetry in the velocity space. The phase space in a cylindrical geometry is then described by 1D3V coordinates $(\rho, w, \vartheta, \varphi)$.

Curvilinear coordinates modify the form of the spatial advection operator $\boldsymbol{w} \cdot \boldsymbol{\nabla}$ appearing in the VFP

equation as

$$\begin{aligned}\{\boldsymbol{w}\cdot\boldsymbol{\nabla}f\}_{\mathrm{p}} &= \mu w\partial_z,\\ \{\boldsymbol{w}\cdot\boldsymbol{\nabla}f\}_{\mathrm{s}} &= \mu w\partial_r + \frac{w}{r}(1-\mu^2)\partial_\mu,\\ \{\boldsymbol{w}\cdot\boldsymbol{\nabla}f\}_{\mathrm{c}} &= \mu w\partial_\rho + \frac{w}{\rho}(1-\mu^2)\sin^2\varphi\partial_\mu - \frac{w}{\rho}\mu\cot\varphi\partial_\varphi,\end{aligned} \tag{3.95}$$

where the labels 'p', 's', and 'c' refer to planar, spherical, and cylindrical, respectively. A derivation of the advection operator in cylindrical and spherical coordinates and their projections onto the spherical harmonic basis are presented below. Flows in spherical and cylindrical geometries also introduce additional contributions through the $\boldsymbol{u}\cdot\boldsymbol{\nabla}$ and $\boldsymbol{w}\cdot(\boldsymbol{\nabla}\boldsymbol{u})\cdot\boldsymbol{\nabla}_{\boldsymbol{w}}$ terms. For the purposes of this work, we do not consider flows in spherical and cylindrical geometries and so these terms are not considered.

Here we prove these expressions. The velocity space is always described in a spherical coordinate system $d\boldsymbol{w} = dw\hat{\boldsymbol{w}} + wd\vartheta\hat{\boldsymbol{\vartheta}} + w\sin\vartheta d\varphi\hat{\boldsymbol{\varphi}}$ for the spherical harmonics expansion. The spatial advection term in the Vlasov operator appears differently in different spatial coordinate systems. For phase space coordinates $\boldsymbol{Z} = (\boldsymbol{x}, \boldsymbol{w})$,

$$\boldsymbol{\nabla}_{\boldsymbol{x}} = \sum_a(\boldsymbol{\nabla}_{\boldsymbol{x}}Z_a)\partial_{Z_a}, \quad \boldsymbol{\nabla}_{\boldsymbol{w}} = \sum_a(\boldsymbol{\nabla}_{\boldsymbol{w}}Z_a)\partial_{Z_a}, \tag{3.96}$$

Since the spatial coordinates are independent of the velocity coordinates, the velocity gradient always reduces to the velocity gradient in spherical polar coordinates. In Cartesian spatial coordinates $d\boldsymbol{x} = dx\hat{\boldsymbol{x}} + dy\hat{\boldsymbol{y}} + dz\hat{\boldsymbol{z}}$, the velocity coordinates are independent of spatial position, therefore

$$\boldsymbol{\nabla}_{\boldsymbol{x}} = \hat{\boldsymbol{x}}\partial_x + \hat{\boldsymbol{y}}\partial_y + \hat{\boldsymbol{z}}\partial_z + (\boldsymbol{\nabla}_{\boldsymbol{x}}w)\partial_w + (\boldsymbol{\nabla}_{\boldsymbol{x}}\mu)\partial_\mu + (\boldsymbol{\nabla}_{\boldsymbol{x}}\varphi)\partial_\varphi = \hat{\boldsymbol{z}}\partial_z. \tag{3.97}$$

The x and y derivatives have been dropped since a slab planar geometry in the z direction is considered. In the planar geometry, all of the gradients of the velocity coordinates $\boldsymbol{\nabla}_{\boldsymbol{x}}(w,\mu,\varphi)$ are zero, since their definition does not vary with z with a fixed velocity $\boldsymbol{w}$. However, in other spatial geometries, we define the velocity coordinates to depend on the spatial position so we may use a 1D3V treatment. The cost of this choice is that the spatial gradient term now picks up additional contributions from the velocity coordinates changing with spatial position.

3.5.1 Spherical spatial coordinates

In spherical spatial coordinates (r,θ,ϕ) with spherical symmetry in θ and ϕ, the velocity space must also be azimuthally symmetric over φ. The gradient is

$$\boldsymbol{\nabla}_{\boldsymbol{x}} = \hat{\boldsymbol{r}}\partial_r + (\boldsymbol{\nabla}_{\boldsymbol{x}}\mu)\partial_\mu. \tag{3.98}$$

Since $\mu = \boldsymbol{w}\cdot\hat{\boldsymbol{r}}/w$, the gradient of μ may be evaluated as

$$\boldsymbol{\nabla}_{\boldsymbol{x}}\mu = \frac{\boldsymbol{w}}{w}\cdot\boldsymbol{\nabla}\hat{\boldsymbol{r}} = \frac{\boldsymbol{w}}{wr}\cdot(\mathbb{I}-\hat{\boldsymbol{r}}\hat{\boldsymbol{r}}) = \frac{1}{wr}(\boldsymbol{w}-\mu w\hat{\boldsymbol{r}}), \tag{3.99}$$

therefore

$$\{\boldsymbol{w}\cdot\boldsymbol{\nabla}f\}_s = \boldsymbol{w}\cdot\left(\hat{\boldsymbol{r}}\partial_r + \frac{1}{wr}(\boldsymbol{w}-\mu w\hat{\boldsymbol{r}})\partial_\mu\right)f = \mu w\partial_r f + \frac{w}{r}(1-\mu^2)\partial_\mu f. \tag{3.100}$$

The projection of this advection term on the spherical harmonic basis is then

$$\langle l,m|\boldsymbol{v}\cdot\boldsymbol{\nabla}f\rangle = w\partial_r\langle l,m|\mu f\rangle + \frac{w}{r}\langle l,m|(1-\mu^2)\partial_\mu f\rangle, \tag{3.101}$$

where both projections are provided by Swanekamp et al. [109], with the new term using the projection of the parallel electric field

$$\langle l,m|(1-\mu^2)\partial_\mu f\rangle = \frac{(l+2)(l+1-m)}{2l+1}f^{(l+1,m)} - \frac{(l-1)(l+m)}{2l+1}f^{(l-1,m)}. \tag{3.102}$$

3.5.2 Cylindrical spatial coordinates

In cylindrical spatial coordinates (ρ,ϕ,z) with cylindrical symmetry in ϕ and translational symmetry in z,

$$\boldsymbol{\nabla}_{\boldsymbol{x}} = \hat{\boldsymbol{\rho}}\partial_\rho + (\boldsymbol{\nabla}_{\boldsymbol{x}}\mu)\partial_\mu + (\boldsymbol{\nabla}_{\boldsymbol{x}}\varphi)\partial_\varphi. \tag{3.103}$$

The polar angle term changes from the spherical case, since in cylindrical coordinates $\boldsymbol{\nabla}_{\boldsymbol{x}}\hat{\boldsymbol{\rho}} = \frac{1}{\rho}\hat{\boldsymbol{\phi}}\hat{\boldsymbol{\phi}}$. The gradient of μ is

$$\boldsymbol{\nabla}_{\boldsymbol{x}}\mu = \frac{\boldsymbol{w}}{w}\cdot\frac{1}{\rho}\hat{\boldsymbol{\phi}}\hat{\boldsymbol{\phi}} = \frac{1}{\rho}\sqrt{1-\mu^2}\sin\varphi\,\hat{\boldsymbol{\phi}}, \tag{3.104}$$

which contributes to the ∂_μ term as

$$\boldsymbol{w}\cdot(\boldsymbol{\nabla}_{\boldsymbol{x}}\mu)\partial_\mu = \frac{w}{\rho}(1-\mu^2)\sin^2\varphi\partial_\mu, \tag{3.105}$$

where we have used $\boldsymbol{w}\cdot\hat{\boldsymbol{\phi}} = w\sqrt{1-\mu^2}\sin\varphi$. For the azimuthal term, we write the azimuthal velocity angle as

$$\boldsymbol{w}\cdot\hat{\boldsymbol{z}} = w\sqrt{1-\mu^2}\cos\varphi \quad\Rightarrow\quad \varphi = \arccos\left(\frac{\boldsymbol{w}\cdot\hat{\boldsymbol{z}}}{|\boldsymbol{w}-(\boldsymbol{w}\cdot\hat{\boldsymbol{\rho}})\hat{\boldsymbol{\rho}}|}\right) = \arccos\left(\frac{\boldsymbol{w}\cdot\hat{\boldsymbol{z}}}{w\sqrt{1-\mu^2}}\right), \tag{3.106}$$

therefore its gradient becomes

$$\begin{aligned}\boldsymbol{\nabla}_{\boldsymbol{x}}\varphi &= -\frac{1}{\sqrt{1-\left(\frac{\boldsymbol{w}\cdot\hat{\boldsymbol{z}}}{w\sqrt{1-\mu^2}}\right)^2}}\frac{\boldsymbol{w}\cdot\hat{\boldsymbol{z}}}{w}\boldsymbol{\nabla}_{\boldsymbol{x}}((1-\mu^2)^{-1/2}) \\ &= -\frac{w\sqrt{1-\mu^2}}{\sqrt{w^2(1-\mu^2)-(\boldsymbol{w}\cdot\hat{\boldsymbol{z}})^2}}\frac{\boldsymbol{w}\cdot\hat{\boldsymbol{z}}}{w}\mu(1-\mu^2)^{-3/2}\boldsymbol{\nabla}_{\boldsymbol{x}}\mu \\ &= -\frac{1}{\rho}\frac{\mu}{1-\mu^2}\frac{\cos\varphi}{\sin\varphi}(\hat{\boldsymbol{w}}-\mu\hat{\boldsymbol{\rho}}),\end{aligned} \tag{3.107}$$

which contributes to the advection term as

$$\boldsymbol{w}\cdot(\boldsymbol{\nabla}_{\boldsymbol{x}}\varphi)\partial_\varphi = -\frac{1}{w\rho}\frac{\mu}{1-\mu^2}\frac{\cos\varphi}{\sin\varphi}\boldsymbol{w}\cdot(\boldsymbol{w}-\mu w\hat{\boldsymbol{\rho}})\partial_\varphi = -\frac{w}{\rho}\mu\frac{\cos\varphi}{\sin\varphi}\partial_\varphi. \tag{3.108}$$

Collecting terms, the advection operator in cylindrical coordinates is then

$$\{\boldsymbol{w}\cdot\boldsymbol{\nabla}f\}_{\mathrm{c}} = \mu w\partial_\rho f + \frac{w}{\rho}(1-\mu^2)\sin^2\varphi\partial_\mu f - \frac{w}{\rho}\mu\cot\varphi\partial_\varphi f. \tag{3.109}$$

The two additional terms are then projected onto the spherical harmonic basis as

$$\begin{aligned}\langle l,m|\mu\frac{\cos\varphi}{\sin\varphi}\partial_\varphi f\rangle &= \sum_{k=0}^{\infty}\sum_{n=-k}^{k}\frac{2k+1}{4\pi}\frac{(k-n)!}{(k+n)!}inf^{(k,n)}\int_{-1}^{1}d\mu\,\mu P_l^m P_k^n \underbrace{\int_0^{2\pi}d\varphi\,\frac{\cos\varphi}{\sin\varphi}e^{i(n-m)\varphi}}_{=2\pi i\mathrm{sgn}(n-m)\text{ for even }n-m\neq 0} \\ &= -\sum_{k=0}^{\infty}\sum_{r=-\lfloor(k+m)/2\rfloor,r\neq 0}^{\lfloor(k-m)/2\rfloor}p_{l,k}(m,r)f^{(k,m+2r)},\end{aligned} \tag{3.110}$$

where the integral over φ is evaluated using contour integration, and

$$\begin{aligned}\langle l,m|(1-\mu^2)\sin^2\varphi\partial_\mu f\rangle &= \sum_{k=0}^{\infty}\sum_{n=-k}^{k}\frac{2k+1}{4\pi}\frac{(k-n)!}{(k+n)!}f^{(k,n)}\int_{-1}^{1}d\mu\,P_l^m(1-\mu^2)\partial_\mu P_k^n \underbrace{\int_0^{2\pi}d\varphi\,e^{i(n-m)\varphi}\sin^2\varphi}_{=2\pi(\frac{1}{2}\delta_{n,m}-\frac{1}{4}\delta_{n,m+2}-\frac{1}{4}\delta_{n,m-2})} \\ &= \frac{1}{2}\left(\frac{(l+2)(l+1-m)}{2l+1}f^{(l+1,m)}-\frac{(l-1)(l+m)}{2l+1}f^{(l-1,m)}\right) \\ &\quad -\frac{1}{4}\sum_{k=0}^{\infty}\left(q_{l,k}^{+}(m)f^{(k,m+2)}+q_{l,k}^{-}(m)f^{(k,m-2)}\right)\end{aligned} \tag{3.111}$$

where

$$\begin{aligned}p_{l,k}(m,r) &= \frac{2k+1}{2}\frac{(k-(m+2r))!}{(k+m+2r)!}(m+2r)\mathrm{sgn}(r)\int_{-1}^{1}d\mu\,\mu P_l^m(\mu)P_k^{m+2r}(\mu), \\ q_{l,k}^{\pm}(m) &\coloneqq \frac{2k+1}{2}\frac{(k-(m\pm 2))!}{(k+(m\pm 2))!}\int_{-1}^{1}d\mu\,(1-\mu^2)P_l^m(\mu)\frac{dP_k^{m\pm 2}(\mu)}{d\mu}.\end{aligned} \tag{3.112}$$

Similarly to the other matrix elements from Swanekamp et al. [109], these matrix elements are evaluated symbolically and tabulated for use in the RKM.

CHAPTER 4

Unmagnetised Single Species Results

To initially demonstrate the RKM and investigate nonlocal transport, a simple case without the complications of multiple ion species or magnetic fields is considered. We consider the electron RKM in a simple isochoric ($n_e = n_0$) unmagnetised ($\chi_e = 0$) hydrogen ($Z^* = 1$) plasma with temperature gradient of the form

$$T_e(z) = \frac{T_{\text{left}} + T_{\text{right}}}{2} - \frac{T_{\text{left}} - T_{\text{right}}}{2}\text{erf}\left(\frac{z}{L}\right) , \tag{4.1}$$

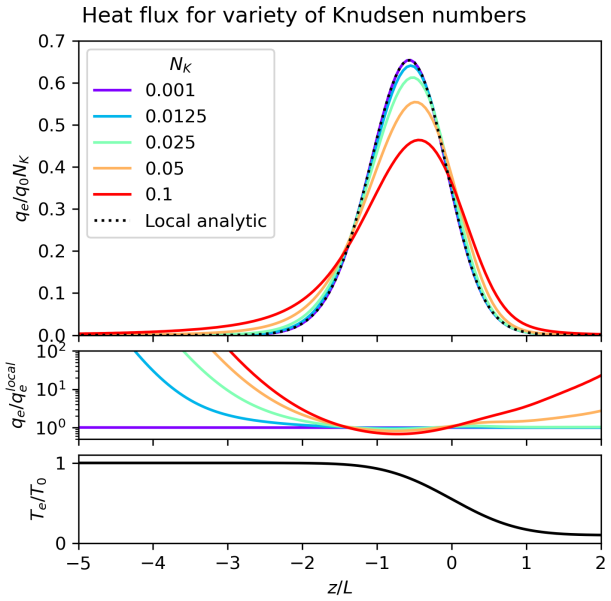
with $T_{\text{left}}/T_{\text{right}} = 10$ for a variety of Knudsen numbers $N_K = \lambda_0/L$, where $\lambda_0 = \lambda_{\text{th},e}(z \to -\infty)$ is the thermal MFP at the hot end. For this case, the hyperparameters $\Delta z/\lambda_0 = 0.1$, $\Delta w/v_0 = 0.1$, $N_l = 4$, $w_{\text{max}}/v_0 = 5$, and $N_{\text{iterations}} = 3$ are used, which provide good convergence as demonstrated by convergence studies in Section 4.3.

4.1 Nonlocal Transport Fluxes

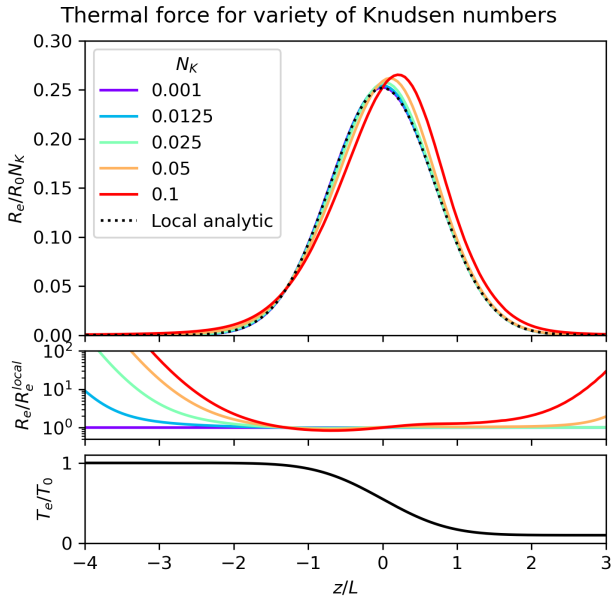
Figure 4.1 shows the nonlocal conductive heat flux and thermal force obtained from the RKM from a variety of Knudsen numbers from $N_K = 0.1$ to $N_K = 0.001$. The heat flux scales proportionally to the temperature gradient $|\boldsymbol{\nabla} \ln T_e|$ and therefore Knudsen number N_K. To conduct a meaningful comparison between the local and nonlocal heat fluxes, they are then normalised by the Knudsen number N_K.

Dimensional quantities such as length, density, and others have been scaled out of the kinetic equation, leaving a set of dimensionless PDEs dependent on the shape of the hydrodynamic profiles and Knudsen number. Varying the Knudsen number may then be considered to be varying the length scale of the profiles L, or equivalently as varying the characteristic mean free path λ_0 due to different characteristic temperatures or densities. In the RKM solver, the dimensionless length scale of the profiles L/λ_0 is varied to obtain cases of various Knudsen number.

For small Knudsen number $N_K \lesssim 0.001$, both the conductive heat flux and thermal force from the RKM agree extremely well with the local analytic results. We emphasise that this agreement is obtained with the RKM solver having no prior knowledge of the local analytic results for q_e^T and R_e^T, but reproduces them



(a) Conductive heat flux q_e^T



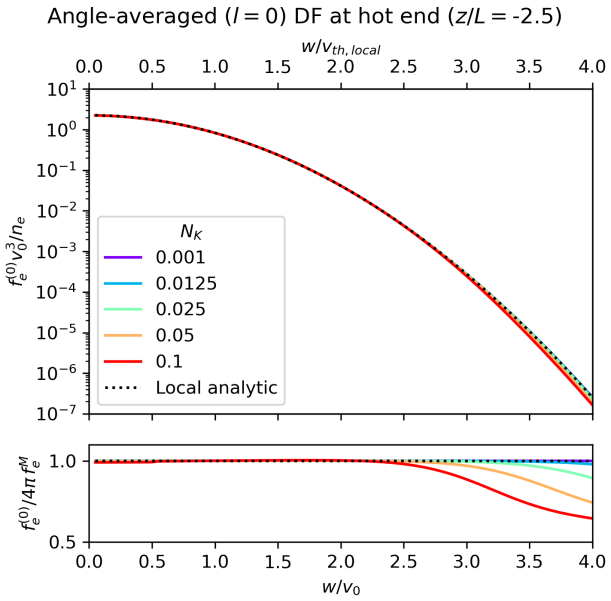
(b) Thermal force R_e^T

Figure 4.1: Nonlocal electron conductive heat flux and thermal force for a variety of Knudsen numbers N_K.

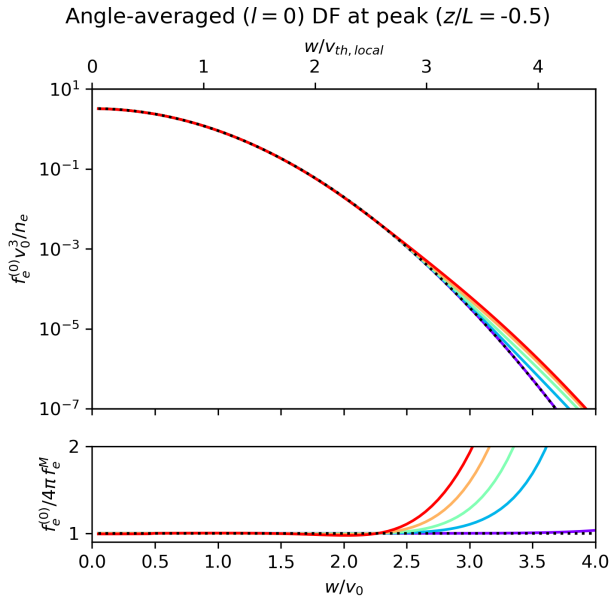
naturally since the approach is first-principles. Strong agreement of the RKM in the local limit ($N_K \ll 1$) with local analytic results are consistent throughout the remainder of this work.

Around $N_K \approx 0.0125 \approx 1/3^4$, deviations of the heat flux away from the local analytic result become apparent, i.e. the $N_K = 0.0125$ blue line of 4.1a is visually slightly different from the local analytic black dotted line. This matches well with particles of $w/v_{\text{th},e} \lesssim 3$ that contribute to the heat flux with MFPs $\lambda = (w/v_{\text{th},e})^4 \lambda_{\text{th}} \sim 81\,\lambda_{\text{th}}$ being able to stream across the temperature gradient and give rise to nonlocal deviations of q_e^T. In contrast, the thermal force appears unaffected at this Knudsen number, since it is a lower velocity moment of the DF which is not noticeably affected by nonlocal behaviour of suprathermal particles at $w/v_{\text{th},e} \sim 3$.

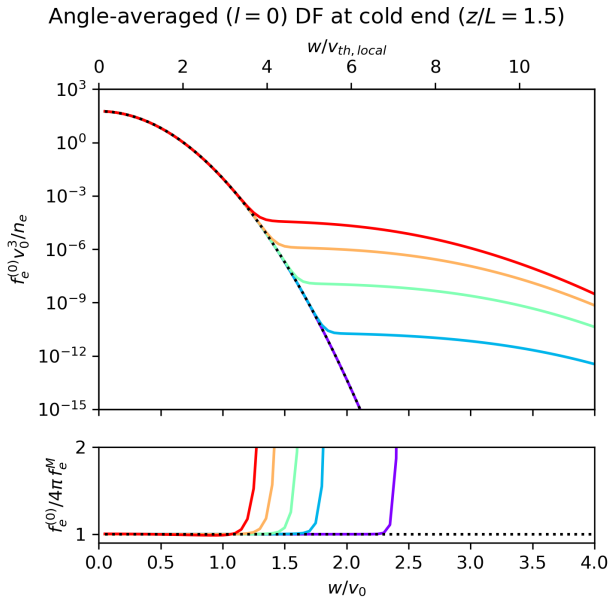
For higher Knudsen numbers, a significant preheat forms in the cold end $z/L \gtrsim 0.5$. This preheat is explained physically by the streaming suprathermal particles from the hot end depositing their heat in the cold end. A similar enhancement of the heat flux in nonlocal cases is also seen in the hot end, although considering the heat flux in the temperature equation $\frac{3}{2} n_e \partial_t T_e = -\boldsymbol{\nabla} \cdot \boldsymbol{q}_e + \ldots$, the fractional rate of change of temperature $(\partial_t T_e)/T_e$ due to enhanced heat flux from nonlocal kinetic effects will be more pronounced in the cold end than the hot end.



(a) $f_e^{(0,0)}$ at hot end



(b) $f_e^{(0,0)}$ at centre



(c) $f_e^{(0,0)}$ at cold end

Figure 4.2: Angle-averaged DF across space.

4.2 Nonlocal Distribution Function

4.2.1 Angle-averaged distribution function

Since the RKM solves for $\delta f_e^{(l,m)}(z,w)$, these modes of the DDF may be directly plotted. Figure 4.2 shows the isotropic $l = 0$ component, i.e. angle-averaged (within a factor of 4π), distribution function

$$f_e^{(0)}(z,w) = f_e^{(0,0)}(z,w) = \int d^2\Omega \; f_e(z,w,\vartheta,\varphi) \tag{4.2}$$

at three spatial positions $z/L = -2.5,\ -0.5,\ 1.5$, corresponding to the hot end, the peak heat flux, and cold end, respectively. The horizontal scales show the velocities normalised to both the hot thermal velocity v_0 and the local thermal velocity $v_{\text{th,local}}$.

For small Knudsen number $N_K = 0.001$, the DFs across space are close to Maxwellian for almost all velocities, with deviations apparent only very far out in the tail. For higher Knudsen numbers, these deviations occur less far out in the tail. Since the length scale of the temperature gradient is shorter, lower velocity particles with shorter MFPs are allowed to stream across the gradient and give rise to deviations in the tail of the DF. In the hot end, the tail is reduced since suprathermal tail particles with long MFPs may leave the hot end, and in the centre and cold end, these same particles enhance the tail of the DF.

4.2.2 First angular moment of distribution function

Figure 4.3 shows the first spherical harmonic $l, m = 1, 0$ component, i.e. the first angular moment

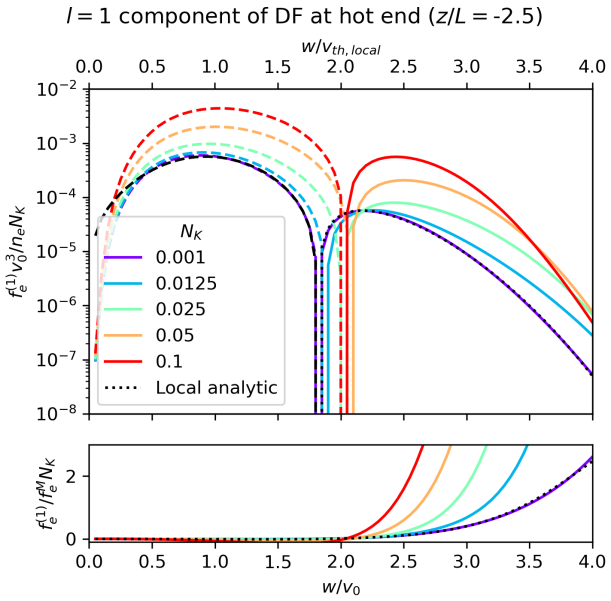
$$f_e^{(1)}(z, w) = f_e^{(1,0)}(z, w) = \int d^2\Omega\ \cos\vartheta\, f_e(z, w, \vartheta, \varphi) \tag{4.3}$$

of the distribution function at these same three spatial positions. Similarly to the conductive heat flux and thermal force, $f_e^{(1)}$ is normalised to the Knudsen number N_K for a meaningful comparison, since the local result is directly proportional to $|\boldsymbol{\nabla} \ln T_e|$.

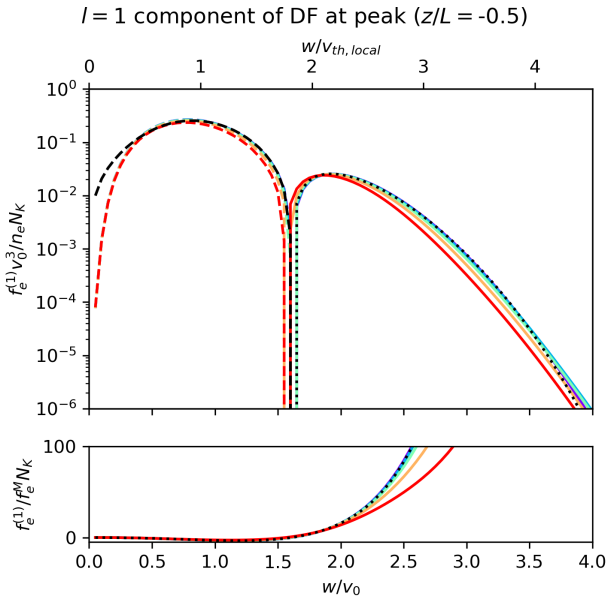
For small Knudsen number $N_K = 0.001$, the RKM result agrees extremely well with the local analytic result. This agreement is recovered naturally, i.e. the RKM has no knowledge of the local analytic solution before solving, but matches up with it in the appropriate limit. This then demonstrates the high accuracy of the RKM.

In contrast to the isotropic component, the local result for the $l = 1$ component is small in the hot and cold ends since the temperature gradient is small at those positions. At the hot end, the high Knudsen number results are orders of magnitude larger than the local result across w due to advected parts of the solution from the centre where the gradient is large. However, at larger $w/v_0 \gtrsim 3.5$, the high Knudsen number $N_K = 0.1$ result still has a reduced tail due to streaming suprathermal particles. At the centre, the local solution is not small due to the local gradient, so the high Knudsen number solutions are not dramatically larger than it. At higher Knudsen numbers, the tail is reduced due to nonlocal streaming. This manifests itself in the heat flux as the reduced peak flux.

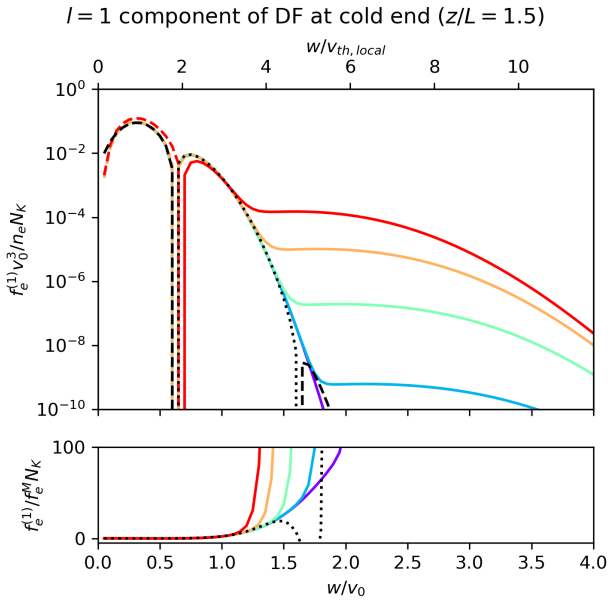
In the cold end, the tail of the DF is enhanced due to streaming particles. Even for the low Knudsen number solution $N_K = 0.001$, the DF is enhanced far out in the tail due to nonlocal streaming, but far out enough where the heat flux is not noticeably influenced. The local analytic solution, shown in black, breaks down in the tail at $w/v_{\text{th},e} \gtrsim 4$. This local solution was computed using six Laguerre polynomials in the expansion. If more were included, this solution would be valid for $N_K \ll 1$ further out in the tail.



(a) $f_e^{(1,0)}$ at hot end



(b) $f_e^{(1,0)}$ at centre



(c) $f_e^{(1,0)}$ at cold end

Figure 4.3: First spherical harmonic component of DF across space. Due to the logarithmic scale, negative values are shown as dashed lines.

4.2.3 First angular moment across space

Figure 4.4 shows the first angular moment $f_e^{(1)}$ from the RKM and local analytic solution in (z, w) space for the nonlocal $N_K = 0.1$ case, as well as the background electron Maxwellian. The local analytic solution, as detailed in Appendix C, has the form

$$\delta f_e^{(1),\text{local}} \propto f_e^M \boldsymbol{w} \cdot \boldsymbol{\nabla} \ln T_e. \tag{4.4}$$

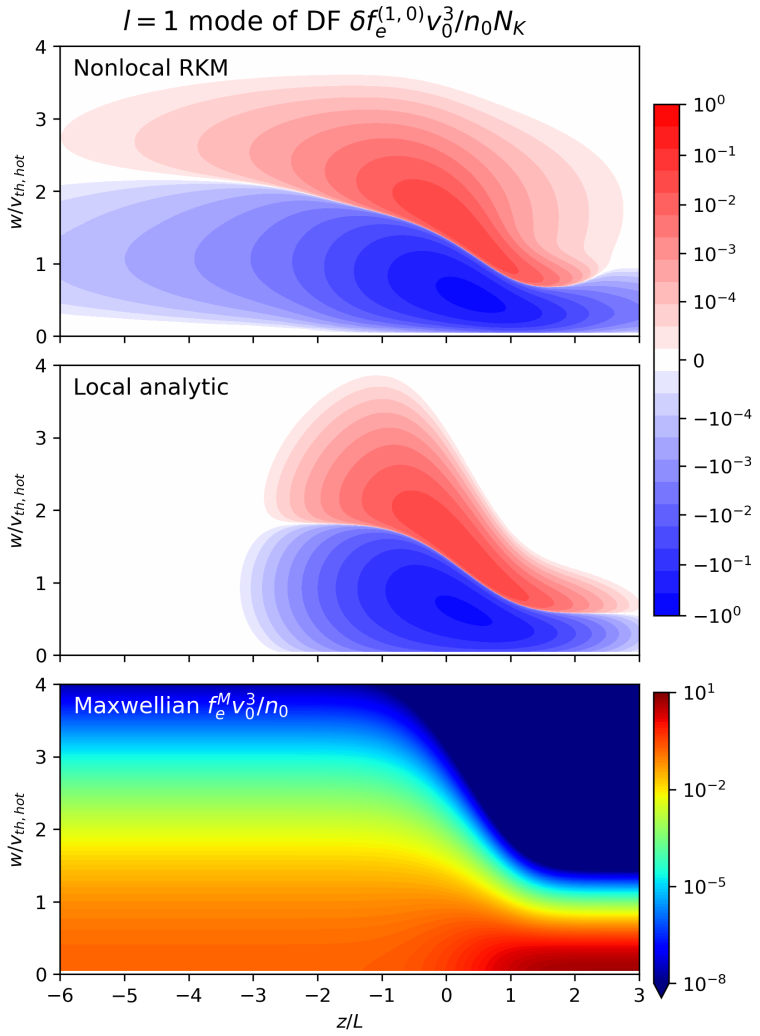


Figure 4.4: First spherical harmonic component of DF in phase space for the $N_K = 0.1$ solution. Note that the symmetric logarithmic colourmap has a linear section through zero. The Maxwellian distribution is shown on the bottom row of subplots on the same spatial axes to show the structure of the bulk distribution. Nonlocal effects are clearly present on the top row of subplots, with beam-like features extending well beyond the main gradient region around $z = 0$.

Away from the centre $|z/L| \lesssim 1.5$, the temperature gradient and therefore local analytic solution become exponentially small. However, the nonlocal solution extends far into the hot end $z/L \lesssim -1.5$ on the hot thermal velocity scale $w/v_{\text{th,hot}} \lesssim 3$. In the cold end $|z/L| \gtrsim 1.5$, the local solution is present on velocities $w/v_0 \lesssim 1$ since the cold thermal velocity $v_{\text{th,cold}}/v_0 \approx 0.32$. However, the nonlocal solution contains a hot beam-like structure on the scale of the hot thermal velocity that penetrates into the cold end.

4.2.4 Heat flux integrand

Figure 4.5 shows the integrand of the z component of the heat flux

$$\frac{dq_e}{dw} = \frac{1}{2} m_e w^5 f_e^{(1,0)}, \tag{4.5}$$

again with an appropriate normalisation to the Knudsen number. This is essentially Figure 4.4 multiplied by w^5, but the now linear heatmap emphasises the magnitude of heat flux that different components of phase

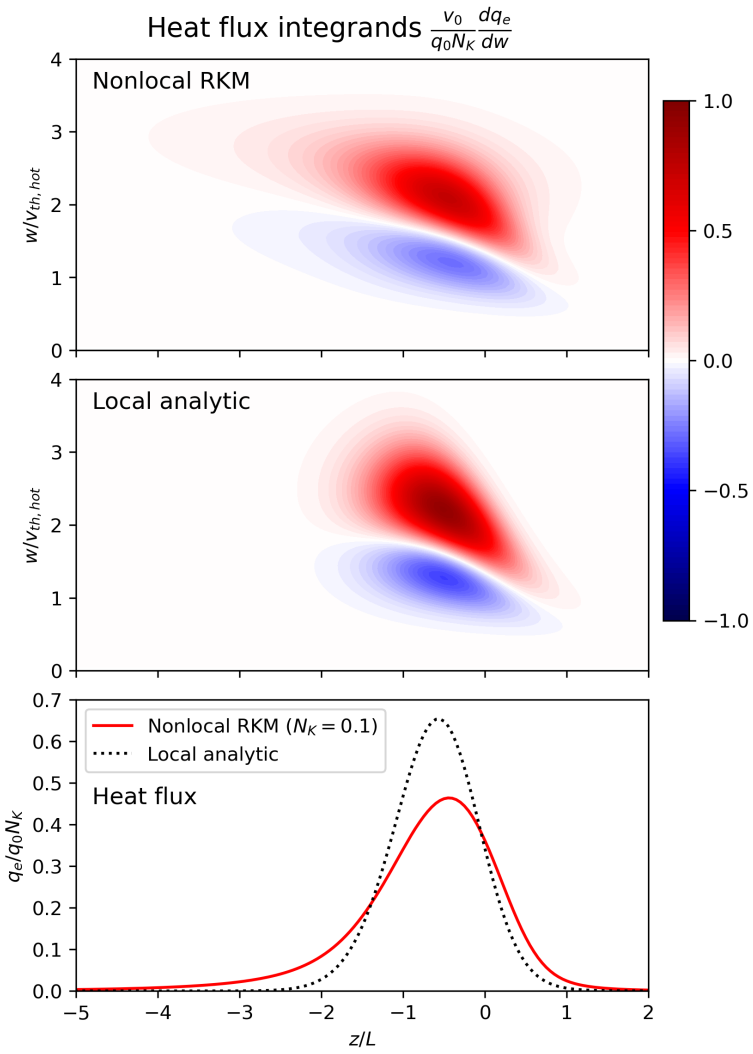


Figure 4.5: Integrand of heat flux in phase space. Note that the colourmap here is linear, so the brightness directly relates to contribution to the integrand. Reproduced from [3].

space contribute to. The hot beam in the cold end and suppression of the peak heat flux is clear.

4.2.5 Validity of linearising collision operator

The key assumption of the RKM is neglecting the nonlinear component of the collision operator, which is the last term when expanding the collision operator

$$C_{\alpha\beta}\{f_\alpha, f_\beta\} = C_{\alpha\beta}\{f_\alpha^M, f_\beta^M\} + C_{\alpha\beta}\{f_\alpha^M, \delta f_\beta\} + C_{\alpha\beta}\{\delta f_\alpha, f_\beta^M\} + C_{\alpha\beta}\{\delta f_\alpha, \delta f_\beta\} \tag{4.6}$$

where general species subscripts α and β are reintroduced to emphasise that $C_{\alpha\beta}$ represents collisions of species α against species β. The basis of this assumption originates from the form of the Landau collision operator, written in Rosenbluth form as

$$C_{\alpha\beta}\{f_\alpha, f_\beta\} = L_{\alpha\beta}\frac{\partial}{\partial v_i}\left[-\frac{m_\alpha}{m_\beta}\frac{\partial \mathcal{H}\{f_\beta\}}{\partial v_i} f_\alpha + \frac{1}{2}\frac{\partial^2 \mathcal{G}\{f_\beta\}}{\partial v_i \partial v_j}\frac{\partial f_\alpha}{\partial v_j}\right], \tag{4.7}$$

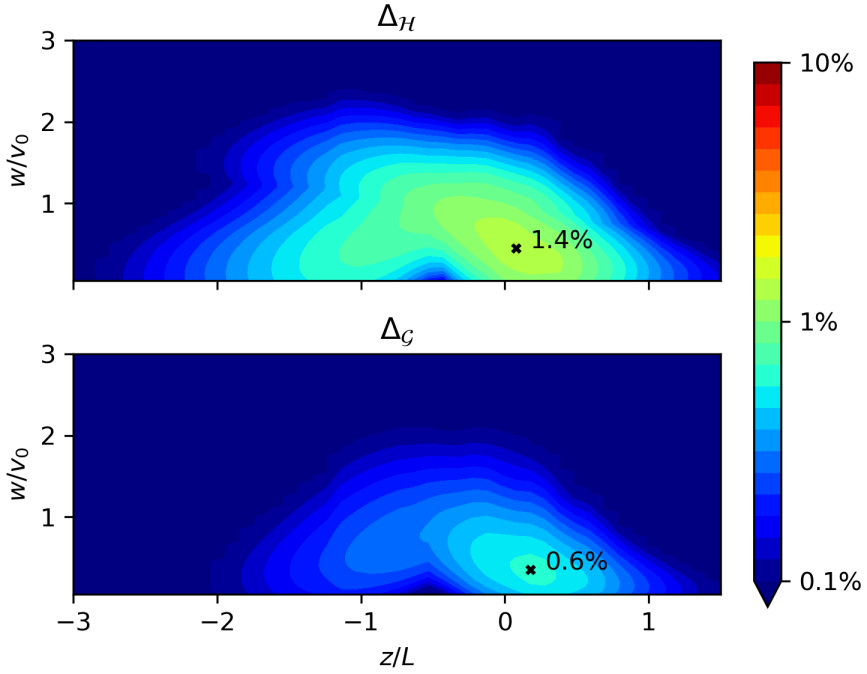


Figure 4.6: *A posteriori* justification to the smallness of the nonlocal correction to the electron Rosenbluth potentials $\mathcal{H}$ and $\mathcal{G}$ for the case of an isochoric unmagnetised plasma with a temperature gradient with $N_K = 1/10$. The smallness of these ratios ($\lesssim 1\%$) across phase space justifies neglecting the nonlinear component of the collision operator for $N_K \lesssim 1/10$. Reproduced from [3].

where $L_{\alpha\beta} \equiv \frac{1}{4\pi}\left(\frac{q_\alpha q_\beta}{\varepsilon_0 m_\alpha}\right)^2 \ln\Lambda_{\alpha\beta}$ and the Rosenbluth potentials are defined as

$$\mathcal{H}\{f_\beta\} \equiv \int d^3\boldsymbol{v}'\, \frac{1}{u} f_\beta(\boldsymbol{v}'), \quad \mathcal{G}\{f_\beta\} \equiv \int d^3\boldsymbol{v}'\, u f_\beta(\boldsymbol{v}'), \tag{4.8}$$

with $u = |\boldsymbol{v} - \boldsymbol{v}'|$. Focusing on the last two terms in the collision operator expansion, the test-particle and nonlinear components, we have

$$C_{\alpha\beta}\{\delta f_\alpha, f_\beta^M\} + C_{\alpha\beta}\{\delta f_\alpha, \delta f_\beta\} \equiv C_{\alpha\beta}\{\delta f_\alpha, f_\beta\}. \tag{4.9}$$

Neglecting the nonlinear component compared to the test-particle operator is then equivalent to approximating the Rosenbluth potentials appearing in this operator as those sampled from a Maxwellian, i.e.

$$\mathcal{H}\{f_\beta\} \approx \mathcal{H}\{f_\beta^M\}, \quad \mathcal{G}\{f_\beta\} \approx \mathcal{G}\{f_\beta^M\}. \tag{4.10}$$

This assumption is justified *a posteriori* by checking the ratios of the deviation of the Rosenbluth potentials $\delta\mathcal{H}_\beta \equiv \mathcal{H}\{\delta f_\beta\}$ from their Maxwellian results $\mathcal{H}_\beta^M \equiv \mathcal{H}\{f_\beta^M\}$ (and identically for $\mathcal{G}$) are small.

Figure 4.6 shows the deviation of the Rosenbluth potentials from their Maxwellian results for the unmagnetised temperature gradient case with $N_K = 0.1$. The deviation of $\mathcal{H}$ is defined as

$$\Delta_{\mathcal{H}} \equiv \frac{1}{|\mathcal{H}^M|} \sum_l \sum_m \frac{2l+1}{4\pi} \frac{(l-m)!}{(l+m)!} |\delta\mathcal{H}^{(l,m)}|, \tag{4.11}$$

which is an upper bound for $|\delta\mathcal{H}/\mathcal{H}^{\mathcal{M}}| \leq \Delta_{\mathcal{H}}$ over velocity angle space, and similarly for $\mathcal{G}$. The maximum deviations are $\Delta_{\mathcal{H}}^{\max} \approx 1.4\%$ and $\Delta_{\mathcal{G}}^{\max} \approx 0.6\%$, justifying the assumption of neglecting the nonlinear component of the collision operator for Knudsen numbers $N_K \lesssim 1/10$.

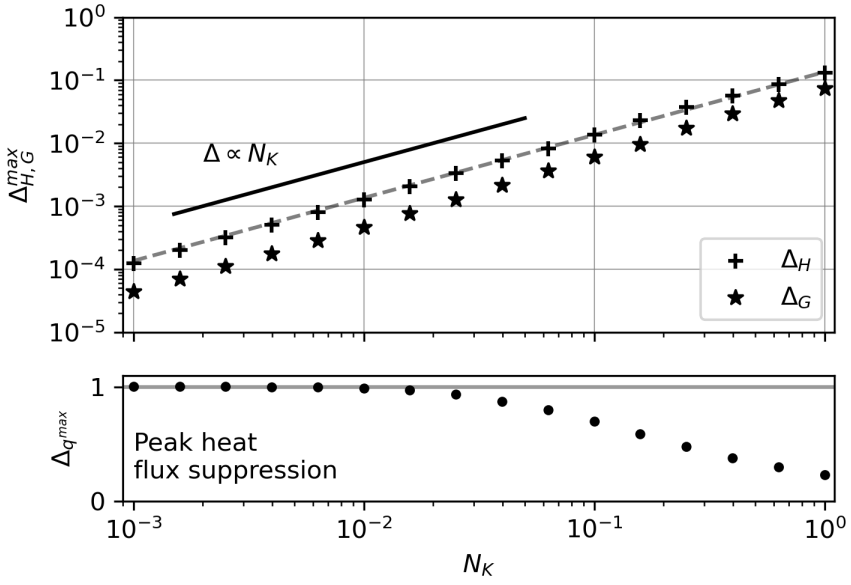


Figure 4.7: Maximum deviation of Rosenbluth potentials $\Delta^{\max}_{\mathcal{H},\mathcal{G}} = \max_{z,w}(\Delta_{\mathcal{H},\mathcal{G}})$ across a wide range of Knudsen numbers for the unmagnetised temperature step case and peak heat flux suppression $\Delta_{q^{\max}} = \max_z(|q_e^{\text{nonlocal}}|)/\max_z(|q_e^{\text{local}}|)$.

Figure 4.7 shows the maximum deviation of the Rosenbluth potentials $\Delta^{\max}_{\mathcal{H},\mathcal{G}}$ over a wide range of Knudsen numbers for the unmagnetised temperature step case, as well as the reduction of the peak heat flow. The deviations of the Rosenbluth potentials increase linearly with Knudsen number, with fits $\Delta_{\mathcal{H}}^{\max} \approx 0.14 N_K$ and $\Delta_{\mathcal{G}}^{\max} \approx 0.08 N_K$. The linearisation of the collision operator is robust where $\Delta^{\max}_{\mathcal{H},\mathcal{G}} \lesssim 0.1$, and therefore over the semi-collisional regime $N_K \lesssim 1$.

4.3 Convergence Studies

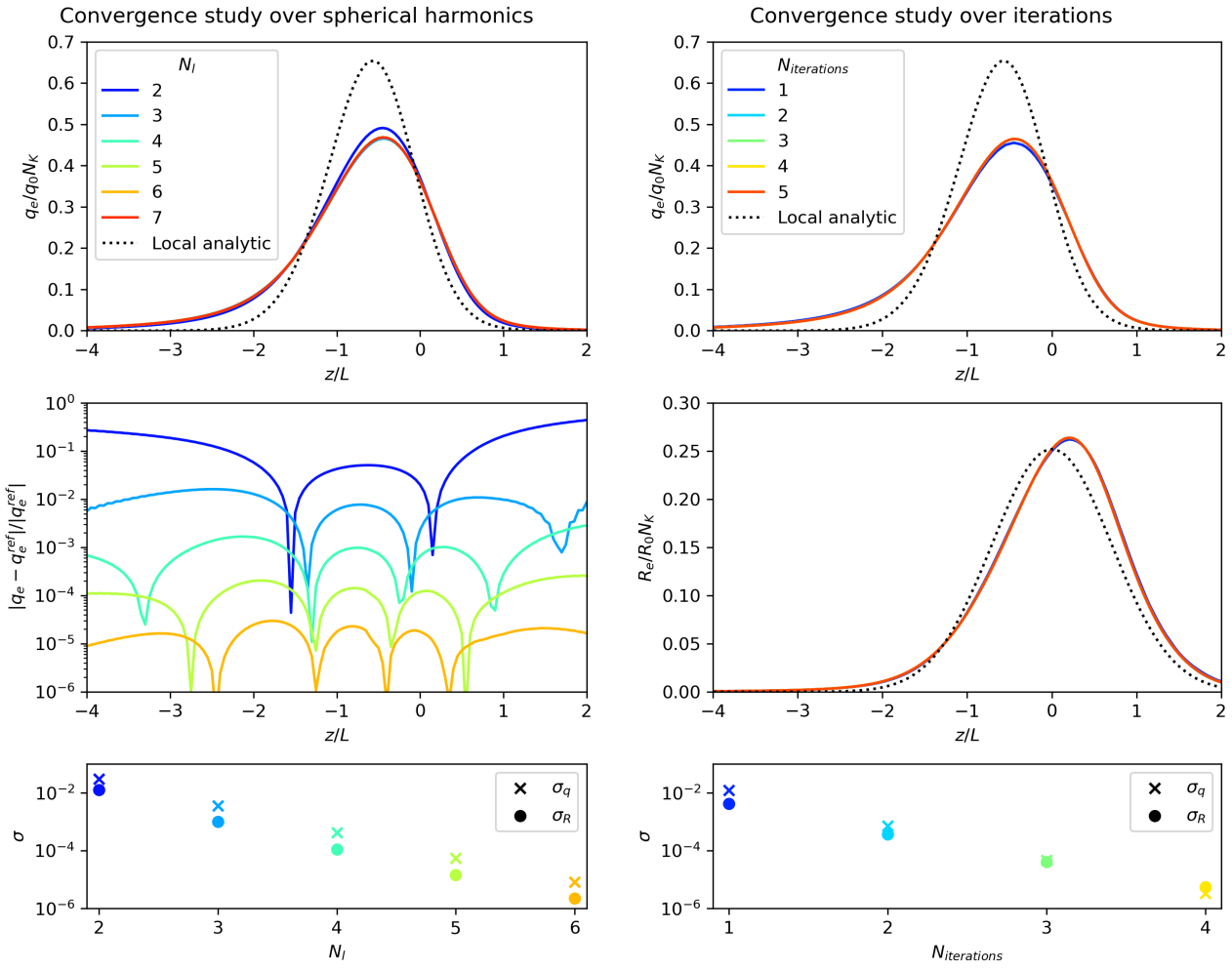
In the RKM, there are various hyperparameters that must be chosen to ensure a good balance between accuracy of the solution versus computational tractability. For example, the spatial and velocity resolutions, Δz and Δw, respectively. These are chosen by default at suitably low values ($\Delta z/l_0 = 0.1$ and $\Delta w/v_0 = 0.1$) which, given the author's experience with the RKM code, provide good accuracy and convergence while remaining tractable. There are two other hyperparameters of particular interest: the number of spherical harmonics N_l kept in the expansion of the DF, and the number of iterations $N_{\text{iterations}}$ the RKM is run for to obtain a solution with a self-consistent momentum exchange.

To measure convergence of the heat flux q_e, its integrated deviation across space is introduced as

$$\sigma_q = \frac{1}{q_0 \lambda_0} \int dz \, |q_e - q_e^{\text{ref.}}|, \tag{4.12}$$

where the reference heat flux $q_e^{\text{ref.}}$ is chosen as the value with the most accurate value, i.e. with largest N_l

(here $N_l^{\text{ref.}} = 7$) or largest $N_{\text{iterations}}$ (here $N_{\text{iterations}}^{\text{ref.}} = 5$). The quantity σ_R is defined analogously to measure convergence of the momentum exchange R_e.



(a) Convergence over N_l

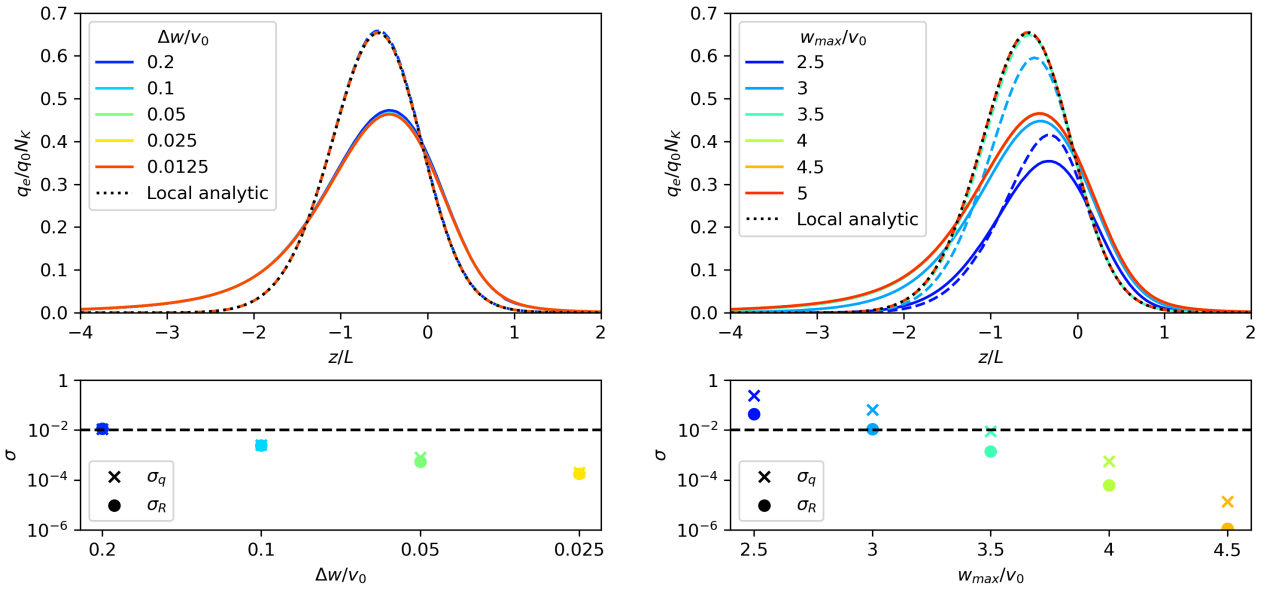
(b) Convergence over $N_{\text{iterations}}$

Figure 4.8: Convergence studies for a) number of spherical harmonics kept in DF expansion, and b) number of iterations to obtain a self-consistent momentum exchange R_e. The lower subplots show the convergence metric defined in Equation 4.12.

Figure 4.8a shows the convergence study over the number of spherical harmonics. With only $N_l = 2$ harmonics, i.e. only including the $l = 0, 1$ components, the nonlocal heat flux is not converged to the higher order solutions and therefore not quite sufficient for describing nonlocal transport accurately. Using only two harmonics $N_l = 2$ is equivalent to closures such as SNB which expand the distribution function as $f_e = f_e^0 + \hat{\boldsymbol{w}} \cdot \boldsymbol{f}_1$. The heat flux and thermal force then quickly converge with more spherical harmonics, although even at $N_l = 3$ there are regions $z/L \approx -2, -0.5, +1$ where the heat flux differs by $\sim 1\%$. A subplot of the thermal force is not included here since all N_l visually produce the same R_e, but its convergence is better than the heat flux as shown by $\sigma_R < \sigma_q$ on the bottom subplot.

Figure 4.8b shows the convergence study over the number of iterations. A single iteration $N_{\text{iterations}} = 1$

uses the local expression for the thermal force $R_e^T = -\beta_\parallel n_e \partial_z T_e$ appearing in the DDF equation, and runs the RKM solver to obtain δf_e and nonlocal transport quantities including q_e and R_e. An additional iteration uses this previous nonlocal result for q_e and R_e as the terms appearing in the DDF equation to solve the RKM again. The convergence study shows that even a single iteration where the RKM solver is only run once is fairly accurate, and then converges very quickly even with only one additional iteration.



(a) Convergence over Δw

(b) Convergence over $w_{\max}$

Figure 4.9: Convergence studies over a) Δw and b) $w_{\max}$. The top subplots show the heat flux obtained from the RKM in the standard unmagnetised temperature gradient case, with solid lines showing nonlocal $N_K = 0.1$ cases and dashed lines showing local $N_K = 0.001$ cases. The lower subplots show the convergence metric defined in Equation 4.12, with a black dashed line indicating a $\sigma = 1\%$ threshold.

Figure 4.9a shows the convergence study for the velocity resolution $\Delta w/v_0$. Good convergence with smaller velocity cell sizes $\Delta w/v_0 \leq 0.1$ is demonstrated. Figure 4.9b shows the convergence study for the maximum velocity $w_{\max}/v_0$. For $w_{\max}/v_0 < 3.5$, convergence is poor since the tail of the heat flux integrand is not included in the domain. For $w_{\max}/v_0 \geq 3.5$, the heat flux then converges rapidly.

4.4 Isobaric versus Isochoric

The cases so far have all involved the same temperature profile with an isochoric (uniform) density $n_e = n_0$. In general, the density affects the collisionality and therefore transport. However, the unmagnetised local analytic results for the conductive heat flux and thermal force,

$$q_e^T = -\hat{\kappa}_\parallel \frac{n_e T_e \tau_{ee}}{m_e} \partial_z T_e, \qquad R_e^T = -\hat{\beta}_\parallel n_e \partial_z T_e, \tag{4.13}$$

have simple density scalings. The factor of n_e appearing in the heat flux is somewhat misleading; since the collision times $\tau_{ee} \propto 1/n_e$, the heat flux q_e^T is independent of n_e. The thermal force scales proportionally to

n_e, so R_e^T/n_e is also independent of n_e. In contrast, nonlocal transport is dependent on the collisionality, and therefore density n_e, in the local vicinity. Nonlocal results for q_e^T and R_e^T are therefore expected to behave differently in isobaric and isochoric cases.

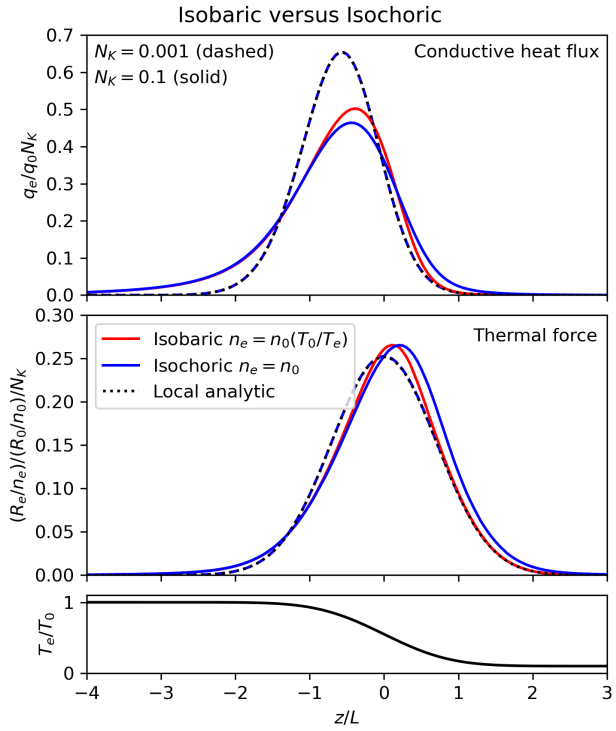


Figure 4.10: Nonlocal electron transport for an isobaric versus an isochoric profile. The thermal force is shown as R_e/n_e rather than R_e such that the local results match between the two cases since $R_e^T/n_e = -\hat{\beta}_\parallel \partial_z T_e$. The local analytic results (black dotted) match up extremely well with the local case (dashed lines), and is therefore hard to see.

Figure 4.10 compares the conductive heat flux and the thermal force for the isochoric case, as shown before, against the isobaric case with the same temperature profile but density profile chosen as $n_e = n_0 T_0/T_e$ such that $p_e = p_0$ is constant. In the local limit, the two cases produce the same result and agree well with the local Braginskii result, since the local results for q_e^T and R_e^T/n_e are independent of n_e.

In the nonlocal cases with $N_K = 0.1$, the isobaric and isochoric transport results differ. They match well for $z/L \lesssim -1$ where the density of the isobaric cases matches the isochoric case. However, the isochoric heat flux forms a preheating region in the cold end $0 \lesssim z/L \lesssim 1$, whereas the isobaric heat flux does not. This is expected since the higher density in the cold end of the isobaric case gives a higher collisionality, therefore fast particles streaming from the hot end do not penetrate as far. The thermal force also forms a significant 'preheat' in the isochoric case but not in the isobaric case for the same reason.

4.5 Operator Comparison

Figure 4.11 shows the $l, m = 1, 0$ components of terms in the DDF equation for the nonlocal $N_K = 0.1$ case, in particular the total electron collision operator $\mathcal{C}_e^{(1,0)}$, Vlasov operator $\mathcal{V}_e^{(1,0)}$ containing the advection term

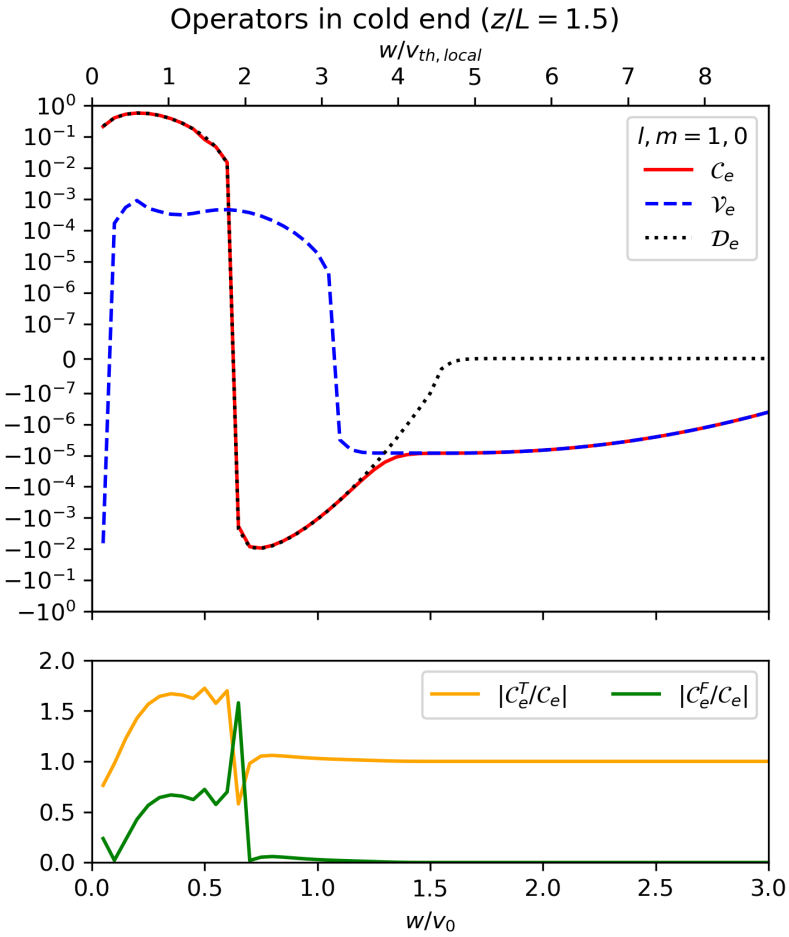


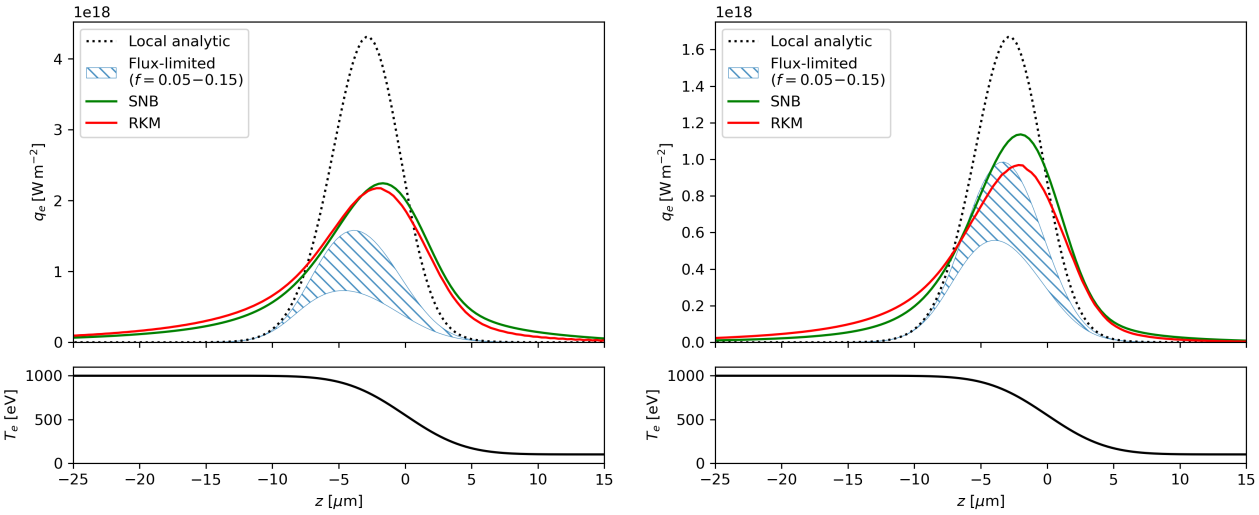
Figure 4.11: Comparison of operators in cold end ($z/L = 1.5$) for $l, m = 1, 0$ for the nonlocal $N_K = 0.1$ case. Note that the vertical scale in the top subplot is symmetrical logarithmic with a linear section through zero. There is a switch of dominant balances in the equation in the tail of the distribution, switching from a balance of the driving term with the collision term at lower velocities to the Vlasov advection term with the collision term at higher velocities.

$\langle 1, 0|\boldsymbol{w} \cdot \boldsymbol{\nabla}\delta f_e\rangle$, and driving term $\mathcal{D}_e^{(1,0)}$. For low, cold velocities, the collision operator balances with the driving term, with the Vlasov term subleading similarly to the local case where the Chapman-Enskog ordering applies. At a particular velocity $w/v_{\text{th,local}} \gtrsim 3.5$, the dominant balance in the DDF equation swaps from the collision term and driving term to the collision term and Vlasov term. This corresponds to the hot suprathermal beam streaming from the hot end and slowing due to collision with the cold background.

The lower subplot shows the test-particle and field-particle components of the collision operator normalised against the total collision operator. At low, cold velocities, both the test-particle and field-particle terms make up order-unity fractions of the total collision operator, therefore are both required to obtain the correct solution at low velocities and the local solution. Further into the tail $w/v_0 \gtrsim 0.75$, even before the swap of dominant balances, the test-particle term quickly dominates the field-particle term. This shows that even though the local solution and total heat flux require the field-particle term for a correct solution, the nonlocal tail behaviour is only subject to field-particle collisions. If there is then a suitable way to adapt the RKM to only solve for the

nonlocal tail behaviour, but keep the correct local solution at lower w, the complicated and computationally expensive field-particle term may be dropped while keeping a first-principles description.

4.6 SNB Comparison



(a) Hydrogen ($Z = 1$)

(b) Nitrogen ($Z = 7$)

Figure 4.12: Comparison of nonlocal electron conductive heat flux from the RKM, SNB method, and flux-limited approaches for a uniform density $n_e = 10^{28}\,\mathrm{m}^{-3}$ with a sharp temperature gradient of length scale $L = 5\,\mu\mathrm{m}$.

The RKM heat flux may be compared to the heat flux as predicted by other nonlocal transport models, namely the SNB approach and flux limiters. Figure 4.12 shows a comparison of the nonlocal electron heat flux from the RKM solver and SNB approach for simple hydrogen ($Z = 1$) and nitrogen ($Z = 7$) plasmas with a uniform density and error-function temperature profile with $L = 5\,\mu\mathrm{m}$. For the chosen values that may be encountered in ICF experiments $n_e = 10^{28}$ m^{-3}, $T_{\mathrm{max}} = 1000$ eV, $T_{\mathrm{min}} = 100$ eV, and $\ln\Lambda_{ee} = \ln\Lambda_{ei} = 10$, the characteristic electron mean free path at the hottest temperature is $\lambda_0 = 1.54\,\mu$m. The SNB implementation used here, provided by Martin Reed from FLF, follows the implicit iSNB algorithm from Cao et al. [112].

In addition to SNB, a flux-limited heat flux is included for comparison. The flux limiter takes the simple harmonic-averaged form

$$q_{\mathrm{f.l.}} = \frac{q_{\mathrm{Brag.}}}{1 + |q_{\mathrm{Brag.}}/(f q_{\mathrm{f.s.}})|}, \tag{4.14}$$

where $q_{\mathrm{f.l.}}$ is the flux-limited heat flux, $q_{\mathrm{Brag.}}$ is the local Braginskii heat flux result, $q_{\mathrm{f.s.}} = n_e T_e v_{\mathrm{th},e}$ is a characteristic free-streaming heat flux, and f is the flux-limiter parameter. Here, a range of values $0.05 \leq f \leq 0.15$ are chosen. The flux-limited heat flux fails to capture enhanced heating in the colder region in comparison to the SNB and RKM approaches.

The heat flow obtained from SNB and RKM are qualitatively similar, with reduced peak heat flow and preheat in both the hot and cold ends of the plasma present. In the hydrogen case, the two results are quantitatively very similar, although SNB appears to overpredict heat flow in the cold end, and underpredict

heat flow in the hot end in comparison to RKM. In contrast, the two heat flows are significantly different in the nitrogen case, with substantially different peak heat flows and preheats.

4.7 Solving for Nonlocal Deviation

The DDF equation may be written as

$$D = (\hat{C}^T + \hat{C}^F - \hat{V} - \hat{B})\delta f, \tag{4.15}$$

where test-particle and field-particle operators are written separately and species subscripts are dropped for brevity. The local leading-order Chapman-Enskog solution for the DDF is obtained by solving Equation 4.15 to leading order in Knudsen number, which then becomes

$$D^{(0)} = (\hat{C}^T + \hat{C}^F - \hat{B})\delta f^{\text{local}}. \tag{4.16}$$

If the DDF is decomposed via $\delta f = \delta f^{\text{local}} + g$, then the equation for the nonlocal correction g is obtained by subtracting Equation 4.16 from Equation 4.15 to yield

$$D' = (\hat{C}^T + \hat{C}^F - \hat{V} - \hat{B})g, \tag{4.17}$$

where the new inhomogeneous driving term $D' \equiv D - D^{(0)} + \hat{V}\delta f^{\text{local}} \approx \hat{V}\delta f^{\text{local}}$. Equation 4.17 appears to be just as complex as the original DDF equation, only with a different inhomogeneous term on the left hand side. However, there is additional computational benefit to this decomposition. The test-particle collision operator is a differential operator in velocity space, whereas the field-particle operator is an integral operator in velocity space. When discretising, the test-particle operator is then sparse in the velocity index, only linking nearest neighbours $j \pm 1$, whereas the field-particle operator is dense in the velocity index, linking all j for given spatial position i and harmonic l, m. The RKM is still tractable with the field-particle operator included, but would be more computationally efficient without it. Discarding the field-particle operator from the DDF equation is unjustified in a first-principles description, and doing so means that the local limit is no longer reproduced. However, when solving for the nonlocal correction g, dropping the field-particle operator may be justified since the field-particle operator is only significant in the bulk of the distribution, whereas nonlocal effects are most significant in the tail. Discarding $\hat{C}^F g$ leaves

$$D' \approx (\hat{C}^T - \hat{V} - \hat{B})g, \tag{4.18}$$

which naturally reproduces the local limit since g will be subleading to δf^{local} for velocities relevant to transport for sufficiently small $N_K \lesssim 1/100$.

Figure 4.13 compares the approaches of solving for δf and g with and without the field-particle operator included. When solving for δf, discarding the field-particle operator yields an incorrect result for the local and nonlocal heat flow. The local result has a conductivity reduced by $\sim 10\%$, and the peak nonlocal heat flow is also reduced, but the preheat predictions of the nonlocal heat flow still matches well with the full result,

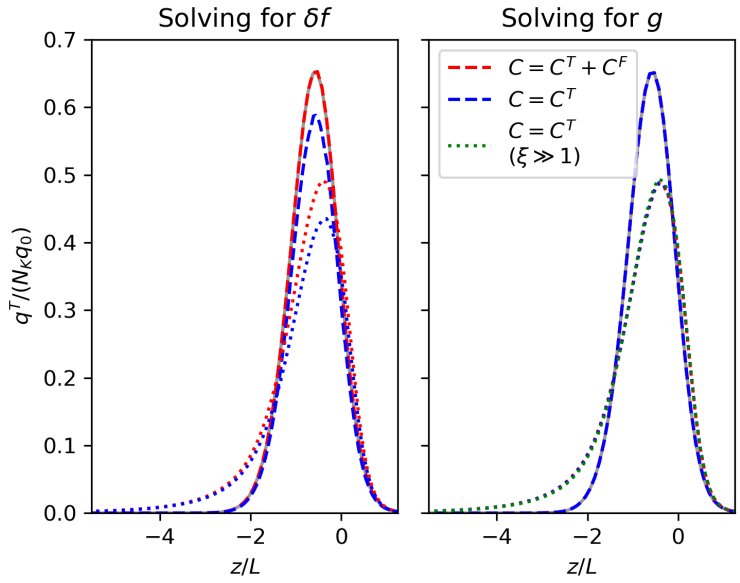


Figure 4.13: Comparison of unmagnetised nonlocal conductive heat flux for RKM solving for $g = f - f^M - \delta f^{\text{local}}$ versus $\delta f = f - f^M$ with and without the field-particle operator included for $N_K = 0.001$ (dashed lines) and $N_K = 0.1$ (dotted lines). The g-approach still reproduces the correct local and nonlocal result even when the field-particle collision operator is discarded and the asymptotic forms of the collision frequencies for $\xi \gg 1$ are used. Reproduced from [3].

suggesting that nonlocal heat flow is governed by test-particle collisions. When solving for g, the local limit is naturally reproduced. The nonlocal heat flow obtained from g is practically unchanged when the field-particle operator is discarded, leaving an even more tractable first-principles approach.

Furthermore, since the nonlocal deviation g is largest in the tail of the distribution where $\xi \equiv w/v_{\text{th},e} \gtrsim 1$, we may use the asymptotic limits for the velocity-dependent collision frequencies appearing in the test-particle operator. This leaves the operator in the simpler form

$$\hat{C}^T g \approx \hat{\nu}_{ee}(\boldsymbol{x}) \left[-\frac{1+Z}{2\xi^3}\hat{\mathcal{L}}_\mu + \frac{1}{\xi^2}\partial_\xi\left(1 + \frac{1}{2\xi}\partial_\xi\right)\right] g. \tag{4.19}$$

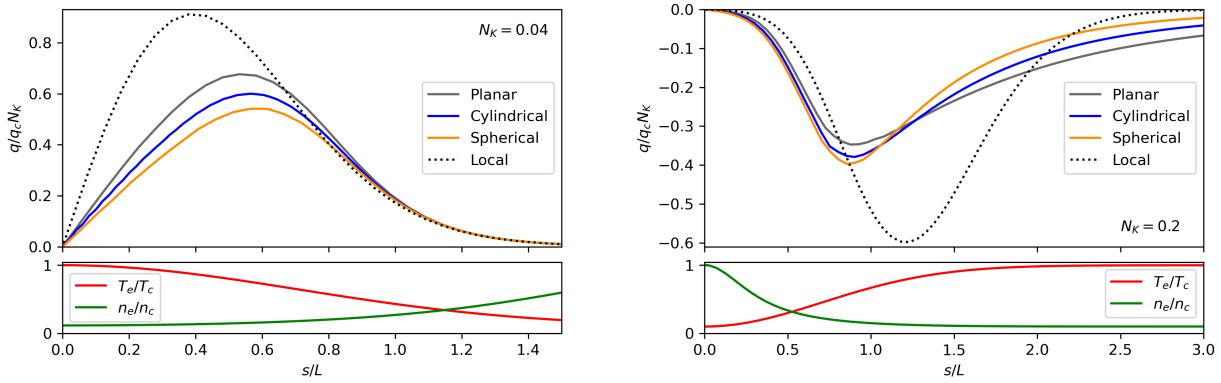
The resulting nonlocal heat flux from this approximation with the leading order $\xi \gg 1$ asymptotic expansions for ν_D, ν_s, and $\nu_\parallel$ is also shown in Figure 4.13, which is still in very good agreement with the original result. Equation 4.18 with these asymptotic forms for the collision frequencies is then an especially simple form of the first-principles RKM which could be tractable in multiple spatial dimensions. It has been verified that dropping any of the test-particle terms originating from ν_D, ν_s, or $\nu_\parallel$ strongly disturbs the nonlocal solution, even if only done for $l = 0$ or $l \geq 1$ terms. The test-particle operator may therefore not be simplified further by dropping such terms.

4.8 Cylindrical and Spherical Geometries

To compare the effect of these three different geometries on nonlocal heat flux, a simple isobaric hydrogen plasma is considered with a temperature profile

$$T(s) = T_\infty + (T_0 - T_\infty)\exp(-(s/L)^2), \tag{4.20}$$

where s is the single spatial coordinate for the corresponding geometry ($s = z$ for planar, $s = r$ for spherical, and $s = \rho$ for cylindrical). For spherical and cylindrical coordinates, $s \geq 0$ with an appropriate boundary condition at $s = 0^-$. For the planar geometry, the spatial coordinate $-\infty < s < \infty$, which gives an appropriate comparison to the other two geometries given the symmetry around $s = 0$. A hotspot-like profile with $T_0/T_\infty = 10$ and coldspot-like profile with $T_0/T_\infty = 1/10$ are considered.



(a) Hotspot in different geometries

(b) Coldspot in different geometries

Figure 4.14: Comparison of nonlocal electron conductive heat flux for an isobaric (a) hotspot and (b) coldspot in planar, cylindrical, and spherical geometries. Differences in the nonlocal heat flow are clearly present due to the geometry itself.

Figure 4.14 shows the nonlocal electron conductive heat flux in a planar, cylindrical, and spherical spatial geometry for the (a) hotspot and (b) coldspot cases. Let us introduce the 'divergence factor' D that appears in the volume element $dV \propto s^D ds$, so $D = 0, 1, 2$ for planar, cylindrical, and spherical geometries, respectively. For larger D, the volume element increases for larger $|s|$. For the hotspot case 4.14a, the nonlocal heat flux is further suppressed for increasing D. Suprathermal particles stream radially outwards from the hotspot near the origin to larger s, providing the nonlocal contribution to the heat flux. For larger divergence factor, these hot particles diverge in space more as they stream to larger s, leading to a smaller heat flux. In contrast for the coldspot case 4.14b, the suprathermal particles are streaming from larger s towards the origin and converge in the cold end, leading to a larger heat flux and enhanced preheat.

This chapter has provided an initial demonstration of the RKM in the simplest case. The next chapter considers the additional complications of magnetic fields and current-driven transport.

CHAPTER 5

Nonlocal Electron Transport Results

This chapter presents results for nonlocal electron transport with magnetic fields and current-driven heat flow. A particularly novel finding is included, in particular that nonlocality of current-driven transport is governed not only by the Knudsen number N_K, but also a second dimensionless parameter N_u associated with the strength of the flow.

5.1 Thermally-Driven Terms

To investigate nonlocality of the conductive electron heat flux $\boldsymbol{q}_e^T$ and thermal force $\boldsymbol{R}_e^T$, a temperature gradient of the form

$$T_e(z) = \frac{T_{\text{left}} + T_{\text{right}}}{2} - \frac{T_{\text{left}} - T_{\text{right}}}{2}\text{erf}\left(\frac{z}{L}\right) , \tag{5.1}$$

is considered again with $T_{\text{left}}/T_{\text{right}} = 10$ for a variety of Knudsen numbers $N_K = \lambda_0/L$, where $\lambda_0 = \lambda_{\text{th},e}(z \to -\infty)$ is the thermal MFP at the hot end. An unmagnetised case is considered, then a magnetised case with a uniform magnetic field $\boldsymbol{B} = B_0\hat{\boldsymbol{x}}$, parametrised by the electron Hall parameter at the hot end $\chi_0 = \chi_e(z \to -\infty)$.

Figure 5.1 shows the conductive heat flux for a small and large Knudsen number ($N_K = 0.001,\, 0.1$ respectively) in an unmagnetised and moderately magnetised case ($\chi_0 = 0,\, 0.5$ respectively). The local analytic result for each component of the conductive heat flux $\boldsymbol{q}^T_{e,(\parallel,\perp,\times)}$ are naturally recovered for small Knudsen number $N_K = 0.001$, i.e. the RKM solver has no prior information about the local analytic results, but reproduces them nonetheless for sufficiently small Knudsen number. This is in contrast with many other nonlocal closures which reproduce local transport results by construction of the method.

For high Knudsen number $N_K = 0.1$, the peak heat flux of each component is reduced for increasing Knudsen number, and a preheat develops in the cold end $0 \lesssim z/L \lesssim 1.5$ as expected from physical arguments and VFP simulations. For even moderately large Hall parameter $\chi_0 \gtrsim 10$, the magnetic field counteracts nonlocal effects, restoring transport fluxes back to their local analytic results. This is expected physically, since

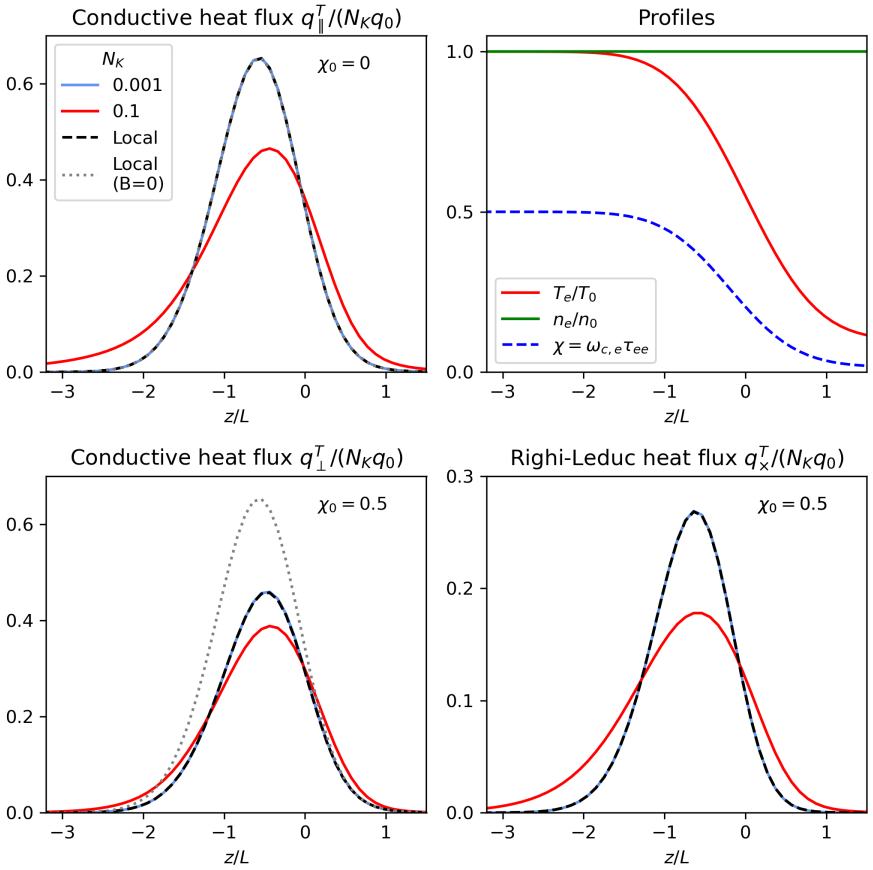


Figure 5.1: Temperature-gradient-driven heat fluxes for an unmagnetised case and moderately magnetised ($\chi_0 = 0.5$) case in a simple hydrogen plasma, appropriately normalised against Knudsen number and a characteristic heat flux $q_0 = n_0 T_0 v_0$, where n_0, T_0, and v_0 are the electron number density, temperature, and thermal velocity at the hot end $z \to -\infty$, respectively. Local unmagnetised (parallel) results are shown in dotted black lines. The parallel results correspond to the unmagnetised $\chi_0 = 0$ case. The normalised profiles of temperature, number density, and Hall parameter are shown. The local unmagnetised results in the z direction are shown in black. Reproduced from [3].

at Hall parameter $\chi_0 \gtrsim 1$ the gyroradius of electrons in the thermal population becomes comparable to or smaller than their mean free paths, restricting their nonlocal streaming.

The Righi-Leduc heat flux $\boldsymbol{q}_{e,\times}^T$ becomes comparable to the other components of the conductive heat flux at intermediate Hall parameter $\chi_0 \sim 1$. At $\chi_0 \lesssim 1$ and high Knudsen number, the Righi-Leduc heat flux is strongly affected by nonlocal effects as has been noted from previous VFP simulations [113]. The Righi-Leduc heat flow reduces thermalisation of cold spikes in ICF implosions, therefore has a detrimental impact to the hotspot temperature and fusion yield [68]. Nonlocal suppression of Righi-Leduc heat flow may then be beneficial for yield.

Figure 5.2 shows the thermal force components $\boldsymbol{R}_{e,(\parallel,\perp,\times)}^T$ for the same cases as Figure 5.1. The thermal force is less impacted by nonlocal effects than the heat flux since it is a lower velocity moment, therefore less sensitive to streaming suprathermal particles. Similarly to the Righi-Leduc heat flow, the Nernst force is significantly more nonlocal compared to its perpendicular counterpart. In ICF implosions, the Nernst effect,

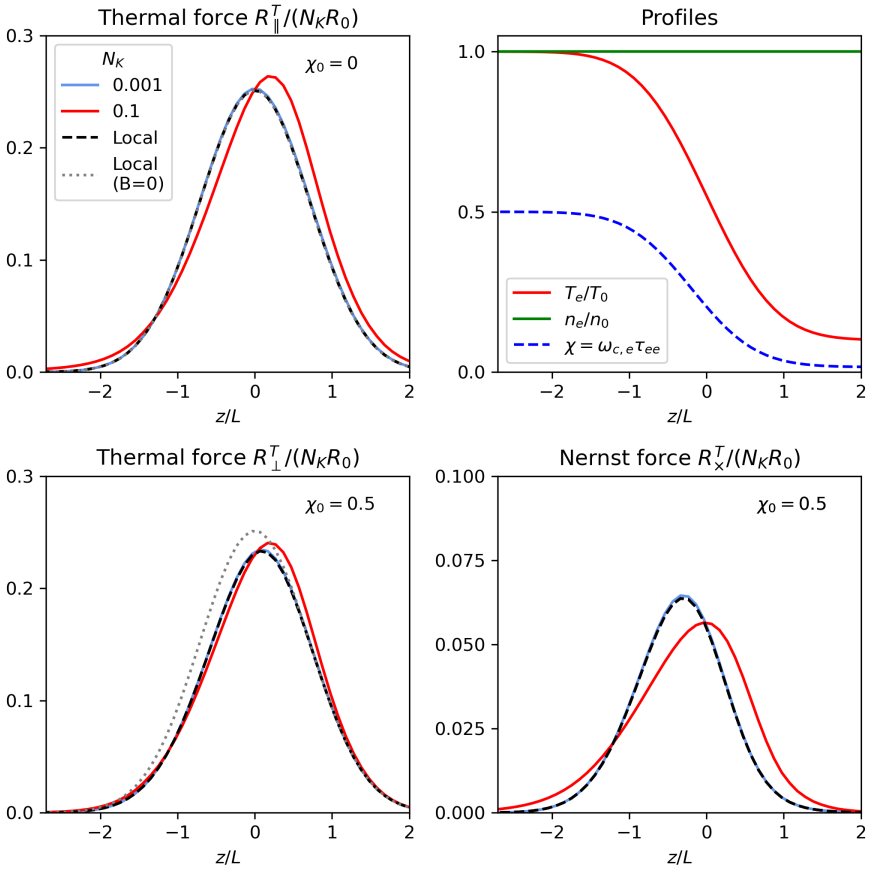


Figure 5.2: Temperature-gradient-driven momentum exchange (thermal force) for an unmagnetised case and moderately magnetised ($\chi_0 = 0.5$) case in a simple hydrogen plasma, appropriately normalised against Knudsen number and a characteristic momentum exchange $R_0 = n_0 m_e v_0 \hat{\nu}_0$, where n_0, T_0, v_0, $\hat{\nu}_0$ are the electron number density, temperature, thermal velocity, and basic collision frequency at the hot end $z \to -\infty$, respectively. Local unmagnetised (parallel) results are shown in dotted black lines. The parallel results correspond to the unmagnetised $\chi_0 = 0$ case. The normalised profiles of temperature, number density, and Hall parameter are shown. The local unmagnetised results in the z direction are shown in black. Reproduced from [3].

originating from $\boldsymbol{R}_e^T$, advects the magnetic field out of the hotspot, therefore demagnetizing thermal transport and having a deleterious impact on maximum temperature and yield.

Under the standard MHD approximations of neglecting electron inertia and displacement current, the thermal force and friction force enter the generalised Ohm's law as $\boldsymbol{E} = -\frac{1}{en_e}\boldsymbol{R}_e + \ldots$, which in turn combines with Faraday's law to form the induction equation $\partial_t \boldsymbol{B} = \boldsymbol{\nabla} \times (\frac{1}{en_e}\boldsymbol{R}_e + \ldots)$. Setting $\boldsymbol{B} = 0$ (and therefore $\boldsymbol{j} = 0$) to focus on the terms responsible for spontaneously generating magnetic fields, the induction equation becomes $(\partial_t \boldsymbol{B})|_{\boldsymbol{B}=0} = \boldsymbol{\nabla} \times (\frac{1}{en_e}\boldsymbol{R}_{e,\parallel}^T) + \frac{1}{e}\boldsymbol{\nabla} T_e \times \boldsymbol{\nabla} \ln n_e$. The latter term is the Biermann battery, typically viewed as the only MHD term that may spontaneously generate magnetic fields in collisional plasmas. Using the local result for the unmagnetised thermal force, the thermal force term vanishes since $\boldsymbol{\nabla} \times (\frac{1}{e}\hat{\beta}_\parallel \boldsymbol{\nabla} T_e) \equiv 0$ by vector identity for uniform Z. However, the unmagnetised thermal force deviates from this curl-free form due to nonlocal effects, thus this term will not vanish and may spontaneously generate magnetic fields. Nonlocal mechanisms for spontaneous field production have been studied by full VFP simulations and other

approaches [114, 115]. This mechanism arises due to electron-ion collisions, indicating that it is related to the generalised Nernst velocity [116] rather than a nonlocal extension of the Biermann term. One can construct a reasonable scenario with aligned temperature and density gradients such that the Biermann term is zero yet the temperature gradient is sharp enough to give a nonlocal thermal force and therefore spontaneous field production without the Biermann battery. This cannot be fully studied in 1D since there must be variation in a second spatial direction, therefore is not investigated further here.

5.2 Current-Driven Terms

To investigate nonlocality of current-driven transport, we consider an isothermal isochoric simple plasma with a flow in the y direction of the form

$$\Delta \boldsymbol{u} = u_0 \exp(-(z/L)^2)\hat{\boldsymbol{y}}, \tag{5.2}$$

with a uniform magnetic field in the $-x$ direction $\boldsymbol{B} = -B_0\hat{\boldsymbol{x}}$ and no ion flow $\boldsymbol{u}_i = 0$. The dimensionless number $N_u^0 = |u_0|/v_{\text{th},e}$ describes the maximum speed of the flow relative to the electron thermal speed, which here is taken as $N_u^0 = 10^{-4} \ll 1$. The Knudsen number $N_K = \lambda_{\text{th},e}/L$ here defines the width of the flow profile rather than the temperature profile.

The local and nonlocal current-driven heat fluxes (Peltier and Ettingshausen) and forces (friction and cross friction) are shown in Figures 5.3 and 5.4, respectively. The Peltier heat flux $\boldsymbol{q}^u_{e,(\parallel,\perp)}$ and Ettingshausen heat flux $\boldsymbol{q}^u_{e,\times}$ are nonlocal for Hall parameters $\chi_0 \lesssim 1$. Similarly to the nonlocal conductive heat flux, the peak heat flux is inhibited, and the heat flux is enhanced away from the peak current. The friction and cross friction are less sensitive to nonlocal effects than the heat fluxes since they are lower velocity moments, but still experience qualitatively similar deviations. Also similarly to the thermally-driven fluxes, the cross components for moderate magnetisations are much more influenced by nonlocal behaviour than their perpendicular counterparts.

5.3 Impact of Fast Flows on Current-Driven Transport

Although considered in a few works, nonlocal modifications to $\boldsymbol{q}^u_e$ have been attributed to the same spatial scales based on the Knudsen number [117, 118]. Since these works relied on simplified rather than first-principles approaches with this assumption essentially built-in, a novel driver of the nonlocal behaviour, the electron flow itself, has been missed.

In this section, we demonstrate that the dimensionless number $N_u \equiv |\Delta \boldsymbol{u}|/v_{\text{th},e}$ plays a role to $\boldsymbol{q}^u_e$ analogous to that N_K plays for $\boldsymbol{q}^T_e$. Although one might expect that the standard local calculation is valid with $N_u \ll 1$, a much more restrictive condition is found to be required. Both an intuitive explanation of the underlying transport physics and first-principles kinetic calculations are presented. A similar but smaller effect is also found on the electron-ion friction $\boldsymbol{R}^u_e$. Deviations from standard results due to this effect are increasingly

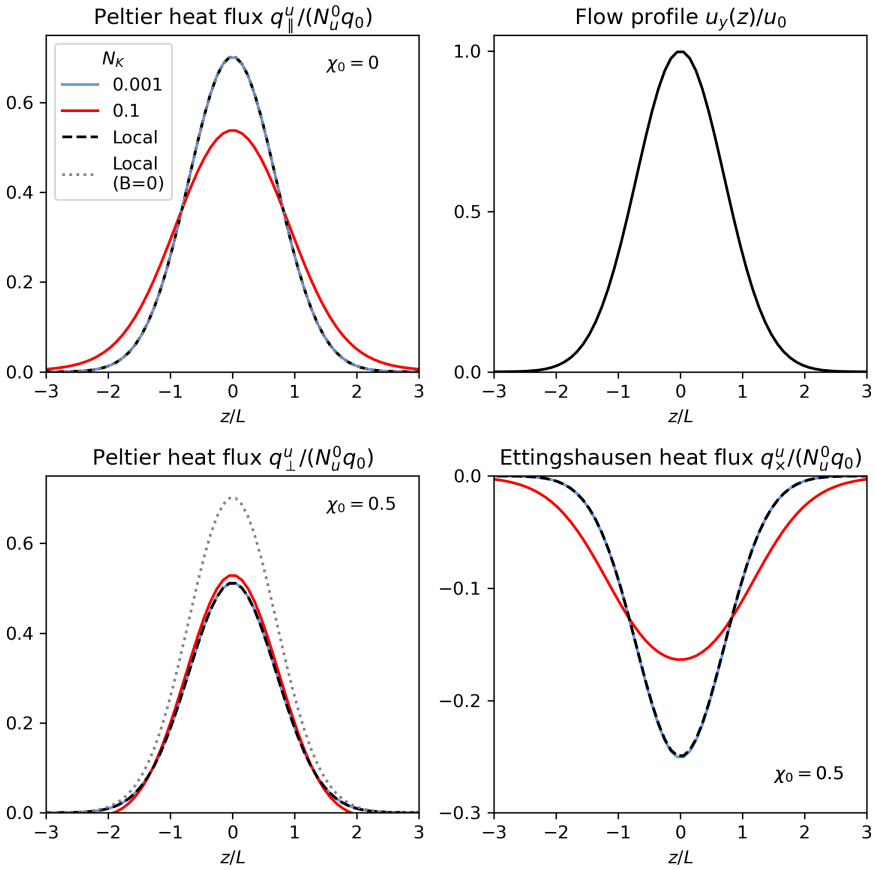


Figure 5.3: Current-driven heat fluxes in a local and nonlocal case for an unmagnetised and moderately magnetised isothermal isochoric simple hydrogen plasma for $N_u^0 = 10^{-4} \ll 1$. The heat fluxes are appropriately normalised against N_u^0 and a characteristic heat flux $q_0 = n_0 T_0 v_0$, where n_0, T_0, and v_0 are the electron number density, temperature, and thermal velocity of the uniform plasma. Reproduced from [3].

prevalent at higher effective ionisations $Z^* \equiv \langle Z^2 \rangle / \langle Z \rangle$ since the relative importance of electron-ion collisions over electron-electron collisions is increased.

Local heat conduction in a collisional magnetised plasma is widely understood, originating from the random motion of electrons that diffuses heat due to a temperature gradient. Analysis of small-angle binary Coulomb collisions shows that the collision frequency of a test electron against an ion background is inversely proportional to the cube of its speed in the frame comoving with the ion population, i.e., $\nu_{ei} \propto 1/|\boldsymbol{v} - \boldsymbol{u}_i|^3$. This fact has the consequence that relative flows, or currents, also drive heat flux as electrons moving in the same direction as the relative drift ($\boldsymbol{w} \cdot \Delta\boldsymbol{u} > 0$, where $\boldsymbol{w} = \boldsymbol{v} - \boldsymbol{u}_e$ is the electron peculiar velocity) are less collisional on average against ions than electrons moving against the relative drift ($\boldsymbol{w} \cdot \Delta\boldsymbol{u} < 0$). The heat carried by these two sides of the electron population then does not cancel and there is a net heat flux in the direction of the relative flow $\boldsymbol{q}_e^u \propto \Delta\boldsymbol{u}$. Currents necessitate the inclusion of magnetic fields which cause electrons to undergo gyro-orbits around the magnetic field lines, suppressing heat transport in the direction perpendicular to the field. However, the gyro-orbits also generate particle motion in the direction perpendicular to both the magnetic field and temperature gradient or relative flow, therefore an additional

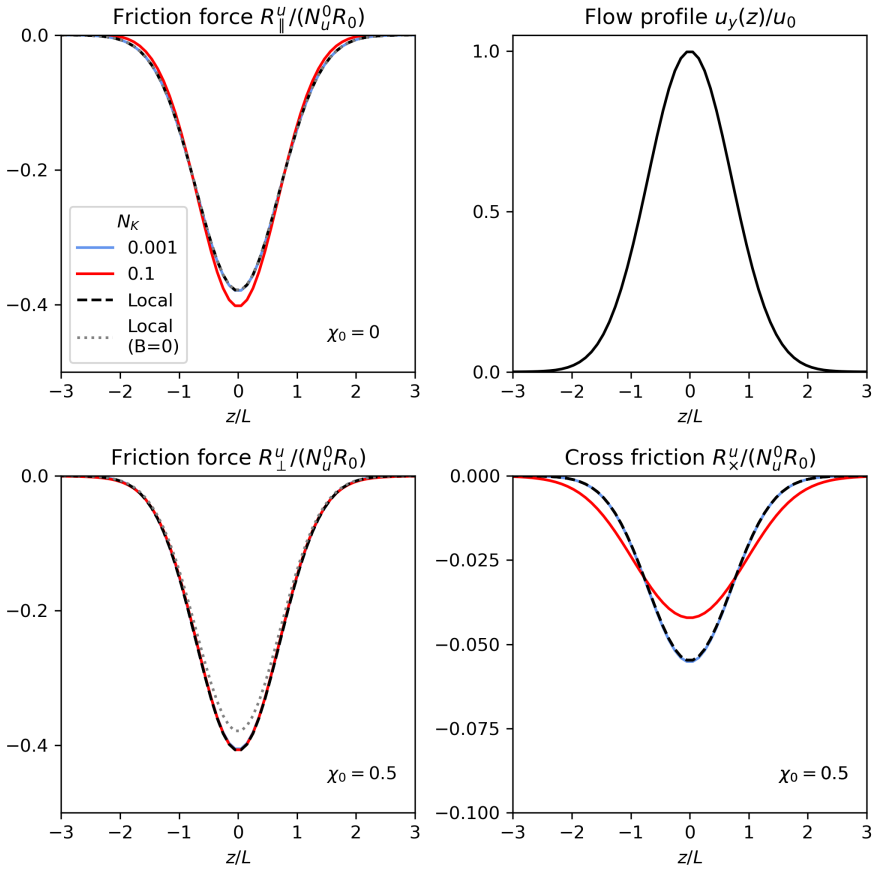


Figure 5.4: Current-driven forces, i.e., friction, in a local and nonlocal case for an unmagnetised and moderately magnetised isothermal isochoric simple hydrogen plasma for $N_u^0 = 10^{-4} \ll 1$. The forces are appropriately normalised against N_u^0 and a characteristic momentum exchange $R_0 = n_0 m_e v_0 \hat{\nu}_0$, where n_0, T_0, v_0, $\hat{\nu}_0$ are the electron number density, temperature, thermal velocity, and basic collision frequency of the uniform plasma. Reproduced from [3].

'cross' component to each of the above transport fluxes is gained in this direction.

The above picture allows a qualitative explanation as to why local current-driven heat flux results [15, 86, 87, 119] break down even for relatively weak electron flows. A nonvanishing net electron flow implies a nonzero electric field set by the bulk electron distribution. This flow being much slower than $v_{\mathrm{th},e}$ is equivalent to the electric field being much less than the Dreicer field [78]. While this ensures the bulk distribution is not in a disruptive runaway scenario, the dynamic friction experienced by suprathermal electrons is lower due to the aforementioned collision frequency scaling. Dynamic friction can then be insufficient to prevent the electric field from driving suprathermal electrons farther away from thermodynamic equilibrium than can be captured by a local transport theory. Since this mechanism accelerates electrons in the direction of the relative flow $\Delta \boldsymbol{u}$, nonlocal behaviour is expected to vary for the different magnetised components of current-driven heat flow in the parallel, perpendicular, and cross directions. We now proceed to the quantitative first-principles description of these nonlocal effects.

To investigate the impact of fast flows on current-driven transport, the same setup as Section 5.2, but with

different values of N_u^0. We may write the electron DDF equation 3.18 explicitly as

$$\begin{aligned} &f_e^M\left[\left(\boldsymbol{R}_e/p_e+\left(\frac{w^2}{v_{\text{th},e}^2}-\frac{5}{2}\right)\boldsymbol{\nabla}\ln T_e\right)\cdot\boldsymbol{w}+\frac{2}{v_{\text{th},e}^2}\boldsymbol{\nabla}\boldsymbol{u}_e\colon\left(\boldsymbol{w}\boldsymbol{w}-\frac{1}{3}w^2\mathbb{I}\right)\right]-C_{ei}\{f_e^M\}\\ &=\hat{C}_{ee}\delta f_e+\hat{C}_{ei}\delta f_e+\frac{e}{m_e}(\boldsymbol{w}\times\boldsymbol{B})\cdot\boldsymbol{\nabla}_{\boldsymbol{w}}\delta f_e-\left[\boldsymbol{w}\cdot\boldsymbol{\nabla}-\left(\boldsymbol{w}\cdot\boldsymbol{\nabla}\boldsymbol{u}_e+\frac{\boldsymbol{R}_e-\boldsymbol{\nabla}p_e}{\rho_e}\right)\cdot\boldsymbol{\nabla}_{\boldsymbol{w}}\right]\delta f_e. \end{aligned} \tag{5.3}$$

Nonlocal deviations conventionally arise from the $\boldsymbol{w}\cdot\boldsymbol{\nabla}\delta f_e$ term in Equation 5.3, which affects transport when

$$\frac{|\boldsymbol{w}\cdot\boldsymbol{\nabla}\delta f_e|}{|\hat{C}_e\delta f_e|}\sim\left(\frac{w}{v_{\text{th},e}}\right)^4 N_K \tag{5.4}$$

is comparable to or greater than unity for particles $w/v_{\text{th},e}\lesssim 4$ that contribute to transport quantities, so where $N_K\gtrsim 1/100$. However, the force term $\boldsymbol{R}_e\cdot\boldsymbol{\nabla}_{\boldsymbol{w}}\delta f_e$ may also cause deviations in δf_e and therefore transport from standard results. Ignoring spatial gradients, this term should affect transport where

$$\frac{|\frac{1}{\rho_e}\boldsymbol{R}_e^u\cdot\boldsymbol{\nabla}_{\boldsymbol{w}}\delta f_e|}{|\hat{C}_e\delta f_e|}\sim\left(\frac{w}{v_{\text{th},e}}\right)^3 N_u \tag{5.5}$$

is comparable to or greater than unity for relevant particle velocities, so where $N_u\gtrsim 1/100$. If all spatial gradient terms are neglected but the force term is included, solutions to δf_e cannot satisfy $\delta f_e(w\to\infty)=0$ since there always exists a sufficiently large velocity in the tail where electrons become prone to runaway, leading to a divergent solution. However, these runaway electrons in the w_y direction can be depleted by spatial advection in the z direction acting as a sink at large w. For sufficiently large length scales in the z direction, this spatial advection can operate at sufficiently high w beyond the velocity space that contributes to the integrand of the heat flux $w\lesssim 4v_{\text{th},e}$ such that the heat flux is not affected by spatial advection, so remains local. Sufficiently large flows can then cause deviations from traditional local transport calculations due to the force term which rely on spatial advection to be convergent, but yield transport fluxes which are dependent on z only through the local flow $\Delta\boldsymbol{u}$, i.e., $\boldsymbol{q}_e^u=\boldsymbol{q}_e^u(\Delta\boldsymbol{u}(\boldsymbol{x}))$ and similarly for $\boldsymbol{R}_e^u$, therefore are 'quasilocal'. Analogously to the Knudsen number N_K characterising the impact of nonlocal effects due to spatial advection from the $\boldsymbol{w}\cdot\boldsymbol{\nabla}$ operator, the number N_u characterises the impact of quasilocal effects due to velocity-space advection from the $\boldsymbol{R}_e^u\cdot\boldsymbol{\nabla}_{\boldsymbol{w}}$ operator. For higher Z^*, the friction force against ions increases relative to the energy-scattering components of the collision operator, which come only from electron-electron collisions since $m_i\gg m_e$. The quasilocal effect should then be more prevalent in higher Z^* plasmas.

Figure 5.5 demonstrates the impact of fast flows on the Ettingshausen heat flux for $Z^*=20$. Typical qualitative nonlocal behaviour is exhibited for low N_u^0. For larger N_u^0, the heat flux is noticeably modified due to the quasilocal effect arising from the $\boldsymbol{R}_e^u\cdot\boldsymbol{\nabla}_{\boldsymbol{w}}\delta f_e$ term in the kinetic equation. For small Knudsen number $N_K=10^{-4}$, the heat flux is enhanced at large N_u, but remains spatially local. For larger Knudsen number, conventional nonlocal effects make the heat flux profile nonlocal in space, reducing and shifting the peak heat flux to $z<0$, and developing significant preheats in regions of small N_u. This shift is in the direction of the flux, or can be interpreted as the direction of the $\boldsymbol{E}\times\boldsymbol{B}$ drift due to the effective electric field. The friction and cross-friction are not shown here since they have very small $\lesssim 5\%$ deviations from local results.

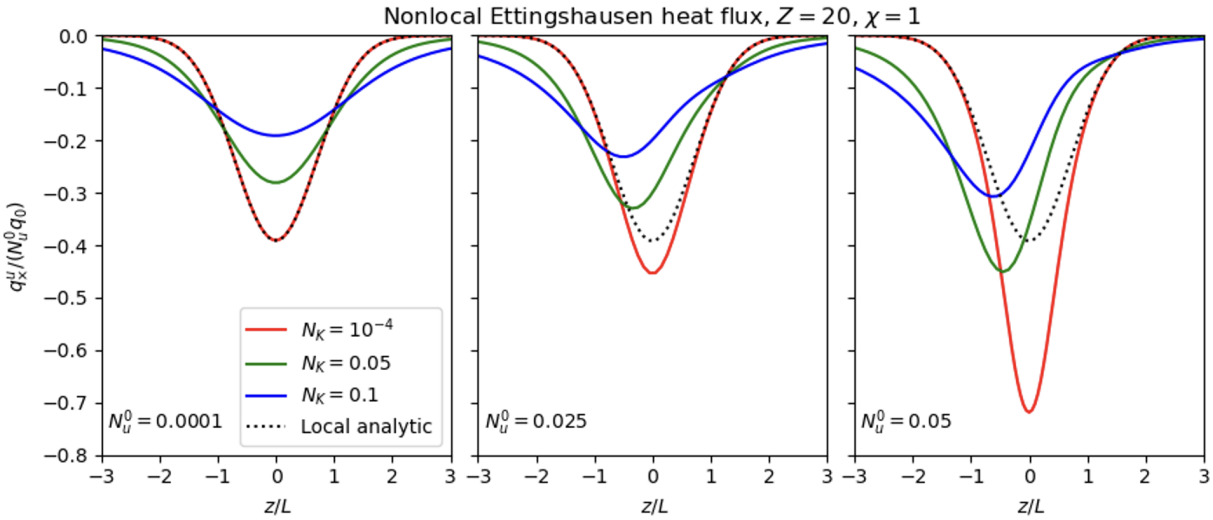


Figure 5.5: Ettingshausen heat flux in a magnetised isothermal isochoric simple plasma with effective ionisation $Z^* = 20$ with the same shape of flow profile as in Figure 5.3. A uniform magnetic field in the $-x$ direction is chosen $\boldsymbol{B} = -B_0\hat{\boldsymbol{x}}$ with a field strength that results in a Hall parameter $\chi = 1$. Different subplots correspond to different peak flows $N_u^0 = 0.0001,\ 0.025,\ 0.05$ which have a noticeable impact on the Ettingshausen heat flux. Reproduced from [2].

Figure 5.6 emphasises the quasilocal effect by plotting the ratio against the local result as a function of $N_u = |\Delta \boldsymbol{u}/v_{\text{th},e}|$. The red line for small Knudsen number $N_K = 10^{-4}$ is one-to-one and returns to a ratio of unity as $N_u \to 0$. This indicates that the Ettingshausen heat flux is still local, i.e., $q^u_{e,\times} = q^u_{e,\times}(u(z))$, but deviates away from the standard analytic result at large $N_u \sim 0.01 - 0.05$ due to the quasilocal effect. The blue and green lines for larger Knudsen numbers form loops, indicating that the heat flux is nonlocal, i.e., $q^u_{e,\times}$ may not be expressed as a function of the local u. The plus and cross markers indicate two spatial positions with the same flow. For the nonlocal case, these positions have very different heat fluxes. For the $N_K = 10^{-4}$ case, the two markers overlap on the red curve, indicating that these two spatial positions still have the same heat flux. The red curve is then not specific to this exact profile, but universal for profiles with sufficiently small Knudsen number for the given ionisation and Hall parameter. Different flow profiles with $N_u^0 = 0.05$ have been verified to reproduce the same red curve for sufficiently small Knudsen number.

Figure 5.7 demonstrates the impact of the quasilocal effect on the integrands of the heat flux in the y and z directions. For high N_u, the integrand at low velocities $w/v_{\text{th},e} \lesssim 2$ experiences only small deviations due to the $\boldsymbol{R}^u_e \cdot \boldsymbol{\nabla}_{\boldsymbol{w}} \delta f_e$ term since the bulk is highly collisional. In the less-collisional region $2 \lesssim w/v_{\text{th},e} \lesssim 5$, the heat flux integrand for high N_u is greatly enhanced from the local result due to electrons starting to become runaway. Electrons that do become runaway are then accelerated to larger velocities $w/v_{\text{th},e} \gtrsim 5$ where they may be depleted to other regions in physical space by spatial advection, even for very small Knudsen number. This spatial advection occurs in regions of velocity space that do not contribute significantly to the heat flux integrand, thus leaving the heat flux local. Even larger N_u, larger Z^*, or smaller χ may then result in divergent integrands, which is indicative of being so far from LTE that fluid models with quasistatic transport closures are not applicable and a full kinetic description is required, such as full VFP [44, 102] or particle-in-cell

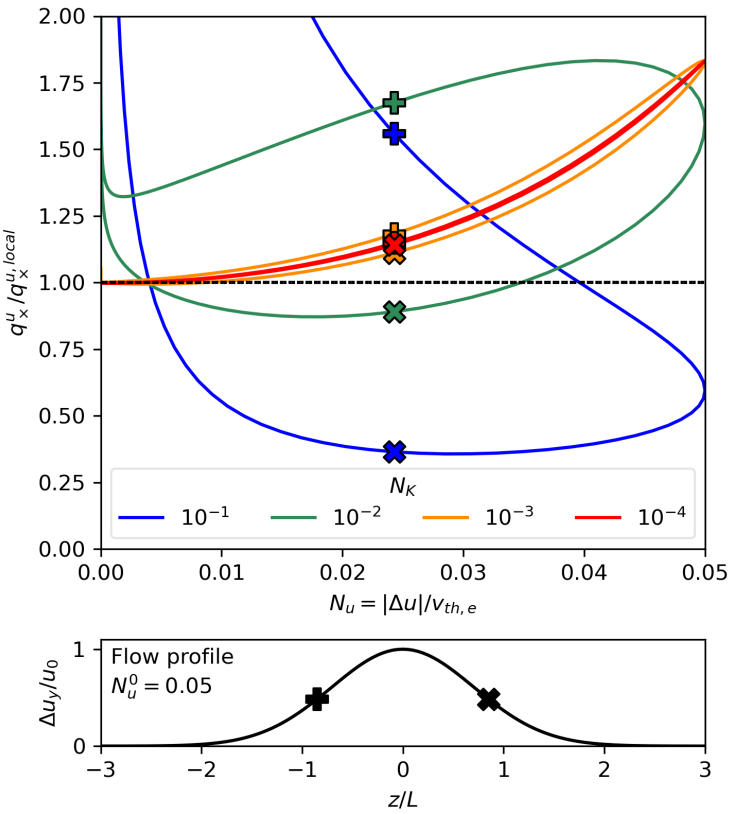


Figure 5.6: Ratio of Ettingshausen heat flux to the local analytic result for peak flow $N_u^0 = 0.05$, Hall parameter $\chi = 1$, and ionisation $Z^* = 20$, plotted as a function of N_u rather than z/L to emphasise the quasilocal effect. A wide variety of Knudsen numbers are chosen to illustrate the transition between the nonlocal and quasilocal regimes. Nonlocal heat fluxes appear as loops on these plots since they are not functions of the local flow. For small Knudsen number, the heat flux tends towards a one-to-one line, showing that the heat flux is local in the sense that $\boldsymbol{q}_e^u(z)$ only depends on the local $\Delta\boldsymbol{u}(z)$. Plus and cross markers are added to indicate how different spatial positions with the same flow N_u yield the same heat flow for small Knudsen number, but different heat flow for larger Knudsen number. Larger Hall parameter χ suppresses both nonlocal and quasilocal deviations, driving these curves closer to the black dashed line. Reproduced from [2].

simulations [13, 120, 121]. Nonlocal transport modelling is further complicated for non-ideal plasmas, where non-binary collisions and quantum degeneracy of electrons can no longer be ignored, and computationally intense methods such as molecular dynamics simulations need to be employed [122].

5.4 Strongly Magnetised Nonlocal Transport

For large Hall parameters $\chi_e \gtrsim 10$, the plasma is sufficiently strongly magnetised that transport is local even for Knudsen numbers $N_K \sim 0.1$. Here, the Larmor radius $\rho_L = v_{\mathrm{th},e}/\omega_{\mathrm{c},e}$ becomes shorter than the gradient lengthscale L, and therefore becomes the limiting factor for nonlocal behaviour. However, such a strongly magnetised regime then increases the maximum Knudsen number for which the fluid model is justified. Figure 5.8 shows the thermally driven and current-driven cases above in a strongly magnetised plasma. Only the cross terms are shown, since these are the dominant transport terms for high magnetisation, assuming the

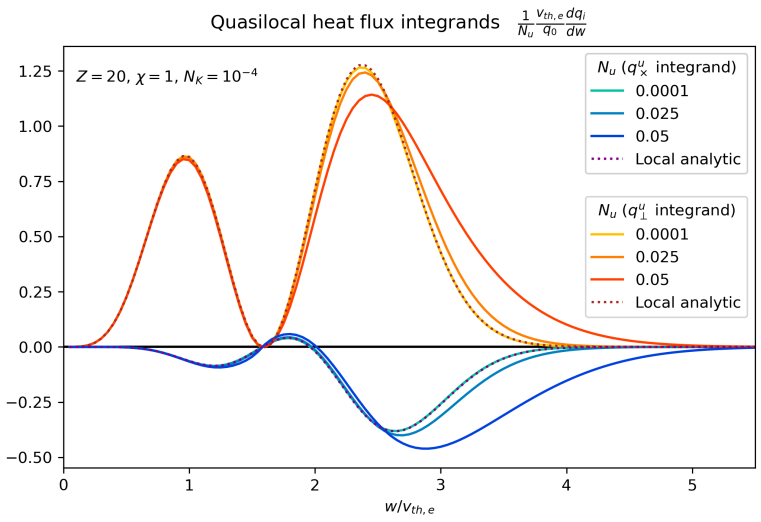


Figure 5.7: Peltier and Ettingshausen heat flux integrands for various flows N_u with ionisation $Z^* = 20$, Hall parameter $\chi = 1$, and very small Knudsen number $N_K \lll 1$. For small $N_u = 10^{-4}$, the heat flux integrands match up extremely well with the local analytic result. For larger $N_u \sim 0.025 - 0.05$, higher energy electrons $w/v_{\mathrm{th},e} \gtrsim 2.5$ are accelerated, shifting the integrand to larger velocity and enhancing the heat fluxes corresponding to the integrated area beneath the curves. The Ettingshausen integrands are more weighted to higher w than the Peltier integrands, i.e., the Ettingshausen heat flow is carried preferentially by faster particles than the Peltier heat flow, explaining why the Ettingshausen heat flow is more impacted by large N_u. Reproduced from [2].

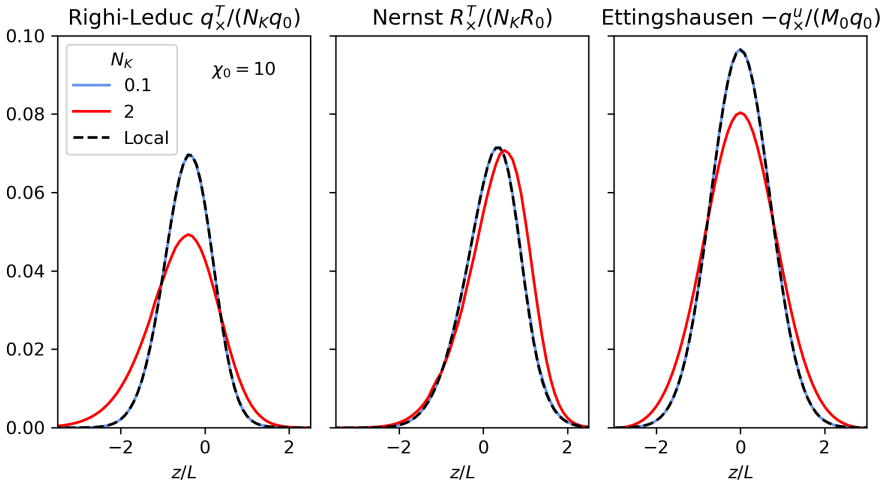


Figure 5.8: Righi-Leduc heat flow, Nernst force, and Ettingshausen heat flow in a strongly magnetised simple hydrogen plasma. The heat flows are appropriately normalised against Knudsen number N_K or flow parameter N_u^0 and a characteristic heat flux $q_0 = n_0 T_0 v_0$, where n_0, T_0, and v_0 are the electron number density, temperature, and thermal velocity at the hot end $z \to -\infty$, respectively. The Nernst force is appropriately normalised against Knudsen number and a characteristic momentum exchange $R_0 = n_0 m_e v_0 \hat{\nu}_0$, where $\hat{\nu}_0$ is the basic collision frequency at the hot end $z \to -\infty$. Reproduced from [3].

thermodynamic drive ($\boldsymbol{\nabla} T_e$ or $\Delta \boldsymbol{u}$) is perpendicular to the magnetic field. For the already large Knudsen number $N_K = 0.1$, the strong magnetic field completely suppresses nonlocal behaviour, forcing the fluxes back to their local results. The strong magnetic field then allows for a higher Knudsen number where a fluid

description is valid, so here a Knudsen number $N_K = 2$ is shown, where the gradient is sufficiently sharp that nonlocal effects emerge again.

5.5 Nonlocal Distribution Function

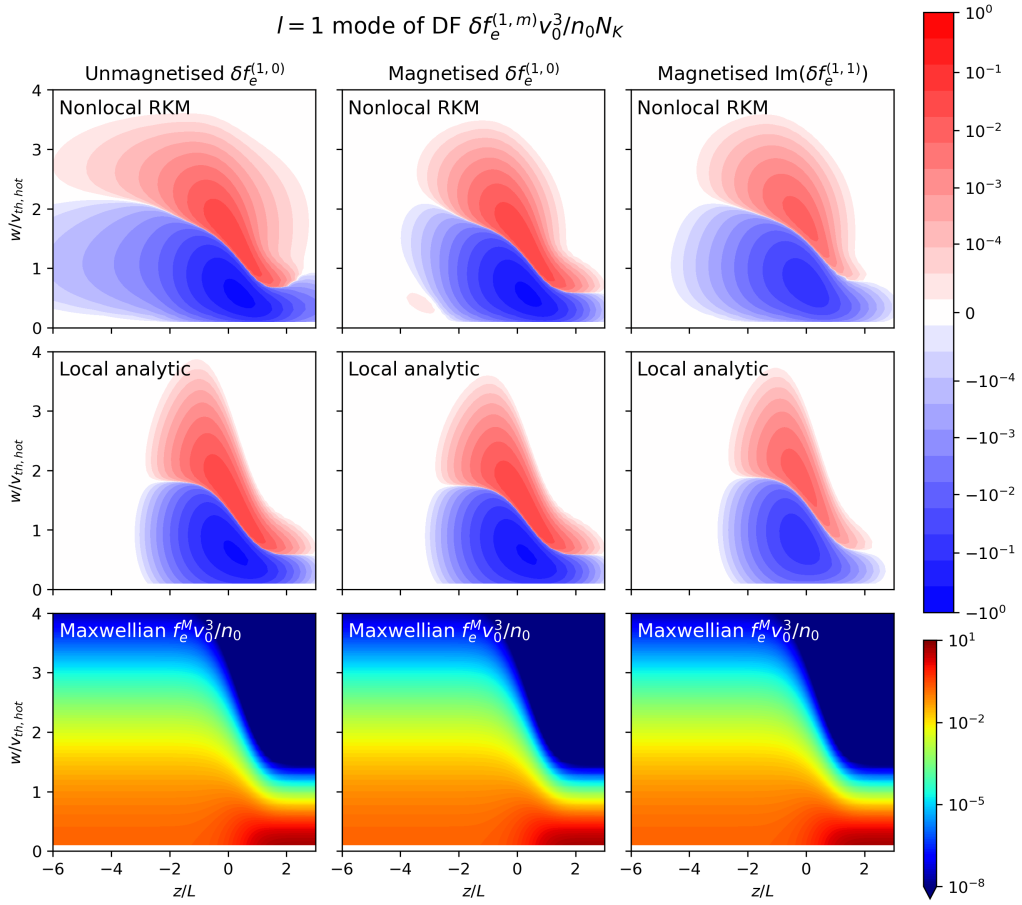


Figure 5.9: $l = 1$ modes of the DDF in the unmagnetised and magnetised ($\chi = 0.5$) cases, similarly to Figure 4.4 of the previous chapter. Note that the symmetric logarithmic colourmap has a linear section through zero. The Maxwellian distribution is shown on the bottom row of subplots on the same spatial axes to show the structure of the bulk distribution. Nonlocal effects are clearly present on the top row of subplots, with beam-like features extending well beyond the main gradient region around $z = 0$.

Figure 5.9 shows the $l = 1$ modes of the DDF similarly to 4.4, but with the magnetised case included. In the magnetised case, the $m = 1$ component is nontrivial and therefore included. Here, we see clearly that the magnetic field with order-unity Hall parameter dramatically suppresses the nonlocal behaviour of the $m = 0$ component of the distribution function itself. The beam-like features in the unmagnetised case are significantly reduced with the magnetic field included. The $m = 1$ component, responsible for the Righi-Leduc heat flow, is slightly weighted to higher w in the local case, and therefore is more subject to nonlocal behaviour.

Nonlocal transport quantities may be evaluated directly by taking appropriate w moments of $\delta f_e^{(l,m)}(z, w)$, but the entire distribution function $\delta f_e(z, w, \vartheta, \varphi)$ may also be reconstructed from the RKM. Figure 5.10 shows the distribution function $f_e(z, w, \vartheta, \varphi)$ in the cold end ($z/L = 0.5$) in the nonlocal magnetised temperature

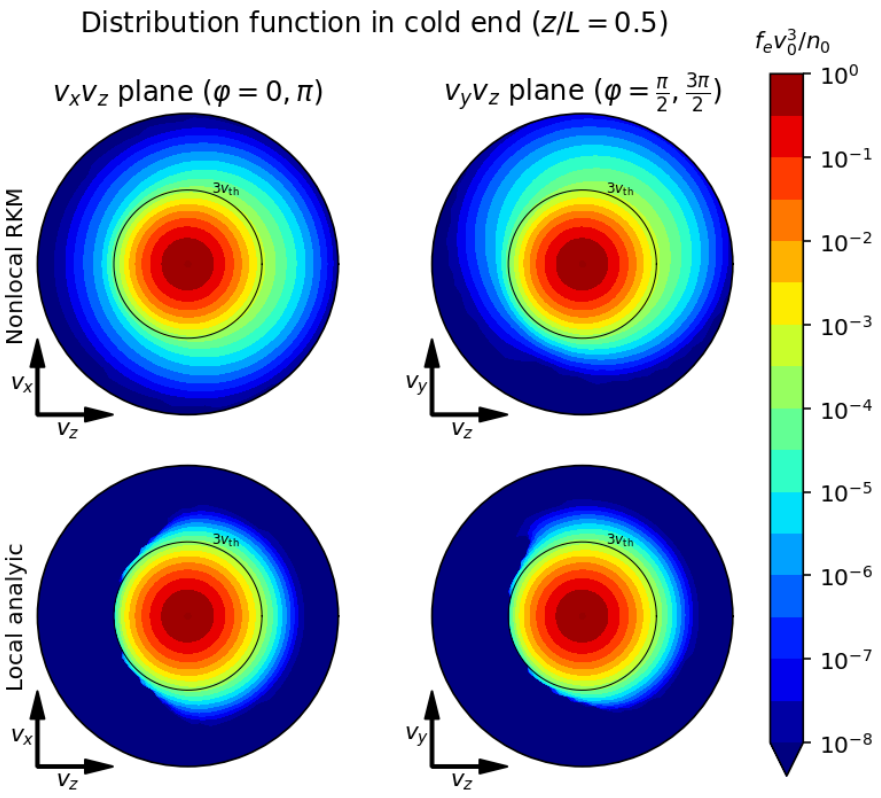


Figure 5.10: Electron distribution function in the cold end ($z/L = 0.5$) for the $N_K = 0.1$ magnetised ($\chi_0 = 0.5$) isochoric temperature step case above. A circle at $w = 3v_{\text{th}}(z/L = 0.5)$ is shown to indicate the radial velocity scale. The sharp edges present in the rear of the local analytic solution are where the distribution is negative, and therefore unphysical. Reproduced from [3].

gradient case in section 5.1 above. Although towards the cold end ($T_e(z/L = 0.5) \approx 0.3\,T_{\text{hot}}$), this chosen spatial position still has a notable temperature gradient and Hall parameter ($\chi(z/L = 0.5) \approx 0.1$) so anisotropy in the local solution is still visible. In the $v_x v_z$ plane, containing the temperature gradient and magnetic field, the local solution is anisotropic in the $+\hat{\boldsymbol{z}} \parallel -\boldsymbol{\nabla} T_e$ direction. In the $v_y v_z$ plane, there is a deflection of this anisotropy in the $+\hat{\boldsymbol{y}} \parallel \boldsymbol{B} \times \boldsymbol{\nabla} T_e$ direction due to the magnetic field. Sufficiently far out in the tail at the rear of the distribution ($w/v_{\text{th}} \gtrsim 3$, $\vartheta \gtrsim 3\pi/4$, where $\vartheta = 0$ is along $v_y = 0, v_z > 0$), the local solution is negative, emphasising the limit of its validity. The tail of the nonlocal distribution is enhanced beyond $w/v_{\text{th}} \gtrsim 3$ due to near-collisionless suprathermal particles streaming from the hot end. Due to the magnetic field, this suprathermal tail is deviated in the $+\hat{\boldsymbol{y}} \parallel \boldsymbol{B} \times \boldsymbol{\nabla} T_e$ direction. The nonlocal solution corrects the unphysical negativeness of the distribution function in the rear of the tail present in the local analytic solution.

5.6 Heat Flux Integrands

To better understand nonlocal and magnetised effects on the conductive heat flow, we may examine the behaviour of the heat flux integrand. Figure 5.11 shows the components of the electron conductive heat flux integrand $\propto w^5 \boldsymbol{S}_{1,e}$ for the unmagnetised and magnetised temperature gradient cases presented above. In the unmagnetised case, nonlocal effects distort the heat flux integrand at higher velocities w where MFPs are

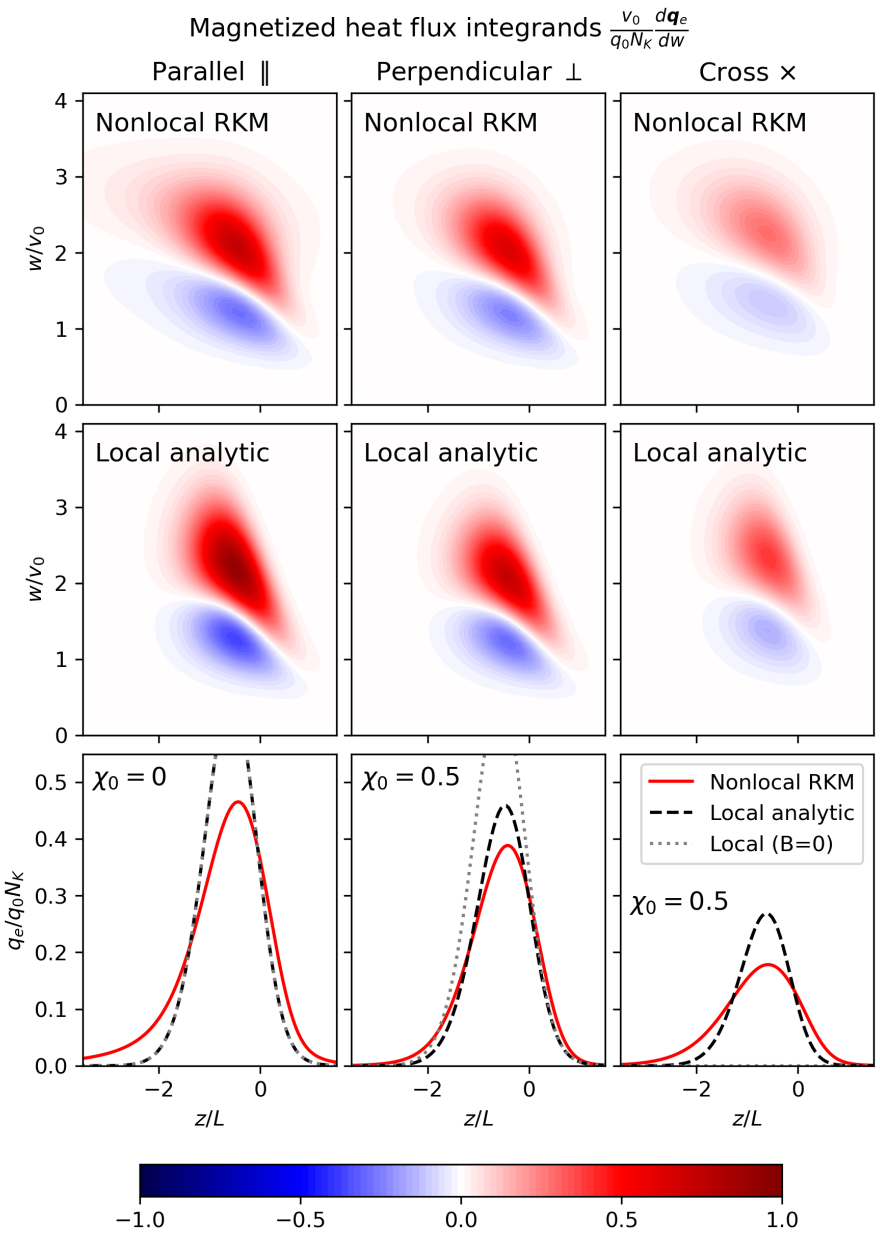


Figure 5.11: Integrand of conductive heat flux components for the unmagnetised and magnetised temperature gradient cases with $N_K = 0.1$ obtained from the RKM and local analytic result. The bottom row of subplots shows the heat flux along the same spatial axes, i.e. is the integrated results of the integrands shown above. Reproduced from [3].

longer, smearing the integrand across the spatial domain. In contrast to the local analytic solution, a beam-like feature penetrating into the cold end for $w \gtrsim 2v_0$ is present, giving rise to the preheat seen in the nonlocal heat flow in the lowest subplot. Similar enhancement is also seen in the hot end, where nonlocal effects allow for suprathermal particles to stream across the gradient.

The magnetic field suppresses this nonlocal behaviour at larger w, largely inhibiting the beam features and preheat seen in the cold end. Nonlocal distortions on the integrand and heat flux are still present, but less than the unmagnetised case. The magnetic field then adds a nontrivial component in the cross $\times$ direction, giving rise to the Righi-Leduc heat flow. The local Righi-Leduc integrand is more weighted towards higher w than the parallel and perpendicular conductive components, therefore nonlocal effects then have a greater

effect on the Righi-Leduc heat flow than the perpendicular component.

5.7 Collision Operator Verification

In Section 4.2.5 of the previous chapter, the linearised Fokker-Planck operator was demonstrated to be valid in the unmagnetised semi-collisional regime. Here, this verification is extended to the magnetised regime of the same temperature-gradient case.

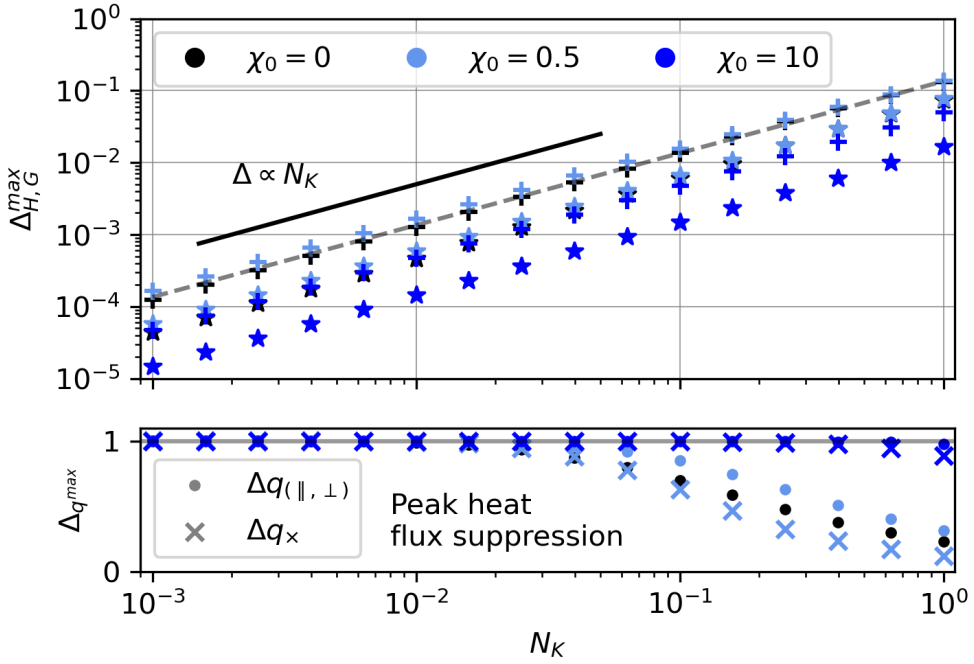


Figure 5.12: Maximum deviation of Rosenbluth potentials $\Delta^{\max}_{\mathcal{H},\mathcal{G}} = \max_{z,w}(\Delta_{\mathcal{H},\mathcal{G}})$ across a wide range of Knudsen numbers for the temperature step case and peak heat flux suppression $\Delta_{q^{\max}} = \max_z(|q_e^{\text{nonlocal}}|)/\max_z(|q_e^{\text{local}}|)$. The black, light blue, and dark blue markers show the unmagnetised, moderately magnetised ($\chi_0 = 0.5$), and strongly magnetised ($\chi_0 = 10$) cases, respectively. The smallness of these ratios $\Delta \lesssim 0.1$ for $N_K \leq 1$ justifies the linearisation of the collision operator in this moderately nonlocal regime. Reproduced from [3].

Figure 5.12 shows the maximum deviation of the Rosenbluth potentials $\Delta^{\max}_{\mathcal{H},\mathcal{G}}$ over a wide range of Knudsen numbers, similarly to Figure 4.7 but including the moderately magnetised and strongly magnetised temperature-gradient cases. The deviations of the Rosenbluth potentials increase linearly with Knudsen number as before. The linear Fokker-Planck collision operator is valid where $\Delta^{\max}_{\mathcal{H},\mathcal{G}} \lesssim 0.1$, and therefore holds up to the semi-collisional regime $N_K \lesssim 1$ as before in unmagnetised and moderately magnetised cases $0 \leq \chi \lesssim 1$. For the strongly magnetised case, the deviations of the Rosenbluth potentials are further reduced by the magnetic field, increasing the upper bound of valid Knudsen numbers.

CHAPTER 6

Nonlocal Ion Transport Results

Nonlocal transport is usually investigated in the context of electron heat conduction [5, 6, 102, 123]. Heat flow is expected to be the most sensitive transport quantity to nonlocal effects since it is carried by higher energy particles, and electrons are far more effective at transporting heat than the much heavier ions. However, there are various scenarios in which the ion heat flux may become comparable to or dominate the electron heat flux. Taking the ratio of the local ion and electron conductive heat fluxes yields

$$\frac{|\boldsymbol{q}_i^T|}{|\boldsymbol{q}_e^T|} \sim \frac{\hat{\kappa}^i_{(\parallel,\perp,\times)}}{\hat{\kappa}^e_{(\parallel,\perp,\times)}} \left(\frac{m_e}{m_i}\right)^{1/2} \left(\frac{T_i}{T_e}\right)^{7/2} \frac{1}{Z^3} \frac{|\boldsymbol{\nabla} \ln T_i|}{|\boldsymbol{\nabla} \ln T_e|}, \tag{6.1}$$

with the ion and electron dimensionless conductivity coefficients dependent on their respective Hall parameters. Ion heat flow is significant in comparison to electron heat flow when this ratio is comparable to or exceeds unity. For large electron Hall parameter $\chi_e \gg 1$, magnetic fields suppress electron heat flow by a factor of $\hat{\kappa}^e_\perp \sim \chi_e^{-2}$ or $\hat{\kappa}^e_\times \sim \chi_e^{-1}$, which can allow ion heat flux to dominate electron heat flux. In addition, the strong dependence on the temperature ratio $(T_i/T_e)^{7/2}$ means even moderately large temperature ratios can also cause ion heat transport to become comparable to electron transport, even in the unmagnetised case. Finally, ion temperature gradients may be significantly sharper than electron temperature gradients, for example in the structure of a collisional shock, where the last term again may cause the ion heat flow to dominate electron heat flow. We may similarly take the ratio of the viscous stress tensors, which shows that the ion viscous effects typically dominate in low-Z plasmas.

6.1 RKM for Single Species Ions

The RKM may be reformulated for a single ion species in a simple plasma with VFP equation

$$\partial_t f_i + \boldsymbol{v} \cdot \boldsymbol{\nabla}_{\boldsymbol{x}} f_i + \frac{Ze}{m_i}\big(\boldsymbol{E} + \boldsymbol{v} \times \boldsymbol{B}\big) \cdot \boldsymbol{\nabla}_{\boldsymbol{v}} f_i = C_{ii} + C_{ie}, \tag{6.2}$$

with a similar derivation leading to the equation for the ion DDF

$$D_i = \big(\hat{C}_i - \hat{V}_i - \hat{B}_i\big)\delta f_i, \tag{6.3}$$

and its projection onto the spherical harmonic basis

$$\mathcal{D}_i^{(l,m)} = \mathcal{C}_i^{(l,m)} - \mathcal{V}_i^{(l,m)} - \mathcal{B}_i^{(l,m)}, \tag{6.4}$$

where terms are defined in Chapter 3.

6.2 Magnetised Viscous Stress

Viscous stress describes the flux of momentum due to gradients in flow. Unlike heat flux, where electron heat flux dominates ion heat flux unless electrons are magnetised or there is a significant temperature separation, ion viscous stress already dominates electron viscous stress. To the author's knowledge, no full VFP studies or closures studying nonlocal viscous stress exist in previous literature, even without a first-principles approach or in the absence of magnetic fields. The RKM naturally includes viscous stress by integrating over the DDF

$$\Pi_i = \int d^3\boldsymbol{w}\; m_i \left(\boldsymbol{w}\boldsymbol{w} - \frac{1}{3} w^2 \mathbb{I} \right) \delta f_i, \tag{6.5}$$

where components are determined by w moments of suitable combinations of $l = 2$ modes specified in Section 3.3.2.

There are many novel features of nonlocal viscous stress from initial studies with the RKM. Firstly, there are two dimensionless numbers that impact the nonlocal behaviour of the viscous stress: the Mach number $M \sim |\boldsymbol{u}_i|/v_{\text{th},i}$ which governs the characteristic speed of the flow, and the Knudsen number $N_K \sim \lambda_{\text{th},ii} |\boldsymbol{\nabla} \ln(|\boldsymbol{u}_i|)$ which governs the length scale over which the flow profile varies. When $N_K \ll 1$ and $M \lesssim \mathcal{O}(1)$, the viscous stress is local. However, when $N_K \gtrsim 1/10$, the viscous stress becomes nonlocal, and in this regime the Mach number $M \sim \mathcal{O}(1)$ has further nonlocal effects on the stress through the $\hat{V}_i \delta f_i$ term. This work takes a fixed $M \sim \mathcal{O}(1)$. Similarly to ion heat flux, ion-electron collisions also impact the local ion viscosity. Here we consider a simple hydrogen plasma with equal temperatures $T_i/T_e = 1$.

There are two types of flows that generate stress: compressive flows where the flow varies in the same direction as the flow $\boldsymbol{u}_i \parallel \boldsymbol{\nabla}$ such as $\boldsymbol{u}_i = u_z(z)\hat{\boldsymbol{z}}$, and shear flows where the flow varies in a direction perpendicular to the flow $\boldsymbol{u}_i \perp \boldsymbol{\nabla}$ such as $\boldsymbol{u}_i = u_y(z)\hat{\boldsymbol{y}}$. For this work, we present results for a shear flow with a uniform magnetic field $\boldsymbol{B} = -B_0\hat{\boldsymbol{x}}$. Figure 6.1 shows the viscous stress components Π_{yz} and Π_{zz} generated by a shear flow

$$\boldsymbol{u}_i(z) = -\frac{1}{2} u_0 \,\text{erf}(z/L)\hat{\boldsymbol{y}}, \tag{6.6}$$

in an isothermal isochoric simple hydrogen plasma. Similarly to results for vectorial transport quantities, the RKM accurately reproduces local analytic results for the viscous stress components for small Knudsen number. For large Knudsen number $N_K = 0.25$, the unmagnetised parallel stress Π_{yz} is significantly modified by nonlocal effects with qualitatively similar behaviour as other transport quantities; the peak flux is inhibited, and a 'preheat' is developed, where the flux away from the main gradient is enhanced due to streaming suprathermal particles. In the magnetised case $\chi_0 = 0.25$, the magnetic field restores the nonlocal perpendicular stress

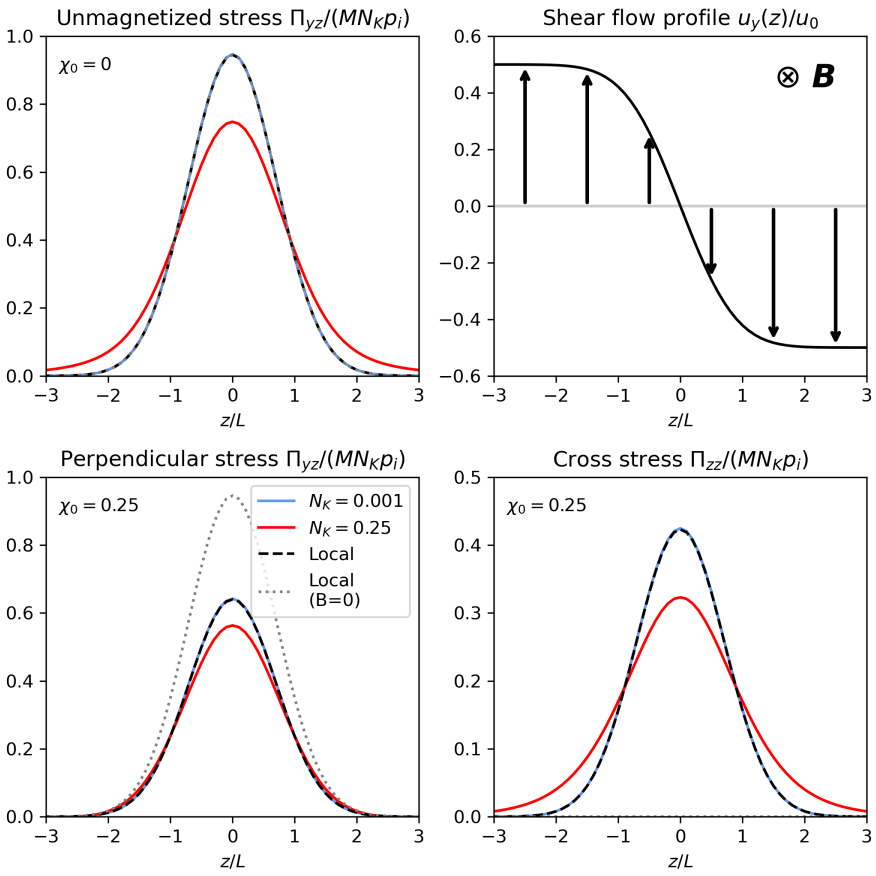


Figure 6.1: Nonlocal ion viscous stress for a shear ion flow $\boldsymbol{u}_i = -\frac{1}{2}u_0 \operatorname{erf}(z/L)\hat{\boldsymbol{y}}$ with Mach number $M = |u_0|/v_{\mathrm{th},i} = 1$. The stresses are normalised against the Mach number M, Knudsen number N_K, and ion pressure $p_i = n_i T_i$. The magnetised cases have an applied uniform magnetic field $\boldsymbol{B} = -B_0\hat{\boldsymbol{x}}$ with B_0 chosen such that the Hall parameter throughout the plasma is $\chi_0 = 0.25$. Reproduced from [3].

closer to its local result. The cross stress Π_{zz} appears more strongly influenced by nonlocal effects than the magnetised shear stress, analogously to the Righi-Leduc heat flux $\boldsymbol{q}^T_{\alpha,\times}$ being more sensitive to nonlocality than the perpendicular counterpart $\boldsymbol{q}^T_{\alpha,\perp}$.

6.3 Impact of Ion-Electron Collisions on Ion Transport

Braginskii [15] derives local analytic closures for collisional transport quantities in a simple plasma including ion heat flux and viscous stress tensor. In deriving the transport coefficients appearing in these local closures, Braginskii neglects ion-electron collisions since the smallness of the mass ratio $m_e/m_i \lessapprox 1/1840$ suggests that their effect is small and should not affect ion transport. However, more recent work by Ji and Held [87, 88] includes ion-electron collisions in the local limit and finds that they do have a notable impact on the ion heat conductivity and viscosity. This section applies the RKM to demonstrate the impact of ion-electron collisions on ion transport in the nonlocal regime.

Braginskii's calculation, which neglects ion-electron collisions, results in magnetised coefficients that are only dependent on the ion Hall parameter $\chi_i = Ze|\boldsymbol{B}|\tau_{ii}/m_i$ and unmagnetised coefficients $(\hat{\kappa}^i_{\parallel})^{\text{Braginskii}}/\sqrt{2} =$

3.906 and $(\hat{\eta}_0^i)^{\text{Braginskii}}/\sqrt{2} = 0.96$, which are numerical constants. Although the ion-electron collision operator is small by a factor of $\sqrt{m_e/m_i}$, there are other considerations that make ion-electron collisions significant enough to notably modify ion transport coefficients. Note that Coulomb collisions are more significant for smaller relative velocities between the two colliding particles. Consider an ion with normalised speed $x_i = w/v_{\text{th},i}$, where $\boldsymbol{w} = \boldsymbol{v} - \boldsymbol{u}_i$ is the particle velocity in the frame comoving with the local ion Maxwellian bulk velocity and $v_{\text{th},i} = \sqrt{2T_i/m_i}$ is the ion thermal velocity. Ions with speeds in the range $1 \lessapprox x_i \lessapprox 4$ are those that contribute significantly to the heat flux, with slower ions not carrying enough kinetic energy and faster ions being too scarce. Mathematically, this is manifested through the integrand of the local heat flux $dq^i \propto (x_i^2 - 5/2)^2 x_i^3 e^{-x_i^2} dx_i$, which has the majority contribution to the resulting integral in this interval. These heat-flow-contributing ions collide with other ions in the tail of the ion distribution, but since these relevant speeds are still much smaller than the electron thermal velocity $w \lesssim 4\, v_{\text{th},i} \ll v_{\text{th},e}$, these ions also collide against the bulk of the electron distribution. Even though a single ion-electron collision is far less impactful on an ion's behaviour than an ion-ion collision, in the tail of the ion distribution there are sufficiently more electrons than ions in the nearby velocity space to collide against, resulting in ion-electron collisions impacting heat flow. Consider a single suprathermal test-particle ion colliding against background ions and electrons. The background Maxwellian ions have a local phase space density $\propto n_i m_i^{3/2} T_i^{-3/2} e^{-x_i^2}$ in the nearby velocity space. In contrast, the much lighter electrons have a broader Maxwellian, so these ions collide against electrons with a phase space density $\propto n_e m_e^{3/2} T_e^{-3/2}$. The ratio of the electron to ion phase space density is then $\frac{1}{Z}(\frac{m_e}{m_i})^{3/2}(\frac{T_i}{T_e})^{3/2} e^{x_i^2}$. For larger ion-electron temperature ratio T_i/T_e, ion-electron collisions become increasingly significant and even dominant over ion-ion collisions.

Ji and Held [88] therefore include the ion-electron collision term, resulting in a dependence of the ion transport coefficients on $\varphi = \frac{1}{Z}\sqrt{\frac{m_e}{m_i}}$ and $\xi = \sqrt{\frac{T_i}{T_e}}$ as well as the ion Hall parameter χ_i. The dependence of the ion transport coefficients on the temperature ratio ξ for a moderately magnetised hydrogen plasma is shown in Figure 6.2. Even for equal temperatures $\frac{T_i}{T_e} = 1$ in a hydrogen plasma, the unmagnetised coefficients for heat conductivity $\hat{\kappa}_\parallel^i$ and viscosity $\hat{\eta}_0^i$ are reduced by 16% and 7% respectively when ion-electron collisions are included. For larger ion-electron temperature ratios, these reductions are much more dramatic, with reductions of 82% and 71% respectively for $\frac{T_i}{T_e} = 10$. In confined fusion schemes, various mechanisms such as collisional shocks [124], neutral beam injection [125], and plasma waves [126] preferentially heat ions over electrons, therefore moderate temperature ratios exceeding unity are realistic and ion-electron collisions should be accounted for. This work investigates the impact of ion-electron collisions in the nonlocal regime.

Figure 6.3 shows the ion heat flux for an isochoric simple hydrogen plasma with a temperature profile

$$T_i(z) = \frac{T_i^{\text{hot}} + T_i^{\text{cold}}}{2} - \frac{T_i^{\text{hot}} - T_i^{\text{cold}}}{2} \text{erf}\left(\frac{z}{L}\right), \tag{6.7}$$

where a temperature step $T_i^{\text{hot}}/T_i^{\text{cold}} = 10$ is chosen. Although the electron and ion temperature profiles may be entirely independent, this work considers cases where they are directly proportional across the spatial domain, i.e. $\xi = \sqrt{T_i(z)/T_e(z)}$ is uniform. The $T_i/T_e = 0$ results correspond to where ion-electron collisions

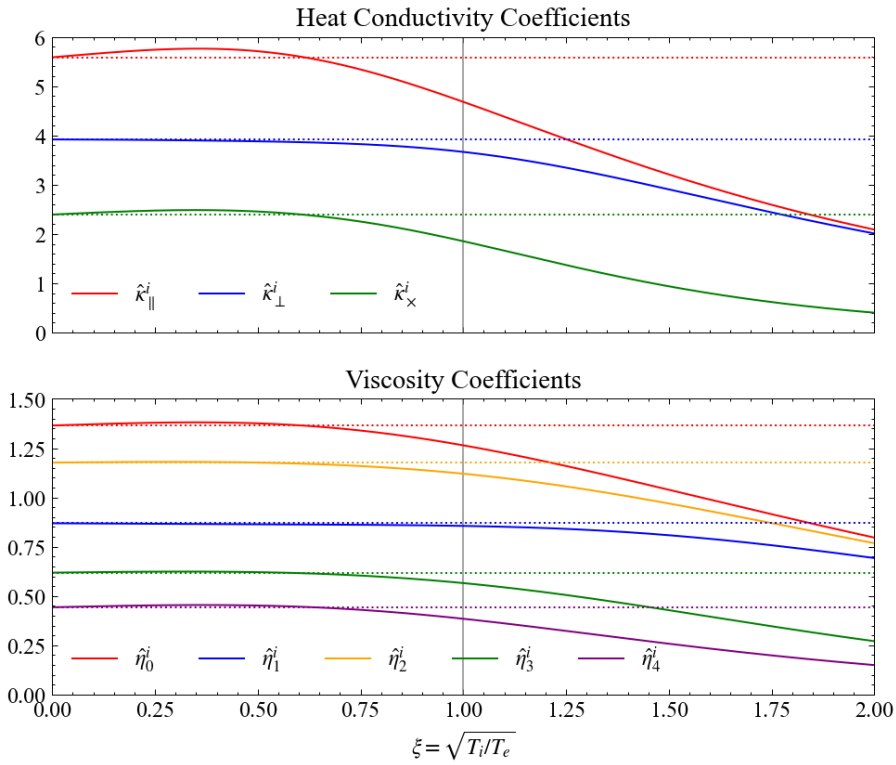


Figure 6.2: Dependence of the dimensionless ion heat conductivity and viscosity coefficients on ion-electron temperature ratio T_i/T_e for an intermediate magnetisation $\chi_i = 0.25$, produced using Ji-Held's fits. Dotted lines correspond to Braginskii's results where ion-electron collisions are neglected, which are then the limiting values for $T_i/T_e \to 0$. The first coefficients $\hat{\kappa}^i_{\parallel}$ and $\hat{\eta}^i_0$ are independent of magnetisation, therefore the red lines also correspond to results for unmagnetised ions. Reproduced from [4].

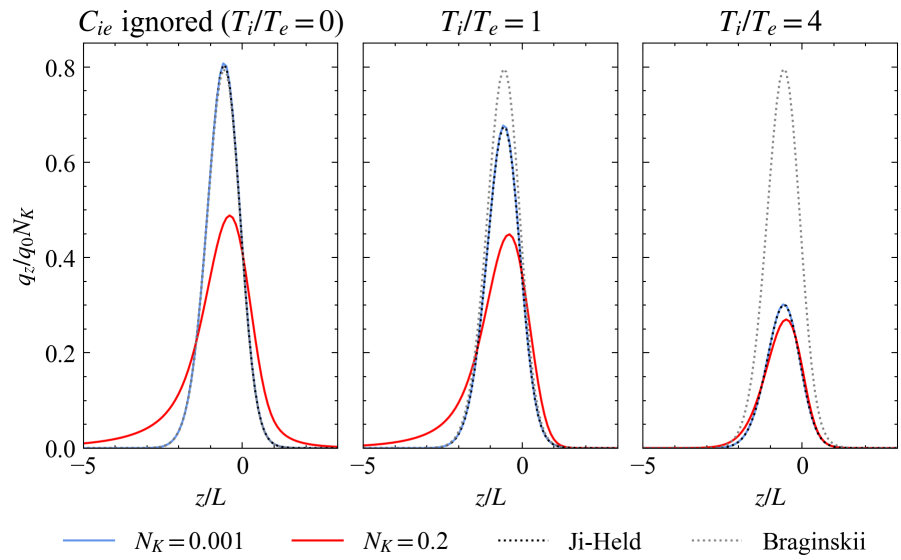


Figure 6.3: Ion conductive heat flux in an unmagnetised simple hydrogen plasma for $N_K = 0.001,\ 0.1$, for different ion-electron temperature ratios. The difference between the results of each subplot is then due solely to ion-electron collisions. The ion Knudsen number is $N_K = \lambda_{\text{th},ii}|_{z\to-\infty}/L$, where the ion-ion thermal MFP is $\lambda_{\text{th},ii} = v_{\text{th},i}/\hat{\nu}_{ii}$. Reproduced from [4].

are neglected, and therefore to Braginskii's result and the results on nonlocal ion heat flux in the previous sections. For equal ion and electron temperatures $T_i/T_e = 1$, the peak heat flow is suppressed by 16% by ion-electron collisions in both the local and nonlocal cases. The nonlocal preheat in the cold end for $0.5 \lesssim z/L \lesssim 2$ is significantly suppressed by ion-electron collisions. This is explained by the behaviour of the slowing collision frequency when ion-electron collisions are included. The ion slowing frequency entering the ion collision operator as $(\hat{C}_i f_i)_{\text{slowing}} = \frac{1}{w^2}\partial_w(w^3\tilde{\nu}_s^i f_i)$ may be written as

$$\tilde{\nu}_s^i = \hat{\nu}_{ii}\Bigg(\underbrace{\frac{2G(x_i)}{x_i}}_{\text{ion-ion}} + \underbrace{\frac{4}{3\sqrt{\pi}}\frac{\ln\Lambda_{ie}}{\ln\Lambda_{ii}}\frac{1}{Z}\sqrt{\frac{m_e}{m_i}}\sqrt{\frac{T_i}{T_e}}}_{\text{ion-electron}}\Bigg). \tag{6.8}$$

For $x_i \gtrsim 2$, $2G(x_i)/x_i \approx 1/x_i^3$. Suprathermal particles that stream from the hot end and give rise to nonlocal heat flow in the cold end typically have velocities on the order of the hot thermal velocity, say $\sim k v_{\text{th},i}^{\text{hot}}$ where $1 \lessapprox k \lessapprox 4$. In the cold end, these particles have a dimensionless velocity $x_i \sim k\sqrt{T_i^{\text{hot}}/T_i^{\text{cold}}}$, i.e. are a factor $\sqrt{T_i^{\text{hot}}/T_i^{\text{cold}}}$ further out into the tail of the ion distribution compared to ions contributing to local heat flow. The ion-ion slowing frequency is small by a factor $\sim \mathcal{O}(1/x_i^3)$, so ions may stream further into the cold end and give rise to a substantial preheating region. However, when included, the ion-electron slowing frequency does not decay further into the tail, therefore assists and even dominates ion-ion collisions in the slowing and scattering of suprathermal ions. The origin of these particles from the hot end means that the relative importance of ion-electron collisions to ion-ion collisions is enhanced by a factor of $\sim (T_i^{\text{hot}}/T_i^{\text{cold}})^{3/2}$, explaining why the nonlocal preheat is more dramatically suppressed by ion-electron collisions than the local heat flux.

For the larger temperature ratio $T_i/T_e = 4$, ion-electron collisions suppress the local result for the heat

flux significantly by 63%. Increased collisionality from ion-electron collisions then mostly inhibits nonlocal behaviour for $N_K = 0.1$, restoring the heat flux to nearly its local result. This is partly due to the definition of the Knudsen number $N_K = \lambda_{\text{th},ii}/L$ being used, which doesn't account for ion-electron effects.

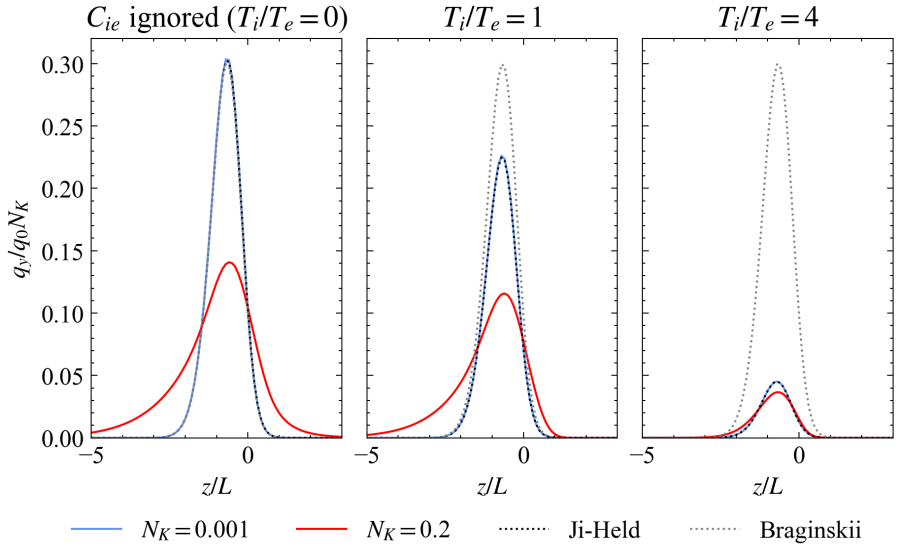


Figure 6.4: Nonlocal ion Righi-Leduc heat flux for a magnetised simple hydrogen plasma with ion Hall parameter $\chi_{i,0} = 0.25$ at the hot end for different ion-electron temperature ratios. The difference between the results of each subplot is then due solely to ion-electron collisions. Reproduced from [4].

Figure 6.4 similarly shows the influence of ion-electron collisions on the ion Righi-Leduc heat flow for the same case as before, but with a magnetic field $\boldsymbol{B} = B_0\hat{\boldsymbol{x}}$ giving an ion Hall parameter $\chi_{i,0} = 0.25$ at the hot end. Similarly to the unmagnetised ion conductive heat flow, accounting for ion-electron collisions for equal ion and electron temperatures significantly modifies the local result and largely suppresses the preheat for the nonlocal heat flow. For the larger temperature separation $T_i/T_e = 4$, the local result is dramatically reduced by ion-electron collisions by 70% and 90% in the hot and cold ends, respectively. This suppression is more dramatic than in the unmagnetised case, since the Righi-Leduc heat flow is sourced from particles with larger velocities w than the parallel and perpendicular counterparts. Mathematically, this is apparent from the integrand of the Righi-Leduc heat flux $dq^i_\times/dw$ being weighted to higher x_i than the parallel and perpendicular flux integrands $dq^i_{(\parallel,\perp)}/dw$.

Figure 6.5 emphasises the above results by showing the ratio of the different components of heat flow with and without ion-electron collisions for the unmagnetised and magnetised cases shown in Figures 6.3 and 6.4. As previously noted, the local unmagnetised heat flow is uniformly suppressed by 16% and 63% in the $T_i/T_e = 1$ and $T_i/T_e = 4$ cases, respectively. The local magnetised results have a small change across the temperature profile since the collisionality increases from the hot to the cold end, therefore the Hall parameter decreases from the hot end to the cold end. In nonlocal cases, the peak heat flow around $-1 \lessapprox z \lessapprox 0$ is not as strongly suppressed by ion-electron collisions as the local heat flow. However, away from the centre of the gradient where nonlocal effects give rise to enhanced heat flow, ion-electron collisions strongly suppress the

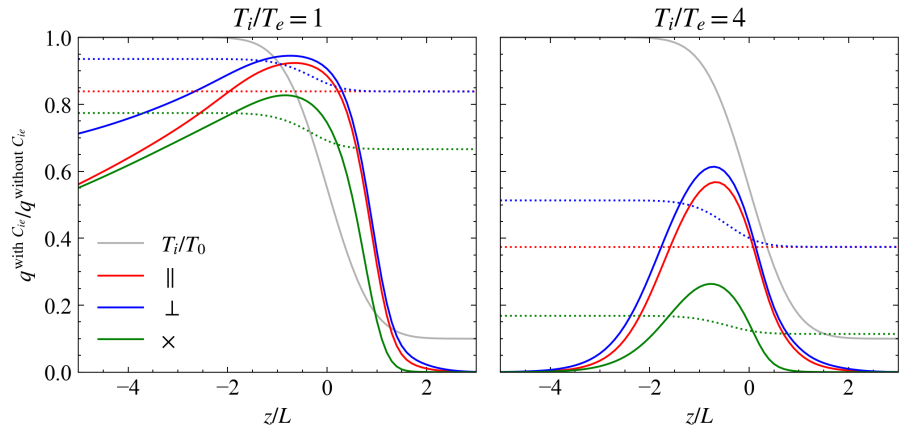


Figure 6.5: Ratio of heat flow with ion-electron collisions included to heat flow without ion-electron collisions included for two different ion-electron temperature ratios. Dotted and solid lines correspond to the local ($N_K = 0.001$) and nonlocal ($N_K = 0.1$) cases. Reproduced from [4].

preheat as previously discussed. This preheat suppression by ion-electron collisions is less impactful on the perpendicular heat flow than the unmagnetised heat flow, but more significant on the Righi-Leduc heat flow than the other components due to its dependence on more energetic ions.

The ion viscous stress tensor is also influenced by ion-electron collisions and nonlocal effects. To investigate the impact of these two effects, the same unmagnetised and magnetised cases as Section 6.2 are considered but with different T_i/T_e and N_K.

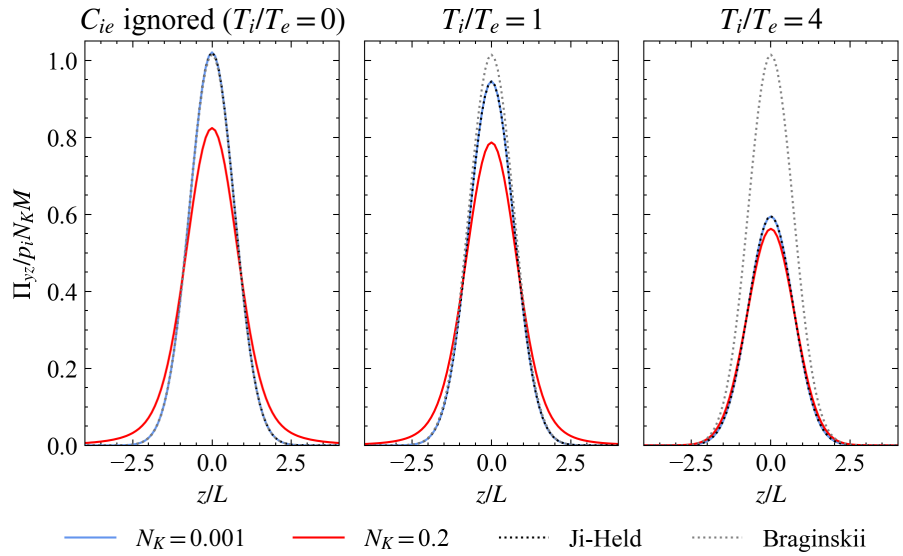


Figure 6.6: Nonlocal ion viscous stress Π_{yz} for an unmagnetised hydrogen plasma due to a shear flow for different ion-electron temperature ratios. The difference between the results of each subplot is then due solely to ion-electron collisions. Reproduced from [4].

Figure 6.6 shows the viscous stress component $\Pi_{i,yz}$ in a simple unmagnetised plasma for different ion-electron temperature ratios. The behaviour is qualitatively similar to the previous heat flow cases; when ion-electron collisions are neglected, Ji-Held and Braginskii agree well, but for temperature ratios of unity

and higher, the stress is suppressed by ion-electron collisions. Nonlocal effects for a high Knudsen number $N_K = 0.2$ suppress the peak stress further, but also give rise to a 'preheat' away from the main gradient at $z = 0$. This enhanced viscous stress then increases momentum transfer away from the main region of shearing flow. For equal temperatures, this preheat is not noticeably modified by ion-electron collisions, but is strongly suppressed at higher ion-electron temperature ratios in the $T_i/T_e = 4$ case where ion-electron collisions almost entirely restore the viscous stress to the local result even for the high Knudsen number $N_K = 0.2$. This is partly due to our definition of Knudsen number that does not include ion-electron collisions, but has been chosen to allow for a straightforward comparison between different cases. The Knudsen number could be redefined to include ion-electron collisions, but it is not clear how this would be done appropriately and consistently.

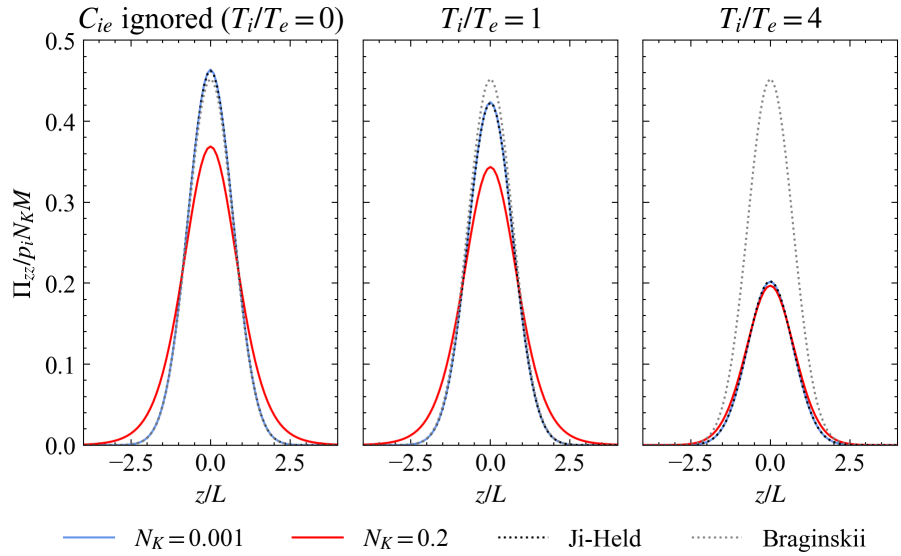


Figure 6.7: Nonlocal ion gyroviscous stress Π_{zz} for a moderately magnetised hydrogen plasma with ion Hall parameter $\chi_i = 0.25$ due to a shear flow for different ion-electron temperature ratios. The difference between the results of each subplot is then due solely to ion-electron collisions. Reproduced from [4].

Figure 6.7 shows the gyroviscous component $\Pi_{i,zz}$ for the shear flow with a magnetic field $\boldsymbol{B} = -B_0\hat{\boldsymbol{x}}$ with B_0 chosen such that the Hall parameter across the domain is $\chi_i = 0.25$. The gyroviscous stress appears to have similar sensitivity to both nonlocal effects and ion-electron collisions as the unmagnetised viscous stress, differing largely from the standard Braginskii result due to high Knudsen number $N_K = 0.2$ or ion-electron temperature ratio $T_i/T_e = 4$.

6.4 Impact of Sonic Flows on Nonlocal Ion Heat Flow

The Vlasov operator appearing in the DDF equation has the form

$$\hat{V} = (\boldsymbol{w} + \boldsymbol{u}) \cdot \boldsymbol{\nabla} + (\dots) \cdot \boldsymbol{\nabla}_{\boldsymbol{w}}, \tag{6.9}$$

where species subscripts have been dropped since the form is similar for electrons and ions. Conventional nonlocal effects have arisen due to the particle advection operator $\boldsymbol{w} \cdot \boldsymbol{\nabla}$. The particle advection term gives

rise to nonlocal behaviour where it becomes significant compared to collision terms for suprathermal particles with speeds $2 \lessapprox w/v_{\text{th}} \lessapprox 4$.

In this section, we notice that the flow advection operator $\boldsymbol{u} \cdot \boldsymbol{\nabla}$ can also become comparable to the collision term and therefore modify the non-Maxwellian component of the distribution δf and transport fluxes if the flow is sufficiently fast. For this effect to be significant, we require

$$\frac{|\boldsymbol{u} \cdot \boldsymbol{\nabla} \delta f|}{|\hat{C} \delta f|} \sim \left(\frac{w}{v_{\text{th}}} \right)^3 M N_K, \tag{6.10}$$

where $M = |\boldsymbol{u}|/v_{\text{th}}$ is the Mach number, to be order unity or larger. For small Knudsen number $N_K \ll 1$, this effect is small unless the Mach number is extremely large $M \gtrsim \mathcal{O}(1/N_K) \gg 1$. However, in the nonlocal transport regime $N_K \sim 1/10$, this effect can become significant for realistic Mach numbers. For the impact of the ion flow to be significant beyond standard nonlocal effects, we require $|\boldsymbol{u}| \gtrsim w \sim v_{\text{th}}$ for transport-relevant particles, which corresponds to order-unity Mach number $M \gtrsim 1$.

As discussed in the previous chapter, a similar criterion $N_u = |\Delta \boldsymbol{u}|/v_{\text{th},e} \sim 1$ cannot be satisfied for near-LTE electrons without the thermal population becoming runaway. For electrons, we still found modifications for $N_u \sim 1/40$, but through a different mechanism manifested through the $\boldsymbol{R}_e^u \cdot \boldsymbol{\nabla}_{\boldsymbol{w}}$ term. In contrast, order-unity Mach number $M \sim 1$ is often achieved for ions since their thermal velocity is much smaller than the electron thermal velocity, and bulk flows are typically bounded by the sound speed $|\boldsymbol{u}_\alpha| \lesssim c_s \sim v_{\text{th},i}$. Ions are not subject to a similar runaway effect as for electrons since suprathermal ions collide against the bulk of the electron distribution. We therefore expect sonic ion flows to impact nonlocal ion transport. Nonlocal ion viscosity is already dependent on the ion flow through its thermodynamic drive, therefore we focus on the impact of sonic flows on the nonlocal ion heat flow.

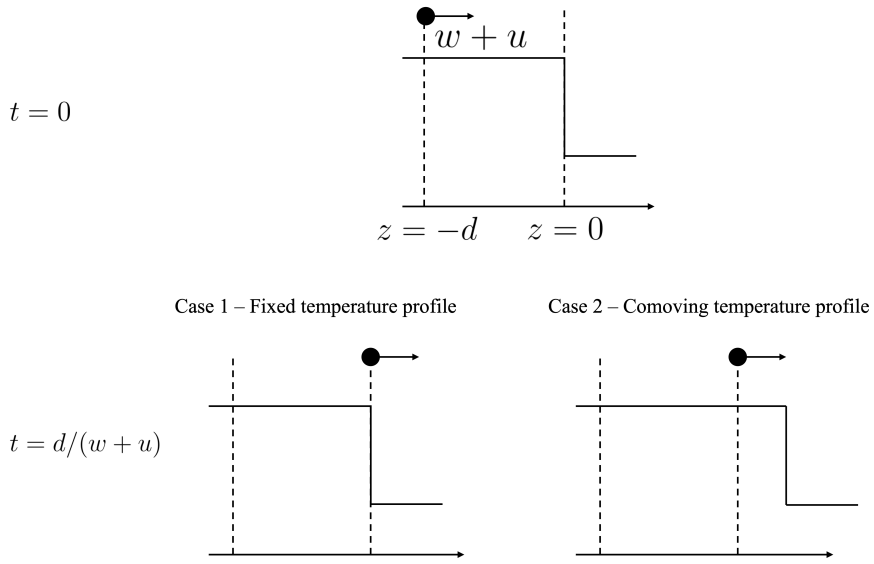


Figure 6.8: Depiction of a particle moving in a temperature profile where the profile is fixed in the lab frame (Case 1, left) or where the temperature profile is comoving with the flow (Case 2, right).

We may be concerned that the flow $\boldsymbol{u}_i$ impacting the heat flux $\boldsymbol{q}$ violates Galilean invariance. The density,

temperature, and heat flux are all defined in the CoM frame as

$$n = \int d^3\boldsymbol{w}\, f, \quad T = \frac{2}{3n}\int d^3\boldsymbol{w}\, \frac{1}{2}mw^2 f, \quad \boldsymbol{q} = \int d^3\boldsymbol{w}\, \frac{1}{2}mw^2\boldsymbol{w} f, \tag{6.11}$$

where $\boldsymbol{w} = \boldsymbol{v} - \boldsymbol{u}$. However, we can argue this effect of flows influencing nonlocal transport is physically sound. Consider a one-dimensional plasma with a temperature profile that has a sharp jump at $z = 0$

$$T(t,z) = \begin{cases} T_{\text{hot}}, & z < 0 \\ T_{\text{cold}}, & z \geq 0 \end{cases} \tag{6.12}$$

and a uniform flow $u > 0$ in the $+z$ direction, as shown in Figure 6.8. A particle starting from $z = -d$ at $t = 0$ with peculiar velocity $w > 0$ takes a time $\Delta t = d/v = d/(w + u)$ to reach the fixed boundary at $z = 0$, experiencing $N = \Delta t/\tau$ collisions. Instead, if the temperature profile is also moving with the flow, i.e.

$$T(t,z) = \begin{cases} T_{\text{hot}}, & z < ut \\ T_{\text{cold}}, & z \geq ut \end{cases} \tag{6.13}$$

then the particle takes a longer time $\Delta t' = d/w$ to reach the moving boundary, experiencing more collisions $N' = \Delta t'/\tau > N$. The particle in the second case has experienced more collisions, and is therefore less likely to stream across the boundary and nonlocally transport heat to the plasma at $z > 0$. The second case is equivalent to a plasma with no flow in the frame comoving with u, which is then distinct from the first case where the flow provides an additional 'boost' to streaming suprathermal particles, allowing more to stream across the boundary carrying more heat. The second case is similar to a shock, where the temperature and other fluid profiles all move at some shock velocity u. The first case which impacts nonlocal heat flow is similar to a boundary where temperature is fixed, perhaps being rapidly cooled or heated by some process such as radiation on either side, but mass flows through the boundary with velocity u. In the RKM, this distinction enters when we set $\partial_{t'}\delta f = 0$ at fixed $\boldsymbol{x}' = \boldsymbol{x}$ and fixed $\boldsymbol{w} = \boldsymbol{v} - \boldsymbol{u}$.

Figure 6.9 shows the nonlocal ion heat flux with a variety of uniform sonic flows $\boldsymbol{u}_i = u_0\hat{\boldsymbol{z}}$. The first (top) subplot shows the heat flux in the local limit $N_K = 1/1000$, where sonic flows in either direction have no significant impact on the heat flux. Here, N_K is sufficiently small that the advection with the flow is still small compared to the effect of collisions $|\boldsymbol{u}\cdot\boldsymbol{\nabla}\delta f|/|\hat{C}\delta f| \ll 1$. The other three subplots show the nonlocal heat flux with a variety of different uniform sonic flows, characterised by their Mach number $M = |u_0|/v_{\text{th},i}$ and direction. Even in the $M = 1$ case, the flow still has a notable impact on the heat flow, enhancing and suppressing the cold-end preheat for the flows in the $\pm\hat{\boldsymbol{z}}$ directions, respectively. This makes physical sense: a sonic flow down the temperature gradient provides an additional boost to suprathermal particles to cross the gradient, increasing nonlocal heat flow in the cold end, whereas a flow up the temperature gradient makes it harder for suprathermal particles to stream against the flow. These effects are increasingly dramatic in the $M = 2$ and $M = 5$ cases, dramatically shifting the nonlocal heat flux profile from the $M = 0$ result.

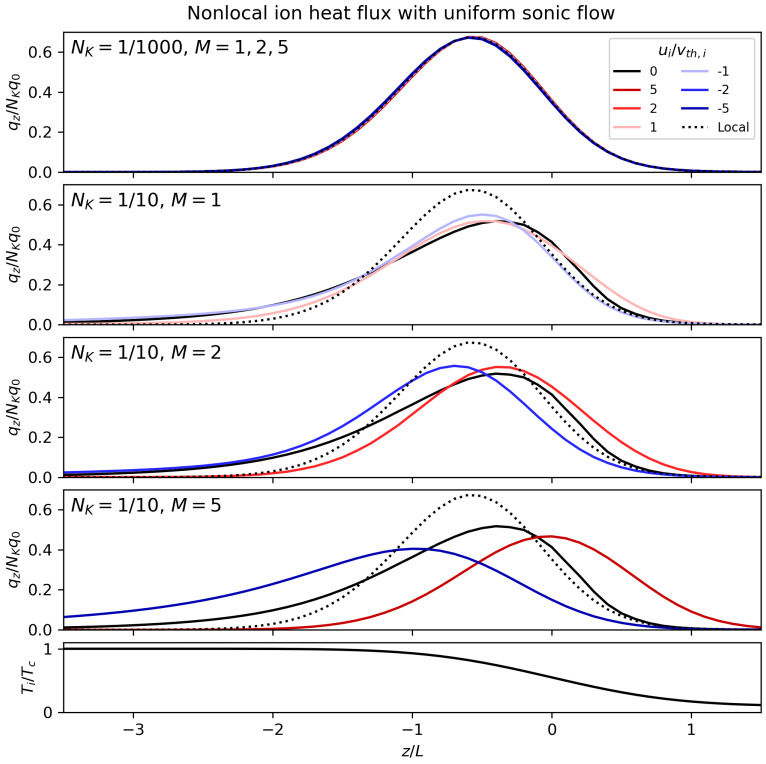


Figure 6.9: Reduced heat flux for an isochoric simple hydrogen plasma with different uniform sonic flows for a variety of Knudsen numbers. The black lines show the cases with no flow and red and blue lines show the cases with flow in the $\pm\hat{\boldsymbol{z}}$ directions, respectively.

6.5 Multi-Species Heat Flow

The above studies have been limited to a single ion species. However, plasmas often have multiple ion species present, for example Deuterium-Tritium (DT) mixtures for fusion fuel or CH_2 for plasmas created by heating plastics which often constitute layers in ICF capsules. Considering an ionic mixture introduces additional physics compared to the single ion species case. Different species may diffuse relative to each other even if the total mixture's state variables ρ_i, $\boldsymbol{u}_i$, and T_i are fixed, which changes the properties and therefore behaviour of the mixture. Confined fusion plasmas typically rely on fusion reactions between different species such as deuterium and tritium, where multi-species effects leading to species separation directly reduce fusion reactivity and total yield. In ICF implosions, high-Z species such as carbon may diffuse or stream into fusion fuel and dramatically increase radiative losses.

For multi-species cases, we define the Knudsen number in a similar manner to the single-species case, but instead using a maximum MFP $N_K = \lambda_{\max}/L$ defined as $\lambda_{\max} = \max_{\alpha,z}(\lambda_{0,\alpha}(z))$, with the MFP of a species α at spatial position z accounting for collisions with all species via $\lambda_{0,\alpha} = v_{\text{th},\alpha}/\sum_\beta \hat{\nu}_{\alpha\beta}$. A 50:50 DT mixture and a fully ionised CH_2 mixture are chosen as multi-species examples to investigate both weakly

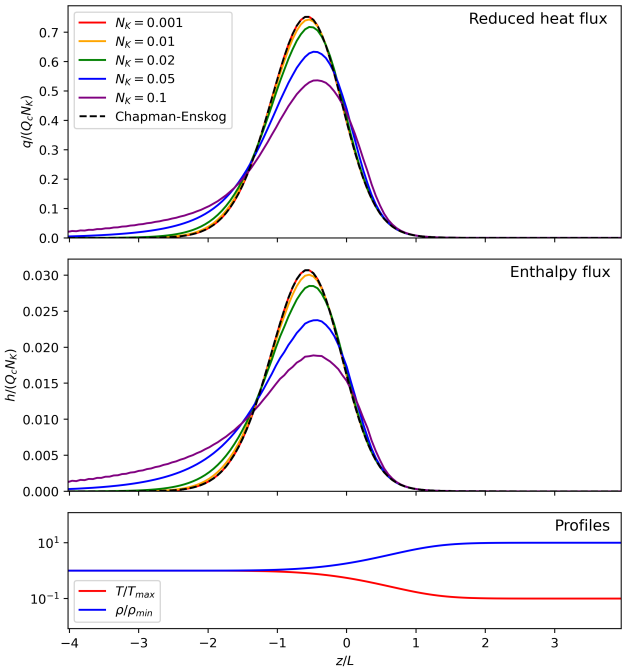
and moderately asymmetric mixtures. Both of these types of mixtures are relevant to ICF-related systems which often use DT fuel and plastic layers. A CH_2 mixture can be considered to be moderately asymmetric in mass, since the masses differ by an order of magnitude. Although the charge ratio is only $Z_C/Z_H = 6$, the charges enter the equations through the collision frequencies $\nu_{\alpha\beta} \propto Z_\alpha^2 Z_\beta^2$, therefore the charge asymmetry is effectively an order of magnitude. Three cases are chosen for each mixture: a temperature gradient at uniform pressure and concentration, a pure pressure gradient at uniform temperature and concentration, and a pure concentration gradient at uniform temperature and pressure. These cases with isolated $\boldsymbol{\nabla} T_i$, $\boldsymbol{\nabla} p_i$, and $\boldsymbol{\nabla} c$ are selected to investigate the sensitivity of the locality of heat fluxes to different driving gradients in temperature, pressure, and concentration. Similarly to the single-species case, the electric field has been set to zero to focus on the nonlocal effects from the aforementioned gradients. These six cases are shown in Figures 6.10 and 6.11 for DT and CH_2 respectively, demonstrating nonlocal effects on the reduced heat flux $\boldsymbol{q}_i'$ and enthalpy flux $\boldsymbol{h}_i$.

All of the multi-species cases show the same basic qualitative behaviour as the single-species cases; increasing Knudsen number inhibits the peak heat flux and enhances the heat flux in some regions away from the peak. However, the multi-species cases do demonstrate additional behaviour of interest. Firstly, nonlocal effects on the heat flux are demonstrated in the absence of a temperature gradient, induced instead by sharp gradients in pressure or concentration. In many of the cases shown, nonlocal effects give rise to enhanced heating in regions $|z/L| \gtrsim 2$ away from the gradient region due to sharp gradients in T_i, p_i, or c. This is in dramatic contrast to the local heat flux in these regions, which is exponentially small for the chosen $\sim \tanh(z/L)$ profiles. In most cases this enhancement only appears significantly on one side of the gradient region, for example the $\boldsymbol{\nabla} p_i$ cases in Figures 6.10b and 6.11b where the nonlocal behaviour is only pronounced on the $z/L > 0$ side of the gradient due to the relatively low collisionality on this side of the gradient region. In contrast, the DT ∇c case in Figure 6.10c has significant nonlocal behaviour in both directions due to the near-symmetry, which is not present in any of the other cases.

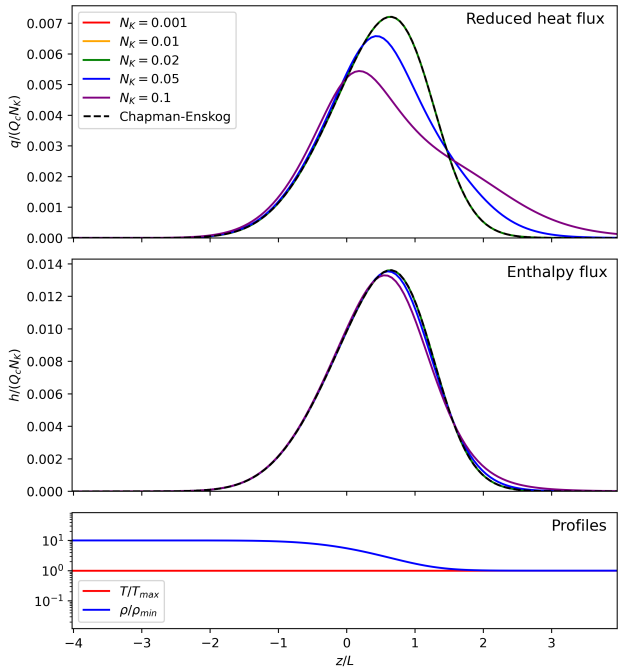
In the temperature gradient cases in Figures 6.10a and 6.11a, both components of the heat flux are similarly sensitive to nonlocal behaviour, and appear similar to the single-species case. Since the enthalpy flux is proportional to the diffusive flux, nonlocal behaviour in the former implies that diffusion can be sensitive to kinetic effects at similar Knudsen numbers at which heat transport is sensitive. In contrast, the DT ∇p case in Figure 6.10b and both ∇c cases in Figures 6.10c and 6.11c have the reduced heat flux q being significantly affected by nonlocal behaviour, whereas the enthalpy flux $\boldsymbol{h}_i$ is quite insensitive to nonlocal behaviour. This leads to cases around the peak flux where $\boldsymbol{q}_i'$ is significantly suppressed and $\boldsymbol{h}_i$ is not, so the latter may be increasingly important and dominant at the peak in nonlocal cases.

6.6 Nonlocal Diffusion

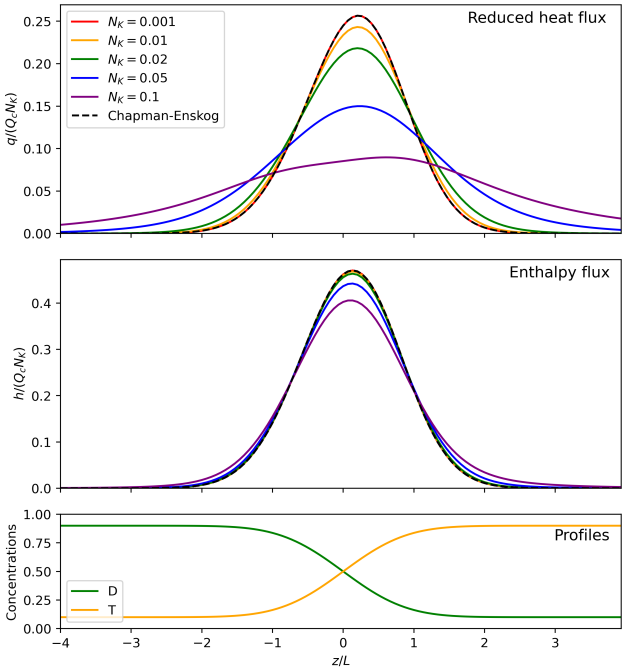
As well as the diffusive velocities contributing to the total ionic heat flux, they are also significant transport fluxes in their own right, responsible for mixing. In this section, the diffusive velocities V_α are shown for the variety of multi-species cases above to demonstrate nonlocal ordinary diffusion, thermo-diffusion, and



(a) DT ∇T



(b) DT ∇p

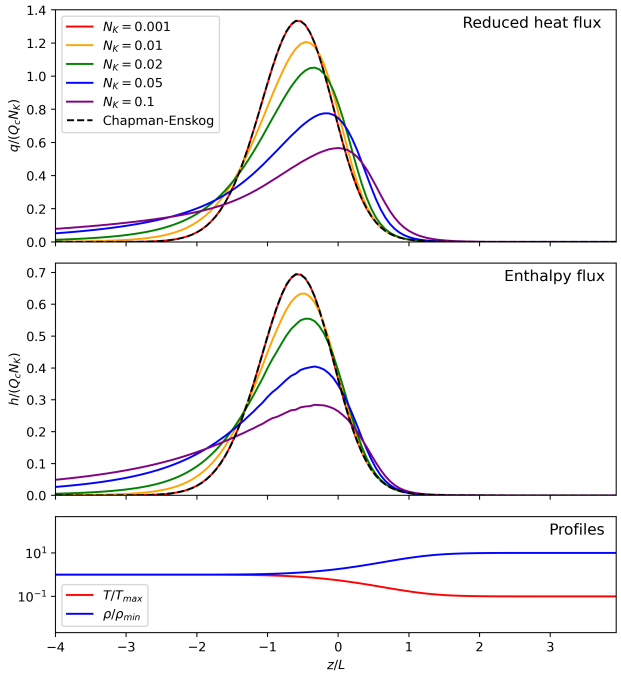


(c) DT ∇c

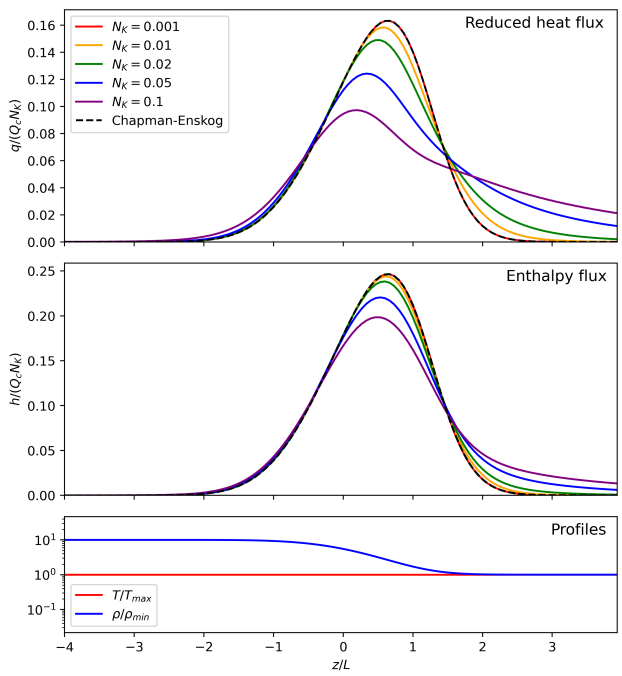
Figure 6.10: Components of heat flux for a DT mixture subject to an isolated temperature gradient (a), isolated pressure gradient (b), and isolated concentration gradient (c). The relevant profiles are shown at the bottom of each subfigure, with undisplayed profiles being fixed constant at unity or concentrations at 0.5. Results for $N_K \leq 0.01$ are not visible owing to strong agreement with the local result. Reproduced from [1].

baro-diffusion in symmetric and asymmetric mixtures.

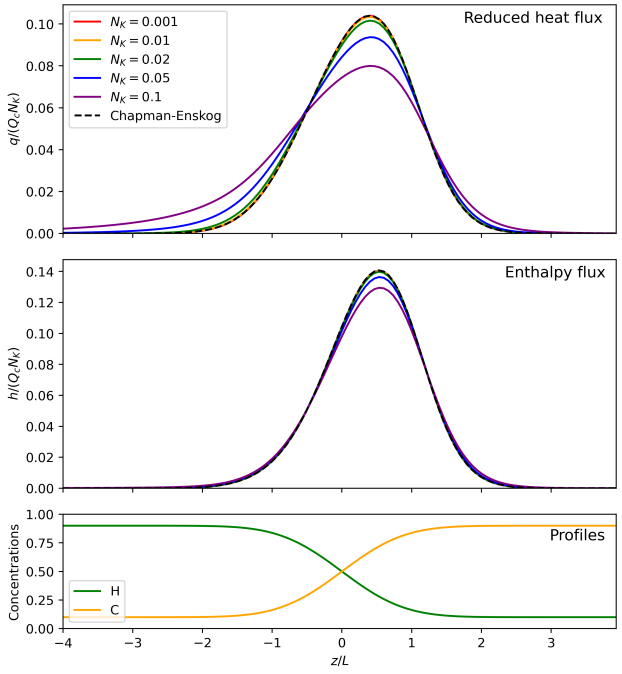
Figure 6.12 shows the local and nonlocal diffusive velocities V_α for a DT and CH_2 mixture subject to a



(a) CH_2 ∇T



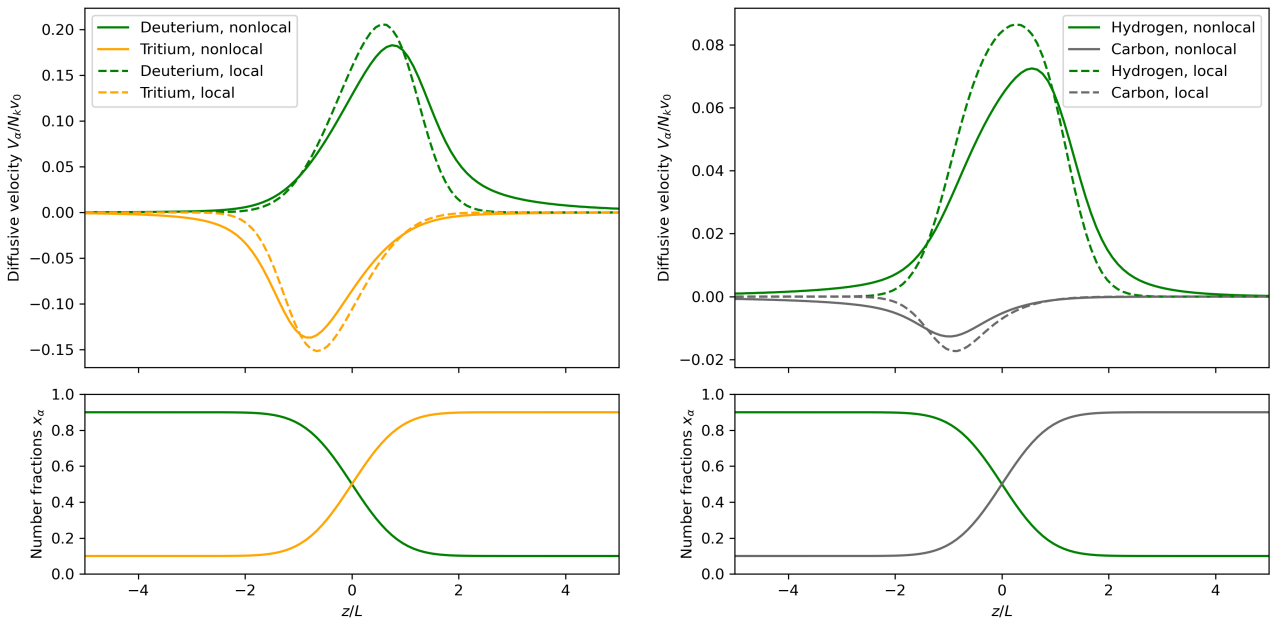
(b) CH_2 ∇p



(c) CH_2 ∇c

Figure 6.11: Components of heat flux for a CH_2 mixture subject to an isolated temperature gradient (a), isolated pressure gradient (b), and isolated concentration gradient (c). The shape of the relevant profiles are shown at the bottom of each subfigure, with undisplayed pressure or temperature profiles being fixed constant at unity or concentrations such that $n_H/n_C = 2$. Reproduced from [1].

gradient in the number fraction $x_\alpha = n_\alpha/n_i$, similar to the ∇c cases in the previous section. The two species diffuse into each other, therefore the diffusive velocity of the lighter species is positive. It has been verified



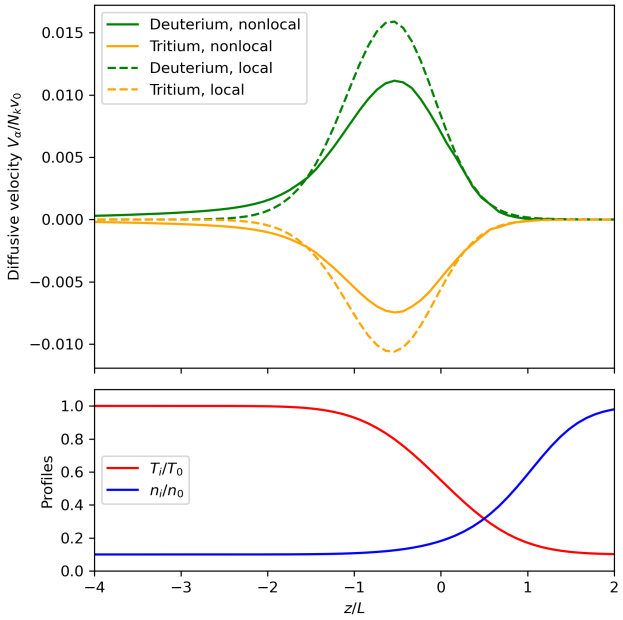
(a) DT ∇x **(b)** CH_2 ∇x

Figure 6.12: Diffusive velocities due to sharp number fraction gradient in symmetric DT mixture and asymmetric CH_2 mixture, showing the nonlocal RKM solution (solid lines) and the local analytic solution (dashed lines). The Knudsen numbers in the nonlocal cases are chosen as $N_K^{\mathrm{DD}} = 0.2$ and $N_K^{\mathrm{HH}} = 1$ in the DT and CH_2 mixtures, respectively.

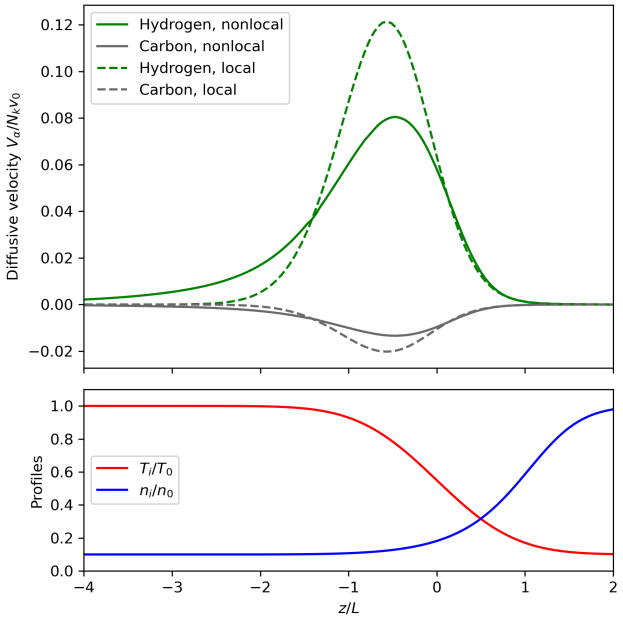
that $\sum_\alpha \rho_\alpha V_\alpha = 0$ in all cases, so the zero-flow constraint is being correctly enforced.

Nonlocal effects give rise to a significant 'preheat' in the diffusive velocity V_α due to suprathermal ions of each species streaming across the gradient region. In the DT case, the diffusive velocities of the two species are near symmetric since the species have similar masses $m_T/m_D \approx 3/2$ and identical charges $Z_T = Z_D = 1$. In the CH_2 case, the hydrogen species diffusive velocity is greater than the carbon diffusive velocity due to the large mass ratio. The CH_2 case is an idealised model of an ablator-fuel boundary that is very often present in ICF implosions. The significantly enhanced carbon diffusion into the hydrogen at negative z is particularly impactful. In an implosion, this kinetic mix deposits high-Z material into the fuel which dramatically enhances radiative losses and degrades yield. In addition, since the effective ionisation relevant to electron transport is $Z^* = \langle Z^2 \rangle / \langle Z \rangle$, even a small amount of high-Z material can dramatically enhance the effective ionisation and significantly impact electron transport, typically suppressing electron heat flow.

Figures 6.13 and 6.14 show nonlocal diffusive velocities for DT and CH_2 cases, but due to a temperature gradient and pressure gradient, respectively. Nonlocal effects on thermo-diffusion and baro-diffusion are clearly present with significant enhancement of the fluxes away from the main gradient region. In symmetric mixtures such as DT, both thermo-diffusion and baro-diffusion are considered to be weak and often insignificant effects. This is quantified by the smallness of the thermo-diffusion and baro-diffusion ratios k_T and k_p for symmetric mixtures [127]. However, nonlocal effects can cause both these effects to become significant away from the boundary relative to the local result where they may have a greater impact.

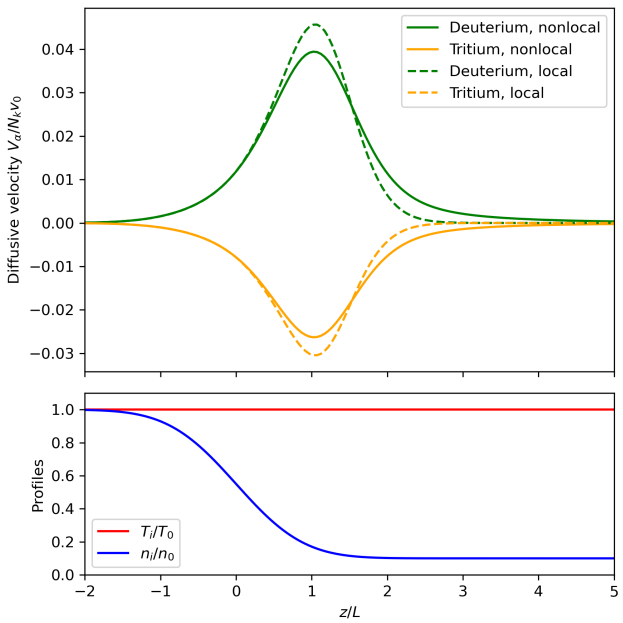


(a) DT ∇T

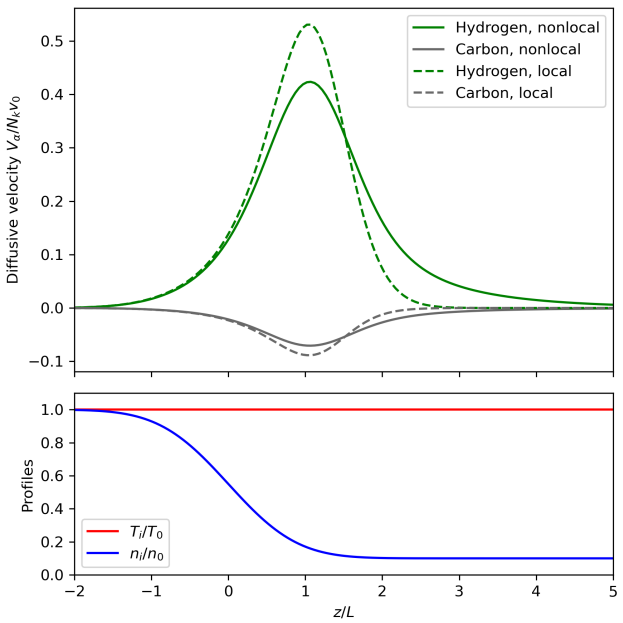


(b) CH_2 ∇T

Figure 6.13: Diffusive velocities due to sharp temperature gradient in symmetric DT mixture and asymmetric CH_2 mixture, showing the nonlocal RKM solution (solid lines) and the local analytic solution (dashed lines). The Knudsen numbers in the nonlocal cases are chosen as $N_K^{\mathrm{DD}} = 0.2$ and $N_K^{\mathrm{HH}} = 1$ in the DT and CH_2 mixtures, respectively.

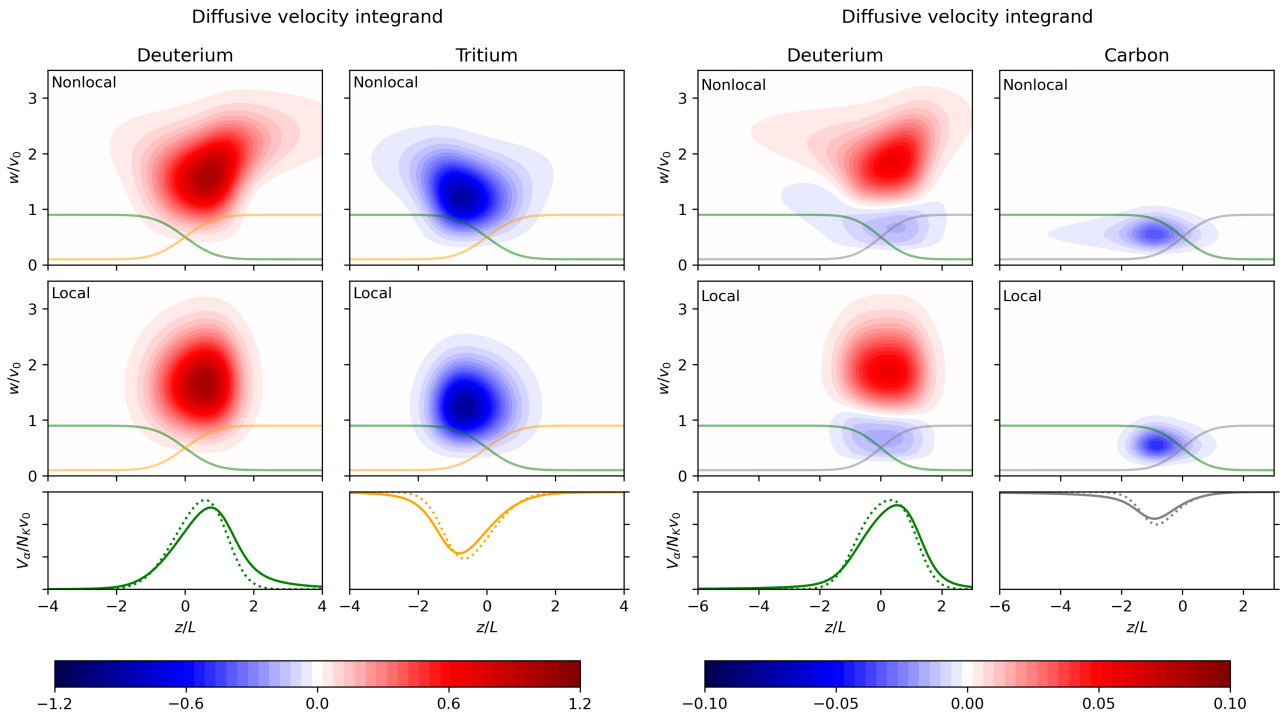


(a) DT ∇p



(b) CH_2 ∇p

Figure 6.14: Nonlocal diffusive velocities due to sharp pressure gradient in symmetric DT mixture and asymmetric CH_2 mixture, showing the nonlocal RKM solution (solid lines) and the local analytic solution (dashed lines). The Knudsen numbers in the nonlocal cases are chosen as $N_K^{\mathrm{DD}} = 0.2$ and $N_K^{\mathrm{HH}} = 1$ in the DT and CH_2 mixtures, respectively.



(a) DT ∇x **(b)** CH_2 ∇x

Figure 6.15: Integrand of diffusive velocity $\frac{1}{N_K}\frac{dV_\alpha}{dw}$ from the same case as Figure 6.12 with a number fraction gradient. The number fraction profiles are overlaid on the heatmaps for deuterium (orange), tritium (green), and carbon (grey).

Figure 6.15 shows the integrands of the diffusive velocities for the cases with a gradient in number fraction. In the DT case, the similarity of the two species results in similar diffusion profiles streaming into each other. In the nonlocal case, thermal ions behave similarly to the local case, but nonlocal beam features are gained for suprathermal ions. This causes deuterons and tritons to counter-stream into each other. In the asymmetric CH_2 case, the carbon ions gain a sharp beam feature that streams much further into the hydrogen than the local case. As discussed above, even a relatively small population of high-Z ions can cause significant disturbances to both radiative losses and electron transport.

6.7 Multi-Species Transport with Ion-Electron Collisions

Having separately considered the impact of ion-electron collisions in the single-species case and then multi-species transport, here the two effects are considered together.

For a binary mixture, the additional fluid variable gained by considering multiple species is the mass concentration of the lighter species $c = \rho_l/\rho_i$ which evolves according to its hydrodynamic equation

$$\partial_t c + \boldsymbol{u}_i \cdot \boldsymbol{\nabla} c + \frac{1}{\rho_i}\boldsymbol{\nabla}\cdot\boldsymbol{i} = 0, \tag{6.14}$$

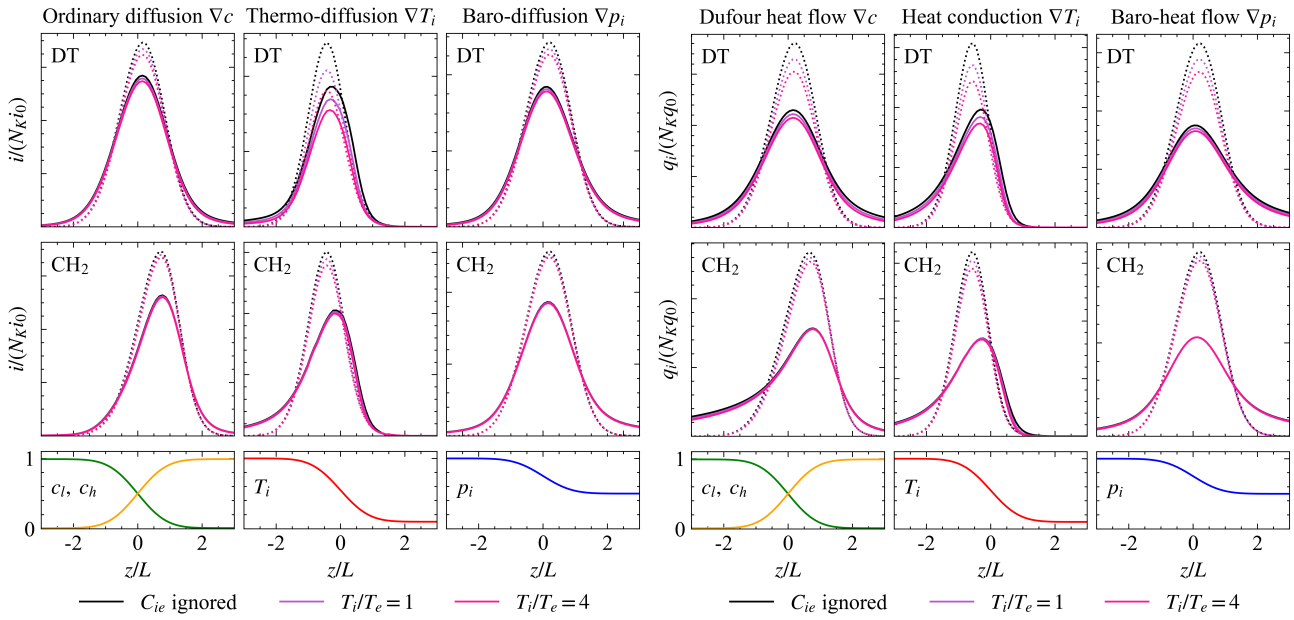
where $\boldsymbol{i} = \rho_l(\boldsymbol{u}_l - \boldsymbol{u}_i)$ is the diffusive mass flux. Its local result may be written in the Landau form [16, 96, 127]

$$\boldsymbol{i}^{\text{local}} = -\rho_i D\Big(\underbrace{\boldsymbol{\nabla} c}_{\substack{\text{Ordinary}\\ \text{diffusion}}} + \underbrace{k_p \boldsymbol{\nabla}\ln p_i}_{\substack{\text{Baro-}\\ \text{diffusion}}} + \underbrace{k_T \boldsymbol{\nabla}\ln T_i}_{\substack{\text{Thermo-}\\ \text{diffusion}}}\Big), \tag{6.15}$$

where D is the ordinary diffusion coefficient, and k_T and k_p are the thermo- and baro-diffusion ratios, respectively. This form emphasises that diffusion is not only driven by concentration gradients, but also temperature and pressure gradients. Here, cases with no electric field are considered so the electro-diffusion term present in previous chapters is ignored. The ion heat flux may be written in an analogous form

$$\boldsymbol{q}_i^{\text{local}} = -T_i \kappa_i \Big(\underbrace{\boldsymbol{\nabla} \ln T_i}_{\substack{\text{Thermal} \\ \text{conduction}}} + \underbrace{h_c \boldsymbol{\nabla} c}_{\substack{\text{Dufour} \\ \text{heat flow}}} + \underbrace{h_p \boldsymbol{\nabla} \ln p_i}_{\substack{\text{Baro-} \\ \text{heat flow}}} \Big), \tag{6.16}$$

where κ_i is the total heat conductivity of the ionic mixture and the dimensionless coefficients h_c and h_p are introduced in a similar manner to the thermo- and baro-diffusion ratios. Ion heat flow in mixtures is then not only driven by temperature gradients, but also concentration gradients and pressure gradients. We then investigate the impact of ion-electron collisions on local and nonlocal multi-species transport in symmetric versus asymmetric mixtures.



(a) Diffusive mass flux $\boldsymbol{i}$ **(b)** Mixture heat flux $\boldsymbol{q}_i$

Figure 6.16: Diffusive mass flux and mixture heat flux for a symmetric DT and asymmetric CH_2 mixture, in three cases driven by a concentration gradient ∇c, temperature gradient ∇T_i, and pressure gradient ∇p_i. Dotted and solid lines correspond to local and nonlocal results, respectively. The line colour indicates the ion-electron temperature ratio, with differences arising due solely to ion-electron collisions. Reproduced from [4].

Figure 6.16a shows the diffusive mass flux $\boldsymbol{i}$ driven by a concentration gradient, temperature gradient, and pressure gradient in a symmetric DT and asymmetric CH_2 mixture. In each case, the other two profiles are uniform so their thermodynamic drives are zero; for example, in the ∇c case, the total ion temperature and pressure are uniform, and in the ∇T_i case, the concentrations and total ion pressure are uniform. The electric field is set to zero in all cases to provide consistency. In the nonlocal cases, the length scale L of the step is chosen such that $N_K^{\text{DD}} = 0.2$ and $N_K^{\text{HH}} = 1$ in the DT and CH_2 cases, respectively. Although these

Knudsen numbers may seem relatively large, the other species (T or C) provides additional collisionality not accounted for in this definition of the Knudsen number. In most cases, the diffusive mass flux is insensitive to ion-electron collisions for equal temperatures $T_i/T_e = 1$. This is expected, since ion-electron collisions are more relevant in the tail of the distribution, whereas the diffusive mass flux is a lower moment of the velocity distribution than other quantities such as the heat flux. The exception is thermo-diffusion in the symmetric DT case, where the local diffusive mass flux is reduced by 15% for equal temperatures when ion-electron collisions are accounted for, and by 25% with $T_i/T_e = 4$. For this higher temperature ratio $T_i/T_e = 4$, ordinary and baro-diffusion remain mostly unaffected by ion-electron collisions. In the local case, the impacts on ordinary diffusion and baro-diffusion are identical to each other. This is expected since the baro-diffusion coefficient k_p is purely thermodynamic, with collisions entering only through the ordinary diffusion coefficient D.

Figure 6.16b shows the total ion heat flux q_i for the same three cases shown in Figure 6.16a. Ion-electron collisions still have only a minor effect on the heat flow for equal ion-electron temperatures. The correction in the symmetric DT case is noticeable for all three thermodynamic drives, with a suppression of 10%, rising to 20% for $T_i/T_e = 4$. In the nonlocal cases, the reductions of the heat fluxes due to ion-electron collisions are similar to the corresponding local results.

CHAPTER 7

Discussion

7.1 Summary of Results

7.1.1 Reduced kinetic method

A reduced kinetic method (RKM) suitable for use as a nonlocal transport closure is derived from first principles, including magnetic fields and multi-species effects. The RKM solves a linear form of the VFP equation with the Fokker-Planck collision operator. The RKM is shown to reproduce all classical (Braginskii-like) transport terms in the highly collisional limit, including magnetised and multi-species effects. In the nonlocal cases, the implemented collision operator has been validated *a posteriori*, with Rosenbluth potentials deviating by $\lesssim 10\%$ from their Maxwellian forms for $N_K \lesssim 1$.

7.1.2 Nonlocal electron transport

Magneto-inertial schemes such as MagLIF [59, 60], Fusion via Low-power Assembly and Rapid Excitation (FLARE) [64], and pulsed magnetic ICF [62] are a promising approach to confined fusion for energy production. These approaches apply external magnetic fields to suppress electron heat conduction or use the $\boldsymbol{j} \times \boldsymbol{B}$ force to compress cylindrical liners to approach the high densities and temperatures required to achieve thermonuclear burn. Even in unmagnetised ICF implosions, the Biermann battery effect can spontaneously generate magnetic fields strong enough to magnetise the plasma [68]. Correct modelling of magnetised transport within simulations of ICF implosions is therefore increasingly important for the path towards inertial fusion energy.

In Chapter 5, the standard nonlocal behaviour of the unmagnetised electron conductive heat flux is demonstrated, where a sharp temperature gradient results in a nonlocal heat flux with an inhibited peak flux and preheats away from the main gradient. Introducing a perpendicular magnetic field suppresses nonlocal effects on the conductive heat flux along the temperature gradient. The magnetic field also introduces the

Righi-Leduc heat flow, which is more sensitive to nonlocal effects than its perpendicular counterpart. Similarly, nonlocal effects are also present on the thermal force and Nernst term.

As well as considering a temperature gradient to investigate nonlocality of temperature-gradient-driven transport, a current profile of different length scales is also studied. These cases demonstrate similar nonlocal effects on current-driven transport, namely the Peltier and Ettingshausen heat flows and electron-ion friction and cross friction.

Strong magnetic fields $\chi \gg 1$ suppress nonlocal behaviour, restoring transport fluxes back to their magnetised local results. For strong magnetisation, it is typically the 'cross' components such as the Righi-Leduc heat flow that dominate over their perpendicular counterparts. At sufficiently high Knudsen numbers, nonlocal effects then reemerge on these cross components.

Current-driven electron heat flux $\boldsymbol{q}_e^u$ becomes nonlocal in the presence of relatively weak spatial gradients with Knudsen numbers $1/100 \lesssim N_K \lesssim 1$, similarly to the conductive heat flux $\boldsymbol{q}_e^T$. Furthermore, a novel nonlocal modification to $\boldsymbol{q}_e^u$ has been found [2], which is driven by a relatively weak electron flow $N_u \equiv |\boldsymbol{u}_e - \boldsymbol{u}_i|/v_{\mathrm{th},e} \gtrsim 1/100$, as opposed to $N_u \gtrsim 1$. The underlying physics has been both captured with a first-principles kinetic model and explained qualitatively and can significantly modify and enhance Ettingshausen heat flow. Such effects may be especially relevant for a variety of collisional plasmas such as plasma staircases [128], dense Z-pinches [129, 130], and ICF implosions [68, 131] where current-driven transport has a notable effect on hydrodynamic evolution and therefore yield.

An alternative formulation of the RKM is also presented, solving for the nonlocal deviation of the DF g rather than the deviation from Maxwellian δf. When solving for δf and discarding the field-particle operator for computational efficiency, both local and nonlocal transport results are noticeably different from their nearly exact counterparts obtained with the full δf method of the previous paragraph. However, when solving for the nonlocal deviation g, both local and nonlocal transport results are found to be unchanged if the field-particle operator is discarded, therefore neglecting it is well justified. The resulting equation for g, with the test-particle collision operator, is more computationally tractable and well suited to act as a nonlocal transport closure.

Full kinetic simulations usually serve as numerical experiments for investigating nonlocal transport rather than closures. Consider using a full VFP simulation to study nonlocal transport in the temperature gradient case of Section 5.1. The DF would be initialised as a Maxwellian distribution with a temperature varying across space. When the simulation is run, the DF evolves to gain an anisotropic component, which relaxes over a few collision times to a quasi-stationary result. For initial profiles with low Knudsen numbers, this quasi-stationary result should match the local Chapman-Enskog solution at each point in space. For large initial Knudsen numbers, the quasi-stationary solution will include nonlocal effects of interest; however, the temperature gradient will partially relax on a similar timescale to the initial relaxation to the quasi-stationary result. The heat flow in this nonlocal case then corresponds to the partially relaxed temperature profile rather than the initial temperature profile. It is then difficult for a full VFP code to provide a robust comparison between different Knudsen numbers for the same shape of profile, a more detailed parameter scan over different

temperature profiles, or as a transport closure to a fluid code. In addition, the DF will also gain some nonzero flow profile during the initial relaxation period. This flow should itself drive heat flow, which cannot be distinguished from the conductive heat flow when integrating over the DF. Some approaches may counteract this by adding sources or sinks of particle number, momentum, or energy to constrain the DF to have the same density, flow, and temperature throughout the initial relaxation period. However, it is not clear if these constraints themselves modify the physics of the heat flow. The initial Maxwellian condition can also lead to strange behaviour of the simulation at early times such as oscillating heat flow [106, 132] and therefore cooling of cold regions. Since the RKM evaluates the DF from the instantaneous fluid profiles, it does not have this issue when finding nonlocal heat flow from hydrodynamic profiles. The RKM could instead be used to initialise the DF accounting for nonlocal effects in full VFP codes to avoid this strange behaviour.

Full kinetic approaches are integrated simulations which do not allow for different nonlocal effects to be clearly studied in isolation, in contrast to the RKM where these effects may be isolated by removing the appropriate terms from the DF equation when solving. For example, a full VFP code is not able to separate out heat flow contributions from temperature gradients versus currents. In the RKM, these correspond to two distinct thermodynamic driving forces, therefore the conductive and current-driven heat flows can be found independently for the same hydrodynamic profiles. This provides a clearer decoupled insight into how different parts of the input hydrodynamic profiles give rise to different nonlocal features.

7.1.3 Nonlocal ion transport

The RKM expands up to an arbitrary order in spherical harmonics, therefore the viscous stress tensor is naturally included in this description. The ion rather than electron viscous stress is presented, since ion viscous effects typically dominate over electron viscous effects. Nonlocal behaviour of the ion viscous stress tensor appears due to sharp shearing ion flows. A magnetic field then suppresses nonlocal effects of the ordinary viscous stress tensor, but also introduces a gyroviscous component which, analogously to the Righi-Leduc heat flow, is more sensitive to these nonlocal effects.

Novel nonlocal features are recovered for the multi-species ion heat transport due to additional thermodynamic drives such as concentration gradients and diffusion of different species in the CoM frame. Results for DFs and heat fluxes in local cases reproduce the analytic results of the Chapman-Enskog expansion [16, 72] for multi-species ion heat flux. Expected qualitative features of nonlocal effects are demonstrated, in particular suppression of the peak heat flux and enhancement of heat flux away from regions of steep gradient. In multi-species cases, nonlocal effects are demonstrated from gradients in temperature, concentration, and pressure, with some cases giving rise to large heat fluxes far away from the gradient region where the local result is small. The multi-species heat flux has been decomposed into two components, the reduced heat flux and enthalpy flux, where the former is the quantity typically employed in hydrodynamic codes and the latter is an inherently multi-species feature due to relative dynamics of the species in the CoM frame. In cases with pressure or concentration gradients, the enthalpy flux is particularly insensitive to nonlocal effects, thus

becoming increasingly important in comparison to the reduced heat flux for high Knudsen numbers.

The ion heat flux, viscous stress, and diffusive mass flux are significantly influenced by ion-electron collisions in nonlocal cases, similarly to their behaviour in the local limit. The RKM captures this effect in a first-principles framework, and to the author's knowledge is the only nonlocal closure that describes ion transport and viscous stress. The nonlocal peak heat flow has minor but noticeable modifications from ion-electron collisions, whereas nonlocal preheats are strongly suppressed by ion-electron collisions even for equal ion-electron temperatures. The nonlocal viscous stress is also reduced at its peak by ion-electron collisions, however the enhanced stress away from the gradient is not noticeably affected. Such effects on ion heat transport are particularly relevant to both inertially and magnetically confined fusion plasmas where magnetic fields suppress electron heat flow and high ion temperatures allow ion heat flow to dominate energy transport and collective plasma behaviour. Since ion viscous effects typically dominate over electron viscous effects, nonlocal viscous stress is more broadly relevant to astrophysical and confined fusion plasmas. The impact on the diffusive mass flux is especially significant in confined fusion plasmas, where different species such as deuterium and tritium can separate in space or high-Z impurities can contaminate the fusing plasma, increasing radiative losses and degrading confinement.

7.2 Future Implications

A clear application of the RKM is integration as a transport closure into a full fluid code in a single and then multiple spatial dimensions. This hybrid RKM-fluid approach would allow fluid simulations of fusion plasmas to capture important kinetic effects while remaining more computationally tractable than current state-of-the-art approaches such as full VFP or PIC simulations. This hybrid framework is of intrinsic physical interest since it pushes the limits of fluid closures, but also of wider interest to the fusion community for integrated simulations of fusion plasmas.

The RKM is ideal for training a surrogate nonlocal closure based on machine learning (ML) techniques for a particularly computationally efficient transport closure. ML transport closures have been developed in other studies. The training sets used in these studies are typically obtained from full VFP or PIC simulations. These approaches are computationally expensive, limiting the size and diversity of the training datasets they can produce. They also face previously discussed limitations such as being explicitly time-dependent simulations, and therefore cannot provide the heat flow for a prescribed temperature profile, only relaxed profiles at later timesteps. The RKM is not subject to these limitations, and is therefore very well suited to providing a dataset to train an ML closure. Alternatively, the set of PDEs that govern the RKM could themselves train a ML method to find a reduced effective PDE that can be solved, leaving a tractable ML closure.

A hybrid RKM-fluid framework for multi-species plasmas would lead naturally to investigating the intersection of multi-species and kinetic effects. Comparisons between multi-fluid, fluid mixture, and multi-species VFP descriptions could be conducted in both local and nonlocal regimes, greatly improving understanding of the significance of various multi-species transport effects in fusion plasmas and the suitability of these

different descriptions for capturing those effects. The RKM-fluid approach would further the physical accuracy and validity of fluid simulations to modelling confined fusion plasmas.

The goal of a confined plasma is to achieve a high fusion yield, and therefore the fusion reactivity must be properly understood and modelled. Reactivity, like transport, is subject to nonlocal effects which often degrade yield [37, 133]. Neutron spectra, also influenced by nonlocal effects, are produced by fusion reactions and are a key diagnostic for burning plasmas by which parameters such as ion temperature can be inferred [134–137]. To improve understanding of inferred quantities from spectra measurements, nonlocal behaviour must be better understood and modelled. Although nonlocal transport is currently the main motivation and application of the RKM, the approach could also have utility in studying reactivity and neutron spectra subject to nonlocal effects. Comparisons of the RKM predictions with yield and neutron spectra from experiments such as NIF implosions would improve links between these measured observables and plasma dynamics, which in turn improves interpretation of measurements and design of confined fusion schemes.

Laser heating of ICF plasmas is often so strong that inverse bremsstrahlung (IB) heating deviates the electron distribution significantly away from Maxwellian and towards a more general super-Gaussian distribution. Underlying transport processes are then modified, not only changing properties such as the thermal conductivity of the plasma but also introducing new transport mechanisms such as pressure-gradient-driven heat flow. Local transport closures for transport in IB-heated plasmas have been found by Ridgers et al. [138]. However, IB-heated plasmas are often sufficiently hot that transport becomes nonlocal. The RKM is the ideal candidate for being extended to describe nonlocal transport in IB-heated plasmas, which would be of interest from a fundamental physics perspective as well as to ICF. These effects are increasingly relevant to modern ICF approaches as laser power and maximum plasma temperature increase, and therefore it is essential to correctly understand and model them in hydrodynamic simulations of fusion plasmas.

Another interesting mathematical problem lying at the interface of kinetic theory and hydrodynamics is determining the structure of shock waves [124]. This is essentially a 1D boundary value problem, but one rich in interesting mathematical features. These include multiple boundary layers connected with matched asymptotics and self-similar behaviour for internal layers. Since the width of the layers is determined by transport processes, the smallest scales are on the order of the mean free path and therefore the Knudsen number is often order unity, where these local transport closures break down. Shock structure is either studied as a stationary fluid problem, where the mathematical structure is clear but closures are invalid, or using full time-dependent kinetic simulations which do not provide a clear insight into the underlying mathematical behaviour. With the RKM developed, shock structure can be studied with a nonlocal transport closure. This approach preserves the many insightful mathematical features of the stationary approach while resolving the problem of transport closures becoming invalid in the shock interior.

As previously mentioned, the RKM could also have applications in modelling and studying MCF plasmas. One of the key issues facing MCF for energy production is the extreme heat loads delivered to the divertor target. No known material can tolerate the heat fluxes projected for power-plant-scale tokamaks. A potential

resolution to this issue is detachment [139], where a buffer region of neutral gas or vapour is maintained between the upstream plasma and target, dissipating the incident heat volumetrically rather than on the surface. An issue facing this approach is the transport of unwanted impurities from the divertor upstream into the core plasma. Accurate modelling of both heat flow and species mixing in detached divertor schemes is therefore essential to their design and optimisation. Divertors are challenging to model partly due to their marginal collisionality. Even where collisions are significant for the thermal bulk of the plasma, particles with mean free paths comparable to the length scales of the divertor may stream and transport momentum, heat, and impurities nonlocally. This nonlocal transport is not captured by diffusive transport closures for species diffusion and heat conduction. Full kinetic descriptions do capture nonlocal transport, but simulations within these frameworks are computationally expensive and often intractable for parameter scans and optimisation. The RKM is an ideal intermediate approach that is computationally efficient while capturing the relevant kinetic physics. RKM studies would provide great physical insight into heat load and impurity mitigation in detached divertors, improving the feasibility of tokamaks for energy production.

7.3 Final Remarks

Nonlocal transport in plasmas is a topic of great importance in both fundamental plasma physics and confined fusion modelling. This thesis has presented a novel first-principles RKM that captures the nonlocal behaviour of the whole suite of different transport fluxes, and has applied it to uncover several previously unrecognised or unstudied features of nonlocal transport in plasmas. The natural next step of this work is to integrate the RKM into fluid simulations of confined fusion schemes, which will have a clear application and impact on modelling, understanding, and optimising confined fusion schemes for energy production.

APPENDIX A

Fluid Equations for Ionic Mixtures

A.1 Definitions of Hydrodynamic Quantities

The number density and flow velocity of species α are defined as

$$n_\alpha = \int d^3\boldsymbol{v}\ f_\alpha, \quad \boldsymbol{u}_\alpha = \frac{1}{n_\alpha}\int d^3\boldsymbol{v}\ \boldsymbol{v} f_\alpha. \tag{A.1}$$

The mass density of species α is simply $\rho_\alpha = m_\alpha n_\alpha$. The total ion mass and number densities of the ionic mixture are then $\rho_i = \sum_\alpha \rho_\alpha$ and $n_i = \sum_\alpha n_\alpha$. The mass concentrations are then defined as $c_\alpha = \rho_\alpha/\rho_i$, satisfying $\sum_\alpha c_\alpha = 1$ by definition. For the ionic mixture, it is convenient to define the centre-of-mass (or hydrodynamic) velocity and diffusive velocities

$$\boldsymbol{u}_i = \sum_\alpha c_\alpha \boldsymbol{u}_\alpha, \quad \boldsymbol{V}_\alpha = \boldsymbol{u}_\alpha - \boldsymbol{u}_i = \frac{1}{n_\alpha}\int d^3\boldsymbol{v}\ (\boldsymbol{v} - \boldsymbol{u}_i) f_\alpha. \tag{A.2}$$

Often the diffusive mass flux $\boldsymbol{i}_\alpha = \rho_\alpha \boldsymbol{V}_\alpha$ is considered rather than the diffusive velocity $\boldsymbol{V}_\alpha$.

The total energy of the ionic mixture in the laboratory frame is

$$\mathcal{E}_i = \sum_\alpha \int d^3\boldsymbol{v}\ \frac{1}{2} m_\alpha v^2 f_\alpha. \tag{A.3}$$

By rewriting in terms of the peculiar velocity $\boldsymbol{w} = \boldsymbol{v} - \boldsymbol{u}_i$, the total energy may be rewritten as

$$\begin{aligned}\mathcal{E}_i &= \underbrace{\sum_\alpha \int d^3\boldsymbol{w}\ \frac{1}{2} m_\alpha w^2 f_\alpha}_{\coloneqq \frac{3}{2} n_i T_i} + \boldsymbol{u}_i \cdot \underbrace{\sum_\alpha m_\alpha \int d^3\boldsymbol{w}\ \boldsymbol{w} f_\alpha}_{=\sum_\alpha \rho_\alpha \boldsymbol{V}_\alpha = 0} + \frac{1}{2} u_i^2 \sum_\alpha m_\alpha \underbrace{\int d^3\boldsymbol{w}\ f_\alpha}_{=n_\alpha} \\ &= \frac{3}{2} n_i T_i + \frac{1}{2}\rho_i u_i^2,\end{aligned} \tag{A.4}$$

where the ion temperature is defined as

$$T_i = \frac{2}{3 n_i}\sum_\alpha \int d^3\boldsymbol{w}\ \frac{1}{2} m_\alpha w^2 f_\alpha. \tag{A.5}$$

A ideal equation of state for the ion and electron pressures $p_i = n_i T_i$ and $p_e = n_e T_e$ are assumed.

A.2 Mass Continuity Equations

Integrating the VFP equation (2.31) over velocity space,

$$\partial_t \int d^3\boldsymbol{v}\; f_\alpha + \boldsymbol{\nabla}\cdot\int d^3\boldsymbol{v}\; \boldsymbol{v} f_\alpha + \int d^3\boldsymbol{v}\; \boldsymbol{\nabla}_{\boldsymbol{v}}\cdot\frac{q_\alpha}{m_\alpha}(\boldsymbol{E}+\boldsymbol{v}\times\boldsymbol{B})f_\alpha = \sum_\beta \int d^3\boldsymbol{v}\; C_{\alpha\beta}\{f_\alpha, f_\beta\}. \tag{A.6}$$

The Lorentz force term vanishes from the divergence theorem since $f_\alpha \to 0$ as $v\to\infty$. Multiplying by m_α and using the appropriate fluid quantities and conservation properties of the collision operator defined earlier, this then yields the mass continuity equation for species α

$$\partial_t \rho_\alpha + \boldsymbol{\nabla}\cdot[\rho_\alpha(\boldsymbol{u}_i + \boldsymbol{V}_\alpha)] = 0. \tag{A.7}$$

A.3 Momentum Equation

Multiplying 2.31 by $m_\alpha \boldsymbol{v}$, summing α over ion species, and integrating over velocity space gives

$$\begin{aligned}\partial_t \underbrace{\sum_\alpha m_\alpha \int d^3\boldsymbol{v}\; \boldsymbol{v} f_\alpha}_{=\sum_\alpha \rho_\alpha \boldsymbol{u}_\alpha = \rho_i \boldsymbol{u}_i} + \boldsymbol{\nabla}\cdot\sum_\alpha m_\alpha \int d^3\boldsymbol{v}\; \boldsymbol{v}\boldsymbol{v} f_\alpha + \sum_\alpha \int d^3\boldsymbol{v}\; m_\alpha \boldsymbol{v}\boldsymbol{\nabla}_{\boldsymbol{v}}\cdot\frac{q_\alpha}{m_\alpha}(\boldsymbol{E}+\boldsymbol{v}\times\boldsymbol{B})f_\alpha \\ = \sum_\alpha\sum_\beta m_\alpha \int d^3\boldsymbol{v}\; \boldsymbol{v} C_{\alpha\beta}\{f_\alpha, f_\beta\}.\end{aligned} \tag{A.8}$$

Rewriting the term inside the spatial divergence using peculiar velocities,

$$\begin{aligned}\sum_\alpha m_\alpha \int d^3\boldsymbol{v}\; \boldsymbol{v}\boldsymbol{v} f_\alpha &= \sum_\alpha m_\alpha \int d^3\boldsymbol{w}\; (\boldsymbol{w}+\boldsymbol{u}_i)(\boldsymbol{w}+\boldsymbol{u}_i) f_\alpha \\ &= \underbrace{\sum_\alpha m_\alpha \int d^3\boldsymbol{w}\; \boldsymbol{w}\boldsymbol{w} f_\alpha}_{:=\mathrm{P}_i} + \boldsymbol{u}_i \underbrace{\sum_\alpha m_\alpha \int d^3\boldsymbol{w}\; \boldsymbol{w} f_\alpha}_{=0} \\ &\quad + \underbrace{\sum_\alpha m_\alpha \int d^3\boldsymbol{w}\; \boldsymbol{w} f_\alpha}_{=0}\boldsymbol{u}_i + \boldsymbol{u}_i\boldsymbol{u}_i \underbrace{\sum_\alpha m_\alpha \int d^3\boldsymbol{w}\; f_\alpha}_{=\rho_i} \\ &= \rho_i \boldsymbol{u}_i\boldsymbol{u}_i + \mathrm{P}_i,\end{aligned} \tag{A.9}$$

where the ion pressure tensor

$$\mathrm{P}_i = \sum_\alpha m_\alpha \int d^3\boldsymbol{w}\; \boldsymbol{w}\boldsymbol{w} f_\alpha. \tag{A.10}$$

The pressure tensor is often decomposed into the isotropic component plus the viscous stress tensor as

$$\mathrm{P}_i = p_i \mathrm{I} + \Pi_i, \quad \text{where} \quad p_i = \frac{1}{3}\mathrm{Tr}(\mathrm{P}_i), \quad \Pi_i = \sum_\alpha m_\alpha \int d^3\boldsymbol{w}\left(\boldsymbol{w}\boldsymbol{w} - \frac{1}{3}w^2\mathrm{I}\right) f_\alpha. \tag{A.11}$$

The Lorentz force term may be evaluated by parts as

$$\begin{aligned}\sum_\alpha q_\alpha \int d^3\boldsymbol{v}\; \boldsymbol{v}\boldsymbol{\nabla}_{\boldsymbol{v}}\cdot(\boldsymbol{E}+\boldsymbol{v}\times\boldsymbol{B}) f_\alpha &= -\sum_\alpha q_\alpha \int d^3\boldsymbol{v}\; (\boldsymbol{E}+\boldsymbol{v}\times\boldsymbol{B}) f_\alpha \\ &= -\sum_\alpha q_\alpha n_\alpha (\boldsymbol{E}+\boldsymbol{u}_i\times\boldsymbol{B}) - \sum_\alpha q_\alpha n_\alpha \boldsymbol{V}_\alpha\times\boldsymbol{B} \\ &= -\boldsymbol{F}_i - \boldsymbol{j}_D\times\boldsymbol{B},\end{aligned} \tag{A.12}$$

where we define the force on the ion mixture and the ion charge density

$$\boldsymbol{F}_i = \sigma_i(\boldsymbol{E} + \boldsymbol{u}_i \times \boldsymbol{B}), \quad \sigma_i = \sum_\alpha q_\alpha n_\alpha \tag{A.13}$$

and the diffusive ion current

$$\boldsymbol{j}_D = \sum_\alpha q_\alpha n_\alpha \boldsymbol{V}_\alpha. \tag{A.14}$$

For the collision term, it is understood that the sum with index α is over ions, whereas the sum over β includes electrons. The ion-ion terms all cancel due to the momentum conservation property of the collision operator, leaving only the ion-electron momentum exchange

$$\boldsymbol{R}_i = \sum_\alpha m_\alpha \int d^3\boldsymbol{v}\ \boldsymbol{v} C_{\alpha e}\{f_\alpha, f_e\} = -\sum_\alpha m_e \int d^3\boldsymbol{v}\ \boldsymbol{v} C_{e\alpha}\{f_e, f_\alpha\} = -\boldsymbol{R}_e. \tag{A.15}$$

The momentum equation for the ionic mixture then becomes

$$\partial_t(\rho_i \boldsymbol{u}_i) + \boldsymbol{\nabla}\cdot[\rho_i \boldsymbol{u}_i \boldsymbol{u}_i + \mathrm{P}_i] = \boldsymbol{F}_i + \boldsymbol{j}_D \times \boldsymbol{B} - \boldsymbol{R}_e \tag{A.16}$$

Using the product rule on the time derivative and rewriting $\partial_t \rho_i = -\boldsymbol{\nabla}\cdot[\rho_i \boldsymbol{u}_i]$ yields

$$\rho_i \partial_t \boldsymbol{u}_i + \rho_i \boldsymbol{u}_i \cdot \boldsymbol{\nabla}\boldsymbol{u}_i = -\boldsymbol{\nabla}\cdot \mathrm{P}_i + \boldsymbol{F}_i + \boldsymbol{j}_D \times \boldsymbol{B} - \boldsymbol{R}_e \tag{A.17}$$

A.4 Pressure Equation

Multiplying 2.31 by $\frac{1}{2}m_\alpha v^2$, summing α over ion species, and integrating over velocity space gives

$$\begin{aligned}\partial_t \underbrace{\sum_\alpha \int d^3\boldsymbol{v}\ \frac{1}{2}m_\alpha v^2 f_\alpha}_{=\mathcal{E}_i} + \boldsymbol{\nabla}\cdot\sum_\alpha \int d^3\boldsymbol{v}\ \frac{1}{2}m_\alpha v^2 \boldsymbol{v} f_\alpha + \sum_\alpha q_\alpha \int d^3\boldsymbol{v}\ \frac{1}{2}v^2 \boldsymbol{\nabla}_{\boldsymbol{v}}\cdot(\boldsymbol{E} + \boldsymbol{v}\times\boldsymbol{B}) f_\alpha \\ = \sum_\alpha \sum_\beta \int d^3\boldsymbol{v}\ \frac{1}{2}m_\alpha v^2 C_{\alpha\beta}\{f_\alpha, f_\beta\}.\end{aligned} \tag{A.18}$$

The term inside the divergence may be rewritten as

$$\begin{aligned}\sum_\alpha \int d^3\boldsymbol{v}\ \frac{1}{2}m_\alpha v^2 \boldsymbol{v} f_\alpha &= \boldsymbol{u}_i \underbrace{\sum_\alpha \int d^3\boldsymbol{v}\ \frac{1}{2}m_\alpha v^2 f_\alpha}_{=\mathcal{E}_i} + \sum_\alpha \int d^3\boldsymbol{v}\ \frac{1}{2}m_\alpha v^2 \boldsymbol{w} f_\alpha \\ &= \mathcal{E}_i \boldsymbol{u}_i + \underbrace{\sum_\alpha \int d^3\boldsymbol{w}\ \frac{1}{2}m_\alpha w^2 \boldsymbol{w} f_\alpha}_{\coloneqq \boldsymbol{q}_i} + \boldsymbol{u}_i \cdot \underbrace{\sum_\alpha \int d^3\boldsymbol{w}\ m_\alpha \boldsymbol{w}\boldsymbol{w} f_\alpha}_{=\mathrm{P}_i} \\ &\quad + \frac{1}{2}u_i^2 \underbrace{\sum_\alpha \int d^3\boldsymbol{w}\ m_\alpha \boldsymbol{w} f_\alpha}_{=0} \\ &= \mathcal{E}_i \boldsymbol{u}_i + \boldsymbol{q}_i + \mathrm{P}_i \cdot \boldsymbol{u}_i,\end{aligned} \tag{A.19}$$

where the ion heat flux is defined as

$$\boldsymbol{q}_i = \sum_\alpha \int d^3\boldsymbol{w}\ \frac{1}{2} m_\alpha w^2 \boldsymbol{w} f_\alpha. \tag{A.20}$$

The force term may be evaluated by parts as

$$\begin{aligned}\sum_\alpha q_\alpha \int d^3\boldsymbol{v}\ \frac{1}{2} v^2 \boldsymbol{\nabla}_{\boldsymbol{v}} \cdot (\boldsymbol{E} + \boldsymbol{v} \times \boldsymbol{B}) f_\alpha &= -\sum_\alpha q_\alpha \int d^3\boldsymbol{v}\ \boldsymbol{v} \cdot (\boldsymbol{E} + \boldsymbol{v} \times \boldsymbol{B}) f_\alpha \\ &= -\sum_\alpha q_\alpha n_\alpha (\boldsymbol{u}_i + \boldsymbol{V}_\alpha) \cdot \boldsymbol{E} \\ &= -\boldsymbol{F}_i \cdot \boldsymbol{u}_i - \boldsymbol{j}_D \cdot \boldsymbol{E}\end{aligned} \tag{A.21}$$

The ion-ion collision terms vanish due to conservation properties of the collision operator, leaving only the ion-electron energy exchange

$$\begin{aligned}W_{ie} &= \sum_\alpha \sum_\beta \int d^3\boldsymbol{v}\ \frac{1}{2} m_\alpha v^2 C_{\alpha\beta}\{f_\alpha, f_\beta\} \\ &= \sum_\alpha \int d^3\boldsymbol{v}\ \frac{1}{2} m_\alpha v^2 C_{\alpha e}\{f_\alpha, f_e\} \\ &= \underbrace{\sum_\alpha \int d^3\boldsymbol{w}\ \frac{1}{2} m_\alpha w^2 C_{\alpha e}\{f_\alpha, f_e\}}_{\coloneqq \tilde{W}_{ie}} + \boldsymbol{u}_i \cdot \underbrace{\sum_\alpha \int d^3\boldsymbol{w}\ m_\alpha \boldsymbol{w} C_{\alpha e}\{f_\alpha, f_e\}}_{=\boldsymbol{R}_i = -\boldsymbol{R}_e} \\ &\quad + \frac{1}{2} u_i^2 \sum_\alpha \underbrace{\int d^3\boldsymbol{w}\ m_\alpha C_{\alpha e}\{f_\alpha, f_e\}}_{=0} \\ &= \tilde{W}_{ie} - \boldsymbol{R}_e \cdot \boldsymbol{u}_i,\end{aligned} \tag{A.22}$$

where $\tilde{W}_{ie}$ is the ion-electron heat exchange. The ion energy equation then becomes

$$\partial_t \mathcal{E}_i + \boldsymbol{\nabla} \cdot \left[\mathcal{E}_i \boldsymbol{u}_i + \boldsymbol{q}_i + \mathrm{P}_i \cdot \boldsymbol{u}_i \right] = \boldsymbol{F}_i \cdot \boldsymbol{u}_i + \boldsymbol{j}_D \cdot \boldsymbol{E} + \tilde{W}_{ie} - \boldsymbol{R}_e \cdot \boldsymbol{u}_i. \tag{A.23}$$

To focus on the internal energy, we subtract the energy contribution from the flow which may be found to be

$$\begin{aligned}\partial_t \left(\frac{1}{2} \rho_i u_i^2 \right) + \boldsymbol{\nabla} \cdot \left[\frac{1}{2} \rho_i u_i^2 \boldsymbol{u}_i \right] &= \underbrace{\frac{1}{2} \boldsymbol{u}_i \cdot \partial_t (\rho_i \boldsymbol{u}_i) + \frac{1}{2} \boldsymbol{u}_i \cdot \boldsymbol{\nabla} \cdot (\rho_i \boldsymbol{u}_i \boldsymbol{u}_i)}_{= \frac{1}{2} \boldsymbol{u}_i \cdot (\boldsymbol{F}_i + \boldsymbol{j}_D \times \boldsymbol{B} - \boldsymbol{R}_e - \boldsymbol{\nabla} \cdot \mathrm{P}_i)} + \underbrace{\frac{1}{2} \rho_i \boldsymbol{u}_i \cdot \partial_t \boldsymbol{u}_i + \frac{1}{2} \rho_i \boldsymbol{u}_i \boldsymbol{u}_i : \boldsymbol{\nabla} \boldsymbol{u}_i}_{= \frac{1}{2} \boldsymbol{u}_i \cdot (\boldsymbol{F}_i + \boldsymbol{j}_D \times \boldsymbol{B} - \boldsymbol{R}_e - \boldsymbol{\nabla} \cdot \mathrm{P}_i)} \\ &= \boldsymbol{u}_i \cdot (\boldsymbol{F}_i + \boldsymbol{j}_D \times \boldsymbol{B} - \boldsymbol{R}_e - \boldsymbol{\nabla} \cdot \mathrm{P}_i),\end{aligned} \tag{A.24}$$

leaving the pressure evolution equation

$$\partial_t \left(\frac{3}{2} n_i T_i \right) + \boldsymbol{\nabla} \cdot \left[\frac{3}{2} n_i T_i \boldsymbol{u}_i + \boldsymbol{q}_i \right] = -\mathrm{P}_i : \boldsymbol{\nabla} \boldsymbol{u}_i + \boldsymbol{j}_D \cdot (\boldsymbol{E} + \boldsymbol{u}_i \times \boldsymbol{B}) + \tilde{W}_{ie}. \tag{A.25}$$

The ion mixture equations in summary are then

$$\begin{aligned}\partial_t \rho_\alpha + \boldsymbol{\nabla} \cdot [\rho_\alpha \boldsymbol{u}_i + \boldsymbol{i}_\alpha] &= 0 \\ \rho_i \partial_t \boldsymbol{u}_i + \rho_i \boldsymbol{u}_i \cdot \boldsymbol{\nabla} \boldsymbol{u}_i &= -\boldsymbol{\nabla} p_i - \boldsymbol{\nabla} \cdot \Pi_i + \sigma_i (\boldsymbol{E} + \boldsymbol{u}_i \times \boldsymbol{B}) + \boldsymbol{j}_D \times \boldsymbol{B} - \boldsymbol{R}_e \\ \partial_t \left(\frac{3}{2} n_i T_i \right) + \boldsymbol{\nabla} \cdot \left[\frac{3}{2} n_i T_i \boldsymbol{u}_i + \boldsymbol{q}_i \right] &= -p_i \boldsymbol{\nabla} \cdot \boldsymbol{u}_i - \Pi_i : \boldsymbol{\nabla} \boldsymbol{u}_i + \boldsymbol{j}_D \cdot (\boldsymbol{E} + \boldsymbol{u}_i \times \boldsymbol{B}) + \tilde{W}_{ie},\end{aligned} \tag{A.26}$$

Similarly, the electron fluid equations are

$$\begin{aligned}
\partial_t \rho_e + \boldsymbol{\nabla} \cdot [\rho_e \boldsymbol{u}_e] &= 0, \\
\rho_e \partial_t \boldsymbol{u}_e + \rho_e \boldsymbol{u}_e \cdot \boldsymbol{\nabla} \boldsymbol{u}_e &= -\boldsymbol{\nabla} p_e - \boldsymbol{\nabla} \cdot \Pi_e - e n_e (\boldsymbol{E} + \boldsymbol{u}_e \times \boldsymbol{B}) + \boldsymbol{R}_e, \\
\partial_t \left(\frac{3}{2} n_e T_e \right) + \boldsymbol{\nabla} \cdot \left[\frac{3}{2} n_e T_e \boldsymbol{u}_e + \boldsymbol{q}_e \right] &= -p_e \boldsymbol{\nabla} \cdot \boldsymbol{u}_e - \Pi_e : \boldsymbol{\nabla} \boldsymbol{u}_e - \tilde{W}_{ie} - \boldsymbol{R}_e \cdot (\boldsymbol{u}_e - \boldsymbol{u}_i).
\end{aligned} \tag{A.27}$$

APPENDIX B

Fokker-Planck Collision Operator

B.1 Derivation of Fokker-Planck Collision Operator

Following Helander and Sigmar [78], the general form of the Fokker-Planck collision operator can be derived. The Fokker-Planck operator describes collisions in a plasma with $\Lambda \gg 1$, i.e. there are many particles inside the Debye sphere, so collisions are primarily long-range small angle deflections, rather than short-range large-angle binary collisions which would be described by the Boltzmann operator. Consider the DF $f_\alpha(\boldsymbol{v}, t)$ for species α at some local point in space, with the spatial coordinate omitted for brevity. Denoting $P_{\alpha\beta}(\boldsymbol{v}, \Delta\boldsymbol{v})$ the probability that the velocity of a particle changes from $\boldsymbol{v} \to \boldsymbol{v} + \Delta\boldsymbol{v}$ due to collisions of species α against species β in time interval $[t, t + \Delta t]$, the DF should obey

$$f_\alpha(\boldsymbol{v}, t + \Delta t)|_{\alpha\beta} = \int d(\Delta\boldsymbol{v}) f_\alpha(\boldsymbol{v} - \Delta\boldsymbol{v}, t) P_{\alpha\beta}(\boldsymbol{v} - \Delta\boldsymbol{v}, \Delta\boldsymbol{v}), \tag{B.1}$$

i.e. summing over all possible collision histories of particles Δt ago that could end up with our final velocity $\boldsymbol{v}$. For our small-angle collisions, we expect only small changes in velocity, therefore $P_{\alpha\beta}(\boldsymbol{v} - \Delta\boldsymbol{v}, \Delta\boldsymbol{v})$ should be sharply peaked around $\Delta\boldsymbol{v} = 0$ in the second argument for short Δt. This allows us to treat $\Delta\boldsymbol{v}$ as a small quantity and therefore expand f and P in their first arguments

$$\begin{aligned} f_\alpha(\boldsymbol{v}, t + \Delta t)|_{\alpha\beta} = \int d(\Delta\boldsymbol{v}) \Bigg[& f_\alpha(\boldsymbol{v}, t) P_{\alpha\beta}(\boldsymbol{v}, \Delta\boldsymbol{v}) - \Delta v_i \frac{\partial (f_\alpha(\boldsymbol{v}, t) P_{\alpha\beta}(\boldsymbol{v}, \Delta\boldsymbol{v}))}{\partial v_i} \\ & + \frac{1}{2} \Delta v_i \Delta v_j \frac{\partial^2 (f_\alpha(\boldsymbol{v}, t) P_{\alpha\beta}(\boldsymbol{v}, \Delta\boldsymbol{v}))}{\partial v_i \partial v_j} + \mathcal{O}((\Delta v)^3) \Bigg] \\ \approx f_\alpha(\boldsymbol{v}, t) & - \frac{\partial (f_\alpha(\boldsymbol{v}, t) \langle \Delta v_i \rangle_{\alpha\beta})}{\partial v_i} + \frac{1}{2} \frac{\partial^2 (f_\alpha(\boldsymbol{v}, t) \langle \Delta v_i \Delta v_j \rangle_{\alpha\beta})}{\partial v_i \partial v_j}, \end{aligned} \tag{B.2}$$

where we have used that the sum of probabilities is unity $\int d(\Delta\boldsymbol{v}) P_{\alpha\beta}(\boldsymbol{v}, \Delta\boldsymbol{v}) = 1$, and defined $\langle \Delta v_i \rangle_{\alpha\beta} \equiv \int d(\Delta\boldsymbol{v}) \Delta v_i P_{\alpha\beta}(\boldsymbol{v}, \Delta\boldsymbol{v})$ and $\langle \Delta v_i \Delta v_j \rangle_{\alpha\beta} \equiv \int d(\Delta\boldsymbol{v}) \Delta v_i \Delta v_j P_{\alpha\beta}(\boldsymbol{v}, \Delta\boldsymbol{v})$. We may then rearrange to find the rate of change of f_α due to collisions of species α against species β as

$$
\begin{aligned}
C_{\alpha\beta} \equiv \left.\frac{df_\alpha}{dt}\right|_{\alpha\beta \text{ collisions}} &= \lim_{\Delta t\to 0}\left(\frac{f_\alpha(\boldsymbol{v}, t+\Delta t)|_{\alpha\beta} - f_\alpha(\boldsymbol{v},t)}{\Delta t}\right) \\
&= -\partial_{v_i}\left(\lim_{\Delta t\to 0}\left(\frac{\langle \Delta v_i\rangle_{\alpha\beta}}{\Delta t}\right) f_\alpha\right) + \frac{1}{2}\partial_{v_i}\partial_{v_j}\left(\lim_{\Delta t\to 0}\left(\frac{\langle \Delta v_i \Delta v_j\rangle_{\alpha\beta}}{\Delta t}\right) f_\alpha\right).
\end{aligned} \tag{B.3}
$$

The friction and diffusion coefficients $\lim_{\Delta t\to 0}\left(\frac{\langle \Delta v_i\rangle_{\alpha\beta}}{\Delta t}\right)$ and $\lim_{\Delta t\to 0}\left(\frac{\langle \Delta v_i \Delta v_j\rangle_{\alpha\beta}}{\Delta t}\right)$ respectively then require consideration of the particular collision dynamics to be evaluated. The total collision operator experienced by f_α is then just the sum of the collision operators over all background species $C_\alpha = \sum_\beta C_{\alpha\beta}$ including $\beta = \alpha$.

B.1.1 Collision dynamics

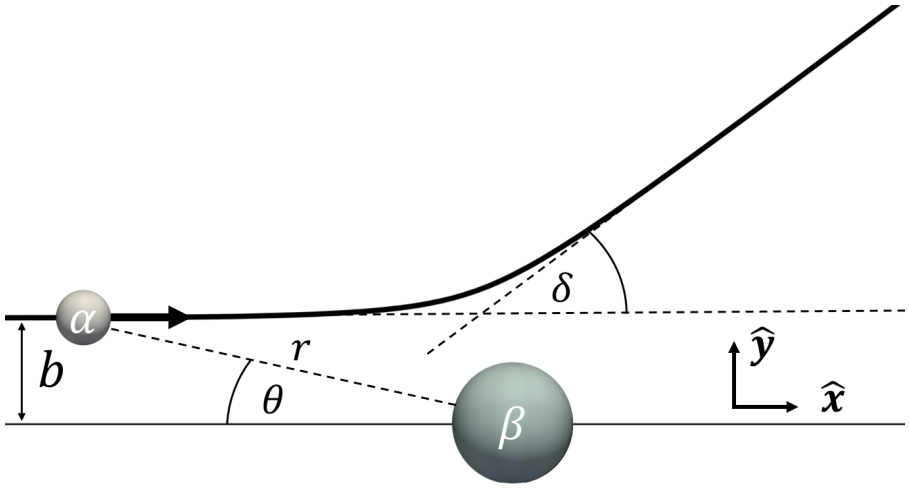


Figure B.1: Particle α scattering off of a fixed particle β

Consider two colliding particles, α and β, where β is fixed at the origin in the laboratory frame and particle α approaches from far away with impact parameter b and initial speed u. The impulse received by α is then

$$
\Delta \boldsymbol{p} = \int_{-\infty}^{\infty} dt\ \boldsymbol{F} = \int_{-\infty}^{\infty} dt\ \frac{q_\alpha q_\beta}{4\pi\varepsilon_0 r^2}(-\cos\theta\hat{\boldsymbol{x}} + \sin\theta\hat{\boldsymbol{y}}) \tag{B.4}
$$

$$
= \int_0^{\pi-\delta} d\theta\ \frac{q_\alpha q_\beta}{4\pi\varepsilon_0 ub}(-\cos\theta\hat{\boldsymbol{x}} + \sin\theta\hat{\boldsymbol{y}}) \tag{B.5}
$$

$$
= \frac{q_\alpha q_\beta}{4\pi\varepsilon_0 ub}\big(\sin(\pi-\delta)\hat{\boldsymbol{x}} - (\cos(\pi-\delta)-1)\hat{\boldsymbol{y}}\big), \tag{B.6}
$$

where we have used angular momentum conservation $J = mub = mr^2\dot{\theta}$ to change integration variables via $dt = \frac{r^2}{ub}d\theta$. Comparing this impulse to the change in momentum $\Delta\boldsymbol{p} = m_\alpha\Delta\boldsymbol{v} = m_\alpha u\big((\cos\delta - 1)\hat{\boldsymbol{x}} + \sin\delta\hat{\boldsymbol{y}}\big)$, we may rearrange to find the scattering angle

$$
\tan(\delta/2) = \frac{q_\alpha q_\beta}{4\pi\varepsilon_0 m_\alpha u^2 b}. \tag{B.7}
$$

The particles entering through the annulus with impact parameters in the range $[b, b+db]$ with area $d\sigma = 2\pi b db$ are then scattered into the solid angle $d\Omega = 2\pi\sin\delta d\delta$. The differential cross section is then defined as

$$
\frac{d\sigma}{d\Omega} = \frac{b}{\sin\delta}\left|\frac{db}{d\delta}\right|. \tag{B.8}
$$

To evaluate the differential cross section for Rutherford scattering, we have

$$b = \frac{q_\alpha q_\beta}{4\pi\varepsilon_0 m_\alpha u^2}\cot(\delta/2) \quad \Rightarrow \quad \frac{db}{d\delta} = -\frac{1}{2}\frac{q_\alpha q_\beta}{4\pi\varepsilon_0 m_\alpha u^2}\frac{1}{\sin^2(\delta/2)}, \tag{B.9}$$

so finally

$$\left(\frac{d\sigma}{d\Omega}\right)_{\text{Rutherford}} = \frac{1}{4}\left(\frac{q_\alpha q_\beta}{4\pi\varepsilon_0 m_\alpha u^2}\right)^2 \frac{1}{\sin^4(\delta/2)}. \tag{B.10}$$

This cross section is very heavily weighted to small δ, meaning that small angle collisions should be the dominant scattering process for binary collisions. This justifies neglecting large angle collisions and taking the scattering angle as roughly

$$\delta \approx \frac{q_\alpha q_\beta}{2\pi\varepsilon_0 m_\alpha u^2 b}. \tag{B.11}$$

Considering now arbitrary masses m_α and m_β that are no longer fixed, the Lagrangian of the system is

$$\begin{aligned}\mathcal{L} &= \frac{1}{2}m_\alpha \dot{\boldsymbol{x}}_\alpha^2 + \frac{1}{2}m_\beta \dot{\boldsymbol{x}}_\beta^2 - \frac{q_\alpha q_\beta}{4\pi\varepsilon_0|\boldsymbol{x}_\alpha - \boldsymbol{x}_\beta|} \\ &= \frac{1}{2}M\dot{\boldsymbol{R}}^2 + \frac{1}{2}\mu\dot{\boldsymbol{r}}^2 - \frac{q_\alpha q_\beta}{4\pi\varepsilon_0 r},\end{aligned} \tag{B.12}$$

where we have changed coordinates to the centre of mass position $\boldsymbol{R} = (m_\alpha \boldsymbol{x}_\alpha + m_\beta \boldsymbol{x}_\beta)/(m_\alpha + m_\beta)$ and relative separation $\boldsymbol{r} = \boldsymbol{x}_\alpha - \boldsymbol{x}_\beta$ between the two particles, and introduced the total mass M and reduced mass μ. Since $\boldsymbol{R}$ is a cyclic coordinate, the first term is a constant so it can be ignored, and now the Lagrangian has the same form as a particle of mass μ that scatters off a fixed particle, therefore has the same scattering angle B.11 with $m_\alpha \to \mu$, where u is the initial relative speed.

Introducing an orthogonal coordinate system (x, y, z) with $\hat{\boldsymbol{x}} \parallel \boldsymbol{u}$, then the relative velocity $\boldsymbol{u} = \dot{\boldsymbol{r}}$ changes by

$$\Delta u_x = u(\cos\delta - 1), \qquad \Delta u_y = u\sin\delta\cos\phi, \qquad \Delta u_z = u\sin\delta\sin\phi. \tag{B.13}$$

Noting that $\boldsymbol{x}_\alpha = \boldsymbol{R} + \frac{m_\beta}{m_\alpha+m_\beta}\boldsymbol{r} \Rightarrow \Delta\boldsymbol{v}_\alpha = \frac{m_\beta}{m_\alpha+m_\beta}\Delta\boldsymbol{u}$, then we obtain

$$\Delta\boldsymbol{v} = \begin{pmatrix}\Delta v_x \\ \Delta v_y \\ \Delta v_z\end{pmatrix} \approx \begin{pmatrix}-(1+\frac{m_\alpha}{m_\beta})(\frac{q_\alpha q_\beta}{2\pi\varepsilon_0 m_\alpha})^2\frac{1}{2b^2u^3} \\ \frac{q_\alpha q_\beta}{2\pi\varepsilon_0 m_\alpha}\frac{\cos\phi}{ub} \\ \frac{q_\alpha q_\beta}{2\pi\varepsilon_0 m_\alpha}\frac{\sin\phi}{ub}.\end{pmatrix} \tag{B.14}$$

B.1.2 Collision statistics

Using the dynamics of a single collision, we may integrate over many collisions in a short time interval. The number of collisions taking place in a time interval Δt between a given particle of species α at velocity $\boldsymbol{v}$ and particles of another species β at velocities $\boldsymbol{v}'$ (so now $\boldsymbol{u} = \boldsymbol{v} - \boldsymbol{v}'$) for impact parameters in the interval $[b, b + db]$ and angles $[\phi, \phi + d\phi]$ is

$$\Delta N_{\text{collisions}} = b\, db\, d\phi \Delta t \int d^3\boldsymbol{v}' f_\beta(\boldsymbol{v}') u, \tag{B.15}$$

coming from the volume $dV = b\, db\, d\phi\, u\Delta t$ swept by the particle in Δt, and then integrating over the velocities of the particles of species β. The rate of collisions provided by B.15 may then multiply B.14 and integrated over b and ϕ to find the averages required for the FP operator B.3 as

$$\frac{\langle \Delta \boldsymbol{v} \rangle_{\alpha\beta}}{\Delta t} = \int_{b_{\min}}^{b_{\max}} db \int_0^{2\pi} d\phi\, \frac{\Delta N_{\text{collisions}}}{\Delta t} \Delta v_x \hat{\boldsymbol{u}} \tag{B.16}$$

$$= -\left(1 + \frac{m_\alpha}{m_\beta}\right)\left(\frac{q_\alpha q_\beta}{2\pi\varepsilon_0 m_\alpha}\right)^2 \underbrace{\int_{b_{\min}}^{b_{\max}} db\, \frac{1}{b}}_{=\ln\Lambda_{\alpha\beta}} \underbrace{\int_0^{2\pi} d\phi}_{=2\pi} \int d^3\boldsymbol{v}' f_\beta(\boldsymbol{v}') \hat{\boldsymbol{u}} \frac{1}{2u^2} \tag{B.17}$$

$$= -\frac{1}{4\pi}\left(1 + \frac{m_\alpha}{m_\beta}\right)\left(\frac{q_\alpha q_\beta}{\varepsilon_0 m_\alpha}\right)^2 \ln\Lambda_{\alpha\beta} \int d^3\boldsymbol{v}' \frac{\boldsymbol{u}}{u^3} f_\beta(\boldsymbol{v}'), \tag{B.18}$$

where we have used the azimuthal ϕ symmetry to note that the y, z integrals vanish. The integral over the impact parameter introduces the Coulomb logarithm as discussed in Section 2.2.3.

Similarly, the $\mathcal{O}((\Delta v)^2)$ terms may be found as

$$\begin{aligned}
\frac{\langle \Delta\boldsymbol{v}\Delta\boldsymbol{v}\rangle_{\alpha\beta}}{\Delta t} &= \frac{\langle(\hat{\boldsymbol{x}}\Delta v_x + \hat{\boldsymbol{y}}\Delta v_y + \hat{\boldsymbol{z}}\Delta v_z)(\hat{\boldsymbol{x}}\Delta v_x + \hat{\boldsymbol{y}}\Delta v_y + \hat{\boldsymbol{z}}\Delta v_z)\rangle}{\Delta t} \\
&= \frac{\langle \hat{\boldsymbol{y}}\hat{\boldsymbol{y}}(\Delta v_y)^2 + \hat{\boldsymbol{z}}\hat{\boldsymbol{z}}(\Delta v_z)^2\rangle}{\Delta t} \\
&= \int_{b_{\min}}^{b_{\max}} db \int_0^{2\pi} d\phi\, \frac{\Delta N_{\text{collisions}}}{\Delta t}(\hat{\boldsymbol{y}}\hat{\boldsymbol{y}}(\Delta v_y)^2 + \hat{\boldsymbol{z}}\hat{\boldsymbol{z}}(\Delta v_z)^2) \\
&= \left(\frac{q_\alpha q_\beta}{2\pi\varepsilon_0 m_\alpha}\right)^2 \int_{b_{\min}}^{b_{\max}} db \frac{1}{b} \int d^3\boldsymbol{v}' f_\beta(\boldsymbol{v}') \frac{1}{u} \int_0^{2\pi} d\phi (\hat{\boldsymbol{y}}\hat{\boldsymbol{y}}\cos^2\phi + \hat{\boldsymbol{z}}\hat{\boldsymbol{z}}\sin^2\phi) \\
&= \frac{1}{4\pi}\left(\frac{q_\alpha q_\beta}{\varepsilon_0 m_\alpha}\right)^2 \ln\Lambda_{\alpha\beta} \int d^3\boldsymbol{v}' f_\beta(\boldsymbol{v}') \frac{1}{u} \underbrace{(\hat{\boldsymbol{y}}\hat{\boldsymbol{y}} + \hat{\boldsymbol{z}}\hat{\boldsymbol{z}})}_{=\mathrm{I} - \hat{\boldsymbol{u}}\hat{\boldsymbol{u}}} \\
&= \frac{1}{4\pi}\left(\frac{q_\alpha q_\beta}{\varepsilon_0 m_\alpha}\right)^2 \ln\Lambda_{\alpha\beta} \int d^3\boldsymbol{v}' \frac{u^2\mathrm{I} - \boldsymbol{u}\boldsymbol{u}}{u^3} f_\beta(\boldsymbol{v}')
\end{aligned} \tag{B.19}$$

where $\langle(\Delta v_x)^2\rangle$ is neglected since it is smaller than a factor $1/\ln\Lambda_{\alpha\beta}$ than the other diffusion terms, and cross terms such as $\langle \Delta v_x \Delta v_y\rangle$ will vanish due to the integrals over ϕ.

B.1.3 Landau form

Substituting these forms directly into the Fokker-Planck operator B.3.

$$C_{\alpha\beta} = \frac{1}{4\pi}\left(\frac{q_\alpha q_\beta}{\varepsilon_0 m_\alpha}\right)^2 \ln\Lambda_{\alpha\beta}\partial_{v_i}\left[\left(1+\frac{m_\alpha}{m_\beta}\right)\int d^3\boldsymbol{v}'\frac{u_i}{u^3}f_\beta(\boldsymbol{v}')f_\alpha(\boldsymbol{v}) + \frac{1}{2}\partial_{v_j}\int d^3\boldsymbol{v}'\mathrm{U}_{ij}f_\beta(\boldsymbol{v}')f_\alpha(\boldsymbol{v})\right] \tag{B.20}$$

$$= \frac{1}{8\pi}\left(\frac{q_\alpha q_\beta}{\varepsilon_0 m_\alpha}\right)^2 \ln\Lambda_{\alpha\beta}\partial_{v_i}\left[\left(1+\frac{m_\alpha}{m_\beta}\right)\int d^3\boldsymbol{v}'\frac{2u_i}{u^3}f_\beta(\boldsymbol{v}')f_\alpha(\boldsymbol{v}) \tag{B.21}$$

$$+ \int d^3\boldsymbol{v}' f_\beta(\boldsymbol{v}')\Big(\underbrace{\partial_{v_j}(\mathrm{U}_{ij})}_{=-2u_i/u^3} f_\alpha(\boldsymbol{v}) + \mathrm{U}_{ij}\partial_{v_j}f_\alpha(\boldsymbol{v})\Big)\Big] \tag{B.22}$$

$$= \frac{1}{8\pi}\left(\frac{q_\alpha q_\beta}{\varepsilon_0 m_\alpha}\right)^2 \ln\Lambda_{\alpha\beta}\partial_{v_i}\left[\frac{m_\alpha}{m_\beta}\int d^3\boldsymbol{v}'\frac{2u_i}{u^3}f_\beta(\boldsymbol{v}')f_\alpha(\boldsymbol{v}) + \int d^3\boldsymbol{v}' f_\beta(\boldsymbol{v}')\mathrm{U}_{ij}\partial_{v_j}f_\alpha(\boldsymbol{v})\right] \tag{B.23}$$

$$= \frac{1}{8\pi}\left(\frac{q_\alpha q_\beta}{\varepsilon_0 m_\alpha}\right)^2 \ln\Lambda_{\alpha\beta}\partial_{v_i}\left[\frac{m_\alpha}{m_\beta}\int d^3\boldsymbol{v}'(\partial_{v'_j}\mathrm{U}_{ij})f_\beta(\boldsymbol{v}')f_\alpha(\boldsymbol{v}) + \int d^3\boldsymbol{v}' f_\beta(\boldsymbol{v}')\mathrm{U}_{ij}\partial_{v_j}f_\alpha(\boldsymbol{v})\right] \tag{B.24}$$

$$= \frac{1}{8\pi}\left(\frac{q_\alpha q_\beta}{\varepsilon_0 m_\alpha}\right)^2 \ln\Lambda_{\alpha\beta}\partial_{v_i}\left[-\frac{m_\alpha}{m_\beta}\int d^3\boldsymbol{v}'\mathrm{U}_{ij}\partial_{v'_j}f_\beta(\boldsymbol{v}')f_\alpha(\boldsymbol{v}) + \int d^3\boldsymbol{v}' f_\beta(\boldsymbol{v}')\mathrm{U}_{ij}\partial_{v_j}f_\alpha(\boldsymbol{v})\right] \tag{B.25}$$

where

$$\mathrm{U}_{ij} = \partial_{v_i}\partial_{v_j}u = \frac{u^2\delta_{ij} - u_i u_j}{u^3}, \tag{B.26}$$

and we have used

$$\partial_{v_j}\mathrm{U}_{ij} = -2u_i/u^3, \quad \partial_{v'_j}\mathrm{U}_{ij} = 2u_i/u^3. \tag{B.27}$$

These manipulations yield the form of the collision operator originally derived by Landau

$$C_{\alpha\beta}\{f_\alpha, f_\beta\} = -\frac{q_\alpha^2 q_\beta^2 \ln\Lambda_{\alpha\beta}}{8\pi\varepsilon_0^2 m_\alpha}\frac{\partial}{\partial v_i}\int d^3\boldsymbol{v}'\,\frac{u^2\delta_{ij} - u_i u_j}{u^3}\left(\frac{f_\alpha(\boldsymbol{v})}{m_\beta}\frac{\partial f_\beta(\boldsymbol{v}')}{\partial v'_j} - \frac{f_\beta(\boldsymbol{v}')}{m_\alpha}\frac{\partial f_\alpha(\boldsymbol{v})}{\partial v_j}\right). \tag{B.28}$$

B.1.4 Rosenbluth form

Alternatively, we may express the collision operator in the Rosenbluth form by defining the 'Rosenbluth potentials'

$$\mathcal{H}_\beta \equiv \int d^3\boldsymbol{v}'\,\frac{1}{u}f_\beta(\boldsymbol{v}'), \quad \mathcal{G}_\beta \equiv \int d^3\boldsymbol{v}'\,u f_\beta(\boldsymbol{v}'). \tag{B.29}$$

Appropriate derivatives of the Rosenbluth potentials yield

$$\partial_{v_i}\mathcal{H}_\beta = -\int d^3\boldsymbol{v}'\,\frac{u_i}{u^3}f_\beta(\boldsymbol{v}'), \quad \partial_{v_i}\partial_{v_j}\mathcal{G}_\beta = \int d^3\boldsymbol{v}'\,\mathrm{U}_{ij}f_\beta(\boldsymbol{v}'). \tag{B.30}$$

and therefore the collision operator may be expressed in terms of the Rosenbluth potentials as

$$C_{\alpha\beta}\{f_\alpha, f_\beta\} = L_{\alpha\beta}\frac{\partial}{\partial v_i}\left[-\frac{m_\alpha}{m_\beta}\frac{\partial\mathcal{H}_\beta}{\partial v_i}f_\alpha + \frac{1}{2}\frac{\partial^2\mathcal{G}_\beta}{\partial v_i\partial v_j}\frac{\partial f_\alpha}{\partial v_j}\right], \tag{B.31}$$

where we have introduced

$$L_{\alpha\beta} \equiv \frac{1}{4\pi}\left(\frac{q_\alpha q_\beta}{\varepsilon_0 m_\alpha}\right)^2 \ln\Lambda_{\alpha\beta} \tag{B.32}$$

for brevity. The Rosenbluth form is particularly convenient for linearising the collision operator.

The functionals $\mathcal{H}_\beta$ and $\mathcal{G}_\beta$ are named 'potentials' since they obey convenient relationships. Firstly, recalling that the Green's function for the Laplacian ∇_v^2 in three dimensions is $G(\boldsymbol{v},\boldsymbol{v}') = -1/4\pi|\boldsymbol{v}-\boldsymbol{v}'|$, that is, $\nabla_v^2(1/u) = -4\pi\delta^3(\boldsymbol{v}-\boldsymbol{v}')$. The Laplacian of $\mathcal{H}_\beta$ is therefore

$$\nabla_v^2\mathcal{H}_\beta = \int d^3\boldsymbol{v}'\,\nabla_v^2(1/u)f_\beta(\boldsymbol{v}') = -4\pi\int d^3\boldsymbol{v}'\,\delta^3(\boldsymbol{v}-\boldsymbol{v}')f_\beta(\boldsymbol{v}') = -4\pi f_\beta(\boldsymbol{v}), \tag{B.33}$$

which has the form of Poisson's equation. Analogously to Newtonian gravity or electrostatics, $\mathcal{H}_\beta$ is the potential due to a charge density $\propto f_\beta$.

Using $U_{ii} = 2/u$, contracting indices of $\partial_{v_i}\partial_{v_j}\mathcal{G}_\beta$ yields

$$\nabla_v^2\mathcal{G}_\beta = 2\mathcal{H}_\beta, \tag{B.34}$$

therefore by a similar analogy, $\mathcal{G}_\beta$ is the potential due to a charge density $\propto \mathcal{H}_\beta$.

B.2 Properties of the Fokker-Planck Collision Operator

Starting from the Landau form

$$C_{\alpha\beta}\{f_\alpha^M, f_\beta^M\} = \frac{\gamma_{\alpha\beta}}{m_\alpha}\boldsymbol{\nabla}_{\boldsymbol{v}}\cdot\left\{\int d^3\boldsymbol{v}'\,\mathrm{U}\cdot\left[\frac{f_\beta(\boldsymbol{v}')}{m_\alpha}\boldsymbol{\nabla}_{\boldsymbol{v}}f_\alpha(\boldsymbol{v}) - \frac{f_\alpha(\boldsymbol{v})}{m_\beta}\boldsymbol{\nabla}_{\boldsymbol{v}'}f_\beta(\boldsymbol{v}')\right]\right\}, \tag{B.35}$$

where $\gamma_{\alpha\beta} \equiv \frac{q_\alpha^2 q_\beta^2 \ln\Lambda}{8\pi\epsilon_0^2} = \gamma_{\beta\alpha}$, we prove some important properties of the Fokker-Planck collision operator:

B.2.1 Particle number conservation

For arbitrary distributions f_α and f_β,

$$\int C_{\alpha\beta}\{f_\alpha^M, f_\beta^M\}\,d^3\boldsymbol{v} = 0. \tag{B.36}$$

The proof is straightforward. By substituting in the Landau form

$$\int d^3\boldsymbol{v}\,\frac{\gamma_{\alpha\beta}}{m_\alpha}\boldsymbol{\nabla}_{\boldsymbol{v}}\cdot\left(\int d^3\boldsymbol{v}'\,\mathrm{U}\cdot\left[\frac{f_\beta(\boldsymbol{v}')}{m_\alpha}\boldsymbol{\nabla}_{\boldsymbol{v}}f_\alpha(\boldsymbol{v}) - \frac{f_\alpha(\boldsymbol{v})}{m_\beta}\boldsymbol{\nabla}_{\boldsymbol{v}'}f_\beta(\boldsymbol{v}')\right]\right), \tag{B.37}$$

which clearly vanishes since it is the integral of a total divergence, so vanishes by Gauss' theorem since the distributions vanish as $v\to\infty$.

B.2.2 Momentum conservation

For arbitrary distributions f_α and f_β,

$$\int m_\alpha\boldsymbol{v}\,C_{\alpha\beta}\{f_\alpha^M, f_\beta^M\}\,d^3\boldsymbol{v} + \int m_\beta\boldsymbol{v}\,C_{\beta\alpha}(f_\beta, f_\alpha)\,d^3\boldsymbol{v} = 0. \tag{B.38}$$

To prove, we focus on the first term:

$$\int m_\alpha \boldsymbol{v} C_{\alpha\beta}\{f_\alpha^M, f_\beta^M\}\, d^3\boldsymbol{v} \tag{B.39}$$

$$= \int d^3\boldsymbol{v}\, m_\alpha \boldsymbol{v} \frac{\gamma_{\alpha\beta}}{m_\alpha} \boldsymbol{\nabla}_{\boldsymbol{v}} \cdot \left\{ \int \mathrm{U} \cdot \left[\frac{f_\beta\left(\boldsymbol{v'}\right)}{m_\alpha} \boldsymbol{\nabla}_{\boldsymbol{v}} f_\alpha\left(\boldsymbol{v}\right) - \frac{f_\alpha\left(\boldsymbol{v}\right)}{m_\beta} \boldsymbol{\nabla}_{\boldsymbol{v'}} f_\beta\left(\boldsymbol{v'}\right) \right] d^3\boldsymbol{v'} \right\}. \tag{B.40}$$

Integrating the $\boldsymbol{v}$ integral by parts, we have

$$= -\gamma_{\alpha\beta} \int d^3\boldsymbol{v} \left\{ \int \mathrm{U} \cdot \left[\frac{f_\beta\left(\boldsymbol{v'}\right)}{m_\alpha} \boldsymbol{\nabla}_{\boldsymbol{v}} f_\alpha\left(\boldsymbol{v}\right) - \frac{f_\alpha\left(\boldsymbol{v}\right)}{m_\beta} \boldsymbol{\nabla}_{\boldsymbol{v'}} f_\beta\left(\boldsymbol{v'}\right) \right] d^3\boldsymbol{v'} \right\} \tag{B.41}$$

$$+ \gamma_{\alpha\beta} \int d^3\boldsymbol{v}\, \boldsymbol{\nabla}_{\boldsymbol{v}} \cdot \left\{ \boldsymbol{v} \int \mathrm{U} \cdot \left[\frac{f_\beta\left(\boldsymbol{v'}\right)}{m_\alpha} \boldsymbol{\nabla}_{\boldsymbol{v}} f_\alpha\left(\boldsymbol{v}\right) - \frac{f_\alpha\left(\boldsymbol{v}\right)}{m_\beta} \boldsymbol{\nabla}_{\boldsymbol{v'}} f_\beta\left(\boldsymbol{v'}\right) \right] d^3\boldsymbol{v'} \right\}. \tag{B.42}$$

The second term is the integral of a total divergence, so vanishes by Gauss' theorem. Writing the remaining term as

$$= -\gamma_{\alpha\beta} \int d^3\boldsymbol{v} \int d^3\boldsymbol{v'} \left\{ \mathrm{U} \cdot \left[\frac{f_\beta\left(\boldsymbol{v'}\right)}{m_\alpha} \boldsymbol{\nabla}_{\boldsymbol{v}} f_\alpha\left(\boldsymbol{v}\right) - \frac{f_\alpha\left(\boldsymbol{v}\right)}{m_\beta} \boldsymbol{\nabla}_{\boldsymbol{v'}} f_\beta\left(\boldsymbol{v'}\right) \right] \right\}, \tag{B.43}$$

we recognise that when swapping labels $\alpha \leftrightarrow \beta$, the result is the same with a minus sign

$$\int m_\beta \boldsymbol{v'} C_{\beta\alpha}(f_\beta, f_\alpha)\, d^3\boldsymbol{v'} \tag{B.44}$$

$$= -\gamma_{\beta\alpha} \int d^3\boldsymbol{v'} \int d^3\boldsymbol{v} \left\{ \mathrm{U} \cdot \left[\frac{f_\alpha\left(\boldsymbol{v}\right)}{m_\beta} \boldsymbol{\nabla}_{\boldsymbol{v'}} f_\beta\left(\boldsymbol{v'}\right) - \frac{f_\beta\left(\boldsymbol{v'}\right)}{m_\alpha} \boldsymbol{\nabla}_{\boldsymbol{v}} f_\alpha\left(\boldsymbol{v}\right) \right] \right\} \tag{B.45}$$

$$= \gamma_{\alpha\beta} \int d^3\boldsymbol{v} \int d^3\boldsymbol{v'} \left\{ \mathrm{U} \cdot \left[\frac{f_\beta\left(\boldsymbol{v'}\right)}{m_\alpha} \boldsymbol{\nabla}_{\boldsymbol{v}} f_\alpha\left(\boldsymbol{v}\right) - \frac{f_\alpha\left(\boldsymbol{v}\right)}{m_\beta} \boldsymbol{\nabla}_{\boldsymbol{v'}} f_\beta\left(\boldsymbol{v'}\right) \right] \right\} \tag{B.46}$$

$$= -\int m_\alpha \boldsymbol{v} C_{\alpha\beta}\{f_\alpha^M, f_\beta^M\}\, d^3\boldsymbol{v}, \tag{B.47}$$

and therefore

$$\int m_\alpha \boldsymbol{v} C_{\alpha\beta}\{f_\alpha^M, f_\beta^M\}\, d^3\boldsymbol{v} + \int m_\beta \boldsymbol{v} C_{\beta\alpha}(f_\beta, f_\alpha)\, d^3\boldsymbol{v} = 0. \tag{B.48}$$

B.2.3 Energy conservation

For arbitrary distributions f_α and f_β,

$$\int \frac{1}{2} m_\alpha v^2 C_{\alpha\beta}\{f_\alpha^M, f_\beta^M\}\, d^3\boldsymbol{v} + \int \frac{1}{2} m_\beta v^2 C_{\beta\alpha}(f_\beta, f_\alpha)\, d^3\boldsymbol{v} = 0. \tag{B.49}$$

To prove, we start with the first term again, integrate by parts, and note the total divergence term vanishes, leaving

$$\int \frac{1}{2} m_\alpha v^2 C_{\alpha\beta}\{f_\alpha^M, f_\beta^M\}\, d^3\boldsymbol{v} \tag{B.50}$$

$$= -\gamma_{\alpha\beta} \int d^3\boldsymbol{v}\, \boldsymbol{v} \cdot \left\{ \int \mathrm{U} \cdot \left[\frac{f_\beta\left(\boldsymbol{v'}\right)}{m_\alpha} \boldsymbol{\nabla}_{\boldsymbol{v}} f_\alpha\left(\boldsymbol{v}\right) - \frac{f_\alpha\left(\boldsymbol{v}\right)}{m_\beta} \boldsymbol{\nabla}_{\boldsymbol{v'}} f_\beta\left(\boldsymbol{v'}\right) \right] d^3\boldsymbol{v'} \right\} \tag{B.51}$$

$$= -\gamma_{\alpha\beta} \int d^3\boldsymbol{v} \int d^3\boldsymbol{v'}\, \boldsymbol{v} \cdot \mathrm{U} \cdot \left[\frac{f_\beta\left(\boldsymbol{v'}\right)}{m_\alpha} \boldsymbol{\nabla}_{\boldsymbol{v}} f_\alpha\left(\boldsymbol{v}\right) - \frac{f_\alpha\left(\boldsymbol{v}\right)}{m_\beta} \boldsymbol{\nabla}_{\boldsymbol{v'}} f_\beta\left(\boldsymbol{v'}\right) \right]. \tag{B.52}$$

Swapping species labels $\alpha \leftrightarrow \beta$ and dummy variables $\boldsymbol{v} \leftrightarrow \boldsymbol{v'}$ yields

$$\int \frac{1}{2} m_\beta v'^2 C_{\beta\alpha}(f_\beta, f_\alpha)\, d^3\boldsymbol{v'} \tag{B.53}$$

$$= \gamma_{\alpha\beta} \int d^3\boldsymbol{v} \int d^3\boldsymbol{v'}\, \boldsymbol{v'} \cdot \mathrm{U} \cdot \left[\frac{f_\beta(\boldsymbol{v'})}{m_\alpha} \boldsymbol{\nabla}_{\boldsymbol{v}} f_\alpha(\boldsymbol{v}) - \frac{f_\alpha(\boldsymbol{v})}{m_\beta} \boldsymbol{\nabla}_{\boldsymbol{v'}} f_\beta(\boldsymbol{v'}) \right]. \tag{B.54}$$

Taking the sum of these results, we have

$$\int \frac{1}{2} m_\alpha v^2 C_{\alpha\beta}\{f_\alpha^M, f_\beta^M\}\, d^3\boldsymbol{v} + \int \frac{1}{2} m_\beta v'^2 C_{\beta\alpha}(f_\beta, f_\alpha)\, d^3\boldsymbol{v'} \tag{B.55}$$

$$= -\gamma_{\alpha\beta} \int d^3\boldsymbol{v} \int d^3\boldsymbol{v'}\, \underbrace{(\boldsymbol{v} - \boldsymbol{v'})}_{=\boldsymbol{u}} \cdot \mathrm{U} \cdot \left[\frac{f_\beta(\boldsymbol{v'})}{m_\alpha} \boldsymbol{\nabla}_{\boldsymbol{v}} f_\alpha(\boldsymbol{v}) - \frac{f_\alpha(\boldsymbol{v})}{m_\beta} \boldsymbol{\nabla}_{\boldsymbol{v'}} f_\beta(\boldsymbol{v'}) \right] \tag{B.56}$$

$$= 0, \tag{B.57}$$

which vanishes since $\boldsymbol{u} \cdot \mathrm{U} = 0$.

B.2.4 Maxwellians are equilibrium distributions

For two Maxwellians f_α^M and f_β^M of common flow and temperature but not necessarily the same species or number density, the collision operator vanishes

$$C_{\alpha\beta}\{f_\alpha^M, f_\beta^M\} = 0 \quad \text{if} \quad \boldsymbol{u}_\alpha = \boldsymbol{u}_\beta \quad \text{and} \quad T_\alpha = T_\beta \tag{B.58}$$

To prove, first note that

$$\boldsymbol{\nabla}_{\boldsymbol{v}} f_\alpha^M = -\frac{m_\alpha}{T_\alpha} (\boldsymbol{v} - \boldsymbol{u}_\alpha) f_\alpha^M, \tag{B.59}$$

so

$$C_{\alpha\beta}\{f_\alpha^M, f_\beta^M\} = \frac{\gamma_{\alpha\beta}}{m_\alpha} \boldsymbol{\nabla}_{\boldsymbol{v}} \cdot \left\{ \int \mathrm{U} \cdot \left[-\frac{1}{T_\alpha} (\boldsymbol{v} - \boldsymbol{u}_\alpha) + \frac{1}{T_\beta} (\boldsymbol{v'} - \boldsymbol{u}_\beta) \right] f_\alpha f_\beta d^3\boldsymbol{v'} \right\}. \tag{B.60}$$

If the flows and temperatures are common between the two species, then this becomes

$$C_{\alpha\beta}\{f_\alpha^M, f_\beta^M\} = \frac{\gamma_{\alpha\beta}}{m_\alpha} \boldsymbol{\nabla}_{\boldsymbol{v}} \cdot \left\{ \int \mathrm{U} \cdot \underbrace{\left[-\boldsymbol{v} + \boldsymbol{v'} \right]}_{=-\boldsymbol{u}} \frac{1}{T} f_\alpha f_\beta d^3\boldsymbol{v'} \right\} = 0, \tag{B.61}$$

which vanishes since $\mathrm{U} \cdot \boldsymbol{u} = 0$.

B.2.5 H-theorem

Consider the entropy density

$$S = -\sum_\alpha \int d^3\boldsymbol{v}\, f_\alpha \ln f_\alpha. \tag{B.62}$$

Its rate of change is

$$\frac{dS}{dt} = -\sum_\alpha \int d^3\boldsymbol{v}\, (1 + \ln f_\alpha) \partial_t f_\alpha. \tag{B.63}$$

The rate of change of entropy due to collisions is therefore

$$\left.\frac{dS}{dt}\right|_{\text{collisions}} = -\sum_\alpha \int d^3\boldsymbol{v}\,(1+\ln f_\alpha)(\partial_t f_\alpha)|_{\text{collisions}} = -\sum_\alpha\sum_\beta \int d^3\boldsymbol{v}\,(1+\ln f_\alpha) C_{\alpha\beta}\{f_\alpha, f_\beta\} \tag{B.64}$$

$$= -\sum_\alpha\sum_\beta \int d^3\boldsymbol{v}\, C_{\alpha\beta}\{f_\alpha, f_\beta\}\ln f_\alpha, \tag{B.65}$$

where the first term vanishes due to particle number conservation. Using the Fokker-Planck operator, this becomes

$$\left.\frac{dS}{dt}\right|_{\text{collisions}} = -\sum_\alpha\sum_\beta \frac{\gamma_{\alpha\beta}}{m_\alpha}\int d^3\boldsymbol{v}\,\ln f_\alpha \boldsymbol{\nabla}_{\boldsymbol{v}}\cdot\left\{\int d^3\boldsymbol{v'}\,\mathrm{U}\cdot\left[\frac{f_\beta(\boldsymbol{v'})}{m_\alpha}\boldsymbol{\nabla}_{\boldsymbol{v}} f_\alpha(\boldsymbol{v}) - \frac{f_\alpha(\boldsymbol{v})}{m_\beta}\boldsymbol{\nabla}_{\boldsymbol{v'}} f_\beta(\boldsymbol{v'})\right]\right\} \tag{B.66}$$

$$= \sum_\alpha\sum_\beta \frac{\gamma_{\alpha\beta}}{m_\alpha}\int d^3\boldsymbol{v}\int d^3\boldsymbol{v'}\,(\boldsymbol{\nabla}_{\boldsymbol{v}}\ln f_\alpha)\cdot\mathrm{U}\cdot\left[\frac{f_\beta(\boldsymbol{v'})}{m_\alpha}\boldsymbol{\nabla}_{\boldsymbol{v}} f_\alpha(\boldsymbol{v}) - \frac{f_\alpha(\boldsymbol{v})}{m_\beta}\boldsymbol{\nabla}_{\boldsymbol{v'}} f_\beta(\boldsymbol{v'})\right] \tag{B.67}$$

$$= \sum_\alpha\sum_\beta \gamma_{\alpha\beta}\int d^3\boldsymbol{v}\int d^3\boldsymbol{v'}\,\frac{1}{m_\alpha}(\boldsymbol{\nabla}_{\boldsymbol{v}}\ln f_\alpha)\cdot\mathrm{U}\cdot\left[\frac{1}{m_\alpha}\boldsymbol{\nabla}_{\boldsymbol{v}}\ln f_\alpha(\boldsymbol{v}) - \frac{1}{m_\beta}\boldsymbol{\nabla}_{\boldsymbol{v'}}\ln f_\beta(\boldsymbol{v'})\right] f_\alpha(\boldsymbol{v}) f_\beta(\boldsymbol{v'}) \tag{B.68}$$

Since the species labels are both dummy variables, we may interchange them $\alpha \leftrightarrow \beta$. Also interchanging the integration variables $\boldsymbol{v} \leftrightarrow \boldsymbol{v'}$, we have

$$\left.\frac{dS}{dt}\right|_{\text{collisions}} = \sum_\beta\sum_\alpha \gamma_{\beta\alpha}\int d^3\boldsymbol{v'}\int d^3\boldsymbol{v}\,\frac{1}{m_\beta}(\boldsymbol{\nabla}_{\boldsymbol{v'}}\ln f_\beta)\cdot\mathrm{U}\cdot\left[\frac{1}{m_\beta}\boldsymbol{\nabla}_{\boldsymbol{v'}}\ln f_\beta(\boldsymbol{v'}) - \frac{1}{m_\alpha}\boldsymbol{\nabla}_{\boldsymbol{v}}\ln f_\alpha(\boldsymbol{v})\right] f_\beta(\boldsymbol{v'}) f_\alpha(\boldsymbol{v}) \tag{B.69}$$

$$= -\sum_\beta\sum_\alpha \gamma_{\alpha\beta}\int d^3\boldsymbol{v}\int d^3\boldsymbol{v'}\,\frac{1}{m_\beta}(\boldsymbol{\nabla}_{\boldsymbol{v'}}\ln f_\beta)\cdot\mathrm{U}\cdot\left[\frac{1}{m_\alpha}\boldsymbol{\nabla}_{\boldsymbol{v}}\ln f_\alpha(\boldsymbol{v}) - \frac{1}{m_\beta}\boldsymbol{\nabla}_{\boldsymbol{v'}}\ln f_\beta(\boldsymbol{v'})\right] f_\alpha(\boldsymbol{v}) f_\beta(\boldsymbol{v'}). \tag{B.70}$$

Taking the mean of these two expressions, we have

$$\left.\frac{dS}{dt}\right|_{\text{collisions}} = \frac{1}{2}\sum_\alpha\sum_\beta \gamma_{\alpha\beta}\int d^3\boldsymbol{v}\int d^3\boldsymbol{v'}\,\left[\frac{1}{m_\alpha}\boldsymbol{\nabla}_{\boldsymbol{v}}\ln f_\alpha(\boldsymbol{v}) - \frac{1}{m_\beta}\boldsymbol{\nabla}_{\boldsymbol{v'}}\ln f_\beta(\boldsymbol{v'})\right]\cdot \tag{B.71}$$

$$\mathrm{U}\cdot\left[\frac{1}{m_\alpha}\boldsymbol{\nabla}_{\boldsymbol{v}}\ln f_\alpha(\boldsymbol{v}) - \frac{1}{m_\beta}\boldsymbol{\nabla}_{\boldsymbol{v'}}\ln f_\beta(\boldsymbol{v'})\right] f_\alpha(\boldsymbol{v}) f_\beta(\boldsymbol{v'}) \tag{B.72}$$

$$= \frac{1}{2}\sum_\alpha\sum_\beta \gamma_{\alpha\beta}\int d^3\boldsymbol{v}\int d^3\boldsymbol{v'}\,(\boldsymbol{X}_{\alpha\beta}\cdot\mathrm{U}\cdot\boldsymbol{X}_{\alpha\beta}) f_\alpha(\boldsymbol{v}) f_\beta(\boldsymbol{v'}), \tag{B.73}$$

where

$$\boldsymbol{X}_{\alpha\beta} = \frac{1}{m_\alpha}\boldsymbol{\nabla}_{\boldsymbol{v}}\ln f_\alpha(\boldsymbol{v}) - \frac{1}{m_\beta}\boldsymbol{\nabla}_{\boldsymbol{v'}}\ln f_\beta(\boldsymbol{v'}). \tag{B.74}$$

The integrand is non-negative since the distributions are non-negative and $(\boldsymbol{X}_{\alpha\beta}\cdot\mathrm{U}\cdot\boldsymbol{X}_{\alpha\beta})$ is a quadratic form with U being a positive semi-definite matrix. We have therefore shown

$$\left.\frac{dS}{dt}\right|_{\text{collisions}} \geq 0, \tag{B.75}$$

i.e. collisions always increase entropy density. We have shown previously that equality, and therefore equilibrium, is achieved here where the distributions are Maxwellians with the same temperature and flow. Collisions therefore drive the distributions towards Maxwellians with common flows and temperatures.

B.3 Linearised Landau Collision Operator

For both local analytic calculations and the RKM, the linearisation of the Landau collision operator around a Maxwellian is used

$$C_{\alpha\beta}\{f_\alpha, f_\beta\} = \underbrace{C_{\alpha\beta}\{f_\alpha^M, f_\beta^M\}}_{\substack{\text{Maxwellian-Maxwellian}\\ \text{collisions}}} + \underbrace{C_{\alpha\beta}\{\delta f_\alpha, f_\beta\}}_{\substack{\text{Test-particle}\\ \text{operator}}} + \underbrace{C_{\alpha\beta}\{f_\alpha, \delta f_\beta\}}_{\substack{\text{Field-particle}\\ \text{operator}}} + \underbrace{C_{\alpha\beta}\{\delta f_\alpha, \delta f_\beta\}}_{\substack{\text{Nonlinear}\\ \text{operator}}}. \tag{B.76}$$

Here we are careful to note that for ionic mixtures, a Maxwellian with a common flow and temperature is expanded around, i.e.

$$f_\alpha^M = n_\alpha \left(\frac{m_\alpha}{2\pi T_i}\right)^{3/2} \exp\left(-\frac{m_\alpha |\boldsymbol{v} - \boldsymbol{u}_i|^2}{2T_i}\right) \tag{B.77}$$

where the peculiar velocity for ion kinetic equations $\boldsymbol{w} = \boldsymbol{v} - \boldsymbol{u}_i$ is then introduced. In contrast, the electron DF is expanded around a Maxwellian with its own distinct flow and temperature

$$f_e^M = n_e \left(\frac{m_e}{2\pi T_e}\right)^{3/2} \exp\left(-\frac{m_e |\boldsymbol{v} - \boldsymbol{u}_e|^2}{2T_e}\right), \tag{B.78}$$

where for the electron kinetic equations the peculiar velocity is $\boldsymbol{w} = \boldsymbol{v} - \boldsymbol{u}_e$. This difference means that the Maxwellian-Maxwellian collision term does not vanish for electron-ion and ion-electron collisions, and the linearised ion-electron operator will have a slightly different form.

B.3.1 Test-particle collision operator

The test-particle operator may be evaluated explicitly. Starting from the Rosenbluth form B.31

$$C_{\alpha\beta}^T\{f_\alpha\} \equiv C_{\alpha\beta}\{\delta f_\alpha, f_\beta^M\} = L_{\alpha\beta} \frac{\partial}{\partial v_i}\left[-\frac{m_\alpha}{m_\beta}\frac{\partial \mathcal{H}_\beta^M}{\partial v_i} f_\alpha + \frac{1}{2}\frac{\partial^2 \mathcal{G}_\beta^M}{\partial v_i \partial v_j}\frac{\partial f_\alpha}{\partial v_j}\right], \tag{B.79}$$

where $\mathcal{H}_\beta^M$ and $\mathcal{G}_\beta^M$ are the Rosenbluth potentials B.29 evaluated for a Maxwellian distribution f_β^M. Since a Maxwellian distribution is isotropic in velocity space, so will the Rosenbluth potentials. The relevant derivatives for the Rosenbluth potentials are

$$\frac{\partial \mathcal{H}_\beta^M}{\partial v_i} = \frac{\partial \mathcal{H}_\beta^M}{\partial w}\frac{\partial w}{\partial v_i} = \frac{\partial \mathcal{H}_\beta^M}{\partial w}\frac{w_i}{w}, \tag{B.80}$$

and

$$\frac{\partial^2 \mathcal{G}_\beta^M}{\partial v_i \partial v_j} = \frac{\partial}{\partial w_i}\left(\frac{\partial \mathcal{G}_\beta^M}{\partial w}\frac{w_j}{w}\right) \tag{B.81}$$

$$= \frac{\partial}{\partial w_i}\left(\frac{\partial \mathcal{G}_\beta^M}{\partial w}\right)\frac{w_j}{w} + \frac{\partial \mathcal{G}_\beta^M}{\partial w}\frac{\partial}{\partial w_i}\left(\frac{w_j}{w}\right) \tag{B.82}$$

$$= \frac{\partial^2 \mathcal{G}_\beta^M}{\partial w^2}\frac{w_i w_j}{w^2} + \frac{\partial \mathcal{G}_\beta^M}{\partial w}\mathrm{W}_{ij} \tag{B.83}$$

where $\mathrm{W}_{ij} = (w^2\delta_{ij} - w_i w_j)/w^3$. Substituting into the Rosenbluth form B.31, the test-particle collision operator becomes

$$C^T_{\alpha\beta}\{f_\alpha\} = L_{\alpha\beta}\frac{\partial}{\partial w_i}\bigg[-\frac{m_\alpha}{m_\beta}\frac{\partial \mathcal{H}^M_\beta}{\partial w}\frac{w_i}{w}f_\alpha + \frac{1}{2}\bigg(\frac{\partial^2 \mathcal{G}^M_\beta}{\partial w^2}\frac{w_i w_j}{w^2} + \frac{\partial \mathcal{G}^M_\beta}{\partial w}\mathrm{W}_{ij}\bigg)\frac{\partial f_\alpha}{\partial w_j}\bigg] \tag{B.84}$$

$$= L_{\alpha\beta}\frac{\partial}{\partial w_i}\bigg[\bigg(-\frac{m_\alpha}{m_\beta}\frac{\partial \mathcal{H}^M_\beta}{\partial w}f_\alpha + \frac{1}{2}\frac{\partial^2 \mathcal{G}^M_\beta}{\partial w^2}\frac{\partial f_\alpha}{\partial w}\bigg)\frac{w_i}{w} + \frac{1}{2}\frac{\partial \mathcal{G}^M_\beta}{\partial w}\mathrm{W}_{ij}\frac{\partial f_\alpha}{\partial w_j}\bigg], \tag{B.85}$$

having used $w_j\partial_{w_j} f_\alpha = w\partial_w f_\alpha$. We note the identity

$$\frac{\partial}{\partial w_i}\bigg(F(w)w_i\bigg) = w\frac{\partial F}{\partial w} + 3F(w) = \frac{1}{w^2}\frac{\partial}{\partial w}\bigg(w^3 F(w)\bigg), \tag{B.86}$$

which simplifies the first term

$$\frac{\partial}{\partial w_i}\bigg[\bigg(-\frac{m_\alpha}{m_\beta}\frac{\partial \mathcal{H}^M_\beta}{\partial w}f_\alpha + \frac{1}{2}\frac{\partial^2 \mathcal{G}^M_\beta}{\partial w^2}\frac{\partial f_\alpha}{\partial w}\bigg)\frac{w_i}{w}\bigg] = \frac{1}{w^2}\frac{\partial}{\partial w}\bigg[w^2\bigg(-\frac{m_\alpha}{m_\beta}\frac{\partial \mathcal{H}^M_\beta}{\partial w}f_\alpha + \frac{1}{2}\frac{\partial^2 \mathcal{G}^M_\beta}{\partial w^2}\frac{\partial f_\alpha}{\partial w}\bigg)\bigg]. \tag{B.87}$$

The last term is handled by noting

$$\partial_{w_i}(F(w)\mathrm{W}_{ij}\partial_{w_j} f) = F'(w)\underbrace{\frac{w_i}{w}\mathrm{W}_{ij}}_{=0}\partial_{w_j} f + F(w)(\partial_{w_i}\mathrm{W}_{ij}\partial_{w_j} f) = F(w)\frac{1}{w^3}\hat{\mathcal{L}}f, \tag{B.88}$$

where we define the Lorentz or 'pitch angle scattering' operator

$$\hat{\mathcal{L}}f \equiv w^3\partial_{w_i}(\mathrm{W}_{ij}\partial_{w_j} f) = \frac{1}{\sin\vartheta}\partial_\vartheta(\sin\vartheta\partial_\vartheta f) + \frac{1}{\sin^2\vartheta}\partial^2_\varphi f = \partial_\mu\big((1-\mu^2)\partial_\mu\big) + \frac{1}{1-\mu^2}\partial^2_\varphi, \tag{B.89}$$

where we write $\hat{\mathcal{L}}$ explicitly in spherical polar velocity coordinates ($\mu = \cos\vartheta$, φ). The Lorentz operator is then the angular part of the Laplacian in spherical polar coordinates

$$\nabla^2_{\boldsymbol{w}} f = \frac{1}{w^2}\partial_w(w^2\partial_w f) + \frac{1}{w^2}\hat{\mathcal{L}}f. \tag{B.90}$$

This suggests that spherical harmonics are eigenfunctions of this operator with eigenvalues $-l(l+1)$, since they are defined when they arise when solving the angular part of a separable solution of Laplace's equation. It also suggests that the Lorentz operator is the part of the test-particle collision operator responsible for angular diffusion in velocity space, with the other terms responsible for energy scattering. When expanding the distribution in spherical harmonics, this term then has a simple form. The last term is then written as

$$\frac{\partial}{\partial w_i}\bigg[\frac{1}{2}\frac{\partial \mathcal{G}^M_\beta}{\partial w}W_{ij}\frac{\partial f_\alpha}{\partial w_j}\bigg] = \frac{1}{2w^3}\frac{\partial \mathcal{G}^M_\beta}{\partial w}\hat{\mathcal{L}}f_\alpha. \tag{B.91}$$

In total, the test-particle operator then becomes

$$C^T_{\alpha\beta}\{f_\alpha\} = L_{\alpha\beta}\bigg(\frac{1}{2w^3}\frac{\partial \mathcal{G}^M_\beta}{\partial w}\hat{\mathcal{L}}f_\alpha + \frac{1}{w^2}\frac{\partial}{\partial w}\bigg[-\frac{m_\alpha}{m_\beta}w^2\frac{\partial \mathcal{H}^M_\beta}{\partial w}f_\alpha + \frac{1}{2}w^2\frac{\partial^2 \mathcal{G}^M_\beta}{\partial w^2}\frac{\partial f_\alpha}{\partial w}\bigg]\bigg). \tag{B.92}$$

The Rosenbluth potentials are then evaluated for a Maxwellian background.

Evaluating Rosenbluth potentials for Maxwellian background

The first Rosenbluth potential may be found recalling the Poisson's equation relationship B.33

$$\nabla_w^2 \mathcal{H}_\beta^M = -4\pi f_\beta^M(w) \quad \Rightarrow \quad \frac{1}{w^2}\partial_w(w^2\partial_w \mathcal{H}_\beta^M) = -4\pi f_\beta^M(w), \tag{B.93}$$

where the isotropy of $f_\beta(\boldsymbol{w}) = f_\beta(w)$ also implies isotropy of $\mathcal{H}_\beta^M(\boldsymbol{w}) = \mathcal{H}_\beta^M(w)$. Integrating,

$$\begin{aligned}
\partial_w \mathcal{H}_\beta^M &= -4\pi \frac{1}{w^2}\int_0^w du\, u^2 f_\beta^M(u) && \text{(B.94)}\\
&= -\frac{2n_\beta}{v_{\text{th},\beta}^2}\frac{1}{\xi_\beta^2}\frac{2}{\sqrt{\pi}}\int_0^{\xi_\beta} dx\, x^2 e^{-x^2} && \text{(B.95)}\\
&= -\frac{2n_\beta}{v_{\text{th},\beta}^2}\frac{1}{\xi_\beta^2}\frac{2}{\sqrt{\pi}}\int_0^{\xi_\beta} dx\, \frac{1}{2}\left(e^{-x^2} - \frac{d}{dx}(xe^{-x^2})\right) && \text{(B.96)}\\
&= -\frac{2n_\beta}{v_{\text{th},\beta}^2}\frac{1}{2\xi_\beta^2}\left(\text{erf}(\xi_\beta) - \frac{2}{\sqrt{\pi}}\xi_\beta e^{-\xi_\beta^2}\right) && \text{(B.97)}\\
&= -\frac{2n_\beta}{v_{\text{th},\beta}^2}G(\xi_\beta) && \text{(B.98)}
\end{aligned}$$

where we introduce the normalised speed coordinates $\xi_\beta = w/v_{\text{th},\beta}$ and the Chandrasekhar function

$$G(x) \equiv \frac{1}{x^2}\frac{2}{\sqrt{\pi}}\int_0^x dy\, y^2 e^{-y^2} \equiv \frac{\text{erf}(x) - \frac{2}{\sqrt{\pi}}xe^{-x^2}}{2x^2} \equiv \frac{\text{erf}(x) - x\frac{d}{dx}\text{erf}(x)}{2x^2}. \tag{B.99}$$

Integrating again,

$$\begin{aligned}
\mathcal{H}_\beta^M(w) &= -\frac{2n_\beta}{v_{\text{th},\beta}^2}\int_0^w du\, G(\xi_\beta) && \text{(B.100)}\\
&= -\frac{n_\beta}{v_{\text{th},\beta}}\int_0^{\xi_\beta} dx\, \left(x^{-2}\text{erf}(x) - x^{-1}\frac{d}{dx}\text{erf}(x)\right) && \text{(B.101)}\\
&= -\frac{n_\beta}{v_{\text{th},\beta}}\int_0^{\xi_\beta} dx\, \frac{d}{dx}\left(-x^{-1}\text{erf}(x)\right) && \text{(B.102)}\\
&= \frac{n_\beta}{v_{\text{th},\beta}}\frac{\text{erf}(\xi_\beta)}{\xi_\beta} && \text{(B.103)}
\end{aligned}$$

The required derivative of $\mathcal{H}_\beta^M$ is then

$$\frac{\partial \mathcal{H}_\beta^M}{\partial w} = -\frac{2n_\beta}{v_{\text{th},\beta}^2}G(\xi_\beta). \tag{B.104}$$

The second Rosenbluth potential is found from

$$\nabla_w^2 \mathcal{G}_\beta^M = 2\mathcal{H}_\beta^M(w) \quad \Rightarrow \quad \frac{1}{w^2}\partial_w(w^2\partial_w \mathcal{G}_\beta^M) = 2\mathcal{H}_\beta^M(w), \tag{B.105}$$

having again used isotropy. Integrating,

$$\partial_w \mathcal{G}_\beta^M = \frac{2}{w^2}\int_0^w du\, u^2 \mathcal{H}_\beta^M(u) \tag{B.106}$$

$$= \frac{2n_\beta}{v_{\text{th},\beta}}\frac{1}{w^2}\int_0^w du\, u^2 \frac{\text{erf}(\xi_\beta)}{\xi_\beta} \tag{B.107}$$

$$= 2n_\beta \frac{1}{\xi_\beta^2}\int_0^{\xi_\beta} dx\, x\text{erf}(x) \tag{B.108}$$

$$= n_\beta \frac{1}{\xi_\beta^2}\left(\xi_\beta^2 \text{erf}(\xi_\beta) - \frac{2}{\sqrt{\pi}}\int_0^{\xi_\beta} dx\, x^2 e^{-x^2}\right) \tag{B.109}$$

$$= n_\beta\Big(\text{erf}(\xi_\beta) - G(\xi_\beta)\Big). \tag{B.110}$$

The second derivative will also be required, which may be found as

$$\partial_w^2 \mathcal{G}_\beta^M = 2\mathcal{H}_\beta^M - \frac{2}{w}\partial_w \mathcal{G}_\beta^M \tag{B.111}$$

$$= 2\frac{n_\beta}{v_{\text{th},\beta}}\frac{\text{erf}(\xi_\beta)}{\xi_\beta} - \frac{2}{w}n_\beta\Big(\text{erf}(\xi_\beta) - G(\xi_\beta)\Big) \tag{B.112}$$

$$= \frac{2n_\beta}{v_{\text{th},\beta}}\frac{G(\xi_\beta)}{\xi_\beta} \tag{B.113}$$

Substituting these derivatives into the test-particle operator, the test-particle operator becomes

$$\hat{C}_{\alpha\beta}^T \delta f_\alpha = \frac{1}{2}\nu_D^{\alpha\beta}\hat{\mathcal{L}}\delta f_\alpha + \frac{1}{w^2}\partial_w\left(\frac{m_\alpha}{m_\alpha + m_\beta}\nu_s^{\alpha\beta} w^3 \delta f_\alpha + \frac{1}{2}\nu_\parallel^{\alpha\beta} w^4 \partial_w \delta f_\alpha\right), \tag{B.114}$$

where we have defined the velocity-dependent test-particle collision frequencies

$$\nu_D^{\alpha\beta} = \hat{\nu}_{\alpha\beta}\frac{\text{erf}(\xi_\beta) - G(\xi_\beta)}{\xi_\alpha^3}, \tag{B.115}$$

$$\nu_s^{\alpha\beta} = 2\hat{\nu}_{\alpha\beta}\frac{m_\alpha + m_\beta}{m_\alpha}\frac{G(\xi_\beta)}{\xi_\alpha}, \tag{B.116}$$

$$\nu_\parallel^{\alpha\beta} = 2\hat{\nu}_{\alpha\beta}\frac{G(\xi_\beta)}{\xi_\alpha^3} \tag{B.117}$$

in terms of a basic (velocity-independent) collision frequency

$$\hat{\nu}_{\alpha\beta} \equiv \frac{n_\beta q_\alpha^2 q_\beta^2 \ln\Lambda_{\alpha\beta}}{4\pi\varepsilon_0^2 m_\alpha^2 v_{\text{th},\alpha}^3}. \tag{B.118}$$

For convenience, we rewrite in terms of a rescaled slowing frequency

$$\tilde{\nu}_s^{\alpha\beta} = \frac{m_\alpha}{m_\alpha + m_\beta}\nu_s^{\alpha\beta} = 2\hat{\nu}_{\alpha\beta}\frac{G(\xi_\beta)}{\xi_\alpha}, \tag{B.119}$$

so that the test-particle operator takes the form

$$\hat{C}_{\alpha\beta}^T \delta f_\alpha = \frac{1}{2}\nu_D^{\alpha\beta}\hat{\mathcal{L}}\delta f_\alpha + \frac{1}{w^2}\partial_w\left(\tilde{\nu}_s^{\alpha\beta} w^3 \delta f_\alpha + \frac{1}{2}\nu_\parallel^{\alpha\beta} w^4 \partial_w \delta f_\alpha\right), \tag{B.120}$$

which straightforwardly sums over species β to become

$$\hat{C}_\alpha^T \delta f_\alpha \equiv \sum_\beta \hat{C}_{\alpha\beta}^T \delta f_\alpha = \frac{1}{2}\nu_D^\alpha \hat{\mathcal{L}}\delta f_\alpha + \frac{1}{w^2}\partial_w\left(\tilde{\nu}_s^\alpha w^3 \delta f_\alpha + \frac{1}{2}\nu_\parallel^\alpha w^4 \partial_w \delta f_\alpha\right), \tag{B.121}$$

where $\nu^\alpha = \sum_\beta \nu^{\alpha\beta}$ for ν_D, $\tilde{\nu}_s$, and $\nu_\parallel$.

B.3.2 Field-particle collision operator

The field particle operator

$$C^F_{\alpha\beta}\{\delta f_\beta\} \equiv C_{\alpha\beta}\{f^M_\alpha, f_\beta\} = L_{\alpha\beta}\frac{\partial}{\partial v_i}\bigg[-\frac{m_\alpha}{m_\beta}\frac{\partial \delta\mathcal{H}_\beta}{\partial v_i} f^M_\alpha + \frac{1}{2}\frac{\partial^2 \delta\mathcal{G}_\beta}{\partial v_i \partial v_j}\frac{\partial f^M_\alpha}{\partial v_j}\bigg], \tag{B.122}$$

where the Rosenbluth potentials $\delta\mathcal{H}_\beta$ and $\delta\mathcal{G}_\beta$ are determined from δf_β. Expanding the outer derivative,

$$C^F_{\alpha\beta}\{\delta f_\beta\} = L_{\alpha\beta}\bigg[-\frac{m_\alpha}{m_\beta} f^M_\alpha \nabla_v^2 \delta\mathcal{H}_\beta - \frac{m_\alpha}{m_\beta}\frac{\partial \delta\mathcal{H}_\beta}{\partial v_i}\frac{\partial f^M_\alpha}{\partial v_i} + \frac{1}{2}\bigg(\frac{\partial}{\partial v_j}\nabla_v^2 \delta\mathcal{G}_\beta\bigg)\frac{\partial f^M_\alpha}{\partial v_j} + \frac{1}{2}\frac{\partial^2 \delta\mathcal{G}_\beta}{\partial v_i \partial v_j}\frac{\partial^2 f^M_\alpha}{\partial v_i \partial v_j}\bigg]. \tag{B.123}$$

Using the Poisson equations for the Rosenbluth potentials (B.33,B.34) and

$$\frac{\partial f^M_\alpha}{\partial v_i} = -\frac{m_\alpha}{T_\alpha} w_i f^M_\alpha, \quad \frac{\partial^2 f^M_\alpha}{\partial v_i \partial v_j} = \frac{m_\alpha^2}{T_\alpha^2} w_i w_j f^M_\alpha - \frac{m_\alpha}{T_\alpha}\delta_{ij} f^M_\alpha, \tag{B.124}$$

the field-particle operator becomes

$$C^F_{\alpha\beta}\{\delta f_\beta\} = L_{\alpha\beta}\frac{m_\alpha}{T_\alpha} f^M_\alpha \bigg[4\pi \frac{T_\alpha}{m_\beta}\delta f_\beta - \delta\mathcal{H}_\beta + \bigg(\frac{m_\alpha}{m_\beta} - 1\bigg) w \frac{\partial \delta\mathcal{H}_\beta}{\partial w} + \frac{m_\alpha w^2}{2T_\alpha}\frac{\partial^2 \delta\mathcal{G}_\beta}{\partial w^2}\bigg]. \tag{B.125}$$

B.3.3 Electron-ion collision operator

For electron-ion and ion-electron collision operators, there are some careful considerations to be kept in mind before applying the multi-species results above. Firstly, the electron distribution may have a significantly different flow and temperature than the ion distribution, therefore the Maxwellian-Maxwellian collision term $C_{e\beta}\{f^M_e, f^M_\beta\}$ is nonvanishing and must be evaluated. On velocity scales relevant to electron kinetics $v \sim v_{\text{th},e}$, the ion distribution is Dirac-delta like since the ion thermal velocity is much smaller $v_{\text{th},i} \ll v_{\text{th},e}$. To leading order in $m_e/m_i \ll 1$, the ion distribution in the electron-ion collision operator may therefore be taken as a Maxwellian, and therefore as a test-particle collision operator

$$C_{e\beta}\{f_e, f_\beta\} \approx C_{e\beta}\{f_e, f^M_\beta\} = C^T_{e\beta}\{f^M_e\} + C^T_{e\beta}\{\delta f_e\}. \tag{B.126}$$

The Maxwellian-Maxwellian term is then evaluated assuming that electron flows are much slower than the electron thermal velocity $|u_e/v_{\text{th},e}| \ll 1$. When this condition is violated, electrons in the bulk of the distribution become runaway so the electron DF is no longer near LTE. In velocity coordinates of the ions $\boldsymbol{w}_i = \boldsymbol{v} - \boldsymbol{u}_i$, the electron Maxwellian is expanded as

$$f^M_e = \frac{n_e}{\pi^{3/2} v^3_{\text{th},e}} \exp\bigg(-\frac{|\boldsymbol{v} - \boldsymbol{u}_e|^2}{v^2_{\text{th},e}}\bigg) = \frac{n_e}{\pi^{3/2} v^3_{\text{th},e}} \exp\bigg(-\frac{|\boldsymbol{w}_i - (\boldsymbol{u}_e - \boldsymbol{u}_i)|^2}{v^2_{\text{th},e}}\bigg) \tag{B.127}$$

$$= \frac{n_e}{\pi^{3/2} v^3_{\text{th},e}} \exp\bigg(-\frac{w_i^2}{v^2_{\text{th},e}}\bigg)\bigg(1 + 2\frac{\boldsymbol{w}_i \cdot \Delta\boldsymbol{u}}{v^2_{\text{th},e}} + \mathcal{O}((u/v_{\text{th},e})^2\bigg) \approx \bigg(1 + 2\frac{\boldsymbol{w}_i \cdot \Delta\boldsymbol{u}}{v^2_{\text{th},e}}\bigg) f^{M0}_e, \tag{B.128}$$

where $\Delta\boldsymbol{u} = \boldsymbol{u}_e - \boldsymbol{u}_i$ and f^{M0}_e is an electron Maxwellian with zero flow in the relevant frame, here the ion frame. Evaluating the Maxwellian-Maxwellian collision term then yields

$$C_{e\beta}\{f^M_e, f^M_\beta\} = C^T_{e\beta}\{f^M_e\} = C^T_{e\beta}\{f^{M0}_e\} + C^T_{e\beta}\{\bigg(2\frac{\boldsymbol{w}_i \cdot \Delta\boldsymbol{u}}{v^2_{\text{th},e}}\bigg) f^{M0}_e\}. \tag{B.129}$$

The test-particle operator B.114 is then applied. Since this collision operator is relevant on velocity scales $v \sim v_{\mathrm{th},e}$, the large-argument asymptotics of the error and Chandrasekhar functions

$$\mathrm{erf}(x) \approx 1, \quad G(x) \approx \frac{1}{2x^2} \quad \text{for } x \gg 1 \tag{B.130}$$

are employed, yielding the test-particle collision frequencies

$$\nu_D^{e\beta} = \hat{\nu}_{e\beta} \frac{\mathrm{erf}(\xi_\beta) - G(\xi_\beta)}{\xi_e^3} \approx \hat{\nu}_{e\beta} \frac{1}{\xi_e^3}, \tag{B.131}$$

$$\nu_s^{e\beta} = 2\hat{\nu}_{e\beta} \frac{m_e + m_\beta}{m_e} \frac{G(\xi_\beta)}{\xi_e} \approx \hat{\nu}_{e\beta} \frac{2m_\beta}{m_e} \frac{1}{2\xi_\beta^2 \xi_e} = \hat{\nu}_{e\beta} \frac{T_\beta}{T_e} \frac{1}{\xi_e^3}, \tag{B.132}$$

$$\nu_\parallel^{e\beta} = 2\hat{\nu}_{e\beta} \frac{G(\xi_\beta)}{\xi_e^3} \approx \hat{\nu}_{e\beta} \frac{m_e}{m_\beta} \frac{T_\beta}{T_e} \frac{1}{\xi_e^5}, \tag{B.133}$$

so the electron-ion test-particle operator becomes

$$C_{e\beta}^T\{f_e\} = \hat{\nu}_{e\beta} \frac{1}{2\xi_e^3} \hat{\mathcal{L}} f_e + \frac{m_e}{m_\beta} \hat{\nu}_{e\beta} \frac{1}{\xi_e^2} \partial_{\xi_e} \left(f_e + \frac{1}{2\xi_e} \partial_{\xi_e} f_e \right) \approx \hat{\nu}_{e\beta} \frac{1}{2\xi_e^3} \hat{\mathcal{L}} f_e \tag{B.134}$$

Even for different electron and ion temperatures, the $C_{e\beta}^T\{f_e^{M0}\}$ term vanishes, even when including the energy scattering terms. The remaining term accounting for the relative flow becomes

$$C_{e\beta}\{f_e^M, f_\beta^M\} = \hat{\nu}_{e\beta} \frac{1}{\xi_e^3} \frac{1}{v_{\mathrm{th},e}^2} f_e^{M0} \hat{\mathcal{L}}(\Delta \boldsymbol{u} \cdot \boldsymbol{w}). \tag{B.135}$$

Writing in spherical velocity coordinates,

$$\hat{\mathcal{L}}(\Delta \boldsymbol{u} \cdot \boldsymbol{w}) = w \Big(\Delta u_x \sin\vartheta \cos\varphi + \Delta u_y \sin\vartheta \sin\varphi + \Delta u_z \cos\vartheta \Big) \tag{B.136}$$

$$= w \hat{\mathcal{L}} \left(\sqrt{1-\mu^2} \frac{\Delta u_x - i\Delta u_y}{2} e^{i\varphi} + \sqrt{1-\mu^2} \frac{\Delta u_x + i\Delta u_y}{2} e^{-i\varphi} + \mu \Delta u_z \right) \tag{B.137}$$

$$= -2w \left(\sqrt{1-\mu^2} \frac{\Delta u_x - i\Delta u_y}{2} e^{i\varphi} + \sqrt{1-\mu^2} \frac{\Delta u_x + i\Delta u_y}{2} e^{-i\varphi} + \mu \Delta u_z \right), \tag{B.138}$$

since these $l = 1$ Legendre functions are eigenfunctions of $\hat{\mathcal{L}}$ with eigenvalue $-l(l+1) = -2$. The collision term is then

$$C_{e\beta}\{f_e^M, f_\beta^M\} \approx -\hat{\nu}_{e\beta} \frac{2}{\xi_e^3} \frac{\Delta \boldsymbol{u} \cdot \boldsymbol{w}}{v_{\mathrm{th},e}^2} f_e^M. \tag{B.139}$$

where the velocity coordinate $\boldsymbol{w} = \boldsymbol{w}_e \approx \boldsymbol{w}_i$ is restored to the electron frame. The electron-ion collision operator against ion species β is finally

$$C_{e\beta}\{f_e, f_\beta\} \approx \hat{\nu}_{e\beta} \frac{1}{\xi_e^3} \left(-\frac{2\Delta \boldsymbol{u} \cdot \boldsymbol{w}}{v_{\mathrm{th},e}^2} f_e^M + \frac{1}{2} \hat{\mathcal{L}} \delta f_e \right). \tag{B.140}$$

Since the particular ion species only enters through the collision frequency prefactor, the final sum over all ion species leaves

$$C_{ei}\{f_e\} \equiv \sum_\beta C_{e\beta}\{f_e, f_\beta\} \approx Z^* \hat{\nu}_{ee} \frac{1}{\xi_e^3} \left(-\frac{2\Delta \boldsymbol{u} \cdot \boldsymbol{w}}{v_{\mathrm{th},e}^2} f_e^M + \frac{1}{2} \hat{\mathcal{L}} \delta f_e \right), \tag{B.141}$$

where the effective ionisation $Z^* = \sum_\beta \hat{\nu}_{e\beta} / \hat{\nu}_{ee}$, which in a simple plasma reduces to the ionisation of the single ion species.

B.3.4 Ion-electron collision operator

To evaluate the ion-electron collision operator, we start by expanding the electron distribution around a Maxwellian at rest in the ion rest frame as

$$f_e(\boldsymbol{w}') \approx f_e^{M0}(w') + f_e'(\boldsymbol{w}') \tag{B.142}$$

where the anisotropic part of the distribution is

$$f_e'(\boldsymbol{w}') = 2\frac{\boldsymbol{w}'\cdot\Delta\boldsymbol{u}}{v_{\text{th},e}^2} f_e^{M0} + \delta f_e(\boldsymbol{w}'), \tag{B.143}$$

which includes both the leading order anisotropic contributions from the drifting Maxwellian and Chapman-Enskog solution.

The ion-electron collision operator is then

$$C_{\alpha e}\{f_\alpha, f_e\} = C_{\alpha e}\{f_\alpha, f_e^{M0}\} + C_{\alpha e}\{f_\alpha, f_e'\} = \hat{C}_{\alpha e}^T f_\alpha + C_{\alpha e}\{f_\alpha, f_e'\}, \tag{B.144}$$

for an ion species α. The collision operator against the electron Maxwellian at rest in the ion frame has become the test-particle collision operator in the ion frame by definition. The remaining collision term is evaluated using the Rosenbluth form of the Fokker-Planck collision operator

$$C_{\alpha e}\{f_\alpha, f_e'\} = \frac{1}{4\pi}\left(\frac{q_\alpha q_e}{\varepsilon_0 m_\alpha}\right)^2 \ln\Lambda_{\alpha e}\frac{\partial}{\partial v_i}\left[-\frac{m_\alpha}{m_e}\frac{\partial \mathcal{H}_e'}{\partial v_i} f_\alpha + \frac{1}{2}\frac{\partial^2 \mathcal{G}_e'}{\partial v_i \partial v_j}\frac{\partial f_\alpha}{\partial v_j}\right], \tag{B.145}$$

where

$$\partial_{v_i}\mathcal{H}_e' = -\int d^3\boldsymbol{v}'\ \frac{u_i}{u^3} f_e'(\boldsymbol{v}'), \quad \partial_{v_i}\partial_{v_j}\mathcal{G}_e' = \int d^3\boldsymbol{v}'\ \mathrm{U}_{ij} f_e'(\boldsymbol{v}'). \tag{B.146}$$

Since the first velocity coordinate $|\boldsymbol{w}| \sim v_{\text{th},i}$, the relative velocity $\boldsymbol{u} = \boldsymbol{w} - \boldsymbol{w}' \approx -\boldsymbol{w}'$, and so

$$\partial_{v_i}\mathcal{H}_e' \approx -\int d^3\boldsymbol{w}'\ \frac{w_i'}{w'^3} f_e'(\boldsymbol{w}'), \quad \partial_{v_i}\partial_{v_j}\mathcal{G}_e' = \int d^3\boldsymbol{w}'\ \mathrm{W}_{ij}' f_e'(\boldsymbol{w}') \tag{B.147}$$

The leading order terms in $f_e'(\boldsymbol{w}')$ are $l = 1$ terms in the spherical harmonic expansion. The second integral is then much smaller than the first. The first term may be written nicely by noting that it relates directly to the electron-ion momentum exchange as

$$\boldsymbol{R}_{e\alpha} = \int d^3\boldsymbol{w}' m_e \boldsymbol{w}' C_{e\alpha}\{f_e', f_\alpha\} = -m_e\hat{\nu}_{e\alpha} v_{\text{th},e}^3 \int d^3\boldsymbol{w}' \frac{\boldsymbol{w}'}{w'^3} f_e'. \tag{B.148}$$

Substituting into the Rosenbluth form of the collision operator, we then have

$$C_{\alpha e}\{f_\alpha, f_e'\} \approx \frac{1}{4\pi}\left(\frac{q_\alpha q_e}{\varepsilon_0 m_\alpha}\right)^2 \ln\Lambda_{\alpha e}\frac{m_\alpha}{m_e^2\hat{\nu}_{e\alpha} v_{\text{th},e}^3} R_{e\alpha,i}\frac{\partial f_\alpha}{\partial v_i} = \frac{1}{\rho_\alpha}\boldsymbol{R}_{e\alpha}\cdot\boldsymbol{\nabla}_{\boldsymbol{w}} f_\alpha. \tag{B.149}$$

The ion-electron collision operator is therefore

$$C_{\alpha e}\{f_\alpha, f_e\} = \frac{1}{\rho_i}\boldsymbol{R}_{e\alpha}\cdot\boldsymbol{\nabla}_{\boldsymbol{w}} f_\alpha + \hat{C}_{\alpha e}^T f_\alpha, \tag{B.150}$$

Evaluating for an ion Maxwellian, this becomes

$$C_{\alpha e}\{f_\alpha^M, f_e\} = \left[-\frac{1}{p_\alpha}\boldsymbol{R}_{e\alpha}\cdot\boldsymbol{w} - \frac{8}{3\sqrt{\pi}}\hat{\nu}_{e\alpha}\frac{\rho_e}{\rho_\alpha}\left(1 - \frac{T_e}{T_\alpha}\right)\left(\frac{w^2}{v_{\text{th},\alpha}^2} - \frac{3}{2}\right)\right] f_\alpha^M. \tag{B.151}$$

B.3.5 Electron-ion Maxwellian exchange terms

Using the earlier result for the electron-ion collision operator

$$C_{ei}\{f_e^M, f_i^M\} = \hat{C}_{ei} f_e^M \approx -\hat{\nu}_{ei} \frac{2}{\xi_e^3} \frac{\Delta \boldsymbol{u} \cdot \boldsymbol{w}}{v_{\mathrm{th},e}^2} f_e^M, \tag{B.152}$$

the electron-ion friction between Maxwellians is

$$\begin{aligned}
\boldsymbol{R}_e^0 &= \int d^3\boldsymbol{v}\; m_e \boldsymbol{v} C_{ei}\{f_e^M, f_i^M\} && \text{(B.153)}\\
&= -\hat{\nu}_{ei} \int d^3\boldsymbol{w}\; m_e \boldsymbol{w} \frac{1}{\xi_e^3} \frac{\Delta \boldsymbol{u} \cdot \boldsymbol{w}}{v_{\mathrm{th},e}^2} f_e^M && \text{(B.154)}\\
&= -\rho_e \pi^{-3/2} v_{\mathrm{th},e}^2 \hat{\nu}_{ei} \Delta \boldsymbol{u} \cdot \underbrace{\int d^3\boldsymbol{\xi}\; \frac{1}{\xi} \hat{\boldsymbol{\xi}}\hat{\boldsymbol{\xi}} e^{-\xi^2}}_{=\frac{4\pi}{3}\mathrm{I}\int_0^\infty d\xi\; \xi e^{-\xi^2} = \frac{2\pi}{3}} && \text{(B.155)}\\
&= -\frac{4}{3\sqrt{\pi}} \hat{\nu}_{ei} \rho_e \Delta \boldsymbol{u} = -\frac{\rho_e}{\tau_{ei}} \Delta \boldsymbol{u}, && \text{(B.156)}
\end{aligned}$$

where, following Braginskii, the electron-ion collision time is defined as $\tau_{ei}^B = \frac{3\sqrt{\pi}}{4}\hat{\nu}_{ei}$ such that the Maxwellian-Maxwellian friction has a prefactor of unity.

Using the earlier result for the ion-electron collision operator

$$C_{ie}\{f_i^M, f_e\} = \left[-\frac{1}{p_i} \boldsymbol{R}_e \cdot \boldsymbol{w} - \frac{8}{3\sqrt{\pi}} \hat{\nu}_{ei} \frac{\rho_e}{\rho_i} \left(1 - \frac{T_e}{T_i}\right) \left(\frac{w^2}{v_{\mathrm{th},i}^2} - \frac{3}{2} \right) \right] f_i^M, \tag{B.157}$$

the ion-electron heat exchange is evaluated as

$$\begin{aligned}
\tilde{W}_{ie} &= \int d^3\boldsymbol{w}\; \frac{1}{2} m_i w^2 C_{ie}\{f_i^M, f_e\} && \text{(B.158)}\\
&= \int d^3\boldsymbol{w}\; \frac{1}{2} m_i w^2 \left[-\frac{1}{p_i} \boldsymbol{R}_e \cdot \boldsymbol{w} - \frac{8}{3\sqrt{\pi}} \hat{\nu}_{ei} \frac{\rho_e}{\rho_i} \left(1 - \frac{T_e}{T_i}\right) \left(\frac{w^2}{v_{\mathrm{th},i}^2} - \frac{3}{2} \right) \right] f_i^M && \text{(B.159)}\\
&= -\frac{16}{3\pi} \hat{\nu}_{ei} \rho_e v_{\mathrm{th},i}^2 \left(1 - \frac{T_e}{T_i}\right) \underbrace{\int_0^\infty d\xi\; \xi^4 \left(\xi^2 - \frac{3}{2} \right) e^{-\xi^2}}_{=\frac{3\sqrt{\pi}}{8}} && \text{(B.160)}\\
&= \frac{4}{\sqrt{\pi}} n_e \hat{\nu}_{ei} \frac{m_e}{m_i} (T_e - T_i). && \text{(B.161)}
\end{aligned}$$

Here, the δf_i contribution is subleading, so this is the leading order result.

B.3.6 Expansion in spherical harmonics

Test-particle operator

Starting from the test-particle collision operator B.114

$$\hat{C}_\alpha^T \delta f_\alpha = \frac{1}{2} \nu_D^\alpha \hat{\mathcal{L}} f_\alpha + \frac{1}{w^2} \partial_w \left(\tilde{\nu}_s^\alpha w^3 f_\alpha + \frac{1}{2} \nu_\parallel^\alpha w^4 \partial_w f_\alpha \right), \tag{B.162}$$

the spherical harmonic projection straightforwardly becomes

$$\begin{aligned}
\mathcal{C}_\alpha^{T,(l,m)} &\equiv \langle l, m | \hat{C}_\alpha^T \delta f_\alpha \rangle && \text{(B.163)}\\
&= -\frac{l(l+1)}{2} \nu_D^\alpha \delta f_\alpha^{(l,m)} + \frac{1}{w^2} \partial_w \left(\tilde{\nu}_s^\alpha w^3 \delta f_\alpha^{(l,m)} + \frac{1}{2} \nu_\parallel^\alpha w^4 \partial_w \delta f_\alpha^{(l,m)} \right), && \text{(B.164)}
\end{aligned}$$

since spherical harmonics are eigenfunctions of the pitch-angle scattering operator via $\hat{\mathcal{L}}(P_l^m e^{im\varphi}) = -l(l+1)P_l^m e^{im\varphi}$.

Field-particle operator

Starting from the field-particle operator

$$\hat{C}^F_{\alpha\beta}\delta f_\beta = L_{\alpha\beta}\frac{m_\alpha}{T_\alpha}f^M_\alpha\left[4\pi\frac{T_\alpha}{m_\beta}\delta f_\beta - \delta\mathcal{H}_\beta + \left(\frac{m_\alpha}{m_\beta}-1\right)w\frac{\partial\delta\mathcal{H}_\beta}{\partial w} + \frac{m_\alpha w^2}{2T_\alpha}\frac{\partial^2\delta\mathcal{G}_\beta}{\partial w^2}\right], \tag{B.165}$$

we project onto the spherical harmonic basis to obtain

$$\mathcal{C}^{F,(l,m)}_{\alpha\beta} \equiv \langle l,m|\hat{C}^F_{\alpha\beta}\delta f_\beta\rangle \tag{B.166}$$

$$= L_{\alpha\beta}\frac{m_\alpha}{T_\alpha}f^M_\alpha\left[4\pi\frac{T_\alpha}{m_\beta}\delta f^{(l,m)}_\beta - \delta\mathcal{H}^{(l,m)}_\beta + \left(\frac{m_\alpha}{m_\beta}-1\right)w\frac{\partial\delta\mathcal{H}^{(l,m)}_\beta}{\partial w} + \frac{m_\alpha w^2}{2T_\alpha}\frac{\partial^2\delta\mathcal{G}^{(l,m)}_\beta}{\partial w^2}\right], \tag{B.167}$$

where the projection of the Rosenbluth potentials

$$\delta\mathcal{H}^{(l,m)}_\beta \equiv \langle l,m|\int d^3\boldsymbol{v}'\,\frac{1}{u}\delta f_\beta(\boldsymbol{v}')\rangle, \quad \delta\mathcal{G}^{(l,m)}_\beta \equiv \langle l,m|\int d^3\boldsymbol{v}'\,u\delta f_\beta(\boldsymbol{v}')\rangle. \tag{B.168}$$

Starting with the projection of the first Rosenbluth potential,

$$\delta\mathcal{H}^{(l,m)}_\beta = \int_0^\infty dw'(w')^2\int d\Omega\, e^{-im\varphi}P_l^m(\mu)\int d\Omega'\,\frac{1}{u}\delta f_\beta(w',\mu',\varphi'). \tag{B.169}$$

Recalling $u = |\boldsymbol{v}-\boldsymbol{v}'| = |\boldsymbol{w}-\boldsymbol{w}'|$, we may expand $1/u$ in Legendre polynomials through their generating function as

$$\frac{1}{u} = \sum_{k=0}^\infty \frac{w_<^k}{w_>^{k+1}}P_k(\cos\gamma), \tag{B.170}$$

where $w_< = \min(w,w')$, $w_> = \max(w,w')$, and $\cos\gamma = \boldsymbol{w}\cdot\boldsymbol{w}'/ww'$ (i.e. γ is the angle between the two velocity vectors). In spherical velocity coordinates, this cosine becomes

$$\cos\gamma = \cos\vartheta\cos\vartheta' + \sin\vartheta\sin\vartheta'\cos(\varphi-\varphi'). \tag{B.171}$$

The addition theorem for spherical harmonics expresses $P_l(\cos\gamma)$ in terms of velocity angles as

$$P_k(\cos\gamma) = \sum_{n=-k}^k \frac{(k-n)!}{(k+n)!}P_k^n(\mu)P_k^n(\mu')e^{in(\varphi-\varphi')}, \tag{B.172}$$

therefore

$$\frac{1}{u} = \sum_{k=0}^\infty\sum_{n=-k}^k \frac{w_<^k}{w_>^{k+1}}\frac{(k-n)!}{(k+n)!}P_k^n(\mu)P_k^n(\mu')e^{in(\varphi-\varphi')}. \tag{B.173}$$

Substituting into the first Rosenbluth potential projection,

$$\delta\mathcal{H}^{(l,m)}_\beta = \int_0^\infty dw'(w')^2\sum_{k=0}^\infty\sum_{n=-k}^k\int d\Omega\, e^{-im\varphi}P_l^m(\mu)\int d\Omega'\,\frac{w_<^k}{w_>^{k+1}}\frac{(k-n)!}{(k+n)!}P_k^n(\mu)P_k^n(\mu')e^{in(\varphi-\varphi')}\delta f_\beta. \tag{B.174}$$

The integral over φ yields $2\pi\delta_{n,m}$, over which the n sum is then evaluated to yield

$$\delta\mathcal{H}_\beta^{(l,m)} = 2\pi\int_0^\infty dw'(w')^2\sum_{k=0}^\infty\int_{-1}^1 d\mu\, P_l^m(\mu)P_k^m(\mu)\int d\Omega'\,\frac{w_<^k}{w_>^{k+1}}\frac{(k-m)!}{(k+m)!}P_k^m(\mu')e^{-im\varphi'}\delta f_\beta. \quad \text{(B.175)}$$

Using orthogonality of associated Legendre functions

$$\int_{-1}^1 d\mu\, P_l^m(\mu)P_k^m(\mu) = \frac{2(l+m)}{(2l+1)(l-m)!}\delta_{l,k}, \quad \text{(B.176)}$$

the μ integral and then sum over k are evaluated, yielding

$$\delta\mathcal{H}_\beta^{(l,m)} = \frac{4\pi}{2l+1}\int_0^\infty dw'(w')^2\,\frac{w_<^l}{w_>^{l+1}}\underbrace{\int d\Omega'\, P_l^m(\mu')e^{-im\varphi'}\delta f_\beta}_{=\delta f_\beta^{(l,m)}} \quad \text{(B.177)}$$

$$= \frac{4\pi}{2l+1}\int_0^\infty dw'(w')^2\,\frac{w_<^l}{w_>^{l+1}}\delta f_\beta^{(l,m)}. \quad \text{(B.178)}$$

It is then convenient to split the integral into the two regions $w' \in [0, w)$ (where $w_< = w'$, $w_> = w$) and $w' \in [w, \infty)$ (where $w_< = w$, $w_> = w'$) to yield

$$\delta\mathcal{H}_\beta^{(l,m)} = \frac{4\pi}{2l+1}\left(w^{-(l+1)}\int_0^w dw'\,(w')^{l+2}\delta f_\beta^{(l,m)} + w^l\int_w^\infty dw'\,(w')^{-(l-1)}\delta f_\beta^{(l,m)}\right). \quad \text{(B.179)}$$

The first derivative is also required, which is evaluated as

$$\partial_w\delta\mathcal{H}_\beta^{(l,m)} = \frac{4\pi}{2l+1}\left(-(l+1)w^{-(l+2)}\int_0^w dw'\,(w')^{l+2}\delta f_\beta^{(l,m)} + lw^{l-1}\int_w^\infty dw'\,(w')^{-(l-1)}\delta f_\beta^{(l,m)}\right), \quad \text{(B.180)}$$

noting that the derivatives of the integrals produce boundary terms, where the $w' = w$ boundary terms cancel exactly and the $w' = 0,\ \infty$ boundary terms vanish.

The projection of the second Rosenbluth potential may be computed similarly. Multiplying B.170 by $u^2 = w^2 + (w')^2 - 2ww'\cos\gamma$,

$$u = \sum_{k=0}^\infty \frac{w_<^k}{w_>^{k+1}}P_k(\cos\gamma)\Big[w^2 + (w')^2 - 2ww'\cos\gamma\Big]. \quad \text{(B.181)}$$

The $P_l(\cos\gamma)\cos\gamma$ term is rewritten using the recursion formula for Legendre polynomials

$$(k+1)P_{k+1}(x) = (2k+1)xP_k(x) - kP_{k-1}(x) \quad \Rightarrow xP_k(x) = \frac{k+1}{2k+1}P_{k+1}(x) + \frac{k}{2k+1}P_{k-1}(x) \quad \text{(B.182)}$$

to yield

$$u = \sum_{k=0}^\infty \frac{w_<^k}{w_>^{k+1}}\left[\Big(w^2 + (w')^2\Big)P_k(\cos\gamma) - 2ww'\left(\frac{k+1}{2k+1}P_{k+1}(\cos\gamma) + \frac{k}{2k+1}P_{k-1}(\cos\gamma)\right)\right]. \quad \text{(B.183)}$$

Shifting the summation index k for the last two terms, this becomes

$$u = \sum_{k=0}^\infty \frac{w_<^k}{w_>^{k+1}}\left[\Big(w^2 + (w')^2\Big) - 2ww'\left(\frac{k}{2k-1}\frac{w_>}{w_<} + \frac{k+1}{2k+3}\frac{w_<}{w_>}\right)\right]P_k(\cos\gamma). \quad \text{(B.184)}$$

The two combinations $w^2 + (w')^2 \equiv w_<^2 + w_>^2$ and $ww' \equiv w_< w_>$ since they are invariant under interchange of $w_<$ and $w_>$. This leaves

$$u = \sum_{k=0}^{\infty} \frac{w_<^k}{w_>^{k+1}} \left[w_<^2 + w_>^2 - 2\left(\frac{k}{2k-1} w_>^2 + \frac{k+1}{2k+3} w_<^2 \right) \right] P_k(\cos\gamma) \tag{B.185}$$

$$= \sum_{k=0}^{\infty} \frac{w_<^k}{w_>^{k+1}} \left[\frac{w_<^2}{2k+3} - \frac{w_>^2}{2k-1} \right] P_k(\cos\gamma). \tag{B.186}$$

Substituting into $\delta\mathcal{G}_\beta^{(l,m)}$, the integrals over φ and μ are evaluated using orthogonality relations identically to the $\delta\mathcal{H}_\beta^{(l,m)}$ procedure, yielding

$$\delta\mathcal{G}_\beta^{(l,m)} = \frac{4\pi}{2l+1} \int_0^\infty dw' (w')^2 \left[\frac{1}{2l+3} \frac{w_<^{l+2}}{w_>^{l+1}} - \frac{1}{2l-1} \frac{w_<^l}{w_>^{l-1}} \right] \delta f_\beta^{(l,m)} \tag{B.187}$$

$$= \frac{4\pi}{2l+1} \left(\int_0^w dw' (w')^2 \left[\frac{1}{2l+3} \frac{(w')^{l+2}}{w^{l+1}} - \frac{1}{2l-1} \frac{(w')^l}{w^{l-1}} \right] \delta f_\beta^{(l,m)} \right. \tag{B.188}$$

$$\left. + \int_w^\infty dw' (w')^2 \left[\frac{1}{2l+3} \frac{w^{l+2}}{(w')^{l+1}} - \frac{1}{2l-1} \frac{w^l}{(w')^{l-1}} \right] \delta f_\beta^{(l,m)} \right) \tag{B.189}$$

$$= \frac{4\pi}{2l+1} \left(\frac{1}{2l+3} w^{-(l+1)} \int_0^w dw' (w')^{l+4} \delta f_\beta^{(l,m)} - \frac{1}{2l-1} w^{-(l-1)} \int_0^w dw' (w')^{l+2} \delta f_\beta^{(l,m)} \right. \tag{B.190}$$

$$\left. + \frac{1}{2l+3} w^{l+2} \int_0^w dw' (w')^{-(l-1)} \delta f_\beta^{(l,m)} - \frac{1}{2l-1} w^l \int_0^w dw' (w')^{-(l-3)} \delta f_\beta^{(l,m)} \right). \tag{B.191}$$

The second derivative is required, which is evaluated as

$$\partial_w^2 \delta\mathcal{G}_\beta^{(l,m)} = \frac{4\pi}{2l+1} \left(\frac{(l+1)(l+2)}{2l+3} w^{-(l+3)} \int_0^w dw' (w')^{l+4} \delta f_\beta^{(l,m)} - \frac{l(l-1)}{2l-1} w^{-(l+1)} \int_0^w dw' (w')^{l+2} \delta f_\beta^{(l,m)} \right. \tag{B.192}$$

$$\left. + \frac{(l+2)(l+1)}{2l+3} w^l \int_0^w dw' (w')^{-(l-1)} \delta f_\beta^{(l,m)} - \frac{l(l-1)}{2l-1} w^{l-2} \int_0^w dw' (w')^{-(l-3)} \delta f_\beta^{(l,m)} \right). \tag{B.193}$$

Substituting in the spherical harmonic expansions of the Rosenbluth potentials into the field-particle operator,

$$\mathcal{C}_{\alpha\beta}^{F,(l,m)} = \left(\frac{q_\alpha q_\beta}{m_\alpha \varepsilon_0} \right)^2 \ln\Lambda_{\alpha\beta} \frac{1}{v_{\text{th},\alpha}^2} f_\alpha^M \left[\frac{m_\alpha}{m_\beta} v_{\text{th},\alpha}^2 \delta f_\beta^{(l,m)} \right. \tag{B.194}$$

$$+ \left(-1 + \left(\frac{m_\alpha}{m_\beta} - 1 \right) l + \frac{(l+1)(l+2)}{2l+3} \frac{w^2}{v_{\text{th},\alpha}^2} \right) \Psi_{\beta,1}^{(l,m)}(w) \tag{B.195}$$

$$+ \left(-1 - \left(\frac{m_\alpha}{m_\beta} - 1 \right) (l+1) - \frac{l(l-1)}{2l-1} \frac{w^2}{v_{\text{th},\alpha}^2} \right) \Psi_{\beta,2}^{(l,m)}(w) \tag{B.196}$$

$$\left. - \frac{l(l-1)}{2l-1} \frac{1}{v_{\text{th},\alpha}^2} \Psi_{\beta,3}^{(l,m)}(w) + \frac{(l+1)(l+2)}{2l+3} \frac{1}{v_{\text{th},\alpha}^2} \Psi_{\beta,4}^{(l,m)}(w) \right], \tag{B.197}$$

where we have introduced the integrals

$$\begin{aligned} \Psi_{\beta,1}^{(l,m)}(w) &= \frac{2}{2l+1} w^l \int_w^\infty du\, u^{1-l} \delta f_\beta^{(l,m)}(u), \quad \Psi_{\beta,2}^{(l,m)}(w) = \frac{2}{2l+1} \frac{1}{w^{l+1}} \int_0^w du\, u^{2+l} \delta f_\beta^{(l,m)}(u), \\ \Psi_{\beta,3}^{(l,m)}(w) &= \frac{2}{2l+1} w^l \int_w^\infty du\, u^{3-l} \delta f_\beta^{(l,m)}(u), \quad \Psi_{\beta,4}^{(l,m)}(w) = \frac{2}{2l+1} \frac{1}{w^{l+1}} \int_0^w du\, u^{4+l} \delta f_\beta^{(l,m)}(u). \end{aligned} \tag{B.198}$$

These integrals are cumulative in velocity, so are more straightforward for numerical implementation than an arbitrary link between w and w'.

APPENDIX C

Local Transport Derivation

C.1 Local Electron Transport

Following Braginskii, we solve the local electron problem for the magnetized transport quantities. The equation for $\delta f_e^{\text{local}}$ is

$$\begin{aligned} &f_e^M\left(\left[\boldsymbol{R}_e/p_e+\left(\frac{w^2}{v_{\text{th},e}^2}-\frac{5}{2}\right)\boldsymbol{\nabla}\ln T_e\right]\cdot\boldsymbol{w}+\frac{2}{v_{\text{th},e}^2}\boldsymbol{\nabla}\boldsymbol{u}_e\colon\left(\boldsymbol{w}\boldsymbol{w}-\frac{1}{3}w^2\mathrm{I}\right)\right)-C_{ei}\{f_e^M\}\\ &=C_{ee}\{\delta f_e^{\text{local}}\}+C_{ei}\{\delta f_e^{\text{local}}\}+\frac{e}{m_e}(\boldsymbol{w}\times\boldsymbol{B})\cdot\boldsymbol{\nabla}_{\boldsymbol{w}}\delta f_e^{\text{local}}\end{aligned} \tag{C.1}$$

Using

$$C_{ei}\{f_e^M\}=-Z\hat{\nu}_{ee}\frac{2}{\xi^3}\frac{\Delta\boldsymbol{u}\cdot\boldsymbol{w}}{v_{\text{th},e}^2}f_e^M \tag{C.2}$$

and

$$\boldsymbol{R}_e=\int d^3\boldsymbol{v}\; m_e\boldsymbol{v}C_{ei}\{f_e\}=-\frac{4Z}{3\sqrt{\pi}}n_em_e\hat{\nu}_{ee}\Delta\boldsymbol{u}+\frac{Z}{2}m_e\hat{\nu}_{ee}\int d^3\boldsymbol{w}\;\boldsymbol{w}\frac{1}{\xi^3}\hat{\mathcal{L}}\delta f_e \tag{C.3}$$

leaves

$$\begin{aligned} &\hat{\nu}_{ee}f_e^M\left(\left[\left(\frac{2}{\xi^3}-\frac{8}{3\sqrt{\pi}}\right)Z\boldsymbol{d}_u+\left(\xi^2-\frac{5}{2}\right)\boldsymbol{d}_T\right]\cdot\boldsymbol{\xi}+2\mathrm{d}_W\colon\left(\boldsymbol{\xi}\boldsymbol{\xi}-\frac{1}{3}\xi^2\mathrm{I}\right)\right)\\ &=\hat{\nu}_{ee}\tilde{C}_{ee}\{\delta f_e^{\text{local}}\}+Z\hat{\nu}_{ee}\tilde{C}_{ei}\{\delta f_e^{\text{local}}\}-\frac{1}{n_e}Z\hat{\nu}_{ee}f_e^M\boldsymbol{\xi}\cdot\int d^3\boldsymbol{w}'\;\boldsymbol{\xi}'\frac{1}{\xi'^3}\hat{\mathcal{L}}\delta f_e^{\text{local}}(\boldsymbol{w}')+\omega_{c,e}(\boldsymbol{\xi}\times\boldsymbol{b})\cdot\boldsymbol{\nabla}_{\boldsymbol{\xi}}\delta f_e^{\text{local}}\end{aligned} \tag{C.4}$$

where the velocity is nondimensionalised as $\boldsymbol{\xi}=\boldsymbol{w}/v_{\text{th},e}$, linearised collision operators are nondimensionalised as $C_{\alpha\beta}=\hat{\nu}_{\alpha\beta}\tilde{C}_{\alpha\beta}$, and the thermodynamic drives are nondimensionalised as

$$\boldsymbol{d}_u=\Delta\boldsymbol{u}/v_{\text{th},e},\quad \boldsymbol{d}_T=\lambda_{\text{th},e}\boldsymbol{\nabla}\ln T_e,\quad \mathrm{d}_W=\frac{\boldsymbol{\nabla}\boldsymbol{u}_e}{\hat{\nu}_{ee}}. \tag{C.5}$$

Since this is a linear problem for $\delta f_e^{\text{local}}$ as a perturbation away from Maxwellian with the drives $\boldsymbol{d}_u$, $\boldsymbol{d}_T$, and d_W, this motivates an ansatz of the form

$$\delta f_e^{\text{local}}=f_e^M\left(\boldsymbol{\Phi}_u(\xi)\cdot\boldsymbol{\xi}+\boldsymbol{\Phi}_T(\xi)\cdot\boldsymbol{\xi}+\hat{\Phi}_W(\xi)\colon\left(\boldsymbol{\xi}\boldsymbol{\xi}-\frac{1}{3}\xi^2\mathrm{I}\right)\right), \tag{C.6}$$

where the dimensionless functions $\boldsymbol{\Phi}_u(\xi)$, $\boldsymbol{\Phi}_T(\xi)$, and $\hat{\Phi}_W(\xi)$ are driven by the dimensionless thermodynamic drives $\boldsymbol{d}_u$, $\boldsymbol{d}_T$, and d_W, respectively. This may be substituted into the local problem, and independent equations for $\boldsymbol{\Phi}_u(\xi)$, $\boldsymbol{\Phi}_T(\xi)$, and $\hat{\Phi}_W(\xi)$ may be obtained from their individual drives. For the flow-driven perturbation, we obtain

$$e^{-\xi^2}\left(\frac{2}{\xi^3}-\frac{8}{3\sqrt{\pi}}\right)Z\boldsymbol{d}_u\cdot\boldsymbol{\xi}=\tilde{C}_{ee}\{\boldsymbol{\Phi}_u\cdot\boldsymbol{\xi}e^{-\xi^2}\}+Z\tilde{C}_{ei}\{\boldsymbol{\Phi}_u\cdot\boldsymbol{\xi}e^{-\xi^2}\} \tag{C.7}$$

$$+2Z\frac{4}{3\sqrt{\pi}}e^{-\xi^2}\boldsymbol{\xi}\cdot\int d\xi'\,\xi'\boldsymbol{\Phi}_u(\xi')e^{-\xi'^2}+\frac{4}{3\sqrt{\pi}}\chi(\boldsymbol{\xi}\times\boldsymbol{b})\cdot\boldsymbol{\Phi}_u e^{-\xi^2} \tag{C.8}$$

having used $\hat{\mathcal{L}}(f(\xi)\hat{\boldsymbol{\xi}})=-2f(\xi)\hat{\boldsymbol{\xi}}$ and $\int d\Omega\,\hat{\boldsymbol{\xi}}\hat{\boldsymbol{\xi}}=\frac{4\pi}{3}\mathrm{I}$, and introducing the electron hall parameter

$$\chi=\omega_{c,e}\tau_{ee}=\frac{3\sqrt{\pi}}{4}\frac{\omega_{c,e}}{\hat{\nu}_{ee}}. \tag{C.9}$$

There are three relevant orthogonal directions, namely parallel to the magnetic field $\boldsymbol{b}=\boldsymbol{B}/B$, perpendicular to the magnetic field but parallel to the drive $(\boldsymbol{b}\times\boldsymbol{d}_u)\times\boldsymbol{b}$, and perpendicular to both $\boldsymbol{b}\times\boldsymbol{d}_u$. A further ansatz for the perturbation is therefore motivated, taking the form

$$\boldsymbol{\Phi}_u(\xi)=\phi_u^{\parallel}(\xi)\boldsymbol{bb}\cdot\boldsymbol{d}_u+\phi_u^{\perp}(\xi)(\mathrm{I}-\boldsymbol{bb})\cdot\boldsymbol{d}_u+\phi_u^{\times}(\xi)(\boldsymbol{b}\times\boldsymbol{d}_u). \tag{C.10}$$

It is sufficient to consider $\boldsymbol{d}_u\perp\boldsymbol{b}$, with parallel $\parallel$ terms recovered from $\perp$ terms for $\chi=0$. Choosing a coordinate system with $\boldsymbol{d}_u=d_u\hat{\boldsymbol{x}}$ and $\boldsymbol{b}=\hat{\boldsymbol{z}}$, we have $\boldsymbol{\xi}\times\boldsymbol{b}=-\xi_x\hat{\boldsymbol{y}}+\xi_y\hat{\boldsymbol{x}}$ and

$$\boldsymbol{\Phi}_u(\xi)=d_u(\phi_u^{\perp}(\xi)\hat{\boldsymbol{x}}+\phi_u^{\times}(\xi)\hat{\boldsymbol{y}}). \tag{C.11}$$

This yields

$$e^{-\xi^2}\left(\frac{2}{\xi^3}-\frac{8}{3\sqrt{\pi}}\right)Z\xi_x=\tilde{C}_{ee}\{(\phi_u^{\perp}\xi_x+\phi_u^{\times}\xi_y)e^{-\xi^2}\}+Z\tilde{C}_{ei}\{(\phi_u^{\perp}\xi_x+\phi_u^{\times}\xi_y)e^{-\xi^2}\} \tag{C.12}$$

$$+2Z\frac{4}{3\sqrt{\pi}}e^{-\xi^2}\xi_x\int_0^{\infty}d\xi'\,\xi'\phi_u^{\perp}(\xi')e^{-\xi'^2}+2Z\frac{4}{3\sqrt{\pi}}e^{-\xi^2}\xi_y\int_0^{\infty}d\xi'\,\xi'\phi_u^{\times}(\xi')e^{-\xi'^2} \tag{C.13}$$

$$-\frac{4}{3\sqrt{\pi}}\chi\xi_x\phi_u^{\times}e^{-\xi^2}+\frac{4}{3\sqrt{\pi}}\chi\xi_y\phi_u^{\perp}e^{-\xi^2} \tag{C.14}$$

Spherical harmonics are eigenfunctions of the linearised collision operator, so we may write

$$\tilde{C}_{\alpha\beta}\{f(\xi)\hat{\boldsymbol{\xi}}\}=\tilde{C}^1_{\alpha\beta}\{f(\xi)\}\hat{\boldsymbol{\xi}}, \tag{C.15}$$

which is the $l=1$ component of the spherical harmonics expansion of the linearised collision operator. In particular, the electron-ion and electron-electron collision operators become

$$\tilde{C}^1_{ei}\{f(\xi)\}=-\frac{1}{\xi^3}f, \tag{C.16}$$

$$\tilde{C}^1_{ee}\{f(\xi)\}=-\frac{\mathrm{erf}(\xi)-G(\xi)}{\xi^3}f+\frac{1}{\xi^2}\frac{d}{d\xi}\left[G(\xi)\left(2\xi^2 f+\xi\frac{df}{d\xi}\right)\right] \tag{C.17}$$

$$+\frac{4}{\sqrt{\pi}}e^{-\xi^2}\left[f+\frac{2}{3}\xi\left(-1+\frac{6}{5}\xi^2\right)\int_{\xi}^{\infty}d\xi' f(\xi')-\frac{2}{3}\frac{1}{\xi^2}\int_0^{\xi}d\xi'\xi'^3 f(\xi')+\frac{4}{5}\frac{1}{\xi^2}\int_0^{\xi}d\xi'\xi'^5 f(\xi')\right]. \tag{C.18}$$

Comparing coefficients for ξ_x, ξ_y yields two equations

$$e^{-\xi^2}\left(\frac{2}{\xi^3}-\frac{8}{3\sqrt{\pi}}\right)Z\xi = \tilde{C}^1_{ee}\{\phi_u^\perp \xi e^{-\xi^2}\} + Z\tilde{C}^1_{ei}\{\phi_u^\perp \xi e^{-\xi^2}\} + \frac{8Z}{3\sqrt{\pi}}e^{-\xi^2}\xi\int_0^\infty d\xi'\ \xi'\phi_u^\perp(\xi')e^{-\xi'^2} - \frac{4\chi}{3\sqrt{\pi}}\xi\phi_u^\times e^{-\xi^2} \tag{C.19}$$

$$0 = \tilde{C}^1_{ee}\{\phi_u^\times \xi e^{-\xi^2}\} + Z\tilde{C}^1_{ei}\{\phi_u^\times \xi e^{-\xi^2}\} + \frac{8Z}{3\sqrt{\pi}}e^{-\xi^2}\xi\int_0^\infty d\xi'\ \xi'\phi_u^\times(\xi')e^{-\xi'^2} + \frac{4\chi}{3\sqrt{\pi}}\xi\phi_u^\perp e^{-\xi^2} \tag{C.20}$$

Defining $\tilde{\phi}_u = \phi_u^\perp + i\phi_u^\times$, these equations are the real and imaginary parts of

$$e^{-\xi^2}\left(\frac{2}{\xi^3}-\frac{8}{3\sqrt{\pi}}\right)Z\xi = \tilde{C}^1_{ee}\{\tilde{\phi}_u \xi e^{-\xi^2}\} + Z\tilde{C}^1_{ei}\{\tilde{\phi}_u \xi e^{-\xi^2}\} + \frac{8Z}{3\sqrt{\pi}}e^{-\xi^2}\xi\int_0^\infty d\xi'\ \xi'\tilde{\phi}_u(\xi')e^{-\xi'^2} + i\frac{4\chi}{3\sqrt{\pi}}\xi\tilde{\phi}_u e^{-\xi^2} \tag{C.21}$$

We then solve by expanding the complex perturbation $\tilde{\phi}_u$ over a convenient set of orthogonal polynomials. Since our solution should be over $\xi \in [0,\infty)$, and we naturally have a weight function $\xi^{2\alpha+1}e^{-\xi^2}$ for some α, the Generalised Laguerre or Sonine polynomials $L_p^{(\alpha)}(\xi^2)$ are an appropriate choice. In particular we choose $\alpha = 3/2$ for the $l = 1$ problem (for the vectorial drives), since in general the Sonine polynomials of index $\alpha = l + 1/2$ are the appropriate set of orthogonal polynomials for the radial coordinate dependence when expanding a function in three dimensions over spherical harmonics, i.e.

$$f(\boldsymbol{\xi}) = \sum_{l=0}^{\infty}\sum_{m=-l}^{l}\sum_{p=0}^{\infty} a_{(l,m,p)}L_p^{(l+1/2)}(\xi^2)\xi^l e^{-\xi^2}P_l^m(\cos\vartheta)e^{im\varphi} \tag{C.22}$$

provides a suitable complete set of orthogonal functions to expand over [84][1]. The complex perturbation $\tilde{\phi}_u$ is therefore expanded over Sonine polynomials as

$$\tilde{\phi}_u = \sum_{p=1}^{\infty}\tilde{a}_p L_p^{(3/2)}(\xi^2), \tag{C.23}$$

where the $p = 0$ term is omitted to constrain zero flow since

$$0 = \int d^3\boldsymbol{w}\ \boldsymbol{w}\delta f_\alpha \propto \int_0^\infty d\xi\ e^{-\xi^2}\xi^4\tilde{\phi}_u \propto \tilde{a}_0. \tag{C.24}$$

Noting the orthogonality relation of the Sonine polynomials

$$\int_0^\infty d\xi\ e^{-\xi^2}\xi^{2\alpha+1}L_p^{(\alpha)}(\xi^2)L_q^{(\alpha)}(\xi^2) = \frac{\Gamma(p+\alpha+1)}{2\Gamma(p+1)}\delta_{pq}, \tag{C.25}$$

and the first few Sonine polynomials $L_0^{(\alpha)}(\xi^2) = 1, \quad L_1^{(\alpha)}(\xi^2) = -\xi^2 + \alpha + 1$, equations for the expansion coefficients $\tilde{a}_p$ may be obtained by integrating over

$$\int_0^\infty d\xi\ \xi^3 L_q^{(3/2)}(\xi^2)\ldots \tag{C.26}$$

[1]Instead of the ansatz introducing $\boldsymbol{\Phi}_{u,T}$, this could have been the initial series expansion for $\delta f_\alpha^{\text{local}}$ which would yield a similar matrix problem for $a_{1,m,p}$ from which the heat flux and friction could be evaluated.

which yields

$$ZG_q^u = \sum_{p=1}^{\infty} \left(A_{qp}^{ee} + ZA_{qp}^{ei} + i\chi B_{qp} \right) \tilde{a}_p, \tag{C.27}$$

where the vectors

$$G_q^u = \int_0^\infty d\xi \, e^{-\xi^2} L_q^{(3/2)}(\xi^2) \left(2\xi - \frac{8}{3\sqrt{\pi}} \xi^4 \right), \tag{C.28}$$

$$B_{qp} = \frac{4}{3\sqrt{\pi}} \frac{\Gamma(q+5/2)}{2\Gamma(q+1)} \delta_{qp}, \tag{C.29}$$

and the matrix elements of the linearised collision operators are

$$A_{qp}^{ee} = \int_0^\infty d\xi \, \xi^3 L_q^{(3/2)}(\xi^2) \tilde{C}_{ee}^1 \{ L_p^{(3/2)}(\xi^2) \xi e^{-\xi^2} \}, \tag{C.30}$$

$$A_{qp}^{ei} = \int_0^\infty d\xi \, \xi^3 L_q^{(3/2)}(\xi^2) \tilde{C}_{ei}^1 \{ L_p^{(3/2)}(\xi^2) \xi e^{-\xi^2} \}. \tag{C.31}$$

Similarly for the temperature-gradient-driven terms, we expand the perturbation

$$\boldsymbol{\Phi}_T(\xi) = \phi_T^{\parallel}(\xi) \boldsymbol{bb} \cdot \boldsymbol{d}_T + \phi_T^{\perp}(\xi) (\mathrm{I} - \boldsymbol{bb}) \cdot \boldsymbol{d}_T + \phi_T^{\times}(\xi) (\boldsymbol{b} \times \boldsymbol{d}_T), \tag{C.32}$$

and then expand over Sonine polynomials

$$\tilde{\phi}_T = \sum_{p=1}^{\infty} \tilde{b}_p L_p^{(3/2)}(\xi^2), \tag{C.33}$$

to obtain an equation for the expansion coefficients

$$G_q^T = \sum_{p=1}^{\infty} \left(A_{qp}^{ee} + ZA_{qp}^{ei} + i\chi B_{qp} \right) \tilde{b}_p, \tag{C.34}$$

where

$$G_q^T = \int_0^\infty d\xi \, e^{-\xi^2} L_q^{(3/2)}(\xi^2) \xi^4 \left(\xi^2 - \frac{5}{2} \right) = -\frac{15\sqrt{\pi}}{16} \delta_{q1}. \tag{C.35}$$

Truncating the Sonine expansion to some maximum order and recasting these equations in matrix form in the $L_q^{(3/2)}$ basis for $q \geq 1$, we have

$$Z\boldsymbol{G}^u = (\hat{A}^{ee} + Z\hat{A}^{ei} + i\chi\hat{B}) \cdot \tilde{\boldsymbol{a}}, \quad \boldsymbol{G}^T = (\hat{A}^{ee} + Z\hat{A}^{ei} + i\chi\hat{B}) \cdot \tilde{\boldsymbol{b}}, \tag{C.36}$$

which may be solved by a simple matrix inversion. Computing these matrix elements, we obtain

$$\hat{A}^{ee} = -\sqrt{2}\begin{pmatrix} 1/2 & 3/8 & 15/64 & \cdots \\ 3/8 & 45/32 & 309/256 & \cdots \\ 15/64 & 309/256 & 5657/2048 & \cdots \\ \vdots & \vdots & \vdots & \ddots \end{pmatrix}, \quad \hat{A}^{ei} = -\begin{pmatrix} 13/8 & 69/32 & 165/64 & \cdots \\ 69/32 & 433/128 & 1077/256 & \cdots \\ 165/64 & 1077/256 & 2957/512 & \cdots \\ \vdots & \vdots & \vdots & \ddots \end{pmatrix}, \tag{C.37}$$

$$\hat{B} = \begin{pmatrix} 5/4 & 0 & 0 & \cdots \\ 0 & 35/16 & 0 & \cdots \\ 0 & 0 & 105/32 & \cdots \\ \vdots & \vdots & \vdots & \ddots \end{pmatrix}, \quad \boldsymbol{G}^u = \begin{pmatrix} 3/2 \\ 15/8 \\ 35/16 \\ \vdots \end{pmatrix}, \quad \boldsymbol{G}^T = -\frac{15\sqrt{\pi}}{16}\begin{pmatrix} 1 \\ 0 \\ 0 \\ \vdots \end{pmatrix}. \tag{C.38}$$

The heat flux may be obtained from

$$\begin{aligned} \boldsymbol{q}_e^{\text{local}} &= \int d^3\boldsymbol{w}\, \frac{1}{2} m_e w^2 \boldsymbol{w} \delta f_e^{\text{local}} && \text{(C.39)} \\ &= \frac{1}{2\pi^{3/2}} n_e m_e v_{\text{th},e}^3 \int d^3\boldsymbol{\xi}\, e^{-\xi^2} \xi^2 \boldsymbol{\xi}\boldsymbol{\xi} \cdot (\Phi_T(\xi) + \Phi_u(\xi)) && \text{(C.40)} \\ &= \frac{1}{2\pi^{3/2}} n_e m_e v_{\text{th},e}^3 \int d\xi\, e^{-\xi^2} \xi^6 \int d\Omega\, \hat{\boldsymbol{\xi}}\hat{\boldsymbol{\xi}} \cdot (\Phi_T(\xi) + \Phi_u(\xi)) && \text{(C.41)} \\ &= n_e T_e v_{\text{th},e} \frac{4}{3\sqrt{\pi}} \int d\xi\, e^{-\xi^2} \xi^6 (\Phi_T(\xi) + \Phi_u(\xi)) && \text{(C.42)} \end{aligned}$$

This then splits the heat flux up into two components $\boldsymbol{q}_e^{\text{local}} = \boldsymbol{q}_e^T + \boldsymbol{q}_e^u$,

$$\begin{aligned} \boldsymbol{q}_e^u &= n_e T_e v_{\text{th},e} \frac{4}{3\sqrt{\pi}} \int d\xi\, e^{-\xi^2} \xi^6 \Phi_u(\xi) && \text{(C.43)} \\ &= n_e T_e v_{\text{th},e} \frac{4}{3\sqrt{\pi}} \int d\xi\, e^{-\xi^2} \xi^6 \Big(\phi_u^{\parallel}(\xi)(\boldsymbol{b}\cdot\boldsymbol{d}_u)\boldsymbol{b} + \phi_u^{\perp}(\xi)(\mathrm{I} - \boldsymbol{b}\boldsymbol{b}) \cdot \boldsymbol{d}_u + \phi_u^{\times}(\xi)(\boldsymbol{b}\times\boldsymbol{d}_u) \Big) && \text{(C.44)} \\ &= n_e T_e \Big(\hat{\beta}_{Tu}^{\parallel} \boldsymbol{b}\boldsymbol{b}\cdot\Delta\boldsymbol{u} + \hat{\beta}_{Tu}^{\perp}(\mathrm{I} - \boldsymbol{b}\boldsymbol{b})\cdot\Delta\boldsymbol{u} + \hat{\beta}_{Tu}^{\times}(\boldsymbol{b}\times\Delta\boldsymbol{u}) \Big), && \text{(C.45)} \end{aligned}$$

where

$$\begin{aligned} \tilde{\beta}_{Tu} \equiv \hat{\beta}_{Tu}^{\perp} + i\hat{\beta}_{Tu}^{\times} &= \frac{4}{3\sqrt{\pi}} \int d\xi\, e^{-\xi^2} \xi^6 \tilde{\phi}_u && \text{(C.46)} \\ &= \frac{4}{3\sqrt{\pi}} \sum_{p=1}^{\infty} \tilde{a}_p \int_0^{\infty} d\xi\, e^{-\xi^2} \xi^6 L_p^{(3/2)}(\xi^2) && \text{(C.47)} \\ &= \frac{4}{3\sqrt{\pi}} \sum_{p=1}^{\infty} \tilde{a}_p \int_0^{\infty} d\xi\, e^{-\xi^2} \xi^4 \left(\frac{5}{2} L_0^{(3/2)}(\xi^2) - L_1^{(3/2)}(\xi^2) \right) L_p^{(3/2)}(\xi^2) && \text{(C.48)} \\ &= -\frac{4}{3\sqrt{\pi}} \frac{\Gamma(7/2)}{2\Gamma(2)} \tilde{a}_1 && \text{(C.49)} \\ &= -\frac{5}{4}\tilde{a}_1 = \frac{4}{3\sqrt{\pi}} \boldsymbol{G}^T \cdot \tilde{\boldsymbol{a}}, && \text{(C.50)} \end{aligned}$$

where in the last line we have noted that we may write this in terms of $\boldsymbol{G}^T$, which will be convenient later. Similarly

$$\boldsymbol{q}_e^T = n_e T_e v_{\text{th},e} \frac{4}{3\sqrt{\pi}} \int d\xi\, e^{-\xi^2} \xi^6 \Phi_T(\xi) \tag{C.51}$$

$$= n_e T_e v_{\text{th},e} \frac{4}{3\sqrt{\pi}} \int d\xi\, e^{-\xi^2} \xi^6 \left(\phi_T^{\parallel}(\xi)(\boldsymbol{b}\cdot\boldsymbol{d}_T)\boldsymbol{b} + \phi_T^{\perp}(\xi)(\mathrm{I}-\boldsymbol{bb})\cdot\boldsymbol{d}_T + \phi_T^{\times}(\xi)(\boldsymbol{b}\times\boldsymbol{d}_T) \right) \tag{C.52}$$

$$= -\frac{n_e T_e \tau_{ee}}{m_e} \left(\hat{\kappa}_e^{\parallel} \boldsymbol{bb}\cdot\boldsymbol{\nabla} T_e + \hat{\kappa}_e^{\perp}(\mathrm{I}-\boldsymbol{bb})\cdot\boldsymbol{\nabla} T_e + \hat{\kappa}_e^{\times}(\boldsymbol{b}\times\boldsymbol{\nabla} T_e) \right), \tag{C.53}$$

where

$$\tilde{\kappa}_e \equiv \hat{\kappa}_e^{\perp} + i\hat{\kappa}_e^{\times} = -\frac{32}{9\pi} \int d\xi\, e^{-\xi^2} \xi^6 \tilde{\phi}_T \tag{C.54}$$

$$= \frac{10}{3\sqrt{\pi}} \tilde{b}_1 = -\frac{32}{9\pi} \boldsymbol{G}^T \cdot \tilde{\boldsymbol{b}} \tag{C.55}$$

The momentum exchange is similarly found as

$$\boldsymbol{R}_e^{\text{local}} = -\frac{4Z}{3\sqrt{\pi}} n_e m_e \hat{\nu}_{ee} \Delta\boldsymbol{u} + Z m_e \hat{\nu}_{ee} \int d^3\boldsymbol{w}\, \boldsymbol{w} \tilde{C}_{ei}\{\delta f_e^{\text{local}}\} \tag{C.56}$$

$$= -\frac{4Z}{3\sqrt{\pi}} n_e m_e \hat{\nu}_{ee} \Delta\boldsymbol{u} + Z m_e \hat{\nu}_{ee} \int d^3\boldsymbol{w}\, \boldsymbol{w} \tilde{C}_{ei}\{f_e^M(\boldsymbol{\Phi}_T(\xi)\cdot\boldsymbol{\xi} + \boldsymbol{\Phi}_u(\xi)\cdot\boldsymbol{\xi}))\} \tag{C.57}$$

$$= -\frac{4Z}{3\sqrt{\pi}} n_e m_e \hat{\nu}_{ee} \Delta\boldsymbol{u} + \pi^{-3/2} Z n_e m_e \hat{\nu}_{ee} v_{\text{th},e} \int d^3\boldsymbol{\xi}\, \hat{\boldsymbol{\xi}}\hat{\boldsymbol{\xi}} \cdot \tilde{C}_{ei}^1\{\xi e^{-\xi^2}(\boldsymbol{\Phi}_T(\xi) + \boldsymbol{\Phi}_u(\xi))\}\xi \tag{C.58}$$

$$= -\frac{4Z}{3\sqrt{\pi}} n_e m_e \hat{\nu}_{ee} \Delta\boldsymbol{u} + \frac{4Z}{3\sqrt{\pi}} n_e m_e \hat{\nu}_{ee} v_{\text{th},e} \int_0^\infty d\xi\, \tilde{C}_{ei}^1\{\xi e^{-\xi^2}(\boldsymbol{\Phi}_T(\xi) + \boldsymbol{\Phi}_u(\xi))\}\xi^3, \tag{C.59}$$

which splits the momentum exchange into two components $\boldsymbol{R}_e^{\text{local}} = \boldsymbol{R}_e^u + \boldsymbol{R}_e^T$,

$$\boldsymbol{R}_e^u = -\frac{4Z}{3\sqrt{\pi}} n_e m_e \hat{\nu}_{ee} \left(\Delta\boldsymbol{u} - v_{\text{th},e} \int_0^\infty d\xi\, \tilde{C}_{ei}^1\{\xi e^{-\xi^2} \boldsymbol{\Phi}_u(\xi)\}\xi^3 \right) \tag{C.60}$$

$$= -\frac{4Z}{3\sqrt{\pi}} n_e m_e \hat{\nu}_{ee} \left(\Delta\boldsymbol{u} - \int_0^\infty d\xi\, \tilde{C}_{ei}^1\{\xi e^{-\xi^2}(\phi_u^{\parallel}(\xi)(\boldsymbol{b}\cdot\Delta\boldsymbol{u})\boldsymbol{b} + \phi_u^{\perp}(\xi)(\mathrm{I}-\boldsymbol{bb})\cdot\Delta\boldsymbol{u} + \phi_u^{\times}(\xi)(\boldsymbol{b}\times\Delta\boldsymbol{u}))\}\xi^3 \right) \tag{C.61}$$

$$= -\frac{n_e m_e}{\tau_{ei}} (\hat{\alpha}^{\parallel}\boldsymbol{bb}\cdot\Delta\boldsymbol{u} + \hat{\alpha}^{\perp}(\mathrm{I}-\boldsymbol{bb})\cdot\Delta\boldsymbol{u} - \hat{\alpha}^{\times}(\boldsymbol{b}\times\Delta\boldsymbol{u})), \tag{C.62}$$

where

$$\tilde{\alpha} \equiv \hat{\alpha}^{\perp} - i\hat{\alpha}^{\times} = 1 - \int_0^\infty d\xi\, \tilde{C}_{ei}^1\{\xi e^{-\xi^2} \tilde{\phi}_u(\xi)\}\xi^3 \tag{C.63}$$

$$= 1 - \sum_{p=1}^{\infty} \tilde{a}_p \int_0^\infty d\xi\, \tilde{C}_{ei}^1\{\xi e^{-\xi^2} L_p^{(3/2)}(\xi^2)\}\xi^3 \tag{C.64}$$

$$= 1 - \sum_{p=1}^{\infty} A_{0p}^{ei} \tilde{a}_p \tag{C.65}$$

$$= 1 + \frac{1}{2} \boldsymbol{G}^u \cdot \tilde{\boldsymbol{a}} \tag{C.66}$$

where we have noted $A^{ei}_{0q} = -\frac{1}{2}G^u_q$. For the thermal force,

$$\boldsymbol{R}^T_e = \frac{4Z}{3\sqrt{\pi}} n_e m_e \hat{\nu}_{ee} v_{\mathrm{th},e} \int_0^\infty d\xi\, \tilde{C}^1_{ei}\{\xi e^{-\xi^2} \boldsymbol{\Phi}_T(\xi)\}\xi^3 \tag{C.67}$$

$$= n_e \frac{8Z}{3\sqrt{\pi}} \int_0^\infty d\xi\, \tilde{C}^1_{ei}\{\xi e^{-\xi^2} (\phi^{\parallel}_T(\xi)(\boldsymbol{b}\cdot\boldsymbol{\nabla}T_e)\boldsymbol{b} + \phi^{\perp}_T(\xi)(\mathrm{I}-\boldsymbol{bb})\cdot\boldsymbol{\nabla}T_e + \phi^{\times}_T(\xi)(\boldsymbol{b}\times\boldsymbol{\nabla}T_e))\}\xi^3 \tag{C.68}$$

$$= -n_e(\hat{\beta}^{\parallel}_{uT}\boldsymbol{bb}\cdot\boldsymbol{\nabla}T_e + \hat{\beta}^{\perp}_{uT}(\mathrm{I}-\boldsymbol{bb})\cdot\boldsymbol{\nabla}T_e + \hat{\beta}^{\times}_{uT}(\boldsymbol{b}\times\boldsymbol{\nabla}T_e)), \tag{C.69}$$

where

$$\tilde{\beta}_{uT} \equiv \hat{\beta}^{\perp}_{uT} + i\hat{\beta}^{\times}_{uT} = -\frac{8Z}{3\sqrt{\pi}} \int_0^\infty d\xi\, \tilde{C}^1_{ei}\{\xi e^{-\xi^2} \tilde{\phi}_T(\xi)\}\xi^3 \tag{C.70}$$

$$= \frac{4Z}{3\sqrt{\pi}} \boldsymbol{G}^u \cdot \tilde{\boldsymbol{b}} \tag{C.71}$$

The coefficients for temperature-gradient-driven force and flow-driven heat flux $\hat{\beta}^{(\parallel,\perp,\times)}_{uT} \equiv \hat{\beta}^{(\parallel,\perp,\times)}_{Tu} \equiv \hat{\beta}^{(\parallel,\perp,\times)}$ are identical due to Onsager symmetry. This may be seen clearly from the matrix problems as we have

$$Z\boldsymbol{G}^u = (\hat{A}^{ee} + Z\hat{A}^{ei} + i\chi\hat{B})\cdot\tilde{\boldsymbol{a}}, \quad \boldsymbol{G}^T = (\hat{A}^{ee} + Z\hat{A}^{ei} + i\chi\hat{B})\cdot\tilde{\boldsymbol{b}}, \tag{C.72}$$

with the coefficients found from

$$\tilde{\beta}_{uT} = \frac{4}{3\sqrt{\pi}} Z\boldsymbol{G}^u\cdot\tilde{\boldsymbol{b}}, \quad \tilde{\beta}_{Tu} = \frac{4}{3\sqrt{\pi}}\boldsymbol{G}^T\cdot\tilde{\boldsymbol{a}}. \tag{C.73}$$

Dotting the $\tilde{\boldsymbol{a}}$ problem through with $\tilde{\boldsymbol{b}}$ and vice-versa, we find

$$Z\boldsymbol{G}^u\cdot\tilde{\boldsymbol{b}} = \tilde{\boldsymbol{b}}\cdot(\hat{A}^{ee} + Z\hat{A}^{ei} + i\chi\hat{B})\cdot\tilde{\boldsymbol{a}} = \tilde{\boldsymbol{a}}\cdot(\hat{A}^{ee} + Z\hat{A}^{ei} + i\chi\hat{B})\cdot\tilde{\boldsymbol{b}} = \boldsymbol{G}^T\cdot\tilde{\boldsymbol{a}} \quad \Rightarrow \quad \tilde{\beta}_{uT} = \tilde{\beta}_{Tu}, \tag{C.74}$$

where the second equality has used the property that the matrix is symmetric since the linear collision operator is self-adjoint.

In summary, the local results for the electron heat flux $\boldsymbol{q}^{\mathrm{local}}_e = \boldsymbol{q}^T_e + \boldsymbol{q}^u_e$ and electron-ion momentum exchange $\boldsymbol{R}^{\mathrm{local}}_e = \boldsymbol{R}^T_e + \boldsymbol{R}^u_e$ are

$$\begin{aligned}
\boldsymbol{q}^T_e &= -\kappa^e_0\big(\underbrace{(\hat{\kappa}_{\parallel}\boldsymbol{bb} + \hat{\kappa}_{\perp}(\mathrm{I}-\boldsymbol{bb}))\cdot\boldsymbol{\nabla}T_e}_{\text{Conduction}} + \underbrace{\hat{\kappa}_{\times}\boldsymbol{b}\times\boldsymbol{\nabla}T_e}_{\text{Righi-Leduc}}\big),\\
\boldsymbol{q}^u_e &= n_eT_e\big(\underbrace{(\hat{\beta}_{\parallel}\boldsymbol{bb} + \hat{\beta}_{\perp}(\mathrm{I}-\boldsymbol{bb}))\cdot\Delta\boldsymbol{u}}_{\text{Peltier}} + \underbrace{\hat{\beta}_{\times}\boldsymbol{b}\times\Delta\boldsymbol{u}}_{\text{Ettingshausen}}\big),\\
\boldsymbol{R}^T_e &= -n_e\big(\underbrace{(\hat{\beta}_{\parallel}\boldsymbol{bb} + \hat{\beta}_{\perp}(\mathrm{I}-\boldsymbol{bb}))\cdot\boldsymbol{\nabla}T_e}_{\text{Cross-Nernst}} + \underbrace{\hat{\beta}_{\times}\boldsymbol{b}\times\boldsymbol{\nabla}T_e}_{\text{Nernst}}\big),\\
\boldsymbol{R}^u_e &= -\frac{n_em_e}{\tau_{ei}}\big(\underbrace{(\hat{\alpha}_{\parallel}\boldsymbol{bb} + \hat{\alpha}_{\perp}(\mathrm{I}-\boldsymbol{bb}))\cdot\Delta\boldsymbol{u}}_{\text{Friction}} - \underbrace{\hat{\alpha}_{\times}\boldsymbol{b}\times\Delta\boldsymbol{u}}_{\text{Cross-friction}}\big).
\end{aligned} \tag{C.75}$$

The dimensionless transport coefficients are computed by first computing the complex values

$$\tilde{\alpha} = 1 + \frac{1}{2}\boldsymbol{G}^u\cdot\tilde{\boldsymbol{a}}, \quad \tilde{\beta} = \frac{4}{3\sqrt{\pi}} Z\boldsymbol{G}^u\cdot\tilde{\boldsymbol{b}} = \frac{4}{3\sqrt{\pi}}\boldsymbol{G}^T\cdot\tilde{\boldsymbol{a}}, \quad \tilde{\kappa} = -\frac{32}{9\pi}\boldsymbol{G}^T\cdot\tilde{\boldsymbol{b}} \tag{C.76}$$

and then recovering the numerical coefficients as

$$\begin{aligned}
\hat{\alpha}^{\perp} &= \Re(\tilde{\alpha}), \qquad \hat{\alpha}^{\times} = -\Im(\tilde{\alpha}), \qquad \hat{\alpha}^{\parallel} = \hat{\alpha}^{\perp}(\chi = 0), \\
\hat{\beta}^{\perp} &= \Re(\tilde{\beta}), \qquad \hat{\beta}^{\times} = \;\; \Im(\tilde{\beta}), \qquad \hat{\beta}^{\parallel} = \hat{\beta}^{\perp}(\chi = 0), \\
\hat{\kappa}^{\perp} &= \Re(\tilde{\kappa}), \qquad \hat{\kappa}^{\times} = \;\; \Im(\tilde{\kappa}), \qquad \hat{\kappa}^{\parallel} = \hat{\kappa}^{\perp}(\chi = 0).
\end{aligned} \tag{C.77}$$

By setting $Z = 0$, single-species ion transport results (ignoring ion-electron collisions) may be found. A similar procedure may be applied to find the local closure for the viscous stress tensor $\Pi_{e,i}$.

The distribution function for one of these drives, say the flow, is then reconstructed as

$$\delta f_e^{\text{local}} = f_e^M \boldsymbol{\xi} \cdot \bigg(\phi_u^{\parallel}(\xi)(\boldsymbol{bb}) \cdot \boldsymbol{d}_u + \phi_u^{\perp}(\xi)(\mathrm{I} - \boldsymbol{bb}) \cdot \boldsymbol{d}_u + \phi_u^{\times}(\xi)(\boldsymbol{b} \times \boldsymbol{d}_u) \bigg). \tag{C.78}$$

To find the spherical harmonic components with the pole aligned with $\hat{\boldsymbol{z}}$, we take the projection

$$(\delta f_e^{\text{local}})^{(l,m)} = \langle l, m | \delta f_e^{\text{local}} \rangle \tag{C.79}$$

$$= f_e^M \xi \bigg(\phi_u^{\parallel}(\xi)(\boldsymbol{bb}) \cdot \boldsymbol{d}_u + \phi_u^{\perp}(\xi)(\mathrm{I} - \boldsymbol{bb}) \cdot \boldsymbol{d}_u + \phi_u^{\times}(\xi)(\boldsymbol{b} \times \boldsymbol{d}_u) \bigg) \cdot \langle l, m | \hat{\boldsymbol{\xi}} \rangle \tag{C.80}$$

where

$$\langle l, m | \hat{\boldsymbol{\xi}} \rangle = \frac{2\pi}{3} \bigg[-2\delta^{m,1}(\hat{\boldsymbol{x}} - i\hat{\boldsymbol{y}}) + \delta^{m,-1}(\hat{\boldsymbol{x}} + i\hat{\boldsymbol{y}}) + 2\delta^{m,0}\hat{\boldsymbol{z}} \bigg] \delta_{l,1}. \tag{C.81}$$

Here we provide a compact Python routine for evaluating local electron transport coefficients, including generating the relevant matrix elements of the collision operator.

```
import numpy as np
from scipy.linalg import solve
from scipy.integrate import quad
from sympy import integrate,symbols,simplify,oo,nsimplify,diff,pi,sqrt,Rational,Matrix
from sympy.functions.special.gamma_functions import gamma
from sympy.functions.special.polynomials import assoc_laguerre as Lg
from sympy.functions.elementary.exponential import exp
from sympy.functions.special.error_functions import erf

x = symbols("x",real=True)

def A_ei_func(q,p):
    Lp,Lq = Lg(p,Rational(3,2),x**2),Lg(q,Rational(3,2),x**2)
    def C1_ei_func(f):
```

```
        return -1/x**3*f
    y = simplify(x**3*Lq*C1_ei_func(Lp*x*exp(-x**2)))
    return simplify(integrate(y,(x,0,oo)))

def G(x):
    return (erf(x)-2/sqrt(pi)*x*exp(-x**2))/(2*x**2)

def A_ee_func(q,p):
    Lp,Lq = Lg(p,Rational(3,2),x**2),Lg(q,Rational(3,2),x**2)
    def C1_ee_func(f):
        result=-(erf(x)-G(x))/x**3*f + 1/x**2*diff(G(x)*(2*x**2*f + x*diff(f)))
        result+=4/sqrt(pi)*exp(-x**2)*f
     result+=4/sqrt(pi)*exp(-x**2)*(x-Rational(6,5)*x**3)*(Rational(2,3)*integrate(f))
        result+=4/sqrt(pi)*exp(-x**2)*(-Rational(2,3)/x**2*integrate(x**3*f))
        result+=4/sqrt(pi)*exp(-x**2)*Rational(4,5)*(1/x**2*integrate(x**5*f))
        return result
    y = simplify(x**3*Lq*C1_ee_func(Lp*x*exp(-x**2)))
    return simplify(integrate(y,(x,0,oo)))

def G_u_func(q):
    Lq = Lg(q,Rational(3,2),x**2)
   return simplify(integrate(exp(-x**2)*Lq*(2*x-Rational(8,3)/sqrt(pi)*x**4 ),(x,0,oo)))

def G_T_func(q):
    if q == 1:
        return -sqrt(pi)*Rational(15,16)
    else:
        return 0

N = 4    ### Number of Laguerre polynomials in expansion (including p=0)
Z = 1    ### Effective ionisation
chi = 0  ### Hall parameter

q_s = np.arange(0,N)
A_ee, A_ei, B = (Matrix(np.zeros((N, N))) for _ in range(3))
G_T, G_u = (Matrix(np.zeros(N)) for _ in range(2))
```

```
for p in q_s[1:]:
    for q in q_s[p:]:
        print(q,p)
        A_ee[q,p],A_ei[q,p] = A_ee_func(q,p), A_ei_func(q,p)
        A_ee[p,q],A_ei[p,q] = A_ee[q,p], A_ei[q,p]
    B[p,p] = 4/(3*sqrt(pi))*gamma(p+Rational(5,2))/(2*gamma(p+1))
    G_u[p],G_T[p]  = G_u_func(p) , G_T_func(p)
M = np.array(A_ee + Z*A_ei + 1j*chi*B ,complex)
M[0,0] = 1
G_u_np , G_T_np = np.array(G_u,complex) , np.array(G_T,complex)
a,b = solve(M,Z*G_u_np) , solve(M,G_T_np)
alpha,beta,kappa=(1+(G_u_np.transpose()@a)[0]/2,
                  -5/4*a[1],10/(3*np.sqrt(np.pi))*b[1])
print(alpha, beta, kappa)
```

C.2 Local Ionic Transport in Mixture Formalism

The local problem for ionic transport in the mixture formalism is

$$\left(\boldsymbol{w}\cdot\frac{n_i}{n_\alpha}\boldsymbol{d}_\alpha+\left(\frac{w^2}{v_{\mathrm{th},\alpha}^2}-\frac{5}{2}\right)\boldsymbol{w}\cdot\boldsymbol{\nabla}\ln T_i+\frac{2}{v_{\mathrm{th},\alpha}^2}\left(\boldsymbol{ww}-\frac{1}{3}\mathrm{I}\right):\boldsymbol{\nabla}\boldsymbol{u}_i\right)f_\alpha^M=\sum_\beta\left(C_{\alpha\beta}^T\{\delta f_\alpha^{\text{local}}\}+C_{\alpha\beta}^F\{\delta f_\beta^{\text{local}}\}\right). \tag{C.82}$$

Here, we follow the procedure of Ferziger and Kaper. Firstly, the DDFs are written as $\delta f_\alpha^{\text{local}}=\phi_\alpha f_\alpha^M$, leaving

$$\left(\boldsymbol{w}\cdot\frac{n_i}{n_\alpha}\boldsymbol{d}_\alpha+\left(\frac{w^2}{v_{\mathrm{th},\alpha}^2}-\frac{5}{2}\right)\boldsymbol{w}\cdot\boldsymbol{\nabla}\ln T_i+\frac{2}{v_{\mathrm{th},\alpha}^2}\left(\boldsymbol{ww}-\frac{1}{3}\mathrm{I}\right):\boldsymbol{\nabla}\boldsymbol{u}_i\right)f_\alpha^M=-\sum_\beta n_\alpha n_\beta I_{\alpha\beta}(\phi_\beta), \tag{C.83}$$

where the linearised collision operator has been written as

$$\sum_\beta\left(C_{\alpha\beta}\{\phi_\alpha f_\alpha^M,f_\beta^M\}+C_{\alpha\beta}\{f_\alpha^M,\phi_\beta f_\beta^M\}\right)\equiv-\sum_\beta n_\alpha n_\beta I_{\alpha\beta}(\phi_\beta). \tag{C.84}$$

This is then a linear problem for ϕ_β, which should then be a linear combination of the thermodynamic drives $\boldsymbol{d}_\alpha$, $\boldsymbol{\nabla}\ln T_i$, and $\boldsymbol{\nabla}\boldsymbol{u}_i$. However, the diffusive driving forces, defined as

$$\boldsymbol{d}_\alpha\equiv\frac{\boldsymbol{\nabla}p_\alpha-c_\alpha\boldsymbol{\nabla}p_i}{p_i}-c_\alpha\frac{\rho_i}{p_i}(\boldsymbol{X}_\alpha-\sum_\beta c_\beta\boldsymbol{X}_\beta),\quad\text{where}\quad\boldsymbol{X}_\alpha=\frac{q_\alpha}{m_\alpha}\boldsymbol{E}'-\frac{1}{\rho_\alpha}\boldsymbol{R}_{e\alpha}, \tag{C.85}$$

are linearly dependent since $\sum_\alpha\boldsymbol{d}_\alpha=0$. It is therefore convenient to introduce a new set of linearly independent drives $\boldsymbol{d}_\alpha^*$ to temporarily replace $\boldsymbol{d}_\alpha$ via

$$\boldsymbol{d}_\alpha=\boldsymbol{d}_\alpha^*-c_\alpha\sum_\gamma\boldsymbol{d}_\gamma^*=\sum_\gamma(\delta_{\alpha\gamma}-c_\alpha)\boldsymbol{d}_\gamma^*. \tag{C.86}$$

The solution is then written as a linear combination of these drives

$$\phi_\beta = -\frac{1}{n_i}\sum_\gamma \boldsymbol{D}_\beta^\gamma \cdot \boldsymbol{d}_\gamma^* - \frac{1}{n_i}\boldsymbol{A}_\beta \cdot \boldsymbol{\nabla}\ln T_i - \frac{1}{n_i}\mathrm{B}_\beta \colon \boldsymbol{\nabla}\boldsymbol{u}_i, \tag{C.87}$$

in terms of the functions $\boldsymbol{D}_\beta^\gamma(\boldsymbol{w})$, $\boldsymbol{A}_\beta(\boldsymbol{w})$, and $\mathrm{B}_\beta(\boldsymbol{w})$. Comparing coefficients in C.82 leads to the integral equations

$$\sum_\beta x_\alpha x_\beta I_{\alpha\beta}(\boldsymbol{D}_\beta^\gamma) = \frac{1}{n_\alpha} f_\alpha^M(\delta_{\alpha\gamma} - c_\alpha)\boldsymbol{w}, \tag{C.88}$$

$$\sum_\beta x_\alpha x_\beta I_{\alpha\beta}(\boldsymbol{A}_\beta) = \frac{1}{n_i} f_\alpha^M\left(\frac{w^2}{v_{\mathrm{th},\alpha}^2} - \frac{5}{2}\right)\boldsymbol{w}, \tag{C.89}$$

$$\sum_\beta x_\alpha x_\beta I_{\alpha\beta}(\mathrm{B}_\beta) = \frac{2}{v_{\mathrm{th},\alpha}^2}\frac{1}{n_i} f_\alpha^M\left(\boldsymbol{w}\boldsymbol{w} - \frac{1}{3}w^2\mathrm{I}\right), \tag{C.90}$$

where $x_\alpha \equiv n_\alpha/n_i$. Since the operators $I_{\alpha\beta}$ are linear and rotationally invariant[2], then the vector functions must take the form

$$\boldsymbol{D}_\beta^\gamma(\boldsymbol{w}) = D_\beta^\gamma(w)\boldsymbol{w}, \quad \boldsymbol{A}_\beta(\boldsymbol{w}) = A_\beta(w)\boldsymbol{w}, \quad \mathrm{B}_\beta(\boldsymbol{w}) = B_\beta(w)\left(\boldsymbol{w}\boldsymbol{w} - \frac{1}{3}w^2\mathrm{I}\right). \tag{C.91}$$

Note that when C.88 is multiplied through by c_γ and summed over γ, the right hand side vanishes, leaving

$$\sum_\beta x_\alpha x_\beta I_{\alpha\beta}\left(\sum_\gamma c_\gamma \boldsymbol{D}_\beta^\gamma\right) = 0. \tag{C.92}$$

This implies that $\sum_\gamma c_\gamma \boldsymbol{D}_\beta^\gamma$ is an invariant for each β. For convenience, these invariants may be set to zero

$$\sum_\gamma c_\gamma \boldsymbol{D}_\beta^\gamma = 0. \tag{C.93}$$

Replacing the vectors $\boldsymbol{d}_\gamma^*$ in C.87 with $\boldsymbol{d}_\gamma^* - c_\gamma \sum_\sigma \boldsymbol{d}_\sigma^*$ then yields

$$\phi_\beta = -\frac{1}{n_i}\sum_\gamma D_\beta^\gamma(w)\boldsymbol{w}\cdot\boldsymbol{d}_\gamma - \frac{1}{n_i}A_\beta(w)\boldsymbol{w}\cdot\boldsymbol{\nabla}\ln T_i - \frac{1}{n_i}B_\beta(w)\left(\boldsymbol{w}\boldsymbol{w} - \frac{1}{3}w^2\mathrm{I}\right)\colon\boldsymbol{\nabla}\boldsymbol{u}_i. \tag{C.94}$$

Equations C.88, C.89, and C.90 may then be solved for the scalar functions D_β^γ, A_β, and B_β via a similar procedure to the electron case by expanding in Sonine polynomials and solving the resulting matrix problems. This procedure is not reproduced here for brevity, but the convenient expressions for the transport coefficients resulting from this procedure are given by [17] and have been implemented in Python. Expressions of the bracket integrals $\bar{A}_{\alpha\beta}^{i,j}$, $\bar{B}_{\alpha\beta}^{i,j}$, $\bar{C}_{\alpha\beta}^{i,j}$, and $\bar{K}_{\alpha\beta}^{i,j}$ to an arbitrary order of Sonine polynomials can be found in the work of Loyalka, Tipton, and Tompson [18–22]. Here, we simply demonstrate that the form of the solution C.94 leads to the local transport closure for mixtures as described in the main text. The required ion transport quantities appearing in the mixture formalism are the total ion heat flux $\boldsymbol{q}_i$, the diffusive velocities $\boldsymbol{V}_\alpha$, and the total ion viscous stress Π_i.

[2]Note that this would not be the case if magnetic fields were included. If they were, a similar process to the electron case can be adopted by expanding the functions $\boldsymbol{A}_\beta$ and similar in orthogonal tensorial combinations of $\boldsymbol{w}$ and $\boldsymbol{b}$ as presented in Ferziger and Kaper. This would then leave the transport coefficients as tensors rather than scalars.

Firstly, the diffusive velocities become

$$\boldsymbol{V}_\alpha^{\text{local}} = \frac{1}{n_\alpha}\int d^3\boldsymbol{w}\ \boldsymbol{w} f_\alpha^M \phi_\alpha \tag{C.95}$$

$$= -\sum_\beta \left(\frac{1}{n_\alpha n_i}\int d^3\boldsymbol{w}\ \boldsymbol{ww} f_\alpha^M D_\alpha^\beta(w)\right)\cdot \boldsymbol{d}_\beta - \left(\frac{1}{n_\alpha n_i}\int d^3\boldsymbol{w}\ \boldsymbol{ww} f_\alpha^M A_\alpha(w)\right)\cdot \boldsymbol{\nabla}\ln T_i \tag{C.96}$$

$$= -\sum_\beta \underbrace{\left(\frac{1}{n_\alpha n_i}\frac{4\pi}{3}\int_0^\infty dw\ w^4 f_\alpha^M D_\alpha^\beta(w)\right)}_{\equiv D_{\alpha\beta}}\boldsymbol{d}_\beta - \underbrace{\left(\frac{1}{n_\alpha n_i}\frac{4\pi}{3}\int_0^\infty dw\ w^4 A_\alpha(w)\right)}_{\equiv D_\alpha^{cT}}\boldsymbol{\nabla}\ln T_i \tag{C.97}$$

$$= -\sum_\beta D_{\alpha\beta}\boldsymbol{d}_\beta - D_\alpha^{cT}\boldsymbol{\nabla}\ln T_i, \tag{C.98}$$

where we have used the identities

$$\int d^3\boldsymbol{w}\ \boldsymbol{w}\left(\boldsymbol{ww} - \frac{1}{3}w^2\mathrm{I}\right)g(w) = 0, \quad \int d^3\boldsymbol{w}\ \boldsymbol{ww}g(w) = \frac{4\pi}{3}\int_0^\infty dw\ w^4 g(w)\mathrm{I}, \tag{C.99}$$

for appropriate isotropic functions $g(w)$. Identically to the main text, the total ion heat flux may be decomposed into two parts $\boldsymbol{q}_i = \boldsymbol{q}_i' + \boldsymbol{h}_i$, the reduced heat flux and enthalpy flux respectively, where

$$\begin{aligned}\boldsymbol{q}_i' &= \sum_\alpha \int d^3\boldsymbol{w}\left(\frac{1}{2}m_\alpha w^2 - \frac{5}{2}T_i\right)\boldsymbol{w} f_\alpha\,,\\ \boldsymbol{h}_i &= \sum_\alpha \frac{5}{2}T_i\int d^3\boldsymbol{w}\ \boldsymbol{w} f_\alpha = \sum_\alpha \frac{5}{2}n_\alpha T_i \boldsymbol{V}_\alpha\,.\end{aligned} \tag{C.100}$$

The enthalpy flux then already has its local closure provided by $\boldsymbol{V}_\alpha^{\text{local}}$. The reduced heat flux becomes

$$\boldsymbol{q}_i'^{\text{local}} = \sum_\alpha \int d^3\boldsymbol{w}\left(\frac{1}{2}m_\alpha w^2 - \frac{5}{2}T_i\right)\boldsymbol{w} f_\alpha^M \phi_\alpha \tag{C.101}$$

$$= -n_i T_i \sum_\beta \left[\sum_\alpha \int d^3\boldsymbol{w}\ \boldsymbol{ww}\left(\frac{m_\alpha w^2}{2T_i} - \frac{5}{2}\right)w^4 f_\alpha^M \frac{1}{n_i^2}D_\alpha^\beta(w)\right]\cdot \boldsymbol{d}_\beta \tag{C.102}$$

$$- \left[\sum_\alpha \int d^3\boldsymbol{w}\left(\frac{m_\alpha w^2}{2T_i} - \frac{5}{2}\right)\boldsymbol{ww} f_\alpha^M \frac{1}{n_i}A_\alpha(w)\right]\cdot \boldsymbol{\nabla}T_i \tag{C.103}$$

$$= -n_i T_i \sum_\beta \underbrace{\left[\sum_\alpha \frac{4\pi}{3}\int_0^\infty dw\ w^4\left(\frac{m_\alpha w^2}{2T_i} - \frac{5}{2}\right)w^4 f_\alpha^M \frac{1}{n_i^2}D_\alpha^\beta(w)\right]}_{\equiv D_\beta^{Tc}}\boldsymbol{d}_\beta \tag{C.104}$$

$$- \underbrace{\left[\sum_\alpha \frac{4\pi}{3}\int_0^\infty dw\ w^4\left(\frac{m_\alpha w^2}{2T_i} - \frac{5}{2}\right)f_\alpha^M \frac{1}{n_i}A_\alpha(w)\right]}_{\equiv \lambda_i'}\boldsymbol{\nabla}T_i \tag{C.105}$$

$$= -\lambda_i'\boldsymbol{\nabla}T_i - n_i T_i \sum_\beta D_\beta^{Tc}\boldsymbol{d}_\beta. \tag{C.106}$$

By taking suitable moments of C.88 and C.89, it is straightforward to show that $D_\beta^{cT} \equiv D_\beta^{Tc} \equiv D_\beta^T$, again a manifestation of Onsager symmetry. Similarly, Onsager symmetry and the condition C.93 also yield useful conditions on the multi-species coefficients

$$D_{\alpha\beta} = D_{\beta\alpha}, \qquad \sum_\beta c_\beta D_{\alpha\beta} = 0, \qquad \sum_\beta c_\beta D_\beta^T = 0. \tag{C.107}$$

Finally, the viscous stress

$$\Pi_i^{\text{local}} = \sum_\alpha \int d^3\boldsymbol{w}\, \left(\boldsymbol{ww} - \frac{1}{3}w^2\mathrm{I}\right) f_\alpha^M \phi_\alpha \tag{C.108}$$

$$= -\left[\sum_\alpha \int d^3\boldsymbol{w}\, \left(\boldsymbol{ww} - \frac{1}{3}w^2\mathrm{I}\right) f_\alpha^M \frac{1}{n_i} B_\alpha(w) \left(\boldsymbol{ww} - \frac{1}{3}w^2\mathrm{I}\right)\right] : \boldsymbol{\nabla} \boldsymbol{u}_i \tag{C.109}$$

$$= -\underbrace{\left[\sum_\alpha \int d^3\boldsymbol{w}\, \frac{1}{10} f_\alpha^M \frac{1}{n_i} \left(\boldsymbol{ww} - \frac{1}{3}w^2\mathrm{I}\right) : \left(\boldsymbol{ww} - \frac{1}{3}w^2\mathrm{I}\right) B_\alpha(w)\right]}_{\equiv \eta_i} \mathrm{W}^i \tag{C.110}$$

$$= -\eta_i \mathrm{W}^i, \tag{C.111}$$

which completes the local closure for ionic mixtures.

It is sometimes preferable to consider the diffusive mass flux $\boldsymbol{i}_\alpha \equiv \rho_\alpha \boldsymbol{V}_\alpha$. For two species, we write the diffusive mass flux of the first (often the lighter) species $\boldsymbol{i} \equiv \boldsymbol{i}_1 \equiv -\boldsymbol{i}_2$ with concentration $c_1 \equiv c$ as

$$\boldsymbol{i}^{\text{local}} = -\rho c \Big[D_{11}\boldsymbol{d}_1 + D_{12}\boldsymbol{d}_2 + D_1^T \boldsymbol{\nabla} \ln T_i \Big], \tag{C.112}$$

$$= -\rho \Big[- D_{12}\boldsymbol{d}_1 + cD_1^T \boldsymbol{\nabla} \ln T_i \Big], \tag{C.113}$$

having used $\sum_\alpha \boldsymbol{d}_\alpha = 0$ (so $\boldsymbol{d}_2 = -\boldsymbol{d}_1$) and $\sum_\beta c_\beta D_{\alpha\beta} = 0$ (so $D_{11} = -\frac{1-c}{c} D_{12}$). We then rewrite in terms of $\boldsymbol{\nabla} c$ and $\boldsymbol{\nabla} \ln p_i$ instead of $\boldsymbol{d}_1$ and $\boldsymbol{d}_2$. The partial pressure of the first species may be written as

$$p_1 = p_i \frac{c/m_1}{c/m_1 + (1-c)/m_2} \Rightarrow \ln p_1 = \ln p_i + \ln c - \ln m_1 - \ln(c/m_1 + (1-c)/m_2), \tag{C.114}$$

and therefore its gradient as

$$\boldsymbol{\nabla} \ln p_1 = \boldsymbol{\nabla} \ln p_i + \left(\frac{1}{c} - \frac{1/m_1 - 1/m_2}{c/m_1 + (1-c)/m_2}\right) \boldsymbol{\nabla} c = \boldsymbol{\nabla} \ln p_i + \frac{1/m_2}{c/m_1 + (1-c)/m_2} \frac{1}{c} \boldsymbol{\nabla} c. \tag{C.115}$$

The diffusive driving force then become

$$\boldsymbol{d}_1 = x \boldsymbol{\nabla} \ln p_1 - c \boldsymbol{\nabla} \ln p_i - \frac{\rho_i}{p_i} c(1-c) \Big(\boldsymbol{X}_1 - \boldsymbol{X}_2 \Big), \tag{C.116}$$

$$\tag{C.117}$$

$$= (x-c) \boldsymbol{\nabla} \ln p_i + \frac{1/m_2}{c/m_1 + (1-c)/m_2} \frac{x}{c} \boldsymbol{\nabla} c - \frac{1}{p_i} \left[\rho_i c(1-c) \left(\frac{q_1}{m_1} - \frac{q_2}{m_2} \right) \boldsymbol{E}' - \Big((1-c)\boldsymbol{R}_{e1} - c\boldsymbol{R}_{e2} \Big) \right]. \tag{C.118}$$

having used that $\boldsymbol{X}_\alpha = \frac{q_\alpha}{m_\alpha} \boldsymbol{E}' - \frac{1}{\rho_\alpha} \boldsymbol{R}_{e\alpha}$. To rewrite the last term, we note

$$\boldsymbol{R}_{e\alpha} = \int d^3\boldsymbol{v}\; m_e \boldsymbol{v} C_{e\alpha}\{f_e\} = \frac{\hat{\nu}_{e\alpha}}{\sum_\beta \hat{\nu}_{e\beta}} \int d^3\boldsymbol{v}\; m_e \boldsymbol{v} C_{ei}\{f_e\}, \tag{C.119}$$

and therefore

$$\boldsymbol{R}_{e\alpha} = \frac{n_\alpha Z_\alpha^2 \ln \Lambda_{e\alpha}}{\sum_\beta n_\beta Z_\beta^2 \ln \Lambda_{e\beta}} \boldsymbol{R}_e = \frac{Z_\alpha^*}{Z^*} \boldsymbol{R}_e \tag{C.120}$$

where the effective ionisation of species α is introduced as

$$Z_\alpha^* = \frac{n_\alpha Z_\alpha^2 \ln \Lambda_{e\alpha}}{n_e \ln \Lambda_{ee}}, \quad Z^* = \sum_\alpha Z_\alpha^*. \tag{C.121}$$

The diffusive driving force becomes

$$\boldsymbol{d}_1 = (x-c)\boldsymbol{\nabla} \ln p_i + \frac{1/m_2}{c/m_1 + (1-c)/m_2}\frac{x}{c}\boldsymbol{\nabla} c - \frac{1}{p_i}\left[\rho_i c(1-c)\left(\frac{q_1}{m_1} - \frac{q_2}{m_2}\right)\boldsymbol{E}' - \frac{(1-c)Z_1^* - cZ_2^*}{Z_1^* + Z_2^*}\boldsymbol{R}_e\right], \tag{C.122}$$

and therefore the diffusive mass flux may be written as

$$\boldsymbol{i}^{\text{local}} = -\rho D\left(\boldsymbol{\nabla} c + k_p \boldsymbol{\nabla} \ln p_i + k_T \boldsymbol{\nabla} \ln T_i - k_E \frac{e}{T_i}\boldsymbol{E}' + k_R \frac{1}{p_i}\boldsymbol{R}_e\right), \tag{C.123}$$

with appropriate definitions for the ordinary diffusion coefficient D and the, baro-, thermo-, electro-, and frictional diffusion ratios k_p, k_T, k_E, and k_R as

$$D = -\frac{1/m_2}{c/m_1 + (1-c)/m_2}\frac{x}{c}D_{12}, \tag{C.124}$$

$$k_p = (x-c)\frac{c/m_1 + (1-c)/m_2}{1/m_2}\frac{c}{x}, \tag{C.125}$$

$$k_T = c\frac{D_1^T}{D}, \tag{C.126}$$

$$k_E = \frac{\rho_i}{n_i}c(1-c)\left(\frac{Z_1}{m_1} - \frac{Z_2}{m_2}\right)\frac{c/m_1 + (1-c)/m_2}{1/m_2}\frac{c}{x}, \tag{C.127}$$

$$k_R = \frac{(1-c)Z_1^* - cZ_2^*}{Z_1^* + Z_2^*}\frac{c/m_1 + (1-c)/m_2}{1/m_2}\frac{c}{x}. \tag{C.128}$$

The friction term $\boldsymbol{R}_e$ can be neglected here since it is expected to be dominated by the other terms.

Table of Mathematical Symbols

Symbol	Description	Other information
Mathematical quantities and coordinates		
$\boldsymbol{x}$	Position vector	
$\boldsymbol{v}$	Velocity in laboratory frame	
$\boldsymbol{Z}$	Phase space coordinates	$= (\boldsymbol{x}, \boldsymbol{v})$
$\boldsymbol{w}$	Peculiar velocity	$= \boldsymbol{v} - \boldsymbol{u}$, where $\boldsymbol{u}$ is either electron fluid velocity or ionic mixture CoM velocity
$\boldsymbol{\xi}_\alpha$	Normalised velocity	$= \boldsymbol{w}/v_{\mathrm{th},\alpha}$
x, y, z	Spatial Cartesian coordinates	
ρ, ϕ, z	Spatial cylindrical coordinates	
r, θ, ϕ	Spatial spherical coordinates	
w, ϑ, φ	Velocity spherical coordinates	Pole aligned with $\hat{\boldsymbol{z}}$ (planar), $\hat{\boldsymbol{\rho}}$ (cylindrical), or $\hat{\boldsymbol{r}}$ (spherical). Usually defined in frame comoving with fluid velocity $\boldsymbol{u}$
μ	Cosine of velocity pitch angle	$= \cos\vartheta$
$d^2\Omega$	Velocity angle element	$= \sin\vartheta \, d\vartheta \, d\varphi = -d\mu \, d\varphi$
δ_{ab}	Kronecker delta	
ε_{abc}	Levi–Civita symbol	
$\delta(x)$	Dirac delta distribution	
$P_l^k(\mu)$	Associated Legendre functions	Basis functions for expansion over velocity pitch angle $\mu = \cos\vartheta$
$L_p^{(\alpha)}(x)$	Generalised Laguerre or Sonine polynomials	Basis functions for expansion over normalised velocity $x = \xi^2$ for local analytic calculations

Symbol		Description	Definition or other information
$f^{(l,m)}$ $\langle l,m\|f\rangle$	$\equiv$	Projection onto spherical harmonic basis	$= \int d^2\Omega\, P_l^k(\mu) e^{-im\varphi} f$

Physical constants

ε_0	Permittivity of free space	$= 8.85418782 \times 10^{-12}\ \mathrm{m^{-3}\,kg^{-1}\,s^4\,A^2}$
e	Electron charge magnitude OR electron species label OR Euler's constant	Charge is $= 1.602176634 \times 10^{-19}\ \mathrm{C}$
k_B	Boltzmann constant	$= 1.380649 \times 10^{-23}\ \mathrm{m^2\,kg\,s^{-2}\,K^{-1}}$. Temperature is often used in energy units, so k_B often does not appear
c	Speed of light in vacuum	$= 2.9979 \times 10^8\ \mathrm{m\,s^{-1}}$
$\hbar$	Reduced Planck constant	$= 1.0546 \times 10^{-34}\ \mathrm{J\,s}$
m_e	Electron rest mass	$= 9.109 \times 10^{-31}\ \mathrm{kg} = 0.5110\ \mathrm{MeV}/c^2$
m_p	Proton rest mass	$= 1.6726 \times 10^{-27}\ \mathrm{kg} = 938.3\ \mathrm{MeV}/c^2$
m_n	Neutron rest mass	$= 1.6749 \times 10^{-27}\ \mathrm{kg} = 939.6\ \mathrm{MeV}/c^2$

Particle properties

m_α	Mass of species α	
q_α	Charge of species α	
Z_α	Ionization of species α	$= q_\alpha/e$

Kinetic quantities

$v_{\mathrm{th},\alpha}$	Thermal velocity	$= \sqrt{2T_\alpha/m_\alpha}$
f_α	Distribution function	
f_α^M	Maxwellian distribution	$= \frac{n_\alpha}{\pi^{3/2} v_{\mathrm{th},\alpha}^3} \exp[-(w/v_{\mathrm{th},\alpha})^2]$
$\delta f_\alpha^{(l,m)}$	(l,m) spherical harmonic	$= \langle l,m\|\delta f_\alpha\rangle$
$\delta f_\alpha^{(l)}$	$m=0$ spherical harmonic	$= \delta f_\alpha^{(l,0)}$
$C_{\alpha\beta}$	Fokker–Planck collision operator	
$\hat{C}_{\alpha\beta}$	Linear collision operator	
$\mathcal{C}_{\alpha\beta}^{(l,m)}$	Harmonic projection	$= \langle l,m\|\hat{C}_{\alpha\beta}\delta f_\alpha\rangle$
$\ln\Lambda_{\alpha\beta}$	Coulomb logarithm	Common $\ln\Lambda$ assumed unless stated
$\hat{\nu}_{\alpha\beta}$	Collision frequency	$= \frac{n_\beta q_\alpha^2 q_\beta^2 \ln\Lambda_{\alpha\beta}}{4\pi\varepsilon_0^2 m_\alpha^2 v_{\mathrm{th},\alpha}^3}$

Symbol	Description	Definition or other information
$\tau_{\alpha\beta}$	Collision time	$= \frac{3\sqrt{\pi}}{4\hat{\nu}_{\alpha\beta}}$
$\lambda_{\mathrm{th},\alpha\beta}$	Thermal mean free path	$= v_{\mathrm{th},\alpha}/\hat{\nu}_{\alpha\beta}$
Z^*_α	Effective ionization of species α	$= n_\alpha Z_\alpha^2 \ln\Lambda_{e\alpha}/(n_e \ln\Lambda_{ee})$
Z^*	Effective ionization	$= \sum_\alpha Z^*_\alpha$
$\rho_{\mathrm{L},\alpha}$	Thermal Larmor radius of species α	$\rho_{\mathrm{L},\alpha} = v_{\mathrm{th},\alpha}/\omega_{\mathrm{c},\alpha}$
Fluid quantities		
n_α	Number density	$\int d^3\boldsymbol{v}\, f_\alpha$
ρ_α	Mass density	$= m_\alpha n_\alpha$
n_i	Total ion number density	$= \sum_\alpha n_\alpha$
ρ_i	Total ion mass density	$= \sum_\alpha \rho_\alpha$
x_α	Number fraction	$= n_\alpha/n_i$
c_α	Mass concentration	$= \rho_\alpha/\rho_i$
T_α	Temperature	Energy units unless stated
$\boldsymbol{u}_\alpha$	Flow velocity	$= \frac{1}{n_\alpha}\int d^3\boldsymbol{v}\,\boldsymbol{v} f_\alpha$
$\boldsymbol{u}_i$	Ion centre-of-momentum velocity	$= \sum_\alpha c_\alpha \boldsymbol{u}_\alpha$
$\Delta\boldsymbol{u}$	Electron–ion relative flow	$= \boldsymbol{u}_e - \boldsymbol{u}_i$
$\boldsymbol{E}$	Electric field	
$\boldsymbol{B}$	Magnetic field	
$\boldsymbol{E}'$	Effective electric field	$= \boldsymbol{E} + \boldsymbol{u}_i \times \boldsymbol{B}$
Transport quantities		
$\boldsymbol{q}_e$	Electron heat flux	$= \int d^3\boldsymbol{w}\, \frac{1}{2} m_e w^2 \boldsymbol{w} f_e$
$\boldsymbol{q}_i$	Total ion heat flux	$= \sum_\alpha \int d^3\boldsymbol{w}\, \frac{1}{2} m_\alpha w^2 \boldsymbol{w} f_\alpha$
$\boldsymbol{q}'_i$	Reduced ion heat flux	$= \sum_\alpha \int d^3\boldsymbol{w} (\frac{1}{2} m_\alpha w^2 - \frac{5}{2} T_i)\boldsymbol{w} f_\alpha$
$\boldsymbol{h}_i$	Ion enthalpy flux	$= \sum_\alpha \frac{5}{2} n_\alpha T_\alpha \boldsymbol{V}_\alpha$
$\boldsymbol{V}_\alpha$	Diffusive velocity	$= \frac{1}{n_\alpha}\int d^3\boldsymbol{w}\,\boldsymbol{w} f_\alpha$
$\boldsymbol{i}_\alpha$	Diffusive mass flux	$= \rho_\alpha \boldsymbol{V}_\alpha$
Π_e	Electron viscous stress	$= m_e \int d^3\boldsymbol{w} (\boldsymbol{w}\boldsymbol{w} - \frac{1}{3} w^2 \mathbb{I}) f_e$
Π_i	Ion viscous stress	$= \sum_\alpha m_\alpha \int d^3\boldsymbol{w} (\boldsymbol{w}\boldsymbol{w} - \frac{1}{3} w^2 \mathbb{I}) f_\alpha$
Dimensionless numbers		

Symbol	Description	Definition or other information
χ_α	Hall parameter	$= q_\alpha B / m_\alpha$
N_K	Knudsen number	$= \lambda_{\text{th}} / L$
N_u	Electron flow strength	$= \lvert \Delta \boldsymbol{u} \rvert / v_{\text{th},e}$

List of Acronyms

BBGKY Bogoliubov–Born–Green–Kirkwood–Yvon

CBET Cross-Beam Energy Transfer

CoM centre-of-momentum

DDF deviation of distribution function from Maxwellian

DF distribution function

FLARE Fusion via Low-power Assembly and Rapid Excitation

FLF First Light Fusion

IB inverse bremsstrahlung

ICF inertial confinement fusion

IFE Inertial Fusion for Energy production

LPIs Laser-plasma instabilities

LTE local thermal equilibrium

MagLIF Magnetized liner inertial fusion

MCF magnetic confinement fusion

MD molecular dynamics

MFP mean free path

MHD magnetohydrodynamics

ML machine learning

NIF National Ignition Facility

PDE partial differential equation

PIC particle-in-cell

RKM reduced kinetic method

RTI Rayleigh-Taylor instability

SBS Stimulated Brillouin Scattering

SNB Schurtz-Nicolaï-Busquet

SRS Stimulated Raman Scattering

TPD Two-Plasmon Decay

VFP Vlasov-Fokker-Planck

WDM warm dense matter

List of Figures

2.1 Depiction of a basic ICF capsule implosion (not to scale). 17

2.2 Depiction of a direct drive implosion. 19

2.3 Depiction of an indirect drive implosion using a hohlraum through the xz plane, where the hohlraum is cylindrically symmetric around the horizontal z axis. 20

2.4 Depiction of a MagLIF-like implosion. 21

2.5 Validity of models across different regimes of collisionality parametrised by the Knudsen number N_K. 23

2.6 Debye shielding in a simple plasma due to a positive charge at the centre. Negative charges shift towards this central positive charge, forming a shielded potential $V(\boldsymbol{r}) \propto e^{-r/\lambda_\mathrm{D}}/r$. Inside the Debye sphere, charged particles experience the individual Coulomb force of the central charge. Outside the Debye sphere $r \gtrsim \lambda_\mathrm{D}$, the potential is exponentially small, and charged particles are shielded from the individual effect of the central charge. 26

2.7 Slab of plasma disturbed from quasineutrality 27

2.8 The cylinder traced out describing the collision of two hard spheres of species α (white ball) against species β (blue ball). 29

2.9 Parameter space of plasma temperature versus number density with different regimes, confined fusion schemes, and relevant scales roughly indicated. The indicated regions for ICF, MCF, stellar cores, and WDM are a rough quantitative guide rather than strict definitions of these types of plasma. The indicated ICF refers to the plasma during the implosion; before the implosion, the material is not ionised, but quickly transitions to the plasma regime during laser heating. 33

2.10 Rectangular region in phase space with particle fluxes in and out. 34

2.11 Depiction of the Klimontovich distribution (black) for a particular microstate over phase space. In the top right plot, each dot represents a Dirac delta at that location in phase space, with histograms in space and velocity shown below and to the left, respectively. The red box shows the coarse-graining volume $\mathcal{V}$ from which the smooth distribution function is obtained. 37

2.12 Depiction of contours of a beam-like DF subject to pitch-angle scattering due to collisions against a fixed Dirac-delta-like distribution. 42
2.13 Two particles transporting energy through a surface at $z = z_0$. 47
2.14 Physical origin of 'off-diagonal' transport terms $\boldsymbol{q}_e^u$ and $\boldsymbol{R}_e^T$. 48
2.15 Magnetised electron heat conduction. For ions, the direction of the gyro-orbits is reversed so the ion Righi-Leduc heat flow is in the $+\boldsymbol{b} \times \boldsymbol{\nabla} T_i$ direction. 49
2.16 Physical origin of viscous stress. 54
2.17 Dimensionless conductivities for electrons and ions for a simple hydrogen plasma ($Z = 1$, $m_i/m_e \approx 1840$, $T_i/T_e = 1$) as a function of Hall parameters. Electron heat transport dominates for $\chi_e \lesssim 10$, but ion heat transport dominates at larger magnetizations. For $10^{-4} \lesssim \chi_i \lesssim 10^{-1}$, ion transport dominates but is still unmagnetised, then becomes magnetised beyond $\chi_i \gtrsim 10^{-1}$. In these regimes, nonlocal unmagnetised and magnetised ion transport are both relevant. . . 56
2.18 Depiction of streaming suprathermal particles in the tail of the distribution giving rise to nonlocal effects. 64
2.19 Integrands of the local electron conductive heat flux for $Z = 1$, $\chi = 1$, normalised to have equal area when integrated over ξ. The parallel component is unaffected by magnetisation, therefore corresponds to the unmagnetised result. The shaded areas represent the highest velocity section of the tail that provides 10% contribution to the whole heat flux integral. . . 66
2.20 Comparison of correct transport coefficients for $Z = 1$ (solid lines) to transport coefficients obtained with the rescaled Lorentz collision operator (dashed lines). 68

3.1 Stencil for cell (i, j, l). 87
3.2 Nonzero elements in the Jacobian $\hat{M}_{k_1,k_2}$ for the RKM with $N_l = 3$, $N_i = 4$, $N_j = 6$ for the unmagnetised single species solver. Elements are arranged according to $k(i, l, j) = j + N_j(l + N_l(i))$. 88
3.3 Diagrams visualizing spherical and cylindrical spatial coordinates with spherical velocity coordinates. 89

4.1 Nonlocal electron conductive heat flux and thermal force for a variety of Knudsen numbers N_K. 94
4.2 Angle-averaged DF across space. 95
4.3 First spherical harmonic component of DF across space. Due to the logarithmic scale, negative values are shown as dashed lines. 97
4.4 First spherical harmonic component of DF in phase space for the $N_K = 0.1$ solution. Note that the symmetric logarithmic colourmap has a linear section through zero. The Maxwellian distribution is shown on the bottom row of subplots on the same spatial axes to show the structure of the bulk distribution. Nonlocal effects are clearly present on the top row of subplots, with beam-like features extending well beyond the main gradient region around $z = 0$. . . . 98

4.5 Integrand of heat flux in phase space. Note that the colourmap here is linear, so the brightness directly relates to contribution to the integrand. Reproduced from [3]. 99

4.6 *A posteriori* justification to the smallness of the nonlocal correction to the electron Rosenbluth potentials $\mathcal{H}$ and $\mathcal{G}$ for the case of an isochoric unmagnetised plasma with a temperature gradient with $N_K = 1/10$. The smallness of these ratios ($\lesssim 1\%$) across phase space justifies neglecting the nonlinear component of the collision operator for $N_K \lesssim 1/10$. Reproduced from [3]. 100

4.7 Maximum deviation of Rosenbluth potentials $\Delta^{\max}_{\mathcal{H},\mathcal{G}} = \max_{z,w}(\Delta_{\mathcal{H},\mathcal{G}})$ across a wide range of Knudsen numbers for the unmagnetised temperature step case and peak heat flux suppression $\Delta_{q^{\max}} = \max_z(|q_e^{\text{nonlocal}}|)/\max_z(|q_e^{\text{local}}|)$. 101

4.8 Convergence studies for a) number of spherical harmonics kept in DF expansion, and b) number of iterations to obtain a self-consistent momentum exchange R_e. The lower subplots show the convergence metric defined in Equation 4.12. 102

4.9 Convergence studies over a) Δw and b) $w_{\max}$. The top subplots show the heat flux obtained from the RKM in the standard unmagnetised temperature gradient case, with solid lines showing nonlocal $N_K = 0.1$ cases and dashed lines showing local $N_K = 0.001$ cases. The lower subplots show the convergence metric defined in Equation 4.12, with a black dashed line indicating a $\sigma = 1\%$ threshold. 103

4.10 Nonlocal electron transport for an isobaric versus an isochoric profile. The thermal force is shown as R_e/n_e rather than R_e such that the local results match between the two cases since $R_e^T/n_e = -\hat{\beta}_\parallel \partial_z T_e$. The local analytic results (black dotted) match up extremely well with the local case (dashed lines), and is therefore hard to see. 104

4.11 Comparison of operators in cold end ($z/L = 1.5$) for $l, m = 1, 0$ for the nonlocal $N_K = 0.1$ case. Note that the vertical scale in the top subplot is symmetrical logarithmic with a linear section through zero. There is a switch of dominant balances in the equation in the tail of the distribution, switching from a balance of the driving term with the collision term at lower velocities to the Vlasov advection term with the collision term at higher velocities. 105

4.12 Comparison of nonlocal electron conductive heat flux from the RKM, SNB method, and flux-limited approaches for a uniform density $n_e = 10^{28}\,\mathrm{m}^{-3}$ with a sharp temperature gradient of length scale $L = 5\,\mu\mathrm{m}$. 106

4.13 Comparison of unmagnetised nonlocal conductive heat flux for RKM solving for $g = f - f^M - \delta f^{\text{local}}$ versus $\delta f = f - f^M$ with and without the field-particle operator included for $N_K = 0.001$ (dashed lines) and $N_K = 0.1$ (dotted lines). The g-approach still reproduces the correct local and nonlocal result even when the field-particle collision operator is discarded and the asymptotic forms of the collision frequencies for $\xi \gg 1$ are used. Reproduced from [3]. 108

4.14 Comparison of nonlocal electron conductive heat flux for an isobaric (a) hotspot and (b) coldspot in planar, cylindrical, and spherical geometries. Differences in the nonlocal heat flow are clearly present due to the geometry itself. 109

5.1 Temperature-gradient-driven heat fluxes for an unmagnetised case and moderately magnetised ($\chi_0 = 0.5$) case in a simple hydrogen plasma, appropriately normalised against Knudsen number and a characteristic heat flux $q_0 = n_0 T_0 v_0$, where n_0, T_0, and v_0 are the electron number density, temperature, and thermal velocity at the hot end $z \to -\infty$, respectively. Local unmagnetised (parallel) results are shown in dotted black lines. The parallel results correspond to the unmagnetised $\chi_0 = 0$ case. The normalised profiles of temperature, number density, and Hall parameter are shown. The local unmagnetised results in the z direction are shown in black. Reproduced from [3]. 111

5.2 Temperature-gradient-driven momentum exchange (thermal force) for an unmagnetised case and moderately magnetised ($\chi_0 = 0.5$) case in a simple hydrogen plasma, appropriately normalised against Knudsen number and a characteristic momentum exchange $R_0 = n_0 m_e v_0 \hat{\nu}_0$, where n_0, T_0, v_0, $\hat{\nu}_0$ are the electron number density, temperature, thermal velocity, and basic collision frequency at the hot end $z \to -\infty$, respectively. Local unmagnetised (parallel) results are shown in dotted black lines. The parallel results correspond to the unmagnetised $\chi_0 = 0$ case. The normalised profiles of temperature, number density, and Hall parameter are shown. The local unmagnetised results in the z direction are shown in black. Reproduced from [3]. . 112

5.3 Current-driven heat fluxes in a local and nonlocal case for an unmagnetised and moderately magnetised isothermal isochoric simple hydrogen plasma for $N_u^0 = 10^{-4} \ll 1$. The heat fluxes are appropriately normalised against N_u^0 and a characteristic heat flux $q_0 = n_0 T_0 v_0$, where n_0, T_0, and v_0 are the electron number density, temperature, and thermal velocity of the uniform plasma. Reproduced from [3]. 114

5.4 Current-driven forces, i.e., friction, in a local and nonlocal case for an unmagnetised and moderately magnetised isothermal isochoric simple hydrogen plasma for $N_u^0 = 10^{-4} \ll 1$. The forces are appropriately normalised against N_u^0 and a characteristic momentum exchange $R_0 = n_0 m_e v_0 \hat{\nu}_0$, where n_0, T_0, v_0, $\hat{\nu}_0$ are the electron number density, temperature, thermal velocity, and basic collision frequency of the uniform plasma. Reproduced from [3]. 115

5.5 Ettingshausen heat flux in a magnetised isothermal isochoric simple plasma with effective ionisation $Z^* = 20$ with the same shape of flow profile as in Figure 5.3. A uniform magnetic field in the $-x$ direction is chosen $\boldsymbol{B} = -B_0 \hat{\boldsymbol{x}}$ with a field strength that results in a Hall parameter $\chi = 1$. Different subplots correspond to different peak flows $N_u^0 = 0.0001,\ 0.025,\ 0.05$ which have a noticeable impact on the Ettingshausen heat flux. Reproduced from [2]. 117

5.6 Ratio of Ettingshausen heat flux to the local analytic result for peak flow $N_u^0 = 0.05$, Hall parameter $\chi = 1$, and ionisation $Z^* = 20$, plotted as a function of N_u rather than z/L to emphasise the quasilocal effect. A wide variety of Knudsen numbers are chosen to illustrate the transition between the nonlocal and quasilocal regimes. Nonlocal heat fluxes appear as loops on these plots since they are not functions of the local flow. For small Knudsen number, the heat flux tends towards a one-to-one line, showing that the heat flux is local in the sense that $\boldsymbol{q}_e^u(z)$ only depends on the local $\Delta\boldsymbol{u}(z)$. Plus and cross markers are added to indicate how different spatial positions with the same flow N_u yield the same heat flow for small Knudsen number, but different heat flow for larger Knudsen number. Larger Hall parameter χ suppresses both nonlocal and quasilocal deviations, driving these curves closer to the black dashed line. Reproduced from [2]. 118

5.7 Peltier and Ettingshausen heat flux integrands for various flows N_u with ionisation $Z^* = 20$, Hall parameter $\chi = 1$, and very small Knudsen number $N_K \lll 1$. For small $N_u = 10^{-4}$, the heat flux integrands match up extremely well with the local analytic result. For larger $N_u \sim 0.025 - 0.05$, higher energy electrons $w/v_{\text{th},e} \gtrsim 2.5$ are accelerated, shifting the integrand to larger velocity and enhancing the heat fluxes corresponding to the integrated area beneath the curves. The Ettingshausen integrands are more weighted to higher w than the Peltier integrands, i.e., the Ettingshausen heat flow is carried preferentially by faster particles than the Peltier heat flow, explaining why the Ettingshausen heat flow is more impacted by large N_u. Reproduced from [2]. 119

5.8 Righi-Leduc heat flow, Nernst force, and Ettingshausen heat flow in a strongly magnetised simple hydrogen plasma. The heat flows are appropriately normalised against Knudsen number N_K or flow parameter N_u^0 and a characteristic heat flux $q_0 = n_0 T_0 v_0$, where n_0, T_0, and v_0 are the electron number density, temperature, and thermal velocity at the hot end $z \to -\infty$, respectively. The Nernst force is appropriately normalised against Knudsen number and a characteristic momentum exchange $R_0 = n_0 m_e v_0 \hat{\nu}_0$, where $\hat{\nu}_0$ is the basic collision frequency at the hot end $z \to -\infty$. Reproduced from [3]. 119

5.9 $l = 1$ modes of the DDF in the unmagnetised and magnetised ($\chi = 0.5$) cases, similarly to Figure 4.4 of the previous chapter. Note that the symmetric logarithmic colourmap has a linear section through zero. The Maxwellian distribution is shown on the bottom row of subplots on the same spatial axes to show the structure of the bulk distribution. Nonlocal effects are clearly present on the top row of subplots, with beam-like features extending well beyond the main gradient region around $z = 0$. 120

5.10 Electron distribution function in the cold end ($z/L = 0.5$) for the $N_K = 0.1$ magnetised ($\chi_0 = 0.5$) isochoric temperature step case above. A circle at $w = 3v_{\text{th}}(z/L = 0.5)$ is shown to indicate the radial velocity scale. The sharp edges present in the rear of the local analytic solution are where the distribution is negative, and therefore unphysical. Reproduced from [3]. 121

5.11 Integrand of conductive heat flux components for the unmagnetised and magnetised temperature gradient cases with $N_K = 0.1$ obtained from the RKM and local analytic result. The bottom row of subplots shows the heat flux along the same spatial axes, i.e. is the integrated results of the integrands shown above. Reproduced from [3]. 122

5.12 Maximum deviation of Rosenbluth potentials $\Delta^{\max}_{\mathcal{H},\mathcal{G}} = \max_{z,w}(\Delta_{\mathcal{H},\mathcal{G}})$ across a wide range of Knudsen numbers for the temperature step case and peak heat flux suppression $\Delta_{q^{\max}} = \max_z(|q_e^{\text{nonlocal}}|)/\max_z(|q_e^{\text{local}}|)$. The black, light blue, and dark blue markers show the unmagnetised, moderately magnetised ($\chi_0 = 0.5$), and strongly magnetised ($\chi_0 = 10$) cases, respectively. The smallness of these ratios $\Delta \lesssim 0.1$ for $N_K \leq 1$ justifies the linearisation of the collision operator in this moderately nonlocal regime. Reproduced from [3]. 123

6.1 Nonlocal ion viscous stress for a shear ion flow $\boldsymbol{u}_i = -\frac{1}{2}u_0 \operatorname{erf}(z/L)\hat{\boldsymbol{y}}$ with Mach number $M = |u_0|/v_{\text{th},i} = 1$. The stresses are normalised against the Mach number M, Knudsen number N_K, and ion pressure $p_i = n_i T_i$. The magnetised cases have an applied uniform magnetic field $\boldsymbol{B} = -B_0\hat{\boldsymbol{x}}$ with B_0 chosen such that the Hall parameter throughout the plasma is $\chi_0 = 0.25$. Reproduced from [3]. 126

6.2 Dependence of the dimensionless ion heat conductivity and viscosity coefficients on ion-electron temperature ratio T_i/T_e for an intermediate magnetisation $\chi_i = 0.25$, produced using Ji-Held's fits. Dotted lines correspond to Braginskii's results where ion-electron collisions are neglected, which are then the limiting values for $T_i/T_e \to 0$. The first coefficients $\hat{\kappa}^i_{\parallel}$ and $\hat{\eta}^i_0$ are independent of magnetisation, therefore the red lines also correspond to results for unmagnetised ions. Reproduced from [4]. 128

6.3 Ion conductive heat flux in an unmagnetised simple hydrogen plasma for $N_K = 0.001,\ 0.1$, for different ion-electron temperature ratios. The difference between the results of each subplot is then due solely to ion-electron collisions. The ion Knudsen number is $N_K = \lambda_{\text{th},ii}|_{z\to-\infty}/L$, where the ion-ion thermal MFP is $\lambda_{\text{th},ii} = v_{\text{th},i}/\hat{\nu}_{ii}$. Reproduced from [4]. 129

6.4 Nonlocal ion Righi-Leduc heat flux for a magnetised simple hydrogen plasma with ion Hall parameter $\chi_{i,0} = 0.25$ at the hot end for different ion-electron temperature ratios. The difference between the results of each subplot is then due solely to ion-electron collisions. Reproduced from [4]. 130

6.5 Ratio of heat flow with ion-electron collisions included to heat flow without ion-electron collisions included for two different ion-electron temperature ratios. Dotted and solid lines correspond to the local ($N_K = 0.001$) and nonlocal ($N_K = 0.1$) cases. Reproduced from [4]. . 131

6.6 Nonlocal ion viscous stress Π_{yz} for an unmagnetised hydrogen plasma due to a shear flow for different ion-electron temperature ratios. The difference between the results of each subplot is then due solely to ion-electron collisions. Reproduced from [4]. 131

6.7 Nonlocal ion gyroviscous stress Π_{zz} for a moderately magnetised hydrogen plasma with ion Hall parameter $\chi_i = 0.25$ due to a shear flow for different ion-electron temperature ratios. The difference between the results of each subplot is then due solely to ion-electron collisions. Reproduced from [4]. 132

6.8 Depiction of a particle moving in a temperature profile where the profile is fixed in the lab frame (Case 1, left) or where the temperature profile is comoving with the flow (Case 2, right). 133

6.9 Reduced heat flux for an isochoric simple hydrogen plasma with different uniform sonic flows for a variety of Knudsen numbers. The black lines show the cases with no flow and red and blue lines show the cases with flow in the $\pm\hat{\boldsymbol{z}}$ directions, respectively. 135

6.10 Components of heat flux for a DT mixture subject to an isolated temperature gradient (a), isolated pressure gradient (b), and isolated concentration gradient (c). The relevant profiles are shown at the bottom of each subfigure, with undisplayed profiles being fixed constant at unity or concentrations at 0.5. Results for $N_K \leq 0.01$ are not visible owing to strong agreement with the local result. Reproduced from [1]. 137

6.11 Components of heat flux for a CH_2 mixture subject to an isolated temperature gradient (a), isolated pressure gradient (b), and isolated concentration gradient (c). The shape of the relevant profiles are shown at the bottom of each subfigure, with undisplayed pressure or temperature profiles being fixed constant at unity or concentrations such that $n_H/n_C = 2$. Reproduced from [1]. 138

6.12 Diffusive velocities due to sharp number fraction gradient in symmetric DT mixture and asymmetric CH_2 mixture, showing the nonlocal RKM solution (solid lines) and the local analytic solution (dashed lines). The Knudsen numbers in the nonlocal cases are chosen as $N_K^{\mathrm{DD}} = 0.2$ and $N_K^{\mathrm{HH}} = 1$ in the DT and CH_2 mixtures, respectively. 139

6.13 Diffusive velocities due to sharp temperature gradient in symmetric DT mixture and asymmetric CH_2 mixture, showing the nonlocal RKM solution (solid lines) and the local analytic solution (dashed lines). The Knudsen numbers in the nonlocal cases are chosen as $N_K^{\mathrm{DD}} = 0.2$ and $N_K^{\mathrm{HH}} = 1$ in the DT and CH_2 mixtures, respectively. 140

6.14 Nonlocal diffusive velocities due to sharp pressure gradient in symmetric DT mixture and asymmetric CH_2 mixture, showing the nonlocal RKM solution (solid lines) and the local analytic solution (dashed lines). The Knudsen numbers in the nonlocal cases are chosen as $N_K^{\mathrm{DD}} = 0.2$ and $N_K^{\mathrm{HH}} = 1$ in the DT and CH_2 mixtures, respectively. 140

6.15 Integrand of diffusive velocity $\frac{1}{N_K}\frac{dV_\alpha}{dw}$ from the same case as Figure 6.12 with a number fraction gradient. The number fraction profiles are overlaid on the heatmaps for deuterium (orange), tritium (green), and carbon (grey). 141

6.16 Diffusive mass flux and mixture heat flux for a symmetric DT and asymmetric CH_2 mixture, in three cases driven by a concentration gradient ∇c, temperature gradient ∇T_i, and pressure gradient ∇p_i. Dotted and solid lines correspond to local and nonlocal results, respectively. The line colour indicates the ion-electron temperature ratio, with differences arising due solely to ion-electron collisions. Reproduced from [4]. 142

B.1 Particle α scattering off of a fixed particle β 156

List of Tables

2.1 Summary of local vectorial electron transport. The 'cross' $\times$ terms gained in the $\boldsymbol{b}\times(-\boldsymbol{\nabla}T_e, \Delta\boldsymbol{u})$ direction are shown in italics. The relevant transport coefficients for each term are also indicated, highlighting the Onsager symmetry between the off-diagonal terms. 53

2.2 Summary of local vectorial ionic mixture transport. Note that the diffusive driving forces $\boldsymbol{d}_\alpha$ are linear combinations of concentration gradients $\boldsymbol{\nabla}c_\alpha$, pressure gradients $\boldsymbol{\nabla}p_\alpha$, the electric field $\boldsymbol{E}$, and electron-ion momentum exchange $\boldsymbol{R}_e$. The relevant transport coefficients for each term are also indicated, highlighting the Onsager symmetry between the off-diagonal terms. 59

3.1 Associated Legendre functions $P_\ell^m(\mu)$ for $\ell = 0, 1, 2$. 82

3.2 Conventions for nondimensionalising quantities in the RKM for numerical implementation. . 84

3.3 Relationship between (l, m) and (a, b) indices. 85

Bibliography

[1] Mitchell N T, Chapman D A, McDevitt C J, Read M P and Kagan G 2024 *Plasma Physics and Controlled Fusion* **66** 075005 ISSN 0741-3335 publisher: IOP Publishing URL https://doi.org/10.1088/1361-6587/ad4740

[2] Mitchell N, Chapman D and Kagan G 2025 *Phys. Rev. E* **112** L053202 publisher: American Physical Society URL https://link.aps.org/doi/10.1103/jn8x-nfv2

[3] Mitchell N, Chapman D and Kagan G 2026 *Plasma Physics and Controlled Fusion* URL http://iopscience.iop.org/article/10.1088/1361-6587/ae6531

[4] Mitchell N, Chapman D and Kagan G 2026 *(in preparation)*

[5] Epperlein E M and Short R W 1991 *Physics of Fluids B: Plasma Physics* **3** 3092–3098 ISSN 0899-8221 URL https://doi.org/10.1063/1.859789

[6] Schurtz G P, Nicolaï P D and Busquet M 2000 *Physics of Plasmas* **7** 4238–4249 ISSN 1070-664X URL https://doi.org/10.1063/1.1289512

[7] Nicolaï P D, Feugeas J L A and Schurtz G P 2006 *Physics of Plasmas* **13** 032701 ISSN 1070-664X URL https://doi.org/10.1063/1.2179392

[8] Held E D, Callen J D, Hegna C C and Sovinec C R 2001 *Physics of Plasmas* **8** 1171–1179 ISSN 1070-664X URL https://doi.org/10.1063/1.1349876

[9] Holec M, Nikl J and Weber S 2018 *Physics of Plasmas* **25** 032704 ISSN 1070-664X URL https://doi.org/10.1063/1.5011818

[10] Brodrick J P, Kingham R J, Marinak M M, Patel M V, Chankin A V, Omotani J, Umansky M, Sorbo D D, Dudson B, Parker J T, Kerbel G D, Sherlock M and Ridgers C P 2017 *Physics of Plasmas* **24** 092309 ISSN 1070-664X, 1089-7674 arXiv:1704.08963 [physics] URL http://arxiv.org/abs/1704.08963

[11] Arran C, Holec M, Sherlock M, Marinak M and Ridgers C P 2025 *Physics of Plasmas* **32** 043908 ISSN 1070-664X URL https://doi.org/10.1063/5.0250147

[12] Marocchino A, Tzoufras M, Atzeni S, Schiavi A, Nicolaï P D, Mallet J, Tikhonchuk V and Feugeas J L 2013 *Physics of Plasmas* **20** 022702 ISSN 1070-664X URL https://doi.org/10.1063/1.4789878

[13] Lezhnin K V, Totorica S R, Hyder A S, Griff-McMahon J, Adams M B P, Tzeferacos P, Diallo A and Fox W 2025 *Physics of Plasmas* **32** 022701 ISSN 1070-664X URL https://doi.org/10.1063/5.0240547

[14] Held E D 2003 *Physics of Plasmas* **10** 4708–4715 ISSN 1070-664X URL https://doi.org/10.1063/1.1626681

[15] Braginskii S I 1965 *Reviews of Plasma Physics* **1**

[16] Ferziger J H and Kaper H G 1972 *Mathematical Theory of Transport Processes in Gases* (Amsterdam: Elsevier Science Publishing Co Inc.,U.S.) ISBN 978-0-7204-2046-3

[17] Kagan G and Baalrud S D 2018 Transport formulas for multi-component plasmas within the effective potential theory framework arXiv:1611.09872 [physics] URL http://arxiv.org/abs/1611.09872

[18] Loyalka S K, Tipton E L and Tompson R V 2007 *Physica A: Statistical Mechanics and its Applications* **379** 417–435 ISSN 0378-4371 URL https://www.sciencedirect.com/science/article/pii/S0378437106013264

[19] Tipton E L, Tompson R V and Loyalka S K 2009 *European Journal of Mechanics - B/Fluids* **28** 335–352 ISSN 0997-7546 URL https://www.sciencedirect.com/science/article/pii/S0997754608000988

[20] Tipton E L, Tompson R V and Loyalka S K 2009 *European Journal of Mechanics - B/Fluids* **28** 353–386 ISSN 0997-7546 URL https://www.sciencedirect.com/science/article/pii/S0997754608001222

[21] Tompson R V, Tipton E L and Loyalka S K 2009 *European Journal of Mechanics - B/Fluids* **28** 695–721 ISSN 0997-7546 URL https://www.sciencedirect.com/science/article/pii/S0997754609000612

[22] Tompson R V, Tipton E L and Loyalka S K 2010 *European Journal of Mechanics - B/Fluids* **29** 153–179 ISSN 0997-7546 URL https://www.sciencedirect.com/science/article/pii/S0997754609000983

[23] Bosch H S and Hale G M 1992 *Nuclear Fusion* **32** 611 ISSN 0029-5515 URL https://doi.org/10.1088/0029-5515/32/4/I07

[24] Wurzel S E and Hsu S C 2022 *Physics of Plasmas* **29** 062103 ISSN 1070-664X URL https://doi.org/10.1063/5.0083990

[25] MAIMAN T 1960 Stimulated optical radiation in ruby URL https://www.nature.com/articles/187493a0

[26] Nuckolls J, Wood L, Thiessen A and Zimmerman G 1972 *Nature* **239** 139–142 ISSN 1476-4687 publisher: Nature Publishing Group URL https://www.nature.com/articles/239139a0

[27] Nuckolls J H 1998 Early steps toward inertial fusion energy (IFE) (1952 to 1962) Tech. Rep. UCRL-ID–131075 Lawrence Livermore National Lab., CA (United States) URL https://www.osti.gov/biblio/658936

[28] Hurricane O, Patel P, Betti R, Froula D, Regan S, Slutz S, Gomez M and Sweeney M 2023 *Reviews of Modern Physics* **95** 025005 publisher: American Physical Society URL https://link.aps.org/doi/10.1103/RevModPhys.95.025005

[29] Zylstra A B, Hurricane O A, Callahan D A, Kritcher A L, Ralph J E, Robey H F, Ross J S, Young C V, Baker K L, Casey D T, Döppner T, Divol L, Hohenberger M, Le Pape S, Pak A, Patel P K, Tommasini R, Ali S J, Amendt P A, Atherton L J, Bachmann B, Bailey D, Benedetti L R, Berzak Hopkins L, Betti R, Bhandarkar S D, Biener J, Bionta R M, Birge N W, Bond E J, Bradley D K, Braun T, Briggs T M, Bruhn M W, Celliers P M, Chang B, Chapman T, Chen H, Choate C, Christopherson A R, Clark D S, Crippen J W, Dewald E L, Dittrich T R, Edwards M J, Farmer W A, Field J E, Fittinghoff D, Frenje J, Gaffney J, Gatu Johnson M, Glenzer S H, Grim G P, Haan S, Hahn K D, Hall G N, Hammel B A, Harte J, Hartouni E, Heebner J E, Hernandez V J, Herrmann H, Herrmann M C, Hinkel D E, Ho D D, Holder J P, Hsing W W, Huang H, Humbird K D, Izumi N, Jarrott L C, Jeet J, Jones O, Kerbel G D, Kerr S M, Khan S F, Kilkenny J, Kim Y, Geppert Kleinrath H, Geppert Kleinrath V, Kong C, Koning J M, Kroll J J, Kruse M K G, Kustowski B, Landen O L, Langer S, Larson D, Lemos N C, Lindl J D, Ma T, MacDonald M J, MacGowan B J, Mackinnon A J, MacLaren S A, MacPhee A G, Marinak M M, Mariscal D A, Marley E V, Masse L, Meaney K, Meezan N B, Michel P A, Millot M, Milovich J L, Moody J D, Moore A S, Morton J W, Murphy T, Newman K, Di Nicola J M G, Nikroo A, Nora R, Patel M V, Pelz L J, Peterson J L, Ping Y, Pollock B B, Ratledge M, Rice N G, Rinderknecht H, Rosen M, Rubery M S, Salmonson J D, Sater J, Schiaffino S, Schlossberg D J, Schneider M B, Schroeder C R, Scott H A, Sepke S M, Sequoia K, Sherlock M W, Shin S, Smalyuk V A, Spears B K, Springer P T, Stadermann M, Stoupin S, Strozzi D J, Suter L J, Thomas C A, Town R P J, Tubman E R, Trosseille C, Volegov P L, Weber C R, Widmann K, Wild C, Wilde C H, Van Wonterghem B M, Woods D T, Woodworth B N, Yamaguchi M, Yang S T and Zimmerman G B 2022 *Nature* **601** 542–548 ISSN 0028-0836 URL https://pmc.ncbi.nlm.nih.gov/articles/PMC8791836/

[30] Kritcher A L, Zylstra A B, Callahan D A, Hurricane O A, Weber C R, Clark D S, Young C V, Ralph J E, Casey D T, Pak A, Landen O L, Bachmann B, Baker K L, Berzak Hopkins L, Bhandarkar S D, Biener J, Bionta R M, Birge N W, Braun T, Briggs T M, Celliers P M, Chen H, Choate C, Divol L, Döppner T, Fittinghoff D, Edwards M J, Gatu Johnson M, Gharibyan N, Haan S, Hahn K D, Hartouni E, Hinkel D E, Ho

D D, Hohenberger M, Holder J P, Huang H, Izumi N, Jeet J, Jones O, Kerr S M, Khan S F, Geppert Kleinrath H, Geppert Kleinrath V, Kong C, Lamb K M, Le Pape S, Lemos N C, Lindl J D, MacGowan B J, Mackinnon A J, MacPhee A G, Marley E V, Meaney K, Millot M, Moore A S, Newman K, Di Nicola J M G, Nikroo A, Nora R, Patel P K, Rice N G, Rubery M S, Sater J, Schlossberg D J, Sepke S M, Sequoia K, Shin S J, Stadermann M, Stoupin S, Strozzi D J, Thomas C A, Tommasini R, Trosseille C, Tubman E R, Volegov P L, Wild C, Woods D T and Yang S T 2022 *Physical Review E* **106** 025201 publisher: American Physical Society URL https://link.aps.org/doi/10.1103/PhysRevE.106.025201

[31] Zhou Y, Sadler J D and Hurricane O A 2025 *Annual Review of Fluid Mechanics* **57** 197–225 ISSN 0066-4189, 1545-4479 publisher: Annual Reviews URL https://www.annualreviews.org/content/journals/10.1146/annurev-fluid-022824-110008

[32] Zhao Y, Weng S M, Ma H H, Bai X J and Sheng Z M 2023 *Reviews of Modern Plasma Physics* **7** 1 URL https://ui.adsabs.harvard.edu/abs/2023RvMPP...7....1Z/abstract

[33] Scott R H H, Glize K, Antonelli L, Khan M, Theobald W, Wei M, Betti R, Stoeckl C, Seaton A G, Arber T D, Barlow D, Goffrey T, Bennett K, Garbett W, Atzeni S, Casner A, Batani D, Li C and Woolsey N 2021 *Phys. Rev. Lett.* **127**(6) 065001 URL https://link.aps.org/doi/10.1103/PhysRevLett.127.065001

[34] Rinderknecht H G, Amendt P A, Wilks S C and Collins G 2018 *Plasma Physics and Controlled Fusion* **60** ISSN 0741-3335 institution: Lawrence Livermore National Lab. (LLNL), Livermore, CA (United States) Number: LLNL-JRNL–742100; LLNL-JRNL–755501 Publisher: IOP Science URL https://www.osti.gov/pages/biblio/1438636

[35] Huang C K, Molvig K, Albright B J, Dodd E S, Vold E L, Kagan G and Hoffman N M 2017 *Physics of Plasmas* **24** 022704 ISSN 1070-664X URL https://doi.org/10.1063/1.4976323

[36] Peigney B E, Larroche O and Tikhonchuk V 2014 *Physics of Plasmas* **21** 122709 ISSN 1070-664X URL https://doi.org/10.1063/1.4904212

[37] Kagan G, Svyatskiy D, Rinderknecht H, Rosenberg M, Zylstra A, Huang C K and McDevitt C 2015 *Physical Review Letters* **115** 105002 publisher: American Physical Society URL https://link.aps.org/doi/10.1103/PhysRevLett.115.105002

[38] Tang X Z, Berk H L, Guo Z and McDevitt C J 2014 *Physics of Plasmas* **21** 032707 ISSN 1070-664X URL https://doi.org/10.1063/1.4868731

[39] Tang X Z, McDevitt C J, Guo Z and Berk H L 2014 *Europhysics Letters* **105** 32001 publisher: EDP Sciences, IOP Publishing and Società Italiana di Fisica URL https://doi.org/10.1209/0295-5075/105/32001

[40] Tang X Z, McDevitt C J, Guo Z and Berk H L 2014 *Physics of Plasmas* **21** 032706 ISSN 1070-664X URL https://doi.org/10.1063/1.4868733

[41] Hu S X, Shaffer N R, Arnold B, Nichols K A, Karasiev V V, Zhang S and Goncharov V N 2025 *Phys. Rev. E* **111** L053202 publisher: American Physical Society URL https://link.aps.org/doi/10.1103/PhysRevE.111.L053202

[42] Zhang S and Hu S X 2020 *Phys. Rev. Lett.* **125** 105001 publisher: American Physical Society URL https://link.aps.org/doi/10.1103/PhysRevLett.125.105001

[43] Haines B M, Shah R C, Smidt J M, Albright B J, Cardenas T, Douglas M R, Forrest C, Glebov V Y, Gunderson M A, Hamilton C E, Henderson K C, Kim Y, Lee M N, Murphy T J, Oertel J A, Olson R E, Patterson B M, Randolph R B and Schmidt D W 2020 *Nature Communications* **11** 544 ISSN 2041-1723 URL https://doi.org/10.1038/s41467-020-14412-y

[44] Casanova M, Larroche O and Matte J P 1991 *Phys. Rev. Lett.* **67** 2143–2146 publisher: American Physical Society URL https://link.aps.org/doi/10.1103/PhysRevLett.67.2143

[45] Keenan B D, Simakov A N, Chacón L and Taitano W T 2017 *Phys. Rev. E* **96** 053203 publisher: American Physical Society URL https://link.aps.org/doi/10.1103/PhysRevE.96.053203

[46] Zhang X, Liu Q k, Zhang W s, Zhang E h, Ning X c, Meng F q, Wang Y p, Cai H b and Zhu S p 2024 *Nuclear Fusion* **64** 096005 publisher: IOP Publishing URL https://doi.org/10.1088/1741-4326/ad61fd

[47] Keenan B D, Taitano W T, Simakov A N, Chacón L and Albright B J 2020 *Physics of Plasmas* **27** 022704 ISSN 1070-664X URL https://doi.org/10.1063/1.5140361

[48] Anderson S E, Chacón L, Taitano W T, Simakov A N and Keenan B D 2021 *Phys. Rev. E* **104** 055205 publisher: American Physical Society URL https://link.aps.org/doi/10.1103/PhysRevE.104.055205

[49] Angus J R, Dun J, Farmer W, Geyko V, Grote D, Larson D, van de Wetering J J and Zimmerman G 2025 *Phys. Rev. E* **112** 065201 URL https://link.aps.org/doi/10.1103/pr7n-48wl

[50] François M, Dieckmann M E, Ribeyre X and d'Humières E 2026 *Physics of Plasmas* **33** 012105 ISSN 1070-664X URL https://doi.org/10.1063/5.0293079

[51] Gregori G, Glenzer S H, Knight J, Niemann C, Price D, Froula D H, Edwards M J, Town R P J, Brantov A, Rozmus W and Bychenkov V Y 2004 *Physical Review Letters* **92** 205006 publisher: American Physical Society URL https://link.aps.org/doi/10.1103/PhysRevLett.92.205006

[52] Chen Z, Yang X, Zhang G, Ma Y, Yan R, Xu H, Sheng Z, Shao F and Zhang J 2024 *Nuclear Fusion* **64** 126029 ISSN 0029-5515 publisher: IOP Publishing URL https://dx.doi.org/10.1088/1741-4326/ad7f6d

[53] Meezan N B, Woods D T, Izumi N, Chen H, Scott H A, Schneider M B, Liedahl D A, Jones O S, Zimmerman G B, Moody J D, Landen O L and Hsing W W 2020 *Physics of Plasmas* **27** 102704 ISSN 1070-664X URL https://doi.org/10.1063/5.0018733

[54] Craxton R S, Anderson K S, Boehly T R, Goncharov V N, Harding D R, Knauer J P, McCrory R L, McKenty P W, Meyerhofer D D, Myatt J F, Schmitt A J, Sethian J D, Short R W, Skupsky S, Theobald W, Kruer W L, Tanaka K, Betti R, Collins T J B, Delettrez J A, Hu S X, Marozas J A, Maximov A V, Michel D T, Radha P B, Regan S P, Sangster T C, Seka W, Solodov A A, Soures J M, Stoeckl C and Zuegel J D 2015 *Physics of Plasmas* **22** 110501 ISSN 1070-664X URL https://doi.org/10.1063/1.4934714

[55] Kritcher A L, Zylstra A B, Weber C R, Hurricane O A, Callahan D A, Clark D S, Divol L, Hinkel D E, Humbird K, Jones O, Lindl J D, Maclaren S, Strozzi D J, Young C V, Allen A, Bachmann B, Baker K L, Braun T, Brunton G, Casey D T, Chapman T, Choate C, Dewald E, Di Nicola J M G, Edwards M J, Haan S, Fehrenbach T, Hohenberger M, Kur E, Kustowski B, Kong C, Landen O L, Larson D, MacGowan B J, Marinak M, Millot M, Nikroo A, Nora R, Pak A, Patel P K, Ralph J E, Ratledge M, Rubery M S, Schlossberg D J, Sepke S M, Stadermann M, Suratwala T I, Tommasini R, Town R, Woodworth B, Van Wonterghem B and Wild C 2024 *Phys. Rev. E* **109** 025204 publisher: American Physical Society URL https://link.aps.org/doi/10.1103/PhysRevE.109.025204

[56] Abu-Shawareb H e a (The Indirect Drive ICF Collaboration) 2024 *Phys. Rev. Lett.* **132**(6) 065102 URL https://link.aps.org/doi/10.1103/PhysRevLett.132.065102

[57] Zylstra A B, Kritcher A L, Hurricane O A, Callahan D A, Ralph J E, Casey D T, Pak A, Landen O L, Bachmann B, Baker K L, Berzak Hopkins L, Bhandarkar S D, Biener J, Bionta R M, Birge N W, Braun T, Briggs T M, Celliers P M, Chen H, Choate C, Clark D S, Divol L, Döppner T, Fittinghoff D, Edwards M J, Gatu Johnson M, Gharibyan N, Haan S, Hahn K D, Hartouni E, Hinkel D E, Ho D D, Hohenberger M, Holder J P, Huang H, Izumi N, Jeet J, Jones O, Kerr S M, Khan S F, Geppert Kleinrath H, Geppert Kleinrath V, Kong C, Lamb K M, Le Pape S, Lemos N C, Lindl J D, MacGowan B J, Mackinnon A J, MacPhee A G, Marley E V, Meaney K, Millot M, Moore A S, Newman K, Di Nicola J M G, Nikroo A, Nora R, Patel P K, Rice N G, Rubery M S, Sater J, Schlossberg D J, Sepke S M, Sequoia K, Shin S J, Stadermann M, Stoupin S, Strozzi D J, Thomas C A, Tommasini R, Trosseille C, Tubman E R, Volegov P L, Weber C R, Wild C, Woods D T, Yang S T and Young C V 2022 *Phys. Rev. E* **106**(2) 025202 URL https://link.aps.org/doi/10.1103/PhysRevE.106.025202

[58] Pak A, Zylstra A B, Baker K L, Casey D T, Dewald E, Divol L, Hohenberger M, Moore A S, Ralph J E, Schlossberg D J, Tommasini R, Aybar N, Bachmann B, Bionta R M, Fittinghoff D, Gatu Johnson M, Geppert Kleinrath H, Geppert Kleinrath V, Hahn K D, Rubery M S, Landen O L, Moody J D, Aghaian L, Allen A, Baxamusa S H, Bhandarkar S D, Biener J, Birge N W, Braun T, Briggs T M, Choate C, Clark D S, Crippen J W, Danly C, Döppner T, Durocher M, Erickson M, Fehrenbach T, Freeman M, Havre M, Hayes

S, Hilsabeck T, Holder J P, Humbird K D, Hurricane O A, Izumi N, Kerr S M, Khan S F, Kim Y H, Kong C, Jeet J, Kozioziemski B, Kritcher A L, Lamb K M, Lemos N C, MacGowan B J, Mackinnon A J, MacPhee A G, Marley E V, Meaney K, Millot M, Di Nicola J M G, Nikroo A, Nora R, Ratledge M, Ross J S, Shin S J, Smalyuk V A, Stadermann M, Stoupin S, Suratwala T, Trosseille C, Van Wonterghem B, Weber C R, Wild C, Wilde C, Wooddy P T, Woodworth B N and Young C V 2024 *Phys. Rev. E* **109**(2) 025203 URL https://link.aps.org/doi/10.1103/PhysRevE.109.025203

[59] Slutz S A and Vesey R A 2012 *Physical Review Letters* **108** 025003 publisher: American Physical Society URL https://link.aps.org/doi/10.1103/PhysRevLett.108.025003

[60] Yager-Elorriaga D, Gomez M, Ruiz D, Slutz S, Harvey-Thompson A, Jennings C, Knapp P, Schmit P, Weis M, Awe T, Chandler G, Mangan M, Myers C, Fein J, Galloway B, Geissel M, Glinsky M, Hansen S, Harding E, Lamppa D, Lewis W, Rambo P, Robertson G, Savage M, Shipley G, Smith I, Schwarz J, Ampleford D, Beckwith K, Peterson K, Porter J, Rochau G and Sinars D 2022 *Nuclear Fusion* **62** 042015 publisher: IOP Publishing URL https://doi.org/10.1088/1741-4326/ac2dbe

[61] Weis M R, Ruiz D E, Gomez M R, Harvey-Thompson A J, Jennings C A, Yager-Elorriaga D A, Lewis W E, Slutz S A, Shulenburger L, Ampleford D J, Beckwith K and Koning J M 2025 *Physics of Plasmas* **32** 022708 ISSN 1070-664X URL https://doi.org/10.1063/5.0244304

[62] Alexander A, Benedetti L R, Bhattacharyya I, Bowen J, Cabatu J, Cacdac V, Chhavi C, Chen C, Chen K, Clark D, Clark J, Cope T, Dannemann W, Davidson S, DeHaan D, Dugan J, Eihusen M, Ellison C L, Esquivel C, Ethridge D, Ferguson B, Ferguson B, Fry J, Garcia-Rubio F, Goyal T, Grim G, Grodman J, Haid B, Howland F, Huynh V, John V, Knapp P, Kravitz I, Lander E S, Langendorf S, LeChien K, Link A, Meezan N, Miller D S, Nardelli N, Ogirri Q, Peng J H, Pinto A, Powser R, Puno F R, Quang K, Rahn B, Regan W, Reichenbach K, Reyes A, Richardson C, Rose D, Samaniego J, Schmit P F, Silva V, Simon N, Sitaraman S, Sullan H, Trebesch J, Truong M, Muench C V, Waltz C, Williams D, Wood E, Wu S and Zylstra A B 2025 *Physics of Plasmas* **32** 092703 ISSN 1070-664X URL https://doi.org/10.1063/5.0273277

[63] Ellison C L, Garcia V, Gomez M, Grim G P, Hammer J H, Jennings C A, Knapp P, LeChien K R, Meezan N, Peterson R, Reyes A, Steiner A, Stygar W A, Tzeferacos P, Welch D and Zylstra A 2025 *Physics of Plasmas* **32** 090601 ISSN 1070-664X URL https://doi.org/10.1063/5.0273577

[64] FLARE A bold strategy to unlock fusion power 2025 URL https://firstlightfusion.com/flare/

[65] Lee S, Damideh V and Btaiche J C 2023 *Vacuum* **216** 112471 ISSN 0042-207X URL https://www.sciencedirect.com/science/article/pii/S0042207X23006681

[66] Vold E L, Joglekar A S, Ortega M I, Moll R, Fenn D and Molvig K 2015 *Physics of Plasmas* **22** 112708 ISSN 1070-664X URL https://doi.org/10.1063/1.4935906

[67] Rinderknecht H, Amendt P, Rosenberg M, Li C, Frenje J, Gatu Johnson M, Sio H, Séguin F, Petrasso R, Zylstra A, Kagan G, Hoffman N, Svyatsky D, Wilks S, Glebov V Y, Stoeckl C and Sangster T 2017 *Nuclear Fusion* **57** 066014 URL https://doi.org/10.1088/1741-4326/aa69d9

[68] Walsh C, Chittenden J, McGlinchey K, Niasse N and Appelbe B 2017 *Physical Review Letters* **118** 155001 publisher: American Physical Society URL https://link.aps.org/doi/10.1103/PhysRevLett.118.155001

[69] Gibbon P, Beg F N, Clark E L, Evans R G and Zepf M 2004 *Physics of Plasmas* **11** 4032–4040 ISSN 1070-664X URL https://doi.org/10.1063/1.1767096

[70] Takizuka T and Abe H 1977 *Journal of Computational Physics* **25** 205–219 ISSN 0021-9991 URL https://www.sciencedirect.com/science/article/pii/0021999177900997

[71] Nanbu K 1997 *Phys. Rev. E* **55** 4642–4652 URL https://link.aps.org/doi/10.1103/PhysRevE.55.4642

[72] Chapman S 1939 *The Mathematical Theory Of Nonuniform Gases* (Cambridge At The University Press) URL http://archive.org/details/dli.ernet.206077

[73] Krommes J A 2019 *Journal of Plasma Physics* **85** ISSN 1469-7807 URL http://dx.doi.org/10.1017/S0022377818001319

[74] Beresnyak A 2023 2023 nrl plasma formulary Tech. rep. Naval Research Laboratory Washington, DC supported by the Office of Naval Research URL https://www.nrl.navy.mil/ppd/content/nrl-plasma-formulary

[75] Klimontovich I L, Massey H S H, Blunn O M and Haar D t 1967 *The statistical theory of non-equilibrium processes in a plasma* (M.I.T. Press)

[76] Callen J D 2018 Plasma Kinetic Theory published: Lecture notes

[77] Schekochihin A 2015 Kinetic theory: Lecture notes MMathPhys Kinetic Theory course lecture notes course materials for Oxford Kinetic Theory URL https://www-thphys.physics.ox.ac.uk/people/AlexanderSchekochihin/KT/2015/KTLectureNotes.pdf

[78] Helander P and Sigmar D 2005 *Collisional Transport in Magnetized Plasmas* Cambridge Monographs on Plasma Physics (Cambridge University Press) ISBN 978-0-521-02098-5 URL https://books.google.co.uk/books?id=nm-V01E0H2MC

[79] Landau L and CALIF G D S D 1958 *The Kinetic Equation in the Case of Coulomb Interaction* (Defense Technical Information Center) URL https://books.google.co.uk/books?id=HdPUNwAACAAJ

[80] Rosenbluth M N, MacDonald W M and Judd D L 1957 *Phys. Rev.* **107** 1–6 publisher: American Physical Society URL https://link.aps.org/doi/10.1103/PhysRev.107.1

[81] Chandrasekhar S 1943 *The Astrophysical Journal* **97** 255–262 URL https://ui.adsabs.harvard.edu/abs/1943ApJ....97..255C/abstract

[82] Nishimura S 2015 *Physics of Plasmas* **22** 122503 ISSN 1070-664X URL https://doi.org/10.1063/1.4936799

[83] Lyman F, Aeronautics U S N and Administration S 1965 *Expansion of the Fokker-Planck Equation in Spherical Harmonics* NASA technical note (National Aeronautics and Space Administration) URL https://books.google.co.uk/books?id=Ml4Lyq5NIpUC

[84] Zhdanov V M 2014 *Transport Processes in Multicomponent Plasma* (Boca Raton, FL : CRC Press) ISBN 978-1-4822-6510-1 978-0-415-27920-8 URL http://archive.org/details/transportprocess0000zhda

[85] Parra F I 2018 Collisional plasma physics: Lecture notes for an oxford mmathphys course Tech. rep. University of Oxford, Rudolf Peierls Centre for Theoretical Physics version as hosted online, accessed 2025-10-17 URL https://www-thphys.physics.ox.ac.uk/people/FelixParra/CollisionalPlasmaPhysics/CollisionalPlasmaPhysics.html

[86] Epperlein E M and Haines M G 1986 *The Physics of Fluids* **29** 1029–1041 ISSN 0031-9171 URL https://doi.org/10.1063/1.865901

[87] Ji J Y and Held E D 2013 *Physics of Plasmas* **20** 042114 ISSN 1070-664X URL https://doi.org/10.1063/1.4801022

[88] Ji J Y and Held E D 2015 *Physics of Plasmas* **22** 062114 ISSN 1070-664X URL https://doi.org/10.1063/1.4922755

[89] Stacey Jr W M and Sigmar D J 1985 *The Physics of Fluids* **28** 2800–2807 ISSN 0031-9171 URL https://doi.org/10.1063/1.865240

[90] Casey D T, Frenje J A, Gatu Johnson M, Manuel M J E, Rinderknecht H G, Sinenian N, Séguin F H, Li C K, Petrasso R D, Radha P B, Delettrez J A, Glebov V Y, Meyerhofer D D, Sangster T C, McNabb D P, Amendt P A, Boyd R N, Rygg J R, Herrmann H W, Kim Y H and Bacher A D 2012 *Phys. Rev. Lett.* **108**(7) 075002 URL https://link.aps.org/doi/10.1103/PhysRevLett.108.075002

[91] Rinderknecht H G, Sio H, Li C K, Zylstra A B, Rosenberg M J, Amendt P, Delettrez J, Bellei C, Frenje J A, Gatu Johnson M, Séguin F H, Petrasso R D, Betti R, Glebov V Y, Meyerhofer D D, Sangster T C, Stoeckl C, Landen O, Smalyuk V A, Wilks S, Greenwood A and Nikroo A 2014 *Phys. Rev. Lett.* **112**(13) 135001 URL https://link.aps.org/doi/10.1103/PhysRevLett.112.135001

[92] Rosenberg M J, Rinderknecht H G, Hoffman N M, Amendt P A, Atzeni S, Zylstra A B, Li C K, Séguin F H, Sio H, Johnson M G, Frenje J A, Petrasso R D, Glebov V Y, Stoeckl C, Seka W, Marshall F J, Delettrez J A, Sangster T C, Betti R, Goncharov V N, Meyerhofer D D, Skupsky S, Bellei C, Pino J, Wilks S C, Kagan G, Molvig K and Nikroo A 2014 *Phys. Rev. Lett.* **112**(18) 185001 URL https://link.aps.org/doi/10.1103/PhysRevLett.112.185001

[93] Amendt P, Landen O L, Robey H F, Li C K and Petrasso R D 2010 *Phys. Rev. Lett.* **105**(11) 115005 URL https://link.aps.org/doi/10.1103/PhysRevLett.105.115005

[94] Kagan G and Baalrud S D 2018 Transport formulas for multi-component plasmas within the effective potential theory framework (*Preprint* 1611.09872) URL https://arxiv.org/abs/1611.09872

[95] Kagan G and Tang X Z 2012 *Physics of Plasmas* **19** 082709 ISSN 1070-664X URL https://doi.org/10.1063/1.4745869

[96] LANDAU L D and LIFSHITZ E M 1987 CHAPTER VI - DIFFUSION *Fluid Mechanics (Second Edition)* ed LANDAU L D and LIFSHITZ E M (Pergamon) pp 227–237 second edition ed ISBN 978-0-08-033933-7 URL https://www.sciencedirect.com/science/article/pii/B9780080339337500143

[97] Sadler J D, Li H and Flippo K A 2020 *Philosophical Transactions of the Royal Society A: Mathematical, Physical and Engineering Sciences* **378** 20200045 ISSN 1364-503X URL https://doi.org/10.1098/rsta.2020.0045

[98] Sadler J D and Li H 2020 *Physics of Plasmas* **27** 122110 ISSN 1070-664X URL https://doi.org/10.1063/5.0027210

[99] Walsh C A and Clark D S 2021 *Physics of Plasmas* **28** 092705 ISSN 1070-664X URL https://doi.org/10.1063/5.0059366

[100] Morse R L and Nielson C W 1973 *The Physics of Fluids* **16** 909–920 ISSN 0031-9171 URL https://doi.org/10.1063/1.1694445

[101] Hoffman N M, Zimmerman G B, Molvig K, Rinderknecht H G, Rosenberg M J, Albright B J, Simakov A N, Sio H, Zylstra A B, Gatu Johnson M, Séguin F H, Frenje J A, Li C K, Petrasso R D, Higdon D M, Srinivasan G, Glebov V Y, Stoeckl C, Seka W and Sangster T C 2015 *Physics of Plasmas* **22** 052707 ISSN 1070-664X URL https://doi.org/10.1063/1.4921130

[102] Bell A R, Evans R G and Nicholas D J 1981 *Physical Review Letters* **46** 243–246 publisher: American Physical Society URL https://link.aps.org/doi/10.1103/PhysRevLett.46.243

[103] Matte J P and Virmont J 1982 *Physical Review Letters* **49** 1936–1939 publisher: American Physical Society URL https://link.aps.org/doi/10.1103/PhysRevLett.49.1936

[104] Luciani J F, Mora P and Bendib A 1985 *Phys. Rev. Lett.* **55** 2421–2424 URL https://link.aps.org/doi/10.1103/PhysRevLett.55.2421

[105] Sherlock M, Brodrick J P and Ridgers C P 2017 *Physics of Plasmas* **24** 082706 ISSN 1070-664X URL https://doi.org/10.1063/1.4986095

[106] Zhao H, Sheng Z and Weng S 2022 *Matter and Radiation at Extremes* **7** 045901 ISSN 2468-2047 URL https://doi.org/10.1063/5.0086783

[107] Brodrick J P, Del Sorbo D and Ridgers C P 2023 *Physics of Plasmas* **30** 054501 ISSN 1070-664X URL https://doi.org/10.1063/5.0134966

[108] Abramowitz M 2013 *Handbook of Mathematical Functions: With Formulas, Graphs, and Mathematical Tables* (New York, NY: Dover Publications Inc) ISBN 978-0-486-61272-0

[109] Swanekamp S B, Ottinger P F, Adamson P E, Giuliani J L, Petrova T B, Richardson A S and Rittersdorf I M 2019 *Physics of Plasmas* **26** 103506 ISSN 1070-664X URL https://doi.org/10.1063/1.5109430

[110] McDevitt C J, Tang X Z, Guo Z and Berk H L 2014 *Physics of Plasmas* **21** 032708 ISSN 1070-664X URL https://doi.org/10.1063/1.4868732

[111] Chang J S and Cooper G 1970 *Journal of Computational Physics* **6** 1–16 ISSN 0021-9991 URL https://www.sciencedirect.com/science/article/pii/002199917090001X

[112] Cao D, Moses G and Delettrez J 2015 *Physics of Plasmas* **22** 082308 ISSN 1070-664X URL https://doi.org/10.1063/1.4928445

[113] Brodrick J P, Sherlock M, Farmer W A, Joglekar A S, Barrois R, Wengraf J, Bissell J J, Kingham R J, Sorbo D D, Read M P and Ridgers C P 2018 *Plasma Physics and Controlled Fusion* **60** 084009 publisher: IOP Publishing URL https://doi.org/10.1088/1361-6587/aaca0b

[114] Kingham R J and Bell A R 2002 *Physical Review Letters* **88** 045004 URL https://link.aps.org/doi/10.1103/PhysRevLett.88.045004

[115] Ridgers C P, Arran C, Bissell J J and Kingham R J 2021 *Philosophical transactions. Series A, Mathematical, physical, and engineering sciences* **379** 20200017 ISSN 1364-503X URL https://pmc.ncbi.nlm.nih.gov/articles/PMC7741009/

[116] Sherlock M and Bissell J 2020 *Physical Review Letters* **124** 055001 URL https://link.aps.org/doi/10.1103/PhysRevLett.124.055001

[117] Bennaceur-Doumaz D and Bendib A 2006 *Physics of Plasmas* **13** 092308 ISSN 1070-664X URL https://doi.org/10.1063/1.2337789

[118] Watkins H C 2019 *Studies of Magnetised and Non-local Transport in Laser-plasma Interactions* PhD Thesis Imperial College London

[119] Spitzer Lyman J and Seeger R J 1963 *American Journal of Physics* **31** 890–891 ISSN 0002-9505 URL https://doi.org/10.1119/1.1969155

[120] Zhang W s, Cai H b, Du B, Kang D g, Zou S y and Zhu S p 2021 *Phys. Rev. E* **103** 023213 publisher: American Physical Society URL https://link.aps.org/doi/10.1103/PhysRevE.103.023213

[121] Luo M, Heaton C, Wang Y, Plummer D, Fitzgerald M, Miniati F, Vinko S M and Gregori G 2025 *Phys. Rev. Res.* **7** L042017 publisher: American Physical Society URL https://link.aps.org/doi/10.1103/m215-3f6c

[122] Hu S X, Collins L A, Boehly T R, Kress J D, Goncharov V N and Skupsky S 2014 *Phys. Rev. E* **89** 043105 publisher: American Physical Society URL https://link.aps.org/doi/10.1103/PhysRevE.89.043105

[123] Del Sorbo D, Feugeas J L, Nicolaï P, Olazabal-Loumé M, Dubroca B, Guisset S, Touati M and Tikhonchuk V 2015 *Physics of Plasmas* **22** 082706 ISSN 1070-664X URL https://doi.org/10.1063/1.4926824

[124] Zel'dovich Y B and Raizer Y P 1967 *Physics of shock waves and high-temperature hydrodynamic phenomena* (Academic Press)

[125] Koch R 2004 *Fusion Science and Technology* **45** 183–192 URL https://doi.org/10.13182/FST04-A482

[126] Hwang D Q, Hosea J, Thompson H, Wilson J R, Davis S, Herndon D, Kaita R, Mueller D, Suckewer S, Daughney C and Colestock P 1983 *Phys. Rev. Lett.* **51** 1865–1868 URL https://link.aps.org/doi/10.1103/PhysRevLett.51.1865

[127] Kagan G and Tang X Z 2014 *Physics Letters A* **378** 1531–1535 ISSN 0375-9601 URL https://www.sciencedirect.com/science/article/pii/S0375960114003521

[128] Lopez N A, Bott A F A and Schekochihin A A 2025 *Journal of Plasma Physics* **91** E45 ISSN 0022-3778, 1469-7807 publisher: Cambridge University Press URL https://www.cambridge.org/core/journals/journal-of-plasma-physics/article/collisional-whistler-instability-and-electron-temperature-staircase-in-inhomogeneous-p9DB8549243477939A59F88A003691A71

[129] Chittenden J P and Haines M G 1993 *Journal of Physics D: Applied Physics* **26** 1048 URL https://doi.org/10.1088/0022-3727/26/7/006

[130] Farrow G, Chittenden J P and Kagan G 2022 *Physics of Plasmas* **29** 032703 ISSN 1070-664X URL https://doi.org/10.1063/5.0082435

[131] Walsh C 2018 Extended magneto-hydrodynamic effects in indirect-drive inertial confinement fusion experiments URL http://hdl.handle.net/10044/1/66631

[132] Dearling A D 2024 *Transport in laser-produced plasmas* phd University of York URL https://etheses.whiterose.ac.uk/id/eprint/36197/

[133] Albright B J, Molvig K, Huang C K, Simakov A N, Dodd E S, Hoffman N M, Kagan G and Schmit P F 2013 *Physics of Plasmas* **20** 122705 ISSN 1070-664X URL https://doi.org/10.1063/1.4833639

[134] Johnson M G, Frenje J A, Casey D T, Li C K, Séguin F H, Petrasso R, Ashabranner R, Bionta R M, Bleuel D L, Bond E J, Caggiano J A, Carpenter A, Cerjan C J, Clancy T J, Doeppner T, Eckart M J, Edwards M J, Friedrich S, Glenzer S H, Haan S W, Hartouni E P, Hatarik R, Hatchett S P, Jones O S, Kyrala G, Le Pape S, Lerche R A, Landen O L, Ma T, MacKinnon A J, McKernan M A, Moran M J, Moses E, Munro D H, McNaney J, Park H S, Ralph J, Remington B, Rygg J R, Sepke S M, Smalyuk V, Spears B, Springer P T, Yeamans C B, Farrell M, Jasion D, Kilkenny J D, Nikroo A, Paguio R, Knauer J P, Yu Glebov V, Sangster T C, Betti R, Stoeckl C, Magoon J, Shoup M J I, Grim G P, Kline J, Morgan G L, Murphy T J, Leeper R J, Ruiz C L, Cooper G W and Nelson A J 2012 *Review of Scientific Instruments* **83** 10D308 ISSN 0034-6748 URL https://doi.org/10.1063/1.4728095

[135] Appelbe B D, Taitano W T, Crilly A J, Mannion O M, Forrest C J and Chittenden J P 2023 Primary Neutron Spectra in Ion Vlasov-Fokker-Planck Simulations arXiv:2305.02403 [physics] version: 1 URL http://arxiv.org/abs/2305.02403

[136] Crilly A, Appelbe B, Mannion O, Taitano W, Hartouni E, Moore A, Gatu-Johnson M and Chittenden J 2022 *Nuclear Fusion* **62** 126015 ISSN 0029-5515 URL https://dx.doi.org/10.1088/1741-4326/ac90d5

[137] Appelbe B and Chittenden J 2014 *High Energy Density Physics* **11** 30–35 ISSN 1574-1818 URL https://www.sciencedirect.com/science/article/pii/S1574181814000135

[138] Ridgers C P, Thomas A G R, Kingham R J and Robinson A P L 2008 *Physics of Plasmas* **15** 092311 ISSN 1070-664X URL https://doi.org/10.1063/1.2978092

[139] Krasheninnikov S I, Kukushkin A S and Pshenov A A 2016 *Physics of Plasmas* **23** 055602 ISSN 1070-664X URL https://doi.org/10.1063/1.4948273